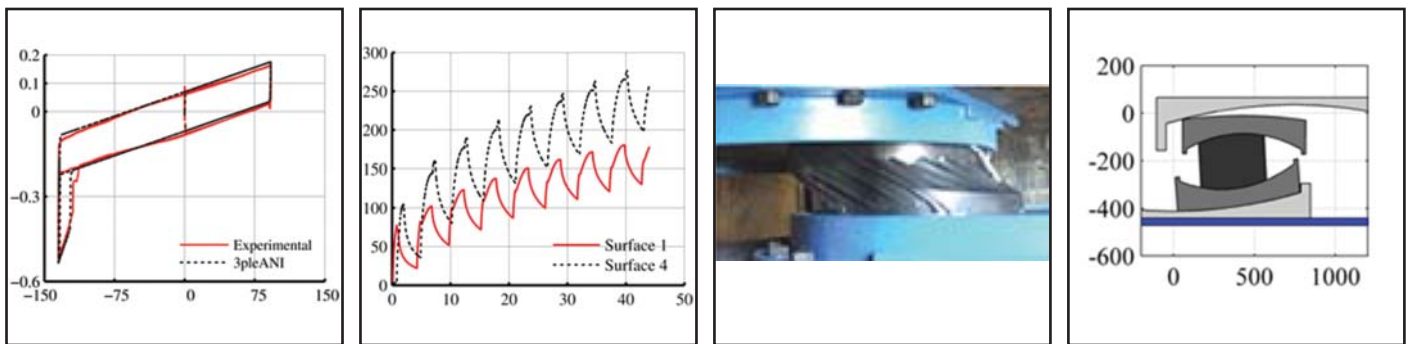


Model of Triple Friction Pendulum Bearing for General Geometric and Frictional Parameters and for Uplift Conditions

by
Apostolos A. Sarlis and Michael C. Constantinou



Technical Report MCEER-13-0010

July 1, 2013

NOTICE

This report was prepared by the University at Buffalo, State University of New York, as a result of research sponsored by MCEER. Neither MCEER, associates of MCEER, its sponsors, the University at Buffalo, State University of New York, nor any person acting on their behalf:

- a. makes any warranty, express or implied, with respect to the use of any information, apparatus, method, or process disclosed in this report or that such use may not infringe upon privately owned rights; or
- b. assumes any liabilities of whatsoever kind with respect to the use of, or the damage resulting from the use of, any information, apparatus, method, or process disclosed in this report.

Any opinions, findings, and conclusions or recommendations expressed in this publication are those of the author(s) and do not necessarily reflect the views of MCEER or other sponsors.

Model of Triple Friction Pendulum Bearing for General Geometric and Frictional Parameters and for Uplift Conditions

by

Apostolos A. Sarlis¹ and Michael Constantinou²

Publication Date: July 1, 2013

Submittal Date: June 27, 2013

Technical Report MCEER-13-0010

MCEER Thrust Area 3, Innovative Technologies

- 1 Ph.D. Candidate, Department of Civil, Structural and Environmental Engineering, University at Buffalo, State University of New York
- 2 Professor, Department of Civil, Structural and Environmental Engineering, University at Buffalo, State University of New York

MCEER

University at Buffalo, State University of New York

133A Ketter Hall, Buffalo, NY 14260

Phone: (716) 645-3391; Fax (716) 645-3399

E-mail: mceer@buffalo.edu; WWW Site: <http://mceer.buffalo.edu>

Preface

MCEER is a national center of excellence dedicated to the discovery and development of new knowledge, tools and technologies that equip communities to become more disaster resilient in the face of earthquakes and other extreme events. MCEER accomplishes this through a system of multidisciplinary, multi-hazard research, in tandem with complimentary education and outreach initiatives.

Headquartered at the University at Buffalo, The State University of New York, MCEER was originally established by the National Science Foundation in 1986, as the first National Center for Earthquake Engineering Research (NCEER). In 1998, it became known as the Multidisciplinary Center for Earthquake Engineering Research (MCEER), from which the current name, MCEER, evolved.

Comprising a consortium of researchers and industry partners from numerous disciplines and institutions throughout the United States, MCEER's mission has expanded from its original focus on earthquake engineering to one which addresses the technical and socio-economic impacts of a variety of hazards, both natural and man-made, on critical infrastructure, facilities, and society.

The Center derives support from several Federal agencies, including the National Science Foundation, Federal Highway Administration, National Institute of Standards and Technology, Department of Homeland Security/Federal Emergency Management Agency, and the State of New York, other state governments, academic institutions, foreign governments and private industry.

This report presents a revised model of the behavior of the Triple Friction Pendulum bearing in which no assumptions are made on the location of the resultant forces at each sliding surface and no constraints on the values of the coefficient of friction are required, provided that all sliding surfaces are in full contact. To accomplish this, the number of degrees of freedom describing the behavior of the bearing is increased to include the location of the resultant force at each sliding surface and equations of moment equilibrium are introduced to relate these degrees of freedom to forces. Moreover, the inertia effects of each of the moving parts of the bearing are accounted for in the derivation of the equations describing its behavior. The model explicitly calculates the motion of each of the components of friction pendulum bearings so that any dependence of the coefficient of friction on the sliding velocity can be explicitly accounted for and calculations of heat flux and temperature increase at each sliding surface can be made.

In a further extension of this model, the uplift behavior of the Triple Friction Pendulum bearing is modeled by explicitly modeling the dynamic response of its internal components and the effect of the rubber seal stiffness while satisfying the conditions of compatibility and equilibrium. Finally, an additional model is developed that can capture the Triple Friction Pendulum behavior when in compression and when in uplift. This model is useful in capturing more complicated phenomena such as flying, overturning, and point contact of the various parts of the isolator.

ABSTRACT

Current models that describe the behavior of the Triple Friction Pendulum bearing (Fenz and Constantinou, 2008a to 2008e; Morgan, 2007) are based on the assumption that the resultant force of the contact pressure acts at the center of each sliding surface. Accordingly, these models only rely on equilibrium in the horizontal direction to arrive at the equations describing its behavior. This is sufficient for most practical applications where certain constraints on the friction coefficient values apply. Moreover, none of the existing models is capable of describing the behavior of the bearing under uplift conditions.

This report presents a revised model of the behavior of the Triple Friction Pendulum bearing in which no assumptions are made on the location of the resultant forces at each sliding surface and no constraints on the values of the coefficient of friction are required, provided that all sliding surfaces are in full contact. To accomplish this, the number of degrees of freedom describing the behavior of the bearing is increased to include the location of the resultant force at each sliding surface and equations of moment equilibrium are introduced to relate these degrees of freedom to forces. Moreover, the inertia effects of each of the moving parts of the bearing are accounted for in the derivation of the equations describing its behavior.

The model explicitly calculates the motion of each of the components of friction pendulum bearings so that any dependence of the coefficient of friction on the sliding velocity can be explicitly accounted for and calculations of heat flux and temperature increase at each sliding surface can be made.

In a further extension of this model, the uplift behavior of the Triple Friction Pendulum bearing is modeled by explicitly modeling the dynamic response of its internal components and the effect of the rubber seal stiffness while satisfying the conditions of compatibility and equilibrium.

Finally, an additional model is developed that can capture the Triple Friction Pendulum behavior when in compression and when in uplift. This model is useful in capturing more complicated phenomena such as flying, overturning, and point contact of the various parts of the isolator.

ACKNOWLEDGEMENTS

Partial financial support for this project was provided by Earthquake Protection Systems, Inc., Vallejo, CA.

TABLE OF CONTENTS

SECTION	TITLE	PAGE
1	INTRODUCTION.....	1
2	SINGLE AND DOUBLE FRICTION PENDULUM BEARING BEHAVIOR.....	7
3	TRIPLE FRICTION PENDULUM BEHAVIOR WITH SURFACES IN FULL CONTACT.....	11
3.1	General Equations.....	11
3.2	TFP Bearing of Configuration A ($\mu_2 R_2/R_{eff2} < \mu_3 R_3/R_{eff3} < \mu_1 R_4/R_{eff4} < \mu_4 R_4/R_{eff4}$).....	16
3.2.1	Transition Point I.....	17
3.2.2	Transition Point II.....	18
3.2.3	Transition Point III.....	19
3.2.4	Transition Point IV.....	20
3.2.5	Transition Point V.....	21
3.2.6	Force-Displacement Relation.....	22
3.3	TFP Bearing of Configuration B ($\mu_1 R_1/R_{eff1} < \mu_4 R_4/R_{eff4} < \mu_2 R_2/R_{eff2} < \mu_3 R_3/R_{eff3}$).....	23
3.3.1	Transition Point I.....	24
3.3.2	Transition Point II.....	24
3.3.3	Transition Point III.....	25
3.3.4	Transition Point IV.....	26
3.3.5	Transition Point V.....	27
3.4	Examples of Force-displacement Relations of Triple FP Bearings.....	29
3.5	Additional Results on the Behavior of Triple FP Bearings Based on Considerations of Moment Equilibrium.....	31
4	MODELING TRIPLE FRICTION PENDULUM BEARINGS WITH SURFACES IN FULL CONTACT FOR RESPONSE HISTORY ANALYSIS.....	35
4.1	Introduction.....	35
4.2	Equations of Motion Including Inertia Effects.....	35

4.3	Triple Friction Pendulum Element for Analysis in Prescribed Motion (Displacement Controlled Test).....	44
4.4	Analysis for Non-Zero Top Concave Plate and Bottom Concave Plate Rotation.....	44
4.5	Verification of Triple Friction Pendulum Bearing Element	47
4.6	Comparison of Current Model to the Fenz and Constantinou Series Model.....	53
4.7	Effect of Initial Offsets on TFP Behavior.....	55
4.8	Effect of top concave plate and bottom concave plate rotation on TFP behavior.....	56
4.9	Heating effects on TFP behavior	60
4.10	Inertia Effects of Triple FP Bearing Internal Components.....	63
4.11	Comparison of Current Model to Becker and Mahin (2011) model.....	66
4.12	Comparison of Current Model to Experimental Results.....	67
5	TRIPLE FRICTION PENDULUM BEARING BEHAVIOR UNDER UPLIFT CONDITIONS AND FULL CONTACT.....	71
5.1	Introduction to Uplift.....	71
5.2	Definition of Uplift Displacement	74
5.3	Modeling of Triple FP Bearing during Uplift with Parts in Full Contact.....	75
5.4	Modeling of Landing	89
5.5	Additional Considerations for Uplift Analysis	91
5.5.1	Landing prior to end of uplift excitation.....	91
5.5.2	Collapse or instability of TFP isolators	92
5.6	Summary of Uplift Analysis	93
5.7	Verification Examples	95
6	MODEL FOR BEARING UPLIFT AND LANDING INCLUDING SLIDING, ROCKING, OVERTURNING, FLYING AND CONTACT OF BEARING COMPONENTS.....	101
6.1	Formulation of Equations of Motion	101
6.2	Model Verification and Demonstration of Analysis Capabilities.....	124
7	PROGRAM 3pleANI.....	131
8	EXAMPLES OF TRIPLE FP ANALYSIS WITH UPLIFT.....	133
8.1	Introduction.....	133
8.2	Example 1	134

8.3	Example 2	141
8.4	Example 3	146
8.5	Example 4	151
8.6	Example 5	160
8.7	Example 6	165
8.8	Example 7 (Imperial Units)	174
9	CONCLUSIONS	189
10	REFERENCES.....	191

APPENDICES

A	3pleANI Friction Pendulum Isolator Analysis and Animation Program: User's Guide and Reference Manual
B	3pleANI Friction Pendulum Isolator Analysis and Animation Program: Analysis and Verification Examples

LIST OF ILLUSTRATIONS

1-1: Schematic of Triple FP bearing and definition of parameters.....	2
1-2: Force-displacement relation of Triple FP	2
1-3: (a) Rigid block sliding on flat surface (b) Rigid block sliding on spherical surface.....	3
2-1: Deformed single friction pendulum isolator.....	8
2-2: Double Friction Pendulum bearing with rigid slider	9
3-1: Free body diagrams of components of a Triple Friction Pendulum bearing.....	13
3-2: Deformed bearing and definition of sliding angles	13
3-3: Force-displacement of Triple FP bearing of Configuration A with $R_1 = R_4, \mu_2 = \mu_3, R_2 = R_3, h_1 = h_4$ and based on the current theory	23
3-4: Force-displacement of Triple FP bearing of Configuration A with $R_1 = R_4, \mu_2 = \mu_3, R_2 = R_3, h_1 = h_4$ and based on the theory of Fenz and Constantinou	23
3-5: Force-displacement of Triple FP bearing of Configuration B with $R_1 = R_4, R_2 = R_3, \mu_1 < \mu_4 < \mu_2 = \mu_3, h_1 = h_4, d_2 = d_3, d_1 < d_4$ and based on the current theory	28
3-6: Force-displacement of Triple FP bearing of Configuration B with $R_1 = R_4, R_2 = R_3, \mu_1 = \mu_4 < \mu_2 = \mu_3, h_1 = h_4, d_2 = d_3, d_1 < d_4$ and based on the Fenz and Constantinou theory	28
3-7: Force-displacement relation of bearings of Table 3-2 as predicted by two theories.....	31
3-8: Triple FP bearing behavior when $S_2 < S_3$ and forces are assumed acting at center of each surface.....	32
3-9: Triple FP bearing behavior when $S_2 < S_3$ and forces are assumed acting at a location determined by moment equilibrium.....	33
3-10: Triple FP bearing (a) un-deformed and (b) at maximum displacement	34
4-1: Free body diagrams of components of a Triple Friction Pendulum bearing including inertia effects	37
4-2: TFP isolator with rotated top and bottom concave plates	45

4-3: Comparison of results obtained using algebraic equations of Section 3 and the hysteretic element of Section 4 for model scale bearing-A with $\mu_1 = 0.1, \mu_2 = \mu_3 = 0.05, \mu_4 = 0.15$	49
4-4: Comparison of results obtained using algebraic equations of Section 3 and the hysteretic element of Section 4 for model scale bearing-B with $\mu_1 = \mu_2 = \mu_3 = \mu_4 = 0.1$	50
4-5: Comparison of results obtained using algebraic equations of Section 3 and the hysteretic element of Section 4 for full scale bearing-A with $\mu_1 = 0.075, \mu_2 = 0.05, \mu_3 = 0.01, \mu_4 = 0.125$.	51
4-6: Comparison of results obtained using algebraic equations of Section 3 and the hysteretic element of Section 4 for full scale bearing-B with $\mu_1 = 0.075, \mu_2 = \mu_3 = 0.05, \mu_4 = 0.125$	52
4-7: Ground motion used for the analysis of SDOF system isolated with TFP	53
4-8: Comparison of results obtained by the series model in SAP2000 and the hysteretic model in MATLAB for the full scale bearing of Table 3-2, case A and $\mu_2 \neq \mu_3$	54
4-9: Comparison of results obtained by the series model in SAP2000 using $\mu_2 = \mu_3 = 0.03$ and the hysteretic model in MATLAB using $\mu_2 = 0.05, \mu_3 = 0.01$ for the full scale bearing of Table 3-2, case B and $\mu_2 = \mu_3 = 0.05$	54
4-10: Two cases of initial offsets of internal components	55
4-11: Effect of initial offsets of internal components on TFP behavior	56
4-12: Comparison of results for various values of rotation of the bottom concave plate	57
4-13: Comparison of results for various values of rotation of the top concave plate	58
4-14: Comparison of results for various values of rotation of the top and bottom concave plate (both plates have equal rotations)	59
4-15: Results of heating analysis of TFP isolator subjected to a four-cycle sinusoidal displacement history applied at the TCP with 0.09Hz frequency and 1040mm amplitude.....	61
4-16: Comparison of results in dynamic analysis of the structure of Section 4.6 for cases with heating effects and without heating effects on the friction coefficient.....	62
4-17: Comparison of results with and without inertia effects of bearing components for the full scale bearing of Table 3-2, case B with $\mu_2 = \mu_3 = 0.05$ and load of 1500kN	64
4-18: Comparison of results with and without inertia effects of bearing moving components for the full scale bearing of Table 3-2, case B with $\mu_2 = \mu_3 = 0.05$ and load of 300kN.....	65

4-19: Force-displacement loops produced by the current theory and the Becker and Mahin (2011) model.....	67
4-20: String-pot instrumentation of Triple FP bearing internal components.....	68
4-21: Comparison of numerical and experimental results for bearing A with $\mu_1 = \mu_2 = \mu_3 = \mu_4$ in motion of 0.02Hz frequency and 140mm amplitude.....	69
4-22: Comparison of numerical and experimental results for bearing A with $\mu_1 = \mu_2 = \mu_3 = \mu_4$ in motion of 0.02Hz frequency and 140mm amplitude-close view.....	70
5-1: Horizontal and uplift displacement histories of TFP isolator in three states during an earthquake event and theories to perform analysis.....	73
5-2: Definition of input displacements for uplift analysis.....	74
5-3: Slider assembly of a deformed Triple FP bearing.....	79
5-4: Slider assembly and inner seal forces on top and bottom slide plates.....	80
5-5: Slider assembly of an un-deformed Triple FP bearing that shows the existence of bulging of the seal.....	83
5-6: Schematics of rubber seal with initial bulge.....	83
5-7: Comparison of seal force-deformation relation based on Equations (5-15) (Linear elastic) and (5-16) (Nonlinear elastic).....	84
5-8: Seal parameter definitions.....	85
5-9: View of TFP under uplift conditions and contact between the TCP and TSP.....	89
5-10: Vertical contact forces acting on the TSP.....	89
5-11: TFP isolator at the end of uplift event and after landing event.....	90
5-12: TFP undergoing landing prior to the end of uplift excitation.....	92
5-13: View of deformed TFP isolator when collapse is imminent.....	93
5-14: Flow diagram of uplift analysis of TFP isolator.....	94
5-15: Simple verification example with sliding allowed only on surface 1.....	96
5-16: Comparison of results obtained by the model of Section 5 and closed form solution for the verification example of sliding on surface 1 subject to initial conditions.....	98
5-17: Simple verification example with sliding allowed only on surface 2.....	98
5-18: Comparison of results obtained by the model of Section 5 and closed form solution for the verification example of sliding on surface 2 subject to initial conditions.....	99

5-19: Simple verification example with sliding allowed only on surface 3	100
5-20: Comparison of results obtained by the model of Section 5 and closed form solution for the verification example of sliding on surface 3 subject to initial velocity	100
6-1: Definition of contact and sliding surfaces.....	102
6-2: Definition of contact points and corresponding sliding points.....	103
6-3: Free body diagram and kinematics of BSP	106
6-4: Free body diagram and kinematics of RS.....	107
6-5: Free body diagram of TSP.....	108
6-6: Free body diagram of TCP	109
6-7: Notation for position vectors of restrainers	118
6-8: Notation of position vectors of rubber seal	120
6-9: Friction force during uplift and contact between TCP and TSP	121
6-10: Comparison of results obtained by model of Section 4 and model of Section 6 for the full scale isolator-configuration B of Table 3-2 subjected to TCP motion of 1000mm amplitude, 0.15Hz frequency and load of 6675kN.....	125
6-11: Comparison of results obtained by model of Section 4 and model of Section 6 for the full scale isolator-configuration B of Table 3-2 subjected to TCP motion of 1000mm amplitude, 1Hz frequency and load of 1335kN.....	126
6-12: Comparison of results obtained by model of Section 4 and model of Section 6 for the full scale isolator-configuration B of Table 3-2 with $\mu_1 = \mu_4 = 0.065, \mu_2 = \mu_3 = 0.045$ and subjected to TCP motion of 1000mm amplitude, 0.15Hz frequency and load of 6675kN.....	127
6-13: Force-displacement loops and snapshots of TFP isolator subjected to displacement amplitude larger than the displacement capacity	128
6-14: Comparison of force-displacement loops of TFP isolator with rotation of the TCP.....	129
6-15: Comparison of force-displacement loops of TFP isolator with rotational spring connected to the TCP	130
8-1: Analyzed Triple FP bearing.....	134
8-2: Horizontal (top) and vertical motion (bottom) of top node of one bearing of isolated structure calculated in program ETABS (Sarkisian et al., 2012).....	136

8-3: Program 3pleANI results of analysis of bearing of example 1 with uplift using full contact theory and without rubber seal.....	137
8-4: Animation of the bearing motion during the uplift duration by program 3pleANI for example 1 using full contact theory and without rubber seal	138
8-5: Program 3pleANI results of analysis of bearing of example 1 with uplift using advanced theory and without rubber seal.....	139
8-6: Animation of the bearing motion during the uplift duration by program 3pleANI for example 1 using advanced theory and without rubber seal	140
8-7: Seal force-deformation relationship for example 2	141
8-8: Program 3pleANI results of analysis of bearing of example 2 with uplift using full contact theory and linear elastic rubber seal.....	142
8-9: Animation of the bearing motion during the uplift duration by program 3pleANI for example 2 using full contact theory and linear elastic rubber seal	143
8-10: Program 3pleANI results of analysis of bearing of example 2 with uplift using advanced theory and linear elastic rubber seal.....	144
8-11: Animation of the bearing motion during the uplift duration by program 3pleANI for example 2 using advanced theory and linear elastic rubber seal	145
8-12: Comparison of seal force-deformation relations used in examples 2 and 3.....	146
8-13: Program 3pleANI results of analysis of bearing of example 3 with uplift using full contact theory and nonlinear elastic rubber seal.....	147
8-14: Animation of the bearing motion during the uplift duration by program 3pleANI for example 3 using full contact theory and nonlinear elastic rubber seal	148
8-15: Program 3pleANI results of analysis of bearing of example 3 with uplift using advanced theory and nonlinear elastic rubber seal.....	149
8-16: Animation of the bearing motion during the uplift duration by program 3pleANI for example 3 using advanced theory and nonlinear elastic rubber seal	150
8-17: Horizontal and vertical displacement histories in uplift test of San Bernardino Courthouse bearing.....	151
8-18: Captured frames in uplift experiment at 900mm horizontal displacement and 100mm uplift displacement (read row by row)	152
8-19: Seal force-deformation relations in analysis of example 4	154

8-20: Comparison of results on final position of parts following separation of TCP from TSP of tested isolator as obtained by 3pleANI and experimental	155
8-21: Comparison of results on position of parts of tested isolator after landing as obtained by 3pleANI and experimental.....	157
8-22: Comparison of analytical results obtained by 3pleANI for analyses 1, 3 and 5 in Table 8-3	158
8-23: Comparison of analytical results obtained by 3pleANI for analyses 2, 4 and 6 in Table 8-3	159
8-24: Animation of the bearing motion during the uplift episode as calculated in 3pleANI for analysis case 6.....	160
8-25: Horizontal and vertical displacement of TCP in example 5.....	161
8-26: Captured frames from uplift experiment of example 5 (read row by row)	162
8-27: Animation obtained by 3pleANI for example 5 during the uplift episode.....	163
8-28: Comparison of analytical and experimental results in example 5 when motion of the inner TFP parts stopped and when the bearing was reloaded	163
8-29: Histories of calculated displacements and rotations of parts, traces of displacements and force-displacement loop of analyzed bearing in example 5.....	164
8-30: Horizontal and vertical displacement of TCP in example 6.....	165
8-31: Captured frames in the uplift experiment of example 6 during the uplift episode (read row by row).....	167
8-32: Captured frames in the uplift experiment of example 6 during the l episode (read row by row).....	168
8-33: Illustrations of observed behavior of tested isolator during uplift	169
8-34: Animation of motion in case 1 obtained by 3pleANI for example 6 during uplift episode	170
8-35: Animation of motion in case 2 obtained by 3pleANI for example 6 during uplift episode	171
8-36: Animation of motion in case 3 (surface 3 restrainer deactivated) obtained by 3pleANI for example 6 during the uplift portion when the TCP moves upward	172
8-37: Animation of motion in case 3(surface 3 restrainer deactivated) obtained by 3pleANI for example 6 during the uplift portion when the TCP reverses direction of motion.....	173

8-38: Animation of motion in case 3 (surface 3 restrainer deactivated) obtained by 3pleANI for example 6 during the uplift portion when the TCP lands	174
8-39: Analyzed slender 16-story isolated structure of example 7.....	175
8-40: Force -displacement relation of isolator in example 7	176
8-41: Ground motion used for response history analysis in example 7	176
8-42: Displacement histories of isolators as calculated in SAP2000.....	178
8-43: 3pleANI animation of TFP-1 isolator based on full contact theory	179
8-44: Program 3pleANI results of analysis for bearing TFP-1 using full contact theory.....	180
8-45: 3pleANI animation of TFP-1 isolator without seal using advanced theory	181
8-46: Program 3pleANI results of analysis for bearing TFP-1 using advanced theory.....	182
8-47: 3pleANI animation of TFP-3 isolator based on full contact theory-isolator instability....	183
8-48: Program 3pleANI results of analysis for bearing TFP-3 using full contact theory-isolator instability.....	184
8-49: 3pleANI animation of TFP-3 modified isolator (increased restrainer height) based on full contact theory.....	185
8-50: Program 3pleANI results of analysis for modified bearing TFP-3 (increased restrainer height) using full contact theory	186
8-51: 3pleANI animation of TFP-3 modified isolator (increased restrainer height) based on full contact theory.....	187
8-52: Program 3pleANI results of analysis for modified bearing TFP-3 (increased restrainer height) using advanced theory	188

LIST OF TABLES

3-1: Triple FP configurations analyzed in this report	16
3-2: Analyzed Triple FP bearings	30
4-1: Sets of properties used to investigate the validity of the Becker and Mahin (2011) model..	66
8-1: Geometric and frictional properties of analyzed bearing	135
8-2: Friction coefficient values for load of 6675kN in example 4.....	153
8-3: Parameters used in uplift analysis of example 4	154
8-4: Theory and parameters used in analysis of example 6 in 3pleANI.....	166
8-5: Properties of TFP isolator in example 7	175

SECTION 1

INTROCUITION

The behavior of the Triple Friction Pendulum (FP) isolator has been previously described by Fenz and Constantinou (2008a to 2008e) and Morgan (2007). The Triple FP isolator exhibits multiple changes in stiffness and strength with increasing amplitude of displacement. The construction of the force-displacement loop is complex as it may contain several transition points which depend on the geometric and frictional properties. Figure 1-1 shows the geometry of a Triple FP bearing and its parameters. Its behavior is characterized by radii R_1 , R_2 , R_3 and R_4 (typically $R_1=R_4$ and $R_2=R_3$), heights h_1 , h_2 , h_3 and h_4 (typically $h_1=h_4$ and $h_2=h_3$), distances (related to displacement capacities) d_1 , d_2 , d_3 and d_4 (typically $d_2=d_3$ and $d_1=d_4$) and friction coefficients μ_1 , μ_2 , μ_3 and μ_4 (typically $\mu_2 = \mu_3 < \mu_1 \leq \mu_4$). The force displacement relation of a Triple FP bearing subject to the conditions $\mu_2 = \mu_3 < \mu_1 \leq \mu_4$ is shown in Figure 1-2 (Fenz and Constantinou, 2008a to 2008e). The Triple FP bearing exhibits five regimes of operation. Regime I starts at point I when sliding initiates simultaneously on surfaces 2 and 3 and terminates at point II when sliding stops on surface 2 and initiates on surface 1. Between points II and III (Regime II), sliding occurs only on surfaces 1 and 3. At point III, sliding stops on surface 3 and initiates on 4. Between points III and IV, sliding occurs on surfaces 1 and 4. At point IV, the displacement capacity of surface 1 is consumed and sliding starts on surface 2. Between points IV and V, sliding occurs on surfaces 2 and 4 until the displacement capacity of surface 4 is consumed. After point V, sliding continues on surfaces 2 and 3 until the displacement capacities of surfaces 2 and 3 are consumed.

The behavior shown in Figure 1-2 is derived on the assumption that the resultants of tractions at each sliding surface act at the center of each sliding surface so that only horizontal equilibrium is needed for the derivation of the force-displacement relation. In reality, when a lateral force is applied at the top of the bearing, the resultants of surface tractions develop at points away from the center so that equilibrium of moments is satisfied. In effect, this requires that a force larger than the friction force at the sliding surface is needed for sliding to initiate.

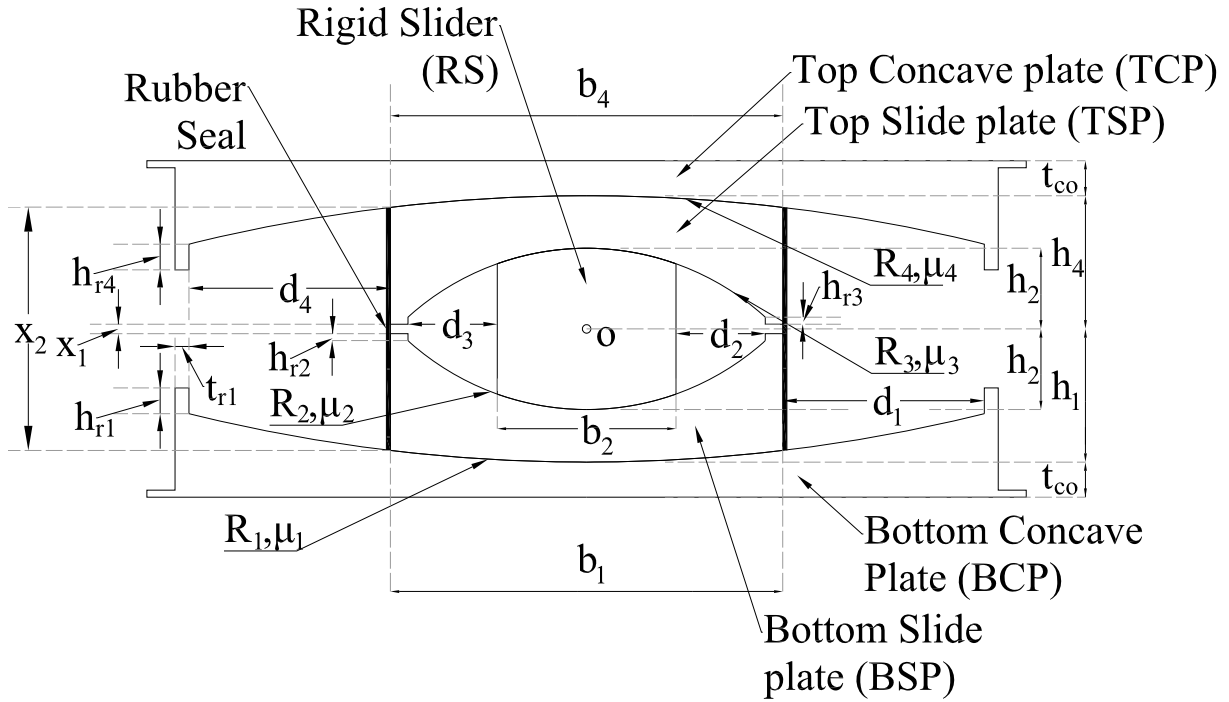


Figure 1-1: Schematic of Triple FP bearing and definition of parameters

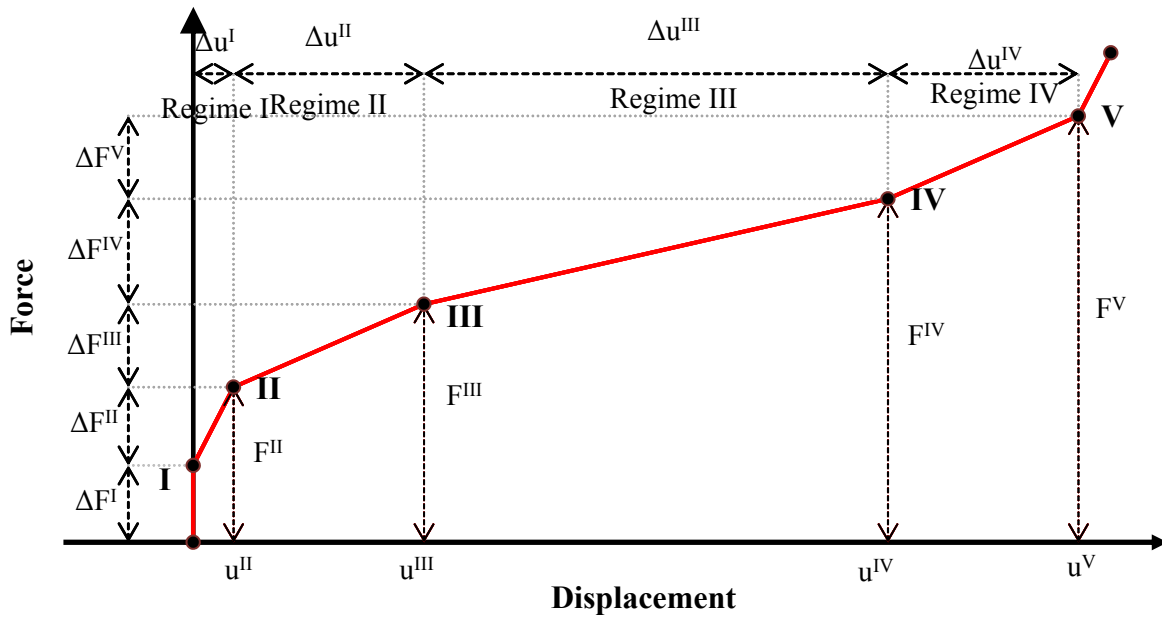


Figure 1-2: Force-displacement relation of Triple FP

In order to better explain this phenomenon and demonstrate the effect of moment equilibrium on the behavior of the Triple FP bearing, consider the simple examples shown in Figure 1-3. Figure 1-3 (a) shows a rigid block on a flat surface under a vertical load W . Consider a lateral force F

acting at the top of the block. Moment equilibrium requires that the contact forces at the sliding surface apply at a distance r from the center of the sliding block. Sliding will initiate when the friction force $S = \mu W$ is equal to the applied force so that $F = S = \mu W$, where μ is the coefficient of friction. In this case, the force needed for sliding to initiate is independent of the location of the contact forces. Consider now the case of Figure 1-3(b) where the block rests on a spherical surface. Moment equilibrium requires that the normal force is inclined at an angle θ_s . Therefore, a force F equal to $\mu W + W\theta_s$ is now needed for sliding to initiate. Accounting for equilibrium of moments, the lateral force at initiation of motion is:

$$F = \mu \frac{R}{R-h} W \quad (1-1)$$

Force F required to initiate motion in Equation (1-1) is larger than the friction force μW . Note that the values of the coefficient of friction in the model of Fenz and Constantinou (2008a to 2008e) are determined from experiments of Triple FP bearings so that the values already contain the spherical surface effect.

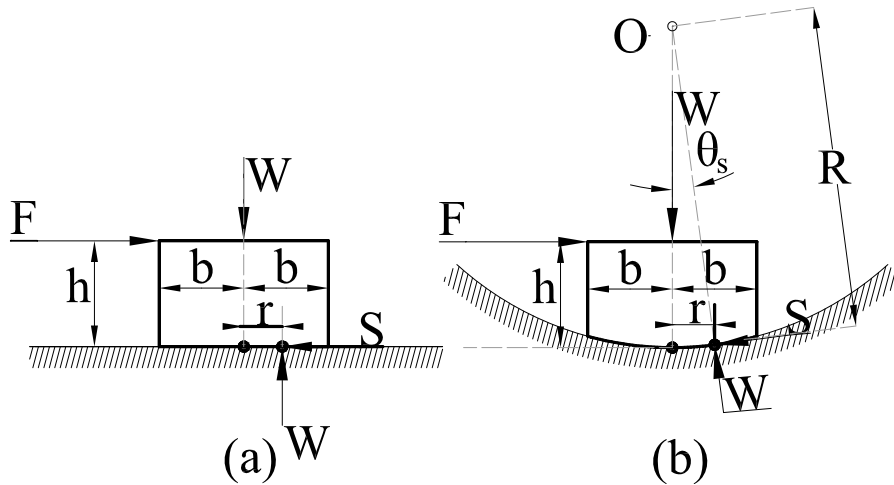


Figure 1-3: (a) Rigid block sliding on flat surface (b) Rigid block sliding on spherical surface

Note that in the free body diagrams of Figure 1-3, the normal force at the sliding surface is shown equal to the vertical load W . This is not exact for the spherical surface where the normal component of the force actually equals $W / \cos \theta_s + S \tan \theta_s$. To arrive at this expression, it is necessary to consider equilibrium of forces in the vertical direction in addition to the equilibrium equations of forces in the horizontal direction and of moments. However, in the limit of small

values of angle θ_s , for which the theory of Fenz and Constantinou (2008a to 2008e) and the theory presented herein are based, the normal force is equal to load W within a first order approximation.

The inclusion of moment equilibrium leads to various new features that will be shown throughout this report: (a) there are no restrictions on the geometry and properties of any of the sliding surfaces, (b) the sliding displacement and velocities can be explicitly calculated at each surface, (c) variations of the friction coefficients due to temperature and velocity can be correctly captured and (d) concave plate rotations and misalignments can be accounted for. Also as a direct consequence of (b) above, the Triple FP model can be extended to capture uplift behavior since uplift modeling requires the surface sliding displacements and velocities as initial conditions.

This report contains the following:

- In Section 2, the mechanics of the single and double friction pendulum bearings with consideration of moment equilibrium are discussed.
- In Section 3, the equations for the mechanics of the Triple Friction Pendulum (TFP) bearings with consideration of moment equilibrium are given. These equations are valid for any random geometry. Algebraic solutions for simple cases are presented.
- In Section 4, a model for use in dynamic analysis of the TFP isolator is presented. This model has no restriction on properties and can be used to conduct complex analysis that includes rotations of the top and bottom concave plate, temperature calculations and variation of friction coefficient values due to temperature at the sliding interfaces and velocity.
- In Section 5, a model that can capture the TFP behavior under uplift conditions is described. The combination of the uplift model, with the model presented in Section 4, can be used to model the TFP under any state.
- In Section 6, an additional theory is presented that can capture the TFP behavior under any state (compression and uplift) and can model complex phenomena that may occur during the isolator's response, such as flying, overturning, full and point contact of the TFP parts.

- In Section 7, program 3pleANI, which can be used to conduct dynamic response history analysis of buildings and bridges while accounting for the features of the new theory of the TFP, is described. Program 3pleANI can also be used to conduct uplift analysis of TFP under specified conditions of motion. A feature of the program is that it can generate animation of motion of parts of the TFP.
- In Section 8, examples of uplift analysis using program 3pleANI are provided.
- Appendices contain the user's and verification manuals of 3pleANI.

SECTION 2
SINGLE AND DOUBLE FRICTION PENDULUM
BEARING BEHAVIOR

The Single and Double Friction Pendulum bearings are treated first as simpler cases of the Triple Friction Pendulum bearing. Consider the Single FP bearing deformed as shown in Figure 2-1. Note that the angles are shown large in the figure for clarity but they are presumed to be small so that the normal force at each sliding surface is equal to load W within the first order of approximation. The top concave plate is considered horizontal. Angle θ is the “sliding angle” defined, for small values, as $\theta = u/(R + h)$ where u is the bearing top displacement. Angle θ_s is the angle formed by the lines connecting the center of curvature of the top concave plate and (a) the point of application of the resultant force at the top surface of the slider (point A) and (b) the center of the slider (point B). Angle θ_r is the angle formed by (a) the vertical axis and (b) the axis connecting the center of curvature of the bottom surface of the slider and the point of application of the resultant force at the bottom surface of the slider (point C).

The coefficient of friction for sliding on the top concave plate is μ and the coefficient of friction for sliding on the bottom of the articulated slider is μ_r . The corresponding friction forces are:

$$\begin{aligned} S_r &= \mu_r W \\ S &= \mu W \end{aligned} \tag{2-1}$$

The forces shown in Figure 2-1 act at the surfaces of the articulated slider (highlighted in the figure). The equations of equilibrium considered are for the articulated slider for forces in the horizontal direction and for moments about point C, and the equation of equilibrium of forces in the horizontal direction of the top concave plate. Note that equilibrium in the vertical direction is already satisfied for small values of the angles since the normal components of force have been considered equal to load W . Moment equilibrium of the articulated slider about point C, force equilibrium of the articulated slider in the horizontal direction and force equilibrium of the top concave plate in the horizontal direction give the three equations below:

$$\begin{aligned}
\theta_s h' + \mu h' - \theta_s R - R_r \theta_r &= 0 \\
\theta_s + \mu &= \theta_r + \mu_r \\
W(\theta + \theta_s) + \mu W &= F
\end{aligned}
\tag{2-2}$$

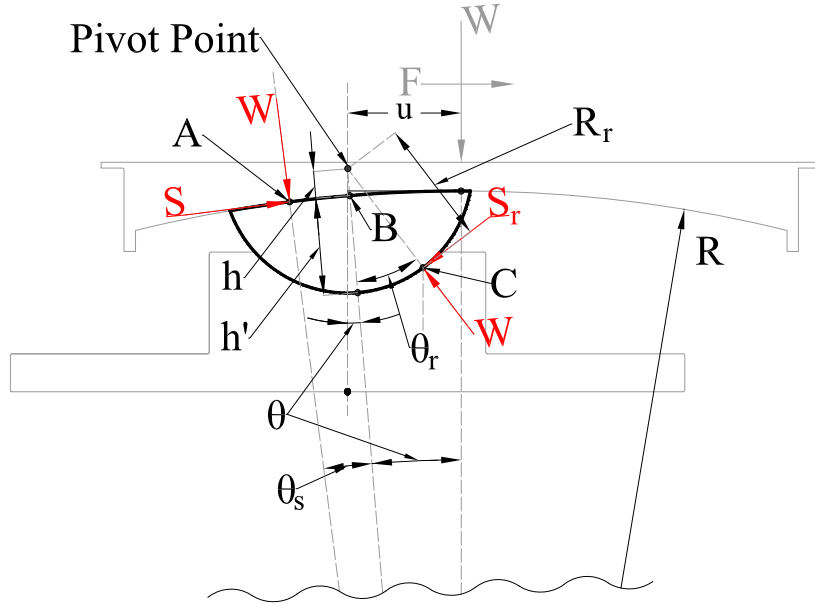


Figure 2-1: Deformed single friction pendulum isolator

Solution of the equations above yield the following expressions for angle θ_s , which defines the location of the point of application of the resultant force, and the force displacement relation:

$$\begin{aligned}
\theta_s &= \frac{\mu_r R_r - \mu h}{R + h} \\
F &= \frac{\mu R + \mu_r R_r}{R + h} W + \frac{W}{R + h} u
\end{aligned}
\tag{2-3}$$

Note that the effective friction coefficient is $(\mu R + \mu_r R_r)/(R + h)$ and not μ , which is the coefficient of friction for a flat sliding surface as predicted when assuming that the resultant forces act at the center of each sliding surface. Also note that the “effective radius” in Equation (2-3), $R_{eff} = R + h$ is also equal to $R_{eff} = R + R_r - h'$. This observation will later be used to demonstrate that the single and double FP bearings have behavior described by exactly the same equations.

Consider now the Double Friction Pendulum bearing with a rigid slider as shown in Figure 2-2. Again, the angles are considered small so that the normal components of force are equal to load W .

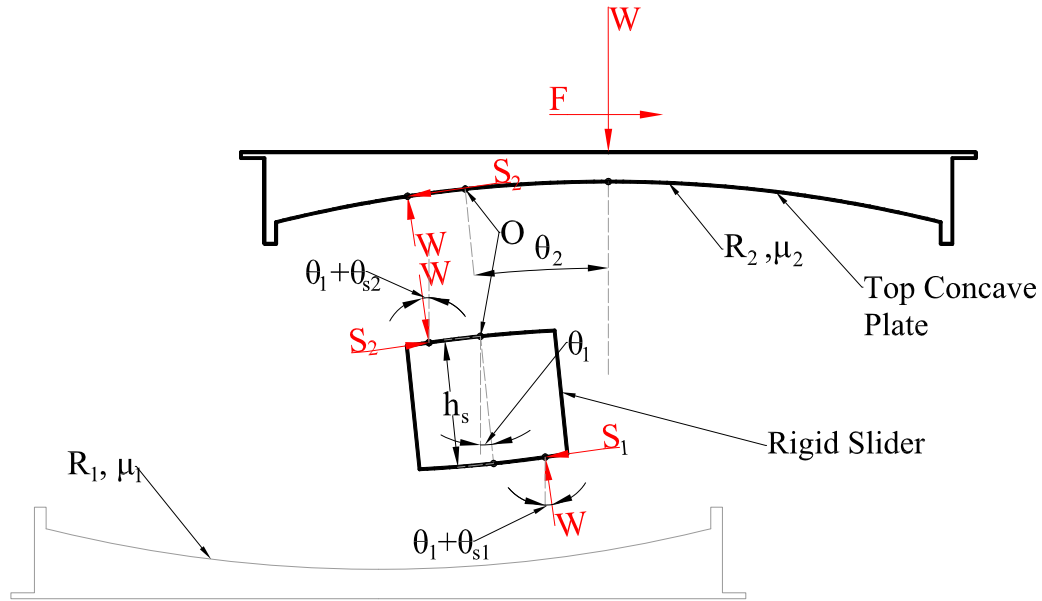


Figure 2-2: Double Friction Pendulum bearing with rigid slider

Equilibrium of force in the horizontal direction and equilibrium of moments for the rigid slider, and equilibrium of forces in the horizontal direction of the top concave plate result in the following:

$$\begin{aligned}
 W\theta_{s2} + S_2 &= S_1 + W\theta_{s1} \\
 0 &= W(\theta_{s2}R_2 + \theta_{s1}R_1) - W\theta_{s1}h_s - S_1h_s \\
 W(\theta_1 + \theta_{s2}) + S_2 &= F
 \end{aligned}
 \tag{2-4}$$

Note that the equations above do not require that the top plate is horizontal. When this constraint is imposed so that $\theta_1 = \theta_2$, the result is:

$$\begin{aligned}
 \theta_{s1} &= \frac{-\mu_1 h_s + R_2(\mu_1 - \mu_2)}{R_1 + R_2 - h_s} \\
 \theta_{s2} &= \frac{\mu_1 R_1 + \mu_2 h_s - \mu_2 R_1}{R_1 + R_2 - h_s}
 \end{aligned}
 \tag{2-5}$$

Considering that the total displacement of the top concave plate is given by $u = (R_1 - h_s)\theta_1 + R_2\theta_2$ and substituting Equations (2-5) into Equations (2-4), the force-displacement relation of the bearing is determined to be:

$$F = \frac{\mu_1 R_1 + \mu_2 R_2}{R_1 + R_2 - h_s} W + \frac{W}{R_1 + R_2 - h_s} u \quad (2-6)$$

Note that the above equation is valid during sliding on both concave surfaces and that the complete description of the behavior requires additional considerations (see Fenz and Constantinou, 2008a for details when moment equilibrium is ignored).

Equation (2-6) demonstrates that the effective friction coefficient is given by $(\mu_1 R_1 + \mu_2 R_2)/(R_1 + R_2 - h_s)$ whereas the theory that ignores moment equilibrium predicts that the effective friction is given by $[\mu_1(R_1 - h_s/2) + \mu_2(R_2 - h_s/2)]/(R_1 + R_2 - h_s)$ (Fenz and Constantinou, 2008a). The difference between the two theories is best illustrated for the common case of $\mu_1 = \mu_2 = \mu$ where the Fenz and Constantinou theory predicts the effective friction coefficient to be equal to μ , whereas the current theory predicts the coefficient to be $[\mu(R_1 + R_2)]/(R_1 + R_2 - h_s)$, which is larger than μ .

Also, note that Equation (2-6) predicts that the effective radius of the bearing is $R_{eff} = R_1 + R_2 - h_s$, which demonstrates that the behavior of the Double FP bearing is identical to that of the Single FP as previously discussed.

SECTION 3

TRIPLE FRICTION PENDULUM BEHAVIOR WITH SURFACES IN FULL CONTACT

3.1 General Equations

Triple Friction Pendulum bearings typically have their geometric and frictional properties satisfy the conditions: $R_1 = R_4, R_2 = R_3, \mu_2 = \mu_3, h_1 = h_4, d_1 = d_4, d_2 = d_3$. The theory presented herein is not restricted by any of these conditions although at some point, conditions will be imposed to develop the rules for constructing hysteresis loops using algebraic equations for two different configurations. The construction of hysteresis rules for random properties using the algebraic equations is beyond the scope of this report and can be constructed by the reader following the procedures presented in this section. Moreover, the theory is restricted by the condition that all sliding surfaces are in full contact and that rotations are small (also $\mu_i \theta_i \approx 0$). The behavior of the bearing under uplift conditions is described later in this report. Moreover, an additional theory free of any restriction is presented in Section 6.

Figure 3-1 shows free body diagrams of individual components of a Triple FP bearing and Figure 3-2 shows a deformed Triple FP bearing with the sliding angles defined. Note that the free body diagrams shown are identical to those of Fenz and Constantinou (2008a) but with the resultant force at each sliding surface acting at a point different than the center; the location being identified by the value of an offset angle. Specifically, the offset angle of surface i, θ_{si} , is formed by (a) the line extending between the point of application of the resultant force and the center of curvature of sliding surface i and (b) the line extending between the center of contact surface i (defined as the one of least diameter among the two in contact) and the center of curvature of sliding surface i (defined as the one of larger diameter among the two in contact). Note that in the Fenz and Constantinou (2008a) model, this angle is zero. Sliding on any of the surfaces is described by angle θ_i which is formed by (a) the line extending between the center of the contact surface and the center of curvature of the sliding surface and (b) the line extending between the center of the sliding surface and the center of curvature of the sliding surface. The definition of the sliding angles is identical to the Fenz and Constantinou (2008a) model.

The effective radius for each concave surface is defined as (see notation in Figure 1-1):

$$R_{effi} = R_i - h_i, \quad i = 1, 2, 3, 4 \quad (3-1)$$

The total displacement of the isolator, u , can be calculated from the geometry of Figure 3-2 as:

$$u = (R_1 - h_1 - h_4)\theta_1 + (R_2 - h_2 - h_4)\theta_2 + (R_3 + h_4 - h_3)\theta_3 + R_4\theta_4 \quad (3-2)$$

Equilibrium is now considered as described below and subject to the condition that angles are small. When the effect of the weight of the individual components of the TFP is ignored, equilibrium in the vertical direction for the forces shown in Figure 3-1 results in:

$$W_1 = W_2 = W_3 = W_4 = W \quad (3-3)$$

The effect of the weight of the TFP components will be considered later when an element for use in response history analysis will be developed. An additional outcome of the small angle approximation is that the vertical distance between the points of application of the resultant friction forces of surfaces 1 and 2 is equal to $h_1 - h_2$, for surfaces 2 and 3 it is $h_2 + h_3$ and for surfaces 3 and 4 is $h_4 - h_3$.

Also, horizontal restrainer forces, F_{ri} , develop when contact occurs at restrainers of each surface. These forces are not shown in the free body diagrams of Figure 3-1 for clarity. The restrainer forces are zero if $|\theta_i| < d_i/R_i$ and become nonzero when $|\theta_i| = d_i/R_i$ (see notation in Figure 1-1). Their exact value is determined by the solution of the equilibrium equations if contact is made with the restrainers.

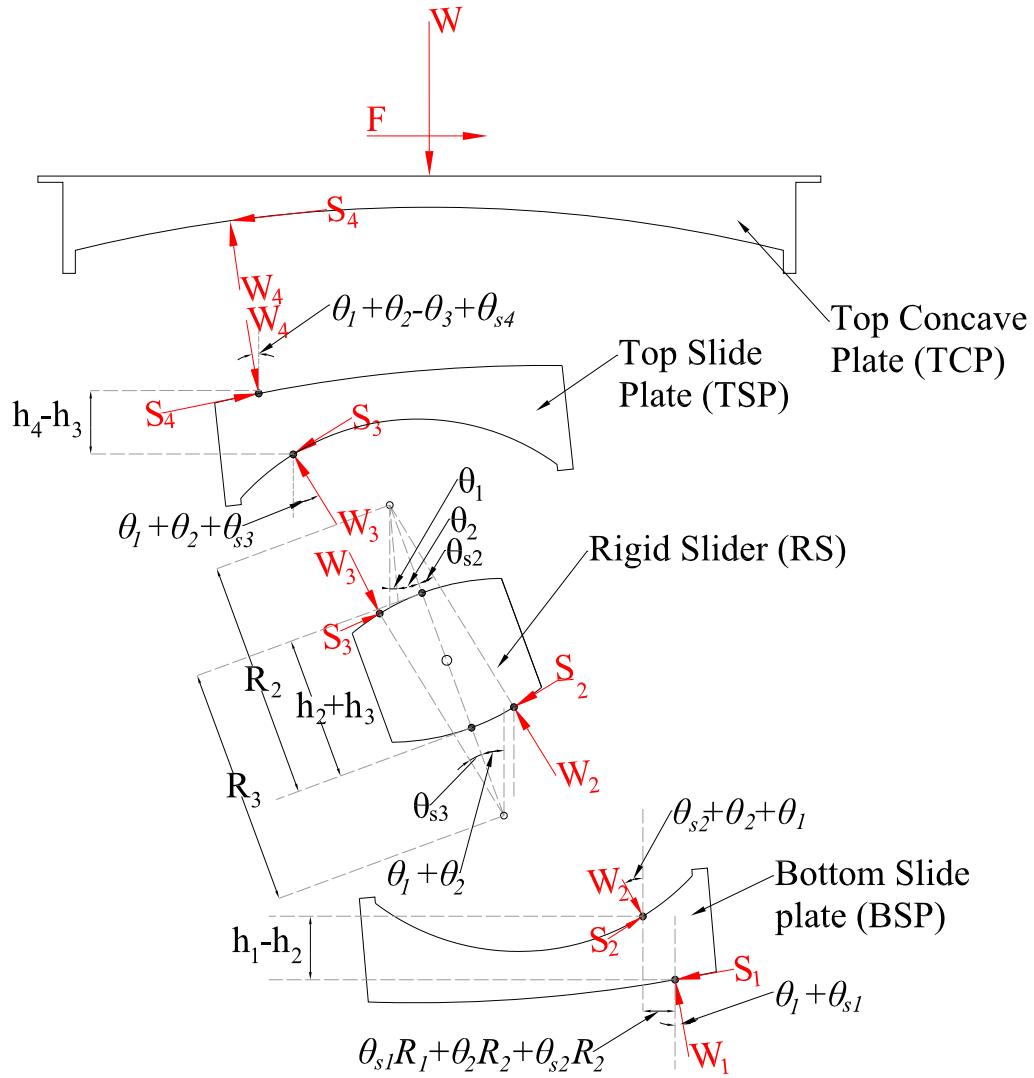


Figure 3-1: Free body diagrams of components of a Triple Friction Pendulum bearing

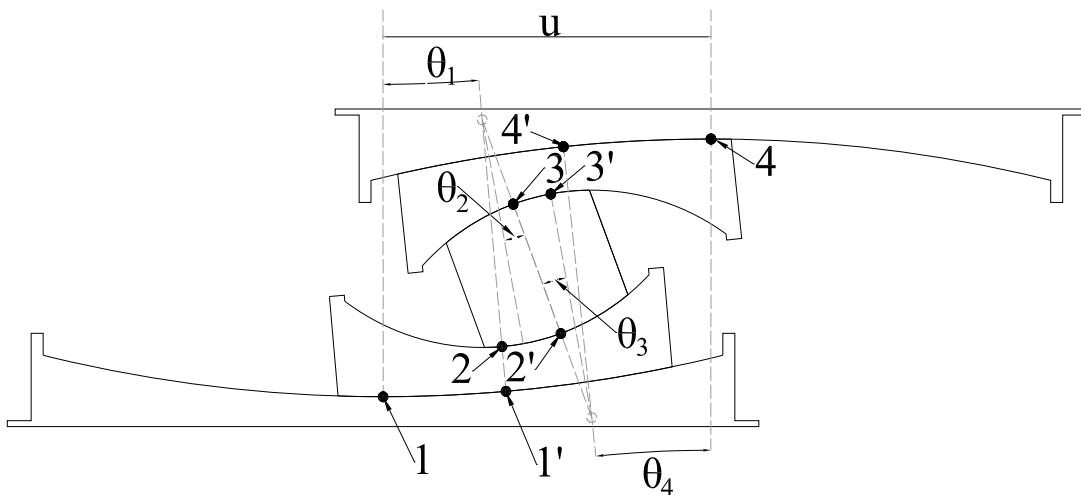


Figure 3-2: Deformed bearing and definition of sliding angles

Equilibrium of moments for the rigid slider about the point of application of forces on surface 3:

$$0 = W(\theta_{s2}R_2 + \theta_{s3}R_3) - (W\theta_{s2} + S_2 + F_{r2})(h_2 + h_3) \quad (3-4)$$

Equilibrium of forces in the horizontal direction for the rigid slider:

$$W\theta_{s2} + S_2 + F_{r2} = W\theta_{s3} + S_3 + F_{r3} \quad (3-5)$$

Equilibrium of forces in the horizontal direction for the bottom sliding plate:

$$W(\theta_2 + \theta_{s2}) + S_2 + F_{r2} = S_1 + W\theta_{s1} + F_{r1} \quad (3-6)$$

Equilibrium of moments about the force application point at surface 1 for the bottom sliding plate:

$$0 = W(\theta_{s1}R_1 - \theta_2R_2 - \theta_{s2}R_2) - (h_1 - h_2)[W(\theta_{s2} + \theta_2) + S_2 + F_{r2}] \quad (3-7)$$

Equilibrium of moments about the force application point at surface 4 for the top sliding plate:

$$0 = W(\theta_{s4}R_4 - \theta_3R_3 - \theta_{s3}R_3) - (h_4 - h_3)[W(\theta_{s3} + \theta_3) + S_3 + F_{r3}] \quad (3-8)$$

Equilibrium of forces in the horizontal direction for the top sliding plate:

$$W(\theta_3 + \theta_{s3}) + S_3 + F_{r3} = S_4 + W\theta_{s4} + F_{r4} \quad (3-9)$$

From force equilibrium of the top concave plate:

$$F = W(\theta_1 + \theta_2 - \theta_3 + \theta_{s4}) + S_4 + F_{r4} \quad (3-10)$$

Restraining the top plate to have zero rotation (top plate is horizontal) requires that:

$$\theta_1 + \theta_2 - \theta_3 - \theta_4 = 0 \quad (3-11)$$

Alternatively, if the top of the bearing is connected to a flexible structure with rotational stiffness K_s , Equation (3-11) above can be modified to the following after neglecting the effect of the top plate thickness:

$$K_s(\theta_1 + \theta_2 - \theta_3 - \theta_4) + WR_4\theta_{s4} = 0 \quad (3-12)$$

Moreover, when misalignment of the top concave plate is considered, Equation (3-11) is modified to Equation (3-13) in which angle θ_c is the known top plate misalignment or deviation from the horizontal:

$$\theta_1 + \theta_2 - \theta_3 - \theta_4 = \theta_c \quad (3-13)$$

Note that the rotation of the bottom concave plate is more complex to include since it has to be accounted for in Equation (3-13) and in the equilibrium Equations (3-4) to (3-10). This case is omitted in this section for simplicity but is presented later in Section 4.

The procedure followed for the calculation of the Triple FP bearing force-displacement relation requires solution of Equations (3-4) to (3-11) during each phase of motion that is characterized by either initiation of motion or stop of motion on one or more sliding surfaces. Note that depending on the phase, the number of variables to solve varies. The total displacement u can either be calculated using Equation (3-2) after all rotations are known or can be included as a variable in Equations (3-4) to (3-11) after eliminating one of the sliding angles.

We now proceed to develop algebraic force-displacement relationships for Triple FP bearings for some selected combinations of parameters that are of practical interest. The constraints on the parameters and the resulting algebraic equations for the behavior of the bearing have similarity to those presented by Fenz and Constantinou (2008a to 2008c). Note that with the presented formulation, algebraic force-displacement relations for arbitrary TFP combinations of properties can be derived. However, the process is cumbersome, of limited practical interest and beyond the scope of this report. Later in Section 4 we will present a more general formulation that can be used for response history analysis but which requires solution of systems of differential equations that describe the constitutive relation of the bearing. In the latter case, there are no constraints on the values of parameters of the bearing.

Table 3-1 presents two configurations of Triple FP bearings with certain geometric and frictional constraints considered in this report. Note the difference in the constraints of Table 3-1 to those in the theory of Fenz and Constantinou (2008a to 2008e), which only involve the coefficient of friction of the four sliding surfaces. By comparison, the constraints of the configurations in

Table 3-1 involve products of the coefficient of friction and the related radii of curvature. However, there is a difference in what is the coefficient of friction in the two formulations. As explained in Section 1, the current formulation utilizes the actual coefficient of friction at each sliding interface. The model of Fenz and Constantinou (2008a to 2008e) utilizes a coefficient of friction obtained in the testing of the bearings, which due to the spherical geometry and the requirement for equilibrium of moments, is an effective coefficient of friction $\bar{\mu}_i$ larger than the actual coefficient μ_i and given by:

$$\bar{\mu}_i = \mu_i \frac{R_i}{R_i - h_i} \quad (3-14)$$

It is the effective friction coefficient that determines the conditions of initiation of sliding and transition between regimes.

Table 3-1: Triple FP configurations analyzed in this report

Configuration	Friction Coefficients
A	$\mu_2 \frac{R_2}{R_{eff2}} < \mu_3 \frac{R_3}{R_{eff3}} < \mu_1 \frac{R_1}{R_{eff1}} < \mu_4 \frac{R_4}{R_{eff4}}$
B	$\mu_1 \frac{R_1}{R_{eff1}} < \mu_4 \frac{R_4}{R_{eff4}} < \mu_2 \frac{R_2}{R_{eff2}} < \mu_3 \frac{R_3}{R_{eff3}}$

Configuration A is similar to the one considered by Fenz and Constantinou (2008a to 2008e) but generalized to have different values of the effective friction coefficient for the two inner surfaces (2 and 3). Configuration B describes a case where the inner two surfaces have coefficients of friction larger than the two outer surfaces. While this is an unusual configuration that has not been implemented, it has been tested and the results will be reported herein.

3.2 TFP Bearing of Configuration A ($\mu_2 R_2/R_{eff2} < \mu_3 R_3/R_{eff3} < \mu_1 R_1/R_{eff1} < \mu_4 R_4/R_{eff4}$)

The force-displacement relation for the bearing is determined for the case when the top concave plate is horizontal; that is, Equation (3-11) is valid.

3.2.1 Transition Point I

Surface 2 is the one of least friction. Accordingly, as lateral load F in Figure 3-1 increases, one would expect sliding to initiate on that surface when $F = \mu_2 W R_2 / R_{eff2}$. However, this would violate the conditions of compatibility or full contact would be lost. For motion to initiate, the smallest of the friction forces at one of the two bottom surfaces ($S_1 = \mu_1 W$ or $S_2 = \mu_2 W$) and the smallest of the friction forces at one of the top two surface surfaces ($S_3 = \mu_3 W$ or $S_4 = \mu_4 W$) must be reached so that motion on two surfaces can simultaneously occur. Based on the conditions for Configuration A (see Table 3-1), motion will first initiate when $S_2 = \mu_2 W$ and $S_3 = \mu_3 W$. Substituting $S_2 = \mu_2 W$, $S_3 = \mu_3 W$, $\theta_1 = \theta_2 = \theta_3 = \theta_4 = 0$ in Equations (3-4) to (3-11), using Equation (3-2) and solving for unknowns $F, u, \theta_{s1}, \theta_{s2}, \theta_{s3}, \theta_{s4}, S_1, S_4$, one can determine that sliding will initiate when the force and displacement satisfy the conditions:

$$F^I = \frac{\mu_2 R_2 + \mu_3 R_3}{R_{eff2} + R_{eff3}}, \quad (3-15)$$

$$u^I = 0$$

The offset angles that determine the location of the resultant forces on each surface at initiation of sliding are given by:

$$\theta_{s2}^I = \frac{2\mu_2 h_2 - (\mu_2 - \mu_3) R_3}{R_{eff2} + R_{eff3}}, \quad \theta_{s3}^I = \frac{2\mu_3 h_2 + (\mu_2 - \mu_3) R_3}{R_{eff2} + R_{eff3}} \quad (3-16)$$

$$\theta_{s1}^I = \frac{\mu_3 R_3 (R_{eff2} + h_1) - \mu_2 R_2 (R_{eff3} - h_1)}{(R_{eff2} + R_{eff3}) R_1}; \quad \theta_{s4}^I = \frac{\mu_2 R_2 (R_{eff3} + h_4) - \mu_3 R_3 (R_{eff2} - h_4)}{(R_{eff2} + R_{eff3}) R_4} \quad (3-17)$$

Note that the superscripts in Equations (3-15) to (3-17) denote the transition point in consistency with the notation in Figure 1-2.

Following initiation of motion at a value of force given by Equation (3-15), sliding occurs simultaneously on surfaces 2 and 3 and the force-displacement relation of the isolator is given by:

$$F = \frac{\mu_2 R_2 + \mu_3 R_3}{R_{eff2} + R_{eff3}} + \frac{W}{R_{eff2} + R_{eff3}} u \quad (3-18)$$

Note that the slope of the force-displacement curve (or stiffness) is given by the same term ($W / (R_{eff2} + R_{eff3})$) as the one predicted by the theory of Fenz and Constantinou (2008a to 2008e).

3.2.2 Transition Point II

Motion on surface 2 and 3 continues until $S_1 = \mu_1 W$ on surface 1. Substituting $S_1 = \mu_1 W$, $S_2 = \mu_2 W$, $S_3 = \mu_3 W$, $\theta_1 = \theta_4 = 0$ in Equations (3-4) to (3-11), using Equation (3-2) and solving for the unknowns $F, u, \theta_{s1}, \theta_{s2}, \theta_{s3}, \theta_{s4}, S_4, \theta_2, \theta_3$, results in the following expressions for the force and displacement at transition point II:

$$\begin{aligned} F^{II} &= \frac{\mu_1 R_1 - \mu_2 R_2}{R_{eff1} - R_{eff2}} W; \\ u^{II} &= \frac{\mu_1 R_1 (R_{eff2} + R_{eff3}) - \mu_2 R_2 (R_{eff1} + R_{eff2}) - \mu_3 R_3 (R_{eff1} - R_{eff2})}{R_{eff1} - R_{eff2}} \end{aligned} \quad (3-19)$$

The offset angles that determine the location of the resultant forces on surfaces 2 and 3 at transition point II are still given by Equation (3-16), which implies that during sliding these angles remain unchanged. The offset angles that determine the location of the resultant forces on surfaces 1 and 4 at transition point II are given by:

$$\theta_{s1}^{II} = \frac{\mu_1 (R_{eff2} + h_1) - \mu_2 R_2}{R_{eff1} - R_{eff2}}; \quad \theta_{s4}^{II} = \frac{(\mu_1 R_1 - \mu_2 R_2)(R_{eff3} + h_4) - \mu_3 R_3 (R_{eff1} - R_{eff2})}{(R_{eff1} - R_{eff2}) R_4} \quad (3-20)$$

The increase in the offset angles of surfaces 1 and 4 (determined by a comparison of Equations (3-17) and (3-20)) is due to the fact that during sliding on surfaces 2 and 3, the force acting on surface 1 shifts its point of application in order to satisfy the condition of moment equilibrium of the slide plate. The sliding rotation angles at surfaces 2 and 3 at the transition point II are given by:

$$\begin{aligned} \theta_2^{II} &= \frac{\mu_1 R_1 - \mu_3 (R_{eff1} - R_{eff2}) - \mu_2 R_2}{R_{eff1} - R_{eff2}} + \frac{(\mu_3 - \mu_2) R_2 - 2h_2 \mu_3}{R_{eff2} + R_{eff3}} \\ \theta_3^{II} &= \frac{\mu_1 R_1 - \mu_2 R_{eff1} - \mu_2 h_2}{R_{eff1} - R_{eff2}} - \frac{2h_2 \mu_2 + (\mu_3 - \mu_2) R_3}{R_{eff2} + R_{eff3}} \end{aligned} \quad (3-21)$$

The force-displacement relation beyond the transition point II is given by:

$$F = \frac{\mu_1 R_1 + \mu_3 R_3}{R_{eff1} + R_{eff3}} + \frac{W}{R_{eff1} + R_{eff3}} u \quad (3-22)$$

Note that following transition point II, motion occurs simultaneously on surfaces 1 and 3.

3.2.3 Transition Point III

Motion continues on surfaces 1 and 3 until $S_4 = \mu_4 W$ on surface 4. Substitution of $S_4 = \mu_4 W$, $S_1 = \mu_1 W$, $S_2 = \mu_2 W$, $S_3 = \mu_3 W$, $\theta_4 = 0$ into Equations (3-4) to (3-11), using Equation (3-2) and solving for the unknowns $F, u, \theta_{s1}, \theta_{s2}, \theta_{s3}, \theta_{s4}, \theta_1, \theta_2, \theta_3$, results in the following results for the force and displacement at transition point III:

$$F^{III} = \frac{\mu_4 R_4 - \mu_3 R_3}{R_{eff4} - R_{eff3}} W$$

$$u^{III} = \frac{\mu_4 R_4 (R_{eff1} + R_{eff3}) - \mu_1 R_1 (R_{eff4} - R_{eff3}) - \mu_3 R_3 (R_{eff4} + R_{eff1})}{R_{eff4} - R_{eff3}} \quad (3-23)$$

The offset angle that determines the location of the resultant force for surface 1 is still given by Equation (3-20). The offset angles that determine the location of the resultant forces for surfaces 2 and 3 are given by Equation (3-16). The offset angle that determines the location of the resultant force for surface 4 at transition point III changes due to motion on surface 3 and is given by the following expression:

$$\theta_{s4}^{III} = \frac{\mu_4 (R_3 - h_2 + h_4) - \mu_3 R_3}{R_{eff4} - R_{eff3}} \quad (3-24)$$

The sliding angle of surface 2 is given by Equation (3-21) which demonstrates that motion stopped on surface 2 when motion started on surface 1 and, therefore, the increment in displacement u described by the difference between Equations (3-23) and (3-19) is due to motion on surfaces 1 and 3. The sliding angles for surfaces 1 and 3 at the transition point III are given by:

$$\begin{aligned}\theta_1^{III} &= \frac{\mu_4(R_{eff1} - R_{eff2}) - \mu_1R_1 + \mu_2R_2}{R_{eff1} - R_{eff2}} + \frac{\mu_4(R_{eff3} + h_4) - \mu_3R_3}{R_{eff4} - R_{eff3}} \\ \theta_3^{III} &= \frac{\mu_4R_4 - \mu_3R_3}{R_{eff4} - R_{eff3}} - \frac{\mu_2R_2 + \mu_3R_3}{R_{eff2} + R_{eff3}}\end{aligned}\quad (3-25)$$

The force-displacement relation beyond the transition point III is given by:

$$F = \frac{\mu_4R_4 + \mu_1R_1}{R_{eff1} + R_{eff4}}W + \frac{W}{R_{eff1} + R_{eff4}}u \quad (3-26)$$

Note that beyond transition point III, motion occurs on surfaces 1 and 4.

3.2.4 Transition Point IV

Motion continues on surfaces 1 and 4 until the displacement capacity on surface 1 is consumed and the moving slider comes into contact with the restrainer of surface 1. Substitution of $S_4 = \mu_4W$, $S_1 = \mu_1W$, $S_2 = \mu_2W$, $S_3 = \mu_3W$, $\theta_1 = d_1/R_1$ in Equations (3-4) to (3-11), using Equation (3-2) and solving for the unknowns $F, u, \theta_{s1}, \theta_{s2}, \theta_{s3}, \theta_{s4}, \theta_2, \theta_3, \theta_4$, results in the following results for the force and displacement at transition point IV (F_{r1} is still zero since transition point IV describes the instant at which contact initiates):

$$\begin{aligned}F^{IV} &= \frac{\mu_1R_1 - \mu_2R_2}{R_{eff1} - R_{eff2}}W + \frac{d_1}{R_1}W \\ u^{IV} &= \frac{d_1(R_{eff1} + h_4)}{R_1} + \mu_1R_1 \frac{R_{eff2} + R_{eff4}}{R_{eff1} - R_{eff2}} - \mu_2R_2 \frac{R_{eff1} + R_{eff4}}{R_{eff1} - R_{eff2}} - \mu_4R_4\end{aligned}\quad (3-27)$$

The offset angles that determine the location of the resultant forces on each surface do not change between stages III and IV and for transition point IV are given by Equation (3-20) for θ_{s1} , Equation (3-16) for θ_{s2} and θ_{s3} and Equation (3-24) for θ_{s4} . The sliding angles of surfaces 2 and 3 are given by Equation (3-21) for surface 2 and Equation (3-25) for surface 3. This implies that between transition points III and IV, there was no motion on surfaces 2 and 3. The sliding angle for surface 4 at transition point IV is given by:

$$\theta_4^{IV} = \frac{\mu_1R_1 - \mu_4(R_{eff1} - R_{eff2}) - \mu_2R_2}{R_{eff1} - R_{eff2}} + \frac{\mu_3R_3 - \mu_4(h_4 + R_{eff3})}{R_{eff4} - R_{eff3}} + \frac{d_1}{R_1} \quad (3-28)$$

The force-displacement relation beyond the transition point IV is given by:

$$F = \frac{\mu_2 R_2 + \mu_4 R_4}{R_{eff4} + R_{eff2}} W - \frac{R_{eff1} - R_{eff2}}{R_{eff4} + R_{eff2}} \frac{d_1}{R_1} W + \frac{W}{R_{eff4} + R_{eff2}} u \quad (3-29)$$

Note that beyond transition point IV, motion occurs on surfaces 2 and 4.

3.2.5 Transition Point V

Motion continues on surfaces 2 and 4 until the displacement capacity on surface 4 is consumed and the moving slider comes into contact with the restrainer of surface 4. Substitution of $S_4 = \mu_4 W$, $S_1 = \mu_1 W$, $S_2 = \mu_2 W$, $S_3 = \mu_3 W$, $\theta_1 = d_1/R_1$, $\theta_4 = d_4/R_4$ into Equations (3-4) to (3-11), using Equation (3-2) and solving for the unknowns $F, u, \theta_{s1}, \theta_{s2}, \theta_{s3}, \theta_{s4}, F_{r1}, \theta_2, \theta_3$, results in the following results for the force and displacement at transition point V (note that the restrainer force of surface 1 is now nonzero and included in the unknown):

$$F^V = \frac{\mu_4 R_4 - \mu_3 R_3}{R_{eff4} - R_{eff3}} W + \frac{d_4}{R_4} W$$

$$u^V = d_4 \frac{R_{eff2} + R_{eff4}}{R_4} + d_1 \frac{R_{eff1} - R_{eff2}}{R_1} - R_2 \mu_2 + \frac{\mu_4 R_4 (R_{eff2} + R_{eff3}) - \mu_3 R_3 (R_{eff4} + R_{eff3})}{R_{eff4} - R_{eff3}} \quad (3-30)$$

The offset angles that determine the location of the resultant forces on each surface are given by Equation (3-16) for θ_{s2} and θ_{s3} and Equation (3-24) for θ_{s4} . Angle θ_{s1} changes and is given by:

$$\theta_{s1}^V = \frac{-R_2 \mu_2 - (R_{eff2} + h_1) \left(\frac{\mu_3 R_3 - \mu_4 R_4}{R_{eff4} - R_{eff3}} + \frac{d_1}{R_1} - \frac{d_4}{R_4} \right)}{R_1} \quad (3-31)$$

The sliding angle of surface 3 is still given by Equation (3-25) and the sliding angle for surface 2 is given by:

$$\theta_2^V = -\frac{\mu_2 R_2 + \mu_3 R_3}{R_{eff2} + R_{eff3}} + \frac{\mu_4 R_4 - \mu_3 R_3}{R_{eff4} - R_{eff3}} - \frac{d_1}{R_1} + \frac{d_4}{R_4} \quad (3-32)$$

The force-displacement relation beyond the transition point V is given by:

$$F = \frac{\mu_2 R_2 + \mu_3 R_3}{R_{eff2} + R_{eff3}} W - \frac{R_{eff1} - R_{eff2}}{R_{eff2} + R_{eff3}} \frac{d_1}{R_1} W - \frac{R_{eff4} - R_{eff3}}{R_{eff2} + R_{eff3}} \frac{d_4}{R_4} W + \frac{W}{R_{eff2} + R_{eff3}} u \quad (3-33)$$

Note that beyond transition point V, motion occurs on surfaces 2 and 3.

The displacement capacity of the triple FP bearing is reached when the minimum of the displacement capacities of surface 2 or surface 3 is reached. Note that after one of the two displacement capacities is reached, three out of four surfaces of the bearing have reached their displacement capacities. This requires that motion stops as sliding on one surface alone would violate the conditions of compatibility or full contact will be lost.

3.2.6 Force-Displacement Relation

The force-displacement relation for the Triple FP, Configuration A is plotted in Figure 3-3 for the special case of $R_1 = R_4, \mu_2 = \mu_3, R_2 = R_3, h_1 = h_4$ for which comparisons to the theory of Fenz and Constantinou (2008a to 2008e) can be made.

The force-displacement relation of the same configuration using the theory of Fenz and Constantinou (2008a to 2008e) is shown in Figure 3-4. Note that the two theories produce identical force-displacement curves for this case when the friction coefficients in the Fenz and Constantinou model are replaced by the effective friction coefficient given by:

$$\begin{aligned}\bar{\mu}_2 &= \mu_2 \frac{R_2}{R_{eff2}} \\ \bar{\mu}_1 &= \frac{\mu_1 R_1 - \mu_2 R_2}{R_{eff1} - R_{eff2}} \\ \bar{\mu}_4 &= \frac{\mu_4 R_4 - \mu_2 R_2}{R_{eff1} - R_{eff2}}\end{aligned}\tag{3-34}$$

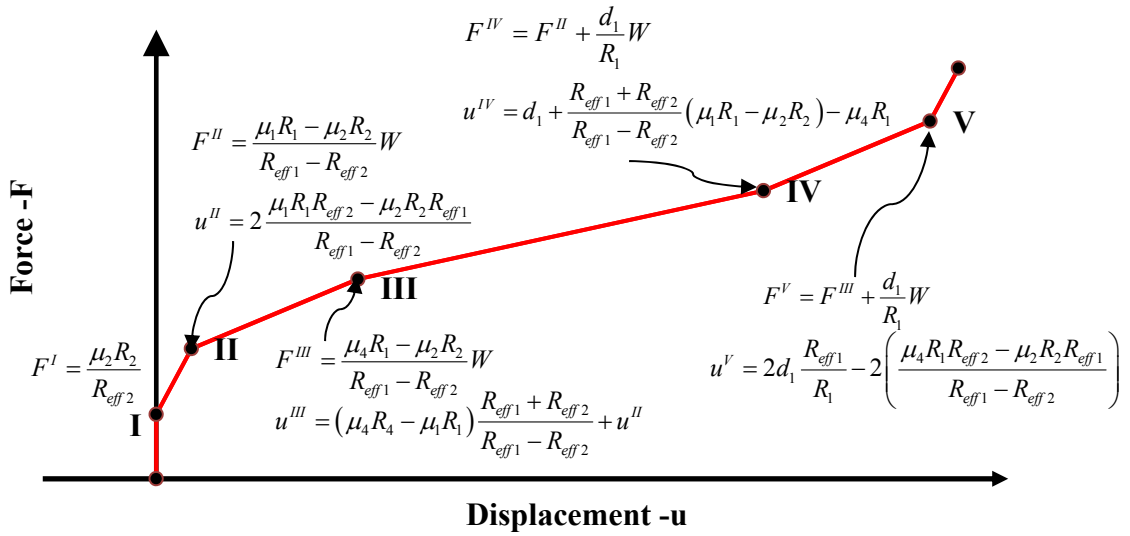


Figure 3-3: Force-displacement of Triple FP bearing of Configuration A with $R_1 = R_4, \mu_2 = \mu_3, R_2 = R_3, h_1 = h_4$ and based on the current theory

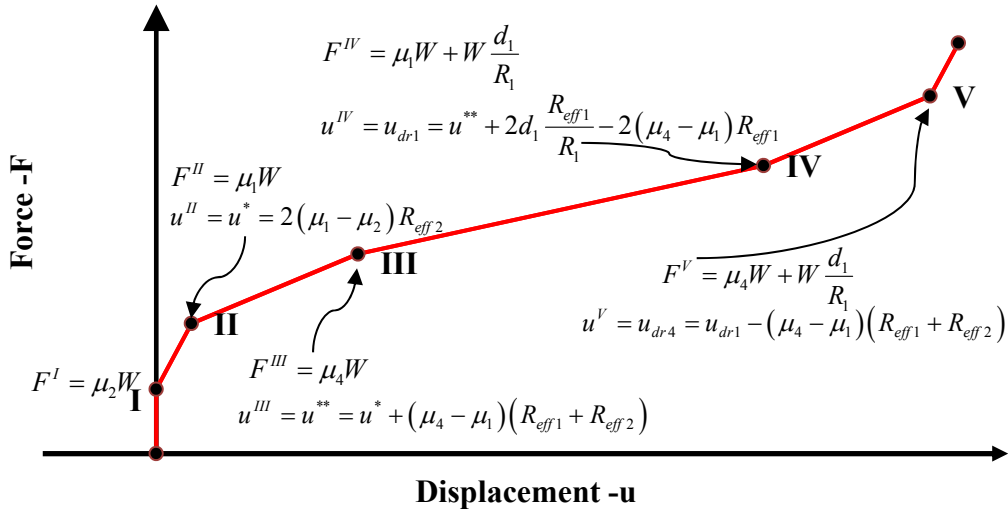


Figure 3-4: Force-displacement of Triple FP bearing of Configuration A with $R_1 = R_4, \mu_2 = \mu_3, R_2 = R_3, h_1 = h_4$ and based on the theory of Fenz and Constantinou

3.3 TFP Bearing of Configuration B ($\mu_1 R_1/R_{eff1} < \mu_4 R_4/R_{eff4} < \mu_2 R_2/R_{eff2} < \mu_3 R_3/R_{eff3}$)

Sliding initiates when the smallest of the friction forces at one of the two bottom surfaces ($S_1 = \mu_1 W$ or $S_2 = \mu_2 W$) and the smallest of the friction forces at one of the top two surfaces ($S_3 = \mu_3 W$ or $S_4 = \mu_4 W$) are overcome. Given the assumptions in Table 3-1, this configuration represents a case where motion initiates first on the outer surfaces (1 and 4). The theory of Fenz

and Constantinou (2008a to 2008e) is not applicable in this case since it is restricted to $\bar{\mu}_2 = \bar{\mu}_3 < \bar{\mu}_1 \leq \bar{\mu}_4$. Analysis for this configuration proceeds along the lines of the analysis for Configuration A but with a different sequence of motion on the various surfaces.

3.3.1 Transition Point I

Based on the conditions for Configuration B (see Table 3-1), motion will initiate when the friction force reaches the value $S_1 = \mu_1 W$ on surface 1 and the value $S_4 = \mu_4 W$ on surface 4. Substituting $S_1 = \mu_1 W, S_4 = \mu_4 W, \theta_1 = \theta_2 = \theta_3 = \theta_4 = 0$ into Equations (3-4) to (3-11), using Equation (3-2) and solving for the unknowns $F, u, \theta_{s1}, \theta_{s2}, \theta_{s3}, \theta_{s4}, S_2, S_3$, one determines that at initiation of motion (transition point I):

$$F^I = \frac{\mu_1 R_1 + \mu_4 R_4}{R_{eff1} + R_{eff4}} W \quad (3-35)$$

$$u^I = 0$$

The offset angles are given by:

$$\theta_{s1}^I = \frac{R_4 \mu_4 - (R_{eff4} - h_1) \mu_1}{(R_{eff1} + R_{eff4})}; \quad \theta_{s4}^I = \frac{\mu_1 R_1 + (h_4 - R_{eff1}) \mu_4}{R_{eff1} + R_{eff4}} \quad (3-36)$$

$$\theta_{s3}^I = \frac{(h_2 + R_{eff4}) \mu_1 R_1 + (h_2 - R_{eff1}) \mu_4 R_4}{R_3 (R_{eff1} + R_{eff4}) W}; \quad \theta_{s2}^I = \frac{(h_2 - R_{eff4}) \mu_1 R_1 + (h_2 + R_{eff1}) \mu_4 R_4}{R_2 (R_{eff1} + R_{eff4}) W}$$

After transition point I, motion occurs simultaneously on surfaces 1 and 4 and the force-displacement relation is given by:

$$F = \frac{\mu_1 R_1 + \mu_4 R_4}{R_{eff1} + R_{eff4}} W + \frac{W}{R_{eff1} + R_{eff4}} u \quad (3-37)$$

3.3.2 Transition Point II

Motion continues on surfaces 1 and 4 until transition point II, where the lesser of the displacement capacities of surfaces 1 and 4 is consumed. While typically the displacement capacities of surfaces 1 and 4 are equal, consider the general case where the displacement capacity of surface 1 is smaller than that of surface 4. Substituting for

$S_1 = \mu_1 W$, $S_4 = \mu_4 W$, $\theta_1 = d_1/R_1$ into Equations (3-4) to (3-11), using Equation (3-2) and solving for the unknowns $F, u, \theta_{s1}, \theta_{s2}, \theta_{s3}, \theta_{s4}, S_2, S_3, \theta_4$, the total force and displacement of the bearing at transition point II are derived to be:

$$F^{II} = \frac{\mu_1 R_1 + \mu_4 R_4}{R_{eff1} + R_{eff4}} W + \frac{d_1}{R_1} W \quad (3-38)$$

$$u^{II} = \left(R_{eff1} + R_{eff4} \right) \frac{d_1}{R_1}$$

The offset angles are given by Equation (3-36) and they remain unchanged during motion between transition points I and II. The sliding angle of surface 4 is equal to that of surface 1:

$$\theta_4^{II} = \theta_1^{II} = \frac{d_1}{R_1} \quad (3-39)$$

At transition point II and due to the fact that friction has not been exceeded on surfaces 2 and 3, Equation (3-11) predicts that the bearing must cease motion and exhibit rigid behavior until the lateral force reaches the value of the friction force on surface 2 (which has less friction than surface 3). For motion to initiate, this condition would still need to be satisfied even if it was assumed that $\mu_2 R_2/R_{eff2} > \mu_3 R_3/R_{eff3}$ (since it was assumed earlier that $d_1 < d_4$).

3.3.3 Transition Point III

At transition point III, motion initiates when the friction force on surface 2 reaches the value of $S_1 = \mu_1 W$. Substituting for $S_1 = \mu_1 W$, $S_4 = \mu_4 W$, $S_2 = \mu_2 W$, $\theta_1 = d_1/R_1$ into Equations (3-4) to (3-11), using Equation (3-2) and solving for the unknowns $F, u, \theta_{s1}, \theta_{s2}, \theta_{s3}, \theta_{s4}, F_{r1}, S_3, \theta_4$, the force and displacement at transition point II are derived to be:

$$F^{III} = \frac{\mu_2 R_2 + \mu_4 R_4}{R_{eff2} + R_{eff4}} W + W \frac{d_1}{R_1} \quad (3-40)$$

$$u^{III} = \left(R_{eff1} + R_{eff4} \right) \frac{d_1}{R_1}$$

Note that $u^{III} = u^{II}$ so that, indeed, the bearing has ceased motion in the interval between transition points II and III. As motion ceased, all offset angles change and are given by:

$$\begin{aligned}\theta_{s1}^{III} &= \frac{R_2\mu_2(h_1 - R_{eff4}) + (h_1 + R_{eff2})R_4\mu_4}{R_1(R_{eff2} + R_{eff4})}; & \theta_{s4}^{III} &= \frac{R_2\mu_2 + (h_4 - R_{eff2})\mu_4}{R_{eff2} + R_{eff4}} \\ \theta_{s2}^{III} &= \frac{(h_2 - R_{eff4})\mu_2 + \mu_4R_4}{R_{eff2} + R_{eff4}}; & \theta_{s3}^{III} &= \frac{(h_2 + R_{eff4})\mu_2R_2 - (R_{eff2} - h_2)\mu_4R_4}{R_3(R_{eff2} + R_{eff4})W}\end{aligned}\quad (3-41)$$

Beyond transition point III, motion occurs on surfaces 2 and 4. The force-displacement relation is given by:

$$F = \frac{\mu_2R_2 + \mu_4R_4}{R_{eff2} + R_{eff4}} - W \frac{R_{eff1} - R_{eff2}}{R_{eff2} + R_{eff4}} \frac{d_1}{R_1} + \frac{W}{R_{eff2} + R_{eff4}} u \quad (3-42)$$

3.3.4 Transition Point IV

At transition point IV, the displacement capacity of surface 4 is consumed. Substituting for $S_1 = \mu_1W, S_4 = \mu_4W, S_2 = \mu_2W, \theta_1 = d_1/R_1, \theta_4 = d_4/R_4$ into Equations (3-4) to (3-11), using Equation (3-2) and solving for the unknowns $F, u, \theta_{s1}, \theta_{s2}, \theta_{s3}, \theta_{s4}, F_{r1}, S_3$, the force and displacement at transition point IV are determined to be:

$$\begin{aligned}F^{IV} &= \frac{\mu_2R_2 + \mu_4R_4}{R_{eff2} + R_{eff4}} W + W \frac{d_4}{R_4} \\ u^{IV} &= (R_{eff1} + R_{eff4}) \frac{d_1}{R_1} + (R_{eff2} - h_4) \left(\frac{d_4}{R_4} - \frac{d_1}{R_1} \right)\end{aligned}\quad (3-43)$$

The offset angles for surfaces 2 and 4 are the same as those at transition point III given by Equations (3-41). The offset angles for surfaces 1 and 3 are given by:

$$\begin{aligned}\theta_{s1}^{IV} &= \frac{(h_1 - h_2)\mu_2}{R_1} + (h_1 + R_{eff2}) \frac{(h_2 - R_{eff4})\mu_2 + \mu_4R_4}{R_1(R_{eff2} + R_{eff4})} + \frac{(h_1 + R_{eff2})}{R_1} \left(\frac{d_4}{R_4} - \frac{d_1}{R_1} \right) \\ \theta_{s3}^{IV} &= \frac{(h_2 + R_{eff4})\mu_2R_2 - (R_{eff2} - h_2)\mu_4R_4}{R_3(R_{eff2} + R_{eff4})}\end{aligned}\quad (3-44)$$

Finally, the sliding angle for surface 2 is given by:

$$\theta_2^{IV} = \frac{d_4}{R_4} - \frac{d_1}{R_1} \quad (3-45)$$

Since the displacement capacities of both surfaces 1 and 4 are reached at transition point IV and the friction force has not been reached on surface 3, the isolator ceases motion again and exhibits rigid behavior until transition point V is reached.

3.3.5 Transition Point V

At transition point V, the friction force is reached on surface 3 and motion starts. Substituting $S_1 = \mu_1 W$, $S_4 = \mu_4 W$, $S_2 = \mu_2 W$, $S_3 = \mu_3 W$, $\theta_1 = d_1/R_1$, $\theta_4 = d_4/R_4$ into Equations (3-4) to (3-11) using Equation (3-2) and solving for the unknowns F , u , θ_{s1} , θ_{s2} , θ_{s3} , θ_{s4} , F_{r1} , F_{r4} , the following are determined for transition point V:

$$\begin{aligned}
 F^V &= \frac{\mu_2 R_2 + \mu_3 R_3}{R_{eff2} + R_{eff3}} + W \frac{d_4}{R_4} \\
 u^V &= u^{IV} \\
 \theta_{s1}^V &= \frac{(h_1 - h_2)\mu_2}{R_1} + (h_1 + R_{eff2}) \frac{2h_2\mu_2 + R_3(\mu_3 - \mu_2)}{R_1(R_{eff2} + R_{eff3})} + \frac{(h_1 + R_{eff2})}{R_1} \left(\frac{d_4}{R_4} - \frac{d_1}{R_1} \right) \\
 \theta_{s4}^V &= \frac{(h_4 + R_{eff3})\mu_2 R_2 + (h_4 - R_{eff2})\mu_3 R_3}{(R_{eff2} + R_{eff3})R_4} \\
 \theta_{s2}^V &= \frac{2h_2\mu_2 + R_3(\mu_3 - \mu_2)}{R_{eff2} + R_{eff3}}; \quad \theta_{s3}^V = \frac{R_2(\mu_2 - \mu_3) + 2h_2\mu_3}{R_{eff2} + R_{eff3}}
 \end{aligned} \tag{3-46}$$

The force-displacement relation beyond transition point V is again given by Equation (3-33).

The displacement capacity of the bearing is consumed when either the displacement capacity of surface 2 or of surface 3, whichever is less, is consumed. If the two capacities are the same and since for this example some motion has already occurred on surface 2 prior to Regime V, the restrainer of surface 2 will be reached first. For practical applications where $d_1 = d_4$, $d_2 = d_3$, the restrainers of surfaces 1 and 4 will be simultaneously reached first and the restrainers of surfaces 2 and 3 will be simultaneously reached next.

The force-displacement relation for Configuration B is plotted in Figure 3-5 for the case $R_1 = R_4$, $R_2 = R_3$, $h_1 = h_4$, $d_2 = d_3$, $d_1 < d_4$. The assumption $d_1 < d_4$, while impractical, allows for some more complex behavior.

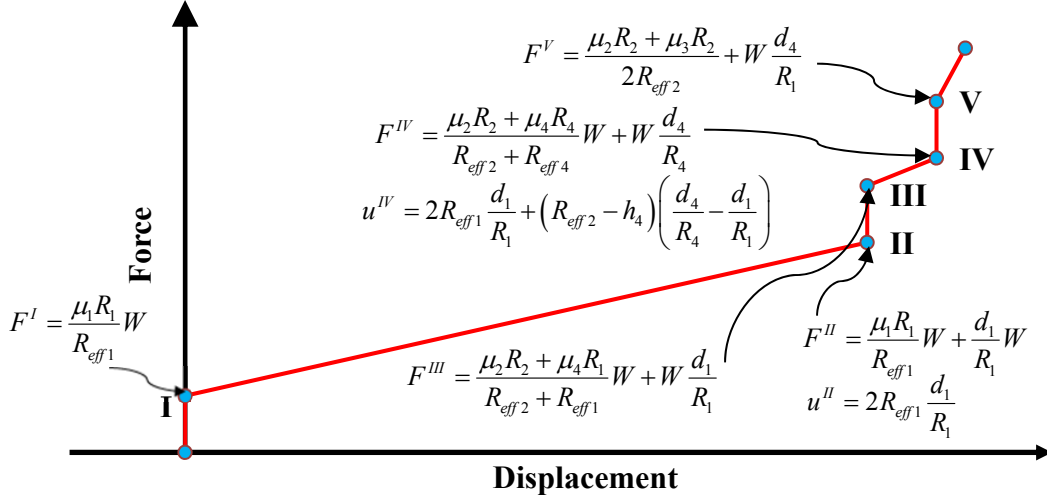


Figure 3-5: Force-displacement of Triple FP bearing of Configuration B with $R_1 = R_4, R_2 = R_3, \mu_1 < \mu_4 < \mu_2 < \mu_3, h_1 = h_4, d_2 = d_3, d_1 < d_4$ and based on the current theory

Figure 3-6 shows the force-displacement of the bearing when the theory of Fenz and Constantinou (2008a to 2008e) is used and for $R_1 = R_4, R_2 = R_3, h_1 = h_4, d_2 = d_3, d_1 = d_4, \mu_2 = \mu_3$. Note that this theory is not valid for this case since it has been developed for the special case where $\mu_2 = \mu_3 < \mu_1 \leq \mu_4, d_2 = d_3, d_1 = d_4$. The Fenz and Constantinou theory cannot predict the sequence of two stops and rather predicts a single stop when the displacement capacity of surfaces 1 and 4 are reached simultaneously.

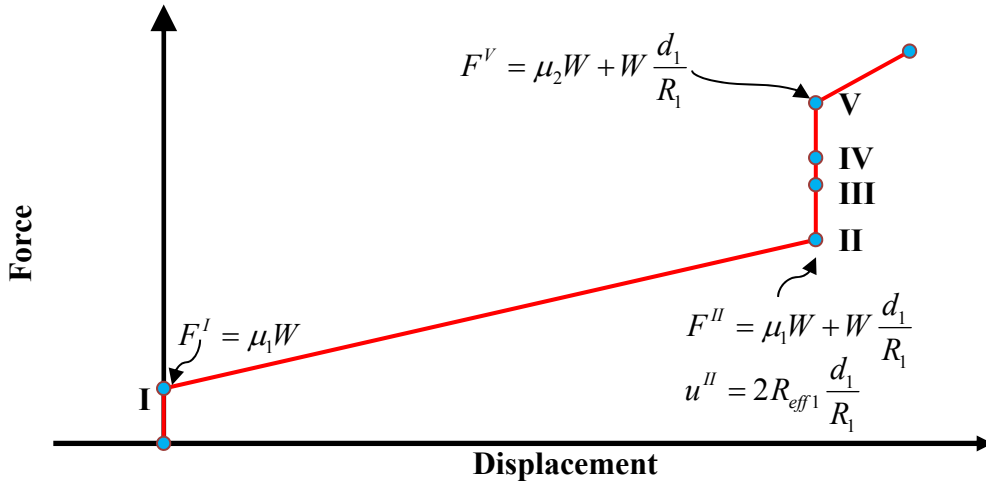


Figure 3-6: Force-displacement of Triple FP bearing of Configuration B with $R_1 = R_4, R_2 = R_3, \mu_1 = \mu_4 < \mu_2 = \mu_3, h_1 = h_4, d_2 = d_3, d_1 = d_4$ and based on the Fenz and Constantinou theory

Note that for the special Configuration B with $\mu_1 = \mu_4 < \mu_2 = \mu_3$, $d_2 = d_3, d_1 = d_4$, the theory of Fenz and Constantinou and the current theory can produce identical results if the following transformation is made (instead of the one given by Equation (3-34)). Note that $\bar{\mu}_i$ is the friction coefficient of surface i in the Fenz and Constantinou model, whereas μ_i is the friction coefficient of surface i in the current model.

$$\begin{aligned}\bar{\mu}_2 = \bar{\mu}_3 &= \mu_2 \frac{R_2}{R_{eff2}} = \mu_3 \frac{R_2}{R_{eff2}} \\ \bar{\mu}_1 = \bar{\mu}_4 &= \mu_1 \frac{R_1}{R_{eff1}} = \mu_4 \frac{R_4}{R_{eff4}}\end{aligned}\tag{3-47}$$

3.4 Examples of Force-displacement Relations of Triple FP Bearings

Consider the Triple FP bearings with the properties presented in Table 3-2. The full scale bearing is an actual bearing used in a building application. The model scale bearing has been tested at the University at Buffalo. The friction coefficient values in Table 3-2 have been randomly selected for the analysis presented here. Force-displacement relations for the four bearings are presented in Figure 3-7 as predicted by the current theory and the theory of Fenz and Constantinou (2008a to 2008e). For the single case in Table 3-2 for which $\mu_2 \neq \mu_3$, the theory of Fenz and Constantinou was used with $\bar{\mu}_2 = \bar{\mu}_3 = 0.0339$ (that is, the average value of the two friction coefficients multiplied by the ratio of the radius to the effective radius). Note that for the Fenz and Constantinou theory, the values of the effective coefficient of friction are used as given by Equation (3-34) for the Model Scale Configuration A, Full Scale Configuration A and Full Scale Configuration B, and as given by Equation (3-47) for the Model Scale Configuration B.

The results of Figure 3-7 demonstrate that the model of Fenz and Constantinou (2008a to 2008e) produces results identical to those of the current theory (presumed exact) for all configurations provided that the friction coefficient is correctly interpreted.

Table 3-2: Analyzed Triple FP bearings

Geometric and Frictional Properties	Model Scale Bearing-Configuration A, $\mu_2 = \mu_3$	Model Scale Bearing-Configuration B, $\mu_2 = \mu_3$	Full Scale Bearing-Configuration A, $\mu_2 \neq \mu_3$	Full Scale Bearing-Configuration B, $\mu_2 = \mu_3$
$R_1 = R_4$ (mm)	473	473	3962	3962
$R_2 = R_3$ (mm)	76	76	991	991
$h_2 = h_3$ (mm)	21	23	115	115
$h_1 = h_4$ (mm)	31	38	165	165
$R_{eff1} = R_{eff4}$ (mm)	442	435	3797	3797
$R_{eff2} = R_{eff3}$ (mm)	55	53	876	876
$d_1 = d_4$ (mm)	64	64	406	406
$d_2 = d_3$ (mm)	19	19	152	152
$d_1^* = d_4^*$ (mm)	59.8	58.9	389.09	389.09
$d_2^* = d_3^*$ (mm)	13.75	13.25	134.4	134.4
$b_1 = b_4$ (mm)	101	101	762	762
$b_2 = b_3$ (mm)	51	51	406.4	406.4
μ_1	0.1	0.1	0.075	0.075
μ_4	0.15	0.1	0.125	0.125
μ_2	0.05	0.1	0.05	0.05
μ_3	0.05	0.1	0.01	0.05
$\bar{\mu}_1$	0.1124	0.1087	0.0848	0.0833
$\bar{\mu}_4$	0.1735	0.1087	0.1662	0.1526
$\bar{\mu}_2$	0.0691	0.1434	0.0339	0.0566
$\bar{\mu}_3$	0.0691	0.1434	0.0339	0.0566
Friction coefficients $\mu_1, \mu_2, \mu_3, \mu_4$ are used in the current model				
Friction coefficients $\bar{\mu}_1, \bar{\mu}_2, \bar{\mu}_3, \bar{\mu}_4$ are used in the Fenz and Constantinou model				
Actual displacement capacities in the Fenz and Constantinou model given by $d_i^* = d_i (R_i - h_i) / R_i$				

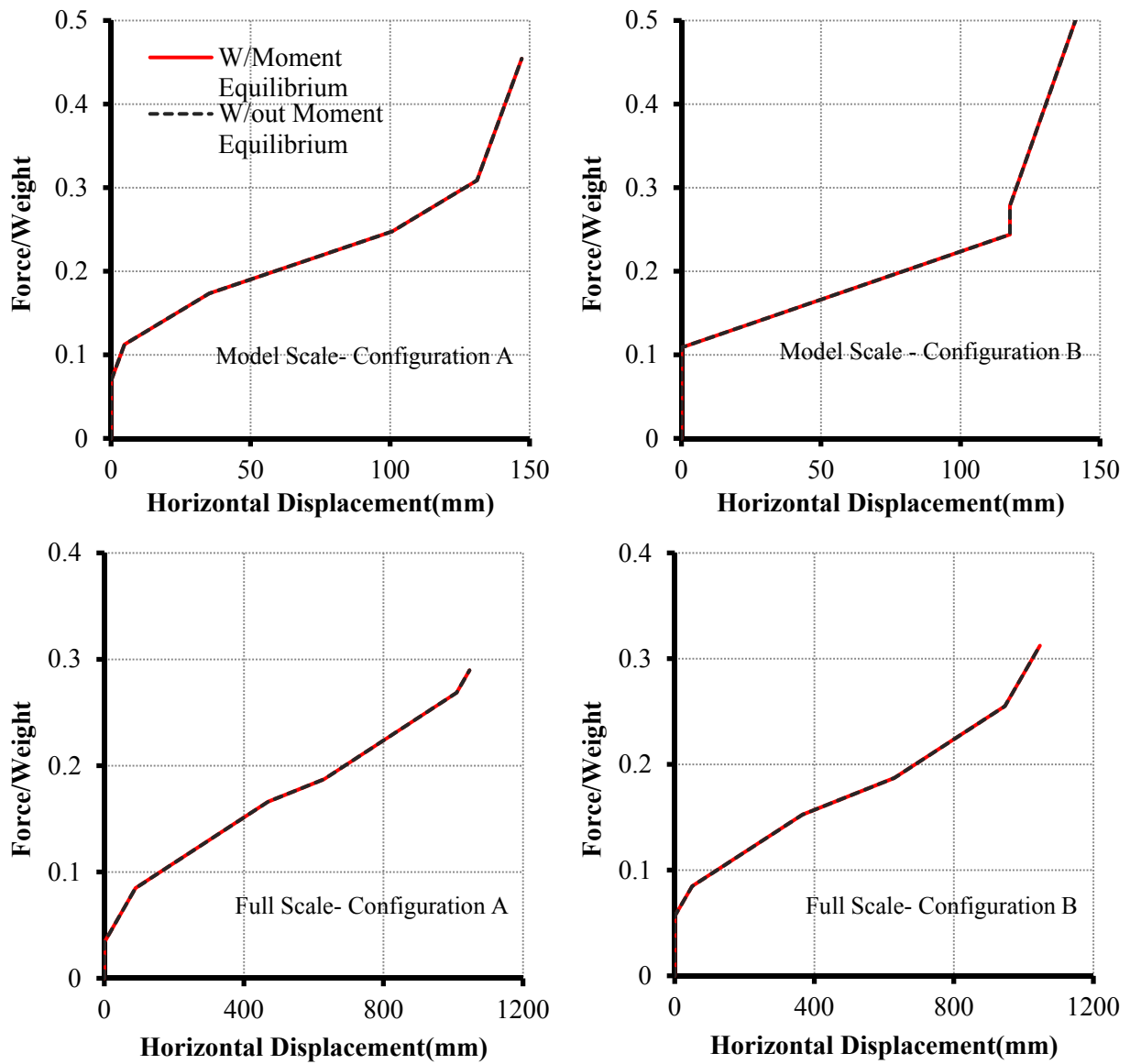


Figure 3-7: Force-displacement relation of bearings of Table 3-2 as predicted by two theories

3.5 Additional Results on the Behavior of Triple FP Bearings Based on Considerations of Moment Equilibrium

Consider the case where $\mu_2 < \mu_3 < \mu_1 < \mu_4$ and the lateral force (also lateral displacement) is small enough so that motion only occurs on surfaces 2 and 3 (that is, surfaces 1 and 4 do not experience any motion). We investigate the behavior of the bearing after initiation of motion

(beyond transition point I) when friction on surfaces 2 and 3 is unequal. The bearing is initially at rest and a lateral force is applied.

If moment equilibrium is disregarded and the resultant forces are assumed to act at the center of the contact surfaces, equilibrium of the rigid slider in the horizontal direction (see Figure 3-1 and consider $\theta_{si}=0$; see Figure 3-8(a) and (b)) requires that $S_2 + W\theta_2 = S_3 + W\theta_2$. Since the friction force S_2 is less than the friction force S_3 , a discrepancy arises. Considering full contact between the sliding surfaces, the motion must then start on surface 2 (of least friction) but not on surface 3 (of higher friction) and therefore it is necessary for the top concave plate to undergo significant free rotation as shown in Figure 3-8(c). This, of course, is not possible as the bearing is connected to a structure so that its top rotation is restrained.

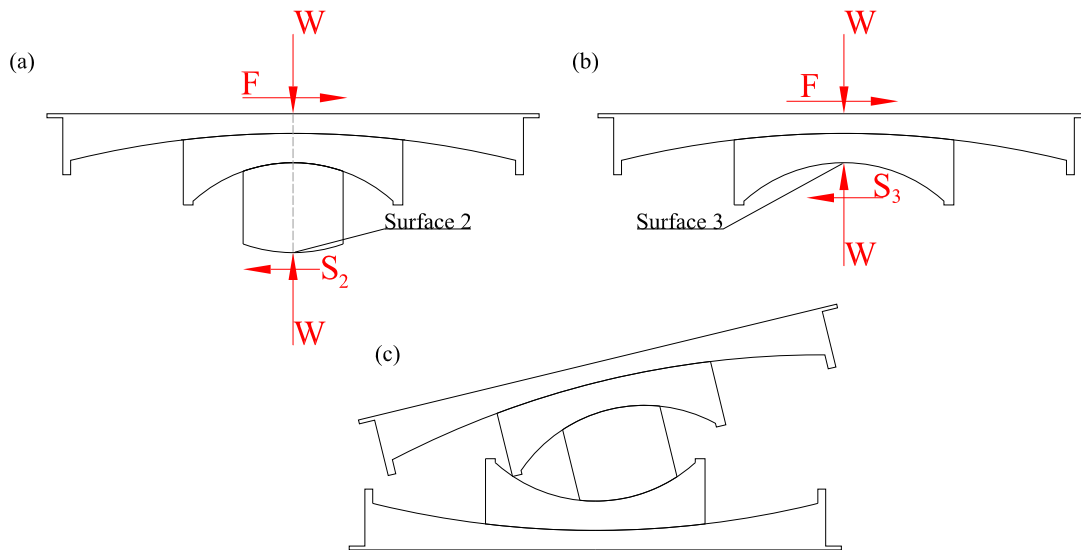


Figure 3-8: Triple FP bearing behavior when $S_2 < S_3$ and forces are assumed acting at center of each surface

The theory presented in this report predicts that motion will initiate when the lateral force reaches the value given by Equation (3-15) ($F = (\mu_2 R_2 + \mu_3 R_3) / (R_{eff2} + R_{eff3})$). The value of this force is larger than the least friction force S_2 and yet the bearing is motionless until the lateral force reaches a value larger than S_2 . This is possible because the points of application of the resultant forces on surfaces 2 and 3 move as lateral force F increases in magnitude (see Figure 3-9 (a) and (b)) so that equilibrium is possible in the horizontal direction. When the lateral force

reaches the value predicted by Equation (3-15), motion occurs on both surfaces 2 and 3 as shown in Figure 3-9(c). This is possible with the top bearing plate remaining horizontal.

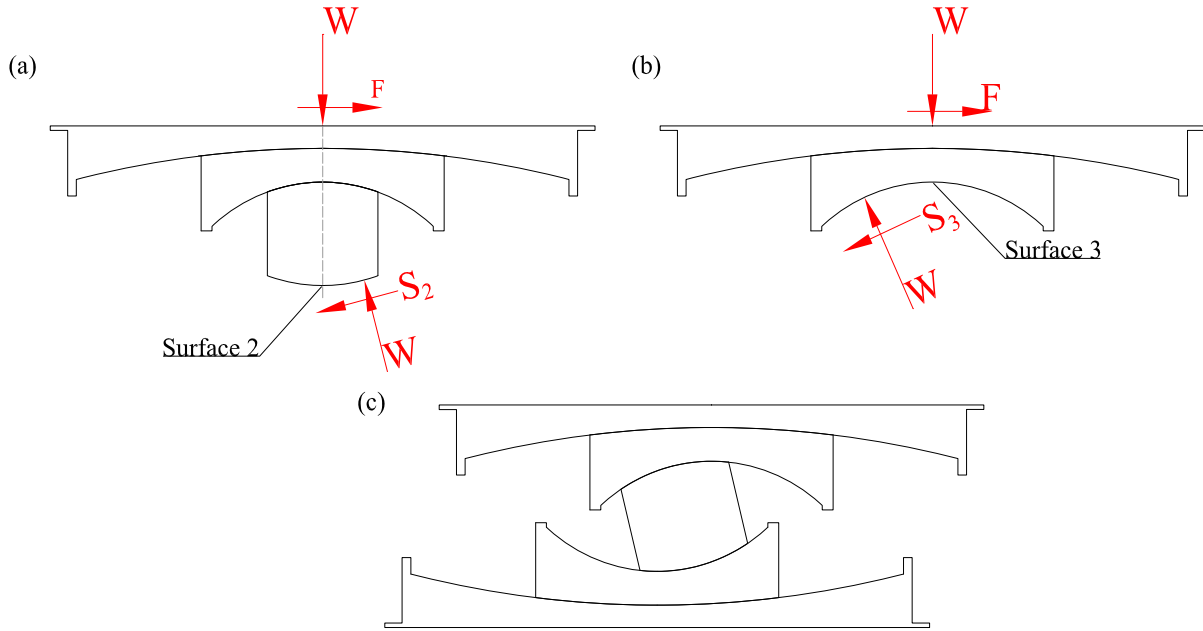


Figure 3-9: Triple FP bearing behavior when $S_2 < S_3$ and forces are assumed acting at a location determined by moment equilibrium

Another result of the current theory is that the displacement capacity of each sliding surface is smaller than d_i and given by:

$$d_i^* = d_i \frac{R_{effi}}{R_i} \quad (3-48)$$

Note that this was not recognized in Fenz and Constantinou (2008a to 2008e) but it was later recognized and corrected in Constantinou et al. (2011).

For the special case where $d_1 = d_4 > d_2 = d_3$, $R_1 = R_4 > R_2 = R_3$, the total displacement capacity of a Triple FP bearing is given by the sum of the displacement capacities of each sliding surface, that is:

$$u_{\max} = \sum_{i=1}^4 \frac{R_{effi}}{R_i} d_i \quad (3-49)$$

However, the total displacement capacity of the TFP bearing is not always the sum of the displacement capacities of its individual sliding surfaces. For an arbitrary combination of the bearing geometric and frictional properties, the total displacement capacity will be less than or equal to the one given by Equation (3-49). That is, Equation (3-49) provides an upper bound. An example is provided in Figure 3-10 where part (b) shows a bearing at maximum displacement. Any attempt to further deform the bearing will result in loss of full contact of the sliding surfaces and uplift of components.

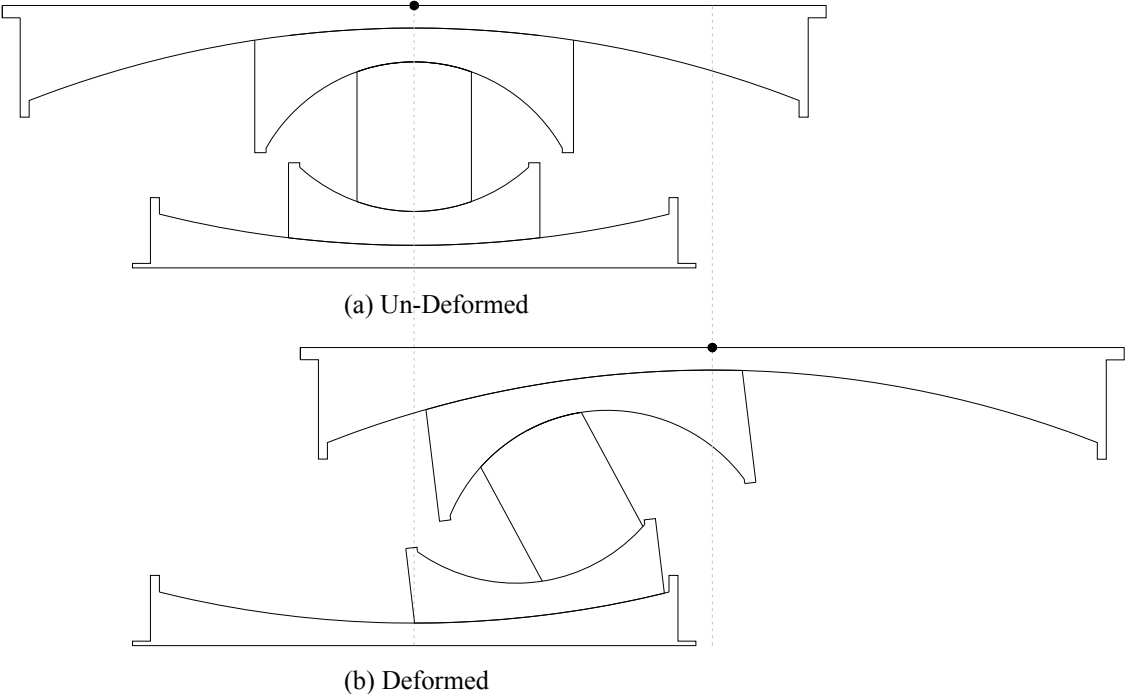


Figure 3-10: Triple FP bearing (a) un-deformed and (b) at maximum displacement

SECTION 4
MODELING TRIPLE FRICTION PENDULUM BEARINGS WITH SURFACES
IN FULL CONTACT FOR RESPONSE HISTORY ANALYSIS

4.1 Introduction

An element is developed that can be used in response history analysis of structures with Triple Friction Pendulum bearings. This element is valid for any combination of parameters of properties and can explicitly calculate the sliding displacement and velocities for each of the four surfaces. The formulation of the element allows for inclusion of the inertia effects of the moving parts of the bearing, different vertical load on each sliding surface due to the effect of self-weight of the components above each surface and variation in the values of the friction coefficient (as functions of sliding velocity, temperature and other parameters). Moreover, the element allows for the top and bottom concave plate to rotate and is capable of performing checks for the stability of the various components of the bearing that can facilitate its use for the analysis of uplift. Finally, with proper selection of geometry and friction parameters, the element is capable of modeling other friction pendulum isolators such as the Double FP with rigid slider, the Double FP with an articulated slider and the Single FP with an articulated slider. The model is restricted to isolators with a maximum of four sliding surfaces.

4.2 Equations of Motion Including Inertia Effects

The equations of motion of the Triple FP bearing are derived for one-directional motion on the basis of the free body diagrams of Figure 3-1 after inclusion of inertia effects. For clarity, Figure 3-1 is complemented by Figure 4-1 where the inertia forces, weights and additional parameters for the Triple FP parts are shown. Also, the normal force of each surface is now considered different and denoted W_i in order to account for the effect of the weight of the individual TFP components on the normal force of each surface (as shown in Figure 3-1). The normal force of each surface is now given by (assuming small angles of rotation and $\mu_i \theta_i \approx 0$):

$$\begin{aligned}
W_1 &= W + m_{TCP}g + m_{TSP}g + m_{RS}g + m_{BSP}g \\
W_2 &= W + m_{TCP}g + m_{TSP}g + m_{RS}g \\
W_3 &= W + m_{TCP}g + m_{TSP}g \\
W_4 &= W + m_{TCP}g
\end{aligned} \tag{4-1}$$

In Figure 4-1, F_{IBSP} , F_{IRS} , F_{ITSP} , F_{ITCP} are the inertia forces of the TFP individual components that act at the center of mass of each body, which is located at distances z_1 from surface 1 for the Bottom Slide Plate (BSP; see Figure 1-1), z_4 from contact surface 4 for the Top Slide Plate (TSP) and z_2 from contact surface 2 and z_3 from contact surface 3 for the Rigid Slider (RS). The inertia forces act in the tangential trajectory of each part. The radial components of the inertia forces are ignored (see Equation (4-1)). M_{IBSP} , M_{IRS} , M_{ITSP} , M_{ITCP} are the mass moments of inertia of the rigid parts BSP, RS, TSP and the Top Concave Plate (TCP) with masses m_{BSP} , m_{RS} , m_{TSP} , m_{TCP} , respectively. The mass moments of inertia can be calculated using the rotational mass moments of inertia I_{BSP} , I_{RS} , I_{TSP} and the rotational acceleration of each body, which can be calculated from double differentiation of rotations θ_1 for the BSP, $\theta_1 + \theta_2$ for the RS, $\theta_1 + \theta_2 - \theta_3$ for the TSP and $\theta_1 + \theta_2 - \theta_3 - \theta_4$ for the TCP. The latter is zero when the TCP is assumed horizontal and therefore the moment equilibrium equation for the top concave plate can be substituted with a constraint equation $\theta_1 + \theta_2 - \theta_3 - \theta_4 = 0$ together with $M_{ITCP} = 0$. Finally, Figure 4-1 shows the restrainer forces F_{ri} which were omitted for clarity in Figure 3-1.

The equilibrium and kinematic equations are presented in Equations (4-2) for the case of horizontal top concave plate (see equation (4-2)(h)). Note that these equations are combined ordinary differential and algebraic equations. Equations (a), (b), (c) and (g) are the horizontal equilibrium equations of the BSP, TSP, TCP and RS, respectively, and equations (d),(e) and (f) are the moment equilibrium equations of the RS, BSP, TSP, respectively. The moment equilibrium equation of the TCP is substituted by the constraint equation (h). It is noted, however, that the same results could have been obtained if moment equilibrium was used for the top concave plate assuming it is connected to a rotational spring that represents the stiffness of an element to which the bearing is connected.

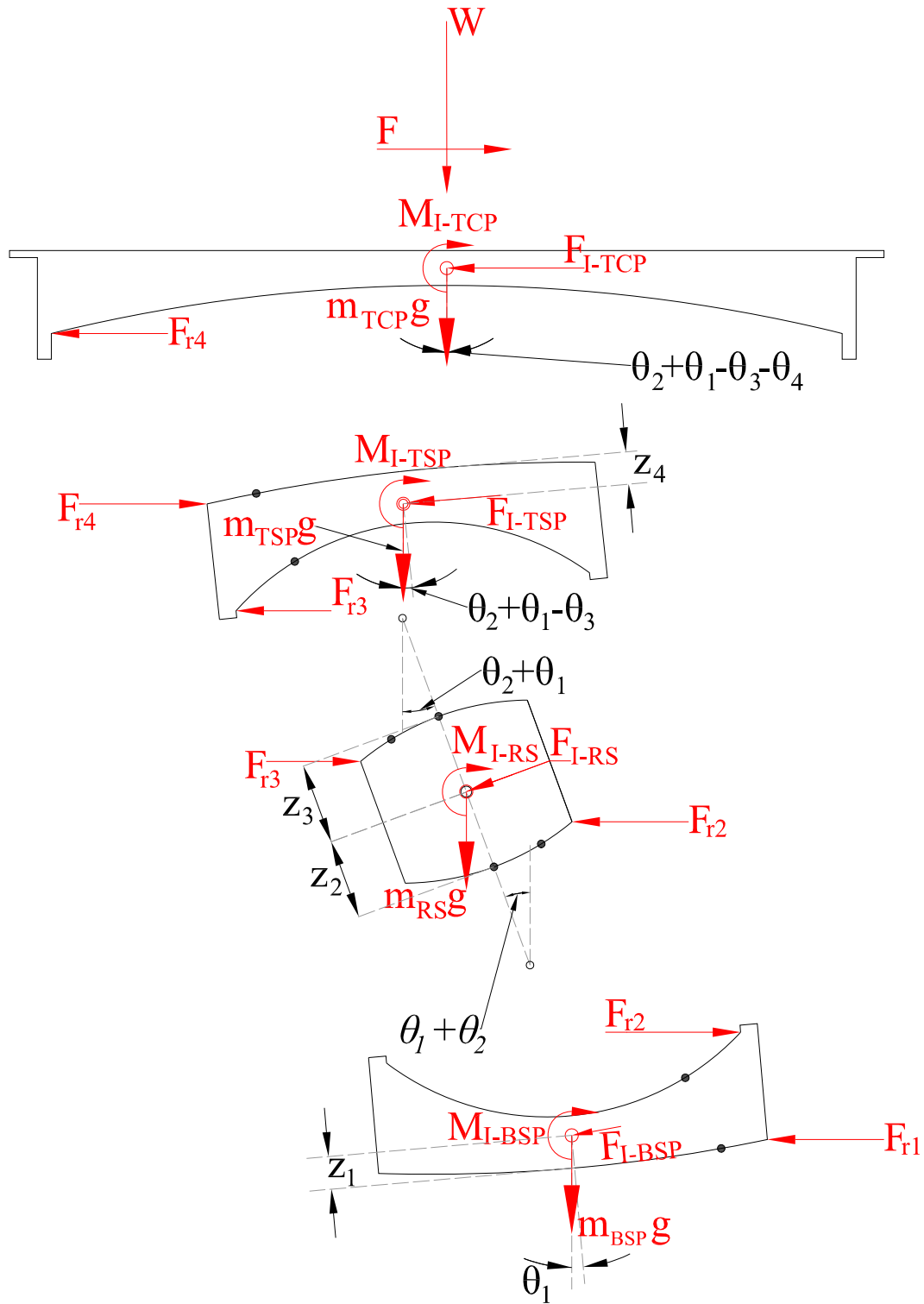


Figure 4-1: Free body diagrams of components of a Triple Friction Pendulum bearing including inertia effects

$$\begin{aligned}
\text{(a): } & W_2(\theta_1 + \theta_2 + \theta_{s2}) + S_2 - S_1 + F_{r2} - F_{r1} - W_1(\theta_1 + \theta_{s1}) - m_{BSP}(R_1 - z_1)\ddot{\theta}_1 - m_{BSP}\ddot{u}_g = 0 \\
\text{(b): } & W_3(\theta_1 + \theta_2 + \theta_{s3}) + S_3 - S_4 + F_{r3} - F_{r4} - W_4(\theta_1 + \theta_2 - \theta_3 + \theta_{s4}) + m_{TSP}(R_{eff1} - h_4 + z_4)\ddot{\theta}_1 + \\
& + m_{TSP}(R_{eff2} - h_4 + z_4)\ddot{\theta}_2 + m_{TSP}(R_{eff3} + h_4 - z_4)\ddot{\theta}_3 + m_{TSP}\ddot{u}_g = 0 \\
\text{(c): } & F - W_4(\theta_1 + \theta_2 - \theta_3 + \theta_{s4}) - S_4 - F_{r4} - m_{TCP}\ddot{u} - m_{TCP}\ddot{u}_g = 0 \\
\text{(d): } & W_2(\theta_{s2}R_2 + \theta_{s3}R_3) - W_2\theta_{s2}(h_2 + h_3) - S_2(h_2 + h_3) - F_{r2}(h_2 + h_3) \\
& - (I_{RS} + m_{RS}(R_{eff1} + h_2 - z_2)z_3)\ddot{\theta}_1 - (I_{RS} + m_{RS}(R_2 - z_2)z_3)\ddot{\theta}_2 \\
& - m_{RS}z_3\ddot{u}_g - m_{RS}g(\theta_1z_3 + \theta_2z_3 + \theta_{s3}R_3) = 0 \\
\text{(e): } & W_2(\theta_{s1}R_1 - \theta_2R_2 - \theta_{s2}R_2) - (h_1 - h_2)[W_2(\theta_{s2} + \theta_2) + S_2 + F_{r2}] - I_{BSP}\ddot{\theta}_1 \\
& + (m_{BSP}(R_1 - z_1)\ddot{\theta}_1 - m_{BSP}\ddot{u}_g)z_1 + m_{BSP}g(\theta_{s1}R_1 + \theta_1z_1) = 0 \\
\text{(f): } & W_3(\theta_{s4}R_4 - \theta_{s3}R_3 - \theta_3R_3) - (h_4 - h_3)[W_3(\theta_{s3} + \theta_3) + S_3 + F_{r3}] \\
& - m_{TSP}g(\theta_{s4}R_4 + (\theta_1 + \theta_2 - \theta_3)z_4) - I_{TSP}(\ddot{\theta}_1 + \ddot{\theta}_2 - \ddot{\theta}_3) \\
& - m_{TSP}z_4[(R_{eff1} - h_4 + z_4)\ddot{\theta}_1 + (R_{eff2} - h_4 + z_4)\ddot{\theta}_2 + (R_{eff3} + h_4 - z_4)\ddot{\theta}_3 + \ddot{u}_g] = 0 \\
\text{(g): } & W_2(\theta_1 + \theta_2 + \theta_{s2}) + S_2 + F_{r2} - W_3(\theta_1 + \theta_2 + \theta_{s3}) - S_3 - F_{r3} \\
& + m_{RS}(R_{eff1} + h_2 - z_2)\ddot{\theta}_1 + m_{RS}(R_2 - z_2)\ddot{\theta}_2 + m_{RS}\ddot{u}_g = 0 \\
\text{(h): } & \theta_1 + \theta_2 - \theta_3 - \theta_4 = 0 \\
\text{(j): } & u = \theta_1R_1 - (h_1 + h_4)\theta_1 + (R_2 - h_2 - h_4)\theta_2 + (R_3 + h_4 - h_3)\theta_3 + R_4\theta_4
\end{aligned} \tag{4-2}$$

The solution of combined differential and algebraic equations is complex so that the two kinematic equations given by (h) and (j) (both for the case of zero rotation of the bearing top plate) are used to eliminate sliding angles θ_3 and θ_4 . Specifically:

$$\begin{aligned}
\theta_4 &= \left(\frac{1}{R_{eff4} - R_{eff3}} \right) u - \left(\frac{R_{eff1} + R_{eff3}}{R_{eff4} - R_{eff3}} \right) \theta_1 - \left(\frac{R_{eff2} + R_{eff3}}{R_{eff4} - R_{eff3}} \right) \theta_2 \\
\theta_3 &= \frac{R_{eff1} + R_{eff4}}{R_{eff4} - R_{eff3}} \theta_1 + \frac{R_{eff2} + R_{eff4}}{R_{eff4} - R_{eff3}} \theta_2 - \frac{u}{R_{eff4} - R_{eff3}}
\end{aligned} \tag{4-3}$$

Substitution of Equations (4-3) into Equations (4-2(a)-(g)) results in the following:

$$\begin{aligned}
\text{(a): } & (W_2 - W_1)\theta_1 + W_2\theta_2 - W_1\theta_{s1} + W_2\theta_{s2} + S_2 - S_1 + F_{r2} - F_{r1} - m_{BSP}(R_1 - z_1)\ddot{\theta}_1 - m_{BSP}\ddot{u}_g = 0 \\
\text{(b): } & [W_3 + W_4C_4]\theta_1 + [W_3 + W_4C_5]\theta_2 - \frac{W_4}{R_{eff4} - R_{eff3}}u + W_3\theta_{s3} - W_4\theta_{s4} + S_3 - S_4 \\
& + F_{r3} - F_{r4} + m_{TSP}(R_4 - z_4)[C_4\ddot{\theta}_1 + C_5\ddot{\theta}_2] - m_{TSP}\left[\frac{C_0 - z_4}{C_1}\right]\ddot{u} + m_{TSP}\ddot{u}_g = 0 \\
\text{(c): } & F - W_4\left(\frac{1}{C_1}u - C_4\theta_1 - C_5\theta_2 + \theta_{s4}\right) - S_4 - F_{r4} - m_{TCP}\ddot{u} - m_{TCP}\ddot{u}_g = 0 \\
\text{(d): } & -m_{RS}gz_3(\theta_1 + \theta_2) + (R_{eff2} - h_3)W_2\theta_{s2} + R_3(W_2 - m_{RS}g)\theta_{s3} - S_2(h_2 + h_3) \\
& - F_{r2}(h_2 + h_3) - (I_{RS} + m_{RS}(R_{eff1} + h_2 - z_2)z_3)\ddot{\theta}_1 - (I_{RS} + m_{RS}(R_2 - z_2)z_3)\ddot{\theta}_2 \\
& - m_{RS}z_3\ddot{u}_g = 0 \\
\text{(e): } & m_{BSP}gz_1\theta_1 - W_2(R_{eff2} + h_1)\theta_2 + (W_2 + m_{BSP}g)R_1\theta_{s1} - W_2(R_{eff2} + h_1)\theta_{s2} \\
& - (h_1 - h_2)(S_2 + F_{r2}) + (m_{BSP}z_1(R_1 - z_1) - I_{BSP})\ddot{\theta}_1 - m_{BSP}\ddot{u}_gz_1 = 0 \\
\text{(f): } & (m_{TSP}gz_4C_4 - W_3C_0C_2)\theta_1 + (m_{TSP}gz_4C_5 - W_3C_0C_3)\theta_2 + \frac{W_3C_0 - m_{TSP}gz_4}{C_1}u \\
& - W_3C_0\theta_{s3} - (h_4 - h_2)(S_3 + F_{r3}) + (W_3 - m_{TSP}g)R_4\theta_{s4} - m_{TSP}z_4\ddot{u}_g \\
& + [I_{TSP} - m_{TSP}z_1(R_4 - z_4)](C_4\ddot{\theta}_1 + C_5\ddot{\theta}_2) + \left(\frac{m_{TSP}z_4(C_0 - z_4)}{C_1} - \frac{I_{TSP}}{C_1}\right)\ddot{u} = 0 \\
\text{(g): } & (W_2 - W_3)\theta_1 + (W_2 - W_3)\theta_2 + W_2\theta_{s2} - W_3\theta_{s3} + S_2 - S_3 + F_{r2} - F_{r3} + \\
& + m_{RS}(R_{eff1} + h_2 - z_2)\ddot{\theta}_1 + m_{RS}(R_2 - z_2)\ddot{\theta}_2 + m_{RS}\ddot{u}_g = 0 \\
& C_0 = R_{eff3} + h_4 \\
& C_1 = R_{eff4} - R_{eff3}, C_2 = \frac{R_{eff1} + R_{eff4}}{R_{eff4} - R_{eff3}}, C_3 = \frac{R_{eff2} + R_{eff4}}{R_{eff4} - R_{eff3}}, C_4 = \frac{R_{eff1} + R_{eff3}}{R_{eff4} - R_{eff3}}, C_5 = \frac{R_{eff2} + R_{eff3}}{R_{eff4} - R_{eff3}}
\end{aligned} \tag{4-4}$$

Equations (4-4) can be written in matrix form as:

$$\mathbf{M}\ddot{\boldsymbol{\theta}}_t + \mathbf{K}\boldsymbol{\theta}_t + \mathbf{S} + \mathbf{F}_g + \mathbf{F}_e = \mathbf{0} \tag{4-5}$$

In Equation (4-5), $\boldsymbol{\theta}_t$ is a vector containing the sliding and offset angles, and the displacement u of the top of the bearing, \mathbf{S} is a vector containing the friction forces, \mathbf{F}_g is a vector containing the restrainer forces and \mathbf{F}_e is a vector containing the excitation (input) terms. Vector $\boldsymbol{\theta}_t$ is given below together with sub-vectors $\boldsymbol{\theta}_s$ (offset angle vector) and $\boldsymbol{\theta}$ arising from partitioning vector $\boldsymbol{\theta}_t$:

$$\begin{aligned}\boldsymbol{\theta}_t &= [\theta_1 \quad \theta_2 \quad u \quad \theta_{s1} \quad \theta_{s2} \quad \theta_{s3} \quad \theta_{s4}] = [\boldsymbol{\theta} \quad \boldsymbol{\theta}_s] \\ \boldsymbol{\theta} &= [\theta_1 \quad \theta_2 \quad u]; \boldsymbol{\theta}_s = [\theta_{s1} \quad \theta_{s2} \quad \theta_{s3} \quad \theta_{s4}]\end{aligned}\quad (4-6)$$

Following the partitioning of vector $\boldsymbol{\theta}_t$, Equation (4-5) can be partitioned as follows:

$$\begin{bmatrix} \mathbf{M}_{aa} & \mathbf{M}_{ab} \\ \mathbf{M}_{ba} & \mathbf{M}_{bb} \end{bmatrix} \begin{Bmatrix} \ddot{\boldsymbol{\theta}} \\ \ddot{\boldsymbol{\theta}}_s \end{Bmatrix} + \begin{bmatrix} \mathbf{K}_{aa} & \mathbf{K}_{ab} \\ \mathbf{K}_{ba} & \mathbf{K}_{bb} \end{bmatrix} \begin{Bmatrix} \boldsymbol{\theta} \\ \boldsymbol{\theta}_s \end{Bmatrix} + \begin{Bmatrix} \mathbf{S}_a \\ \mathbf{S}_b \end{Bmatrix} + \begin{Bmatrix} \mathbf{F}_{ga} \\ \mathbf{F}_{gb} \end{Bmatrix} + \begin{Bmatrix} \mathbf{F}_{ea} \\ \mathbf{F}_{eb} \end{Bmatrix} = \mathbf{0}\quad (4-7)$$

Note that matrices \mathbf{M}_{ab} and \mathbf{M}_{bb} are nil so that Equations (4-7) may be written as:

$$\begin{aligned}\mathbf{M}_{aa} \ddot{\boldsymbol{\theta}} + \mathbf{K}_{aa} \boldsymbol{\theta} + \mathbf{K}_{ab} \boldsymbol{\theta}_s + \mathbf{S}_a + \mathbf{F}_{ga} + \mathbf{F}_{ea} &= \mathbf{0} \\ \mathbf{M}_{ba} \ddot{\boldsymbol{\theta}} + \mathbf{K}_{ba} \boldsymbol{\theta} + \mathbf{K}_{bb} \boldsymbol{\theta}_s + \mathbf{S}_b + \mathbf{F}_{gb} + \mathbf{F}_{eb} &= \mathbf{0}\end{aligned}\quad (4-8)$$

The second Equation in (4-8) can be solved with respect to the offset angle vector:

$$\boldsymbol{\theta}_s = \mathbf{K}_{bb}^{-1} (-\mathbf{F}_{eb} - \mathbf{F}_{gb} - \mathbf{S}_b - \mathbf{K}_{ba} \boldsymbol{\theta} - \mathbf{M}_{ba} \ddot{\boldsymbol{\theta}})\quad (4-9)$$

Substituting Equation (4-9) in the first Equation (4-8), one obtains the condensed equations of motion as:

$$\tilde{\mathbf{M}} \ddot{\boldsymbol{\theta}} + \tilde{\mathbf{K}} \boldsymbol{\theta} + \tilde{\mathbf{S}} + \tilde{\mathbf{F}}_g + \tilde{\mathbf{F}}_e = \mathbf{0}\quad (4-10)$$

Where the condensed vectors and matrices are given by:

$$\begin{aligned}\tilde{\mathbf{M}} &= \mathbf{M}_{aa} - \mathbf{K}_{ab} \mathbf{K}_{bb}^{-1} \mathbf{M}_{ba} \\ \tilde{\mathbf{K}} &= \mathbf{K}_{aa} - \mathbf{K}_{ab} \mathbf{K}_{bb}^{-1} \mathbf{K}_{ba} \\ \tilde{\mathbf{S}} &= \mathbf{S}_a - \mathbf{K}_{ab} \mathbf{K}_{bb}^{-1} \mathbf{S}_b \\ \tilde{\mathbf{F}}_g &= \mathbf{F}_{ga} - \mathbf{K}_{ab} \mathbf{K}_{bb}^{-1} \mathbf{F}_{gb} \\ \tilde{\mathbf{F}}_e &= \mathbf{F}_{ea} - \mathbf{K}_{ab} \mathbf{K}_{bb}^{-1} \mathbf{F}_{eb}\end{aligned}\quad (4-11)$$

The friction force S_i at sliding surface i is modeled using the following formulation, which is based on a modification of the Bouc-Wen model as implemented in program 3D-BASIS (Nagarajiah et al., 1989) (special case of $\beta=0$, $\gamma=1$ and $\eta=2$):

$$\begin{aligned}
S_i &= \mu_i W_i Z_i \\
\dot{Z}_i &= (R_i/Y)(1 - a_i Z_i^2) \dot{\theta}_i \\
a_i &= \begin{cases} 1, & \dot{\theta}_i Z_i > 0 \\ 0, & \dot{\theta}_i Z_i \leq 0 \end{cases}
\end{aligned} \tag{4-12}$$

Note that parameter Y is a ‘‘yield displacement’’ for use in the visco-plastic representation of the friction force. Y should have a small value, generally equal to or less than 1mm for full size bearings.

The coefficient of friction of surface i is considered to be velocity-dependent and assumed to follow the relation (Constantinou et al., 1990):

$$\mu_i = \mu_{fi} - (\mu_{fi} - \mu_{si}) e^{-a_i |v_i|} \tag{4-13}$$

Note that this model also allows for temperature dependence of the friction coefficient to be implemented. In that case, the following relation between the friction coefficient μ_i and the temperature T_i at the sliding interface is assumed for surface i :

$$\mu_i = \mu_{\min,i} + (\mu_{\max,i} - \mu_{\min,i}) e^{-a_h T_i} \tag{4-14}$$

In the above equation, the friction coefficient is equal to μ_{\max} when temperature rise is zero and decreases exponentially with rising temperature. It reaches the minimum value μ_{\min} when the temperature is approximately equal to $1/a_h$. Quantity a_h is the heating rate parameter.

The heat flux and temperature rise histories at each of the four sliding surfaces of the isolator are calculated based on the theory presented in Constantinou et al. (2007). For the calculation of the temperature rise, the heat flux is assumed to be supplied at the center of the sliding surface and given by:

$$Q_i(t) = \begin{cases} 0 & , \theta_i R_i > b_i / 2 \\ \frac{\mu_i W_i \dot{\theta}_i R_i}{A_i} & , \theta_i R_i < b_i / 2 \end{cases} \tag{4-15}$$

In Equation (4-15), A_i is the area of contact surface i ($i=1, 2, 3$ or 4) given by $(A_i = \pi b_i^2 / 4)$, and all other terms were previously defined. If a part of the bearing moves away from the center, the

heat flux is set to zero so that the heat flux is intermittent. The temperature rise at the center of the each surface is calculated by the following convolution integral (Constantinou et al., 2007):

$$T_i(t) = \frac{1}{k} \sqrt{\frac{D}{\pi}} \int_0^t \frac{Q_i(\tau)}{\sqrt{t-\tau}} d\tau \quad (4-16)$$

In Equation (4-16), D and k are the thermal conductivity and thermal diffusivity of the material (herein assumed to be that of stainless steel), respectively. The convolution integral in Equation (4-16) needs to be evaluated numerically and calculated at every integration step in order to update the friction coefficient based on Equation (4-14). However, such a procedure results in large execution times so that an approximate procedure can be used in which the convolution integral is evaluated at selected time steps.

The restrainer force F_{ri} of surface i is modeled as:

$$F_{ri} = \begin{cases} 0 & , |\theta_i| \leq d_i / R_i \\ k_{ri} (\theta_i - \text{sgn}(\theta_i) d_i / R_i) + c_{ri} \dot{\theta}_i & , |\theta_i| > d_i / R_i \end{cases} \quad (4-17)$$

In Equation (4-17), k_{ri} is the stiffness of the restrainer given from:

$$k_{ri} = \frac{\pi (t_{ri}^2 + s_i t_{ri}) F_{ry}}{6Y_r}, \quad i = 1, 4 \quad (4-18)$$

$$k_{ri} = \frac{1}{4} \frac{\pi (b_i^2 - s_i^2) t_{ri} F_{ry}}{6Y_r}, \quad i = 2; \quad k_{ri} = \frac{1}{4} \frac{\pi (b_4^2 - s_i^2) t_{ri} F_{ry}}{6Y_r}, \quad i = 3$$

Also, c_{ri} is an artificial damping constant assigned to the restrainer using an arbitrary damping ratio of $\zeta = 0.01$ (for most cases zero damping is recommended for the restrainers):

$$c_{ri} = \frac{4\pi^2 \zeta W}{gT^2} \quad (4-19)$$

Moreover, F_{ry} is the yield stress of the restrainer in shear (for the typical material used-ductile iron-is 172MPa), t_{ri} is the thickness of restrainer i shown in Figure 1-1 and s_i is the diameter of the sliding surface which is given by:

$$s_i = b_i + 2d_i \quad (4-20)$$

The stiffness value k_{ri} above is based on the shear strength of a 60-degree wedge of the restrainer ring divided by an arbitrary yield displacement Y_r (a value of 2.5mm may be used).

The restrainers have limited strength so that Equation (4-21) instead of Equation (4-17) may be used to model the restrainers. The equation is based on the assumption that brittle failure occurs when the shear stress reaches the limit F_{ry} . Energy dissipation is neglected. Note that Equation (4-21) distinguishes between left and right restrainers so that the failure of the restrainer on one side does not affect the failure of the restrainer on the opposite side.

$$F_{ri} = \begin{cases} 0, & |\theta_i| \leq d_i / R_i \\ k_{ri} (\theta_i - d_i / R_i) + c_{ri} \dot{\theta}_i, & \theta_i > d_i / R_i \text{ \& } |\max[\theta_i(0 \leq t \leq t_n)]| < d_i / R_i + \frac{F_{ry}}{k_{ri}} \\ k_{ri} (\theta_i + d_i / R_i) + c_{ri} \dot{\theta}_i, & \theta_i < -d_i / R_i \text{ \& } |\min[\theta_i(0 \leq t \leq t_n)]| < d_i / R_i + \frac{F_{ry}}{k_{ri}} \\ 0 & elsewhere \end{cases} \quad (4-21)$$

In the equation above, t_n is the time at the n -th integration step and $|\max \theta_i(0 \leq t \leq t_n)|$ denotes the absolute of the maximum value of the sliding angle from time zero up to the n -th integration step.

Sliding angles θ_3 and θ_4 are required in Equations (4-15), (4-17) and (4-21) but are not directly available. Rather, Equations (4-3) are used to calculate these quantities using the known values of angles θ_1 and θ_2 . Also, velocities $\dot{\theta}_3$ and $\dot{\theta}_4$ of surfaces 3 and 4 are required in Equations (4-12) to (4-15) and (4-17), (4-21). These quantities are obtained by differentiation of Equations (4-3) using the known values of $\dot{\theta}_1$, $\dot{\theta}_2$ and \dot{u} .

The equations are written in state space form after defining vector $\mathbf{Q} = [\boldsymbol{\theta} \quad \dot{\boldsymbol{\theta}} \quad \mathbf{Z}]^T$ so that Equations (4-10) and (4-12) take the form:

$$\frac{d\mathbf{Q}}{dt} = \frac{d}{dt} \begin{Bmatrix} \boldsymbol{\theta} \\ \dot{\boldsymbol{\theta}} \\ \mathbf{Z} \end{Bmatrix} = \begin{Bmatrix} \dot{\boldsymbol{\theta}} \\ -\tilde{\mathbf{M}}^{-1} \tilde{\mathbf{K}} \boldsymbol{\theta} - \tilde{\mathbf{M}}^{-1} \tilde{\mathbf{S}} - \tilde{\mathbf{M}}^{-1} \tilde{\mathbf{F}} \\ \dot{\mathbf{Z}} \end{Bmatrix} \quad (4-22)$$

All equations above have been derived assuming that a force is applied at the top of the bearing and a ground acceleration history \ddot{u}_g is applied at the bottom of the bearing. When the element is used in the dynamic analysis of a seismically isolated structure, force $F = 0$ and Equation (4-22) needs to be combined with the equations of motion of the superstructure. In the case that the element is used for the analysis of a single bearing under the action of a known lateral force F , the ground motion is zero.

4.3 Triple Friction Pendulum Element for Analysis in Prescribed Motion (Displacement Controlled Test)

An interesting problem is to specify arbitrary geometric and frictional properties of a Triple FP bearing, the vertical load on the bearing and the lateral displacement history of the top of the bearing, and to calculate the force-displacement relation of the bearing and the motion of its components. In this case, the lateral force F is unknown and needs to be included in the vector of unknowns- θ . Analysis starts with Equations (4-4) and (4-5), a zero ground acceleration history \ddot{u}_g is used, and the now enhanced vector θ_t is partitioned to remove displacement u and include force F :

$$\begin{aligned} \theta_t &= [\theta_1 \quad \theta_2 \quad F \quad \theta_{s1} \quad \theta_{s2} \quad \theta_{s3} \quad \theta_{s4}] = [\theta \quad \theta_s] \\ \theta &= [\theta_1 \quad \theta_2]; \theta_s = [F \quad \theta_{s1} \quad \theta_{s2} \quad \theta_{s3} \quad \theta_{s4}] \end{aligned} \quad (4-23)$$

Note that displacement u and its derivatives are now known and are included in the excitation vector \mathbf{F}_e . After partitioning, the condensation procedure and the reduction to state-space formulation are performed starting from Equations (4-5) and proceeding to Equations (4-7) to (4-11) and (4-22), as described in Section 4.2. Note that in the formulation presented above, the bearing top rotation is zero (horizontal top concave plate).

4.4 Analysis for Non-Zero Top Concave Plate and Bottom Concave Plate Rotation

In this section, we extend the model presented in Section 4.2 to capture the effect of rotations of the TCP and BCP. This model will be useful in modeling the effects of misalignments of the top and bottom plates, and the effects of rotations caused by elements connected above and below the isolator (e.g., a bridge pier).

Consider that the top and bottom concave plates are not horizontal but have rotation θ_c for the TCP and θ_b for the BCP. These rotations can either be constant (misalignments), or varying with time either as imposed excitation or due to the motion of a flexible element connected to the top or the bottom of the TFP. The geometry of the deformed isolator with nonzero top and bottom concave plate rotations is shown in Figure 4-2 below.

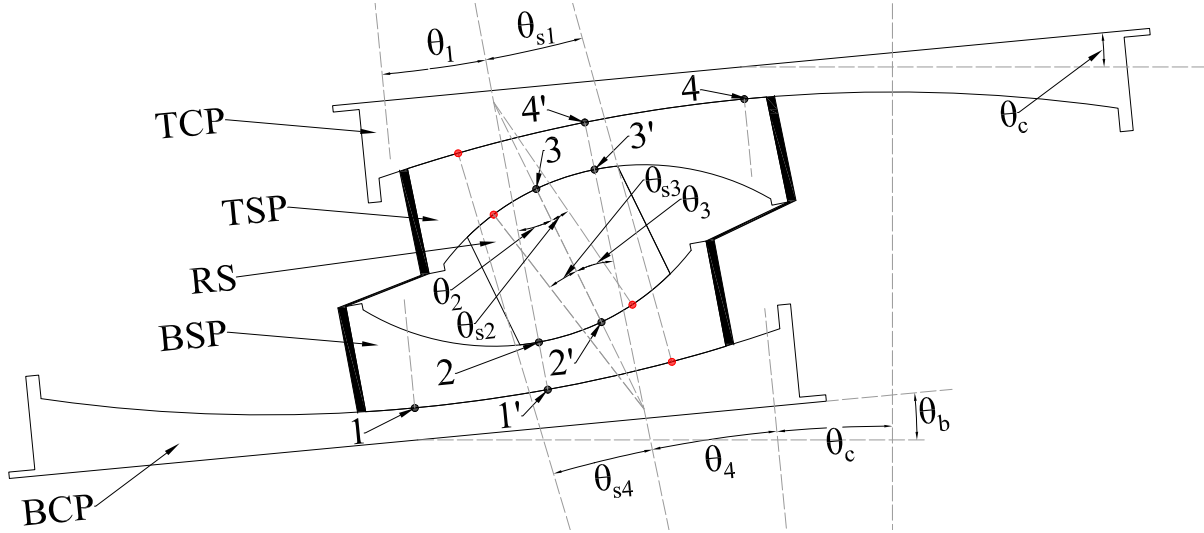


Figure 4-2: TFP isolator with rotated top and bottom concave plates

Equations (4-4) are extended to account for this new geometry. The compatibility equations are now given by:

$$\begin{aligned} \theta_1 + \theta_2 + \theta_b - \theta_3 - \theta_4 - \theta_c &= 0 \\ u &= \theta_1 (R_{eff1} - h_4 - t_{co}) + (R_{eff2} - h_4 - t_{co}) \theta_2 + (R_{eff3} + h_4 + t_{co}) \theta_3 \\ &\quad + (R_4 + t_{co}) \theta_4 - (h_1 + h_4 + t_{co}) \theta_b \end{aligned} \quad (4-24)$$

Solution of Equations (4-24) for θ_3 and θ_4 , result in:

$$\begin{aligned} \theta_3 &= -\frac{u}{R_{eff4} - R_{eff3}} + \frac{R_{eff1} + R_{eff4}}{R_{eff4} - R_{eff3}} \theta_1 + \frac{R_{eff2} + R_{eff4}}{R_{eff4} - R_{eff3}} \theta_2 + \frac{R_{eff4} - h_1 - t_{co}}{R_{eff4} - R_{eff3}} \theta_b - \frac{R_4 + t_{co}}{R_{eff4} - R_{eff3}} \theta_c \\ \theta_4 &= \frac{u}{R_{eff4} - R_{eff3}} - \frac{R_{eff1} + R_{eff3}}{R_{eff4} - R_{eff3}} \theta_1 - \frac{R_{eff2} + R_{eff3}}{R_{eff4} - R_{eff3}} \theta_2 + \frac{h_1 - R_{eff3} + t_{co}}{R_{eff4} - R_{eff3}} \theta_b + \frac{R_{eff3} + h_4 + t_{co}}{R_{eff4} - R_{eff3}} \theta_c \end{aligned} \quad (4-25)$$

The equilibrium equations now have to be re-written by accounting for the rotated BCP and TCP. They are given below after use of Equations (4-25).

$$\begin{aligned}
\text{(a): } & (W_2 - W_1)\theta_1 + W_2\theta_2 - W_1\theta_{s1} + W_2\theta_{s2} + S_2 - S_1 + F_{r2} - F_{r1} - m_{BSP}(R_1 - z_1)\ddot{\theta}_1 - m_{BSP}\ddot{u}_g \\
& (W_2 - W_1)\theta_b = 0 \\
\text{(b): } & [W_3 + W_4C_4]\theta_1 + [W_3 + W_4C_5]\theta_2 - \frac{W_4}{R_{eff4} - R_{eff3}}u + W_3\theta_{s3} - W_4\theta_{s4} + S_3 - S_4 \\
& + F_{r3} - F_{r4} + m_{TSP}(R_4 - z_4)[C_4\ddot{\theta}_1 + C_5\ddot{\theta}_2] - m_{TSP}\left[\frac{C_0 - z_4}{C_1}\right]\ddot{u} + m_{TSP}\ddot{u}_g \\
& (W_3 - W_4)\theta_b + W_4H_1\theta_b + W_4H_2\theta_c = 0 \\
\text{(c): } & F - W_4\left(\frac{1}{C_1}u - C_4\theta_1 - C_5\theta_2 + \theta_{s4}\right) - S_4 - F_{r4} - m_{TCP}\ddot{u} - m_{TCP}\ddot{u}_g \\
& - W_4\theta_b + W_4H_1\theta_b + W_4H_2\theta_c = 0 \\
\text{(d): } & -m_{RS}gz_3(\theta_1 + \theta_2) + (R_{eff2} - h_3)W_2\theta_{s2} + R_3(W_2 - m_{RS}g)\theta_{s3} - S_2(h_2 + h_3) \\
& - F_{r2}(h_2 + h_3) - (I_{RS} + m_{RS}(R_{eff1} + h_2 - z_2)z_3)\ddot{\theta}_1 - (I_{RS} + m_{RS}(R_2 - z_2)z_3)\ddot{\theta}_2 \\
& - m_{RS}z_3\ddot{u}_g - m_{RS}gz_3\theta_b = 0 \\
\text{(e): } & m_{BSP}gz_1\theta_1 - W_2(R_{eff2} + h_1)\theta_2 + (W_2 + m_{BSP}g)R_1\theta_{s1} - W_2(R_{eff2} + h_1)\theta_{s2} \\
& - (h_1 - h_2)(S_2 + F_{r2}) + (m_{BSP}z_1(R_1 - z_1) - I_{BSP})\ddot{\theta}_1 - m_{BSP}\ddot{u}_gz_1 + m_{BSP}gz_1\theta_b = 0 \\
\text{(f): } & (m_{TSP}gz_4C_4 - W_3C_0C_2)\theta_1 + (m_{TSP}gz_4C_5 - W_3C_0C_3)\theta_2 + \frac{W_3C_0 - m_{TSP}gz_4}{C_1}u \\
& - W_3C_0\theta_{s3} - (h_4 - h_2)(S_3 + F_{r3}) + (W_3 - m_{TSP}g)R_4\theta_{s4} - m_{TSP}z_4\ddot{u}_g \\
& + [I_{TSP} - m_{TSP}z_1(R_4 - z_4)](C_4\ddot{\theta}_1 + C_5\ddot{\theta}_2) + \left(\frac{m_{TSP}z_4(C_0 - z_4)}{C_1} - \frac{I_{TSP}}{C_1}\right)\ddot{u} \\
& + [-W_3H_1(h_4 - h_3) - m_{TSP}gz_4 - H_1(R_3W_3 - m_{TSP}gz_4)]\theta_b \\
& + [-W_3H_2(h_4 - h_3) - H_2(R_3W_3 - m_{TSP}gz_4)]\theta_c = 0 \\
\text{(g): } & (W_2 - W_3)\theta_1 + (W_2 - W_3)\theta_2 + W_2\theta_{s2} - W_3\theta_{s3} + S_2 - S_3 + F_{r2} - F_{r3} + \\
& + m_{RS}(R_{eff1} + h_2 - z_2)\ddot{\theta}_1 + m_{RS}(R_2 - z_2)\ddot{\theta}_2 + m_{RS}\ddot{u}_g + (W_2 - W_3)\theta_b = 0 \\
\end{aligned} \tag{4-26}$$

$$\begin{aligned}
C_0 &= R_{eff3} + h_4 \\
C_1 &= R_{eff4} - R_{eff3}, C_2 = \frac{R_{eff1} + R_{eff4}}{R_{eff4} - R_{eff3}}, C_3 = \frac{R_{eff2} + R_{eff4}}{R_{eff4} - R_{eff3}}, C_4 = \frac{R_{eff1} + R_{eff3}}{R_{eff4} - R_{eff3}}, C_5 = \frac{R_{eff2} + R_{eff3}}{R_{eff4} - R_{eff3}} \\
H_1 &= \frac{R_{eff4} - h_1 - t_{co}}{R_{eff4} - R_{eff3}}, H_2 = \frac{-R_4 - t_{co}}{R_{eff4} - R_{eff3}}
\end{aligned}$$

This model can be used in several ways depending on the nature of the BCP and TCP rotations:

1. If θ_b, θ_c are misalignments (assumed constant), or known histories of time, then all terms involving θ_b and θ_c should be included in the excitation vector \mathbf{F}_e .
2. If θ_b results from the connection of the BCP to a flexible element below the isolator (e.g., a bridge pier), rotation θ_b must be included as a degree of freedom. In doing so, in addition to Equations (4-26), horizontal and moment equilibrium equation of the bottom concave plate needs to be included in the analysis. Rotation θ_b is then included as a degree of freedom in vector $\boldsymbol{\theta}$ in Equation (4-6). In this case, the P- Δ moment that is transferred by the isolator to the structure below is given by:

$$M_{BCP} = W_1 (\theta_1 + \theta_{s1}) (R_1 + t_{co}) + (F_{g1} + S_1) t_{co} \quad (4-27)$$

3. If θ_c results from the connection of the TCP to a flexible element above the isolator, rotation θ_c needs again to be included as a degree of freedom. However, the procedure to do this is different than in the case of the bottom concave plate rotation. The first of Equations (4-24) needs to be substituted by the moment equilibrium equation of the TCP and included together with the remaining TFP equilibrium equations. The moment transferred by the isolator to the structure above is given by:

$$M_{TCP} = W_4 (\theta_4 + \theta_{s4}) (R_4 + t_{co}) + (F_{g4} + S_4) t_{co} \quad (4-28)$$

The condensation procedure and the reduction to state-space formulation is identical to the one performed based on Equations (4-7) to (4-11) and (4-22) as described in Section 4.2.

4.5 Verification of Triple Friction Pendulum Bearing Element

Examples are presented for the bearing configurations presented in Table 3-2. Force-displacement loops and angle-displacement loops obtained by the hysteretic element are compared to the results of the algebraic models developed in Section 3. For the comparison, any velocity dependence of the coefficients of friction is ignored and the masses of the moving parts of the bearing are made very small so that their inertia and weight effects are effectively eliminated. Note that in the presented results, the lateral force is normalized by the constant

vertical load on the bearing (W), the lateral displacement, in some graphs, is normalized by the bearing displacement capacity (Equation (4-1)), the offset angles are normalized by the offset angle capacities $\theta_{si,max}$ and the sliding angles are normalized by the sliding angle capacities $\theta_{i,max}$.

The angle capacities are given by:

$$\theta_{si,max} = \frac{b_i}{2R_i} \quad (4-29)$$

$$\theta_{i,max} = \frac{d_i}{R_i} \quad (4-30)$$

In these equations, b_i is the diameter of contact surface i defined as the one of least diameter out of the two in contact (see Figure 1-1). Note that if $|\theta_{si,max}| \geq \theta_{si,max}$, point contact occurs and the reader is referred to the theory presented in Section 6 to better describe this case.

Figure 4-3 compares results for the case of the model scale bearing of Configuration A (Table 3-2). Figure 4-4 compares results for the case of the model scale bearing of Configuration B (Table 3-2). Figure 4-5 compares results for the case of the full scale bearing of Configuration A with unequal friction at surfaces 2 and 3 (Table 3-2), and Figure 4-6 compares results for the full scale Configuration B. Results are almost identical in all cases.

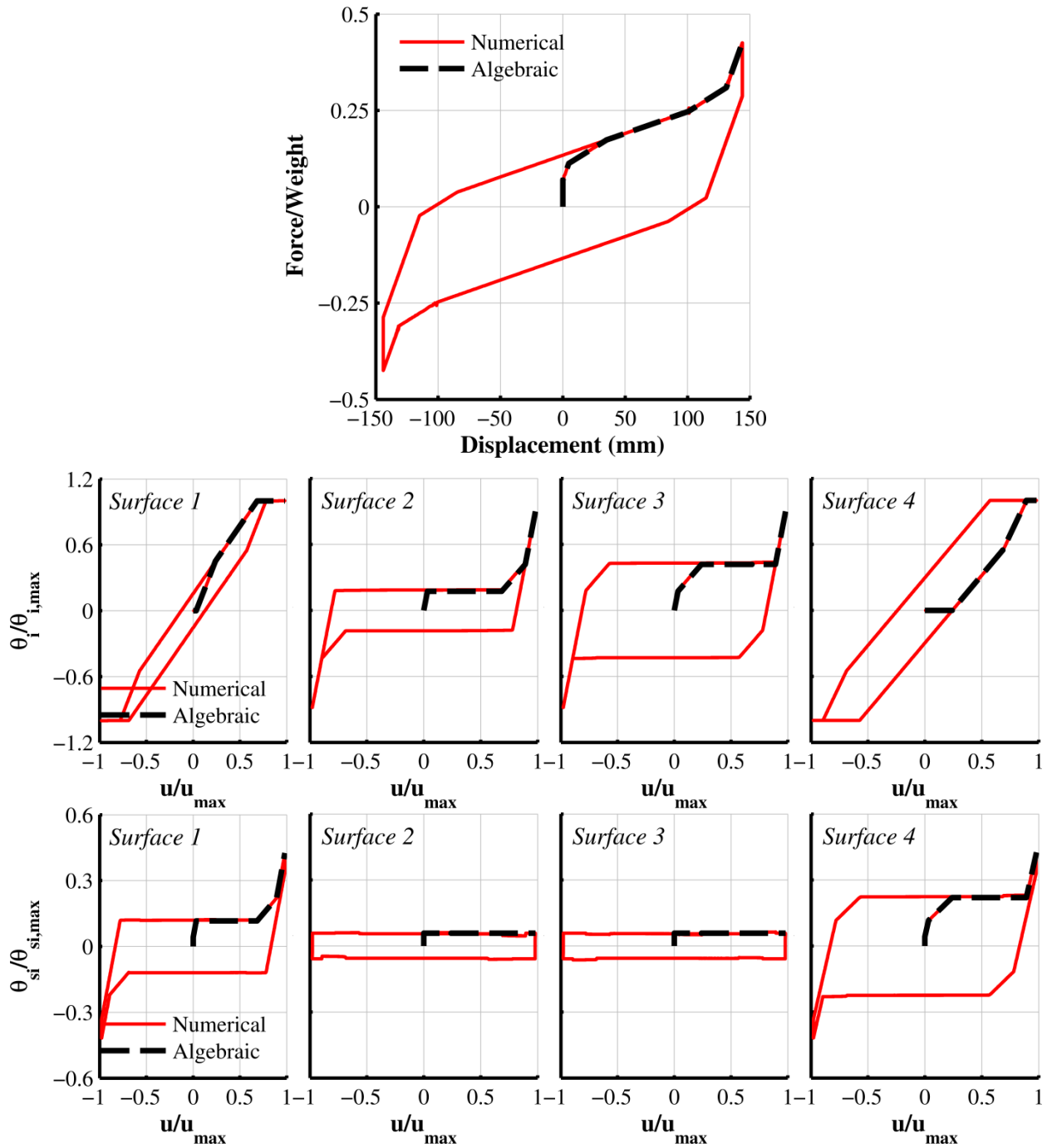


Figure 4-3: Comparison of results obtained using algebraic equations of Section 3 and the hysteretic element of Section 4 for model scale bearing-A with $\mu_1 = 0.1, \mu_2 = \mu_3 = 0.05, \mu_4 = 0.15$

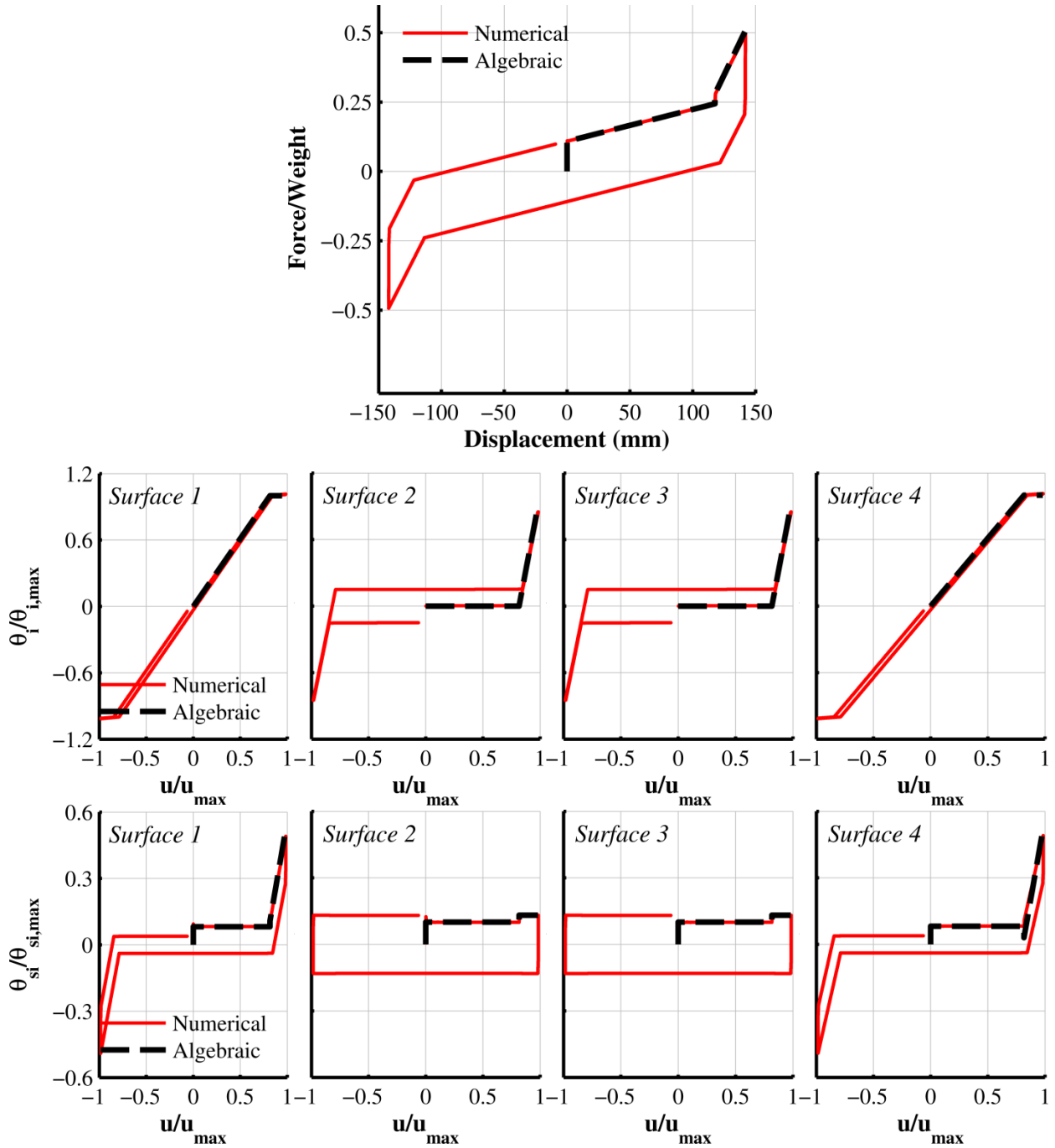


Figure 4-4: Comparison of results obtained using algebraic equations of Section 3 and the hysteretic element of Section 4 for model scale bearing-B with $\mu_1 = \mu_2 = \mu_3 = \mu_4 = 0.1$

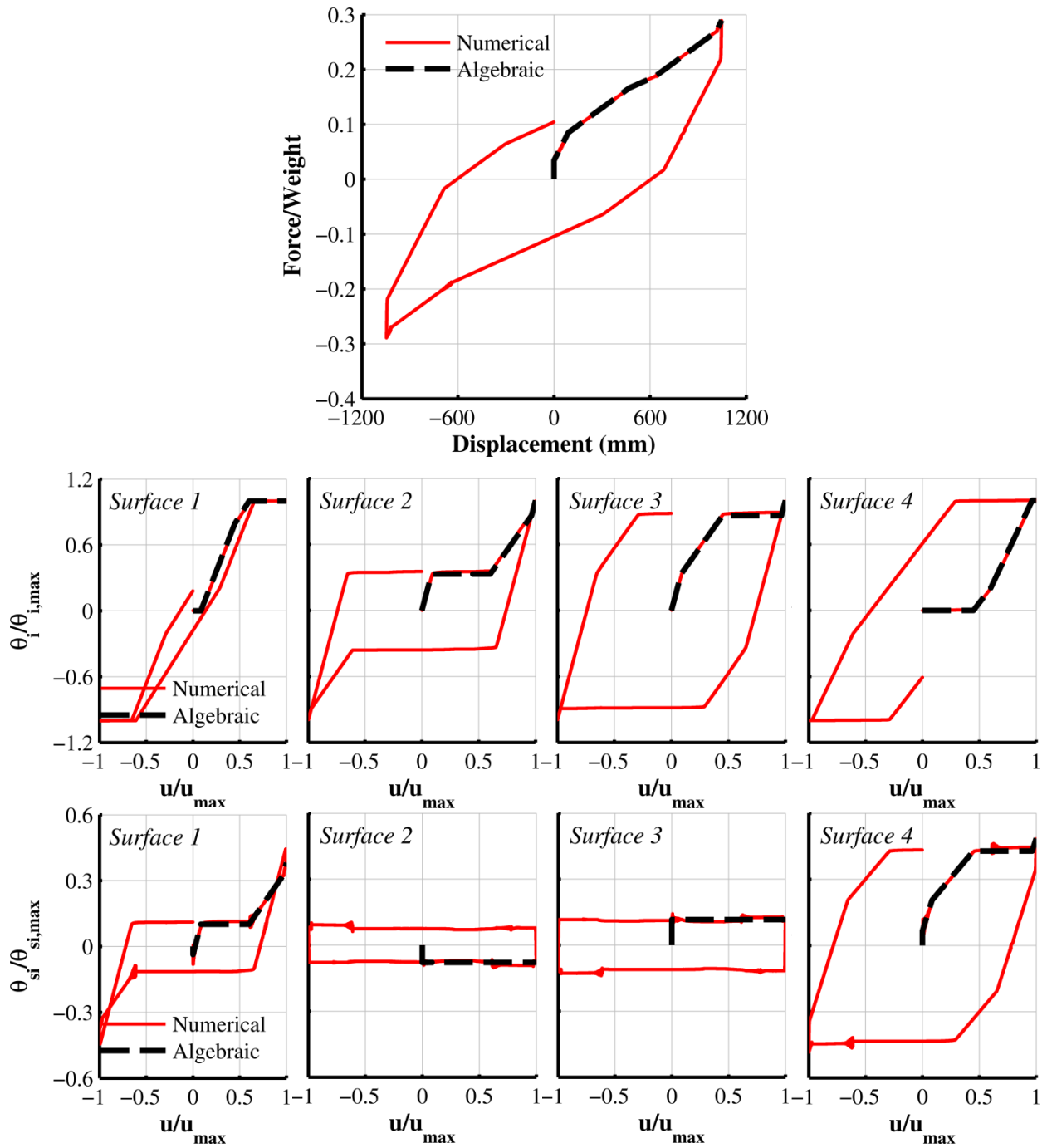


Figure 4-5: Comparison of results obtained using algebraic equations of Section 3 and the hysteretic element of Section 4 for full scale bearing-A with $\mu_1 = 0.075, \mu_2 = 0.05, \mu_3 = 0.01, \mu_4 = 0.125$

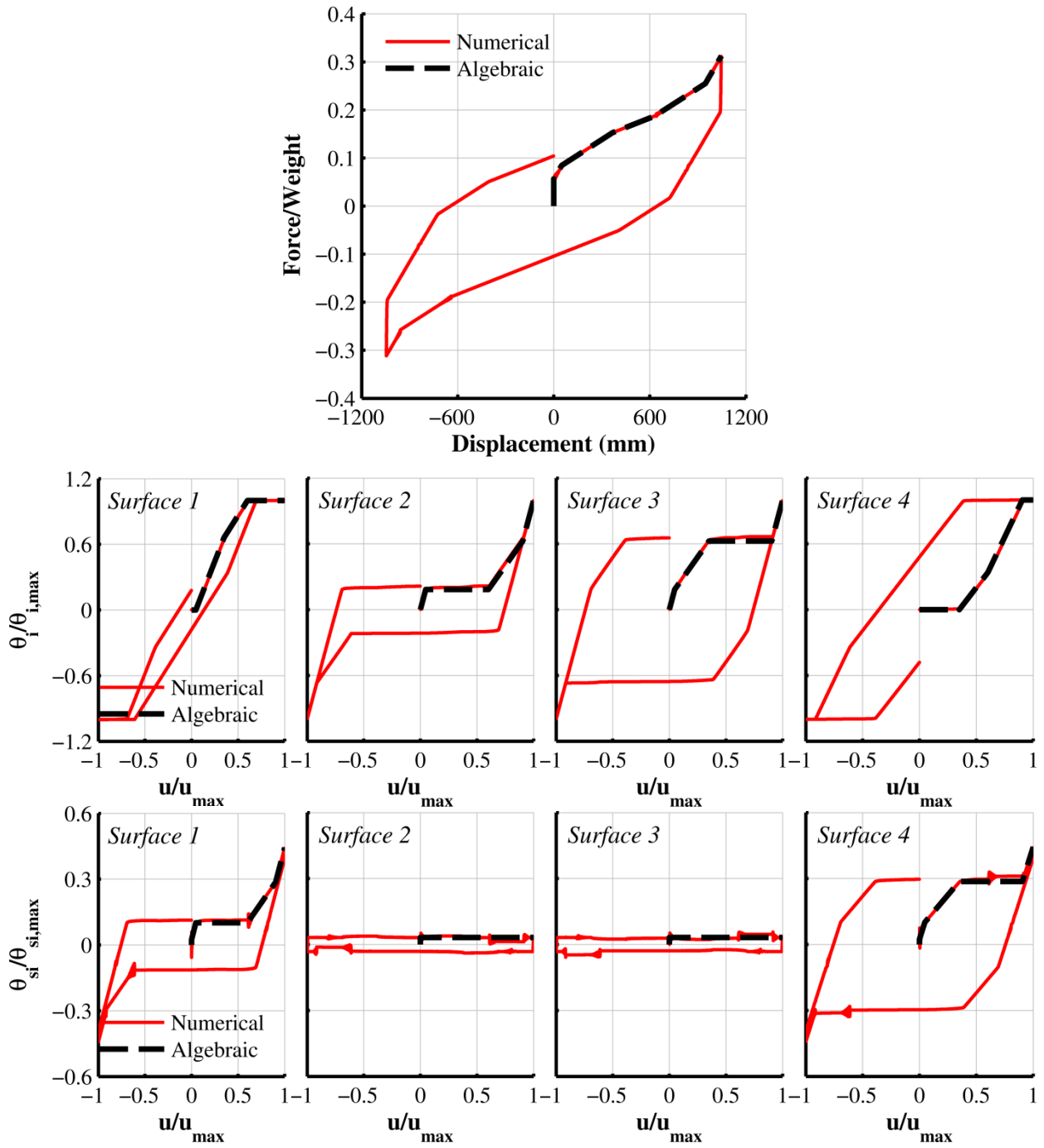


Figure 4-6: Comparison of results obtained using algebraic equations of Section 3 and the hysteretic element of Section 4 for full scale bearing-B with $\mu_1 = 0.075, \mu_2 = \mu_3 = 0.05, \mu_4 = 0.125$

4.6 Comparison of Current Model to the Fenz and Constantinou Series Model

The series model (Fenz and Constantinou, 2008d) is capable of modeling the behavior of triple FP bearings in all regimes of operation provided that the basic assumptions of the Fenz and Constantinou theory ($\mu_2 = \mu_3 < \mu_1 \leq \mu_4$) apply. Herein we compare predictions of the dynamic response of a rigid mass supported on Triple FP bearings using the developed hysteretic model and the series model. The series model has been implemented in program SAP2000 (Computers and Structures, 2007; Fenz and Constantinou 2008c, Sarlis and Constantinou, 2010). The current model has been programmed in MATLAB. For proper comparison, the inertia effects and the weight of the bearing components have been neglected in the current model (artificially small mass and weight values were assigned) as these effects are not accounted for in the series model. Also, any velocity effect on the coefficient of friction has not been modeled in either of the two models because the series model can only approximately determine the sliding displacement and velocity on each surface. The inertia effects are known to have minor or insignificant effects on the force-displacement loops provided that the bearing is not close to or experiencing uplift.

A rigid weight of 1500kN is supported by Triple FP bearings having the geometric and frictional properties of the full scale bearing of Table 3-2. The seismic excitation used consists of one-directional horizontal component the ground motion shown in Figure 4-7.

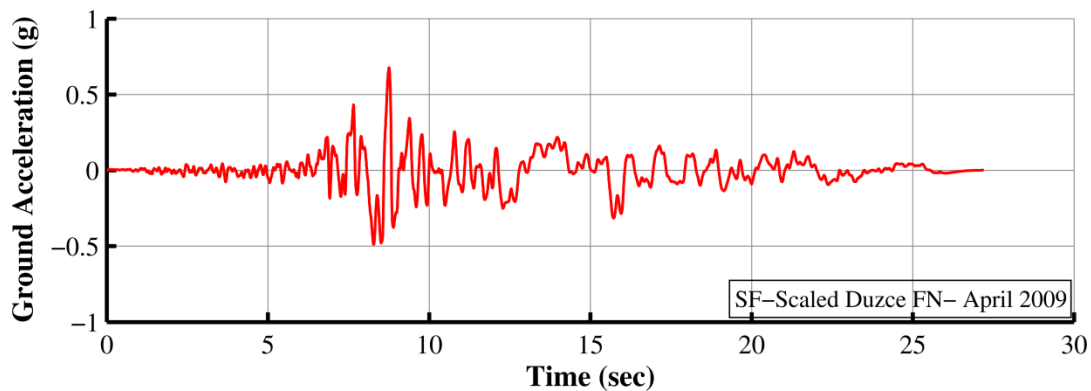


Figure 4-7: Ground motion used for the analysis of SDOF system isolated with TFP

Figure 4-8 compares the predictions of the two analyses in terms of the force-displacement loop using the two models for the case of the full scale bearing of Table 3-2, case A with $\mu_2 = 0.05, \mu_3 = 0.01$. This case cannot be analyzed by the series model so that a compromise is

made and analysis is performed, only for the series model, using $\bar{\mu}_2 = \bar{\mu}_3 = 0.0339$, which is the average of the two friction values multiplied by the ratio of radii to effective radii. Again in the case of the series model, the friction coefficient is interpreted as $\bar{\mu}_i$ in Table 3-2 and displacement capacities are defined as $d_i^* = d_i(R_i - h_i) / R_i$. The results for this case differ but are very close. Figure 4-9 compares the predictions of the two models in terms of the force-displacement loop for the case of the full scale bearing of Table 3-2, case B with $\mu_2 = 0.05, \mu_3 = 0.05$. The results for this case are essentially the same.

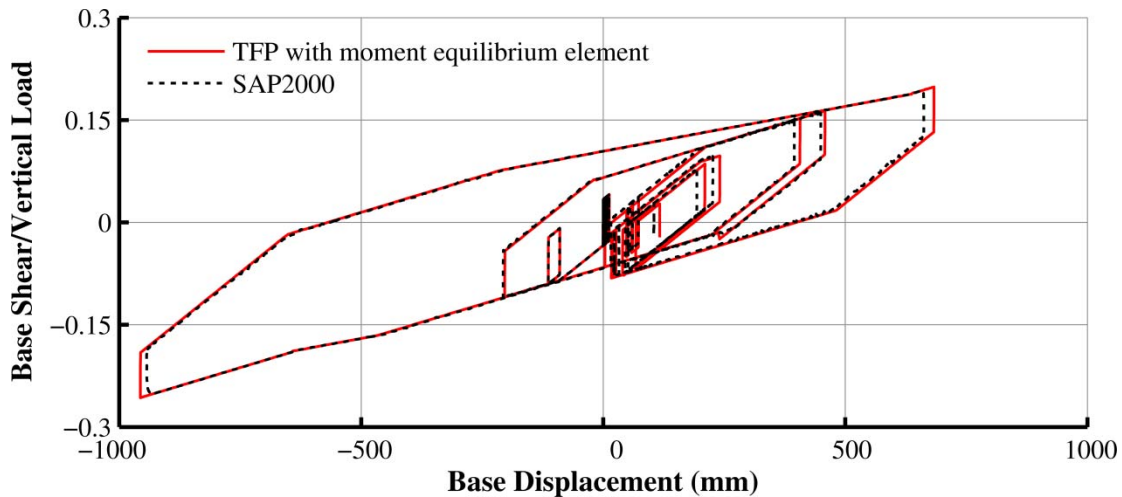


Figure 4-8: Comparison of results obtained by the series model in SAP2000 and the hysteretic model in MATLAB for the full scale bearing of Table 3-2, case A and $\mu_2 \neq \mu_3$

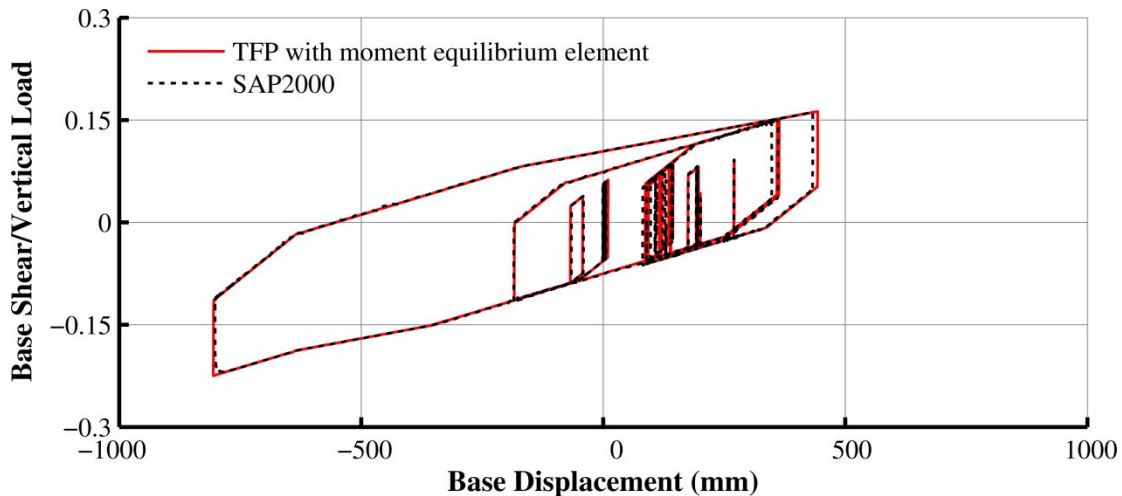


Figure 4-9: Comparison of results obtained by the series model in SAP2000 using $\mu_2 = \mu_3 = 0.03$ and the hysteretic model in MATLAB using $\mu_2 = 0.05, \mu_3 = 0.01$ for the full scale bearing of Table 3-2, case B and $\mu_2 = \mu_3 = 0.05$

4.7 Effect of Initial Offsets on TFP Behavior

The TFP isolators may exhibit two types of permanent displacements:

- a) Isolation system permanent displacement, in which there is the offset between the top and bottom concave plates of the bearing.
- b) Internal component permanent displacements. These permanent displacements always occur even in the absence of isolation system permanent displacements.

The models of Section 4.2 to 4.4 are able to account for initial offsets of the TFP. The TFP model makes use of three degrees of freedom (θ_1 , θ_2 and u) when used for response history analysis and two degrees of freedom (θ_1 and θ_2) when used for prescribed displacement applied at the TCP (displacement controlled test). In order to describe the TFP initial conditions, exactly three out of five (θ_1 , θ_2 , θ_3 , θ_4 and u) variables need to be known. In case the desired degrees of freedom are not directly known, they can be calculated using Equations (4-3) after substituting for the known initial conditions. The others are determined by the conditions of compatibility. Note that in doing so only compatibility is satisfied but not equilibrium. As a consequence, at the first integration step, new values will have to be calculated in order to satisfy equilibrium.

Figure 4-11 compares the response of a Triple FP bearing having the geometric and frictional properties of the Full Scale Bearing-Configuration B shown in Table 3-2 for two different cases of initial conditions shown in Figure 4-10. For both cases, the initial TCP displacement is zero. The bearing is subjected to two different displacement amplitude motions. The force-displacement loops of the TFP are only affected during the first quarter cycle when the internal parts are re-aligned and, thereafter, the behavior is no longer affected. Also note that the displacement capacity of the isolator is not affected by the offset of the internal components.

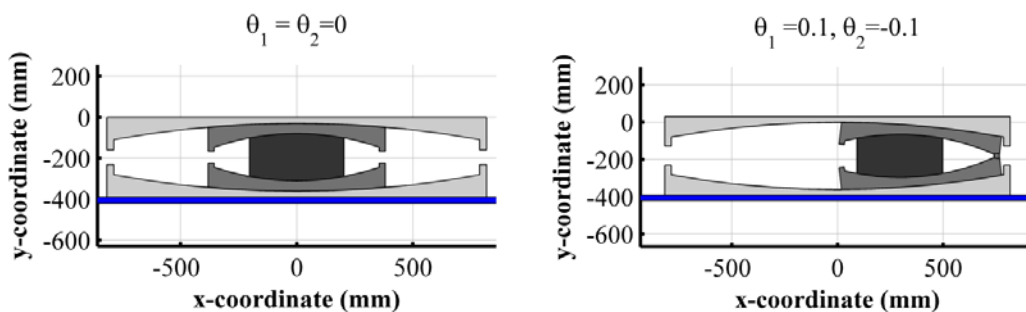


Figure 4-10: Two cases of initial offsets of internal components

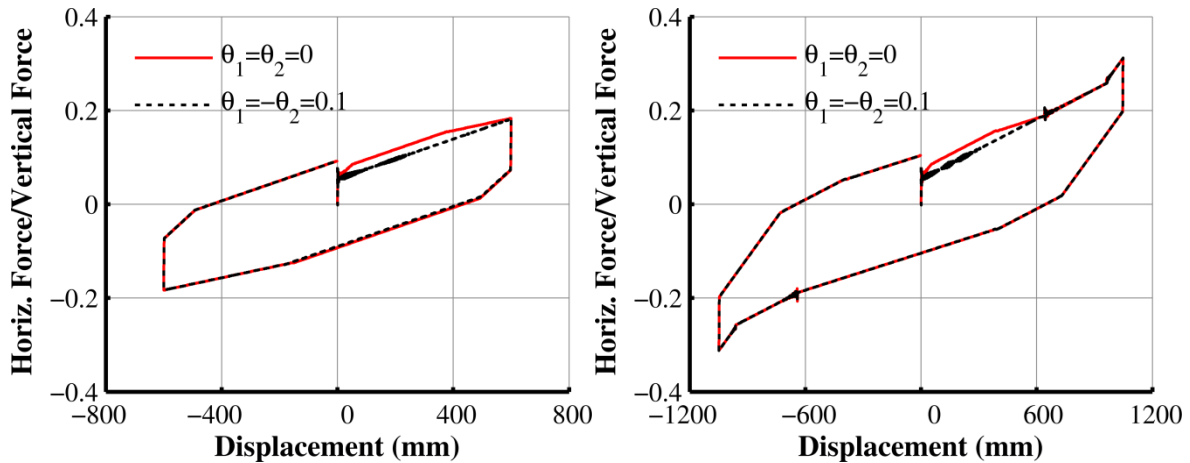


Figure 4-11: Effect of initial offsets of internal components on TFP behavior

4.8 Effect of top concave plate and bottom concave plate rotation on TFP behavior

Consider the bearing with the properties shown in Table 3-2 for Full Scale Bearing – Configuration B. In this section, the model that was developed in Section 4.4 is used to account for misalignment of the top and bottom concave plates. Note that initial misalignments of the TCP and BCP lead to corresponding initial offsets of the internal components.

Consider the case that these misalignments are constant (although the theory of Section 4.4 is not restricted to constant rotations). Figure 4-12 compares results for three different values of BCP rotation θ_b and zero θ_c rotation of the TCP. Figure 4-13 compares results for three different values of TCP rotation θ_c and zero value for θ_b . Figure 4-14 compares results for three different values of rotation for both θ_b and θ_c . For all examples, it was assumed that $\theta_1 = \theta_2 = u = 0$ thus $\theta_3 \neq 0$ and $\theta_4 \neq 0$.

The main effect of concave plate rotations is a shift of the loop along the axis of the force depending on the sign of the misalignment. These observations are similar to the observations for misaligned plates by Fenz and Constantinou (2008a). Another effect is changes in the initiation of the TFP five regimes, which can only be predicted by the current theory.

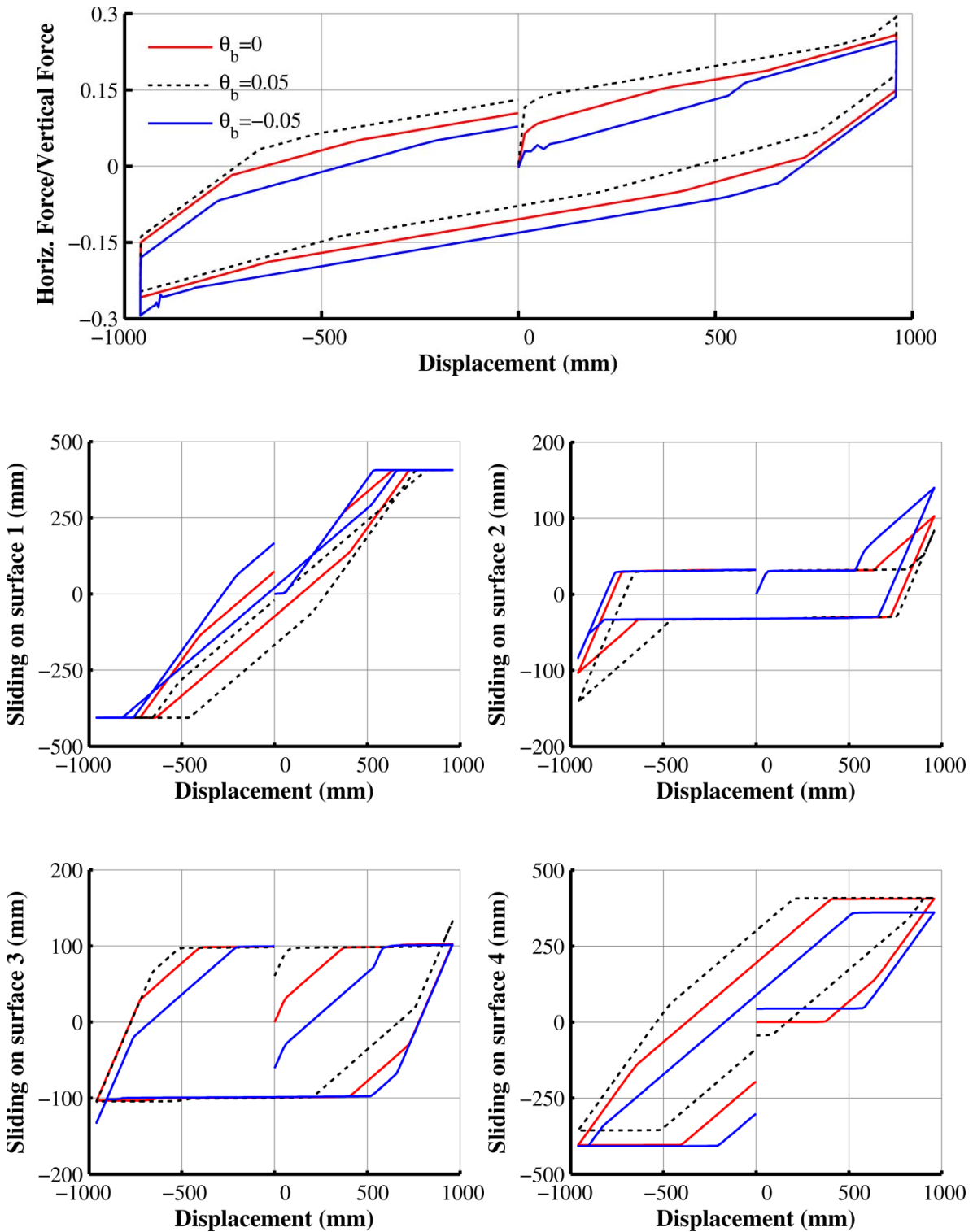


Figure 4-12: Comparison of results for various values of rotation of the bottom concave plate

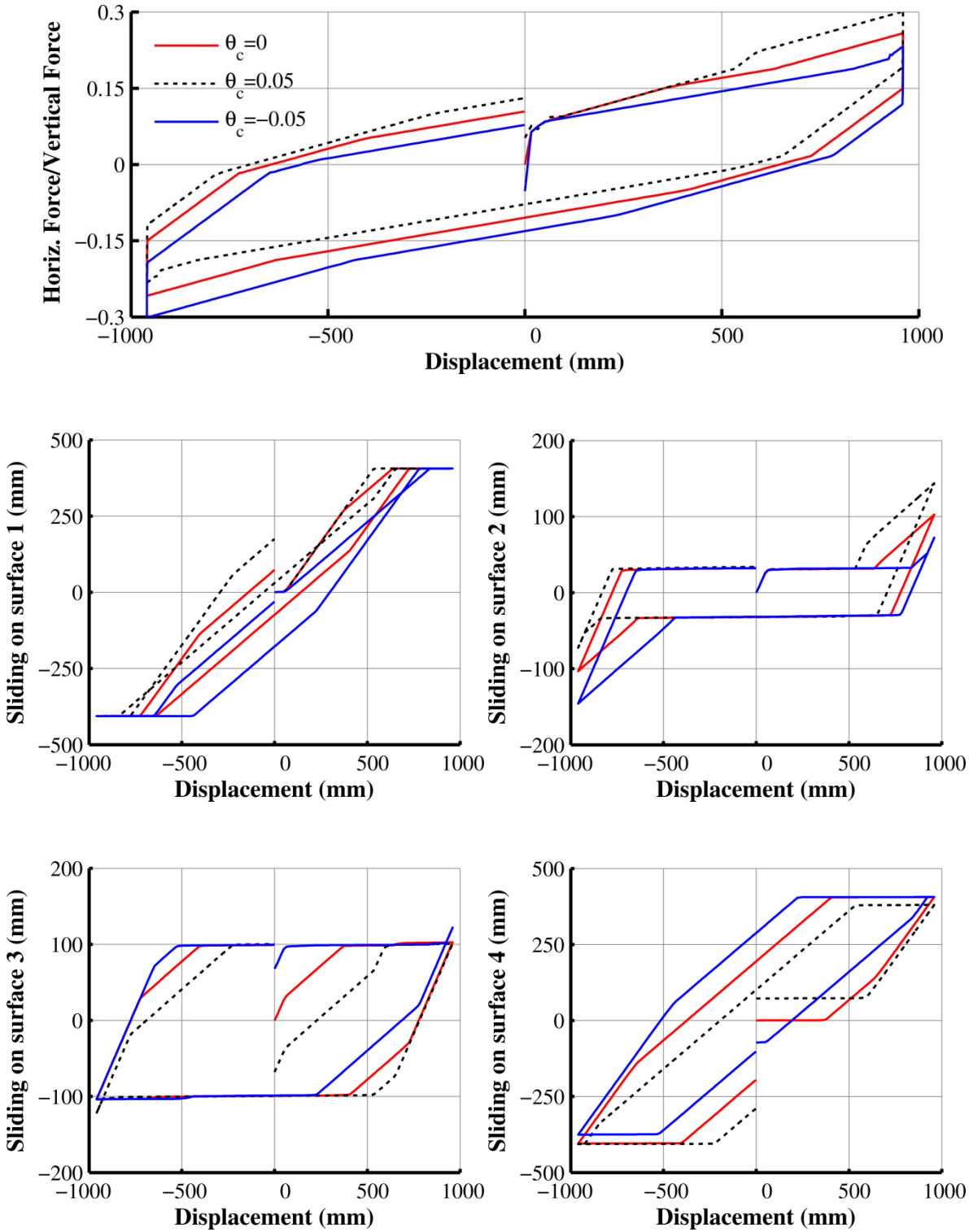


Figure 4-13: Comparison of results for various values of rotation of the top concave plate

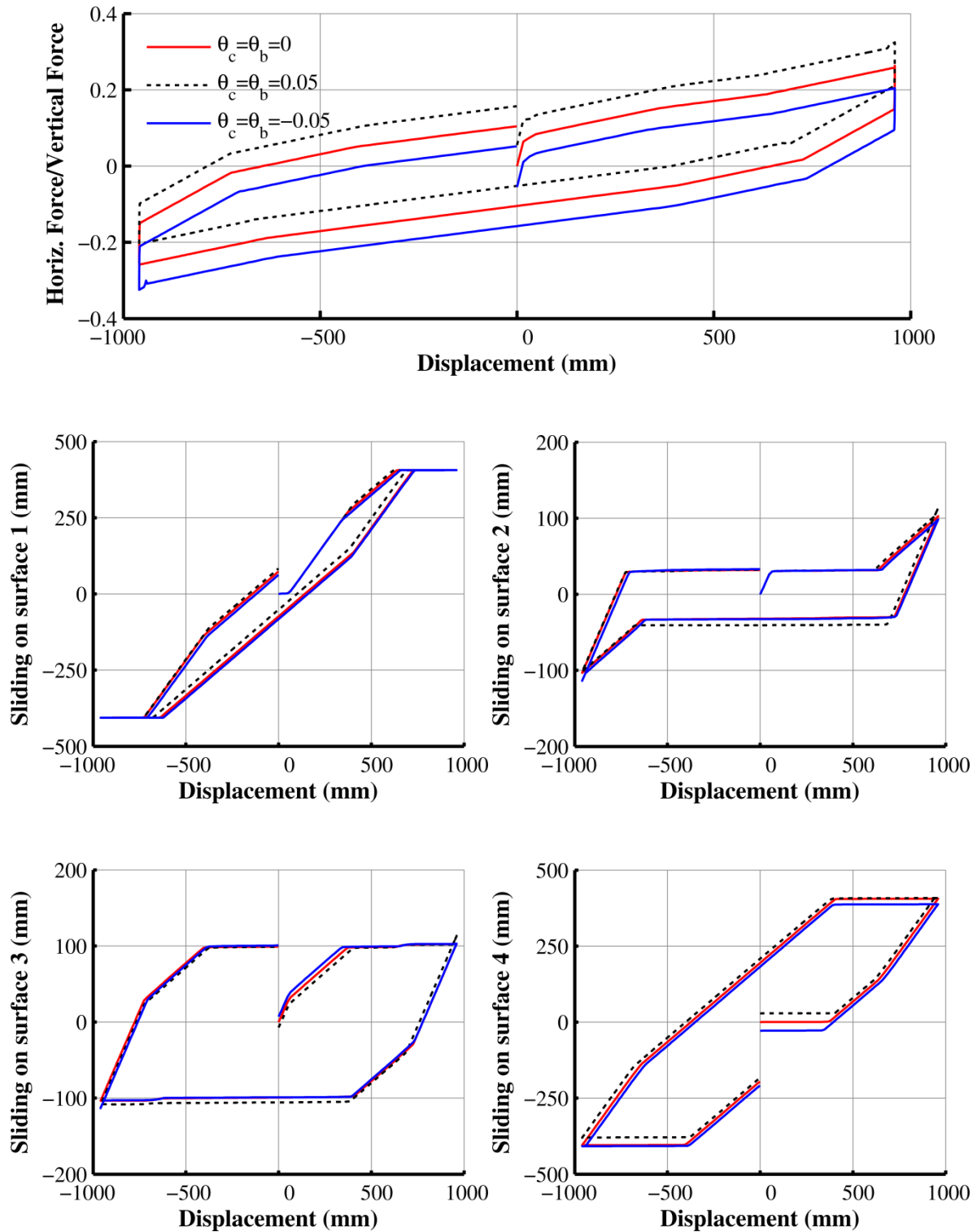


Figure 4-14: Comparison of results for various values of rotation of the top and bottom concave plate (both plates have equal rotations)

4.9 Heating effects on TFP behavior

This section presents an example of heating analysis of the TFP. Figure 4-15 presents results of the analysis of the Full Scale-Configuration B TFP isolator of Table 3-2 when subjected to four cycles of sinusoidal displacement history applied at the TCP at frequency with 0.09Hz and amplitude of 1040mm. The values of the friction coefficients used in Equation (4-14) were $\mu_{\max 1} = 0.075$, $\mu_{\max 2} = \mu_{\max 3} = 0.05$, $\mu_{\max 4} = 0.125$, $\mu_{\min 1} = 0.0375$, $\mu_{\min 4} = 0.0625$, and $\mu_{\min 2} = \mu_{\min 3} = 0.025$. The heat rate parameter was set equal to $0.01/^{\circ}\text{C}$. Results are shown for the normalized force-displacement loop, for the normalized friction force-sliding displacement of each surface and the temperature rise histories of each sliding surface.

Figure 4-16 compares results of response history analysis of the rigid structure of Section 4.6 for three different cases:

- 1) With heating effects: The values of the friction coefficients that were used in Equation (4-14) were $\mu_{\max 1} = 0.075$, $\mu_{\max 2} = \mu_{\max 3} = 0.05$, $\mu_{\max 4} = 0.125$, $\mu_{\min 1} = 0.0375$, $\mu_{\min 4} = 0.0625$ and $\mu_{\min 2} = \mu_{\min 3} = 0.025$.
- 2) Without heating effects on friction and with friction values equal to the maximum values ($\mu = \mu_{\max}$). That is, the friction coefficient values were $\mu_1 = 0.075$, $\mu_2 = \mu_3 = 0.05$, $\mu_4 = 0.125$.
- 3) Without heating effects on friction and with friction values equal to the minimum values ($\mu = \mu_{\min}$). That is, the friction coefficient values were $\mu_1 = 0.0375$, $\mu_2 = \mu_3 = 0.025$, $\mu_4 = 0.0625$.

The results of Figure 4-16 show that heating can have important effects that warrant consideration in analysis. Heating effects also need to be considered when measuring the friction coefficient in tests for use in analysis without the effects of heating. The friction coefficient needs to be measured at the sliding surface temperatures expected to develop during the controlling seismic event.

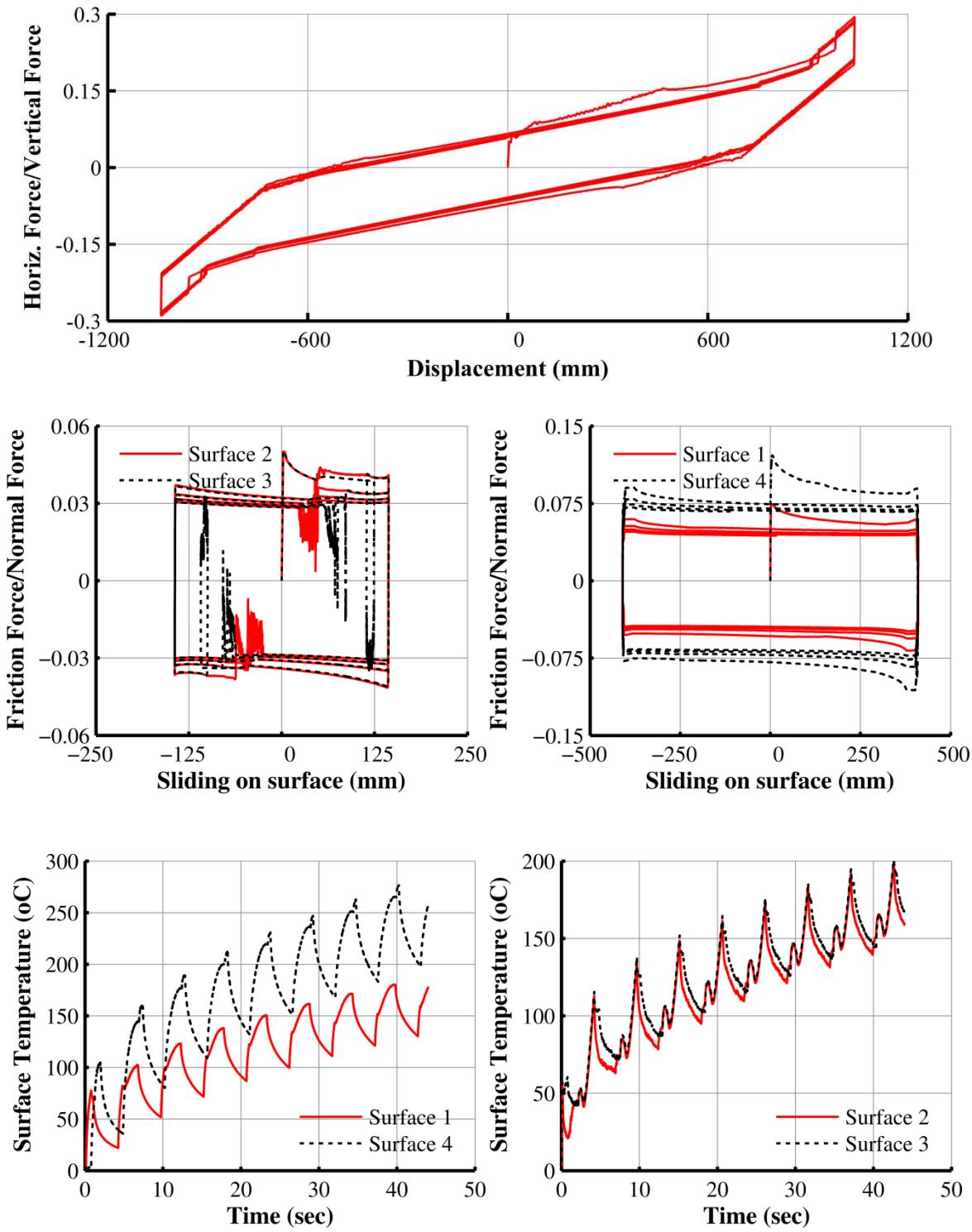


Figure 4-15: Results of heating analysis of TFP isolator subjected to a four-cycle sinusoidal displacement history applied at the TCP with 0.09Hz frequency and 1040mm amplitude

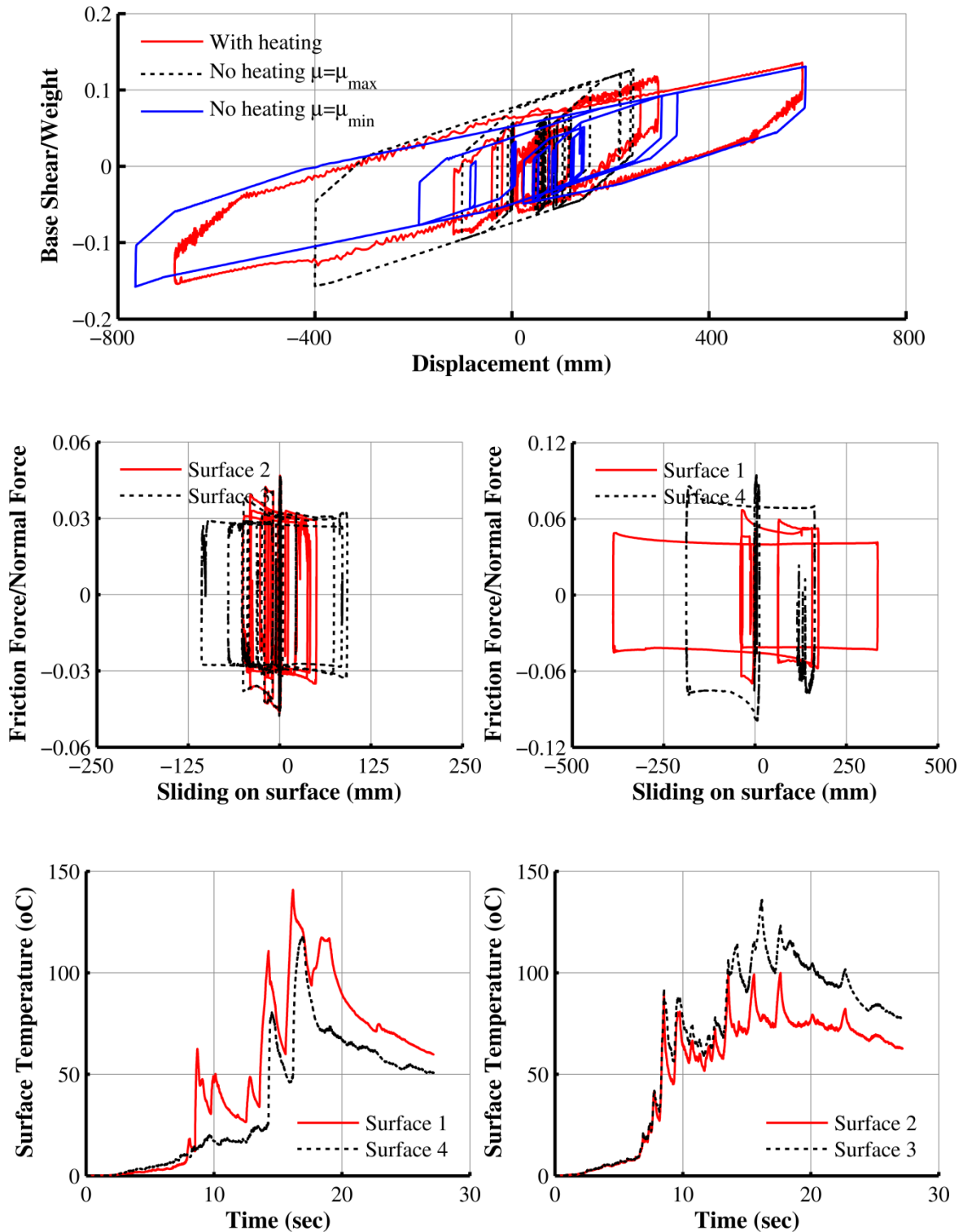


Figure 4-16: Comparison of results in dynamic analysis of the structure of Section 4.6 for cases with heating effects and without heating effects on the friction coefficient

4.10 Inertia Effects of Triple FP Bearing Internal Components

Consider again the rigid structure analyzed in Section 4.6 supported by the Full Scale Bearing-Configuration B of Table 3-2 with $\mu_2 = \mu_3 = 0.05$ and subjected to the ground motion of Figure 4-7. Two analyses are conducted: a) one that considers the inertia and weight effects on the isolators using the actual masses of the TFP parts, and b) one that neglects those effects by assigning artificially small values for the mass of the parts. Results presented in Figure 4-17 show that inertia and weight effects are insignificant for practical purposes as they are very small by comparison to the restoring and frictional forces acting at each sliding surface. Note that this will not be true when the gravity load on the bearing is small - a condition that occurs when uplift is imminent. Results for such a case are presented in Figure 4-18 where the same analyses (with and without inertia effects) are conducted but the supported weight (and axial load on isolators) is reduced to 300kN instead of 1500kN. Now the inertia and weight effects are more pronounced. Under uplift conditions, the gravity load is zero and the inertia of the bearing components becomes even more important in determining the state of the bearing.

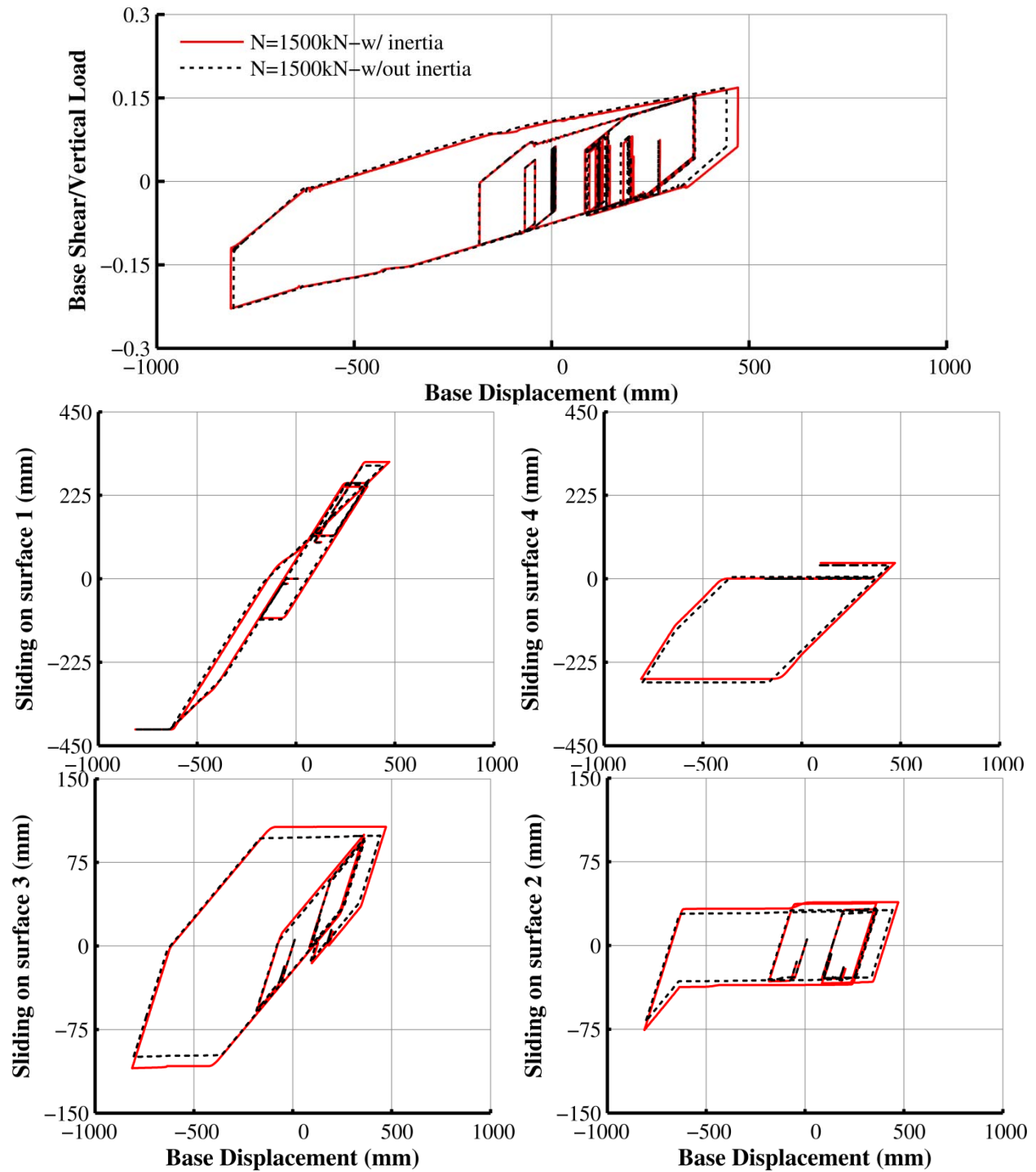


Figure 4-17: Comparison of results with and without inertia effects of bearing components for the full scale bearing of Table 3-2, case B with $\mu_2 = \mu_3 = 0.05$ and load of 1500kN

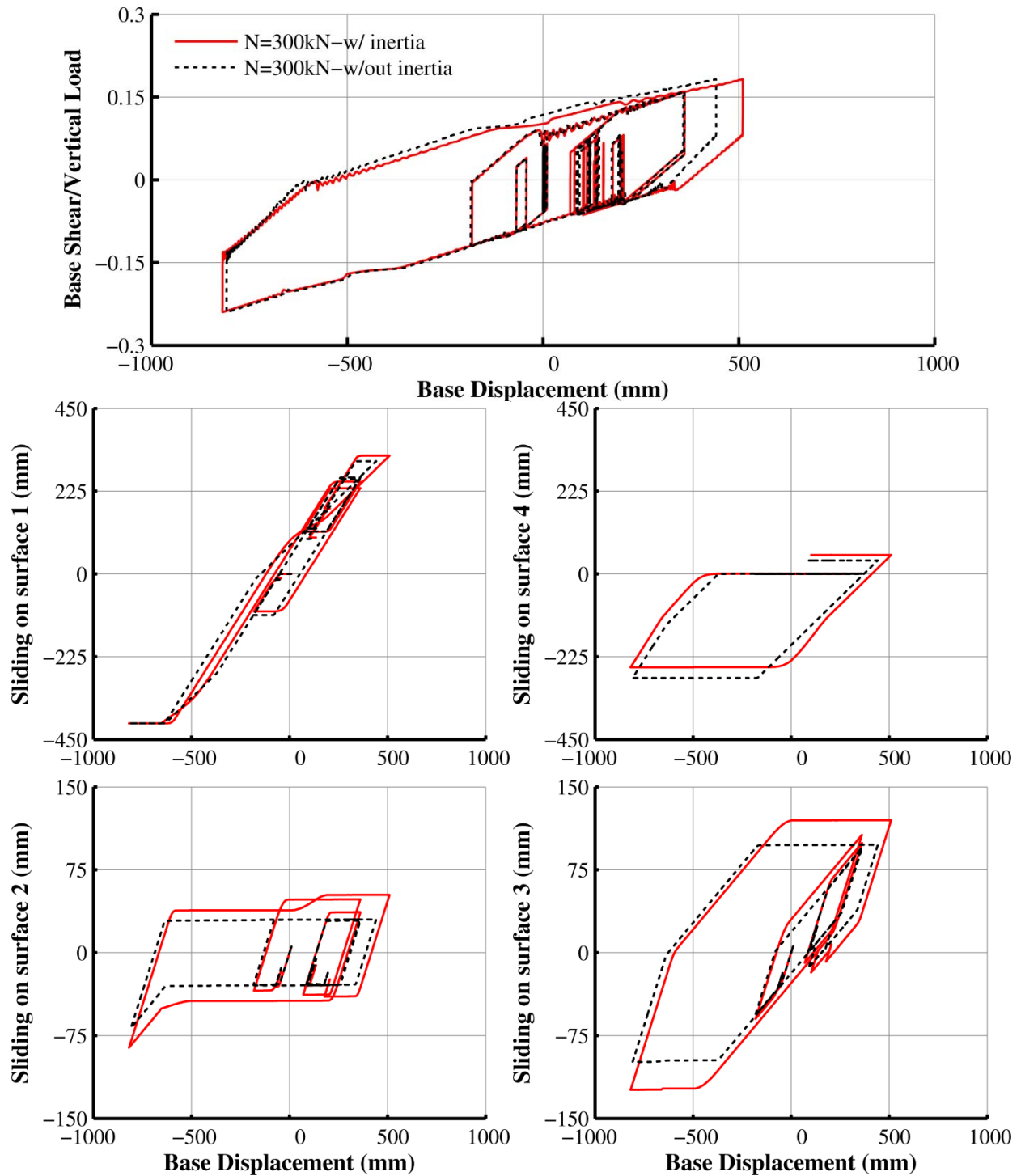


Figure 4-18: Comparison of results with and without inertia effects of bearing moving components for the full scale bearing of Table 3-2, case B with $\mu_2 = \mu_3 = 0.05$ and load of 300kN

4.11 Comparison of Current Model to Becker and Mahin (2011) model

Recently, Becker and Mahin (2011) and Dao et al. (2013) have developed formulations based on plasticity that can model the TFP behavior. These formulations are based on horizontal equilibrium and are subject to the constraints $d_2=d_3$ and $d_1=d_4$, $\mu_2 = \mu_3 < \mu_1 \leq \mu_4$. Under such conditions, all models produce essentially the same results as the Fenz and Constantinou formulation. However, Becker and Mahin (2011) claim that their TFP formulation is valid for any random geometric and frictional parameters. This is not true as the model is based on horizontal equilibrium alone for which the condition $\mu_2=\mu_3$ is necessary (see also Section 3.5). Note that Fenz and Constantinou (2008d) also recognized this and used three elements in the series model implementation of the TFP in SAP2000 instead of four. It is emphasized again here that the complete TFP mechanics that are presented in this report are needed in order to capture the TFP behavior for all cases.

Consider the four sets of TFP geometric and frictional properties presented in Table 4-1, for which results for an imposed cycle of motion are presented in Figure 4-19. The results demonstrate that the Becker and Mahin model is not valid for any random combination of geometric and frictional parameters (although the selected TFP properties are unrealistic and impractical).

Table 4-1: Sets of properties used to investigate the validity of the Becker and Mahin (2011) model

Geometric and Frictional Properties	Property Set 1	Property Set 2	Property Set 3	Property Set 4
$R_1=R_4(\text{cm})$	381	381	381	381
$R_2=R_3(\text{cm})$	30.48	30.48	30.48	30.48
$h_2=h_3(\text{cm})$	7.62	7.62	7.62	7.62
$h_1=h_4(\text{cm})$	11.43	11.43	11.43	11.43
$d_1(\text{cm})$	54.86	54.86	54.86	40.64
$d_4(\text{cm})$	54.86	54.86	54.86	66.04
$d_2(\text{cm})$	5.72	5.72	5.72	5.72
$d_3(\text{cm})$	5.72	5.72	5.72	3.18
μ_1	0.8	0.1	0.3	0.5
μ_2	0.1	0.3	0.1	0.7
μ_3	0.1	0.5	0.5	0.3
μ_4	0.8	0.7	0.7	0.1

Notation is per Fenz and Constantinou (2008a)

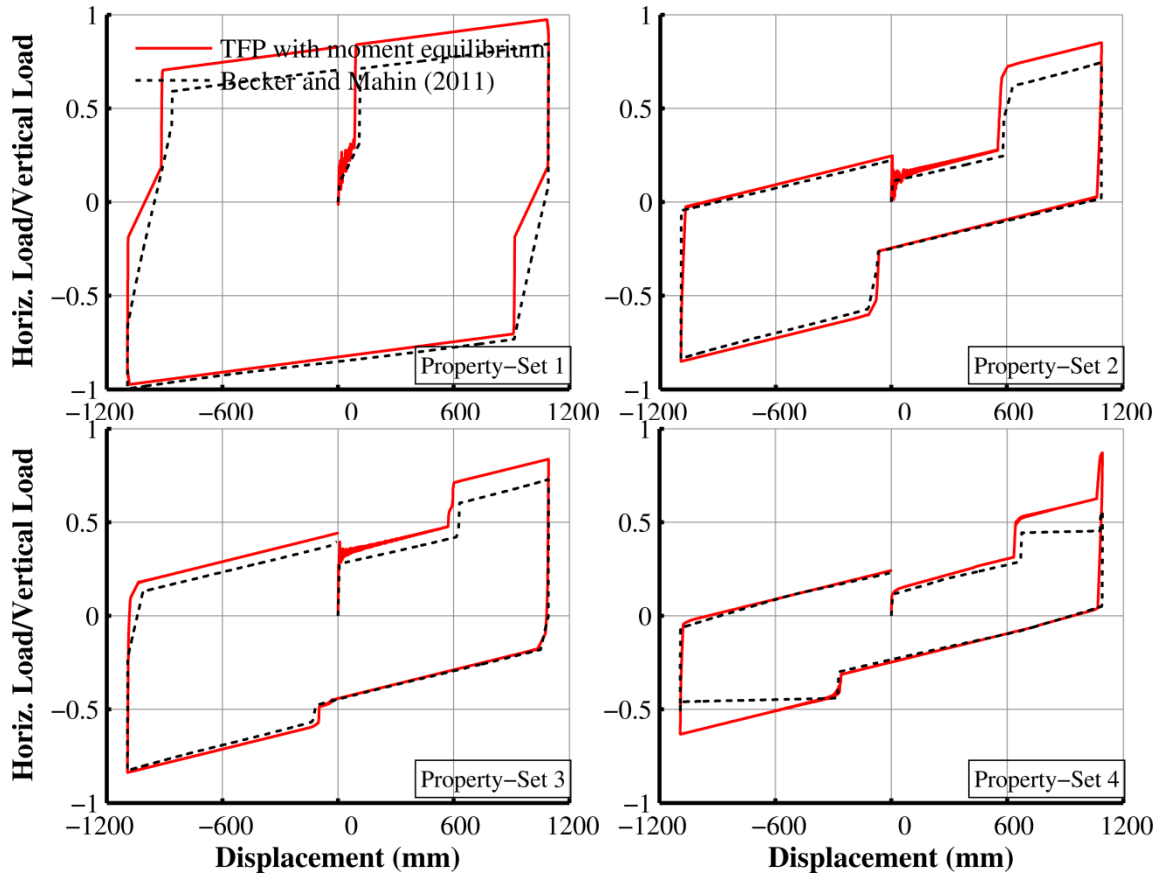


Figure 4-19: Force-displacement loops produced by the current theory and the Becker and Mahin (2011) model

4.12 Comparison of Current Model to Experimental Results

Experiments were conducted at the University at Buffalo using a 3-story steel model structure at quarter length scale and isolated with Triple FP bearings. Two different configurations of bearings were used having the geometric and frictional properties of the scale model bearings in Table 3-2. Note that the bearing of Configuration A with $\mu_2 = \mu_3 < \mu_1 < \mu_4$ is a commonly used configuration, whereas the bearing of Configuration B with $\mu_1 = \mu_4 < \mu_3 = \mu_2$ is highly unusual. The results presented herein were obtained in testing of the bearing of Configuration B with $\mu_1 = \mu_4 < \mu_3 = \mu_2$ in a single bearing testing machine under imposed constant vertical load and one-directional harmonic lateral displacement.

Figure 4-20 shows the instrumentation used to monitor the motion of the three internal components of the bearing. Note that two instruments were needed for each component as the

parts also exhibited torsional motion which was likely caused by uneven distribution of friction tractions, by out-of-plane force offsets due to initial nonzero displacements and by rocking of the bearing machine moving top beam. The average value of the two measurements from each pair of instruments was used for comparison to analytical results.

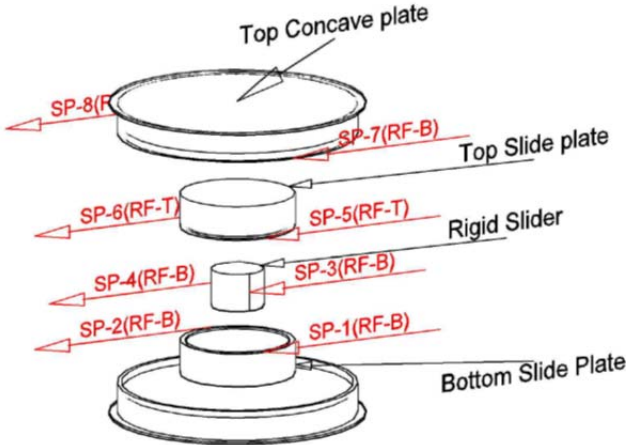


Figure 4-20: String-pot instrumentation of Triple FP bearing internal components

Figure 4-21 compares the experimental normalized force (lateral force divided the vertical load) versus displacement (this is the imposed displacement) loops and the analytically determined loops (using program 3pleANI that uses the theory of this section and is described later in this report). Three cycles of motion were imposed under constant vertical load of 50kN. Note that in this case motion is asymmetric with 100mm amplitude in one direction and large enough amplitude in the other direction (140mm) to engage the displacement restrainers and to exhibit strong stiffening behavior.

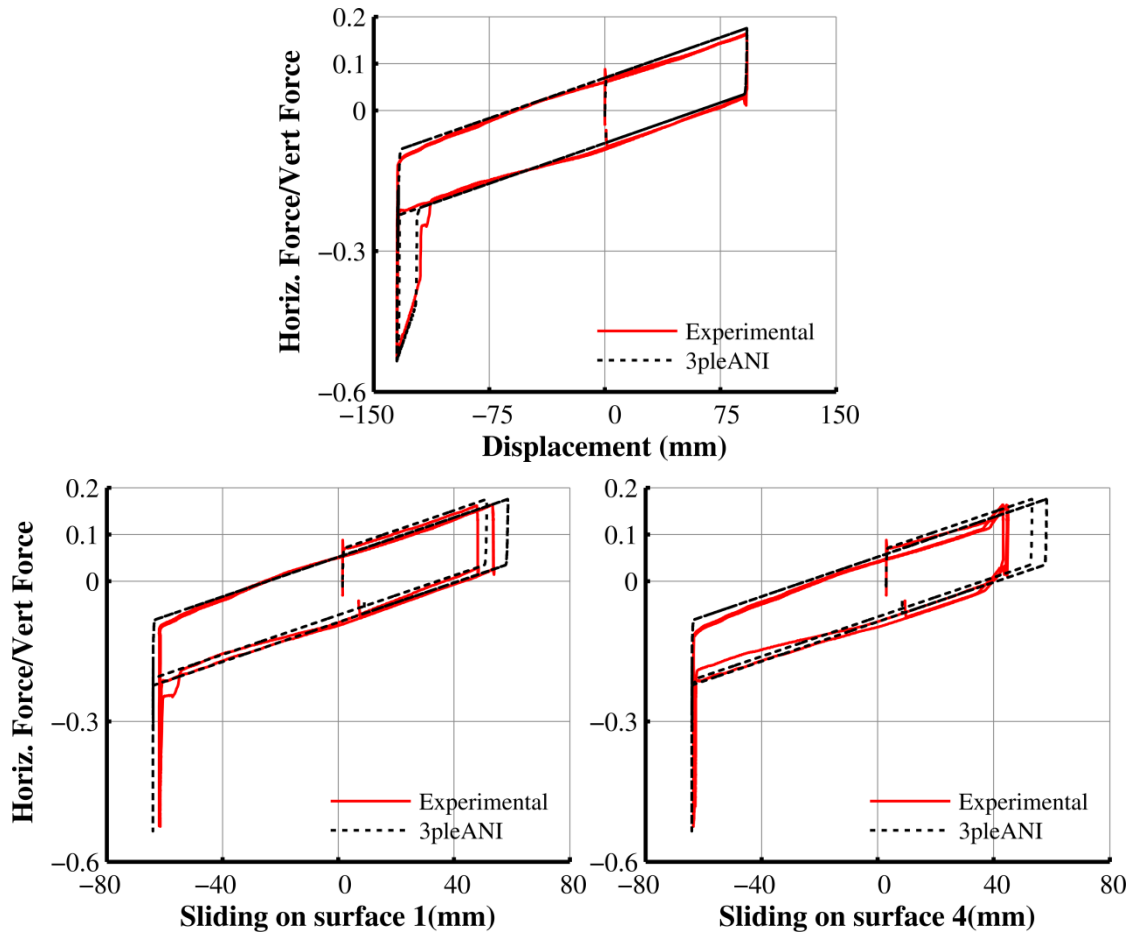


Figure 4-21: Comparison of numerical and experimental results for bearing A with $\mu_1 = \mu_2 = \mu_3 = \mu_4$ in motion of 0.02Hz frequency and 140mm amplitude

The analytical model predicts well the experimental loops but for the following:

- (1) In some cases, as shown in Figure 4-21, the analysis over-predicts the displacement on surface 1 for two of the three cycles of motion. It is likely that the experimental measurement was affected by significant torsional motion of the internal parts. This phenomenon is not predictable by the current theory.
- (2) In the stiffening regime, the analytical model does not predict the existence of the two stops experienced by the bearing. However, the existence of the first stop depends on the exact values of the initial offsets and friction coefficients which cannot be known in experiments. Therefore, results of an additional analysis are presented in Figure 4-22 in which slightly different initial offsets were used. The analytical model can now capture the existence of the first stop (circled in the figure) although the magnitude of the stop is

under-predicted by the model. By experimenting with different values of initial offsets and friction coefficients, the magnitude of the stop could have been predicted more accurately. The interested reader is referred to Sarlis et al (2013) for more comparisons between the experimental results and analytical predictions using the current model.

- (3) The stiffness exhibited in the last regime of operation of the bearing is slightly different than the analytical one. This is most likely due to load cell measurement errors, the effects of large bearing rotations, some small rotation of the top loading beam of the test machine and the effect of the rubber seal. The reader is referred to Sarlis et al (2013) for more details.

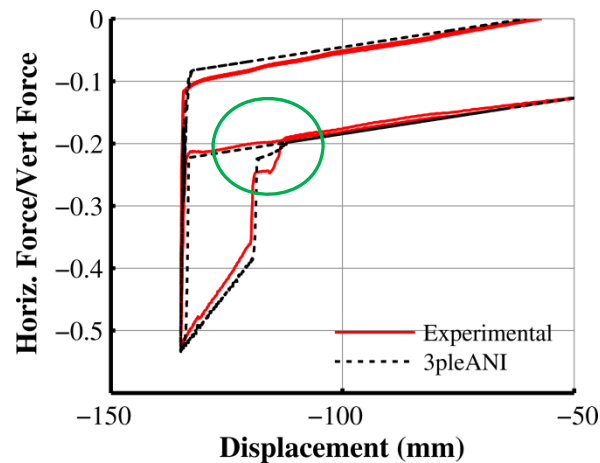


Figure 4-22: Comparison of numerical and experimental results for bearing A with $\mu_1 = \mu_2 = \mu_3 = \mu_4$ in motion of 0.02Hz frequency and 140mm amplitude-close view

SECTION 5

TRIPLE FRICTION PENDULUM BEARING BEHAVIOR UNDER UPLIFT CONDITIONS AND FULL CONTACT

5.1 Introduction to Uplift

Uplift or tension of isolators may occur in slender structures, or in isolators under braced columns, or isolators under shear walls and it depends on the level of seismic excitation. Triple Friction Pendulum isolators are capable of accommodating uplift and are often preferred when such a phenomenon is likely to occur. When uplift occurs, the engineer is interested (a) to know if the internal components of the bearing have stable characteristics during the uplift episode, (b) to know if the bearing behaves properly at the end of the uplift episode (“landing” of the top concave plate), (c) to know the amount of free fall, if any, and (d) to have the capability to animate the motion of the bearing components during a prescribed horizontal and vertical motion with uplift in order to detect problems.

Currently available commercial software such as SAP2000 and ETABS (Computer and Structures, 2007) have the capability to model the behavior of Triple Friction Pendulum bearings through the use of the parallel and series models (Fenz and Constantinou, 2008c; Sarlis and Constantinou, 2010). These models consist of elements connected between two nodes and have proper hysteretic behavior in any horizontal direction, linear compressive stiffness and zero tensile stiffness. When implemented in commercial software, these models can describe the behavior of the bearing in the horizontal directions while in full contact (and provided that the constraints of the Fenz and Constantinou, 2008a to 2008e model prevail), and also calculate the history of horizontal and vertical displacement of the two nodes representing the bearing from the initial position. The availability of these histories of displacement should be sufficient to determine the behavior of the bearing and its various components, including uplift, by physical real time dynamic testing. This is currently impossible as no machine exists that is capable of such performance for large bearings. The only remaining option is to have the capability (a) to analyze the motion of the bearing components given the histories of horizontal and vertical motion of the two nodes of the bearing representation, (b) to be able to animate the motion of the bearing as if it were observed in testing, and (c) to calculate histories of any relevant response

quantity as if it were possible to measure in testing. Therefore, it is important to have a model of the behavior of the Triple FP bearing that accounts for its behavior in its most complex state, including the inertia effects of its moving parts and the stiffness of the rubber seal, and to account for uplift.

A model of uplift behavior is presented in this section. To start, a model is needed to describe the behavior when the bearing is in compression. The model presented in Section 4 is applicable for any combination of geometric and frictional parameters and is suitable for this purpose. During uplift, the lateral force-displacement relation is known (zero force) but the motion of the bearing components needs to be determined in order to correctly calculate the behavior of the bearing at the conclusion of an uplift episode. A model to describe this behavior is presented in this section.

Figure 5-1 depicts a portion of the horizontal and uplift displacement histories of an isolator in three different states as obtained in response history analysis. Figure 5-1 also shows the possible theories (developed in this report) that can be used to model each state of the isolator. The three states of the isolator depicted in Figure 5-1 are:

- 1) The bearing is in compression and all surfaces are in full contact ($0 < t \leq t_1$ and $t \geq t_2$).
For this case, the TFP behavior is fully described by the model presented in Section 4.
- 2) The bearing top concave plate uplifts at time t_1 and uplift lasts for a duration $t_2 - t_1$ ($t_1 \leq t \leq t_2$). The uplift state can be analyzed using two different methods:
 - (a) Using the derivations of Section 5.3 for which the sliding surfaces 1, 2 and 3 are assumed to be in full contact at all times (that is, only the TCP separates from the rest).
 - (b) Full contact is lost so that point contact, sliding, rocking, free fall and overturning of the inner components may occur. This is a very complex problem for which a model of behavior is described in Section 6.
- 3) The top concave plate comes into contact with the components below (“landing”) at time t_2 . Landing is also a very complex problem that involves point contact, sliding, rocking, and free fall of the inner components and it can again be analyzed using two different methods:

- (a) Compatibility and equilibrium of the TFP are restored instantaneously by using the ending conditions from the uplift analysis of Section 5.3 as initial conditions in the analysis presented in Section 4. This is an approximate procedure and it is described in Section 5.4 herein. In this case, $t_3=t_2$ in Figure 5-1; that is, landing has zero duration.
- (b) Complex phenomena such as bouncing-uplift and point contact of components occurs for which landing lasts for a short duration of time until compatibility is restored at time t_3 (see Figure 5-1). This procedure for modeling landing is preferred over the one described in (a) and is described in Section 6.
- 4) When landing is complete (time t_3), the bearing is in compression and analyzed using the model presented in Section 4.

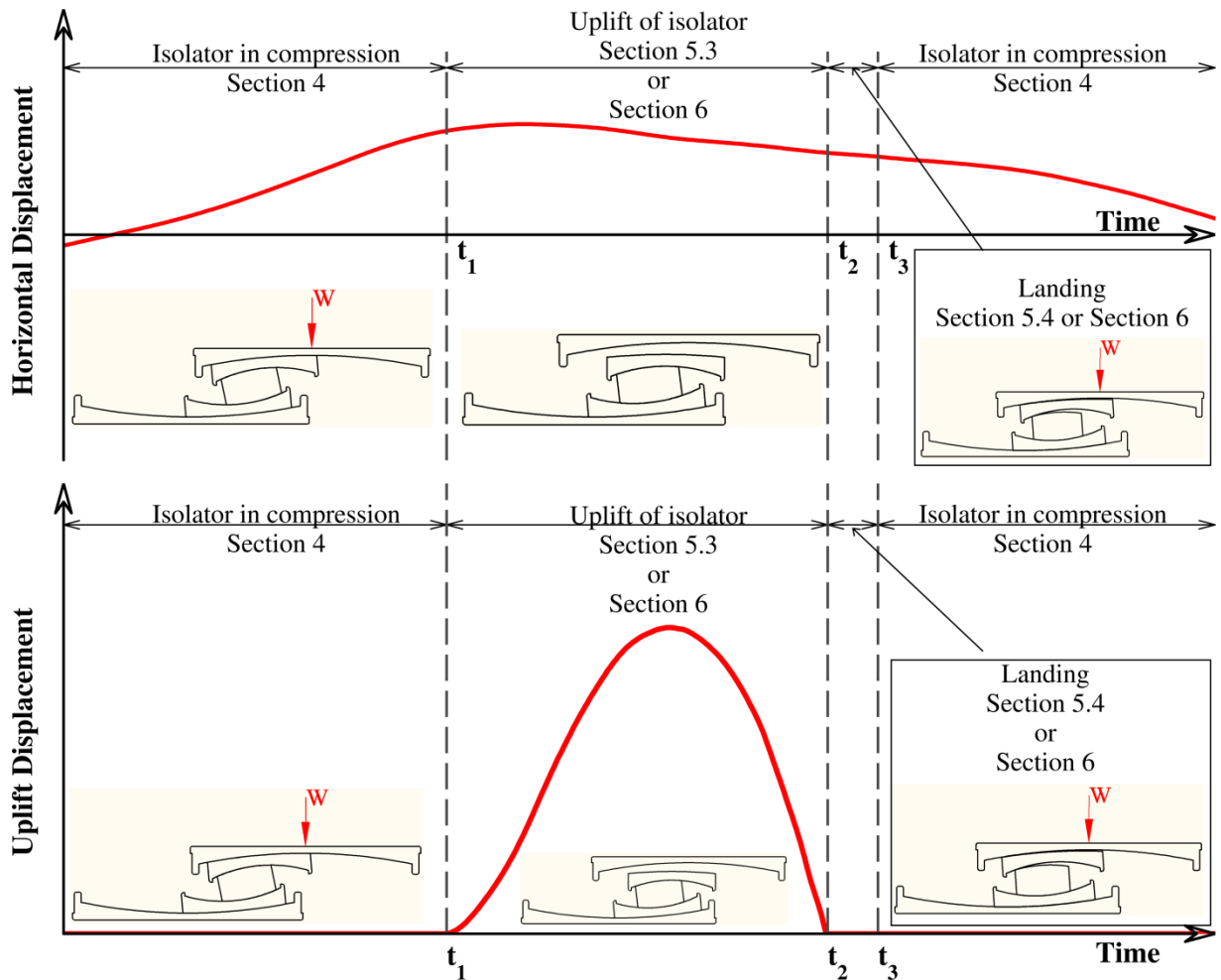


Figure 5-1: Horizontal and uplift displacement histories of TFP isolator in three states during an earthquake event and theories to perform analysis

5.2 Definition of Uplift Displacement

In commercial software such as SAP2000 and ETABS, the vertical behavior of the TFP is modeled using linear elastic springs that represent the isolator stiffness in the vertical direction. Accordingly, these models do not account for the vertical displacements of the isolators due to the pendulum motion. When uplift occurs, the vertical displacement of the bearing due to pendulum motion is very important as it affects any interaction between the TCP and TSP that may bring about collapse of the bearing. This section defines the uplift displacement and its distinction from the total vertical displacement of the bearing. For this, consider the horizontal and vertical displacement history (denoted as v_i) of an isolator that exhibits uplift as shown in Figure 5-2 and obtained in response history analysis performed in software that does not account for the vertical displacement of the TCP due to the pendulum motion. In Figure 5-2, negative vertical displacement values indicate compression of the bearing (the vertical springs representing the bearing have finite stiffness and exhibit deformations).

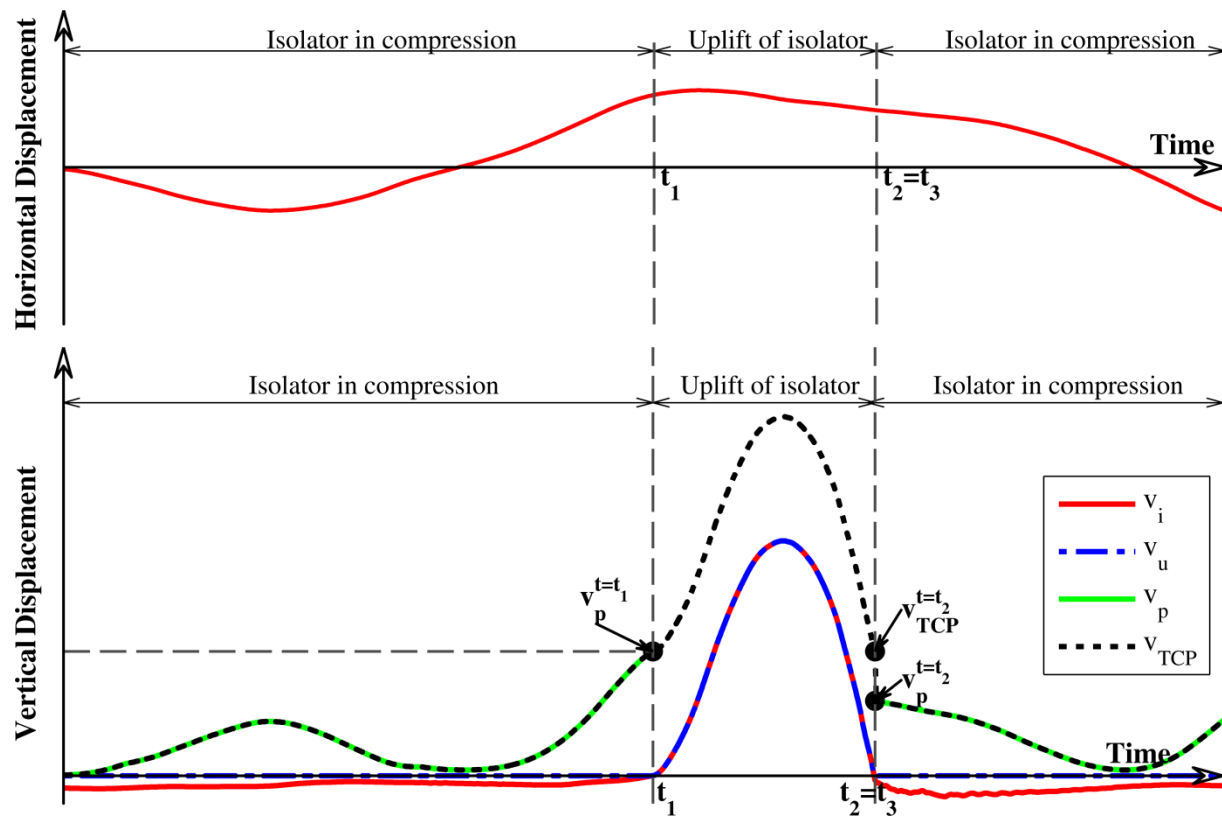


Figure 5-2: Definition of input displacements for uplift analysis

Given the vertical displacement v_i (red line in Figure 5-2), the uplift displacement v_u is first calculated by replacing the small negative values of displacement for times $t < t_1$ and $t > t_2$ with zeros. The resulting uplift displacement history is shown in Figure 5-2 by a blue line. This is not the total vertical displacement of the TCP - rather, is the vertical displacement exclusive of the pendulum motion effect. The vertical displacement due to the pendulum motion is denoted as v_p and is shown with a green line in Figure 5-2. It can be calculated using the theory presented in Section 4 and assuming zero top concave plate rotation as shown in Equation (5-1).

$$v_p = -(R_{eff1} - R_{eff2})\cos\theta_1 - (R_{eff2} + R_{eff3})\cos(\theta_1 + \theta_2) - (R_{eff4} - R_{eff3})\cos\theta_4 + R_{eff1} + R_{eff4}$$

$$v_u = \begin{cases} 0 & , 0 \leq t \leq t_1, t \geq t_2 \\ v_i & , t_1 \leq t \leq t_2 \end{cases} \quad (5-1)$$

The total vertical displacement of the TCP is denoted as v_{TCP} and is shown in Figure 5-2 with a black dotted line. It is given by:

$$v_{TCP} = \begin{cases} v_u + v_p^{t=t_1} & , t_1 \leq t \leq t_2 \\ v_p & , t < t_1, t \geq t_2 \end{cases} \quad (5-2)$$

In Equation (5-2), $v_p^{t=t_1}$ is the vertical displacement of the isolator at the initiation of uplift. Also in Figure 5-2, $v_p^{t=t_2}$ is the vertical displacement of the TCP due to the pendulum motion of the bearing after uplift is completed and after compatibility and equilibrium have been restored in the TFP and the bearing is in compression. This value is different than the vertical displacement of the TCP at the end of the uplift event (given by $v_{TCP}^{t=t_2}$) due to the motion of the TFP inner parts during uplift. The transition from $v_{TCP}^{t=t_1}$ to $v_p^{t=t_2}$ in Figure 5-2 is termed landing of the TFP and modeling techniques for this phase of motion are presented in Sections 5.4 and 6. The vertical displacement difference between $v_{TCP}^{t=t_2}$ and $v_p^{t=t_2}$ represents “free fall” of the TCP.

5.3 Modeling of Triple FP Bearing during Uplift with Parts in Full Contact

This section describes the TFP behavior for times $t_1 < t < t_2$ as shown in Figure 5-2 and assuming full contact between surfaces 1, 2 and 3. When uplift occurs (at time $t=t_1$ in Figure 5-2) and the top concave plate (TCP) separates from the bearing components below (bottom sliding plate or

BSP, rigid slider or RS and top sliding plate or TSP), equilibrium of parts BSP, TSP and RS needs to be considered. The equations of equilibrium of forces in the horizontal direction and of moments of these parts are as follows based on the assumption of small rotations:

$$\begin{aligned}
\text{(a): } & W_2(\theta_1 + \theta_2 + \theta_{s2}) + S_2 - S_1 + F_{r2} - F_{r1} - W_1(\theta_1 + \theta_{s1}) - m_{BSP}(R_1 - z_1)\ddot{\theta}_1 - m_{BSP}\ddot{u}_g + \\
& + F_{bx,l} + F_{bx,r} = 0 \\
\text{(b): } & W_3(\theta_1 + \theta_2 + \theta_{s3}) + S_3 + F_{bx,l} + F_{bx,r} + F_{r3} - F_{r4} + m_{TSP}(R_{eff1} - h_4 + z_4)\ddot{\theta}_1 + \\
& + m_{TSP}(R_{eff2} - h_4 + z_4)\ddot{\theta}_2 + m_{TSP}(R_{eff3} + h_4 - z_4)\ddot{\theta}_3 + m_{TSP}\ddot{u}_g = 0 \\
\text{(c): } & W_2(\theta_{s2}R_2 + \theta_{s3}R_3) - (W_2\theta_{s2} + S_2 + F_{r2})(h_2 + h_3) - (I_{RS} + m_{RS}(R_{eff1} + h_2 - z_2)z_3)\ddot{\theta}_1 - \\
& (I_{RS} + m_s(R_2 - z_2)z_3)\ddot{\theta}_2 - m_{RS}z_3\ddot{u}_g - m_{RS}g(\theta_1z_3 + \theta_2z_3 + \theta_{s3}R_3) = 0 \\
\text{(d): } & W_2(\theta_{s1}R_1 - \theta_2R_2 - \theta_{s2}R_2) - (h_1 - h_2)[W_2(\theta_{s2} + \theta_2) + S_2 + F_{r2}] - I_{BSP}\ddot{\theta}_1 + \\
& (m_{BSP}(R_1 - z_1)\ddot{\theta}_1 - m_{BSP}\ddot{u}_g)z_1 + m_{BSP}g(\theta_{s1}R_1 + \theta_1z_1) \\
& - (h_1 - h_2 + h_{r2} + h_{s2})(F_{bx,l} + F_{bx,r}) - (b_1/2 + \theta_{s1}R_1)F_{by,l} + (b_1/2 - \theta_{s1}R_1)F_{by,r} = 0 \\
\text{(e): } & -W_3R_3(\theta_{s3} + \theta_3) - (h_4 - h_3)[W_3(\theta_{s3} + \theta_3) + S_3 + F_{r3}] - I_{TSP}(\ddot{\theta}_1 + \ddot{\theta}_2 - \ddot{\theta}_3) + \\
& - [m_{TSP}(R_{eff1} - h_4 + z_4)\ddot{\theta}_1 + m_{TSP}(R_{eff2} - h_4 + z_4)\ddot{\theta}_2 + m_{TSP}(R_{eff3} + h_4 - z_4)\ddot{\theta}_3]z_4 + \\
& - m_{TSP}\ddot{u}_g - m_{TSP}g(\theta_1 + \theta_2 - \theta_3)z_4 + (b_4/2)(F_{by,l} - F_{by,r}) \\
& - (h_4 - h_3 + h_{r3} + h_{s3})(F_{bx,l} + F_{bx,r}) + (b_4/2)F_{vg,l} - (b_4/2)F_{vg,r} = 0 \\
\text{(f): } & W_2(\theta_1 + \theta_2 + \theta_{s2}) + S_2 + F_{r2} - W_3(\theta_1 + \theta_2 + \theta_{s3}) - S_3 - F_{r3} \\
& + m_{RS}(R_{eff1} + h_2 - z_2)\ddot{\theta}_1 + m_{RS}(R_2 - z_2)\ddot{\theta}_2 + m_{RS}\ddot{u}_g = 0
\end{aligned} \tag{5-3}$$

The equilibrium equations above are derived using the free body diagrams of Figure 3-1 and Figure 4-1 with the following additional considerations:

1. The rubber seal forces are considered. The horizontal components of these forces are denoted as $F_{bx,l}$ and $F_{bx,r}$ and the vertical components as $F_{by,l}$ and $F_{by,r}$. Note that the subscripts l and r denote the seal forces on the left and the right, respectively.
2. Additional vertical forces, $F_{vg,l}$ and $F_{vg,r}$, applied by the top concave plate (TCP) to the top slide plate (TSP) are considered. These forces are usually zero for the entire duration of uplift and become non-zero only when point contact occurs between the TCP and TSP. A more detailed description follows.

Since there is no normal force applied to surface 4, the moment equilibrium of the TSP (equation (f) in Equations (5-3) above) was considered, for simplicity, about the center of contact surface 4. It should be noted that, alternatively, Equations (5-3) can be directly derived from Equations (4-2) using $W_4=0$ and $\theta_{s4}=0$, and by neglecting equations (h), (j) and (c) (since apart from restrainer force F_{r4} and forces $F_{vg,l}$ and $F_{vg,r}$, the top concave plate is independent of the motion of the inner components).

Loads W_1 , W_2 and W_3 in Equations (5-3) are the normal loads on each surface and are dependent on the weight of the inner components and the vertical components of force from the rubber seal:

$$\begin{aligned} W_1 &= m_{TSP}g + m_{RS}g + m_{BSP}g + F_{vg,l} + F_{vg,r} \\ W_2 &= m_{TSP}g + m_{RS}g + F_{by} + F_{vg,l} + F_{vg,r} \\ W_3 &= m_{TSP}g + F_{by} + F_{vg,l} + F_{vg,r} \end{aligned} \quad (5-4)$$

Note that in Equations (5-4), the vertical contact forces $F_{vg,l}$ and $F_{vg,r}$ could have been neglected. As described later in this report, these forces are mostly zero and become nonzero for extremely small durations. Including these forces in Equations (5-4) may in some cases cause delay in the analysis while they have an insignificant effect on the bearing response.

Equations (5-3) may be written in matrix form:

$$\mathbf{M}\ddot{\boldsymbol{\theta}}_t + \mathbf{K}\boldsymbol{\theta}_t + \mathbf{S} + \mathbf{F}_e + \mathbf{F}_g + \mathbf{F}_{rb} + \mathbf{F}_{vg} = 0 \quad (5-5)$$

where $\boldsymbol{\theta}_t$ is a vector containing the sliding and offset angles, \mathbf{S} is a vector containing all variables related to the friction forces, \mathbf{F}_g is a vector containing all variables related to the restrainer forces, \mathbf{F}_e is a vector containing all variables related to the excitation terms, \mathbf{F}_{rb} is a vector containing all variables related to the inner rubber seal forces acting on the top and bottom slide plates and \mathbf{F}_{vg} is a vector containing all variables related to forces applied by the TCP to the TSP due to point contact. Vector $\boldsymbol{\theta}_t$ is given by:

$$\boldsymbol{\theta}_t = \begin{bmatrix} \theta_1 & \theta_2 & \theta_3 & \theta_{s1} & \theta_{s2} & \theta_{s3} \end{bmatrix}^T \quad (5-6)$$

Vector $\boldsymbol{\theta}_t$, is then partitioned as follows:

$$\boldsymbol{\theta}_t = \begin{Bmatrix} \boldsymbol{\theta} \\ \boldsymbol{\theta}_s \end{Bmatrix}; \quad \boldsymbol{\theta} = [\theta_1 \quad \theta_2 \quad \theta_3]^T$$

$$\boldsymbol{\theta}_s = [\theta_{s1} \quad \theta_{s2} \quad \theta_{s3} \quad \dots]^T \quad (5-7)$$

Using the partitioned vectors, the condensation procedure described by Equations (4-7)-(4-11) is followed again in order to derive the following equation:

$$\tilde{\mathbf{M}}\ddot{\boldsymbol{\theta}} + \tilde{\mathbf{K}}\boldsymbol{\theta} + \tilde{\mathbf{S}} + \tilde{\mathbf{F}}_e + \tilde{\mathbf{F}}_g + \tilde{\mathbf{F}}_{rb} + \tilde{\mathbf{F}}_{vg} = 0 \quad (5-8)$$

The condensed vectors are again given by Equation (4-11) but based on the partitioning of Equation (5-7) and use of Equations (5-3) for matrices \mathbf{K}_{ab} , \mathbf{K}_{bb} , \mathbf{M}_{ab} , etc. The condensed rubber seal force vector is given by:

$$\tilde{\mathbf{F}}_{rb} = \mathbf{F}_{rba} - \mathbf{K}_{ab} \mathbf{K}_{bb}^{-1} \mathbf{F}_{rbb} \quad (5-9)$$

The condensed vertical contact force vector is given in Equation (5-10) - the components will be presented later in this section.

$$\tilde{\mathbf{F}}_{vg} = \mathbf{F}_{vga} - \mathbf{K}_{ab} \mathbf{K}_{bb}^{-1} \mathbf{F}_{vgb} \quad (5-10)$$

The inner rubber seal is a cylindrical flexible tension-only membrane that is attached on the perimeter of the top and bottom slide plates. The seal keeps the slide plates and the rigid slider together and protects the interior from contamination. A rubber seal is shown deformed in the photograph of Figure 5-3. Figure 5-4 shows where the seal is attached and how it deforms during motion of the slider assembly. The rubber seal stiffness is too small to affect the behavior of the bearing when it is under a large vertical load but is large enough to affect the behavior of the slider assembly when the bearing is under uplift conditions and the lateral bearing force is zero. Accordingly, the seal stiffness is accounted for herein only during an uplift episode.

Note that the free length of the seal is less than the height of the slider assembly ($\approx h_1 + h_4$) but on deformation the length that determines the angle of inclination is l_{bd} with an initial value l_{in} . During motion of the slider assembly, the top and bottom slide plates rotate differently and the seal is subjected to tension in some of its body and to compression elsewhere.

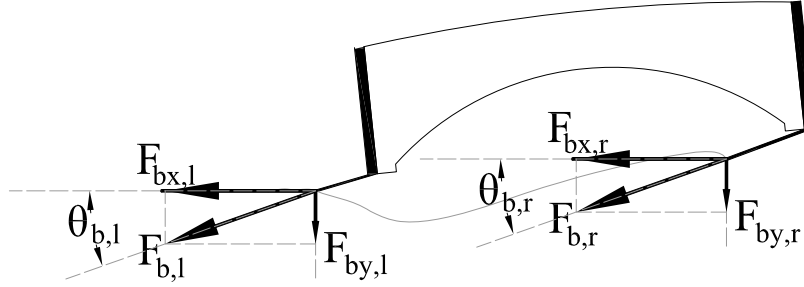


Figure 5-4: Slider assembly and inner seal forces on top and bottom slide plates

The inner rubber seal is represented by two springs; one located on the left and one on the right of the assembly. Each spring generates a pair of forces located at the restrainer tips of the top and bottom slide plates (points B1, B2, B3 and B4 in Figure 5-4). The deformed length of each of these springs is given by (where $\|\dots\|$ represents the magnitude):

$$\begin{aligned} l_{bd,l} &= \|\mathbf{x}_{B2} - \mathbf{x}_{B1}\| \\ l_{bd,r} &= \|\mathbf{x}_{B4} - \mathbf{x}_{B3}\| \end{aligned} \quad (5-11)$$

Subscript l denotes the spring on the left while subscript r denotes the spring on the right. $\mathbf{x}_{B1}, \mathbf{x}_{B2}, \mathbf{x}_{B3}, \mathbf{x}_{B4}$ are 2x1 vectors with the coordinates of points B1, B2, B3 and B4, respectively, (shown in Figure 5-4) with respect to a coordinate system having its origin at the center of curvature of surface 1 and is positive upwards. These vectors are given by:

$$\begin{aligned} \mathbf{x}_{B1} &= \begin{Bmatrix} x_{B1} \\ y_{B1} \end{Bmatrix} = \mathbf{x}_{O1} + \mathbf{T}_{BSP} \mathbf{r}_{B1} \\ \mathbf{x}_{B2} &= \begin{Bmatrix} x_{B2} \\ y_{B2} \end{Bmatrix} = \mathbf{x}_{O4} + \mathbf{T}_{TSP} \mathbf{r}_{B2} \\ \mathbf{x}_{B3} &= \begin{Bmatrix} x_{B3} \\ y_{B3} \end{Bmatrix} = \mathbf{x}_{O1} + \mathbf{T}_{BSP} \mathbf{r}_{B3} \\ \mathbf{x}_{B4} &= \begin{Bmatrix} x_{B4} \\ y_{B4} \end{Bmatrix} = \mathbf{x}_{O4} + \mathbf{T}_{TSP} \mathbf{r}_{B4} \end{aligned} \quad (5-12)$$

In Equation (5-12), $\mathbf{x}_{O1}, \mathbf{x}_{O2}$ are vectors with the coordinates of points O1 and O4 in Figure 5-4 and are given by the Equation (5-13):

$$\mathbf{x}_{O1} = \begin{Bmatrix} R_1 \sin \theta_1 \\ -R_1 \cos \theta_1 \end{Bmatrix}$$

$$\mathbf{x}_{O4} = \begin{Bmatrix} (R_{eff1} - R_{eff2}) \sin \theta_1 + (R_{eff2} + R_{eff3}) \sin(\theta_1 + \theta_2) - R_3 \sin(\theta_1 + \theta_2 - \theta_3) \\ -(R_{eff1} - R_{eff2}) \cos \theta_1 - (R_{eff2} + R_{eff3}) \cos(\theta_1 + \theta_2) + R_3 \cos(\theta_1 + \theta_2 - \theta_3) \end{Bmatrix} \quad (5-13)$$

In the equations above, θ_i are the sliding angles. Also, $\mathbf{r}_{B1}, \mathbf{r}_{B2}, \mathbf{r}_{B3}, \mathbf{r}_{B4}$ in Equation (5-12) are constant vectors that contain the relative coordinates of points O1 and B1, O4 and B2, O1 and B3, and O4 and B4, respectively, and are given by:

$$\mathbf{r}_{B1} = \begin{Bmatrix} -b_1 \\ h_{b1} + h_{r2} + h_{s2} + h_1 - h_2 \end{Bmatrix}; \mathbf{r}_{B2} = \begin{Bmatrix} -b_4 \\ -h_{b1} - h_{r3} - h_{s2} - h_1 + h_2 \end{Bmatrix};$$

$$\mathbf{r}_{B3} = \begin{Bmatrix} b_1 \\ h_{b1} + h_{r2} + h_{s2} + h_1 - h_2 \end{Bmatrix}; \mathbf{r}_{B4} = \begin{Bmatrix} b_4 \\ -h_{b1} - h_{r3} - h_{s2} - h_1 + h_2 \end{Bmatrix}; \quad (5-14)$$

$$h_{si} = R_i - \sqrt{R_i^2 - (d_i + b_i / 2)^2}$$

$$h_{bi} = R_i - \sqrt{R_i^2 - (b_i / 2)^2}$$

where b_i is the diameter of the contact surface i , h_{si} is the height differential between the center and the edge of the sliding surface i , h_{bi} is the height differential between the center and the edge of the contact surface i (the contact surface is the one of least diameter out of the two surfaces in contact and the sliding surface is the one of largest diameter), and h_{r2} and h_{r3} are the heights of the restrainers of surfaces 2 and 3 as shown in Figure 5-4. Finally, $\mathbf{T}_{BSP}, \mathbf{T}_{TSP}$ in Equation (5-12) are given by the Equation (5-15):

$$\mathbf{T}_{BSP} = \begin{bmatrix} \cos \theta_1 & \sin \theta_1 \\ -\sin \theta_1 & \cos \theta_1 \end{bmatrix}; \mathbf{T}_{TSP} = \begin{bmatrix} \cos \theta_1 & \sin \theta_1 \\ -\sin \theta_1 & \cos \theta_1 \end{bmatrix} \quad (5-15)$$

The angles of the springs are given by:

$$\theta_{b,l} = \sin^{-1} \frac{x_{B2} - x_{B1}}{l_{bd,l}}; \theta_{b,r} = \sin^{-1} \frac{x_{B4} - x_{B3}}{l_{bd,r}} \quad (5-16)$$

The force components of the left and right seal forces in the horizontal and vertical directions are given by Equation (5-17). They apply along the lines between points B1-B2 and B3-B4 (Figure 5-4) as pairs opposing each other.

$$\begin{aligned}
 F_{bx,l} &= \begin{cases} k_{b,l} (l_{bd,l} - l_{in}) \sin \theta_{b,l} \\ 0 \end{cases}; & F_{by,l} &= \begin{cases} k_{b,l} (l_{bd,l} - l_{in}) \cos \theta_{b,l} \\ 0 \end{cases} \\
 F_{bx,r} &= \begin{cases} k_{b,r} (l_{bd,r} - l_{in}) \sin \theta_{b,r} \\ 0 \end{cases}; & F_{by,r} &= \begin{cases} k_{b,r} (l_{bd,r} - l_{in}) \cos \theta_{b,r} \\ 0 \end{cases}
 \end{aligned} \tag{5-17}$$

The stiffness of the rubber seal ($k_{b,r}, k_{b,l}$) can be calculated as half of the tensile stiffness of a hollow rubber tube of modulus of elasticity E , thickness t_s , diameter b_1 (see Figure 5-4) and length l_{in} :

$$k_{b,l} = k_{b,r} = \frac{\pi b_1 t_s E}{2l_{in}} \geq \frac{\pi b_1 t_s E}{2(h_1 + h_4)} \tag{5-18}$$

Equation (5-18) assumes linear elastic behavior for the seal. A more realistic behavior can be considered by assuming that the seal is nonlinear elastic due to changes in thickness and length during deformation:

$$\begin{aligned}
 k_{b,l} &= \frac{\pi E b_1 l_{in} t_s}{2l_{bd,l}^2} \\
 k_{b,r} &= \frac{\pi E b_1 l_{in} t_s}{2l_{bd,r}^2}
 \end{aligned} \tag{5-19}$$

In the equation above, the seal is assumed incompressible so that the seal volume is equal to the initial volume prior to deformation. The instantaneous thickness of the seal t' is assumed to vary based on $t' = l_{in} t_s / l_{bd}$. Moreover, the seal stiffness is calculated based on the instantaneous length of the seal. Note also that the left and right spring exhibit different values of stiffness as they have different deformations.

The initial length of the seal in Equation (5-17) to (5-19) is given by the following equation:

$$l_{in} = s_g + h_1 + h_4 - h_{b1} - h_{b4} - h_{s2} - h_{s3} - h_{r2} - h_{r3} \tag{5-20}$$

s_g is a value of deformation that delays the engagement of the seal. In Figure 5-4, this value is shown to be zero as the seal engages from the start of deformation. A nonzero value can be specified in order to model bulging of the seal in the un-deformed position of the TFP assembly. Figure 5-5 shows a photograph of an un-deformed TFP assembly with a bulge. Figure 5-6 shows an example where the seal has an initial circular bulge of radius r . In this case, the seal has to deform by an amount $s_g = \pi r - 2r$ in order to engage and this value should be specified in Equation (5-20). When the seal contains a bulge, the initial seal length should be distinguished from the seal installed length denoted as l_{ip} in Figure 5-6.

The difference in the behavior between Equation (5-18) (Linear Elastic) and Equation (5-19) (Nonlinear Elastic) is significant and the results shown in Figure 5-7 demonstrate this.



Figure 5-5: Slider assembly of an un-deformed Triple FP bearing that shows the existence of bulging of the seal

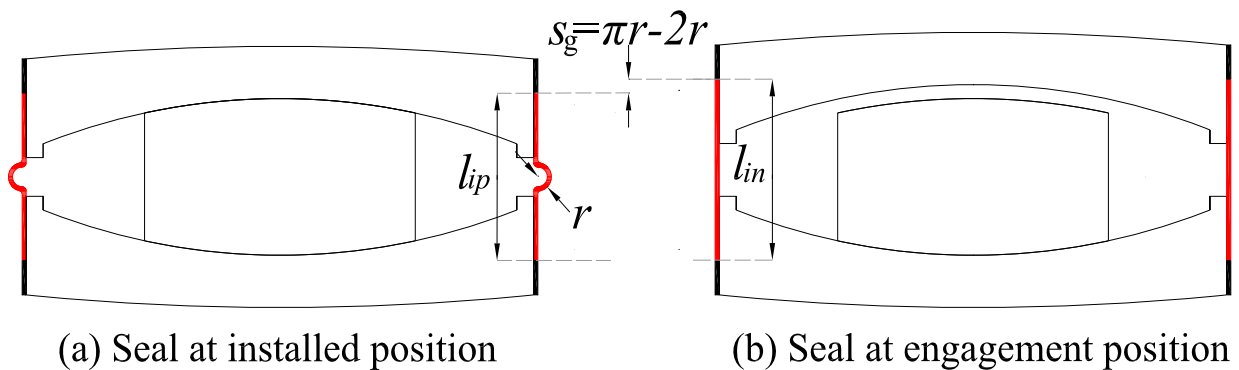


Figure 5-6: Schematics of rubber seal with initial bulge

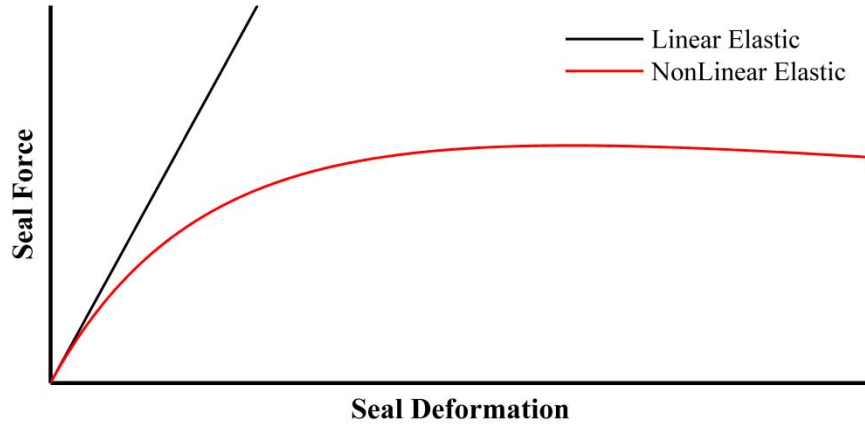


Figure 5-7: Comparison of seal force-deformation relation based on Equations (5-18) (Linear elastic) and (5-19) (Nonlinear elastic)

The model of the seal presented so far is based on the assumption that the seal is attached over the entire height of the perimeter of the TSP and BSP. As a result, it was assumed that the seal was attached at points B1, B2, B3 and B4 in Figure 5-4. This may not be the case in practical applications as demonstrated in the deformed bearing of Figure 5-3. Accordingly, a more complex seal behavior is considered where the seal is assumed to be attached at points different than B1, B2, B3 and B4 (see Figure 5-4).

Consider Figure 5-8(a) where the seal is attached at points C1, C2, C3 and C4 which are located at distance s_{A1} from the edges of contact surface 1 and s_{A4} from the edges of contact surface 4. When the seal is deformed as shown in Figure 5-8(b), the left seal inclination angle is defined by the location of points B1 and C2, while the right seal inclination angle is defined by the location of points C3 and B4. When the seal is deformed as shown Figure 5-8(c), the left seal inclination angle is defined by the location of points C1 and B2, while the right seal inclination angle by the location of points B3 and C4.

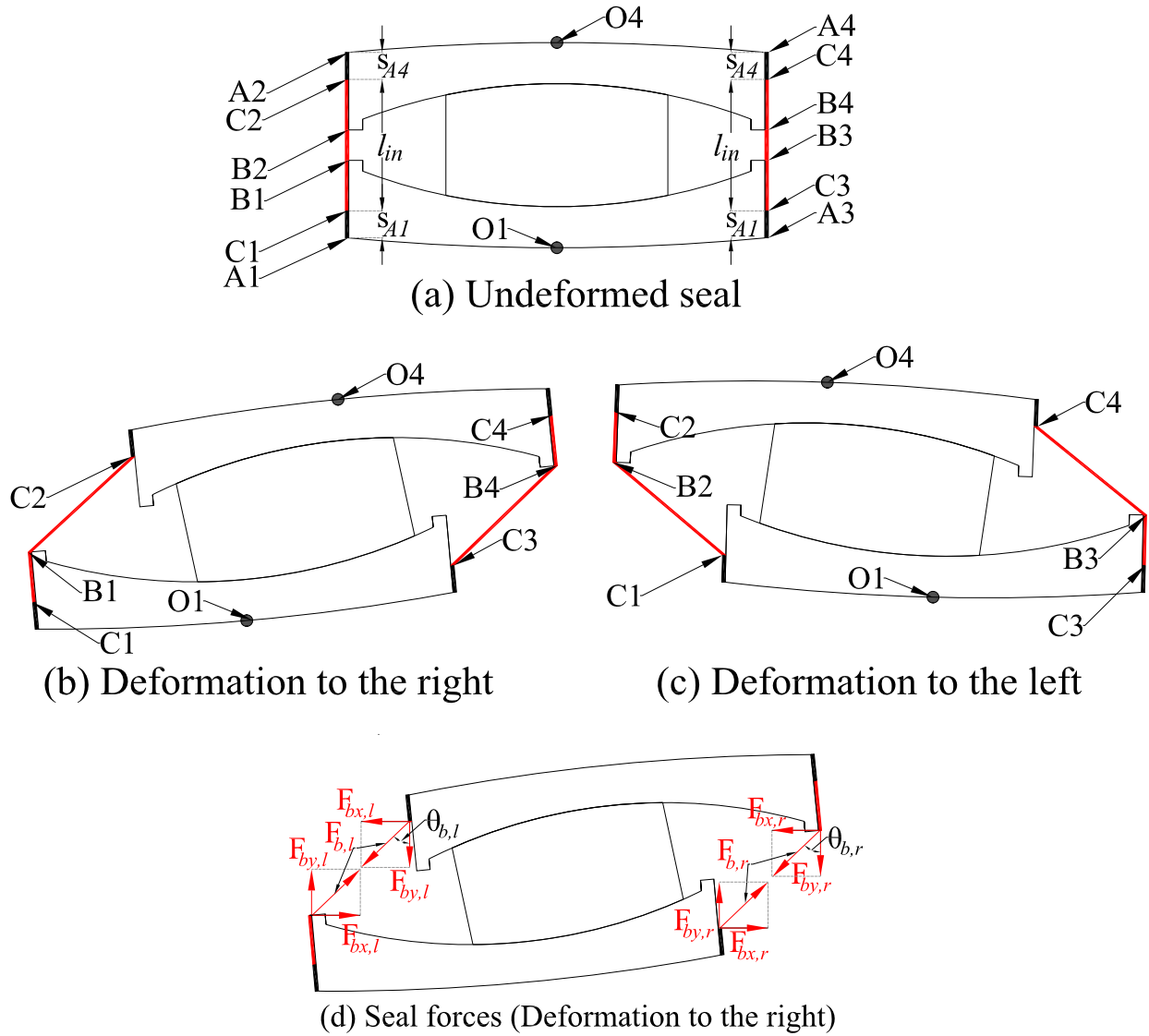


Figure 5-8: Seal parameter definitions

The coordinates of the attachment points are given by:

$$\begin{aligned}
 \mathbf{x}_{C1} &= \begin{Bmatrix} x_{C1} \\ y_{C1} \end{Bmatrix} = \mathbf{x}_{O1} + \mathbf{T}_{BSP} \mathbf{r}_{C1} \\
 \mathbf{x}_{C2} &= \begin{Bmatrix} x_{C2} \\ y_{C2} \end{Bmatrix} = \mathbf{x}_{O4} + \mathbf{T}_{TSP} \mathbf{r}_{C2} \\
 \mathbf{x}_{C3} &= \begin{Bmatrix} x_{C3} \\ y_{C3} \end{Bmatrix} = \mathbf{x}_{O1} + \mathbf{T}_{BSP} \mathbf{r}_{C3} \\
 \mathbf{x}_{C4} &= \begin{Bmatrix} x_{C4} \\ y_{C4} \end{Bmatrix} = \mathbf{x}_{O4} + \mathbf{T}_{TSP} \mathbf{r}_{C4}
 \end{aligned} \tag{5-21}$$

In Equation (5-21), vectors $\mathbf{x}_{O1}, \mathbf{x}_{O2}$ were given by Equation (5-13), $\mathbf{T}_{BSP}, \mathbf{T}_{TSP}$ by Equation (5-15) and $\mathbf{r}_{C1}, \mathbf{r}_{C2}, \mathbf{r}_{C3}, \mathbf{r}_{C4}$ are constant vectors given by:

$$\mathbf{r}_{C1} = \begin{Bmatrix} -b_1 \\ s_{A1} + h_{b1} \end{Bmatrix}; \mathbf{r}_{C2} = \begin{Bmatrix} -b_4 \\ -s_{A4} - h_{b4} \end{Bmatrix}; \mathbf{r}_{C3} = \begin{Bmatrix} b_1 \\ s_{A1} + h_{b1} \end{Bmatrix}; \mathbf{r}_{C4} = \begin{Bmatrix} b_4 \\ -s_{A4} - h_{b4} \end{Bmatrix} \quad (5-22)$$

Note that quantities h_{si} and h_{bi} were defined in Equation (5-14), and quantities s_{A1} and s_{A4} were defined in Figure 5-8(a). Let define vectors $\mathbf{A}_1, \mathbf{A}_2, \mathbf{A}_3$ and \mathbf{A}_4 as:

$$\begin{aligned} \mathbf{A}_1 &= \begin{cases} \mathbf{x}_{C1}, \omega_1 > a_1 \\ \mathbf{x}_{B1}, \omega_1 < a_1 \end{cases}, \mathbf{A}_2 = \begin{cases} \mathbf{x}_{C2}, \omega_2 < a_1 \\ \mathbf{x}_{B2}, \omega_2 > a_1 \end{cases} \\ \mathbf{A}_3 &= \begin{cases} \mathbf{x}_{C3}, \omega_3 > a_2 \\ \mathbf{x}_{B3}, \omega_3 < a_2 \end{cases}, \mathbf{A}_4 = \begin{cases} \mathbf{x}_{C4}, \omega_4 > a_2 \\ \mathbf{x}_{B4}, \omega_4 < a_2 \end{cases} \end{aligned} \quad (5-23)$$

$$\omega_1 = a \tan \frac{x_{B1} - x_{A1}}{y_{B1} - y_{A1}}, \omega_2 = a \tan \frac{x_{B2} - x_{A2}}{y_{B2} - y_{A2}}, \omega_3 = a \tan \frac{x_{A3} - x_{B3}}{y_{A3} - y_{B3}}, \omega_4 = a \tan \frac{x_{B3} - x_{A4}}{y_{B3} - y_{A4}}$$

$$\alpha_1 = a \tan \frac{x_{C2} - x_{C1}}{y_{C2} - y_{C1}}, \alpha_2 = a \tan \frac{x_{C4} - x_{C3}}{y_{C4} - y_{C3}}$$

Vectors $\mathbf{A}_1, \mathbf{A}_2, \mathbf{A}_3$ and \mathbf{A}_4 are used to identify the seal “bending” points which in general are different from the attachment points C1, C2, C3 and C4 as illustrated in Figure 5-8. $\mathbf{A}_1, \mathbf{A}_2, \mathbf{A}_3, \mathbf{A}_4$ determine the location of the bending points of the bottom left, the top left, the bottom right and the top right part of the seal, respectively. For the example of Figure 5-8(b) at the bottom left part of the seal, the attachment point is C1 and the “bending point” is B1 and, therefore, $\mathbf{A}_1 = \mathbf{x}_{B1}$. At the top left part of the seal, the attachment and “bending” points coincide at C2 and, therefore, $\mathbf{A}_2 = \mathbf{x}_{C2}$. At the bottom right part, the attachment and “bending” points coincide at point C3 and, therefore, $\mathbf{A}_3 = \mathbf{x}_{C3}$. For the top right part, the attachment point is C4 and the “bending” point is B4 and, therefore, $\mathbf{A}_4 = \mathbf{x}_{B4}$. In the example of Figure 5-8(c), $\mathbf{A}_1 = \mathbf{x}_{C1}$, $\mathbf{A}_2 = \mathbf{x}_{B2}$, $\mathbf{A}_3 = \mathbf{x}_{B3}$, $\mathbf{A}_4 = \mathbf{x}_{C4}$.

The deformed length of the seal is given by the length of the segments shown in red in Figure 5-8. They are given by:

$$\begin{aligned}
l_{bd,l} &= \|\mathbf{x}_{B1} - \mathbf{A}_1\| + \|\mathbf{A}_1 - \mathbf{A}_2\| + \|\mathbf{A}_2 - \mathbf{x}_{B2}\| \\
l_{bd,r} &= \|\mathbf{x}_{C'} - \mathbf{A}_{BR}\| + \|\mathbf{A}_{BR} - \mathbf{A}_{TR}\| + \|\mathbf{A}_{TR} - \mathbf{x}_{D'}\|
\end{aligned} \tag{5-24}$$

The inclination angles of the seals are used to calculate the vertical and horizontal components of the seal forces and are given by:

$$\theta_{b,l} = \sin^{-1} \frac{A_2^1 - A_1^1}{\|\mathbf{A}_2 - \mathbf{A}_1\|}; \quad \theta_{b,r} = \sin^{-1} \frac{A_4^1 - A_3^1}{\|\mathbf{A}_4 - \mathbf{A}_3\|} \tag{5-25}$$

where A_i^1 is the x-component of vector \mathbf{A}_i .

In summary, the seal forces are given by Equation (5-17), and the stiffness of the seal can be obtained either from Equation (5-18) for linear elastic behavior or from Equation (5-19) for nonlinear elastic behavior.

During uplift, the TCP might come into contact with the inner components of the bearing due to the curvature of surface 4. This is illustrated in Figure 5-9. For the derivations of this section that assume full contact, this event is approximately captured by introducing vertical compression-only forces, $F_{vg,l}$ and $F_{vg,r}$, as shown in Figure 5-10 and given by the following equation:

$$\begin{aligned}
F_{vg,l} &= \begin{cases} k_v (y_{A2} - y_{A2'}), & y_{A2} > y_{A2'} \\ 0, & y_{A2} \leq y_{A2'} \end{cases} \\
F_{vg,r} &= \begin{cases} k_v (y_{A4} - y_{A4'}), & y_{A4} > y_{A4'} \\ 0, & y_{A4} \leq y_{A4'} \end{cases}
\end{aligned} \tag{5-26}$$

In Equation (5-26), $y_{A2}, y_{A2'}, y_{A4}, y_{A4'}$ are the vertical coordinates of the points $A2, A2', A4, A4'$ shown in Figure 5-10 with respect to a coordinate system located at the center of curvature of surface 1 and positive upwards, and k_v is a stiffness of arbitrary and large value in order to minimize or eliminate any penetration between the TSP and TCP. The horizontal and vertical coordinates of points $A2, A4$ (located on the TSP) are:

$$\begin{aligned}
\mathbf{x}_{A2} &= \begin{Bmatrix} x_{A2} \\ y_{A2} \end{Bmatrix} = \mathbf{x}_{O4} + \mathbf{T}_{TSP} \mathbf{r}_{A2} \\
\mathbf{x}_{A4} &= \begin{Bmatrix} x_{A4} \\ y_{A4} \end{Bmatrix} = \mathbf{x}_{O4} + \mathbf{T}_{TSP} \mathbf{r}_{A4}
\end{aligned} \tag{5-27}$$

In Equation (5-27), vectors $\mathbf{x}_{O1}, \mathbf{x}_{O2}$ are given by Equation (5-13), \mathbf{T}_{TCP} is given by Equation (5-15) and $\mathbf{r}_{A2}, \mathbf{r}_{A4}$ are constant vectors given by:

$$\mathbf{r}_{A2} = \begin{Bmatrix} -b_4 \\ -h_{b4} \end{Bmatrix}; \mathbf{r}_{A4} = \begin{Bmatrix} b_4 \\ -h_{b4} \end{Bmatrix} \quad (5-28)$$

The vertical coordinates of points A', B' (located on the TCP) in Figure 5-10 are given by:

$$\begin{aligned} y_{A2'} &= -R_1 + h_1 + h_4 - R_4 + \sqrt{R_4^2 - (u - x_{A2})^2} + v_{TCP} \\ y_{A4'} &= -R_1 + h_1 + h_4 - R_4 + \sqrt{R_4^2 - (u - x_{A4})^2} + v_{TCP} \end{aligned} \quad (5-29)$$

where v_{TCP} is the total vertical displacement of the TCP defined in Section 5.2 and u is the horizontal displacement of the TCP.

Note that for the calculation of the vertical forces in Equation (5-26) and of the seal forces, use is made of the actual rotations of the elements which are large, whereas the model for the bearing in compression and uplift is based on the assumption of small rotations. Note also that the TCP horizontal displacement when considering large rotations ends up being slightly less than the excitation displacement u . This leads to some small incompatibility in the calculation of the coordinates of points $A2, A2', A4, A4'$ at the initiation of the uplift event. This may occasionally lead to nonzero initial vertical contact forces. Depending on the value of stiffness k_v , these forces may become large. This is unrealistic and to be avoided; the TCP displacement v_{TCP} in Equation (5-2) is increased by a quantity equal to $\max(|y_{A2}^{t=t_1} - y_{A2'}^{t=t_1}|, |y_{A4}^{t=t_1} - y_{A4'}^{t=t_1}|)$ (an extremely small value) in order to ensure that there is no penetration at the beginning of the uplift event.

Forces $F_{vg,l}$ and $F_{vg,r}$ cannot be simultaneously nonzero since such a case corresponds to the bearing being in compression and, therefore, the model presented in Section 4 should be used. If simultaneous nonzero values occur during the uplift analysis, the uplift analysis is terminated and resumed with the equations of Section 4. This case is described later.

It should be noted that contact of the type shown in Figure 5-9 between the TCP and TSP might lead to uplifting of the inner components and therefore the modeling described in Section 6 could also be used in that case.

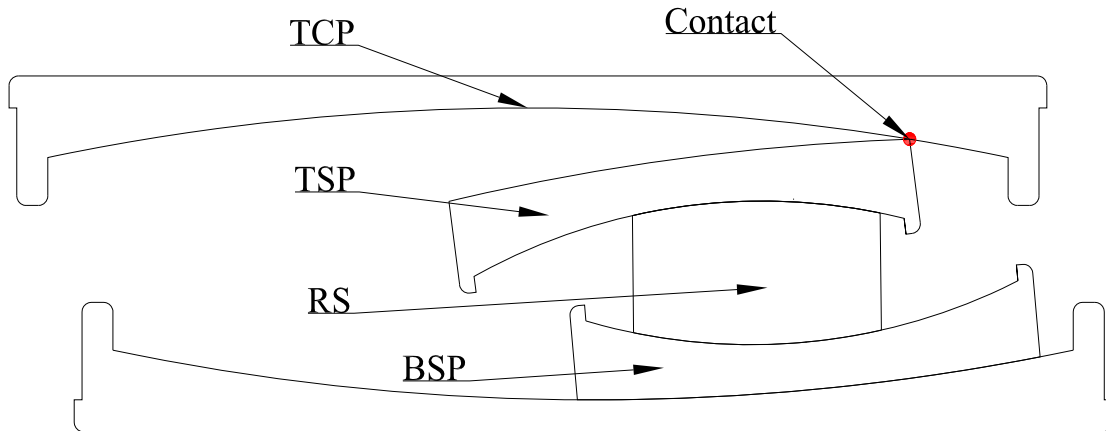


Figure 5-9: View of TFP under uplift conditions and contact between the TCP and TSP

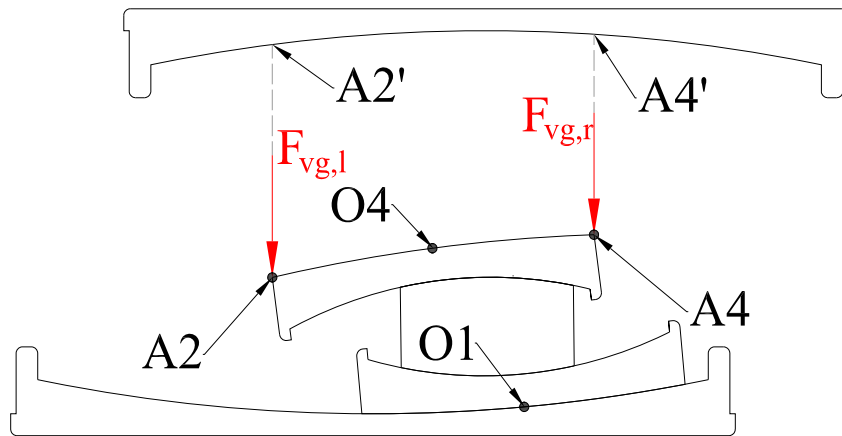


Figure 5-10: Vertical contact forces acting on the TSP

5.4 Modeling of Landing

Landing of the TFP isolator is a complex phenomenon. This behavior is modeled in two distinct methods: (a) a simple method is described in Section 5.4 and (b) another more realistic method, capable of analyzing the behavior of rigid bodies experiencing sliding, rocking, contact, overturning and free fall, is described in Section 6.

The simple model is based on the use of the model for the bearing under load and for full contact of the sliding surfaces presented in Section 4.2 and described by Equations (4-4) to (4-17) but with initial conditions being the values of the angles of the bearing components at the end of the

uplift episode as calculated in the analysis of the bearing during uplift with full contact as described in Section 5.3 or without full contact as described in Section 6.

More specifically, consider the isolator at the end of the uplift event shown in Figure 5-11(a) with sliding angles given by $\theta_{1,u}^{t=t_2}$, $\theta_{2,u}^{t=t_2}$, $\theta_{3,u}^{t=t_2}$. Equations (4-4) to (4-17) require only two initial conditions for displacements (horizontal displacement u is the input; three initial conditions are required when the model is used for dynamic analysis). Rotations $\theta_{1,u}^{t=t_2}$, $\theta_{2,u}^{t=t_2}$ are substituted into Equations (4-4) to (4-17) as initial conditions while the sliding rotation $\theta_{3,u}^{t=t_2}$ is ignored. Also, two initial conditions for the velocities are required. Accordingly, at the end of the uplift event the compatibility Equation (4-3) is not satisfied. At the first integration step of Equation (4-17), new rotations ($\theta_{1,c}^{t=t_2}$, $\theta_{2,c}^{t=t_2}$ and $\theta_{3,c}^{t=t_2}$, $\theta_{4,c}^{t=t_2}$ from compatibility) will be calculated so that equilibrium and compatibility are restored as shown in Figure 5-11(b). The top concave plate will also exhibit a reduction in its vertical displacement given by $v_{TCP}^{t=t_2} - v_p^{t=t_2}$ (see Figure 5-11 and Figure 5-2). Note that the total vertical displacement at the end of the landing event ($v_p^{t=t_2}$ in Figure 5-2) is calculated using Equation (5-1) and the final values $\theta_{1,c}^{t=t_2}$, $\theta_{2,c}^{t=t_2}$, $\theta_{3,c}^{t=t_2}$, $\theta_{4,c}^{t=t_2}$. Therefore, the difference $v_{TCP}^{t=t_2} - v_p^{t=t_2}$ in Figure 5-2 is the vertical displacement undergone by the TCP during the landing event so that compression and full contact is restored in the bearing. This is “free fall” displacement of the TCP.

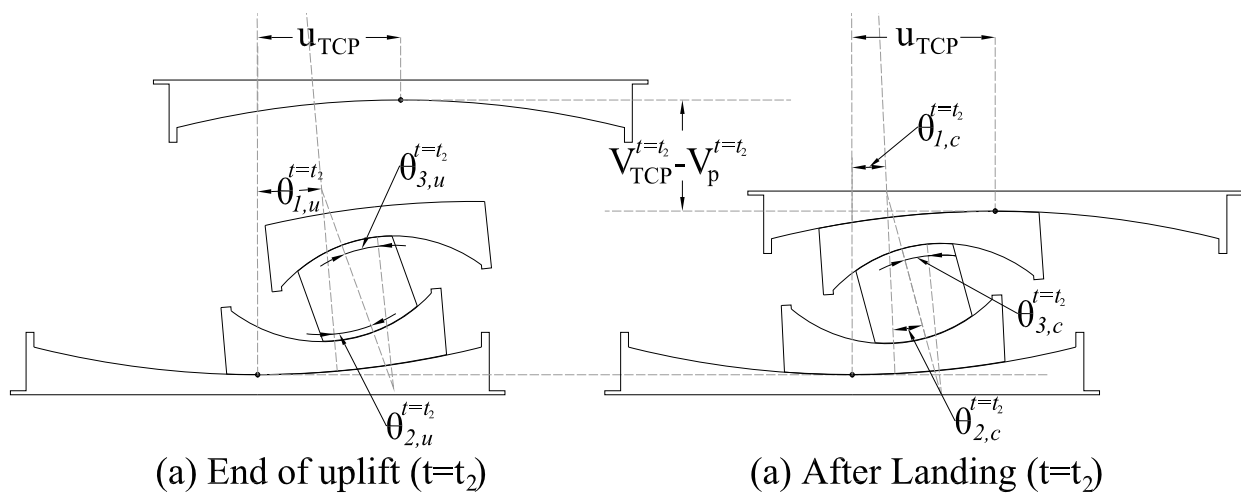


Figure 5-11: TFP isolator at the end of uplift event and after landing event

This model may occasionally produce incorrect results when under extreme conditions; the internal components of the bearing are required to abruptly relocate to a very different position in order to satisfy the conditions of compatibility upon full contact at the end of the uplift episode. For such cases, the more complex model described in Section 6 provides a more realistic prediction of response.

5.5 Additional Considerations for Uplift Analysis

5.5.1 Landing prior to end of uplift excitation

Consider (a) Figure 5-12(a) which shows a bearing in uplift and with the vertical contact force $F_{vg,l}$ being nonzero, (b) Figure 5-12(b) which shows the isolator still in the uplift state but the inner parts have moved to the right and gained height, and (c) Figure 5-12(c) where the height gained by the inner parts is larger than the vertical displacement of the TCP during uplift so that the bearing landed although the uplift displacement is still nonzero. Therefore, criteria are needed for switching back and forth between the equations of Section 4 (bearing in compression) and the equation of Section 5 (bearing in uplift). These criteria are:

- 1) Uplift has ended when the vertical contact forces $F_{vg,l}$ and $F_{vg,r}$ in Figure 5-10 are both nonzero. This condition is written as:

$$y_{A2} - y_{A2'} > 0 \ \& \ y_{A4} - y_{A4'} > 0 \quad (5-30)$$

- 2) Uplift resumes if the TCP displacement, described by Equation (5-2) and assuming uplift, becomes larger than the vertical TCP displacement calculated from the geometry of the deformed TFP isolator in compression and given by v_p in Equation (5-1). This condition is written as:

$$v_{TCP} > v_p \quad (5-31)$$

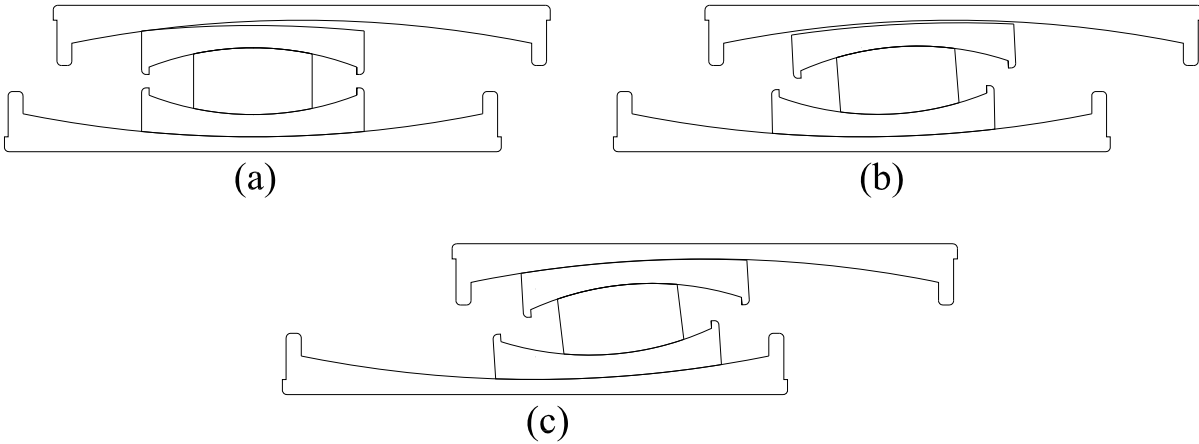


Figure 5-12: TFP undergoing landing prior to the end of uplift excitation

5.5.2 Collapse or instability of TFP isolators

Collapse or instability of the TFP isolator occurs if one of the two following events occurs:

- 1) The tip of the restrainer of surface 4 (point D2 or D4 in Figure 5-13) displaces above the TSP. This situation is depicted in Figure 5-13. This situation is described by the following two equations (the first equation is for the left restrainer while the second equation is for the right restrainer; x and y denote coordinates with respect to an arbitrary coordinate system):

$$\begin{aligned}
 y_{D2} > y_{A2} \ \& \ x_{D2} > x_{A2} \\
 y_{D4} > y_{A4} \ \& \ x_{D4} < x_{A4}
 \end{aligned}
 \tag{5-32}$$

- 2) Overturning of TFP inner parts. The theory that was presented in this section cannot capture overturning. The reader is referred to Section 6 for modeling of overturning. However, the capability of the theory presented in Sections 5 to calculate the contact force offset angles can provide information on when point contact occurs, which is a first step towards instability.

Considering the uncertainties involved in an uplift analysis, and in addition to the criteria above, the evaluation of collapse of the isolator should be mostly based on judgment after review of the analysis results.

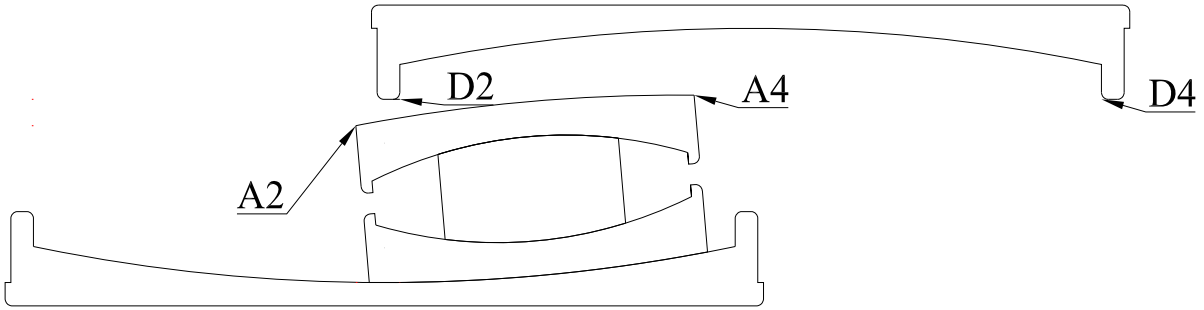


Figure 5-13: View of deformed TFP isolator when collapse is imminent

5.6 Summary of Uplift Analysis

The theory presented in Section 5 makes use of the horizontal and vertical displacement histories of the TCP (denoted as u and v_i ; see Figure 5-2) and simulates the response of the inner parts during the duration of excitation of the TCP. The analysis procedure for a complete uplift analysis is schematically shown in Figure 5-14.

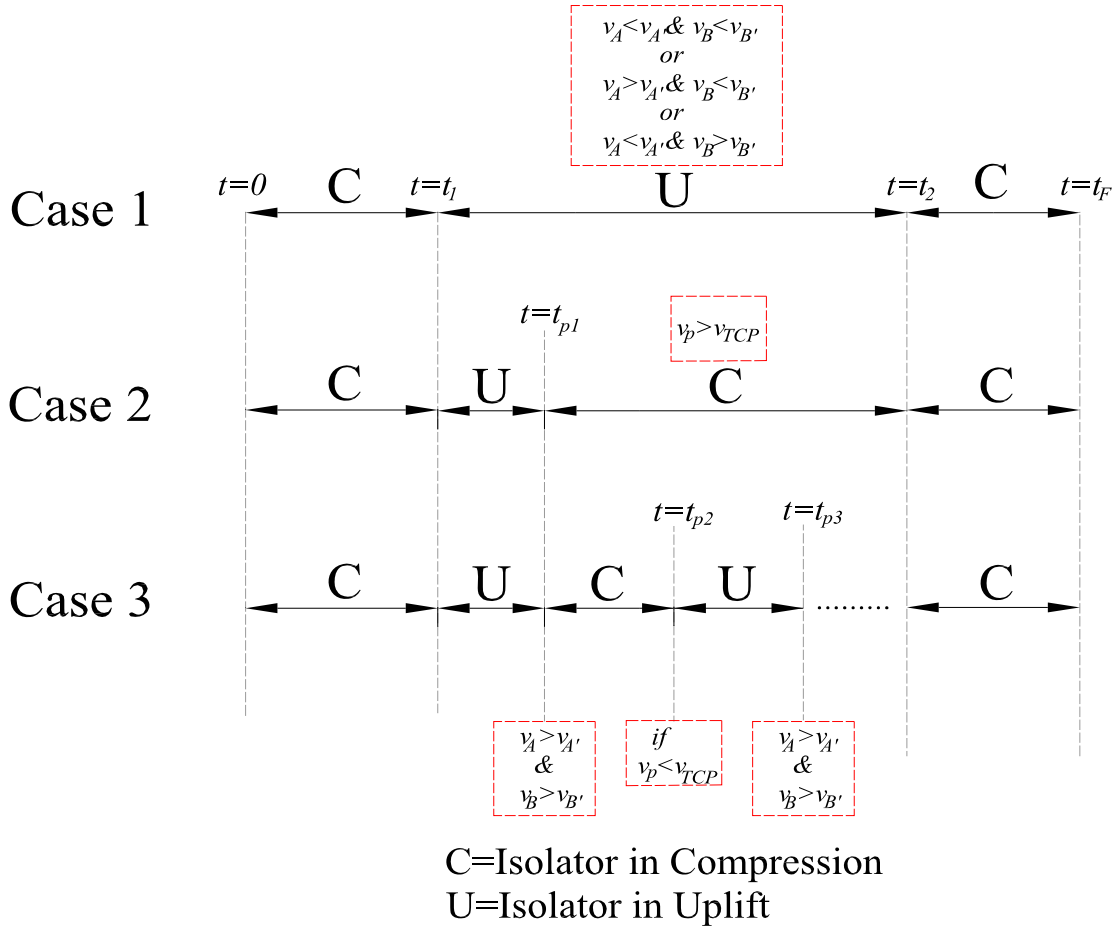


Figure 5-14: Flow diagram of uplift analysis of TFP isolator

A typical uplift analysis involves the following steps:

- 1) The TFP is initially analyzed in compression using the theory of Section 4 (Equations (4-4) to (4-17)) until time t_1 when uplift occurs (see Figure 5-2).
- 2) At time t_1 , Equations (4-4) to (4-17) provide the values for angles $\theta_1^{t=t_1}, \theta_2^{t=t_1}, \theta_3^{t=t_1}, \dot{\theta}_1^{t=t_1}, \dot{\theta}_2^{t=t_1}, \dot{\theta}_3^{t=t_1}$ to be used as initial conditions in Equations (5-1) to (5-14) and carry out the uplift analysis. Also, using the vertical displacement of the TCP at time t_1 , the total vertical displacement of the TCP is calculated using Equation (5-2). If the condition given by Equation (5-30) (with the aid of Equations (5-27) and (5-29)) is violated at all times during the entire uplift duration, the uplift equations are used until time t_2 when landing occurs. Furthermore,
 - a) If during the uplift duration the condition given by Equation (5-30) is satisfied at specific times only and not during the entire duration of uplift, uplift terminates

and compression of the isolator occurs. While in compression, if the condition given by Equation (5-31) is not satisfied at any time, uplift will not occur again until time t_2 so that the compression equations are used for the remainder of the excitation.

- b) If the condition given by Equation (5-31) is satisfied at a time instance, uplift is resumed at that time.
 - c) Steps a) and b) are repeated as many times as needed in the time interval t_1 to t_2 .
- 3) After time t_2 , the theory of Section 4 is used for the remainder of the excitation.

Note that this procedure and the formulations of this section can be used to model the TFP behavior when conducting response history of a structure with the TFP isolators exhibiting uplift. In doing so, a vertical compression-only spring needs to be added at surface 4 to connect the TCP and TSP. The motion of this spring is used to detect uplift and to calculate the uplift displacement during the analysis. During uplift, the isolator generates zero force and, therefore, terms related to the uplifted isolator are removed from the global equations of motion. That is, the horizontal and vertical displacements of the isolator can be calculated from the global equations of motion independently of the isolator below. The equations of Section 5 can then be used to calculate the uplift response of the isolator at every integration time step using the calculated horizontal and vertical displacement histories.

5.7 Verification Examples

This section presents simple examples of verification of the theory presented in Section 5. Consider the example shown in Figure 5-15. Very high values of the friction coefficients are assigned for surfaces 2 and 3 so that sliding only occurs on surface 1. The TSP, the RS and the BSP act as a single rigid body sliding on surface 1 below. Consider now that this rigid body is set in free vibration with initial conditions of displacement u_o and velocity \dot{u}_o .

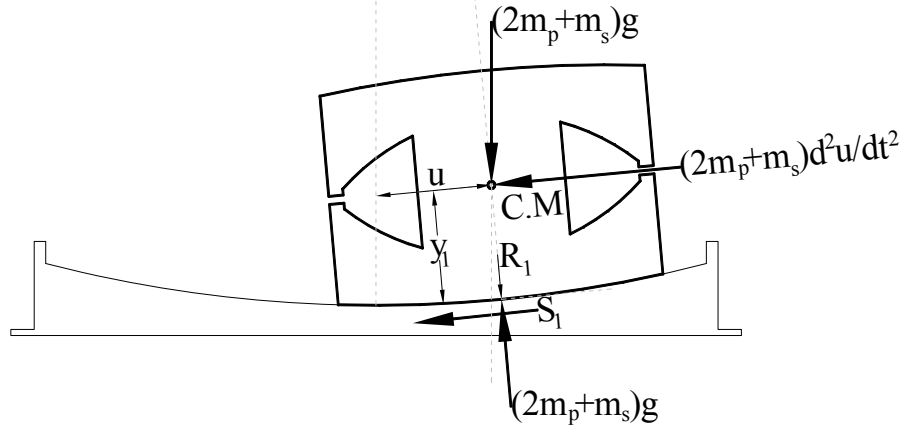


Figure 5-15: Simple verification example with sliding allowed only on surface 1

The closed form solution for the history of displacement, assuming Coulomb friction, is given by (see Chopra, 2012 for an example of analysis):

$$\begin{aligned} (a) : u(t) &= (u_o + u_F) \cos \omega t + (\dot{u}_o / \omega) \sin \omega t - u_F, \dot{u}_o > 0 \\ (b) : u(t) &= (u_o - u_F) \cos \omega t + (\dot{u}_o / \omega) \sin \omega t + u_F, \dot{u}_o < 0 \end{aligned} \quad (5-33)$$

Note that the initial conditions of displacement and velocity are related to the initial conditions of the sliding rotation θ_i and rotational velocity $\dot{\theta}_i$ by:

$$u_o = \theta_i (R_1 - y_1); \quad \dot{u}_o = \dot{\theta}_i (R_1 - y_1) \quad (5-34)$$

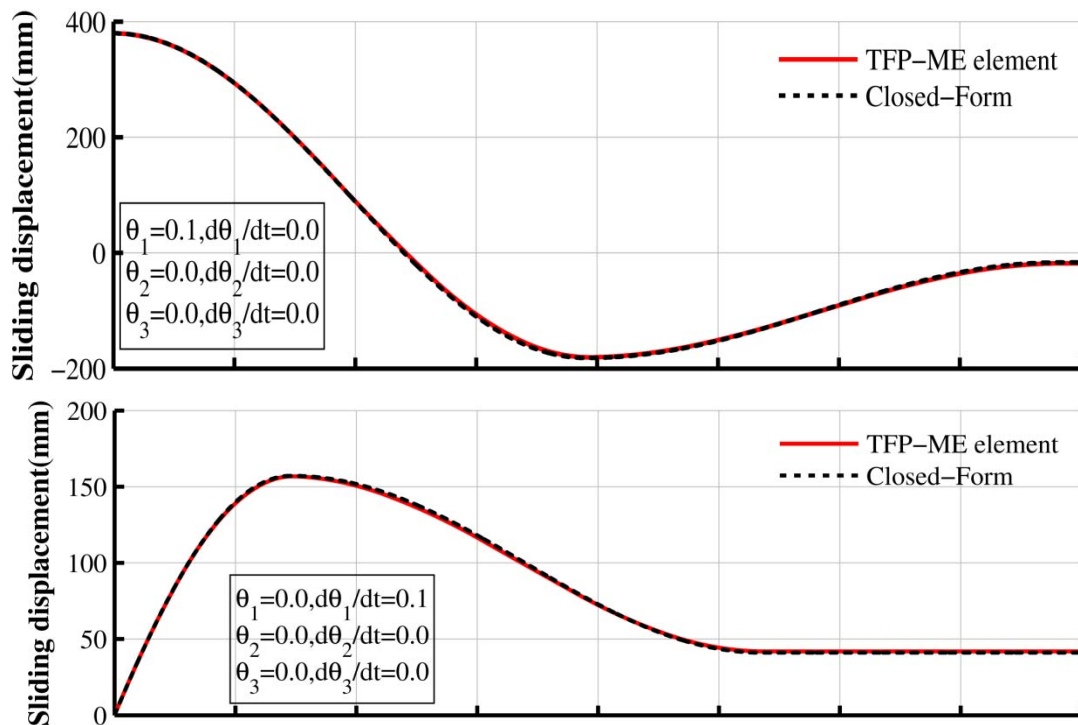
In Equation (5-34), y_1 is the distance of the center of mass of the rigid assembly (BSP, RS and TSP) from sliding surface 1. Also, quantities u_F and ω are given by:

$$u_F = \mu_1 (R_1 - y_1); \quad \omega = \sqrt{g / (R_1 - y_1)} \quad (5-35)$$

Given the initial conditions at $t=0$, either Equation (5-33a) or Equation (5-33b) is utilized. The time at which the velocity becomes zero can be calculated by letting the derivative of the selected equation, say (5-33a) to become zero. The displacement and velocity at that time are also calculated. Once the motion reverses direction, the other equation (now (5-33b) must be used with initial conditions being the final conditions calculated using the previous equation. This procedure needs to be repeated as many times as needed until the motion stops. Motion will stop when $\dot{u} = 0$ and $u(t_{\dot{u}=0}) < u_F$. The equations above assume that there is no impact between the sliding surface and its restrainer.

Figure 5-16 presents a comparison of results of the closed-formed solution to numerical calculations based on the theory presented in Section 5 for three different cases of initial conditions. The isolator has the geometric properties of the bearing Model Scale-Configuration A in Table 3-2 and with the friction coefficient at surface 1 $\mu_1=0.05$. In the first graph, an initial displacement with zero initial velocity is applied. In the second graph, an initial velocity with zero initial displacement is applied. In the last graph, a very large initial velocity with zero initial displacement is applied so that impact with the restrainer of surface 1 occurs.

Evidently, the results of the theory presented in Section 5 are essentially the same as those of the closed-form solution. The small differences are due to the difference in treating friction and the restrainer in the two solutions: visco-plastic friction model and elastic restrainer in the theory presented in Section 5, and Coulomb friction and rigid restrainers in the closed-form solution.



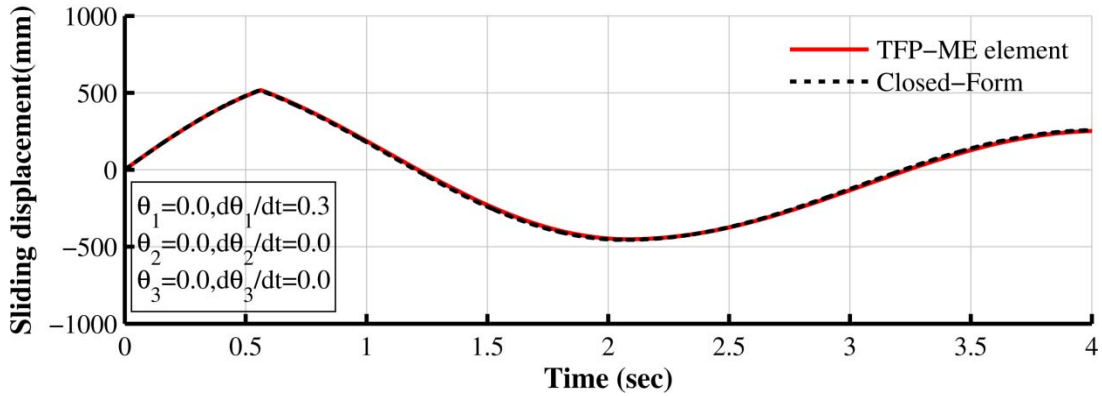


Figure 5-16: Comparison of results obtained by the model presented in Section 5 and closed form solution for the verification example of sliding on surface 1 subject to initial conditions

A second verification example is presented in Figure 5-17. This is similar to the example shown in Figure 5-15 where now sliding is only allowed on surface 2 with friction coefficient $\mu_2=0.05$. As a result, for the closed form solution, Equations (5-33) to (5-35) are valid but subscript 1 needs to be substituted by 2. Results of the theory presented in Section 5 are compared to the closed-form solution in Figure 5-18 for two cases of initial conditions: one of initial displacement with zero initial velocity and one of initial velocity with zero initial displacement. Again, the two solutions are essentially the same.

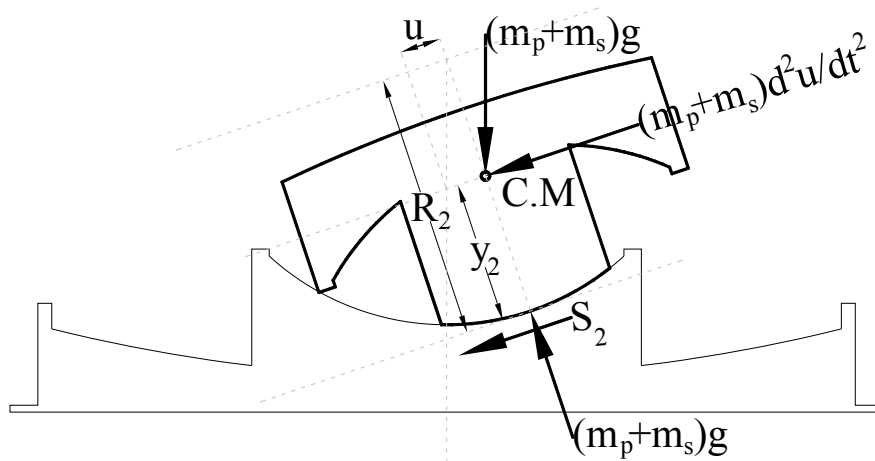


Figure 5-17: Simple verification example with sliding allowed only on surface 2

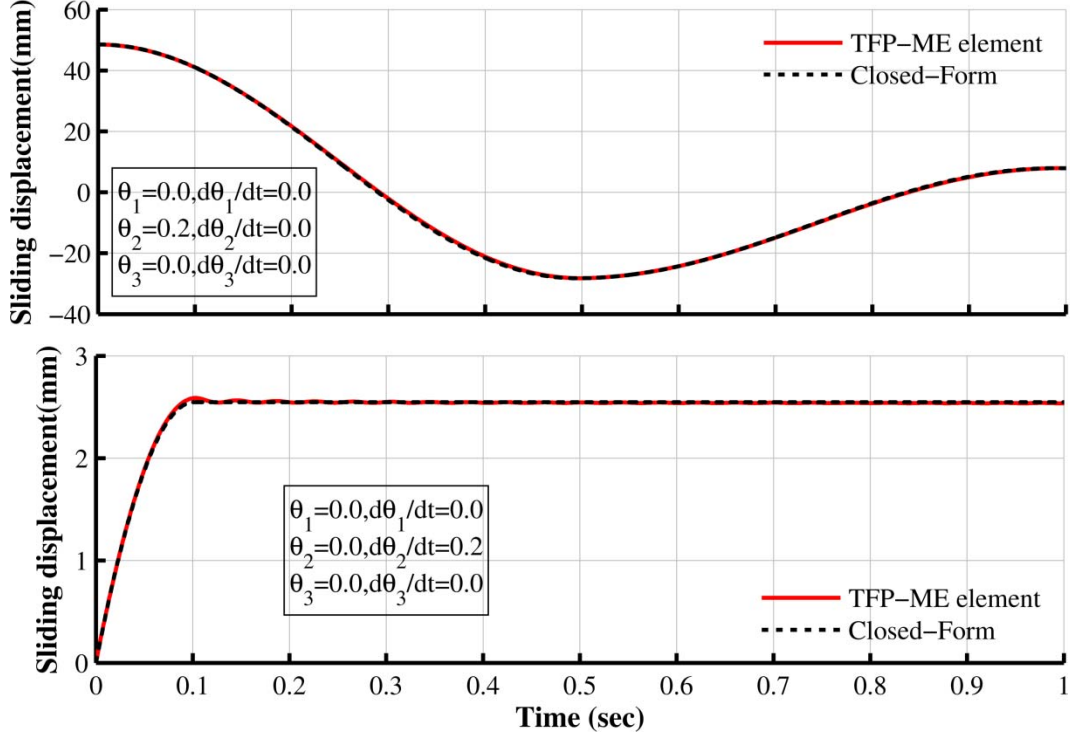


Figure 5-18: Comparison of results obtained by the model presented in Section 5 and closed form solution for the verification example of sliding on surface 2 subject to initial conditions

Finally, consider the example shown in Figure 5-19 where sliding is allowed only on surface 3. This is equivalent to a mass undergoing pendulum motion on a convex surface; an unstable system. For simplicity, we assume that the contact forces are applied at the center of the sliding surface and friction is ignored, so that the differential equation for free vibration is given by:

$$\ddot{u}(t) - (g/R_{eff})u(t) = 0 \quad (5-36)$$

The closed-form solution of this equation for an initial displacement and velocity is given by:

$$u(t) = \frac{1}{2}(u_o + \dot{u}_o)e^{\omega_n t} + \frac{1}{2}(u_o - \dot{u}_o)e^{-\omega_n t} \quad (5-37)$$

Impact on the restrainer of surface 3 occurs when displacement $u(t) = d_3$. The time and velocity at the instance of impact need to be evaluated and then substituted into Equation (5-37) for the solution to restart following impact. The closed-form solution is thus obtained for elastic impact on the restrainer. In the absence of any energy dissipation, motion continues forever.

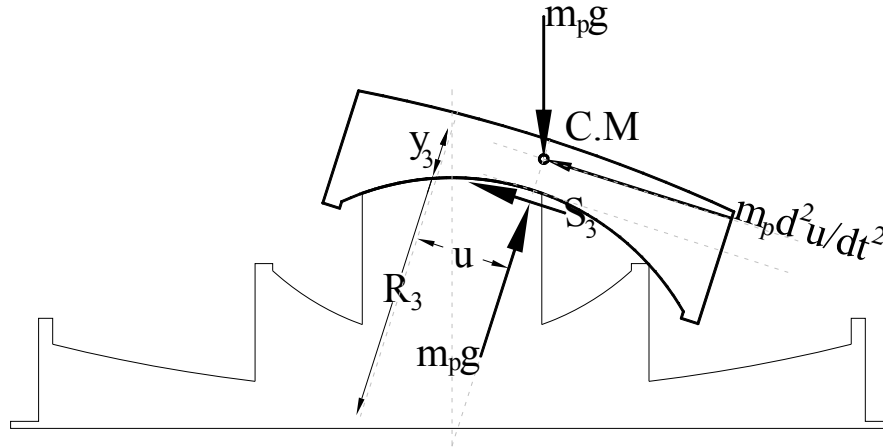


Figure 5-19: Simple verification example with sliding allowed only on surface 3

Results of the theory presented in Section 5 are compared to the closed-form solution and shown in Figure 5-20 for the case of initial velocity with zero initial displacement. Again, the two solutions are essentially the same.

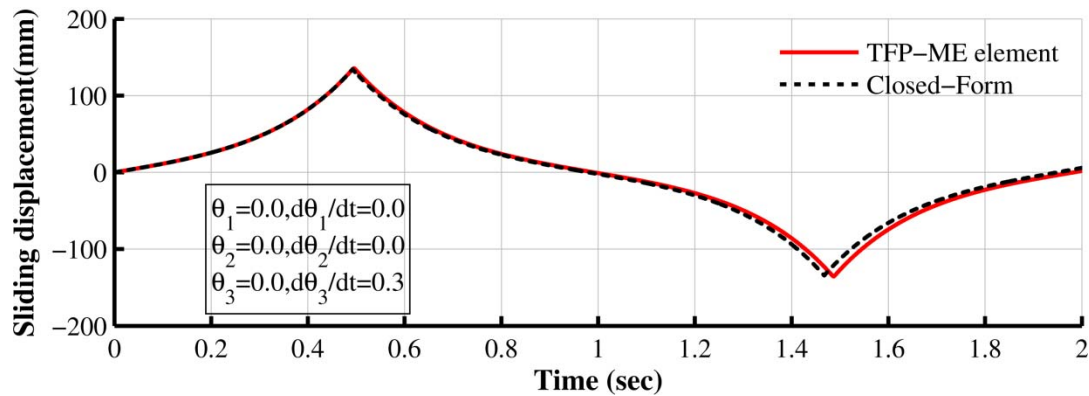


Figure 5-20: Comparison of results obtained by the model presented in Section 5 and closed form solution for the verification example of sliding on surface 3 subject to initial velocity

SECTION 6

MODEL FOR BEARING UPLIFT AND LANDING INCLUDING SLIDING, ROCKING, OVERTURNING, FLYING AND CONTACT OF BEARING COMPONENTS

This model is based on a representation of the parts of the bearing as rigid bodies interconnected with springs and dashpots that would allow for simulation of bearing uplift and landing and of sliding, rocking, overturning, free fall and contact bearing components. When parts come into contact, contact forces are introduced by the use of high stiffness springs that only function in compression. The advantage of this formulation is that one set of equations can be used for any possible state of the isolator (see Figure 5-2) without having to switch equations when a change in conditions occurs (e.g., uplift, landing, contact of TCP during uplift, etc.). However typically, this formulation is more useful when landing occurs where compatibility of the sliding angles needs to be restored in a very short duration of time upon the application of the vertical load or when there is significant interaction between the TCP and TSP (through contact forces F_{r4} , $F_{vg,l}$ and $F_{vg,r}$ in Section 5) and, therefore, likelihood of overturning of internal components.

6.1 Formulation of Equations of Motion

Each surface of the bearing is arbitrarily divided in two components: the *contact surface* and the *sliding surface* as illustrated in Figure 6-1. The *contact surface* is defined as the part of a sliding interface having the smallest diameter, whereas the surface with the largest diameter is termed the *sliding surface*. Note that each sliding surface has a displacement restrainer formed by a perimeter ring. In the notation used, points on a contact surface contain the superscript or subscript C and points located on a sliding surface contain the superscript or subscript S.

"
"
"
"

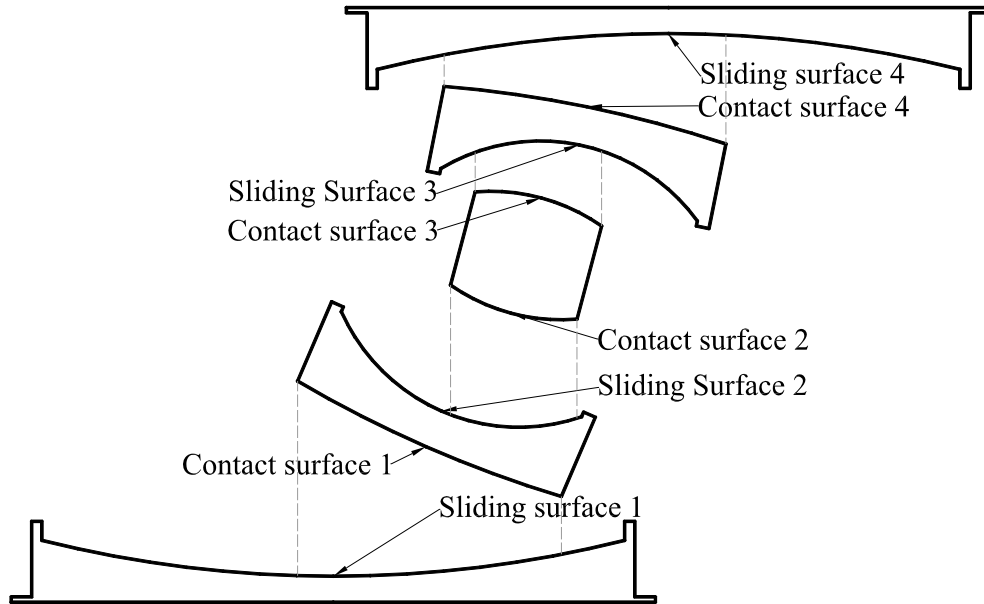


Figure 6-1: Definition of contact and sliding surfaces

Each contact surface is characterized by its two edges, with the one on the left denoted as L and the one on the right edge denoted as R . For each contact edge there is a corresponding point on the sliding surface defined as the intersection of the vertical line passing through the contact edge and the corresponding sliding surface. Figure 6-2 shows each of these points and their designation. For example, for surface 1 the contact edges are located on the bottom sliding plate (BSP) and are denoted as $CL-1$ and $CR-1$. The corresponding sliding points are located on the bottom concave plate (BCP) and are denoted as $SL-1$ and $SR-1$. Each edge has its own pair of contact forces and may experience impact with the restrainers of each sliding surface. The direction of the contact forces depends on the angle of the sliding surface which is calculated as the angle formed by the tangent of the sliding surface at the sliding point that corresponds to the contact point and the horizontal line. The relative vertical displacement between the contact points and the corresponding sliding points determines whether the two points are in contact (when the value is zero) or not in contact. The friction forces depend on the relative velocity of the contact edge and its corresponding point on the sliding surface. It is noted that both contact surfaces and sliding surfaces displace and rotate and this needs to be taken into account.

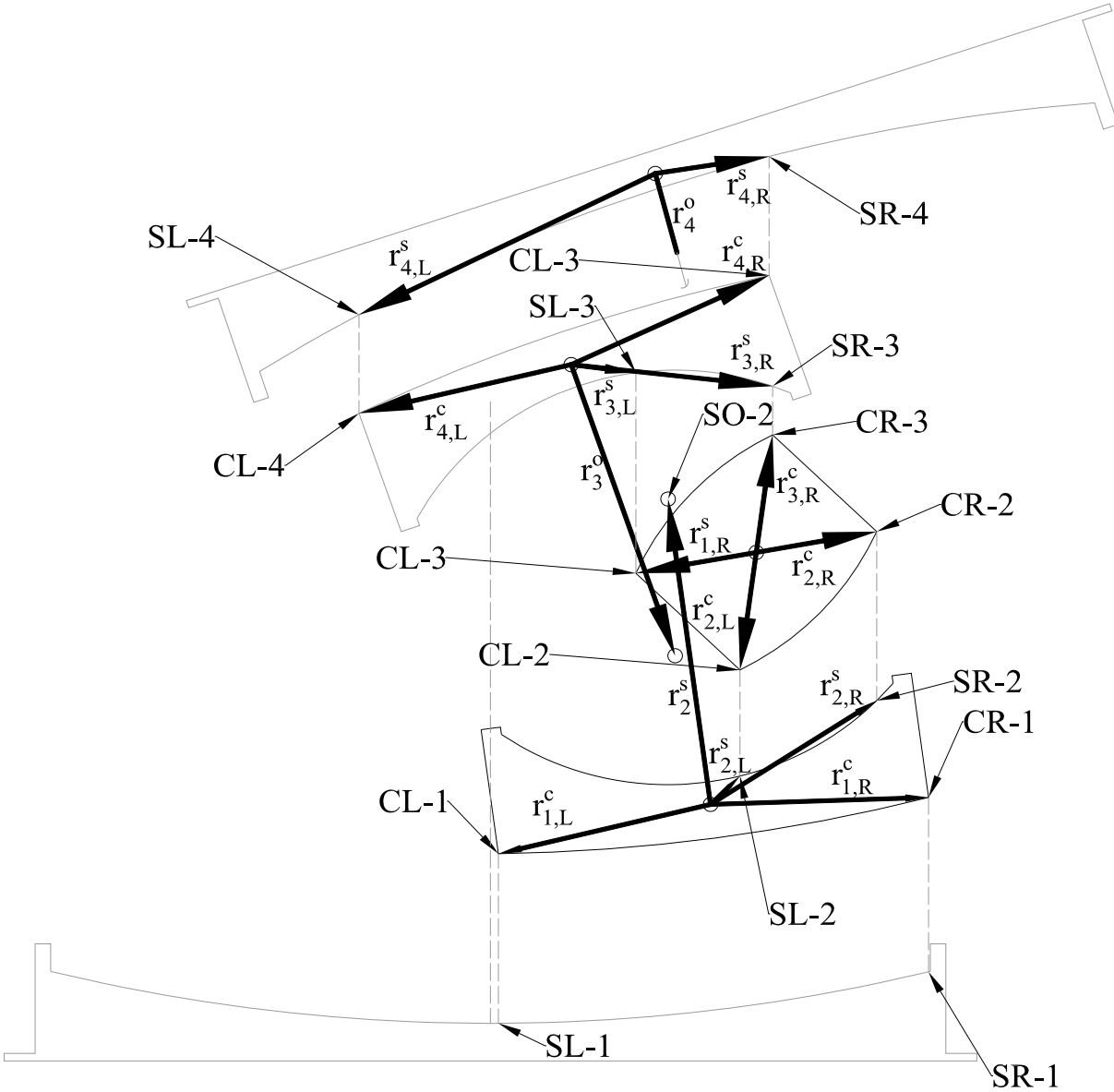


Figure 6-2: Definition of contact points and corresponding sliding points

A global coordinate system is defined with its origin located at the center of curvature of sliding surface 1 (center of circle), with the y-axis pointing downwards and the x-axis pointing to the right. Rotations are positive when counterclockwise. For the following derivations, all vectors denoted by symbol r and shown in Figure 6-2 have to be written at the local coordinate system of the rigid body. The origin of the local coordinate system is located at the center of mass of the rigid body that translates and rotates with the rigid body. As a result, these vectors are constant and independent of the rigid body's motion.

The vectors that connect the center of mass of each rigid body with the contact points located on the rigid body under consideration are defined. Let these vectors for surface i be $\mathbf{r}_{i,L}^c, \mathbf{r}_{i,R}^c$ as shown in Figure 6-2. These vectors are constant and given by:

$$\begin{aligned} \mathbf{r}_{i,L}^c &= \begin{Bmatrix} -b_i/2 \\ Z_{si} \end{Bmatrix}; \quad \mathbf{r}_{i,R}^c = \begin{Bmatrix} b_i/2 \\ Z_{si} \end{Bmatrix}; \quad i=1,2 \\ \mathbf{r}_{i,L}^c &= \begin{Bmatrix} -b_i/2 \\ -Z_{si} \end{Bmatrix}; \quad \mathbf{r}_{i,R}^c = \begin{Bmatrix} b_i/2 \\ -Z_{si} \end{Bmatrix}; \quad i=3,4 \end{aligned} \quad (6-1)$$

In Equation (6-1), quantities Z_{si} are given by:

$$Z_{si} = z_i - \left(R_i - \sqrt{R_i^2 - \left(\frac{b_i}{2}\right)^2} \right), \quad i=1,2,3,4 \quad (6-2)$$

Quantity z_i is the distance of the center of contact surface i to the center of mass of the rigid body that surface i is attached to as shown in Figure 4-1. It has a positive value. Quantities R_i and b_i are radii and diameters defined in Figure 1-1.

Since the sliding surfaces translate and rotate together with the rigid bodies, one can define the vectors connecting the center of mass of the rigid body to the center of curvature of the sliding surface (defined earlier) that translates and rotates with the body. These vectors are constant, denoted as \mathbf{r}_i^o in Figure 6-2 and are given by (see Figure 1-1 for definition of definition of h_i and t_{co}):

$$\begin{aligned} \mathbf{r}_1^o &= [0 \quad -R_1 - t_{co} + Z_5]^T \\ \mathbf{r}_2^o &= [0 \quad -R_2 - h_1 + h_2 + Z_1]^T \\ \mathbf{r}_3^o &= [0 \quad R_3 + h_4 - h_3 - Z_4]^T \\ \mathbf{r}_4^o &= [0 \quad R_4 + t_{co} - Z_5]^T \end{aligned} \quad (6-3)$$

The vectors that connect the center of mass to the sliding points are also defined and denoted as $\mathbf{r}_{i,L}^s, \mathbf{r}_{i,R}^s$, as shown in Figure 6-2. Vectors $\mathbf{r}_{i,L}^s, \mathbf{r}_{i,R}^s$ are again independent of the translation and rotation of the rigid body but are not constant since the location of the sliding points change

based on the locations of their corresponding contact points. Free body diagrams of the parts of the bearing and definitions of the angles and various displacements are shown in Figure 6-3 to Figure 6-6. The degrees of freedom are the horizontal coordinates, u_b , u_r , u_t and u_{tc} , the vertical coordinates, v_b , v_r , v_t and v_{tc} , the rotations, θ_b , θ_r , θ_t and θ_{tc} , of the centers of mass of parts BSP, RS, TSP and TCP and their derivatives $du_b/dt, du_r/dt, du_t/dt, du_{tc}/dt, dv_b/dt, dv_r/dt, dv_t/dt, dv_{tc}/dt, d\theta_b/dt, d\theta_r/dt, d\theta_t/dt, d\theta_{tc}/dt$.

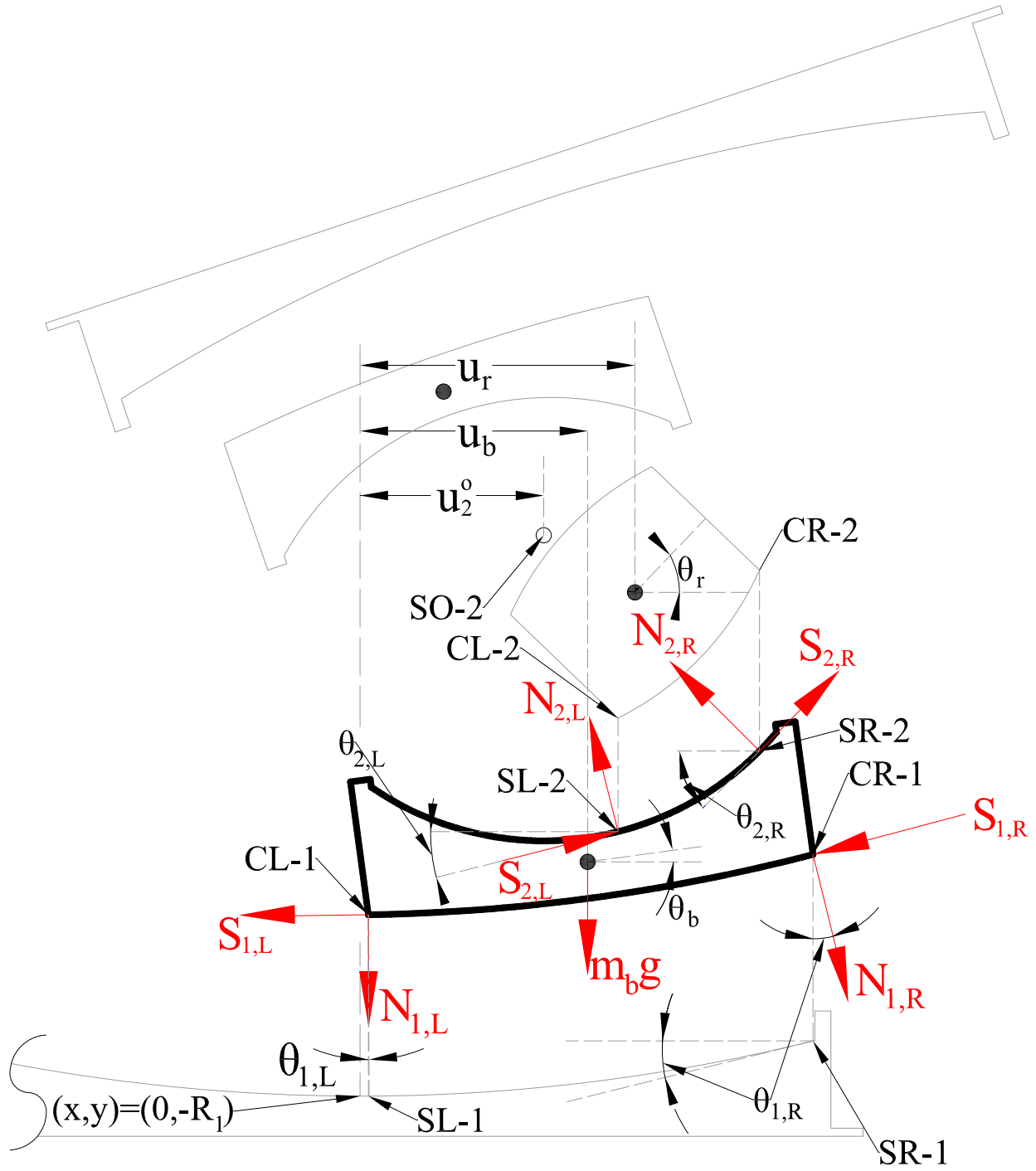


Figure 6-3: Free body diagram and kinematics of BSP

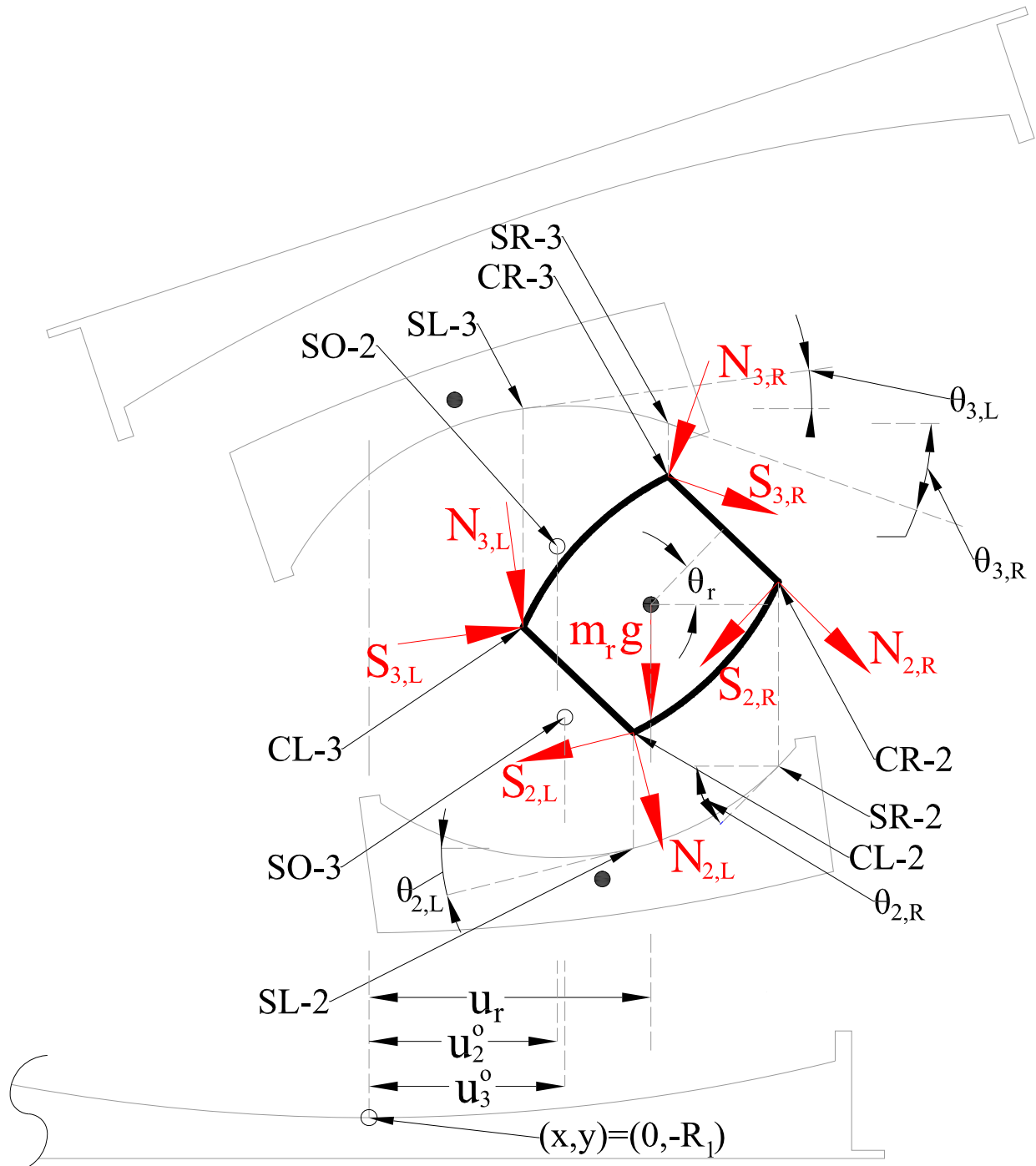


Figure 6-4: Free body diagram and kinematics of RS

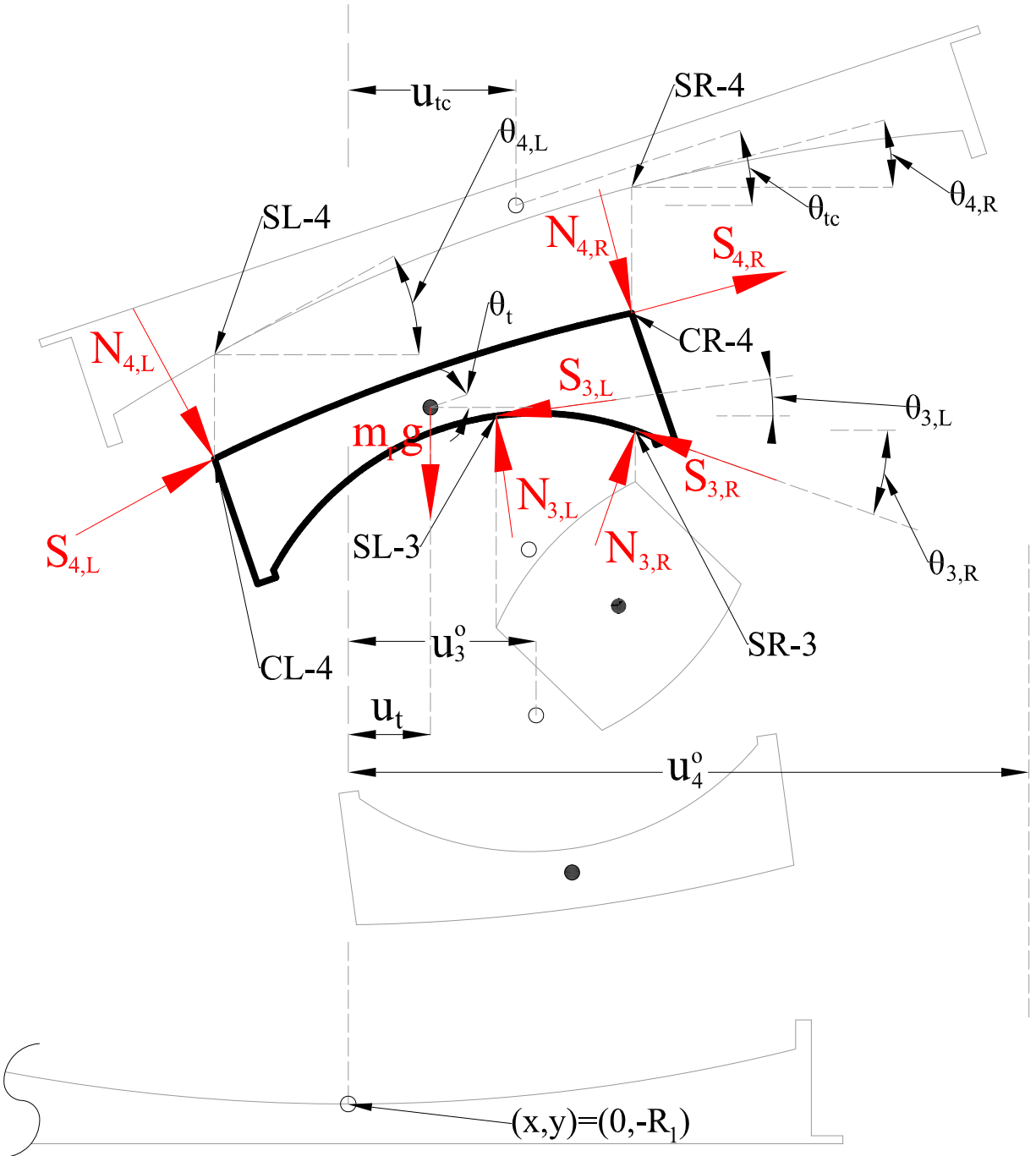


Figure 6-5: Free body diagram of TSP

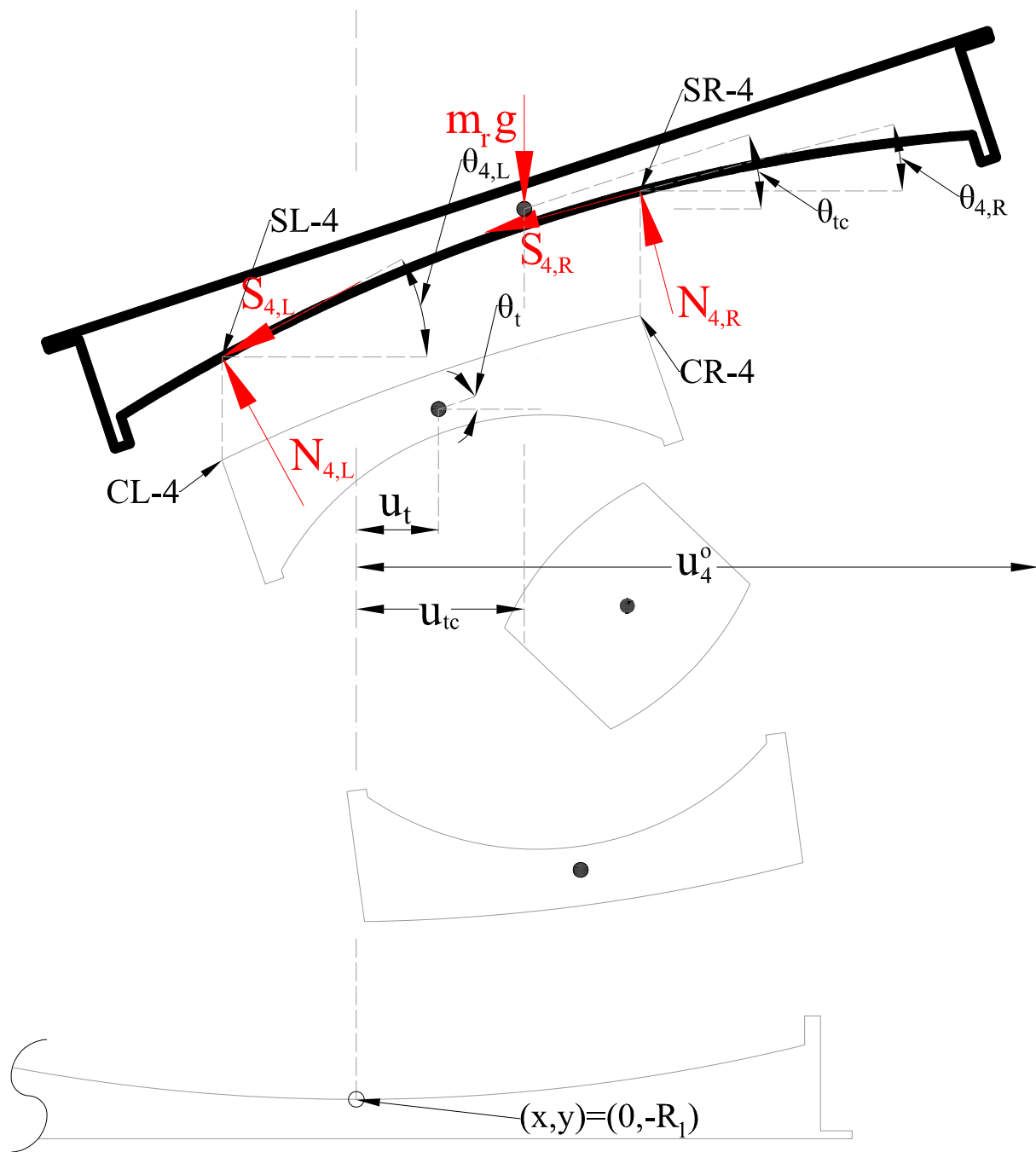


Figure 6-6: Free body diagram of TCP

The motion of each component is described by the horizontal coordinate u and the vertical coordinate v of its center of mass and by the rotation θ of its center of mass. The location vectors of the center of mass of the bottom slide plate, the rigid slider, the top slide plate and the top concave plate are, respectively, given by:

$$\mathbf{u}_b = \begin{Bmatrix} u_b \\ v_b \end{Bmatrix}; \mathbf{u}_r = \begin{Bmatrix} u_r \\ v_r \end{Bmatrix}; \mathbf{u}_t = \begin{Bmatrix} u_t \\ v_t \end{Bmatrix}; \mathbf{u}_{tc} = \begin{Bmatrix} u_{tc} \\ v_{tc} \end{Bmatrix} \quad (6-4)$$

In Equation (6-4), u_b , u_r , u_t and u_{tc} , are the horizontal coordinates of parts BSP, RS, TSP and TCP, respectively, and v_b , v_r , v_t and v_{tc} are the vertical coordinates of same parts.

Upon displacement and rotation of the bearing components, the new coordinates of the contact points (CL-1, CR-1, CL-2, etc. in Figure 6-2) in the global coordinate system are given by the following equations:

$$\mathbf{x}_{i,L}^c = \mathbf{u}_i + \mathbf{T}_i \mathbf{r}_{i,L}^c \quad \mathbf{x}_{i,R}^c = \mathbf{u}_i + \mathbf{T}_i \mathbf{r}_{i,R}^c \quad i = 1, 2, 3, 4 \quad (6-5)$$

In Equations (6-5), the displacement vectors \mathbf{u}_i and transformation matrices \mathbf{T}_i are given by:

$$\begin{aligned} \mathbf{u}_1 = \mathbf{u}_b & \quad ; \mathbf{T}_1 = \mathbf{T}_b \\ \mathbf{u}_2 = \mathbf{u}_3 = \mathbf{u}_r & ; \mathbf{T}_2 = \mathbf{T}_3 = \mathbf{T}_r \\ \mathbf{u}_4 = \mathbf{u}_t & \quad ; \mathbf{T}_4 = \mathbf{T}_t \end{aligned} \quad (6-6)$$

Also, vectors \mathbf{u}_b , \mathbf{u}_r and \mathbf{u}_t are given in Equation (6-4) and vectors $\mathbf{r}_{i,L}^c$ and $\mathbf{r}_{i,R}^c$ were defined in Figure 6-2.

In Equations (6-6), \mathbf{T}_b , \mathbf{T}_r and \mathbf{T}_t are the transformation matrices for parts BSP, RS and TSP, respectively. They relate the position vectors of each part after a rotation to the position prior to the rotation. They are given by:

$$\mathbf{T}_b = \begin{bmatrix} \cos \theta_b & \sin \theta_b \\ -\sin \theta_b & \cos \theta_b \end{bmatrix}; \mathbf{T}_r = \begin{bmatrix} \cos \theta_r & \sin \theta_r \\ -\sin \theta_r & \cos \theta_r \end{bmatrix}; \mathbf{T}_t = \begin{bmatrix} \cos \theta_t & \sin \theta_t \\ -\sin \theta_t & \cos \theta_t \end{bmatrix}; \quad (6-7)$$

Parameters θ_b , θ_r , and θ_t are the rotations of parts BSP, RS and TSP, respectively, and are shown in Figure 6-3 to Figure 6-6. After the rigid bodies displace and rotate, the new coordinates of the center of each sliding surface is given by:

$$\mathbf{x}_i^o = \mathbf{u}_i + \mathbf{T}_i \mathbf{r}_i^o, \quad i = 1, 2, 3, 4 \quad (6-8)$$

In Equation (6-8), displacement vectors \mathbf{u}_i and transformation matrices \mathbf{T}_i are given by Equation (6-9) rather than by Equation (6-6):

$$\begin{aligned} \mathbf{u}_1 &= \mathbf{0}; & \mathbf{T}_1 &= \mathbf{0} \\ \mathbf{u}_2 &= \mathbf{u}_b; & \mathbf{T}_2 &= \mathbf{T}_b \\ \mathbf{u}_3 &= \mathbf{u}_t; & \mathbf{T}_3 &= \mathbf{T}_t \\ \mathbf{u}_4 &= \mathbf{u}_{tc}; & \mathbf{T}_4 &= \mathbf{T}_{tc} \end{aligned} \quad (6-9)$$

Transformation matrices \mathbf{T}_b , \mathbf{T}_r and \mathbf{T}_t are given in Equation (6-7) and matrix \mathbf{T}_{tc} is given by:

$$\mathbf{T}_{tc} = \begin{bmatrix} \cos \theta_{tc} & \sin \theta_{tc} \\ -\sin \theta_{tc} & \cos \theta_{tc} \end{bmatrix} \quad (6-10)$$

Note that θ_{tc} is the rotation of the top concave plate. The equation describing the geometry for each sliding surface is then transformed to the global coordinate system by the following operation after including the translation and rotation of each sliding surface:

$$(\mathbf{x} - \mathbf{x}_i^o) \cdot (\mathbf{x} - \mathbf{x}_i^o) = R_i^2 \quad (6-11)$$

Note that \cdot represents the dot product of the two vectors. To determine if an edge of a body is in contact with its corresponding sliding point, the vertical coordinates of the two points need to be compared. The vertical coordinates of the contact edges can be calculated using vectors $\mathbf{x}_{i,L}^c$ and $\mathbf{x}_{i,R}^c$ given by Equation (6-5). The components of the vectors obtained from Equation (6-5) are explicitly given by:

$$\mathbf{x}_{i,L}^c = \begin{bmatrix} x_{i,L}^c & y_{i,L}^c \end{bmatrix}^T; \quad \mathbf{x}_{i,R}^c = \begin{bmatrix} x_{i,R}^c & y_{i,R}^c \end{bmatrix}^T \quad (6-12)$$

The corresponding components of the sliding surface point vectors are given by:

$$\mathbf{x}_{i,L}^s = \begin{bmatrix} x_{i,L}^c & y_{i,L}^s \end{bmatrix}^T, \mathbf{x}_{i,R}^s = \begin{bmatrix} x_{i,R}^c & y_{i,R}^s \end{bmatrix}^T \quad (6-13)$$

Note that in Equations (6-12) and (6-13) the x-coordinates of the sliding surface points are equal. The y-coordinates of the sliding surface points of surfaces 1 and 2 can be calculated as the first root of Equations (6-11), (6-12) and (6-13):

$$y_{i,L}^s = y_i^o + \sqrt{R_i^2 - (x_{i,L}^c - x_i^o)^2}; \quad y_{i,R}^s = y_i^o + \sqrt{R_i^2 - (x_{i,R}^c - x_i^o)^2}; \quad i = 1, 2 \quad (6-14)$$

For the convex surfaces 3 and 4, the second root of Equations (6-11), (6-12) and (6-13) needs to be used, so that:

$$y_{i,L}^s = y_i^o - \sqrt{R_i^2 - (x_{i,L}^c - x_i^o)^2}; \quad y_{i,R}^s = y_i^o - \sqrt{R_i^2 - (x_{i,R}^c - x_i^o)^2}; \quad i = 3, 4 \quad (6-15)$$

Finally, the inclination of the contact forces shown in Figure 6-3 to Figure 6-6 with respect to the global coordinate system is defined by the slope of the sliding surfaces at the location of the sliding points. They are obtained as the derivatives of Equations (6-14) and (6-15) with respect to x:

$$\theta_{i,L}^s = a \tan^{-1} \frac{dy_{i,L}^s}{dx} = \begin{cases} a \tan \left(\frac{(x_{i,L}^c - x_i^o)}{\sqrt{R_i^2 - (x_{i,L}^c - x_i^o)^2}} \right), i = 1, 2 \\ -a \tan \left(\frac{(x_{i,L}^c - x_i^o)}{\sqrt{R_i^2 - (x_{i,L}^c - x_i^o)^2}} \right), i = 3, 4 \end{cases} \quad (6-16)$$

$$\theta_{i,R}^s = a \tan^{-1} \frac{dy_{i,R}^s}{dx} = \begin{cases} a \tan \left(\frac{(x_{i,R}^c - x_i^o)}{\sqrt{R_i^2 - (x_{i,R}^c - x_i^o)^2}} \right), i = 1, 2 \\ -a \tan \left(\frac{(x_{i,R}^c - x_i^o)}{\sqrt{R_i^2 - (x_{i,R}^c - x_i^o)^2}} \right), i = 3, 4 \end{cases}$$

The following vectors that contain the contact forces of each contact point shown in Figure 6-3 to Figure 6-6 are defined as:

$$\mathbf{R}'_{i,L} = \begin{Bmatrix} S_{i,L} \\ N_{i,L} \end{Bmatrix} ; \mathbf{R}'_{i,R} = \begin{Bmatrix} S_{i,R} \\ N_{i,R} \end{Bmatrix}, i = 1, 2, 3, 4 \quad (6-17)$$

The normal components N_i for the concave surfaces 1 and 2 are given by:

$$N_{i,L} = \begin{cases} -k_{i,L} (y_{i,L}^c - y_{i,L}^s), & y_{i,L}^s \leq y_{i,L}^c \\ 0, & \text{otherwise} \end{cases}; N_{i,R} = \begin{cases} -k_{i,R} (y_{i,R}^c - y_{i,R}^s), & y_{i,R}^s \leq y_{i,R}^c \\ 0, & \text{otherwise} \end{cases}, i = 1, 2 \quad (6-18)$$

For the convex surfaces 3 and 4 these forces are given by:

$$N_{i,L} = \begin{cases} k_{i,L} (y_{i,L}^s - y_{i,L}^c), & y_{i,L}^s \geq y_{i,L}^c \\ 0, & \text{otherwise} \end{cases}; N_{i,R} = \begin{cases} k_{i,R} (y_{i,R}^s - y_{i,R}^c), & y_{i,R}^s \geq y_{i,R}^c \\ 0, & \text{otherwise} \end{cases}, i = 3, 4 \quad (6-19)$$

The friction forces are given by:

$$S_{i,L} = \mu_i N_{i,L} Z_{i,L} ; S_{i,R} = \mu_i N_{i,R} Z_{i,R}, i = 1, 2, 3, 4 \quad (6-20)$$

In Equation (6-20), μ_i is the friction coefficient of each surface. It is assumed equal for the left and right edges. Also, Z_i is a hysteretic parameter to be defined later.

Equations (6-18) and (6-19) imply that if the sliding surface projection is located below the contact surface edge, the two points are not in contact and the normal force and the friction force are zero. In order to develop contact in this model, some small overlap or “penetration” needs to be developed between the two points. The amount of penetration depends on the value of the vertical stiffness of the springs given by $k_{i,L}$ and $k_{i,R}$. If both edge forces are zero ($N_{i,L} = N_{i,R} = 0$), then there is no contact between the bodies. If one of the two forces is nonzero, then there is point contact. If both forces are nonzero, then there is full contact.

In order to transform the contact force vector to the global coordinates, the following transformation needs to be performed:

$$\mathbf{R}_{i,L} = \mathbf{T}_{i,L}^s \mathbf{R}'_{i,L}; \quad \mathbf{R}_{i,R} = \mathbf{T}_{i,R}^s \mathbf{R}'_{i,R} \quad (6-21)$$

In Equation (6-21), $\mathbf{T}_{i,L}^s$ is a transformation matrix that is different for each contact point and is given by:

$$\mathbf{T}_{i,L}^s = \begin{bmatrix} \cos \theta_{i,L}^s & \sin \theta_{i,L}^s \\ -\sin \theta_{i,L}^s & \cos \theta_{i,L}^s \end{bmatrix}; \quad \mathbf{T}_{i,R}^s = \begin{bmatrix} \cos \theta_{i,R}^s & \sin \theta_{i,R}^s \\ -\sin \theta_{i,R}^s & \cos \theta_{i,R}^s \end{bmatrix}, i = 1, 2, 3, 4 \quad (6-22)$$

Where angles $\theta_{i,L}^s$ and $\theta_{i,R}^s$ are given in Equation (6-16).

The velocity vectors of the contact points in the global coordinate system are given by:

$$\frac{d\mathbf{x}_{i,L}^c}{dt} = \frac{d\mathbf{u}_i}{dt} + \frac{d\mathbf{T}_i}{dt} \mathbf{r}_{i,L}^c; \quad \frac{d\mathbf{x}_{i,R}^c}{dt} = \frac{d\mathbf{u}_i}{dt} + \frac{d\mathbf{T}_i}{dt} \mathbf{r}_{i,R}^c \quad i = 1, 2, 3, 4 \quad (6-23)$$

In Equation (6-23), the displacement vectors \mathbf{u}_i and the transformation matrices \mathbf{T}_i are given by Equation (6-6). The derivative of matrix \mathbf{T}_i with respect to time can be calculated from Equation (6-7). The velocity vectors of the contact points, written at the local coordinates of the corresponding sliding points, are given by:

$$\left(\frac{d\mathbf{x}_{i,L}^c}{dt} \right)' = \mathbf{T}_{i,L}^s \left(\frac{d\mathbf{x}_{i,L}^c}{dt} \right); \quad \left(\frac{d\mathbf{x}_{i,R}^c}{dt} \right)' = \mathbf{T}_{i,R}^s \left(\frac{d\mathbf{x}_{i,R}^c}{dt} \right) \quad i = 1, 2, 3, 4 \quad (6-24)$$

The relative coordinates of the sliding surface points with respect to the center of mass of the rigid body considered are given by:

$$\mathbf{r}_{i,L}^s = \mathbf{T}_i^{-1} (\mathbf{x}_{i,L}^s - \mathbf{u}_i); \quad \mathbf{r}_{i,R}^s = \mathbf{T}_i^{-1} (\mathbf{x}_{i,R}^s - \mathbf{u}_i), \quad i = 1, 2, 3, 4 \quad (6-25)$$

In Equation (6-25), the displacement vectors \mathbf{u}_i and the transformation matrices \mathbf{T}_i are given by Equation (6-9).

The velocity of the sliding surface points are given by (note that \mathbf{u}_i and \mathbf{T}_i are given by Equation (6-9)):

$$\frac{d\mathbf{x}_{i,L}^s}{dt} = \frac{d\mathbf{u}_i}{dt} + \frac{d\mathbf{T}_i}{dt} \mathbf{r}_{i,L}^s; \quad \frac{d\mathbf{x}_{i,R}^s}{dt} = \frac{d\mathbf{u}_i}{dt} + \frac{d\mathbf{T}_i}{dt} \mathbf{r}_{i,R}^s, \quad i = 1, 2, 3, 4 \quad (6-26)$$

In the local coordinate system, the velocity of the sliding projections is:

$$\left(\frac{d\mathbf{x}_{i,L}^s}{dt}\right)' = \mathbf{T}_{i,L}^s \frac{d\mathbf{x}_{i,L}^s}{dt}; \quad \left(\frac{d\mathbf{x}_{i,R}^s}{dt}\right)' = \mathbf{T}_{i,R}^s \frac{d\mathbf{x}_{i,R}^s}{dt}, \quad i=1,2,3,4 \quad (6-27)$$

The relative velocity of the contact points with respect to the sliding points in the direction tangential to the sliding surface at the location of the sliding points is given by:

$$\mathbf{v}_{i,L} = \begin{Bmatrix} v_{i,LT} \\ v_{i,LN} \end{Bmatrix} = \left(\frac{d\mathbf{x}_{i,L}^c}{dt}\right)' - \left(\frac{d\mathbf{x}_{i,L}^s}{dt}\right)' = \mathbf{T}_{i,L}^s \left[\frac{d\mathbf{x}_{i,L}^c}{dt} - \frac{d\mathbf{x}_{i,L}^s}{dt} \right] \quad (6-28)$$

$$\mathbf{v}_{i,R} = \begin{Bmatrix} v_{i,RT} \\ v_{i,RN} \end{Bmatrix} = \left(\frac{d\mathbf{x}_{i,R}^c}{dt}\right)' - \left(\frac{d\mathbf{x}_{i,R}^s}{dt}\right)' = \mathbf{T}_{i,R}^s \left[\frac{d\mathbf{x}_{i,R}^c}{dt} - \frac{d\mathbf{x}_{i,R}^s}{dt} \right]$$

The hysteretic parameter for each contact point is defined as:

$$\dot{Z}_{i,L} = (1/Y)(1 - a_{i,L} Z_{i,L}^2) v_{i,LT}; \quad \dot{Z}_{i,R} = (1/Y)(1 - a_{i,R} Z_{i,R}^2) v_{i,RT}$$

$$a_{i,L} = \begin{cases} 1, & v_{i,LT} Z_{i,L} > 0 \\ 0, & v_{i,LT} Z_{i,L} \leq 0 \end{cases}; \quad a_{i,R} = \begin{cases} 1, & v_{i,RT} Z_{i,R} > 0 \\ 0, & v_{i,RT} Z_{i,R} \leq 0 \end{cases} \quad (6-29)$$

In Equation (6-29), Y is a ‘‘yield displacement’’ in the visco-plastic representation of friction (typically assigned small values of less than 1mm), and $v_{i,LT}$ and $v_{i,RT}$ are defined in Equation (6-28).

In order to introduce some damping in the vertical direction, dampers are assigned at each contact point. The damping forces of surfaces 1 and 2 are given by:

$$N_{i,L}^D = \begin{cases} c_{i,L} \left(\frac{dy_{i,L}^c}{dt} - \frac{dy_{i,L}^s}{dt} \right), & \frac{dy_{i,L}^c}{dt} > \frac{dy_{i,L}^s}{dt} \ \& \ y_{i,L}^c > y_{i,L}^s \\ 0, & \text{otherwise} \end{cases} \quad (6-30)$$

$$N_{i,R}^D = \begin{cases} c_{i,R} \left(\frac{dy_{i,R}^c}{dt} - \frac{dy_{i,R}^s}{dt} \right), & \frac{dy_{i,R}^c}{dt} > \frac{dy_{i,R}^s}{dt} \ \& \ y_{i,R}^c > y_{i,R}^s \\ 0, & \text{otherwise} \end{cases}$$

Note that $c_{i,L}$ and $c_{i,R}$ are arbitrary damping constants assigned for the contact point of surface i .

For the convex surfaces 3 and 4 the damping forces are given by:

$$\begin{aligned}
N_{i,L}^D &= \begin{cases} c_{i,L} \left(\frac{dy_{i,L}^c}{dt} - \frac{dy_{i,L}^s}{dt} \right), & \frac{dy_{i,L}^c}{dt} < \frac{dy_{i,L}^s}{dt} \text{ \& } y_{i,L}^c < y_{i,L}^s \\ 0, & \text{otherwise} \end{cases} \\
N_{i,R}^D &= \begin{cases} c_{i,R} \left(\frac{dy_{i,R}^c}{dt} - \frac{dy_{i,R}^s}{dt} \right), & \frac{dy_{i,R}^c}{dt} < \frac{dy_{i,R}^s}{dt} \text{ \& } y_{i,R}^c < y_{i,R}^s \\ 0, & \text{otherwise} \end{cases}
\end{aligned} \tag{6-31}$$

Note that the damping forces act in the vertical direction and are only activated when there is overlap or “penetration” between contact and sliding points and only when this “penetration” increases in magnitude. They do not affect the vertical displacement due to the pendulum motion of the contact surfaces. Also, they do not affect the response in the horizontal direction.

For convenience, the following vectors are defined:

$$\mathbf{N}_{i,L}^D = \begin{Bmatrix} 0 \\ N_{i,L}^D \end{Bmatrix}; \quad \mathbf{N}_{i,R}^D = \begin{Bmatrix} 0 \\ N_{i,R}^D \end{Bmatrix}, i = 1, 2, 3, 4 \tag{6-32}$$

Figure 6-7 introduces additional notation related to the restrainer forces. Note that this notation is identical to the notation that was followed earlier for the contact forces. The following constant vectors are defined for the restrainers based on Figure 6-7:

$$\begin{aligned}
\mathbf{r}_{1,L}^G &= \begin{Bmatrix} -s_1/2 \\ -h_{s1} - t_{co} + Z_{s5} \end{Bmatrix}; & \mathbf{r}_{1,R}^G &= \begin{Bmatrix} s_1/2 \\ -h_{s1} - t_{co} + Z_{s5} \end{Bmatrix} \\
\mathbf{r}_{2,L}^G &= \begin{Bmatrix} -s_2/2 \\ -h_{s2} - h_1 + h_2 + Z_1 \end{Bmatrix}; & \mathbf{r}_{2,R}^G &= \begin{Bmatrix} s_2/2 \\ -h_{s2} - h_1 + h_2 + Z_1 \end{Bmatrix} \\
\mathbf{r}_{3,L}^G &= \begin{Bmatrix} -s_3/2 \\ h_{s3} + h_4 - h_3 - Z_4 \end{Bmatrix}; & \mathbf{r}_{3,R}^G &= \begin{Bmatrix} s_3/2 \\ h_{s3} + h_4 - h_3 - Z_4 \end{Bmatrix} \\
\mathbf{r}_{4,L}^G &= \begin{Bmatrix} -s_4/2 \\ h_{s4} + t_{co} - Z_{s5} \end{Bmatrix}; & \mathbf{r}_{4,R}^G &= \begin{Bmatrix} s_4/2 \\ h_{s4} + t_{co} - Z_{s5} \end{Bmatrix}
\end{aligned} \tag{6-33}$$

$$\begin{aligned}
\mathbf{r}_{1,L}^{GE} &= \begin{Bmatrix} -s_1/2 \\ -h_{s1} - t_{co} + Z_{s5} - h_{r1} \end{Bmatrix} ; \mathbf{r}_{1,R}^{GE} = \begin{Bmatrix} s_1/2 \\ -h_{s1} - t_{co} + Z_{s5} - h_{r1} \end{Bmatrix} \\
\mathbf{r}_{2,L}^{GE} &= \begin{Bmatrix} -s_2/2 \\ -h_{s2} - h_1 + h_2 + Z_1 - h_{r2} \end{Bmatrix} ; \mathbf{r}_{2,R}^{GE} = \begin{Bmatrix} s_2/2 \\ -h_{s2} - h_1 + h_2 + Z_1 - h_{r2} \end{Bmatrix} \\
\mathbf{r}_{3,L}^{GE} &= \begin{Bmatrix} -s_3/2 \\ h_{s3} + h_4 - h_3 - Z_4 + h_{r3} \end{Bmatrix} ; \mathbf{r}_{3,R}^{GE} = \begin{Bmatrix} s_3/2 \\ h_{s3} + h_4 - h_3 - Z_4 + h_{r3} \end{Bmatrix} \\
\mathbf{r}_{4,L}^{GE} &= \begin{Bmatrix} -s_4/2 \\ h_{s4} + t_{co} - Z_{s5} + h_{r4} \end{Bmatrix} ; \mathbf{r}_{4,R}^{GE} = \begin{Bmatrix} s_4/2 \\ h_{s4} + t_{co} - Z_{s5} + h_{r4} \end{Bmatrix}
\end{aligned} \tag{6-34}$$

In these equations, s_i is the diameter of the sliding surface (given by Equation (4-20)) and h_{si} and h_{ri} were defined in Equations (5-14). The restrainer coordinates after translation and rotation of the rigid bodies are given by:

$$\mathbf{x}_{i,L}^G = \begin{Bmatrix} x_{i,L}^G \\ y_{i,L}^G \end{Bmatrix} = \mathbf{u}_i + \mathbf{T}_i \mathbf{r}_{i,L}^G ; \quad \mathbf{x}_{i,R}^G = \begin{Bmatrix} x_{i,R}^G \\ y_{i,R}^G \end{Bmatrix} = \mathbf{u}_i + \mathbf{T}_i \mathbf{r}_{i,R}^G \quad i = 1, 2, 3, 4 \tag{6-35}$$

$$\mathbf{x}_{i,L}^{GE} = \begin{Bmatrix} x_{i,L}^{GE} \\ y_{i,L}^{GE} \end{Bmatrix} = \mathbf{u}_i + \mathbf{T}_i \mathbf{r}_{i,L}^{GE} ; \quad \mathbf{x}_{i,R}^{GE} = \begin{Bmatrix} x_{i,R}^{GE} \\ y_{i,R}^{GE} \end{Bmatrix} = \mathbf{u}_i + \mathbf{T}_i \mathbf{r}_{i,R}^{GE} \quad i = 1, 2, 3, 4 \tag{6-36}$$

where the displacement vectors \mathbf{u}_i and the transformation matrices \mathbf{T}_i are given by Equation (6-9).

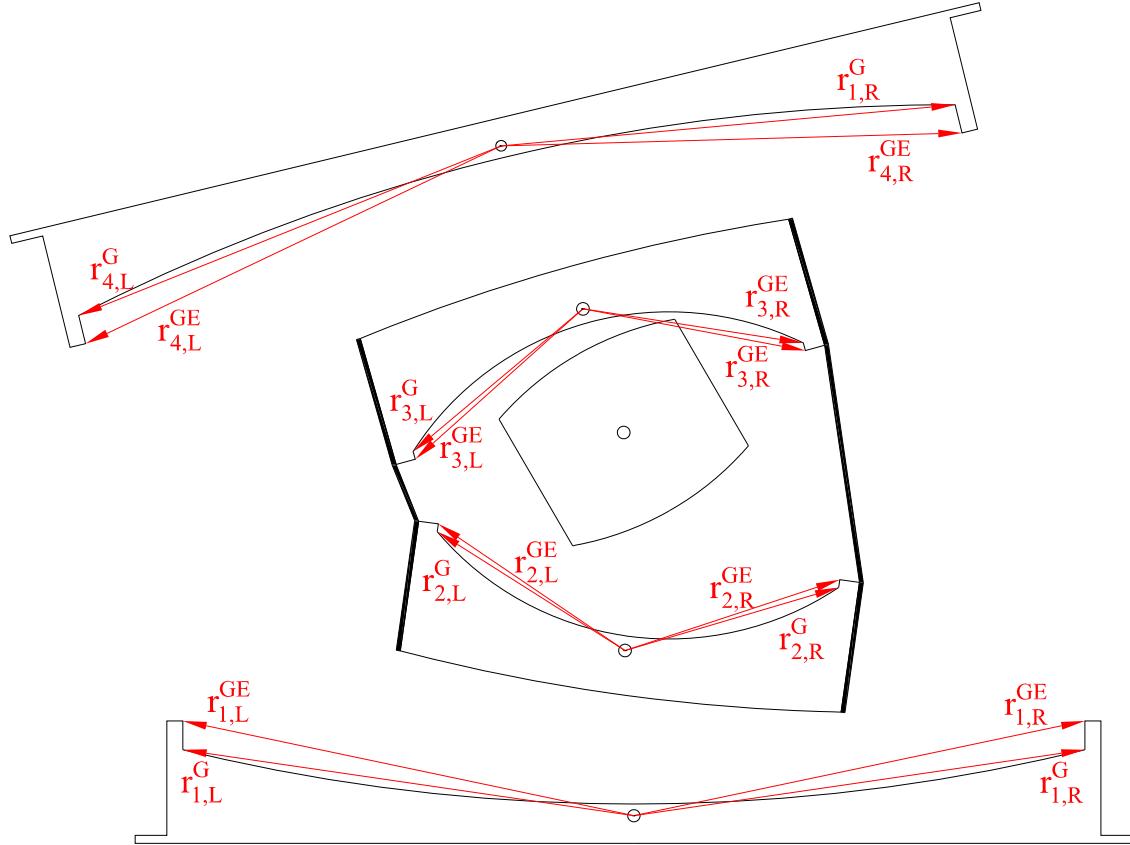


Figure 6-7: Notation for position vectors of restrainers

Contact with the restrainers activates spring forces given by:

$$F_{i,L}^G = \begin{cases} k_{ri} (x_{i,L}^G - x_{i,L}^c), & x_{i,L}^G \geq x_{i,L}^c \\ 0, & x_{i,L}^G < x_{i,L}^c \text{ or } y_{i,L}^{GE} > y_{i,L}^c \end{cases}, i=1,2 \quad (6-37)$$

$$F_{i,R}^G = \begin{cases} k_{ri} (x_{i,R}^c - x_{i,R}^G) & x_{i,R}^c \geq x_{i,R}^G \\ 0 & x_{i,R}^c < x_{i,R}^G \text{ or } y_{i,R}^{GE} > y_{i,R}^c \end{cases} \quad i=1,2$$

$$F_{i,L}^G = \begin{cases} k_{ri} (x_{i,L}^G - x_{i,L}^c), & x_{i,L}^G \geq x_{i,L}^c \\ 0, & x_{i,L}^G < x_{i,L}^c \text{ or } y_{i,L}^{GE} < y_{i,L}^c \end{cases}, i=3,4 \quad (6-38)$$

$$F_{i,R}^G = \begin{cases} k_{ri} (x_{i,R}^c - x_{i,R}^G) & x_{i,R}^c \geq x_{i,R}^G \\ 0 & x_{i,R}^c < x_{i,R}^G \text{ or } y_{i,R}^{GE} < y_{i,R}^c \end{cases} \quad i=3,4$$

In these equations, k_{ri} is the stiffness of the restrainer and is given by Equation (4-17) for linear elastic behavior.

Vectors containing the restrainer forces are defined and given by:

$$\mathbf{F}_{i,L}^G = \begin{Bmatrix} F_{i,L}^G \\ 0 \end{Bmatrix}; \quad \mathbf{F}_{i,R}^G = \begin{Bmatrix} F_{i,R}^G \\ 0 \end{Bmatrix}, i = 1, 2, 3, 4 \quad (6-39)$$

Figure 6-8 introduces additional notation related to the rubber seal forces. Note that notation used for the seal is similar to that used in Figure 5-8 with some differences. The general case of variable seal attachments is described herein. The procedure is similar to that of Section 5.3 with minor changes. The coordinates of the seal attachment points are given by:

$$\begin{aligned} \mathbf{x}_{C1} = \begin{Bmatrix} x_{C1} \\ y_{C2} \end{Bmatrix} &= \mathbf{x}_b + \mathbf{T}_b \mathbf{r}_{C1}; \quad \mathbf{x}_{C2} = \begin{Bmatrix} x_{C2} \\ y_{C2} \end{Bmatrix} = \mathbf{x}_t + \mathbf{T}_t \mathbf{r}_{C2} \\ \mathbf{x}_{C3} = \begin{Bmatrix} x_{C3} \\ y_{C3} \end{Bmatrix} &= \mathbf{x}_b + \mathbf{T}_b \mathbf{r}_{C3}; \quad \mathbf{x}_{C4} = \begin{Bmatrix} x_{C4} \\ y_{C4} \end{Bmatrix} = \mathbf{x}_t + \mathbf{T}_t \mathbf{r}_{C4} \end{aligned} \quad (6-40)$$

The coordinates of the restrainer edges are given by:

$$\begin{aligned} \mathbf{x}_{B1} = \begin{Bmatrix} x_{B1} \\ y_{B2} \end{Bmatrix} &= \mathbf{x}_b + \mathbf{T}_b \mathbf{r}_{B1}; \quad \mathbf{x}_{B2} = \begin{Bmatrix} x_{B2} \\ y_{B2} \end{Bmatrix} = \mathbf{x}_t + \mathbf{T}_t \mathbf{r}_{B2} \\ \mathbf{x}_{B3} = \begin{Bmatrix} x_{B3} \\ y_{B3} \end{Bmatrix} &= \mathbf{x}_b + \mathbf{T}_b \mathbf{r}_{B3}; \quad \mathbf{x}_{B4} = \begin{Bmatrix} x_{B4} \\ y_{B4} \end{Bmatrix} = \mathbf{x}_t + \mathbf{T}_t \mathbf{r}_{B4} \end{aligned} \quad (6-41)$$

In the equations above, vectors \mathbf{r}_{Bi} and \mathbf{r}_{Ci} are given by the expressions below:

$$\begin{aligned} \mathbf{r}_{C1} = \begin{Bmatrix} -b_1 \\ Z_1 - h_{b1} - s_{A1} \end{Bmatrix}; \quad \mathbf{r}_{C2} = \begin{Bmatrix} -b_4 \\ -Z_1 + h_{b1} + s_{A1} \end{Bmatrix}; \\ \mathbf{r}_{C3} = \begin{Bmatrix} b_1 \\ Z_1 - h_{b1} - s_{A1} \end{Bmatrix}; \quad \mathbf{r}_{C4} = \begin{Bmatrix} b_4 \\ -Z_1 + h_{b1} + s_{A1} \end{Bmatrix} \end{aligned} \quad (6-42)$$

$$\begin{aligned} \mathbf{r}_{B1} = \begin{Bmatrix} -b_1 \\ -h_1 + h_2 + Z_1 - h_{s2} - h_{r2} \end{Bmatrix}; \quad \mathbf{r}_{B2} = \begin{Bmatrix} -b_4 \\ h_1 - h_2 - Z_1 + h_{s2} + h_{r3} \end{Bmatrix} \\ \mathbf{r}_{B3} = \begin{Bmatrix} b_1 \\ -h_1 + h_2 + Z_1 - h_{s2} - h_{r2} \end{Bmatrix}; \quad \mathbf{r}_{B4} = \begin{Bmatrix} b_4 \\ h_1 - h_2 - Z_1 + h_{s2} + h_{r3} \end{Bmatrix} \end{aligned} \quad (6-43)$$

Given the definitions above, the procedure for analysis is identical to the one described in Section 5.3 that involves the calculation of vectors $\mathbf{A}_1, \mathbf{A}_2, \mathbf{A}_3$ and \mathbf{A}_4 . These are now given by:

$$\begin{aligned} \mathbf{A}_1 &= \begin{cases} \mathbf{x}_{C1}, \omega_1 \leq a_1 \\ \mathbf{x}_{B1}, \omega_1 > a_1 \end{cases}, \mathbf{A}_2 = \begin{cases} \mathbf{x}_{C2}, \omega_2 > a_1 \\ \mathbf{x}_{B2}, \omega_2 \leq a_1 \end{cases} \\ \mathbf{A}_3 &= \begin{cases} \mathbf{x}_{C3}, \omega_3 > a_2 \\ \mathbf{x}_{B3}, \omega_3 \leq a_2 \end{cases}, \mathbf{A}_4 = \begin{cases} \mathbf{x}_{C4}, \omega_4 \leq a_2 \\ \mathbf{x}_{B4}, \omega_4 > a_2 \end{cases} \end{aligned} \quad (6-44)$$

$$\omega_1 = a \tan \frac{x_{B1} - x_{1,L}^c}{y_{B1} - y_{1,L}^c}, \omega_2 = a \tan \frac{x_{B2} - x_{4,L}^c}{y_{B2} - y_{4,L}^c}, \omega_3 = a \tan \frac{x_{A3} - x_{1,R}^c}{y_{A3} - y_{1,R}^c}, \omega_4 = a \tan \frac{x_{B3} - x_{4,R}^c}{y_{B3} - y_{4,R}^c}$$

$$\alpha_1 = a \tan \frac{x_{C2} - x_{C1}}{y_{C2} - y_{C1}}, \alpha_2 = a \tan \frac{x_{C4} - x_{C3}}{y_{C4} - y_{C3}}$$

The deformed length of the seal, the stiffness of the seal and the seal forces and angles were presented in Section 5.3. The horizontal and vertical components of the seal forces are given by:

$$\mathbf{F}_L^{RS} = \begin{Bmatrix} F_{i,L}^{RS} \sin(\theta_{b,l}) \\ F_{i,L}^{RS} \cos(\theta_{b,l}) \end{Bmatrix}, \mathbf{F}_R^{RS} = \begin{Bmatrix} F_{i,R}^{RS} \sin(\theta_{b,r}) \\ F_{i,R}^{RS} \cos(\theta_{b,r}) \end{Bmatrix} \quad (6-45)$$

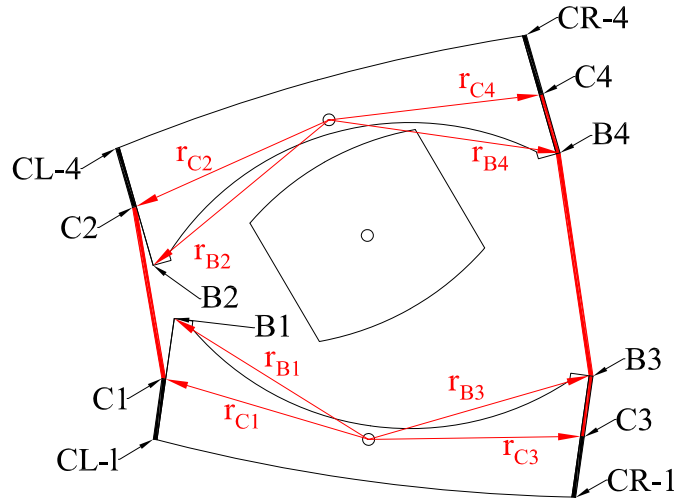


Figure 6-8: Notation of position vectors of rubber seal

Consider also the following vectors that contain the external forces applied to the TFP parts:

$$\mathbf{F}_b^w = \begin{Bmatrix} 0 \\ -m_b g \end{Bmatrix}; \mathbf{F}_r^w = \begin{Bmatrix} 0 \\ -m_r g \end{Bmatrix}; \mathbf{F}_t^w = \begin{Bmatrix} 0 \\ -m_t g \end{Bmatrix}; \mathbf{F}_{ic}^w = \begin{Bmatrix} 0 \\ -m_{ic} g - W \end{Bmatrix} \quad (6-46)$$

where W is the external vertical load applied on the TCP. $W=0$ when the model is combined with a superstructure for dynamic analysis and $W>0$ if a single isolator is analyzed.

Finally, for the uplift duration, a friction force is considered to act in the vertical direction as shown in Figure 6-9. The vectors for the friction forces on the left and the right restrainers are:

$$\mathbf{F}_L^V = \begin{Bmatrix} 0 \\ -\mu_s F_{4,L}^G Z_{V,L} \end{Bmatrix}; \quad \mathbf{F}_R^V = \begin{Bmatrix} 0 \\ -\mu_s F_{4,R}^G Z_{V,R} \end{Bmatrix} \quad (6-47)$$

Quantity μ_s is the friction coefficient between rubber and steel or steel and steel (when there is no rubber seal). The hysteretic variables $Z_{V,L}$ and $Z_{V,R}$ are described by the following equations:

$$\dot{Z}_{V,L} = (1/Y)(1 - a_{i,L} Z_{i,L}^2) \left(\frac{dy_{4,L}^c}{dt} - \frac{dy_{4,L}^G}{dt} \right); \quad \dot{Z}_{i,R} = (1/Y)(1 - a_{i,R} Z_{i,R}^2) \left(\frac{dy_{4,R}^c}{dt} - \frac{dy_{4,R}^G}{dt} \right) \quad (6-48)$$

$$a_{i,L} = \begin{cases} 1, & v_{i,L} Z_{V,L} > 0 \\ 0, & v_{i,L} Z_{V,L} \leq 0 \end{cases}; \quad a_{i,R} = \begin{cases} 1, & v_{i,R} Z_{V,R} > 0 \\ 0, & v_{i,R} Z_{V,R} \leq 0 \end{cases}$$

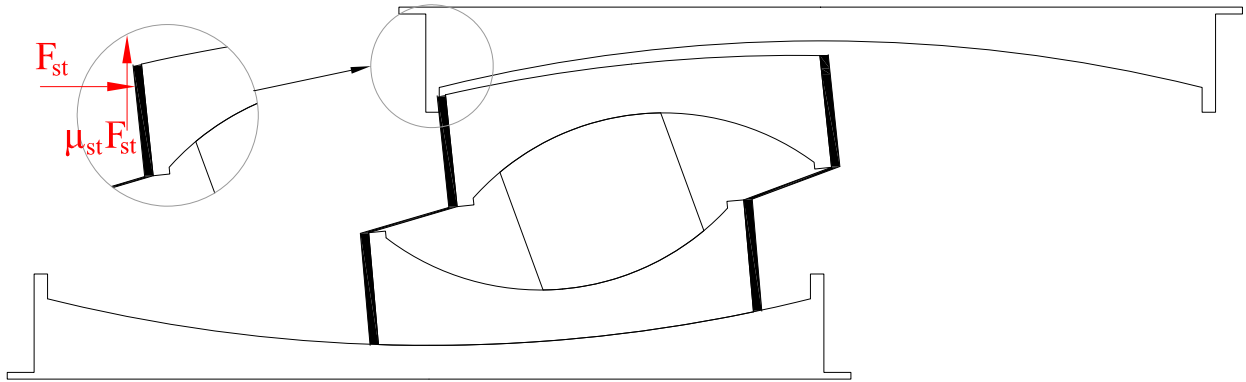


Figure 6-9: Friction force during uplift and contact between TCP and TSP

Moment equilibrium requires that:

$$\begin{aligned}
(a) : & \mathbf{R}_{1,L} \times (\mathbf{T}_b \cdot \mathbf{r}_{1,L}^c) + \mathbf{R}_{1,R} \times (\mathbf{T}_b \cdot \mathbf{r}_{1,R}^c) - \mathbf{R}_{2,L} \times (\mathbf{T}_b \cdot \mathbf{r}_{1,L}^s) - \mathbf{R}_{2,R} \times (\mathbf{T}_b \cdot \mathbf{r}_{1,R}^s) \\
& + \mathbf{F}_{1,L}^G \times (\mathbf{T}_b \cdot \mathbf{r}_{1,L}^c) - \mathbf{F}_{1,R}^G \times (\mathbf{T}_b \cdot \mathbf{r}_{1,R}^c) - \mathbf{F}_{2,L}^G \times (\mathbf{T}_b \cdot \mathbf{r}_{2,L}^G) + \mathbf{F}_{2,R}^G \times (\mathbf{T}_b \cdot \mathbf{r}_{2,R}^G) \\
& - \mathbf{F}_L^{RS} \times (\mathbf{A}_1 - \mathbf{u}_b) - \mathbf{F}_R^{RS} \times (\mathbf{A}_3 - \mathbf{u}_b) = \mathbf{I}_b \times \ddot{\boldsymbol{\theta}}_b \\
(b) : & \mathbf{R}_{2,L} \times (\mathbf{T}_r \cdot \mathbf{r}_{2,L}^c) + \mathbf{R}_{2,R} \times (\mathbf{T}_r \cdot \mathbf{r}_{2,R}^c) + \mathbf{R}_{3,L} \times (\mathbf{T}_r \cdot \mathbf{r}_{3,L}^c) + \mathbf{R}_{3,R} \times (\mathbf{T}_r \cdot \mathbf{r}_{3,R}^c) \\
& + \mathbf{F}_{2,L}^G \times (\mathbf{T}_r \cdot \mathbf{r}_{2,L}^c) - \mathbf{F}_{2,R}^G \times (\mathbf{T}_r \cdot \mathbf{r}_{2,R}^c) + \mathbf{F}_{3,L}^G \times (\mathbf{T}_r \cdot \mathbf{r}_{3,L}^c) - \mathbf{F}_{3,R}^G \times (\mathbf{T}_r \cdot \mathbf{r}_{3,R}^c) \\
& = \mathbf{I}_r \times \ddot{\boldsymbol{\theta}}_r \\
(c) : & -\mathbf{R}_{3,L} \times (\mathbf{T}_t \cdot \mathbf{r}_{3,L}^s) - \mathbf{R}_{3,R} \times (\mathbf{T}_t \cdot \mathbf{r}_{3,R}^s) + \mathbf{R}_{4,L} \times (\mathbf{T}_t \cdot \mathbf{r}_{4,L}^c) + \mathbf{R}_{4,R} \times (\mathbf{T}_t \cdot \mathbf{r}_{4,R}^c) \\
& - \mathbf{F}_{3,L}^G \times (\mathbf{T}_t \cdot \mathbf{r}_{3,L}^G) + \mathbf{F}_{3,R}^G \times (\mathbf{T}_t \cdot \mathbf{r}_{3,R}^G) + \mathbf{F}_{4,L}^G \times (\mathbf{T}_r \cdot \mathbf{r}_{4,L}^c) - \mathbf{F}_{4,R}^G \times (\mathbf{T}_r \cdot \mathbf{r}_{4,R}^c) \\
& + \mathbf{F}_L^{RS} \times (\mathbf{A}_2 - \mathbf{u}_t) + \mathbf{F}_R^{RS} \times (\mathbf{A}_4 - \mathbf{u}_t) + \mathbf{F}_L^V \times (\mathbf{T}_r \cdot \mathbf{r}_{4,L}^c) + \mathbf{F}_R^V \times (\mathbf{T}_r \cdot \mathbf{r}_{4,R}^c) \\
& = \mathbf{I}_t \times \ddot{\boldsymbol{\theta}}_t \\
(d) : & -\mathbf{R}_{4,L} \times (\mathbf{T}_t \cdot \mathbf{r}_{4,L}^s) - \mathbf{R}_{4,R} \times (\mathbf{T}_t \cdot \mathbf{r}_{4,R}^s) - \mathbf{F}_{4,L}^G \times (\mathbf{T}_r \cdot \mathbf{r}_{4,L}^G) + \mathbf{F}_{4,R}^G \times (\mathbf{T}_r \cdot \mathbf{r}_{4,R}^G) \\
& + K_f \boldsymbol{\theta}_{tc} - \mathbf{F}_L^V \times (\mathbf{T}_r \cdot \mathbf{r}_{4,L}^c) - \mathbf{F}_R^V \times (\mathbf{T}_r \cdot \mathbf{r}_{4,R}^c) = \mathbf{I}_{tc} \times \ddot{\boldsymbol{\theta}}_{tc}
\end{aligned} \tag{6-49}$$

Note that the \times symbol denotes the cross product of the vectors. The rotation vectors are given by:

$$\boldsymbol{\theta}_b = \begin{Bmatrix} 0 \\ 0 \\ \theta_b \end{Bmatrix}; \boldsymbol{\theta}_r = \begin{Bmatrix} 0 \\ 0 \\ \theta_r \end{Bmatrix}; \boldsymbol{\theta}_t = \begin{Bmatrix} 0 \\ 0 \\ \theta_t \end{Bmatrix}; \boldsymbol{\theta}_{tc} = \begin{Bmatrix} 0 \\ 0 \\ \theta_{tc} \end{Bmatrix} \tag{6-50}$$

Equilibrium of forces requires that:

$$\begin{aligned}
(a) : & \mathbf{T}_{1,L}^{s-1} \mathbf{R}'_{1,L} + \mathbf{T}_{1,R}^{s-1} \mathbf{R}'_{1,R} - \mathbf{T}_{2,L}^{s-1} \mathbf{R}'_{2,L} - \mathbf{T}_{2,R}^{s-1} \mathbf{R}'_{2,R} + \mathbf{F}_{1,L}^G - \mathbf{F}_{1,R}^G - \mathbf{F}_{2,L}^G + \mathbf{F}_{2,R}^G \\
& - \mathbf{F}_L^{RS} - \mathbf{F}_R^{RS} + \mathbf{F}_b^w + \mathbf{N}_{2,L}^D + \mathbf{N}_{2,R}^D - \mathbf{N}_{1,L}^D - \mathbf{N}_{1,R}^D = m_b \ddot{\mathbf{u}}_b \\
(b) : & \mathbf{T}_{2,L}^{s-1} \mathbf{R}'_{2,L} + \mathbf{T}_{2,R}^{s-1} \mathbf{R}'_{2,R} + \mathbf{T}_{3,L}^{s-1} \mathbf{R}'_{3,L} + \mathbf{T}_{3,R}^{s-1} \mathbf{R}'_{3,R} + \mathbf{F}_{2,L}^G - \mathbf{F}_{2,R}^G + \mathbf{F}_{3,L}^G \\
& - \mathbf{F}_{3,R}^G + \mathbf{F}_r^w + \mathbf{N}_{3,L}^D - \mathbf{N}_{2,L}^D + \mathbf{N}_{3,R}^D - \mathbf{N}_{2,R}^D = m_r \ddot{\mathbf{u}}_r \\
(c) : & \mathbf{T}_{4,L}^{s-1} \mathbf{R}'_{4,L} + \mathbf{T}_{4,R}^{s-1} \mathbf{R}'_{4,R} - \mathbf{T}_{3,L}^{s-1} \mathbf{R}'_{3,L} - \mathbf{T}_{3,R}^{s-1} \mathbf{R}'_{3,R} - \mathbf{F}_{3,L}^G + \mathbf{F}_{3,R}^G + \mathbf{F}_{4,L}^G \\
& - \mathbf{F}_{4,R}^G + \mathbf{F}_L^{RS} + \mathbf{F}_R^{RS} + \mathbf{F}_t^w + \mathbf{F}_L^V + \mathbf{F}_R^V + \mathbf{N}_{4,L}^D - \mathbf{N}_{3,L}^D + \mathbf{N}_{4,R}^D - \mathbf{N}_{3,R}^D = m_t \ddot{\mathbf{u}}_t \\
(d) : & -\mathbf{T}_{4,L}^{s-1} \mathbf{R}'_{4,L} - \mathbf{T}_{4,R}^{s-1} \mathbf{R}'_{4,R} - \mathbf{F}_{4,L}^G + \mathbf{F}_{4,R}^G + \mathbf{F}_{tc}^w - \mathbf{F}_L^V - \mathbf{F}_R^V \\
& - \mathbf{N}_{4,L}^D - \mathbf{N}_{4,R}^D = m_{tc} \ddot{\mathbf{u}}_{tc}
\end{aligned} \tag{6-51}$$

The equations of motion have the following degrees of freedom: $u_b, u_r, u_t, u_{tc}, v_b, v_r, v_t, v_{tc}, \theta_b, \theta_r, \theta_t, \theta_{tc}, du_b/dt, du_r/dt, du_t/dt, du_{tc}/dt, dv_b/dt, dv_r/dt, dv_t/dt, dv_{tc}/dt, d\theta_b/dt, d\theta_r/dt, d\theta_t/dt$ and $d\theta_{tc}/dt$. Equations (6-51) and (6-49) are combined with Equations (6-29) for the hysteretic parameters and written in state space. Collapse of the isolator occurs if the isolator becomes unstable during the analysis or if any of the following conditions are satisfied:

$$\begin{aligned} y_{i,L}^{GE} > y_{i,L}^c \ \& \ x_{i,L}^G > x_{i,L}^c; \quad y_{i,R}^{GE} > y_{i,R}^c \ \& \ x_{i,R}^G < x_{i,R}^c, \ i = 1, 2 \\ y_{i,L}^{GE} < y_{i,L}^c \ \& \ x_{i,L}^G > x_{i,L}^c; \quad y_{i,R}^{GE} < y_{i,R}^c \ \& \ x_{i,R}^G < x_{i,R}^c, \ i = 3, 4 \end{aligned} \quad (6-52)$$

The model as described above is suitable for response history analysis of seismically isolated structures.

When the model is used in analysis of a single isolator under prescribed motion, some modifications are needed. While the isolator is in compression, quantity u_{tc} is prescribed so is not a degree of freedom, whereas v_{tc} is a degree of freedom. During uplift, quantities u_{tc} and v_{tc} are both prescribed and, therefore, both components of the last Equation in (6-51) are ignored (these are the equations of horizontal and vertical equilibrium of the top concave plate). Also, the last of Equation (6-49) is ignored (moment equilibrium of the TCP). During landing, the TCP exhibits free fall (see difference between $v_{TCP}^{t=t_2}$ and $v_p^{t=t_2}$ in Figure 5-2) so that v_{tc} is unknown (a degree of freedom) with an initial value - the value obtained from the end of the uplift duration. As a result, modeling of landing is no different than modeling compression. The initial conditions of the remaining components are also calculated using as initial conditions the conditions calculated at the end of the uplift episode. Note that the model presented in Section 6 can be combined with the models of Sections 4 and 5 in order to analyze various stages of behavior (i.e., compression, uplift and landing) using different theories. This may expedite the execution of the analysis but differences between the models require care in the calculation of the initial conditions for each stage of analysis. Also, it should be noted that in the model presented in Section 6, landing is a phenomenon of finite duration ($t_3 > t_2$ in Figure 5-1), whereas in the model presented in Section 5.3, landing occurs instantaneously ($t_3 = t_2$ in Figure 5-2).

6.2 Model Verification and Demonstration of Analysis Capabilities

Consider the Full Scale-Configuration B isolator described in Table 3-2 subjected to a compressive load of 6675kN and a prescribed horizontal TCP sinusoidal displacement history of 1000mm amplitude and 0.15Hz frequency. Results are obtained using a) the model presented in Section 4, and b) the model presented in Section 6. Results presented in Figure 6-10 demonstrate that the two models produce nearly identical results. Minor differences may be observed at large amplitude of motion and are likely the effect of large rotations which can be accounted for only in the model presented in Section 6.

Figure 6-11 compares results for the same isolator subjected to motion of 1000mm amplitude, frequency of 1Hz and vertical compressive load of 1335kN. Due to the low vertical load and the high frequency of motion, the inertia effects are now more pronounced. Results are again in good agreement but for some small differences in the force-displacement loops which are attributed to numerical errors in the analysis and to differences in accounting for the inertia effects in the two models - the model presented in Section 6 being more accurate. One should note the increase in force upon entering Regime IV when the bearing internal parts engage the restrainer of surface 1. The increase in force is due to impact of the moving parts on the restrainer. This force is much more pronounced (as a portion of the vertical load) than in the analysis shown in Figure 6-10 due to the higher speed of the moving parts and the lower vertical load used in the analysis.

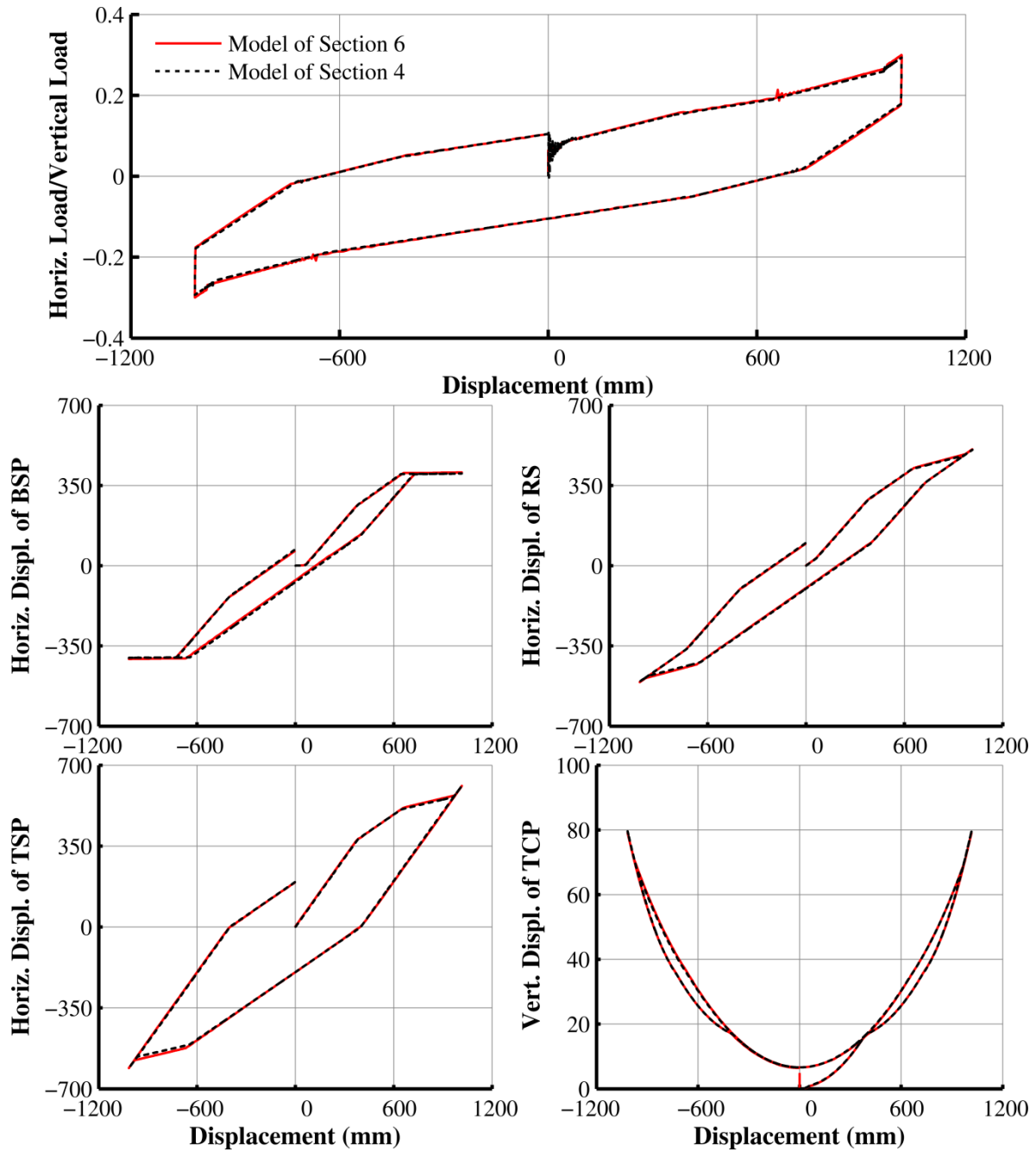


Figure 6-10: Comparison of results obtained by model presented in Section 4 and model presented in Section 6 for the full scale isolator-Configuration B of Table 3-2 subjected to TCP motion of 1000mm amplitude, 0.15Hz frequency and load of 6675kN

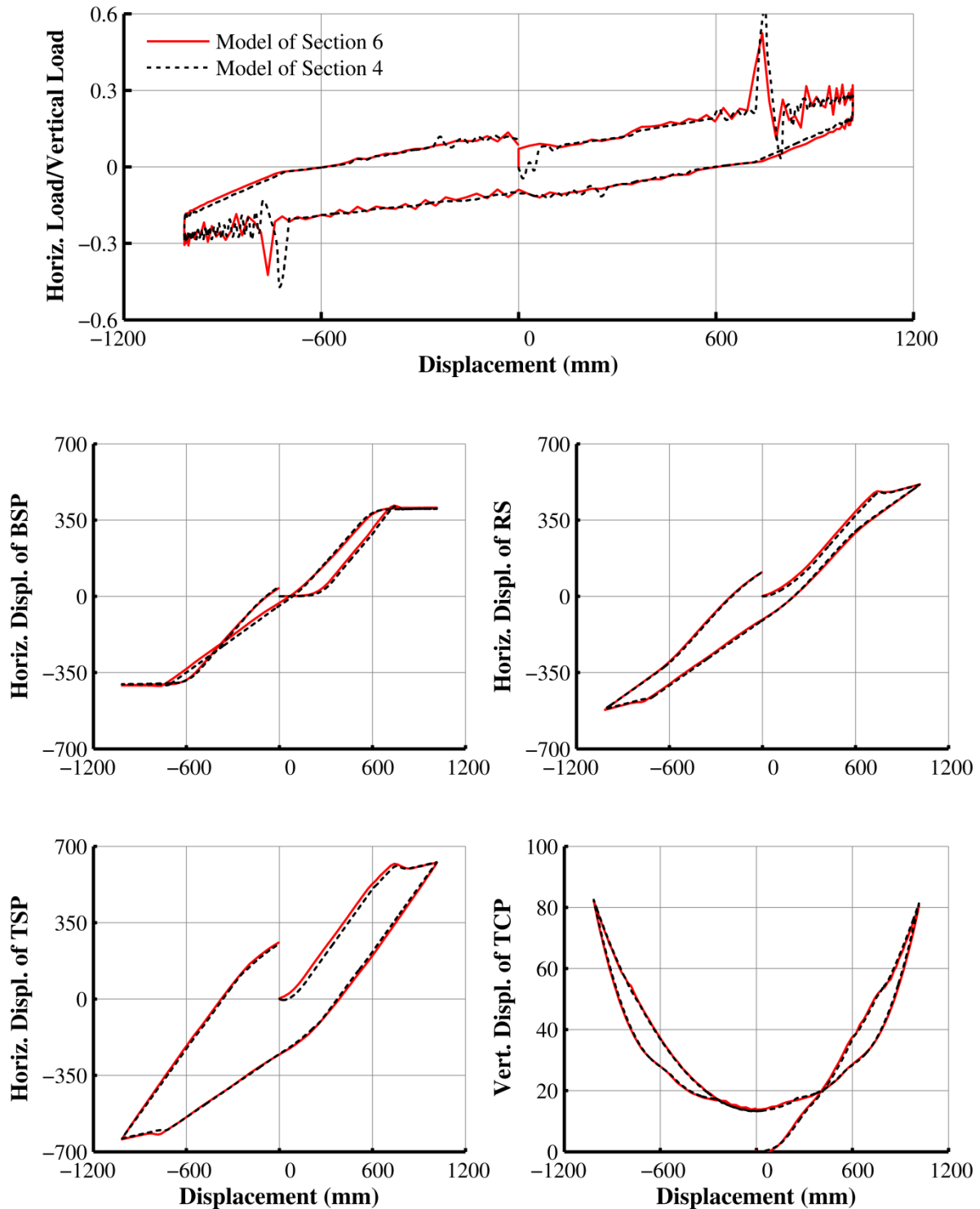


Figure 6-11: Comparison of results obtained by model presented in Section 4 and model presented in Section 6 for the full scale isolator-Configuration B of Table 3-2 subjected to TCP motion of 1000mm amplitude, 1Hz frequency and load of 1335kN

In order to investigate the effect of large rotations, Figure 6-12 compares results of the models of Sections 4 and 6 for the Full Scale-Configuration B isolator of Table 3-2 but with different friction properties ($\mu_1 = \mu_4 = 0.065, \mu_2 = \mu_3 = 0.045$) so that that Regime V extends over a larger displacement range. The motion is of 1000mm amplitude and frequency of 0.15Hz. Note that the model presented in Section 6 accounts for large rotation effects, whereas the model presented in Section 4 does not. The results of the two models are essentially the same. Accordingly, large rotation effects for this large size isolator are not important.

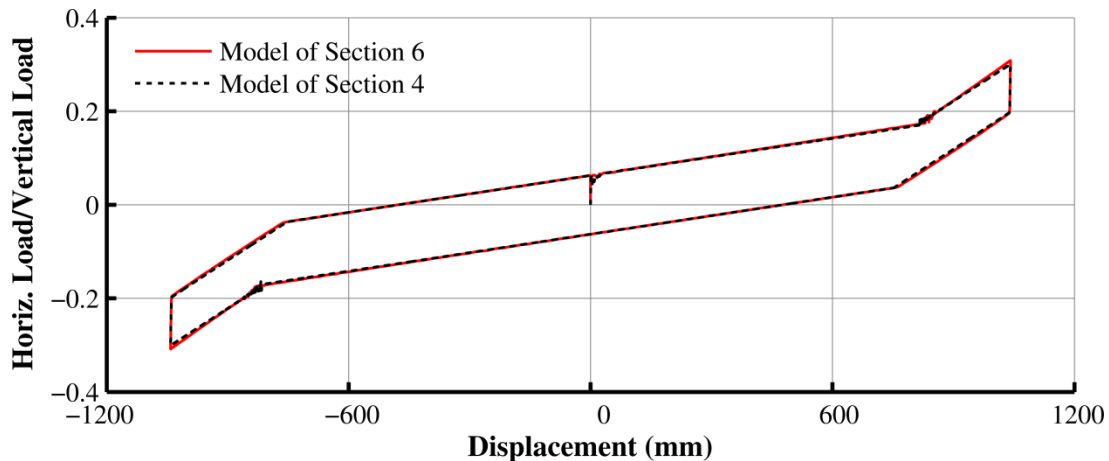


Figure 6-12: Comparison of results obtained by model presented in Section 4 and model presented in Section 6 for the full scale isolator-Configuration B of Table 3-2 with $\mu_1 = \mu_4 = 0.065, \mu_2 = \mu_3 = 0.045$ and subjected to TCP motion of 1000mm amplitude, 0.15Hz frequency and load of 6675kN

Figure 6-13 shows results for the Full Scale-Configuration B isolator described in Table 3-2 and subjected to a compressive load of 6675kN and a prescribed horizontal TCP sinusoidal displacement history of 0.15Hz frequency and displacement amplitude that was larger than the displacement capacity of the bearing. The figure also shows snapshots of the deformed bearing when the displacement is close to its maximum value. Notice that the model is capable of capturing point contact and overturning that may occur at extreme displacements. The model also captures instability of the bearing as indicated by the branch of the force displacement loop with negative stiffness. However, it should be noted that the results shown in Figure 6-13 are based on the assumption of infinite strength for the restrainers. In reality, these restrainers have limited strength, which affects the behavior of the bearing under the conditions analyzed.

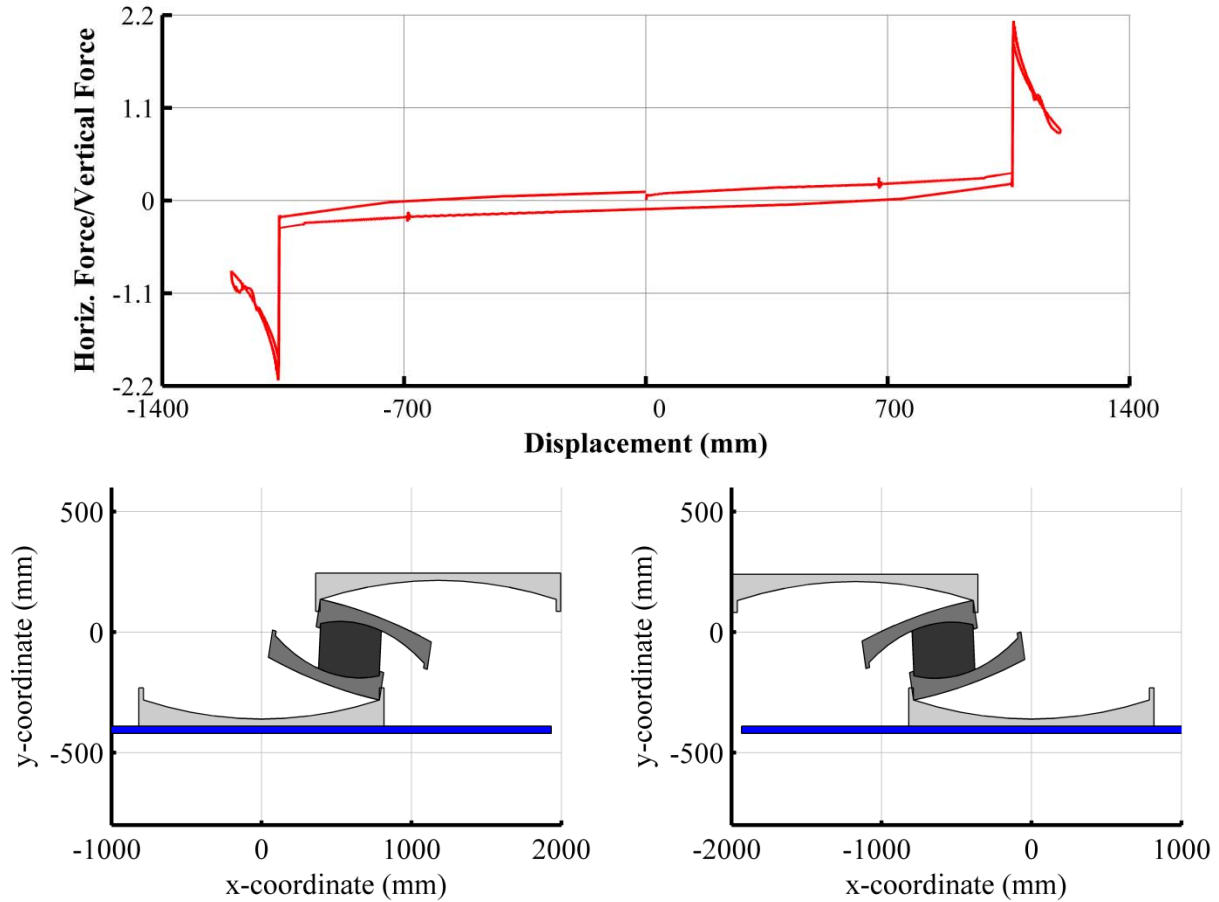


Figure 6-13: Force-displacement loops and snapshots of TFP isolator subjected to displacement amplitude larger than the displacement capacity

Figure 6-14 compares force-displacement loop of the Full Scale-Configuration B isolator described in Table 3-2 and subjected to a compressive load of 6675kN and a prescribed horizontal TCP sinusoidal displacement history of 1000mm amplitude and 0.15Hz frequency when the TCP is leveled or is rotated. The effects of the TCP rotation are to shift the loops along the axis of force and to modify the transition points between regimes.

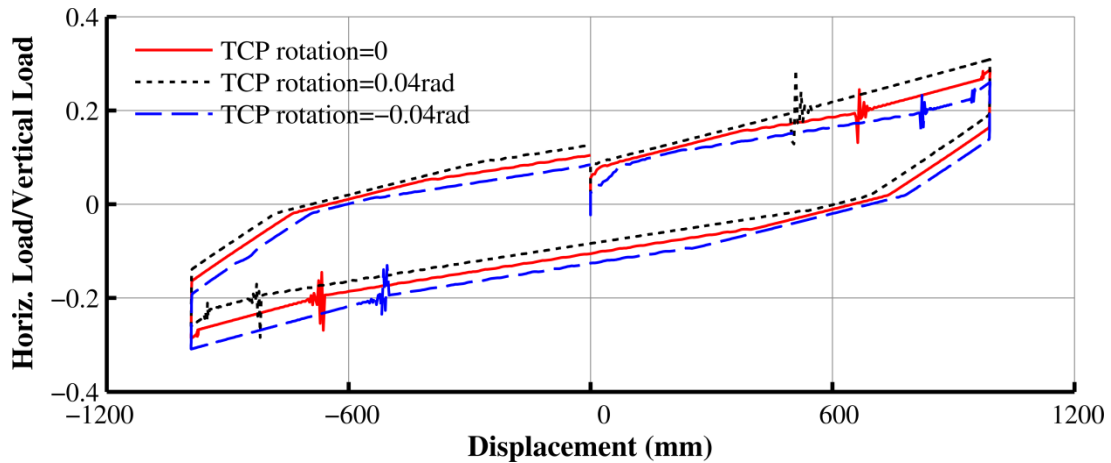


Figure 6-14: Comparison of force-displacement loops of TFP isolator with rotation of the TCP

Finally, Figure 6-15 compares results of the Full Scale-Configuration B isolator described in Table 3-2 and subjected to a compressive load of 6675kN and a prescribed horizontal TCP sinusoidal displacement history of 1000mm amplitude and 0.15Hz frequency when a rotational spring is connected to the TCP. Three values of stiffness are considered: a) Infinite so that the TCP remains horizontal, b) 302MN-m and c) 101MN-m. Noticeable effects are observed as a result of the TCP rotation caused by the overturning moment.

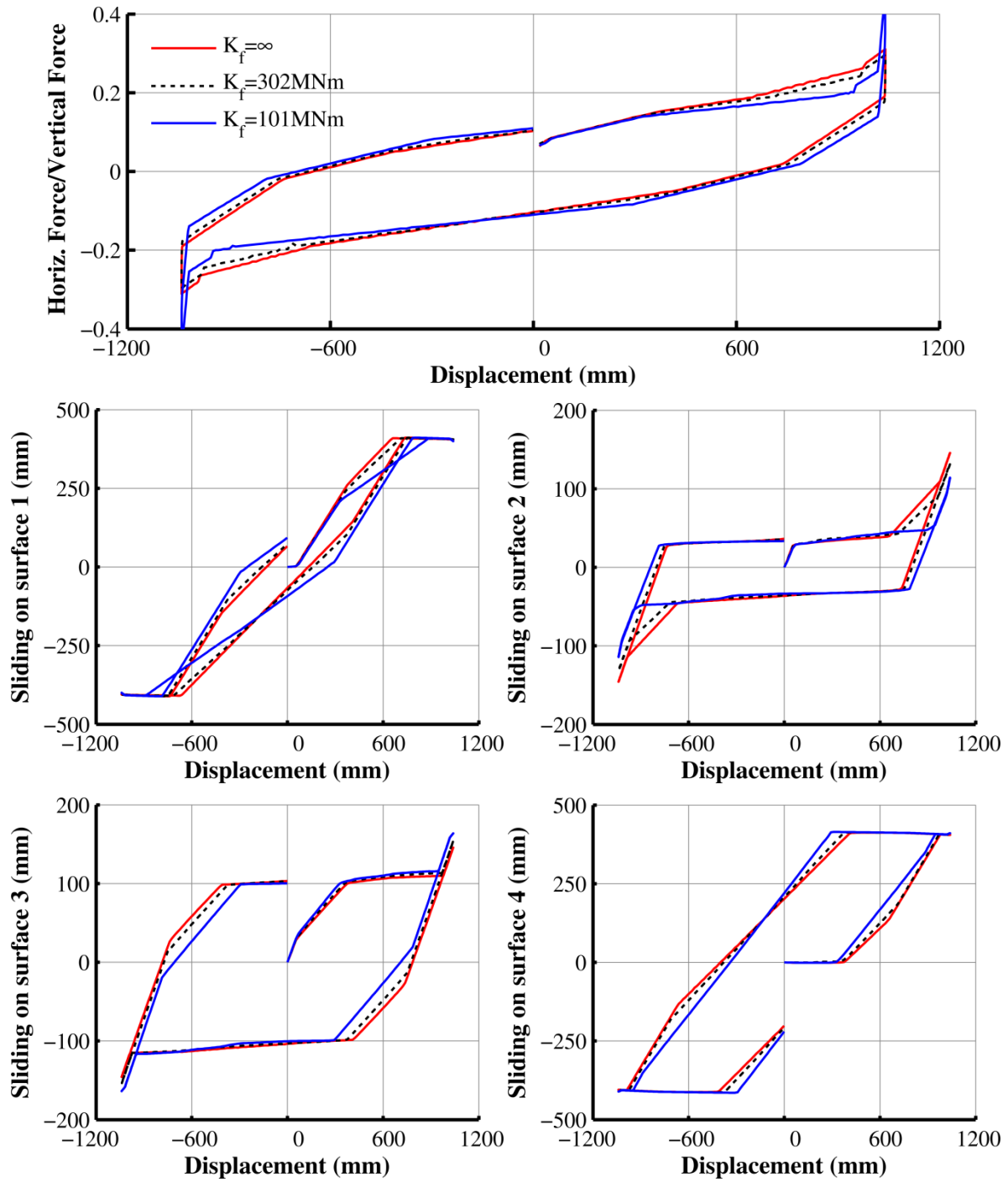


Figure 6-15: Comparison of force-displacement loops of TFP isolator with rotational spring connected to the TCP

SECTION 7

PROGRAM 3pleANI

3pleANI is an analysis program developed in MATLAB that is capable of performing two-dimensional analysis and animation of Triple Friction Pendulum (FP) isolators that cannot be performed by commercially available software. The FP isolators are modeled based on the theory presented in Sections 4 to 6. The program offers the capability to analyze and present animation of motion of the components of isolators under (a) regular conditions when no uplift occurs and (b) uplift conditions that include bouncing of components. Output quantities include global response quantities of the analyzed structural system (total accelerations, total displacements, drift, forces, and floor response spectra) and isolator response quantities (displacements and rotations of parts, velocities at the sliding surfaces, forces at the sliding surfaces, heat flux and temperature rise at each sliding surface).

The program has two analysis options: (a) displacement control analysis and (b) dynamic analysis. The first option allows analysis and animation of motion of the components of sliding isolators under specified histories of horizontal and vertical motion (and constant or variable vertical load). The program can calculate all response quantities related to all sliding surfaces for any geometric and frictional parameters. Advanced analysis options include heating effects at the sliding interfaces, misalignments, non-zero initial conditions, etc. The uplift analysis is the centerpiece of this interface since it allows modeling of the behavior of the inner components that cannot be performed in commercial software.

The second option allows for dynamic analysis of plane seismically isolated structures. Several options for the structure exist:

- (a) A rigid single-degree-of-freedom system,
- (b) A multi-story building with shear type representation in which the parameters are story stiffness and floor masses,
- (c) A multi-story building with one degree-of-freedom per floor but with the stiffness and mass matrices imported,

- (d) A bridge with flexible piers. In this case, analysis options include consideration of P- Δ effects on the pier rotation and consideration of the pier rotation on the behavior of the isolator.

In the dynamic analysis option, the isolators are presumed to be in full contact so that no uplift analysis is performed. A library of ground motion acceleration histories allows the user to select and scale for analysis. Analysis options include (a) calculation of response spectra of input motion, (b) calculation of periods, mode shapes and damping ratios of the superstructure (c) calculation of response of the non-isolated structure, (d) calculation of response of the seismically isolated structure, and (e) display and animation of the calculated response.

Appendix A presents the “Users Guide and Reference Manual” of program 3pleANI where the capabilities of the program are described. The option of program 3pleANI for “displacement controlled analysis” is used for the verification examples of Section 8 that follows.

Appendix B presents an “Analysis and Verification Examples” document for program 3pleANI where predictions of the response of Triple FP bearings and of isolated structures obtained by 3pleANI are compared to theoretical results and to predictions of commercially available programs. The latter case is restricted to combinations of geometric and frictional parameters that can be modeled by existing models in commercial software (see Fenz and Constantinou 2008a to 2008e). All of the examples in Appendix B involve cases where the Triple FP bearings operate in full contact of the sliding surfaces. Also, the “Analysis and Verification Examples” document presents comparisons of results obtained from uplift analysis against closed form solutions that can be obtained for the same cases.

SECTION 8

EXAMPLES OF TRIPLE FP ANALYSIS WITH UPLIFT

8.1 Introduction

The calculation of uplift displacement of Triple FP isolators in the response history analysis of structures is possible in commercially available software (e.g., programs SAP2000 and ETABS). However, the model of the isolator in these programs is generic and does not actually trace the motion of the parts of the isolator to be able to obtain information on the state of the isolator, including permanent offsets of the internal parts, instability and heating of the components. Program 3pleANI is able to provide this information by conducting complex analyses of various degrees of complexity.

An analysis of uplift involves the following steps:

1. Model the isolated structure in commercially available software such as SAP2000 using the series model (Fenz and Constantinou 2008d) or the parallel model (Sarlis and Constantinou 2010). Conduct response history analysis.
2. Export the horizontal and vertical displacement histories of the top joint of the isolators exhibiting uplift. The response histories of all the isolators will be required and not just selected isolators that exhibit the largest uplift displacement since the magnitude of uplift is significant but is not the sole determining factor in assessing the safety of the isolator.
3. Import the displacement histories in program 3pleANI and conduct uplift analysis for each isolator and assuming various scenarios in the analysis (e.g., analyze the isolator with and without the rubber seal, consider different attachment details of the seal, assume various values of the friction coefficient when the bearing uplifts).
4. If unstable behavior is feasible, modify the isolator details (e.g., increase the height of the restrainers) or modify the structural system in order to reduce the uplift displacement or change the uplift characteristics.
5. Conduct experiments to validate the behavior of the modified isolator.

Uplift experiments are difficult to conduct as testing machines with capacity to reproduce complex uplift conditions for large bearings do not exist. Typically, testing is conducted under

quasi-static conditions that provide the ability to make visual observations of behavior. Program 3pleANI can reduce the necessity for physical testing and be used to identify the critical uplift cases that should be experimentally investigated. With increased level of confidence in the use of the program, physical testing for uplift may be eliminated but for the most important applications.

This section presents examples of motion of Triple FP bearings under conditions of uplift. Program 3pleANI is used to obtain results in terms of force-displacement loops and other response parameters. Also, results of animation of the analyzed bearings are presented.

8.2 Example 1

Consider the bearing of Figure 8-1 that is used in the isolation system of the San Bernardino Courthouse in California (Sarkisian et al., 2012). Table 8-1 presents the geometric and frictional properties of the bearing used in the analysis.

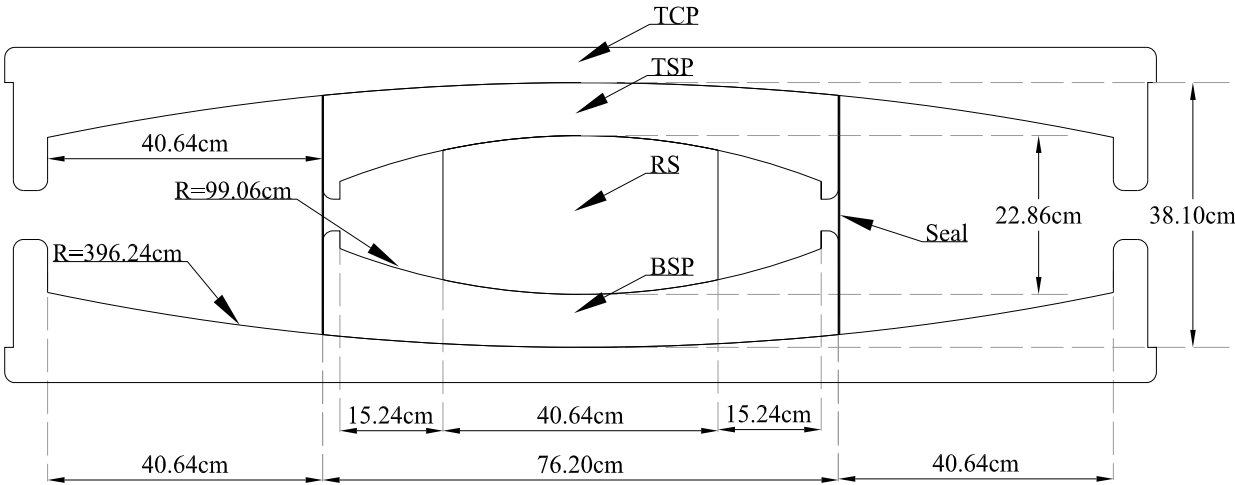


Figure 8-1: Analyzed Triple FP bearing

Analysis of the bearing motion was performed in program 3pleANI using the horizontal and vertical motions shown in Figure 8-2. These histories of motion are those of the two nodes representing one bearing in the ETABS analysis model of the isolated structure in a particular seismic motion as reported in Sarkisian et al. (2012). Note that these motions represent the motion, including uplift, of the top node representing the bearing so that the geometric changes are not included. The geometric changes are explicitly calculated in the 3pleANI program analysis. Load on the bearing was assumed constant at 6675kN and then converted to zero for

the uplift duration, which starts at time of 3.685sec and ends at time of 5.325sec as shown in the vertical displacement history of Figure 8-2. Analysis was conducted with friction assumed independent of velocity and having the values in Table 8-1 while under the compressive load of 6675kN. The values of the friction coefficients were assumed to be twice as much as those of Table 8-1 when the bearing uplifts and the load at each sliding interface is only the weight of the internal components. For this example, it was assumed that there is no rubber seal. Examples 2 and 3 study the effect of the rubber seal.

Table 8-1: Geometric and frictional properties of analyzed bearing

TFP Properties	Value
$R_1 = R_4$ (mm)	3962
$R_2 = R_3$ (mm)	991
$h_2 = h_3$ (mm)	114
$h_1 = h_4$ (mm)	191
$R_{eff1} = R_{eff4}$	148.5
$R_{eff2} = R_{eff3}$ (mm)	34.5
$d_1 = d_4$ (mm)	406.4
$d_2 = d_3$ (mm)	152.4
$b_1 = b_4$ (mm)	762
$b_2 = b_3$ (mm)	406.4
$\mu_1 = \mu_4$	0.08
$\mu_2 = \mu_3$	0.05

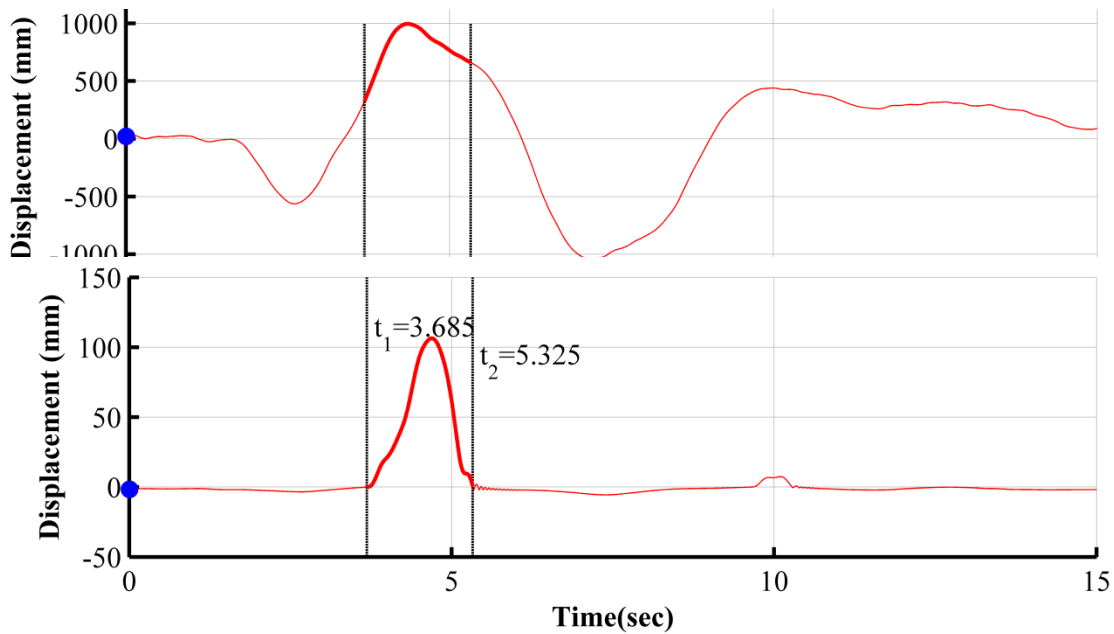


Figure 8-2: Horizontal (top) and vertical motion (bottom) of top node of one bearing of isolated structure calculated in program ETABS (Sarkisian et al., 2012)

Analysis results using the full contact theory of Sections 4 and 5 are shown in Figure 8-3 and Figure 8-4, and analysis results using the advanced theory of Section 6 are shown in Figure 8-5 and Figure 8-6.

Figure 8-3 (full contact theory) and Figure 8-5 (advanced theory) present results from program 3pleANI for the horizontal displacement, vertical displacement and rotation of the center of mass (CM) of each part of the isolator (see notation in Figure 1-1 and Figure 8-1). Also, they present force-displacement loops as calculated by program 3pleANI. The graphs compare the vertical displacement of the TCP calculated in 3pleANI to the ETABS results (also shown in Figure 8-2 for the TCP vertical displacement).

Figure 8-4 (full contact theory) and Figure 8-6 (advanced theory) present captured frames of the isolator's response obtained from 3pleANI for the uplift duration. Note that the two theories predict slightly different behavior for the uplift duration. However, the isolator's position at landing (frames at 5.1446sec and 5.1415sec in Figure 8-4 and Figure 8-6, respectively) is almost the same in both analysis methods. The most significant difference between the two methods is the ability of the advanced modeling to capture point contact and potential overturning of TFP parts. When the seal is not present, the TSP is unstable and uplifts as shown at time 4.6002sec in

Figure 8-6. In this case, the small separation between the TCP and TSP does not allow for overturning and, accordingly, the two methods produce similar results.

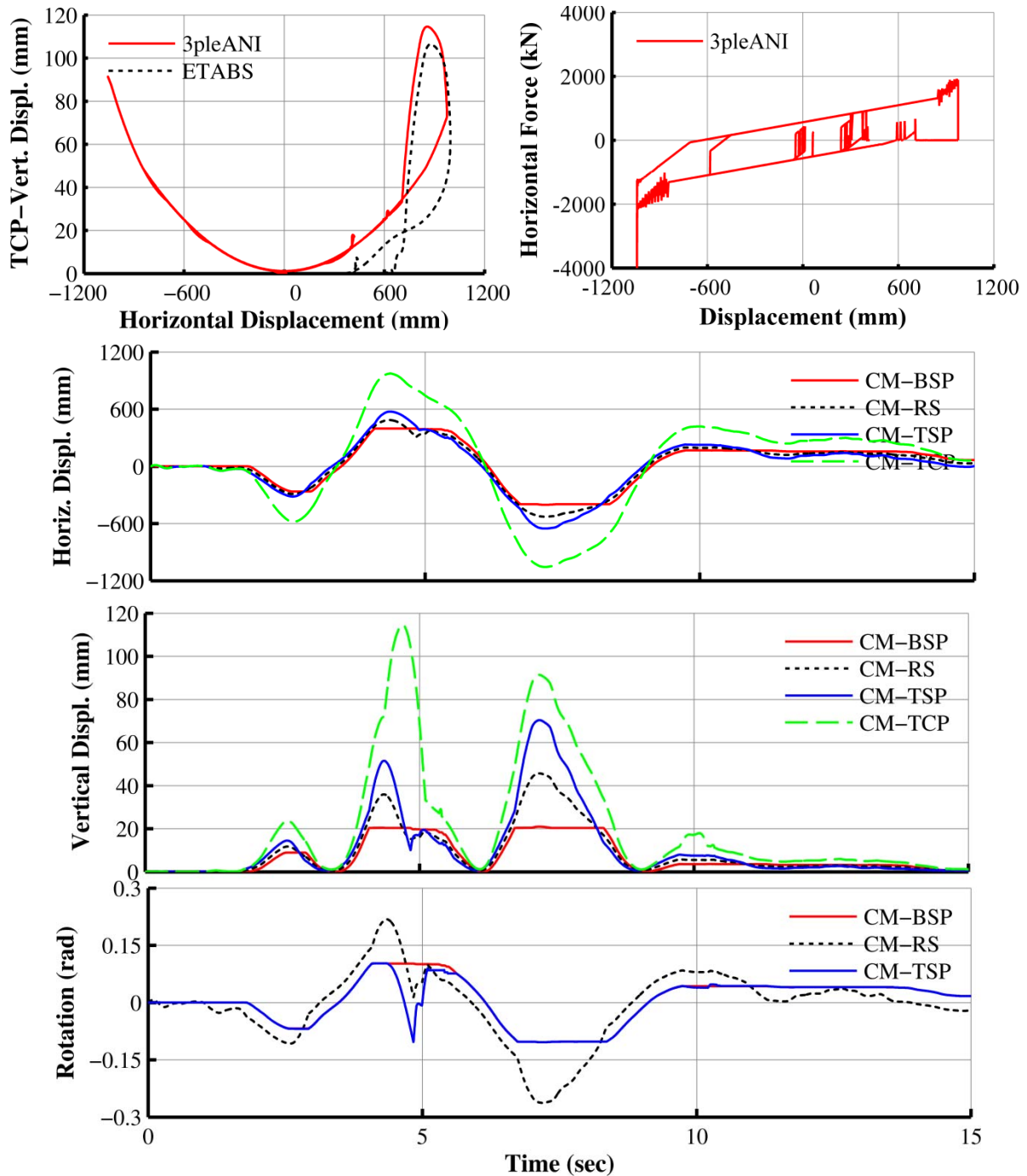


Figure 8-3: Program 3pleANI results of analysis of bearing of Example 1 with uplift using full contact theory and without rubber seal

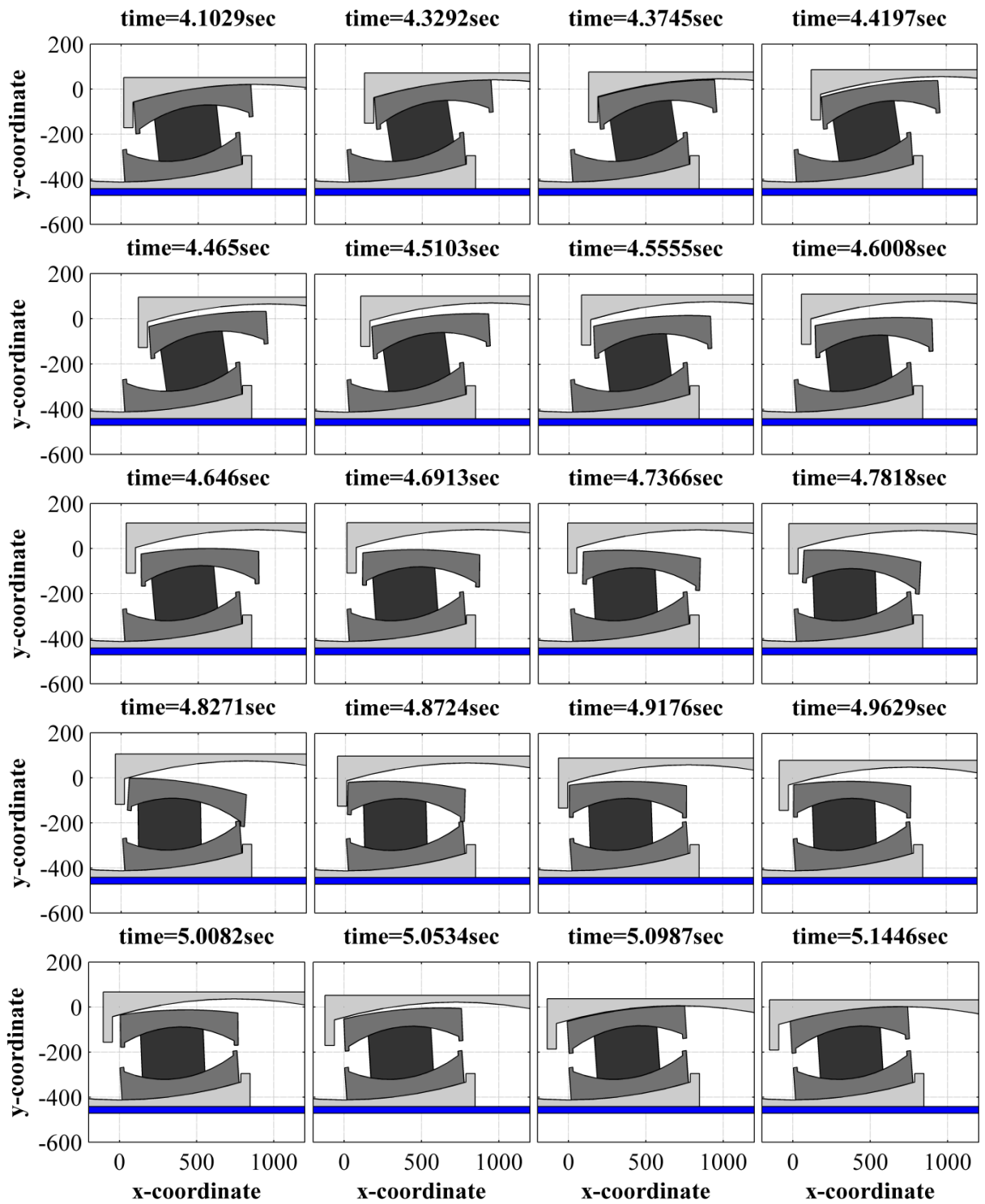


Figure 8-4: Animation of the bearing motion during the uplift duration by program 3pleANI for Example 1 using full contact theory and without rubber seal

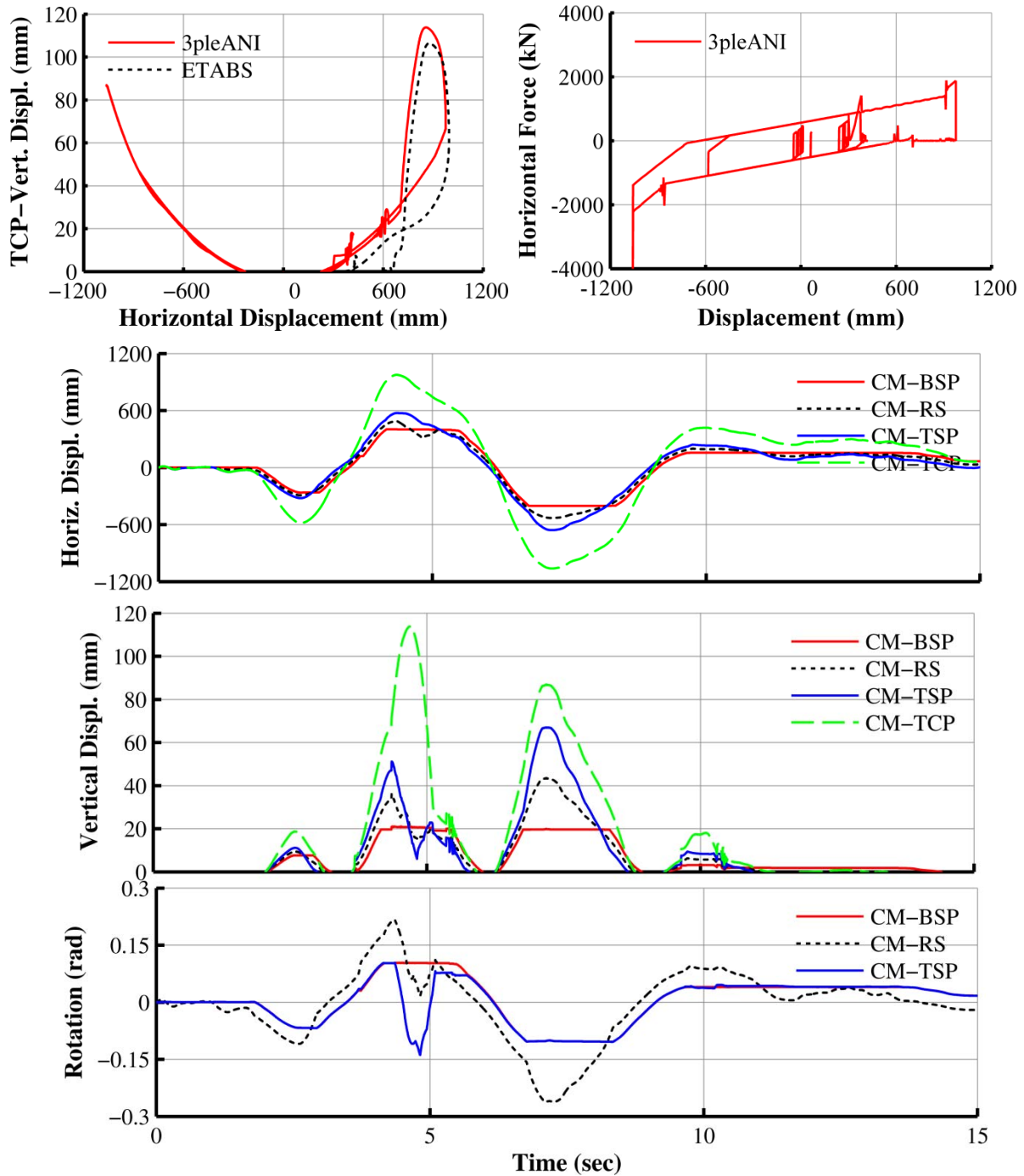


Figure 8-5: Program 3pleANI results of analysis of bearing of Example 1 with uplift using advanced theory and without rubber seal

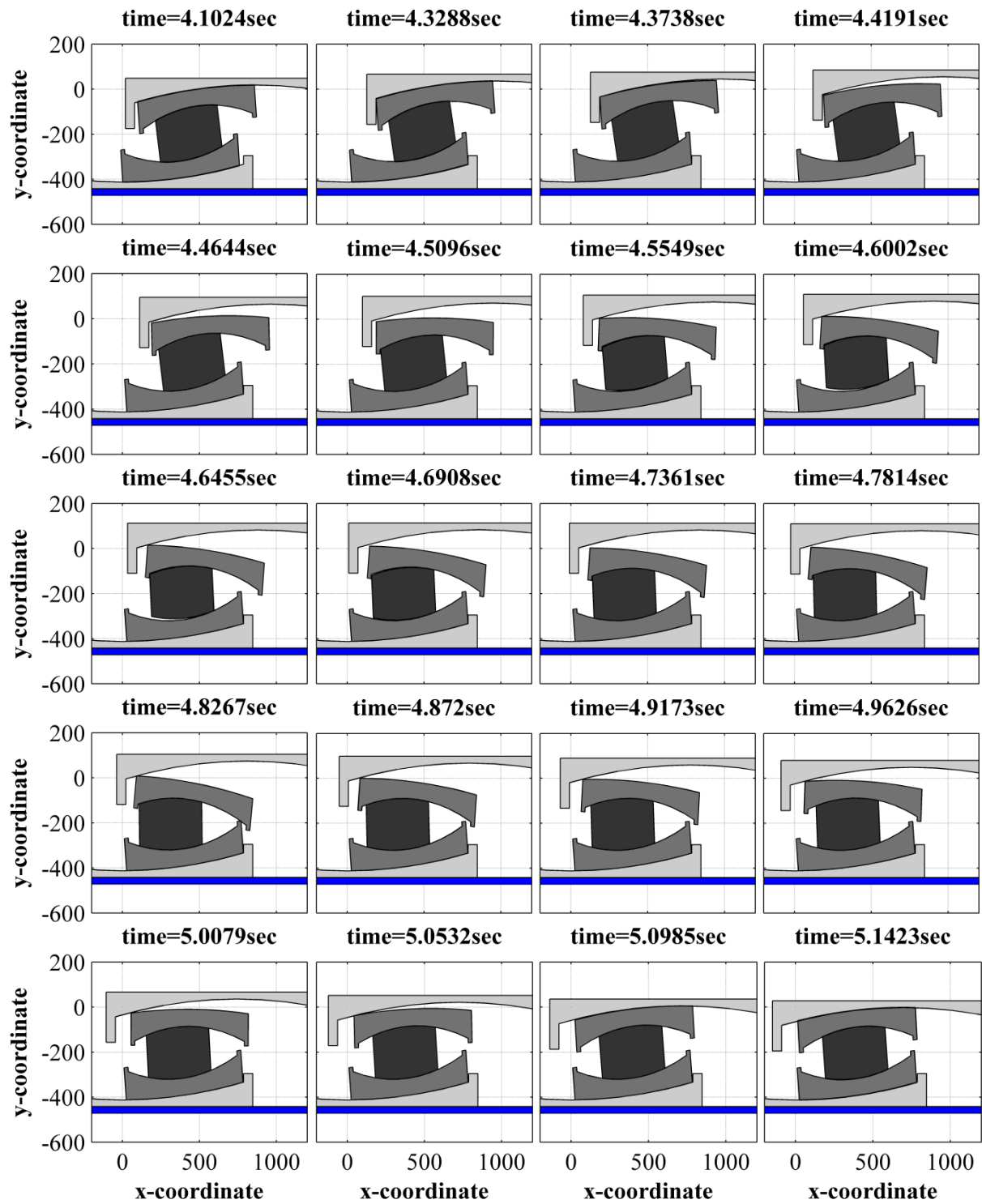


Figure 8-6: Animation of the bearing motion during the uplift duration by program 3pleANI for Example 1 using advanced theory and without rubber seal

8.3 Example 2

Example 1 was re-analyzed for the same bearing motion (shown in Figure 8-2) but with the presence of the rubber seal. For this example, the rubber seal was assumed to be linear elastic with behavior given by Equation (5-18) and $t_s = 1.56\text{mm}$ and $E = 9.65\text{MPa}$. The force-deformation relation of the rubber seal for this example is shown in Figure 8-7. The isolator was analyzed using both the full contact theory (quantitative results are presented in Figure 8-8 and animation results in Figure 8-9) and the advanced theory (quantitative results are presented in Figure 8-10 and animation results in Figure 8-11). The quantities presented in the results were described in Example 1.

Note that for this example, the full contact theory and the advanced theory produce different results for the isolator's response during the uplift episode. However, the final isolator position after landing is essentially the same for the two theories. In this example, the rubber seal is strong enough to lift up the TFP parts so that point contact occurs on surface 1 as predicted by the advanced theory and shown in Figure 8-11, for example at time=4.7316sec. Such phenomena cannot be predicted by the full contact theory.

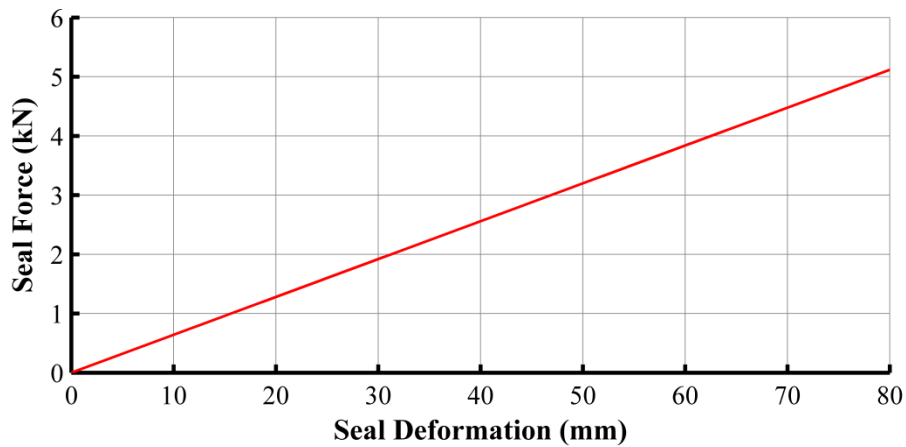


Figure 8-7: Seal force-deformation relationship for Example 2

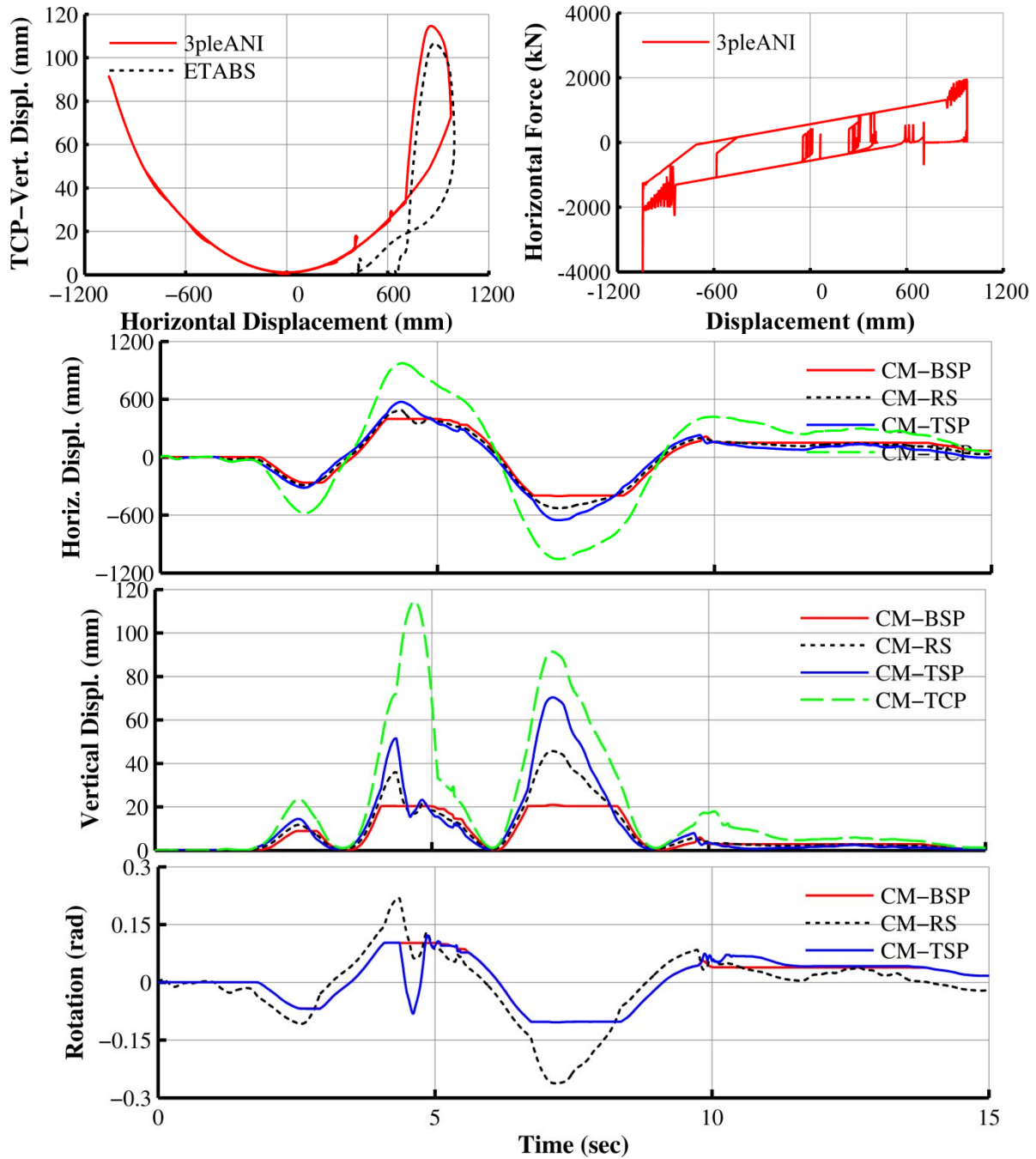


Figure 8-8: Program 3pleANI results of analysis of bearing of Example 2 with uplift using full contact theory and linear elastic rubber seal

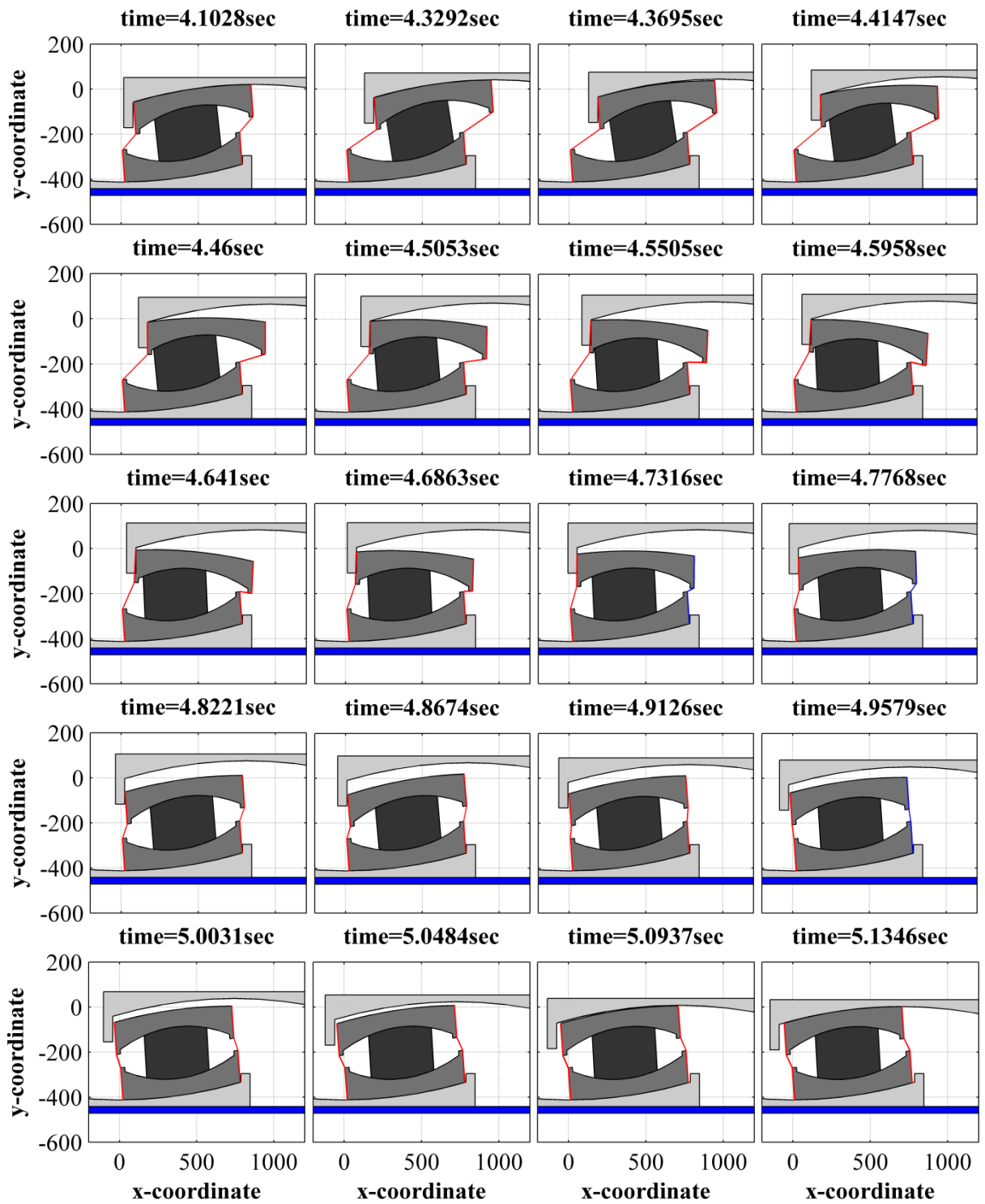


Figure 8-9: Animation of the bearing motion during the uplift duration by program 3pleANI for Example 2 using full contact theory and linear elastic rubber seal

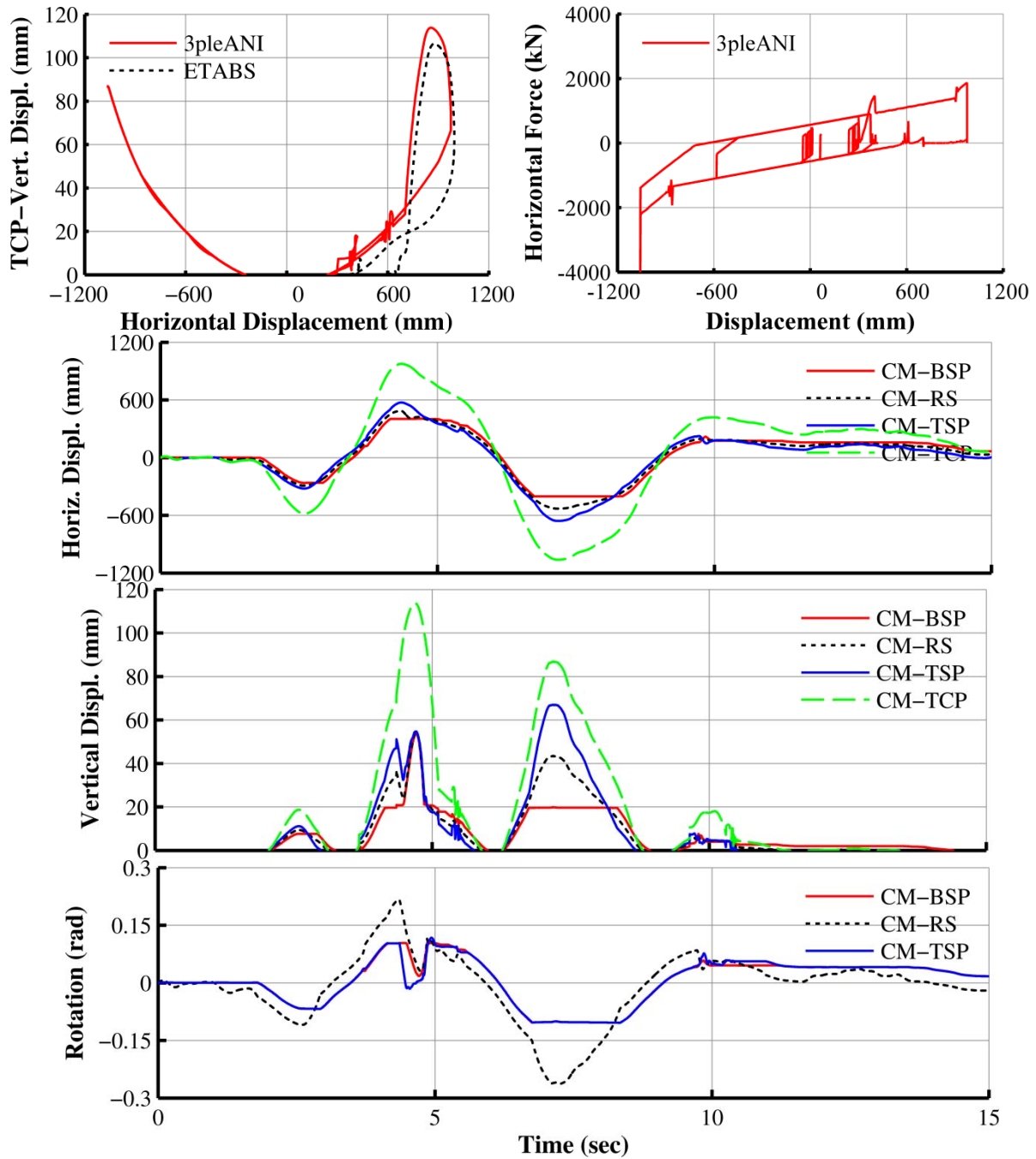


Figure 8-10: Program 3pleANI results of analysis of bearing of Example 2 with uplift using advanced theory and linear elastic rubber seal

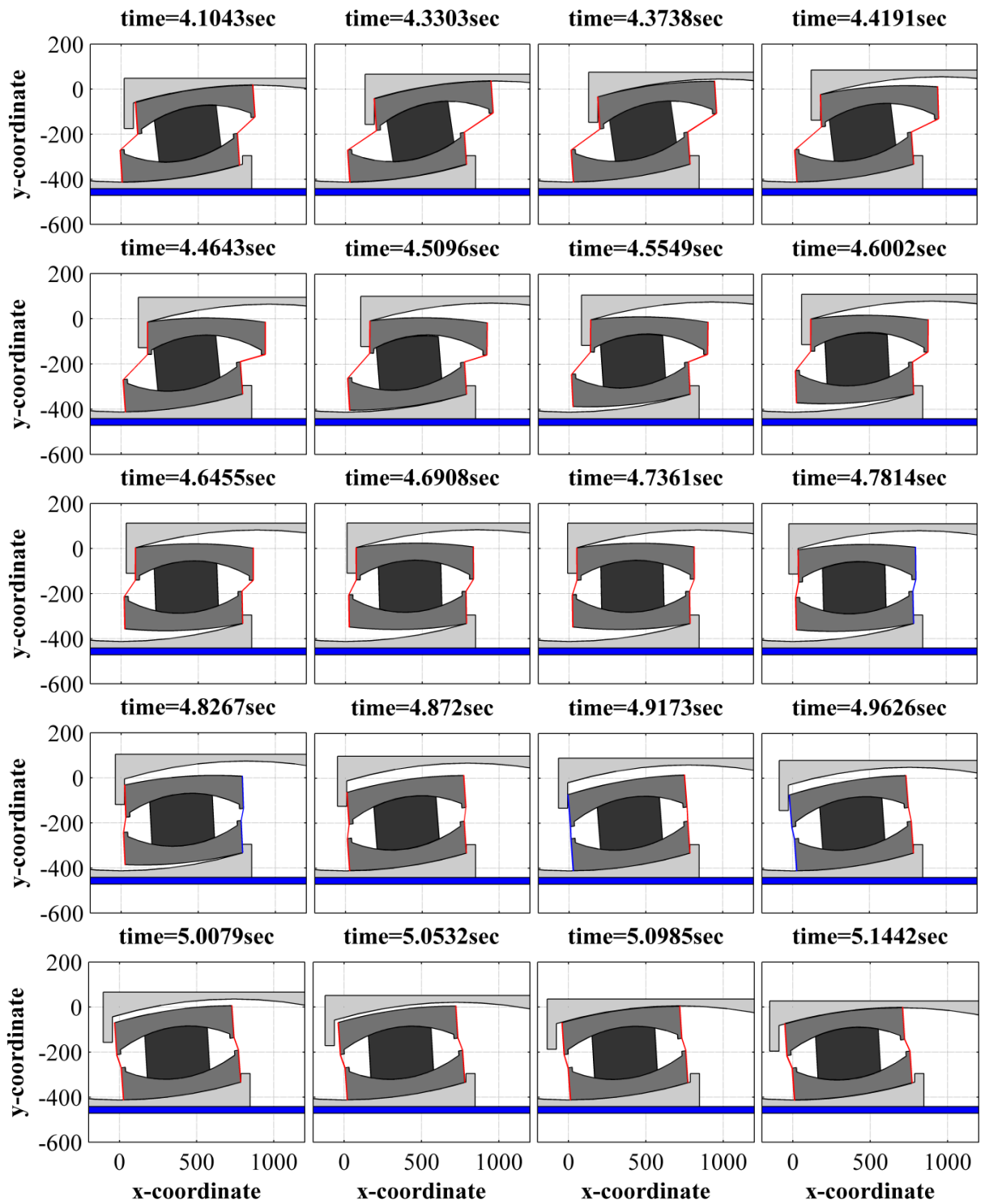


Figure 8-11: Animation of the bearing motion during the uplift duration by program 3pleANI for Example 2 using advanced theory and linear elastic rubber seal

8.4 Example 3

Example 2 was re-analyzed but for a different behavior for the rubber seal. For this example, the rubber seal was assumed to be nonlinear elastic with behavior described by Equation (5-19) with the same properties as Example 2. Note that this type of behavior is more realistic for the seal. A comparison of the seal force-deformation relations used in Examples 2 and 3 is presented in Figure 8-12.

The isolator was analyzed using both the full contact theory (quantitative results are presented in Figure 8-13 and animation results in Figure 8-14) and the advanced theory (quantitative results are presented in Figure 8-15 and animation results in Figure 8-16). The quantities presented in the results were described in Example 1.

Again the full contact theory and advanced theory produce different results for the isolator's response during the uplift episode. Also, note the difference with Example 2: the rubber seal with variable stiffness is not stiff enough to lift up the TFP parts but is stiff enough to re-center the inner parts of the bearing prior to landing.

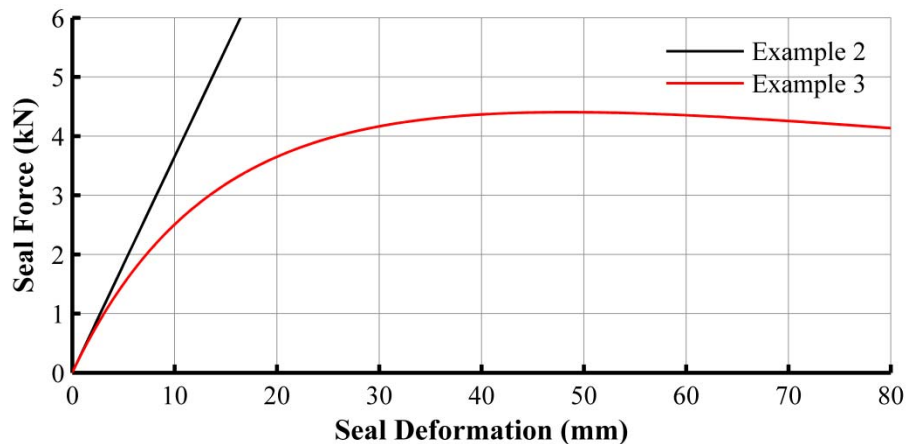


Figure 8-12: Comparison of seal force-deformation relations used in Examples 2 and 3

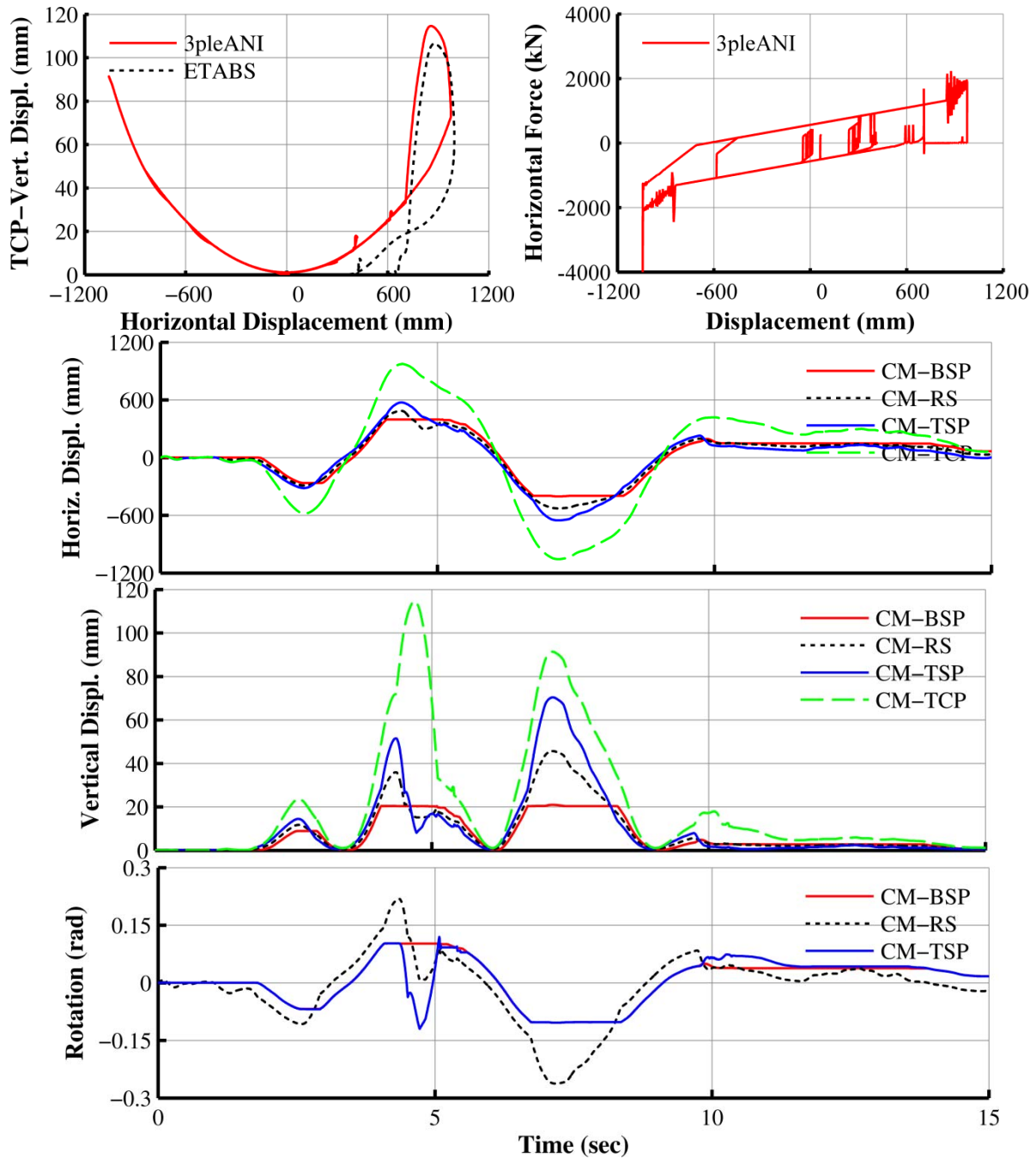


Figure 8-13: Program 3pleANI results of analysis of bearing of Example 3 with uplift using full contact theory and nonlinear elastic rubber seal

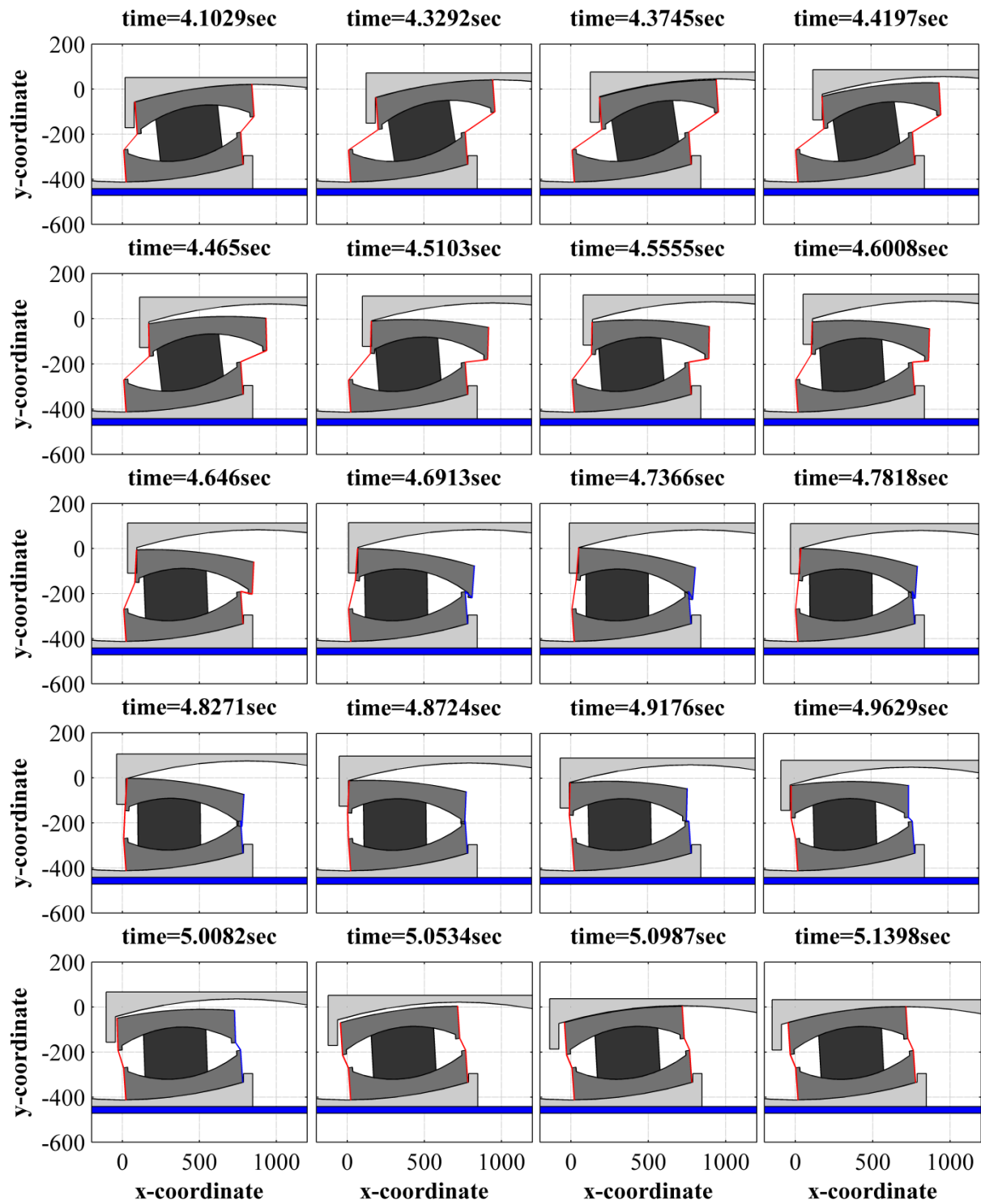


Figure 8-14: Animation of the bearing motion during the uplift duration by program 3pleANI for Example 3 using full contact theory and nonlinear elastic rubber seal

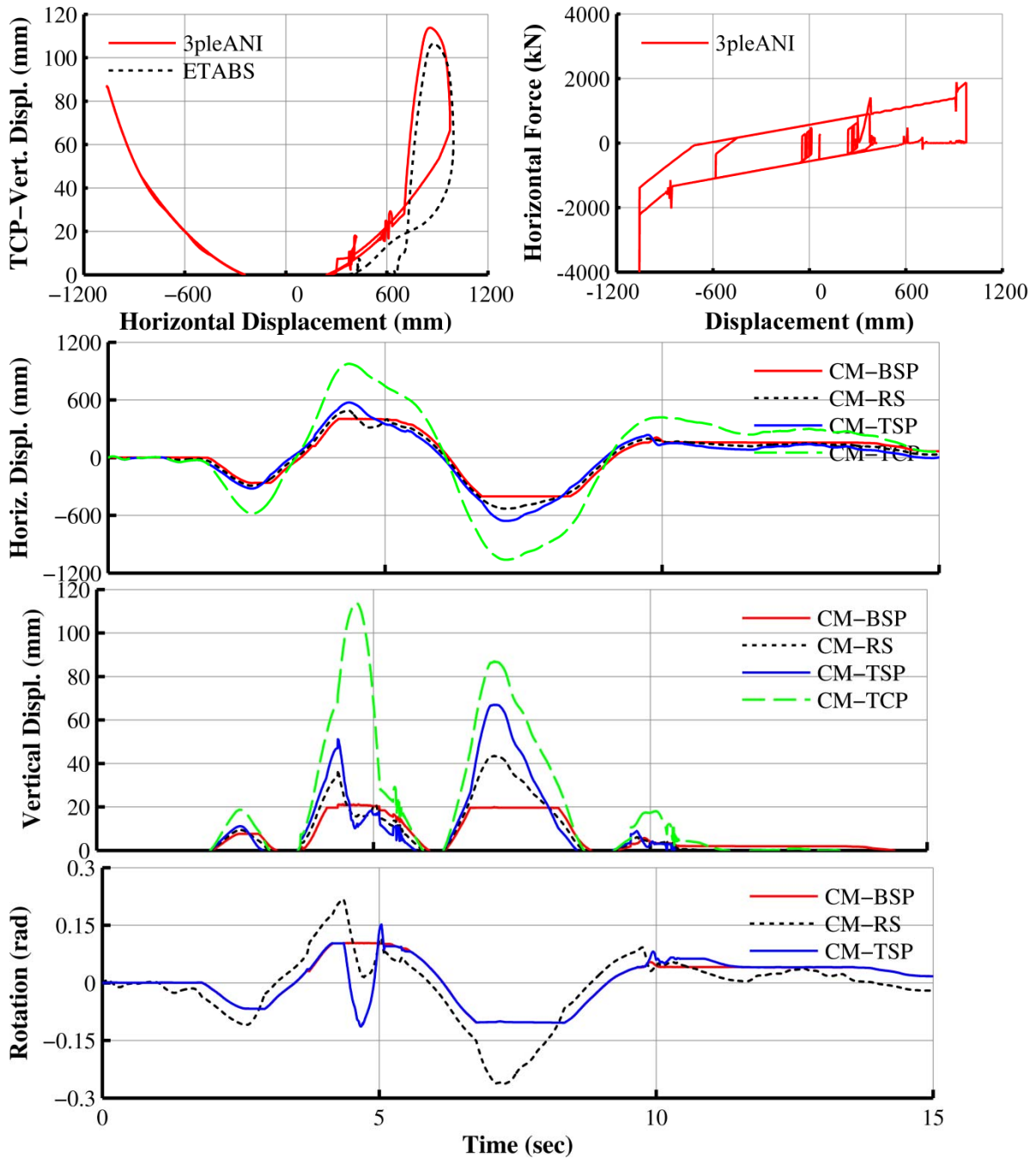


Figure 8-15: Program 3pleANI results of analysis of bearing of Example 3 with uplift using advanced theory and nonlinear elastic rubber seal

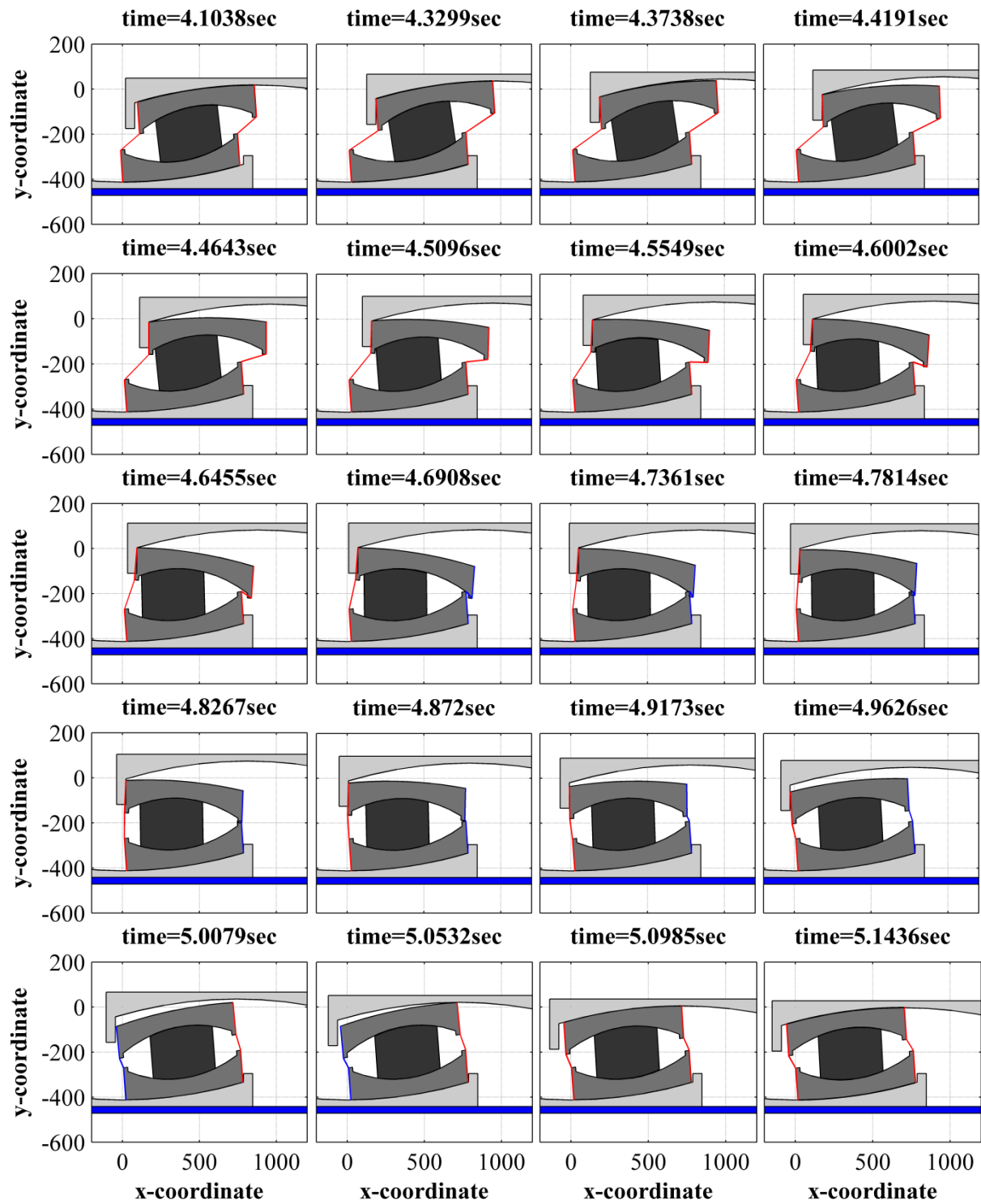


Figure 8-16: Animation of the bearing motion during the uplift duration by program 3pleANI for Example 3 using advanced theory and nonlinear elastic rubber seal

8.5 Example 4

A San Bernardino Courthouse bearing (shown in Figure 8-1) was tested in combined horizontal and vertical motion as shown in Figure 8-17 (Sarkisian et al., 2012). This example compares the experimental results in the uplift test to simulation results of program 3pleANI. In this test, the TCP was loaded to 6675kN, laterally displaced by 900mm and then lifted up by 100mm in slow motion. While in uplifted position, the TCP was moved backwards by 300mm to the 600mm displacement position and re-loaded to 6675kN load. In the numerical simulation in 3pleANI, time was compressed by a factor of three in order to expedite execution but without otherwise altering the dynamic characteristics of the test. Captured frames from the experiments are shown in Figure 8-18 (read row by row). Note in this figure that when uplift occurs, sliding occurs on surfaces 2 and 3 until the TSP hits the restrainer of surface 4. Sliding does not occur on surface 1. After the TCP restrainer moves above the TSP, additional sliding occurs on surfaces 2 and 3 so that the TSP is positioned below the restrainer of surface 4.

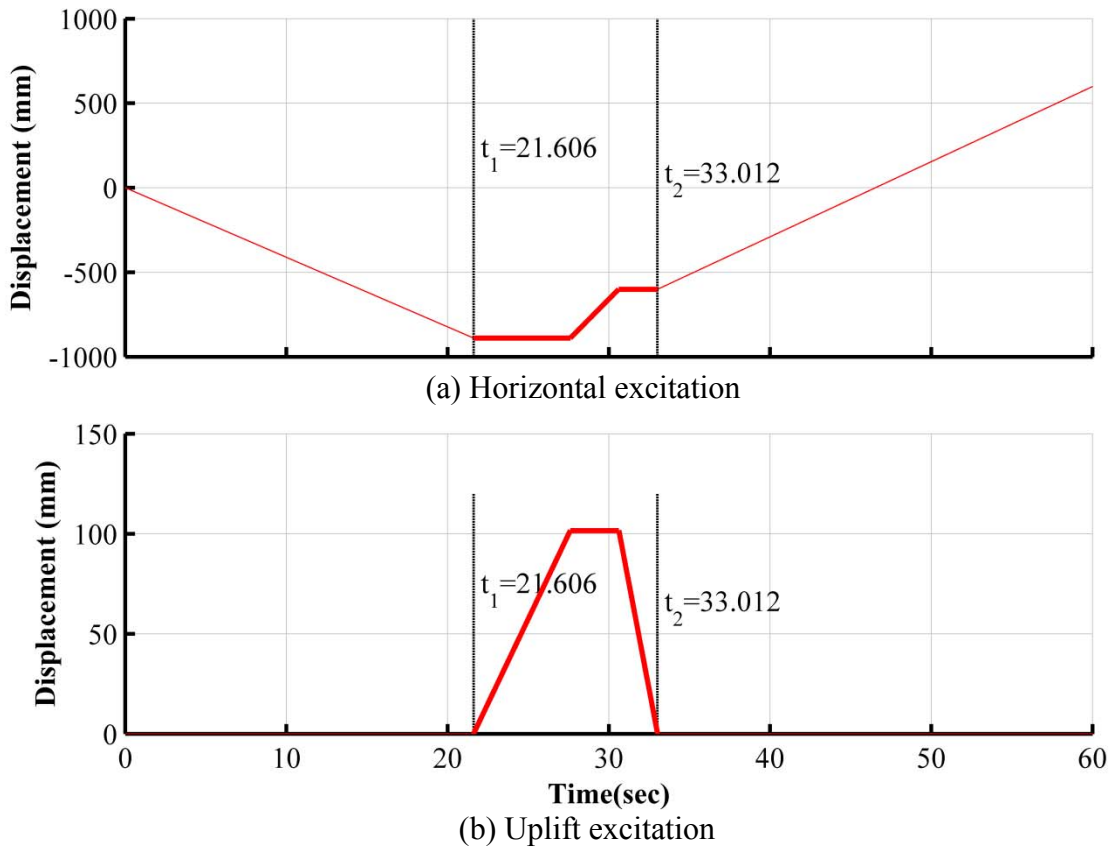


Figure 8-17: Horizontal and vertical displacement histories in uplift test of San Bernardino Courthouse bearing

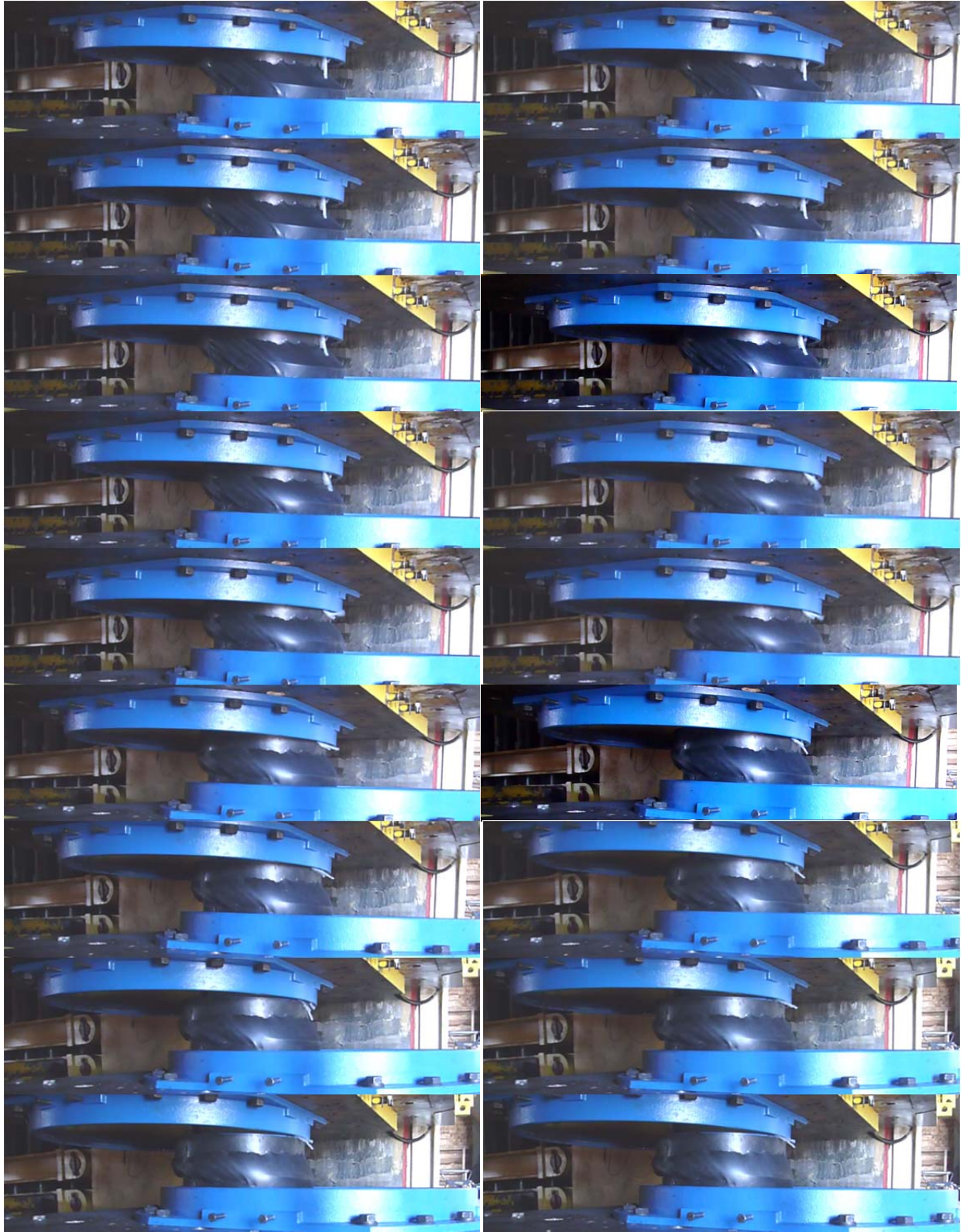


Figure 8-18: Captured frames in uplift experiment at 900mm horizontal displacement and 100mm uplift displacement (read row by row)

The isolator was analyzed in program 3pleANI for the geometry in Table 8-1 and Figure 8-1 and using the friction properties in Table 8-2 below. The difference between the friction values of Table 8-1 and Table 8-2 is a result of different heating conditions in the uplift experiments and the operational conditions of the isolator. The properties in Table 8-1 are those under high speed motion where heating effects significantly affected the friction coefficient values. The properties in Table 8-2 are representative of the uplift test conditions when the bearing was at normal temperature and testing did not have any heating effects.

Table 8-2: Friction coefficient values for load of 6675kN in Example 4

TFP Properties	Value per Fenz and Constantinou	Value per Sarlis and Constantinou
μ_1	0.12	0.101
$\mu_2 = \mu_3$	0.06	0.053
μ_4	0.17	0.137

The isolator was analyzed for the excitation of Figure 8-17 assuming six different sets of parameters that are described in Table 8-3 in order to investigate the effect of the following parameters:

- 1) Behavior of rubber seal as affected by bulges and the location of the points of attachment.
- 2) Friction coefficient during the uplift episode.

Analyses 1 and 2 in Table 8-3 are based on the assumption of nonlinear elastic seal with stiffness given by Equation (5-19) and without any bulges. The seal is assumed attached on the perimeter of the BSP and TSP throughout the height of these elements - from the bottom edge to the tip of the restrainers (points B_1, B_2, B_3, B_4 in Figure 5-4). Analyses 3 and 4 are based on the same behavior for the seal but the seal is at locations attached lower than the restrainer tip. Specifically, it is attached at points $C_1, C_2, C_3, C_4; s_{A1} = s_{A2} = 50mm$, (see Figure 5-8). Note that the attachment points are located significantly lower than the restrainer tips (points B_1, B_2, B_3, B_4 in Figure 5-8). This is a realistic situation that can be clearly observed in the photographs of Figure 8-18. Analyses 5 and 6 have the same seal behavior as analyses 3 and 4 but for the addition of a bulge in the seal. The existence of a bulge in the actual bearing can be seen in the photograph of Figure 5-5. It is also noted that the only difference between analysis 1

and 2 (also between analyses 3 and 4, and between 5 and 6) is that for the uplift episode, the friction coefficients are assumed to be twice as much in analysis 1 and four times as much in analysis 2, as the values of Table 8-2.

Figure 8-19 compares the seal force-deformation relations in the three groups of analyses conducted in program 3pleANI for Example 4.

Table 8-3: Parameters used in uplift analysis of Example 4

Seal Properties $E = 9.65 Mpa, t_s = 1.52 mm$, Equation (5-19)				
ANALYSIS NUMBER	Seal attachment points (see Figure 5-8)	Initial seal length	Initial bulge	Friction multiplier during uplift
1	B1, B2, B3, B4	$l_{in} = 58.3mm$	$s_g = 0$	2
2	B1, B2, B3, B4	$l_{in} = 58.3mm$	$s_g = 0$	4
3	C1, C2, C3, C4; $s_{A1} = s_{A2} = 50mm$	$l_{in} = 243.4mm$	$s_g = 0$	2
4	C1, C2, C3, C4; $s_{A1} = s_{A2} = 50mm$	$l_{in} = 243.4mm$	$s_g = 0$	4
5	C1, C2, C3, C4; $s_{A1} = s_{A2} = 50mm$	$l_{in} = 263.4mm$	$s_g = 20mm$	2
6	C1, C2, C3, C4; $s_{A1} = s_{A2} = 50mm$	$l_{in} = 263.4mm$	$s_g = 20mm$	4

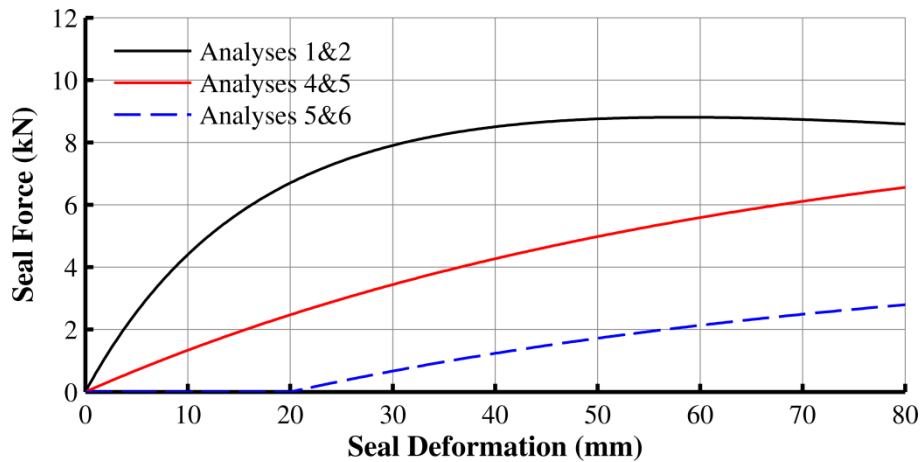
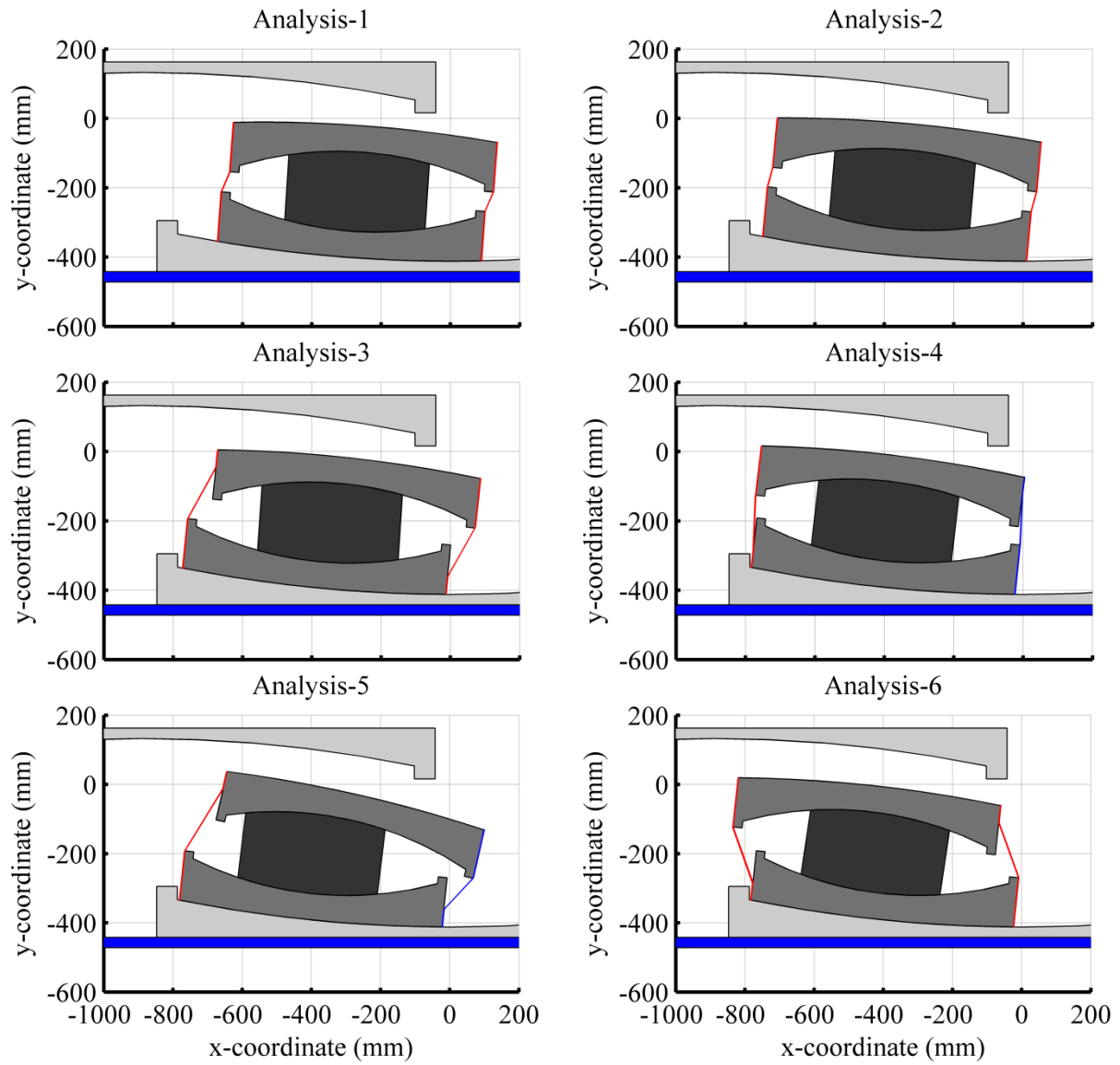


Figure 8-19: Seal force-deformation relations in analysis of Example 4

Figure 8-20 shows comparisons of the isolator position when the TCP is at maximum upper position as predicted by program 3pleANI for each of the six cases of Table 8-3 and the experiment. Note that analysis 6 results in a configuration of parts that is closest to the experimental observation.



Experimental



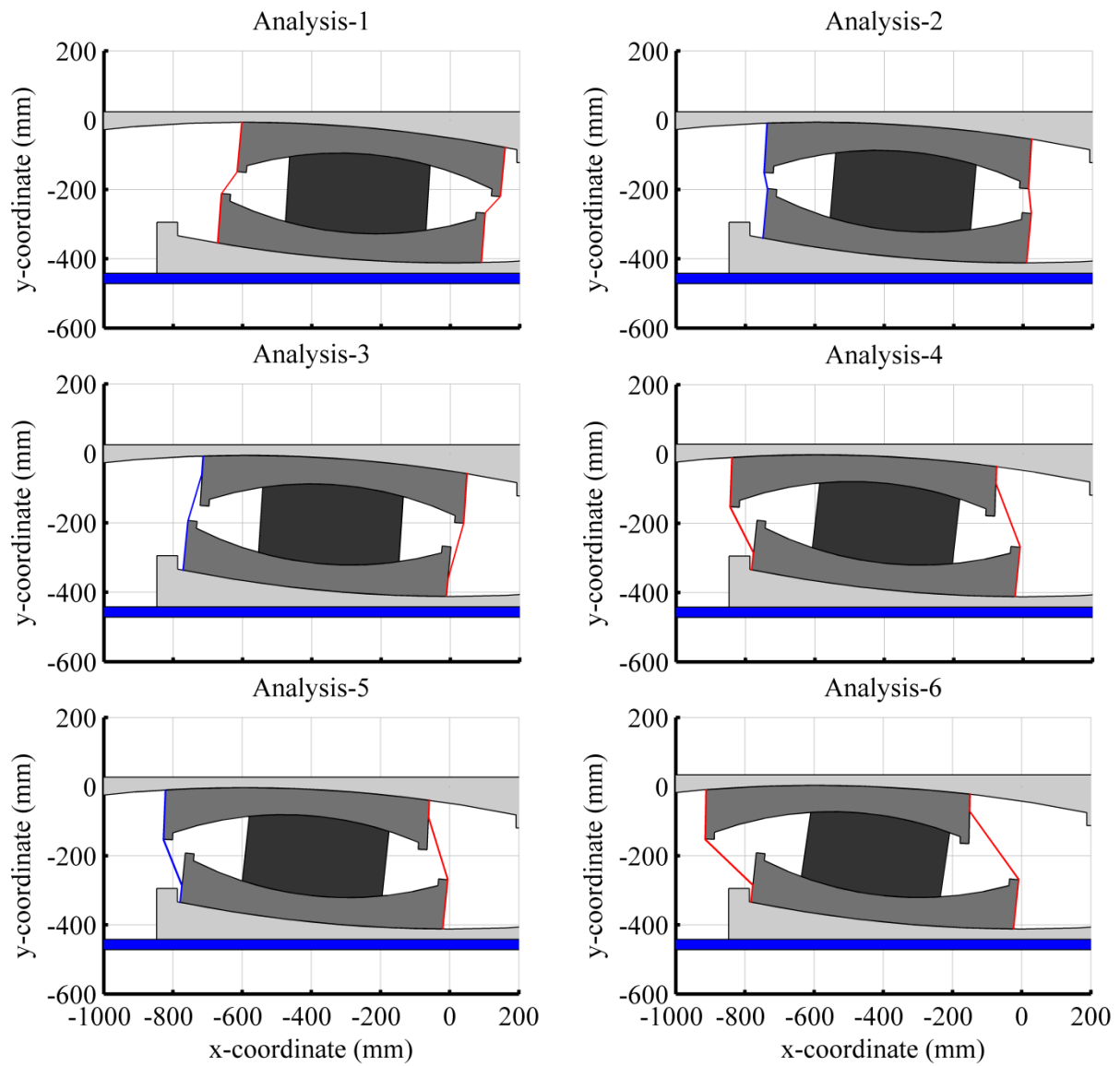
Figure 8-20: Comparison of results on final position of parts following separation of TCP from TSP of tested isolator as obtained by 3pleANI and experimental

Figure 8-21 compares the isolator positions after landing of the TCP as predicted by program 3pleANI and compared with experimental observations. Analysis 6 appears to predict well the observed location of the internal parts although good predictions are also made by analyses 4 and 5.

Figure 8-22 (for analyses 1, 3 and 5) and Figure 8-23 (for analyses 2, 4 and 6) present histories of calculated displacements and rotations of parts, traces of isolator displacements and force-displacement loops of the bearing analyzed for the uplift motion of Figure 8-17. It may be observed that while the force-displacement loops are essentially unaffected, the motion of the internal parts differs in the six analyses.

A more detailed animation of motion for the case of analysis 6 is presented in Figure 8-24. The parameters of analysis 6 appear to be appropriate for the actual conditions of the tested bearing. By comparison of Figure 8-18 to Figure 8-24, it can be concluded that 3pleANI predicted the observed response during the uplift test of Figure 8-17 very well.

The results presented demonstrated the significance of friction and seal modeling in the prediction of the response of the internal parts of a Triple FP bearing during an uplift episode. It is also clear that it is not possible to exactly know the location of the seal attachment points and the existence and size of a bulge in the seal of all bearings. Therefore, analysis should consider variability in properties and geometry of the seal arrangement along the lines of the analysis conducted for this example.



Experimental



Figure 8-21: Comparison of results on position of parts of tested isolator after landing as obtained by 3pleANI and experimental

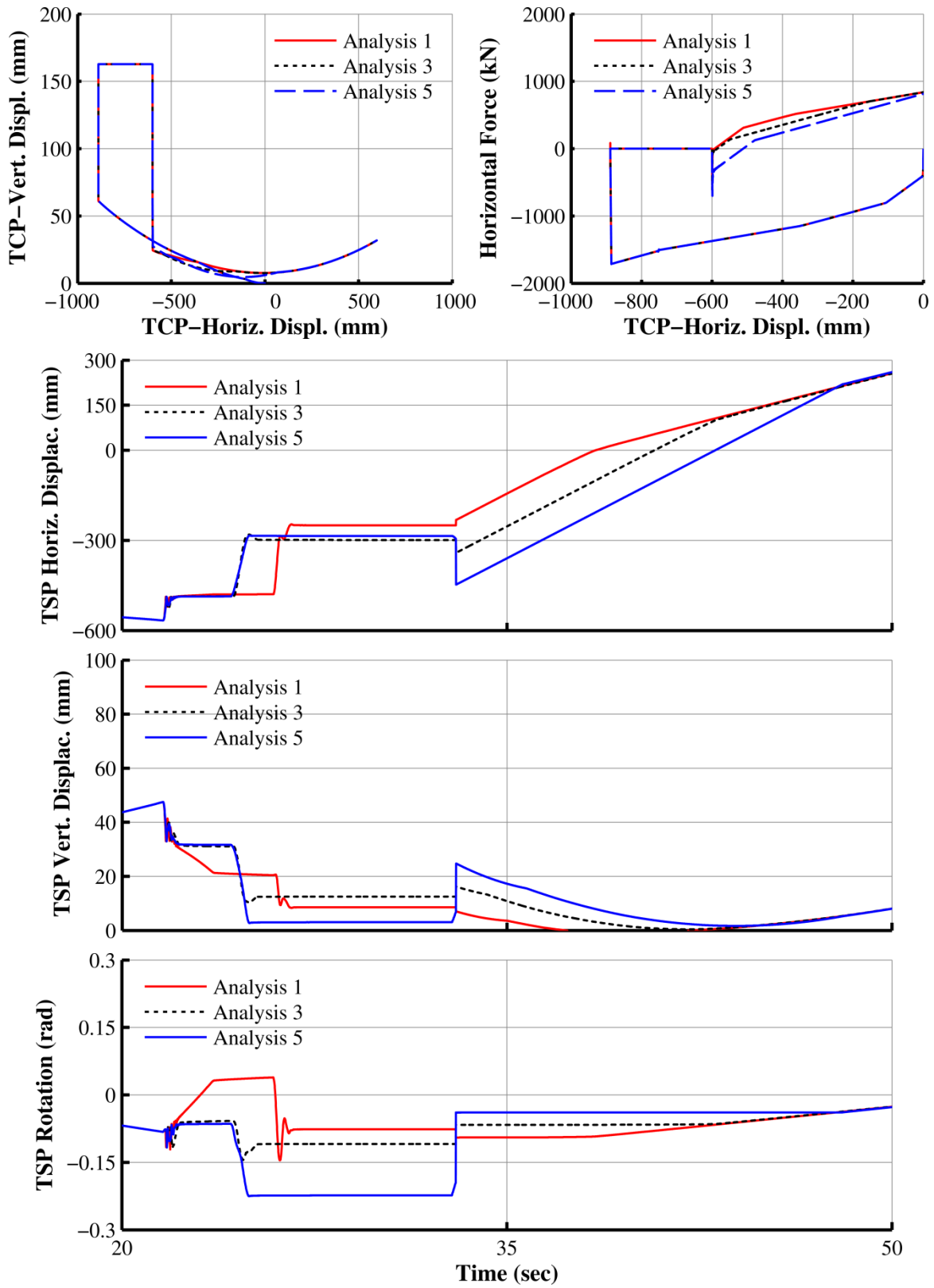


Figure 8-22: Comparison of analytical results obtained by 3pleANI for analyses 1, 3 and 5 in Table 8-3

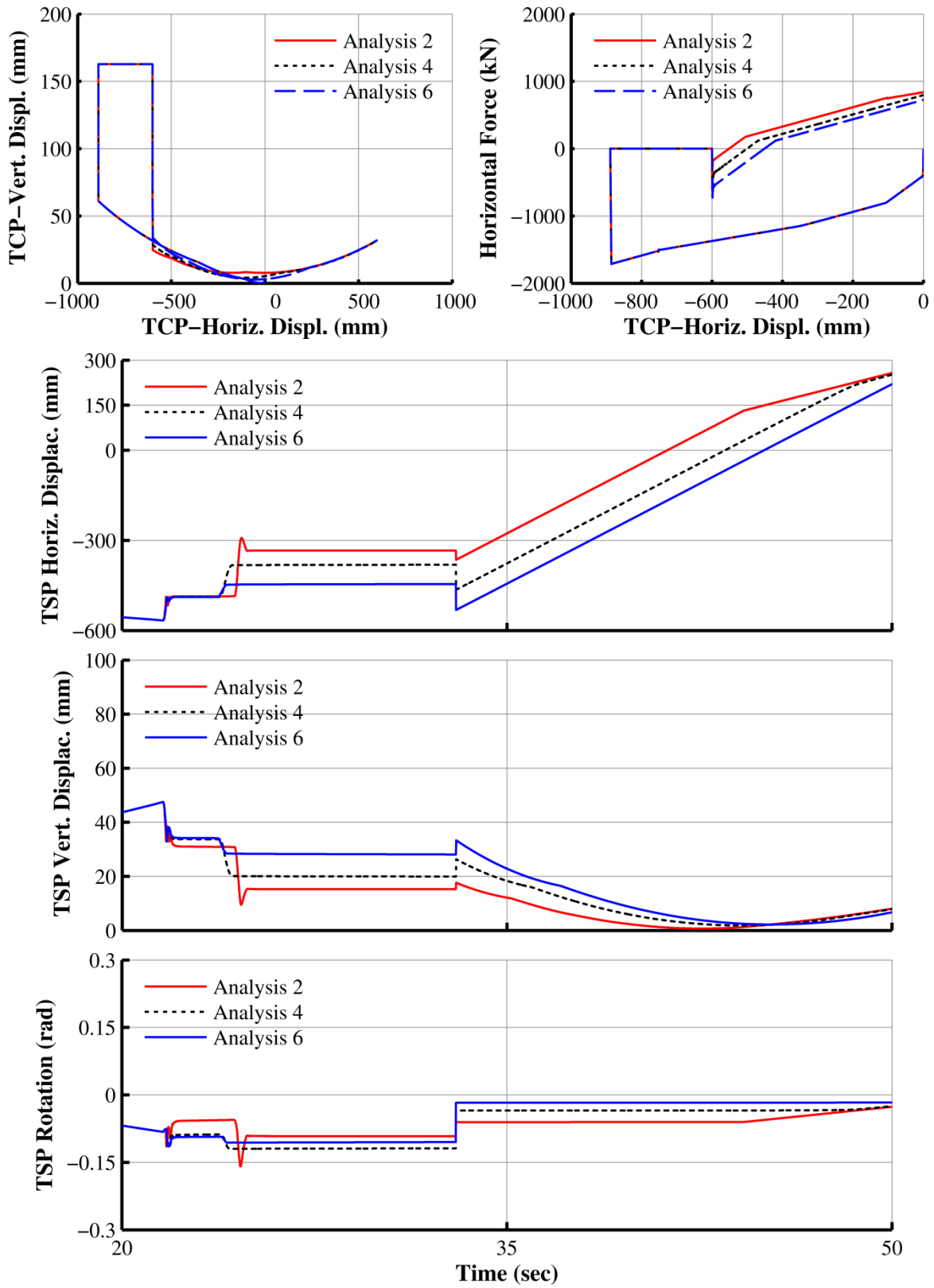


Figure 8-23: Comparison of analytical results obtained by 3pleANI for analyses 2, 4 and 6 in Table 8-3

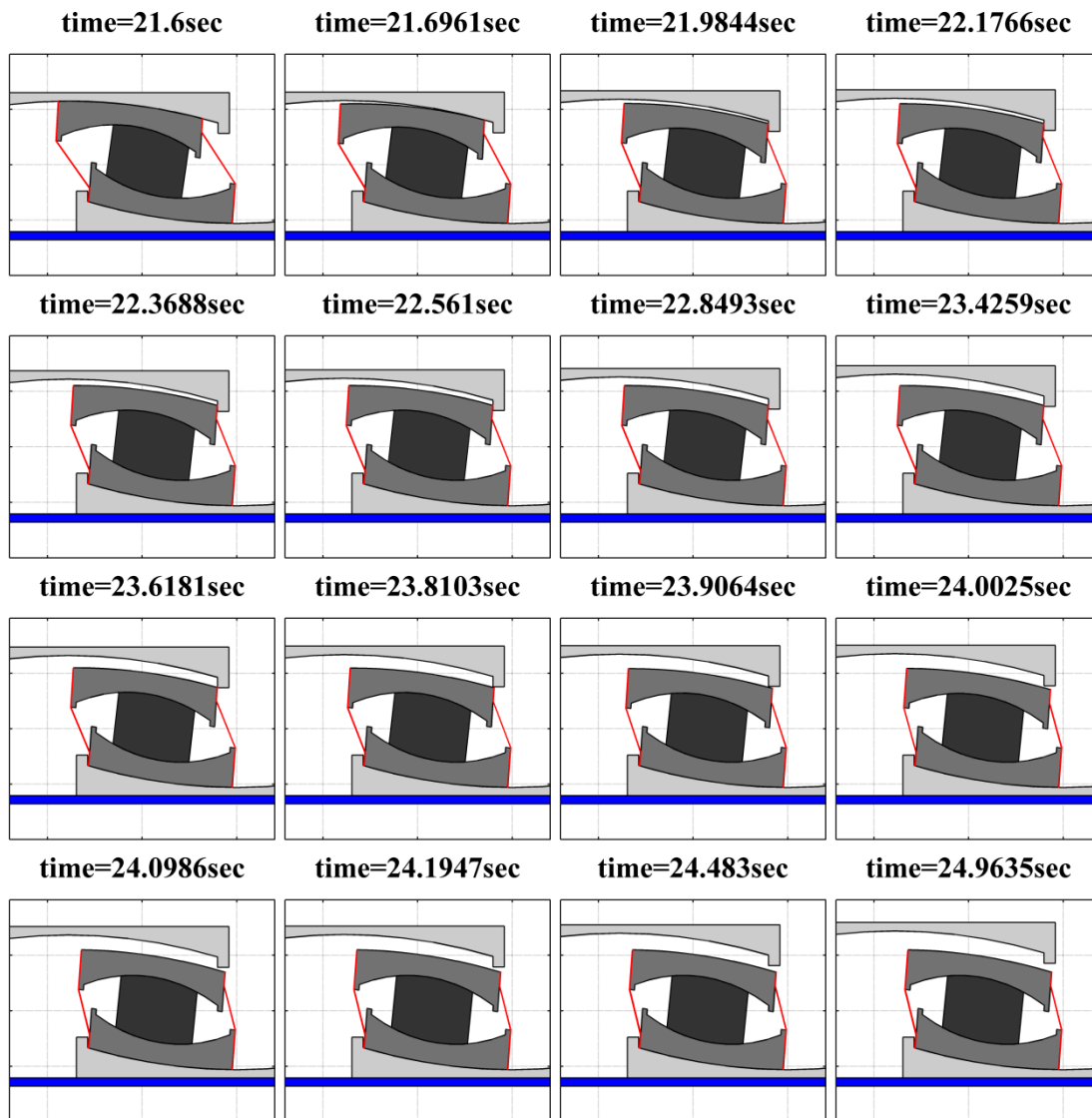


Figure 8-24: Animation of the bearing motion during the uplift episode as calculated in 3pleANI for analysis case 6

8.6 Example 5

This example presents comparisons of 3pleANI simulations for the isolator of Example 4 but for a different uplift experiment. In this test, the TCP of the isolator was loaded to 6675kN, laterally displaced by 640mm and then lifted up by 100mm in slow motion. While in uplifted position, the TCP was moved backwards by 340mm to the 300mm displacement position and re-loaded to 6675kN load. The histories of horizontal and vertical displacements in the test are shown in Figure 8-25.

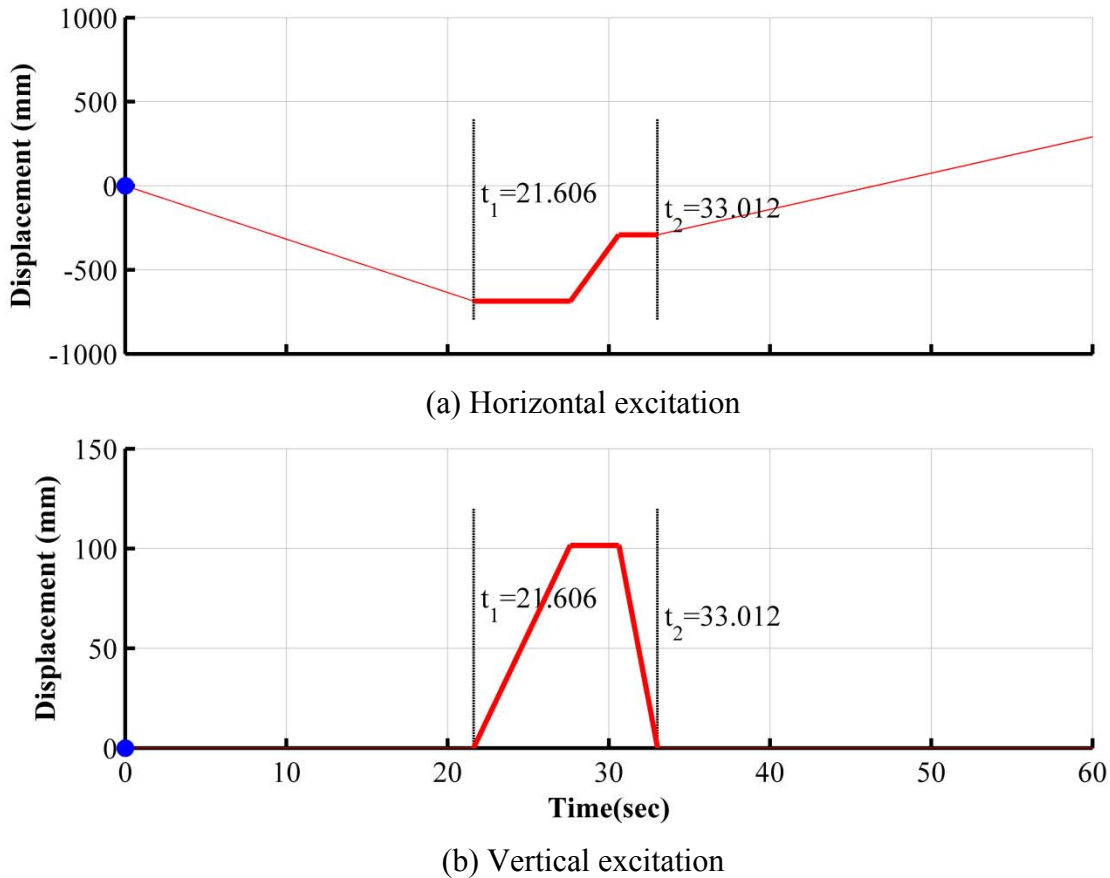


Figure 8-25: Horizontal and vertical displacement of TCP in Example 5

Captured frames from the experiment are presented in Figure 8-26. Observations of the video of the test suggest that during uplift, sliding occurs on surfaces 2 and 3 without sliding on surface 1 until the TSP hits the restrainer of surface 4. After the TCP restrainer moves above the TSP, no additional sliding occurs on any surface and as a result the TSP does not move underneath the restrainer ring.

The bearing was analyzed in program 3pleANI for the displacement histories shown in Figure 8-25 and the parameters of analysis case 6 of Example 4 (see Table 8-3) since this set of parameters accurately predicted the response in Example 4. Figure 8-27 present snapshots of animation of motion of the bearing as predicted by program 3pleANI for a portion of the uplift episode. Figure 8-28 compares the position of the internal parts as predicted by 3pleANI and as observed in the experiment after uplift and when motion of the inner TFP parts stopped and the bearing was reloaded. Note that 3pleANI again predicts the isolator's response very well.



Figure 8-26: Captured frames from uplift experiment of Example 5 (read row by row)

Figure 8-29 presents histories of calculated displacements and rotations of parts, traces of isolator displacements and the force-displacement loop of the bearing analyzed for the uplift motion of Figure 8-25.

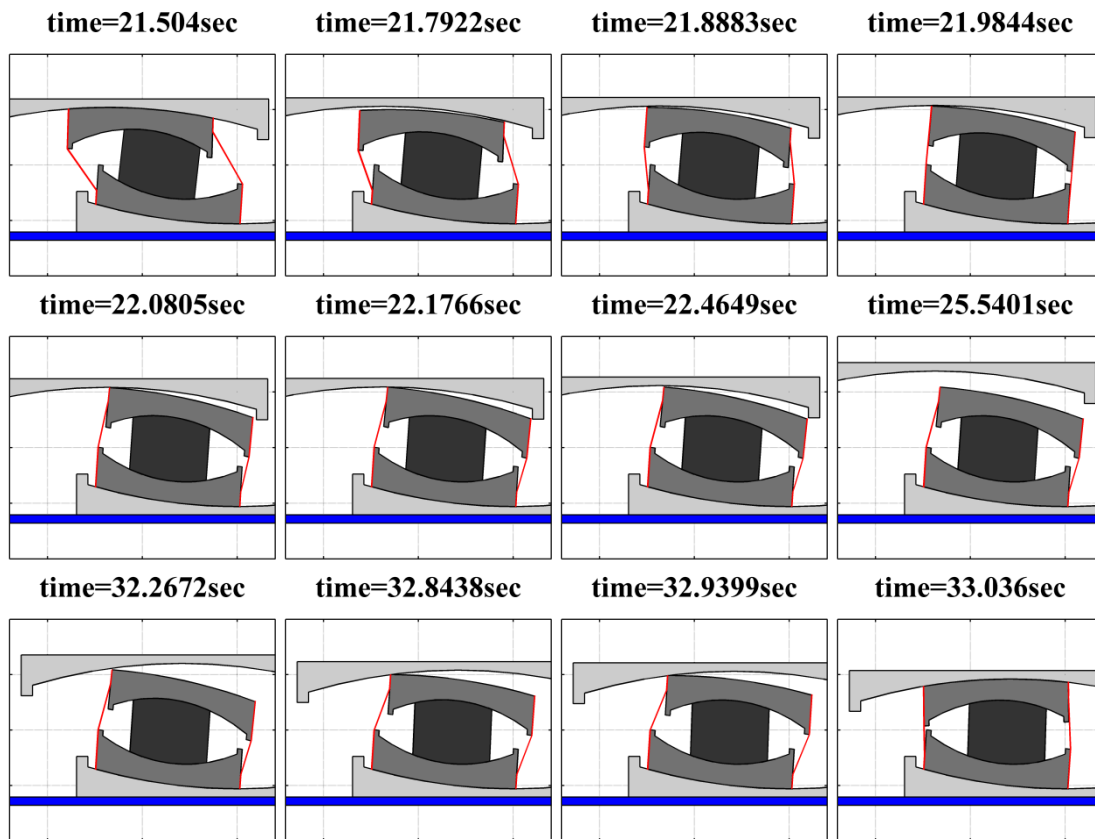


Figure 8-27: Animation obtained by 3pleANI for Example 5 during the uplift episode

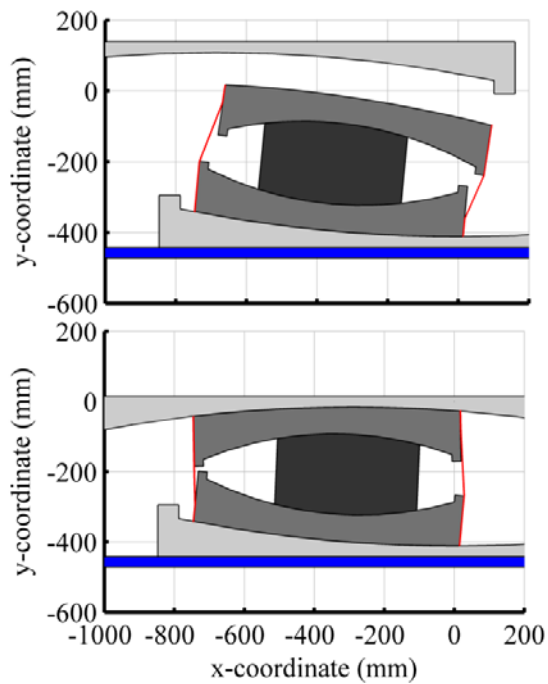


Figure 8-28: Comparison of analytical and experimental results in Example 5 when motion of the inner TFP parts stopped and when the bearing was reloaded

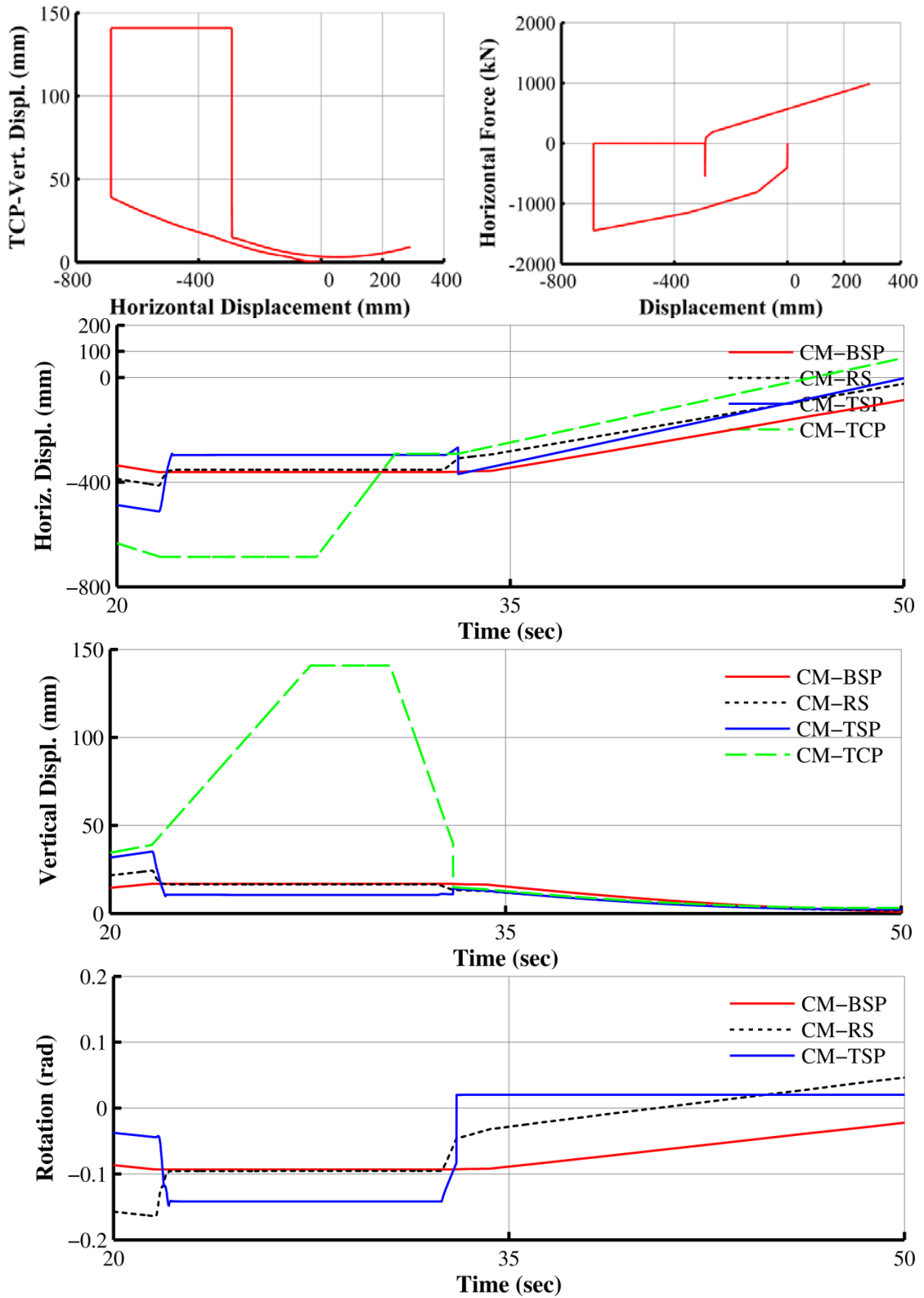


Figure 8-29: Histories of calculated displacements and rotations of parts, traces of displacements and force-displacement loop of analyzed bearing in Example 5

8.7 Example 6

This example presents comparisons of 3pleANI simulations for the isolator of Examples 4 and 5 but for an experiment with large amplitude lateral displacement and uplift. In this test, the TCP of the isolator was loaded to 6675kN, laterally displaced by 1000mm (close to displacement capacity) and then lifted up by 100mm in slow motion. While in uplifted position, the TCP was moved backwards by 200mm to the 800mm displacement position and re-loaded to 6675kN load. The histories of horizontal and vertical displacements in the test are shown in Figure 8-30.

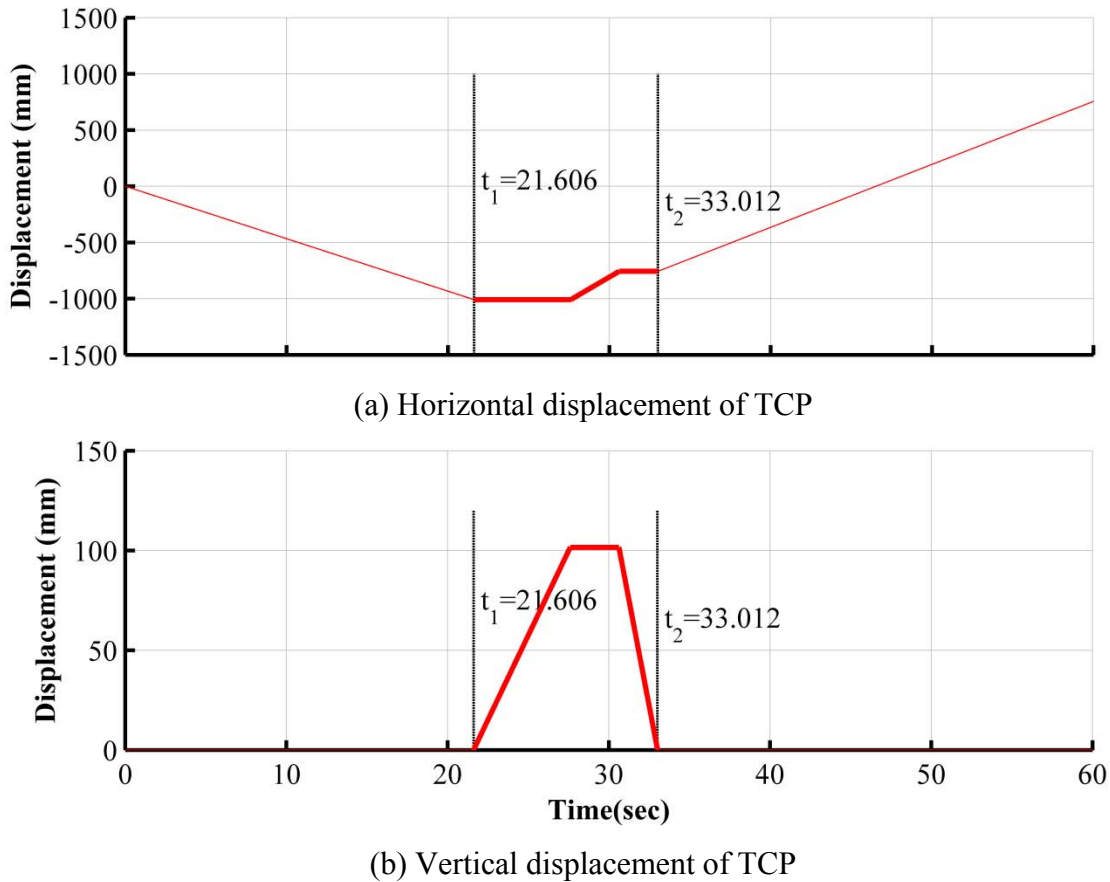


Figure 8-30: Horizontal and vertical displacement of TCP in Example 6

Captured frames from the video of the experiment are shown in Figure 8-31 for a significant portion of the uplift episode and in Figure 8-32 during landing on re-loading the bearing. Observation of these frames reveals the following sequence of events:

- 1) As the TCP moves up, the seal is deformed and pushes against the restrainer of surface 4 resulting in an upward friction force on the TSP. This force tends to cause overturning of the TSP as shown in the illustrations of Figure 8-33.
- 2) The restrainer of surface 3 moves above the sliding surface 3 and the rigid slider slides underneath the restrainer of surface 3.
- 3) The restrainer of surface 3 lands and rests on top of surface 3 for the entire uplift episode as shown in Figure 8-33(b), (c) and (d).
- 4) The TCP moves up and the bearing is unloaded.
- 5) Sliding occurs on surface 2 as shown in Figure 8-33(c).
- 6) Sliding on surface 2 stops, and sliding on surface 1 starts.
- 7) The TSP touches the restrainer of surface 1 and as a result motion stops as shown in Figure 8-33(d).

The isolator was analyzed in program 3pleANI for the motion shown in Figure 8-30. The seal behavior was the same as in analysis 6 of Example 4 (nonlinear elastic with bulge). The isolator was analyzed for four different cases as shown in Table 8-4.

Table 8-4: Theory and parameters used in analysis of Example 6 in 3pleANI

ANALYSIS NUMBER	Theory used	Restrainer stiffness	Friction multiplier during uplift of surface 3
1	Full Contact	Non-zero	4
2	Advanced	Non-zero	4
3	Advanced	Zero	20

Results for analysis case 1 (using the full contact theory) are presented in Figure 8-34. By comparing the analytical and experimental results, it can be seen that the full contact theory cannot capture the complex events shown in Figure 8-31 and Figure 8-33. The advanced theory was then utilized to calculate the motion in the uplift test and results are shown in Figure 8-35. The analysis correctly captures uplifting of the TSP as seen in the last few frames of Figure 8-35 and in most frames of the experimental results in Figure 8-31. However, the analysis resulted in a form of instability as the restrainer of surface 3 has just moved above the RS (see last frame of Figure 8-25).



Figure 8-31: Captured frames in the uplift experiment of Example 6 during the uplift episode (read row by row)



Figure 8-32: Captured frames in the uplift experiment of Example 6 during the landing episode (read row by row)

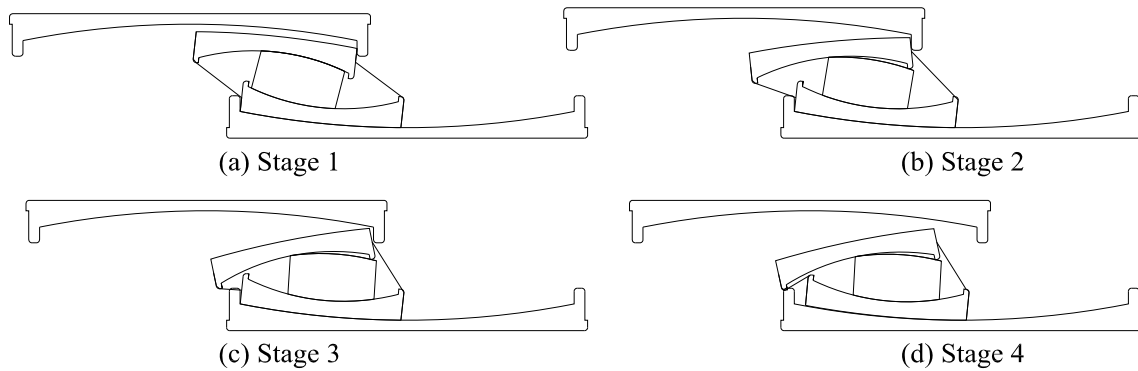


Figure 8-33: Illustrations of observed behavior of tested isolator during uplift

To overcome this numerical complexity, the collapse detection option was deactivated and zero stiffness was assigned for the restrainer of surface 3 in 3pleANI. This is a realistic assumption since, as shown in Figure 8-33, the restrainer actually moved above surface 3 in the test and it did not have any contribution during the uplift episode. Also, very high friction was assigned for surface 3 in order to model the effect of the restrainer sliding on surface 3. Results from this analysis are shown in Figure 8-36, Figure 8-37 and Figure 8-38 for various portions of the uplift and landing episodes. The analytical results are now in very good agreement with experimental results.

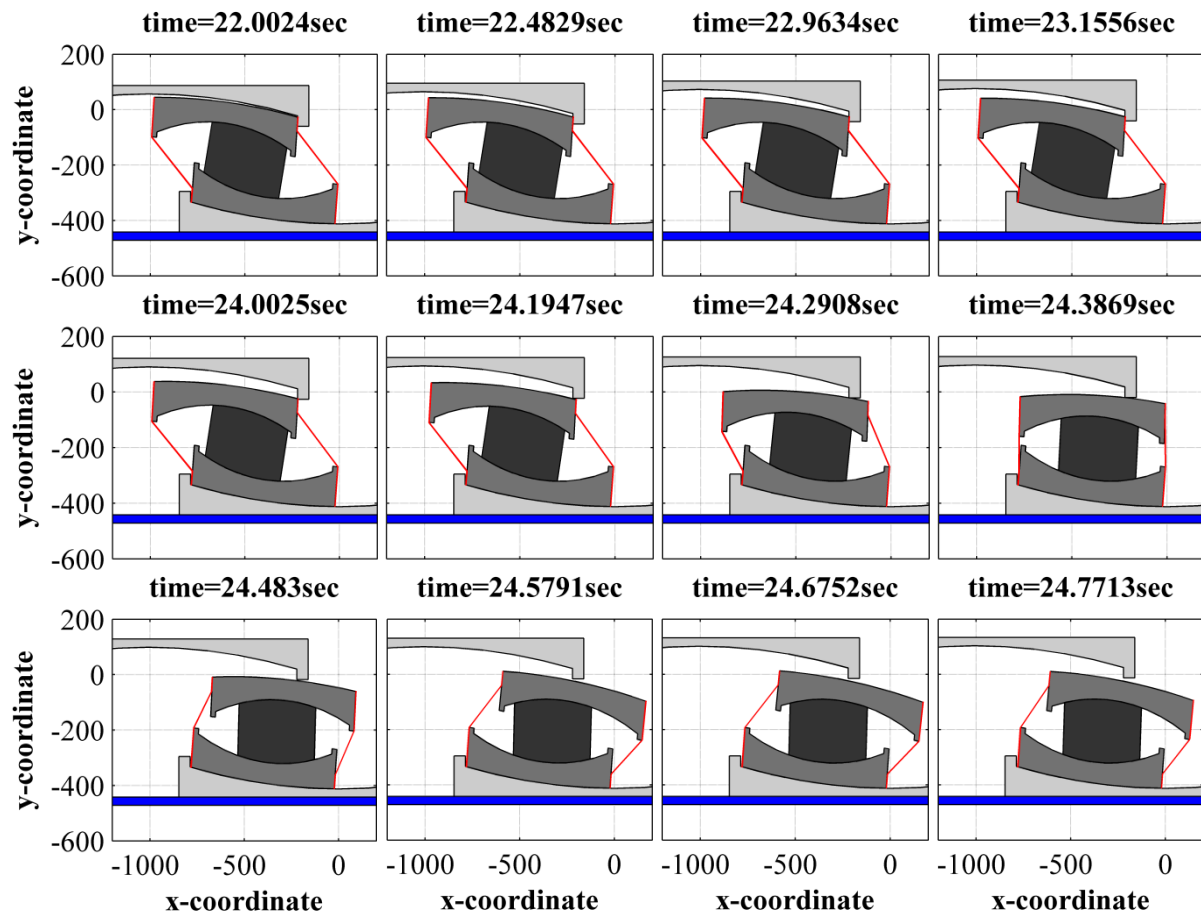


Figure 8-34: Animation of motion in case 1 obtained by 3pleANI for Example 6 during uplift episode

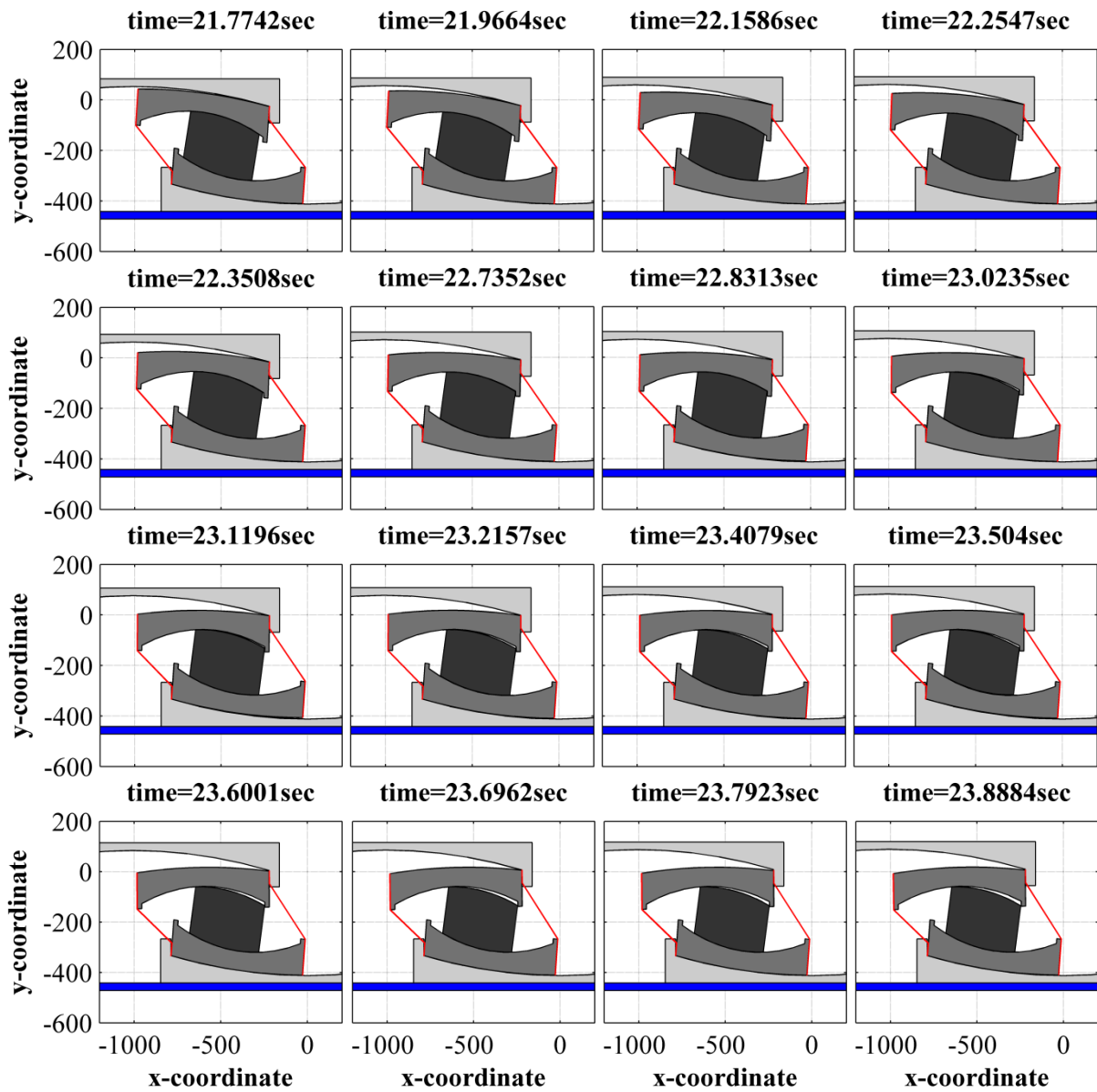


Figure 8-35: Animation of motion in case 2 obtained by 3pleANI for Example 6 during uplift episode

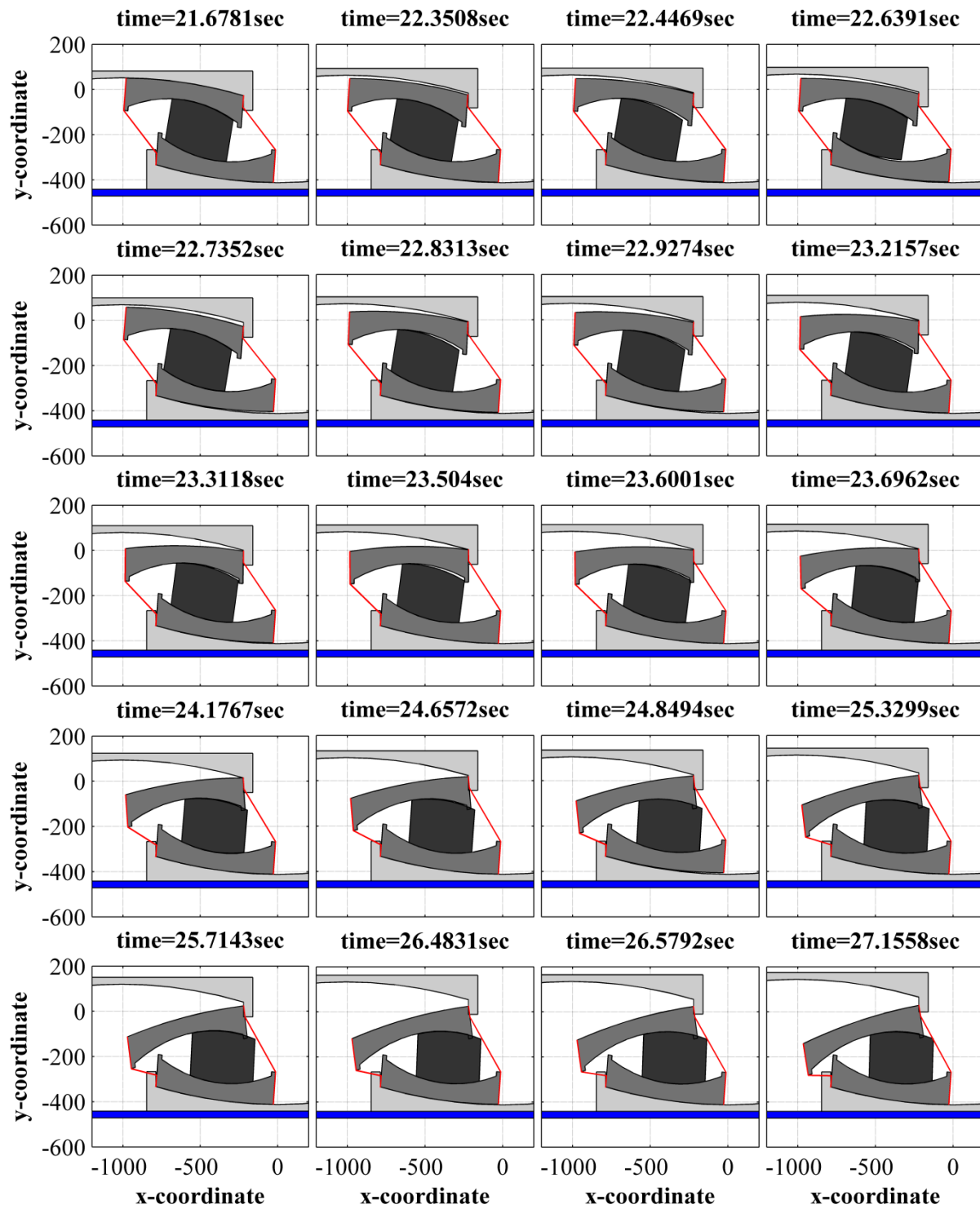


Figure 8-36: Animation of motion in case 3 (surface 3 restrainer deactivated) obtained by 3pleANI for Example 6 during the uplift portion when the TCP moves upward

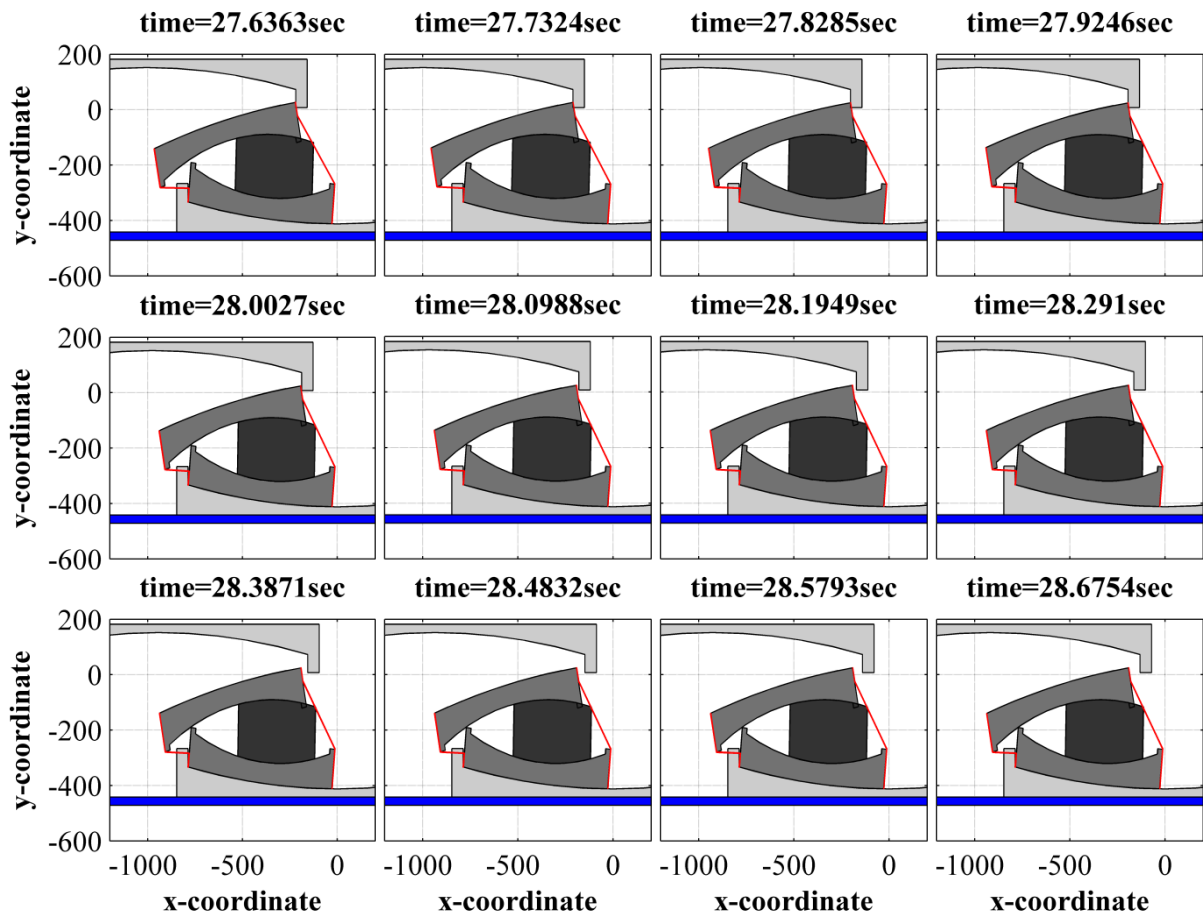


Figure 8-37: Animation of motion in case 3 (surface 3 restrainer deactivated) obtained by 3pleANI for Example 6 during the uplift portion when the TCP reverses direction of motion

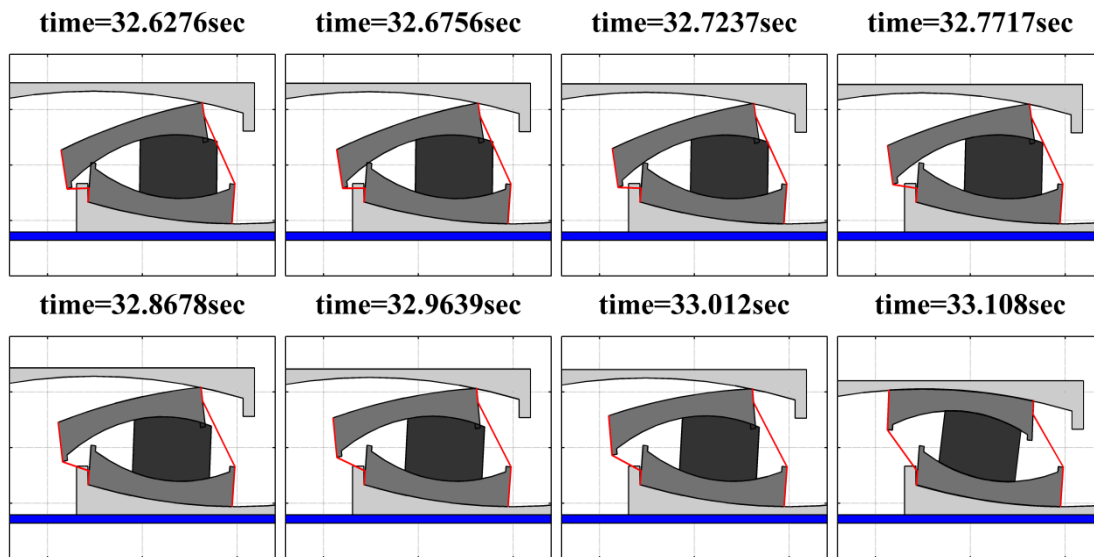


Figure 8-38: Animation of motion in case 3 (surface 3 restrainer deactivated) obtained by 3pleANI for Example 6 during the uplift portion when the TCP lands

8.8 Example 7 (Imperial Units)

This example illustrates the process of analysis in commercial software of an isolated structure with uplift and then analysis of individual isolators in program 3pleANI. Consider the structure shown in Figure 8-39 that was modeled in program SAP2000. It is a slender 16-story braced frame specifically selected in order to maximize the amplitude and duration of uplift and, generally, result in extreme isolator response. The mass of the structure was lumped at the joint locations as shown in Figure 8-39. The structure is supported by 3 isolators with the properties presented in Table 8-5. Isolator force-displacement loops are presented in Figure 8-40. For simplicity, all isolators are assumed to carry an equal load of 5252.7kips. The isolators were modeled in SAP2000 using the series model. The structure was subjected to the ground acceleration history shown in Figure 8-41.

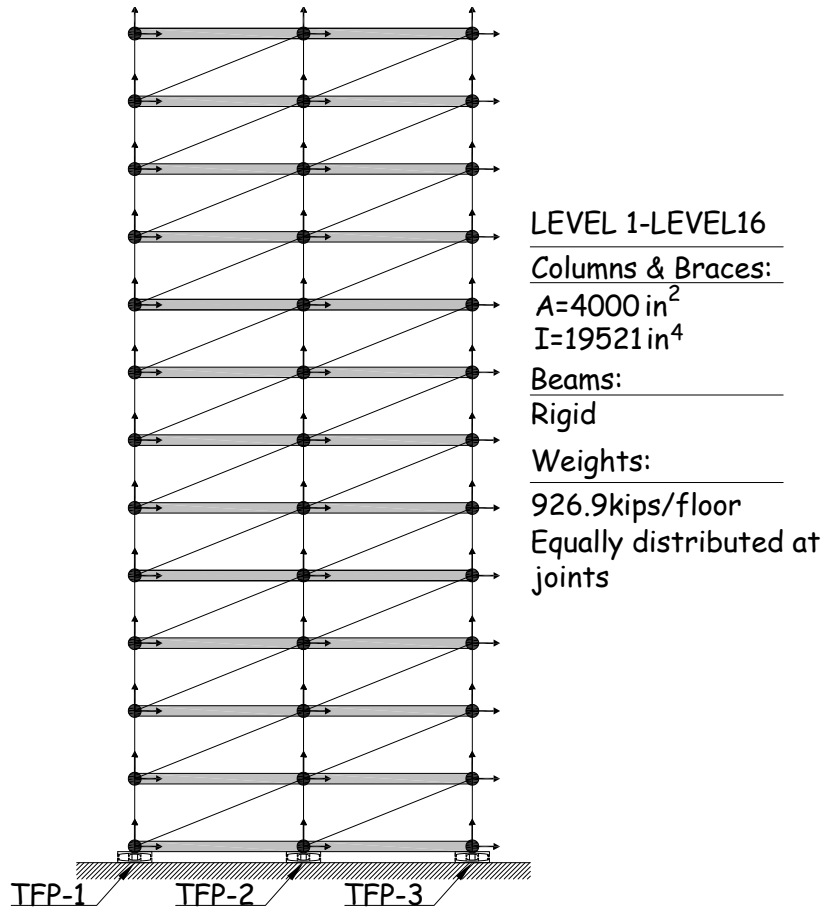


Figure 8-39: Analyzed slender 16-story isolated structure of Example 7

Table 8-5: Properties of TFP isolator in Example 7

Parameters	Values for use in SAP2000 (Fenz and Constantinou model implemented as series model)	Values in 3pleANI (moment equilibrium model)
$R_1 = R_4$ (inch)	156	156
$R_2 = R_3$ (inch)	16	16
Displacement capacity on surfaces 1 and 4 (in)	$d_1^* = d_4^* = 20.77^1$	$d_1 = d_4 = 21.6$
Displacement capacity on surfaces 2 and 3 (in)	$d_2^* = d_3^* = 1.688^1$	$d_2 = d_3 = 2.25$
Friction surface 1 ²	$\bar{\mu}_1 = 0.1$	$\mu_1 = 0.02$
Friction surfaces 2 and 3 ²	$\bar{\mu}_2 = \bar{\mu}_3 = 0.05$	$\mu_2 = \mu_3 = 0.01$
Friction surface 4 ²	$\bar{\mu}_4 = 0.014$	$\mu_4 = 0.065$
$h_1 = h_4$ (inch)	6	6
$h_2 = h_3$ (inch)	4	4

1. $d_i^* = d_i \left(R_{eff} / R_i \right)$, $R_{eff} = R_i - h_i$ 2. All friction values are for high velocity conditions= f_{max}

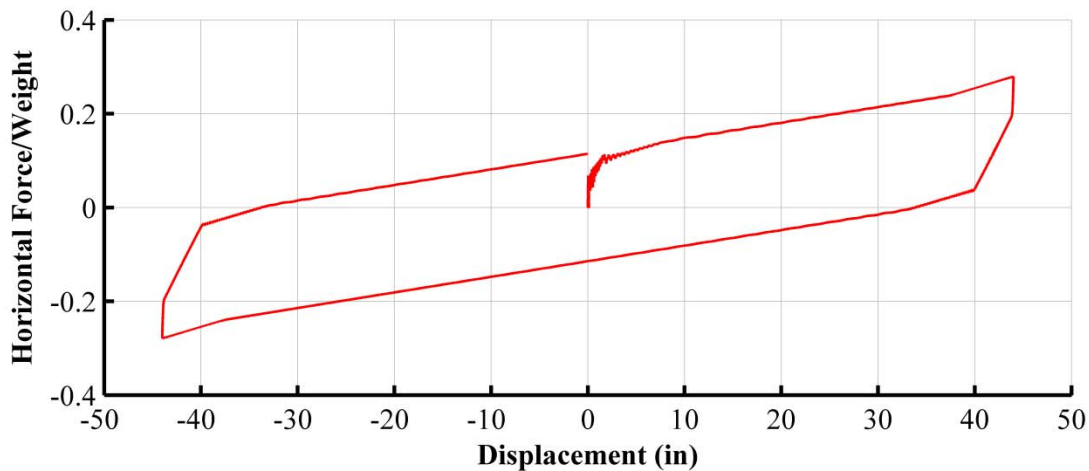


Figure 8-40: Force -displacement relation of isolator in Example 7

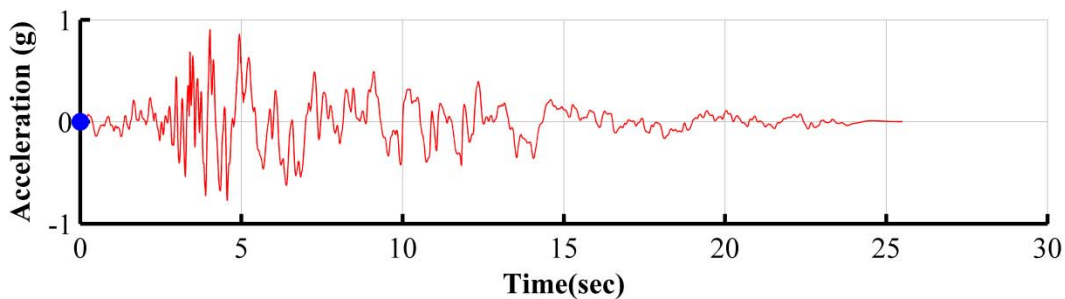


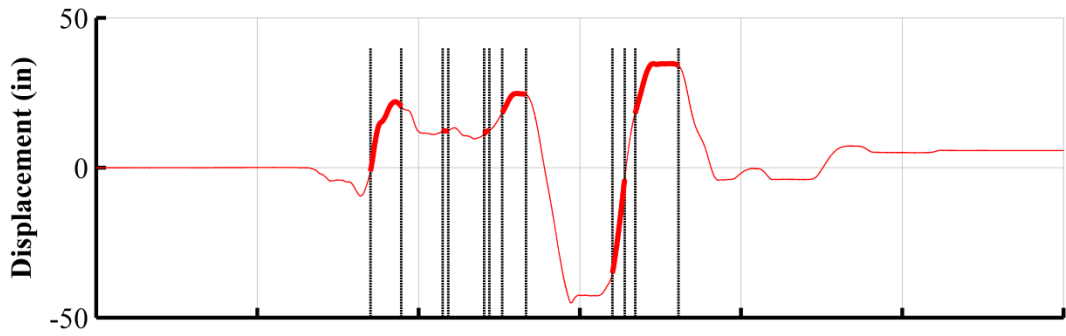
Figure 8-41: Ground motion used for response history analysis in Example 7

All three isolators (TFP-1, TFP-2 and TFP-3 in Figure 8-39) in SAP2000 exhibited uplift. Only TFP-1 and TFP-3 were analyzed in 3pleANI. The horizontal and vertical displacement histories of isolators TFP-1 and TFP-3 are shown in Figure 8-42. The two isolators exhibit several uplift episodes as indicated in bold red line in Figure 8-42. Analysis in program 3pleANI was conducted using the full contact theory in which the parts of the bearing, other than the TCP, remain in contact with each other during the uplift episode.

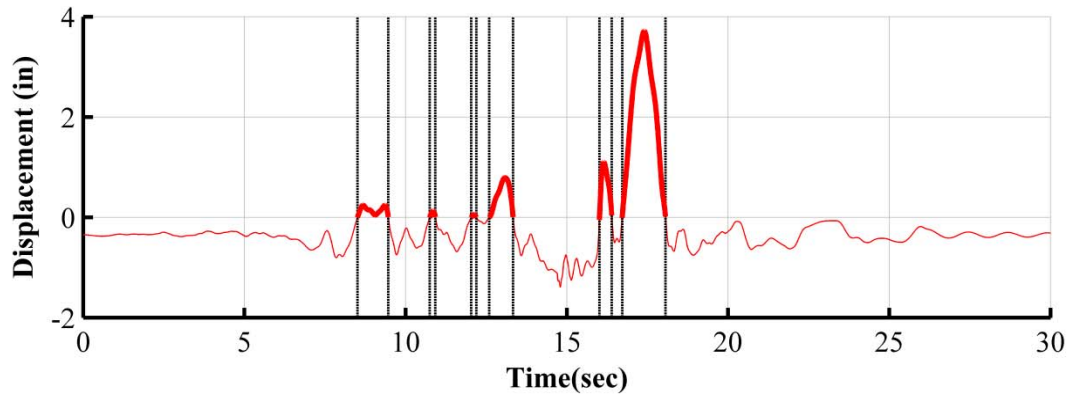
Results of program 3pleANI for bearing TFP-1 are presented in Figure 8-43 for the animation of the bearing motion (for the most significant uplift portion). Figure 8-44 presents results on the histories of displacement of the isolator parts, history of axial load, force-displacement loops and displacement traces as calculated by program 3pleANI. Note that the axial load is assumed to either be constant or zero (during uplift). Figure 8-43 reveals that the bearings exhibit stable behavior but it is known that the full contact theory cannot fully model instability of the inner components so that the advanced theory needs to be used. Results of this analysis are presented

in Figure 8-45 and Figure 8-46. For this analysis, the rubber seal was removed in order to generate a worst case scenario for the stability of the isolator parts. As seen in Figure 8-45, the TFP parts uplift and bounce on the sliding surfaces after impact with the restrainer of surface 4 but they remain stable. The motion of the parts is very similar (other than some small uplift of parts) to those of Figure 8-43 of the full contact theory. Also, results on histories of displacement of the isolator parts, history of axial load, force-displacement loops and displacement traces in Figure 8-46 are very similar to those of Figure 8-43 for the full contact theory but for the peak shear force which is much less in the advanced theory analysis. This is due to the fact that the advanced theory predicted slightly different motion of parts and less loading on the high stiffness restrainer of surface 4.

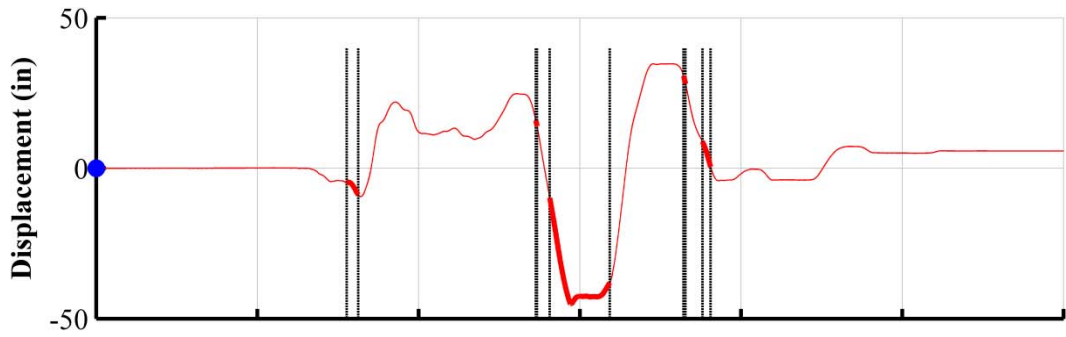
Results for the isolator are presented in Figure 8-47 and Figure 8-48 when using the full contact theory. It may be seen in Figure 8-47, the restrainer of the TCP moves above the TSP - a situation interpreted as instability. Analysis was repeated after the TCP restrainer height was increased to prevent this phenomenon. Results of the modified isolator are shown in Figure 8-49 and Figure 8-50 using the full contact theory and in Figure 8-51 and Figure 8-52 using the advanced theory. Both analyses demonstrate stable operation of the modified isolator.



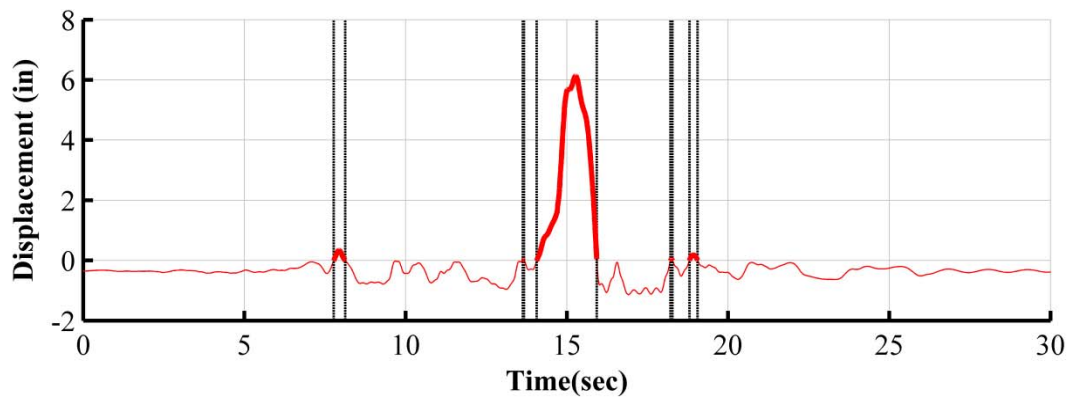
(a) Horizontal Displacement of TFP-1



(a) Vertical Displacement of TFP-1



(c) Horizontal Displacement of TFP-3



(b) Vertical Displacement of TFP-3

Figure 8-42: Displacement histories of isolators as calculated in SAP2000

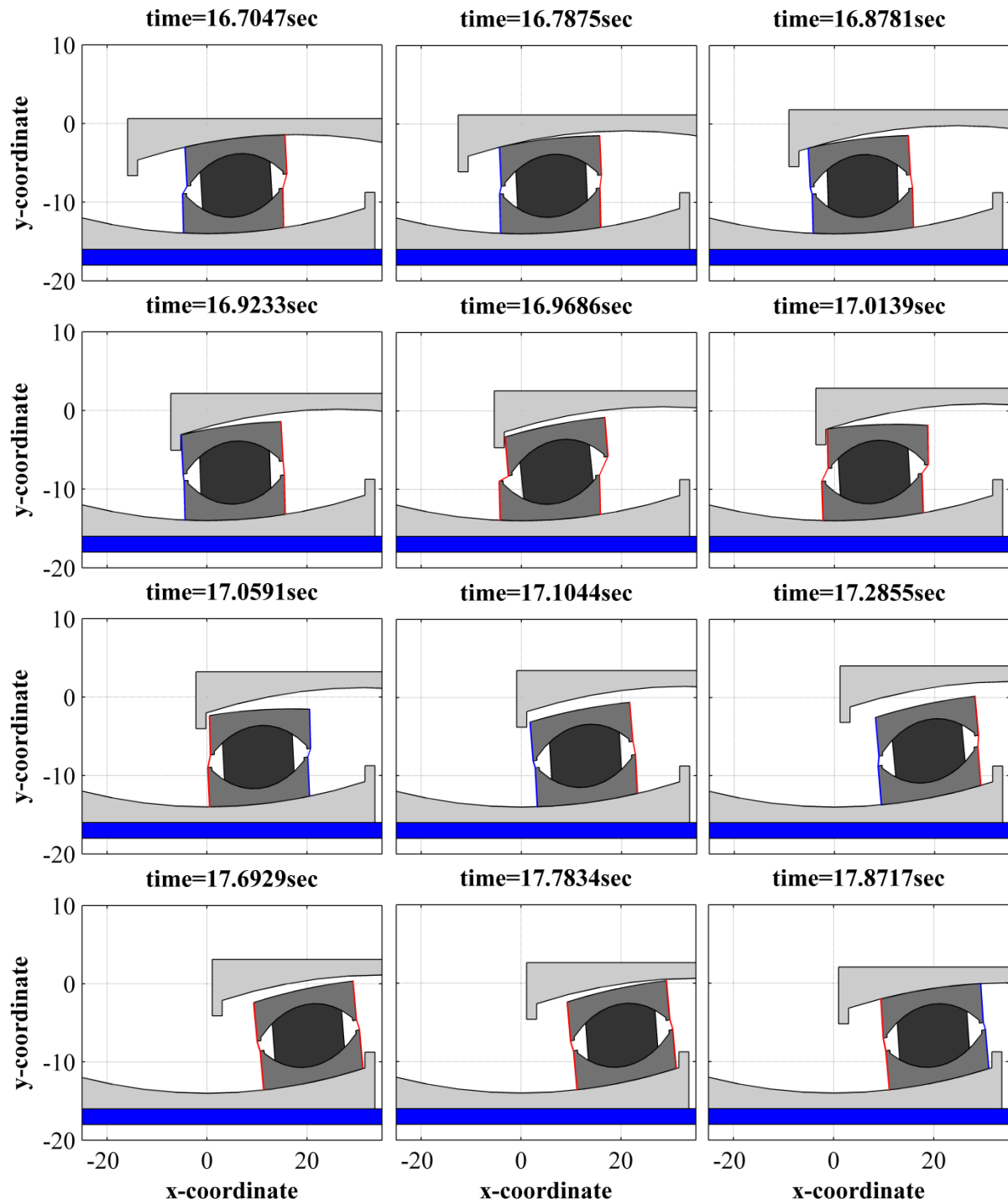


Figure 8-43: 3pleANI animation of TFP-1 isolator based on full contact theory

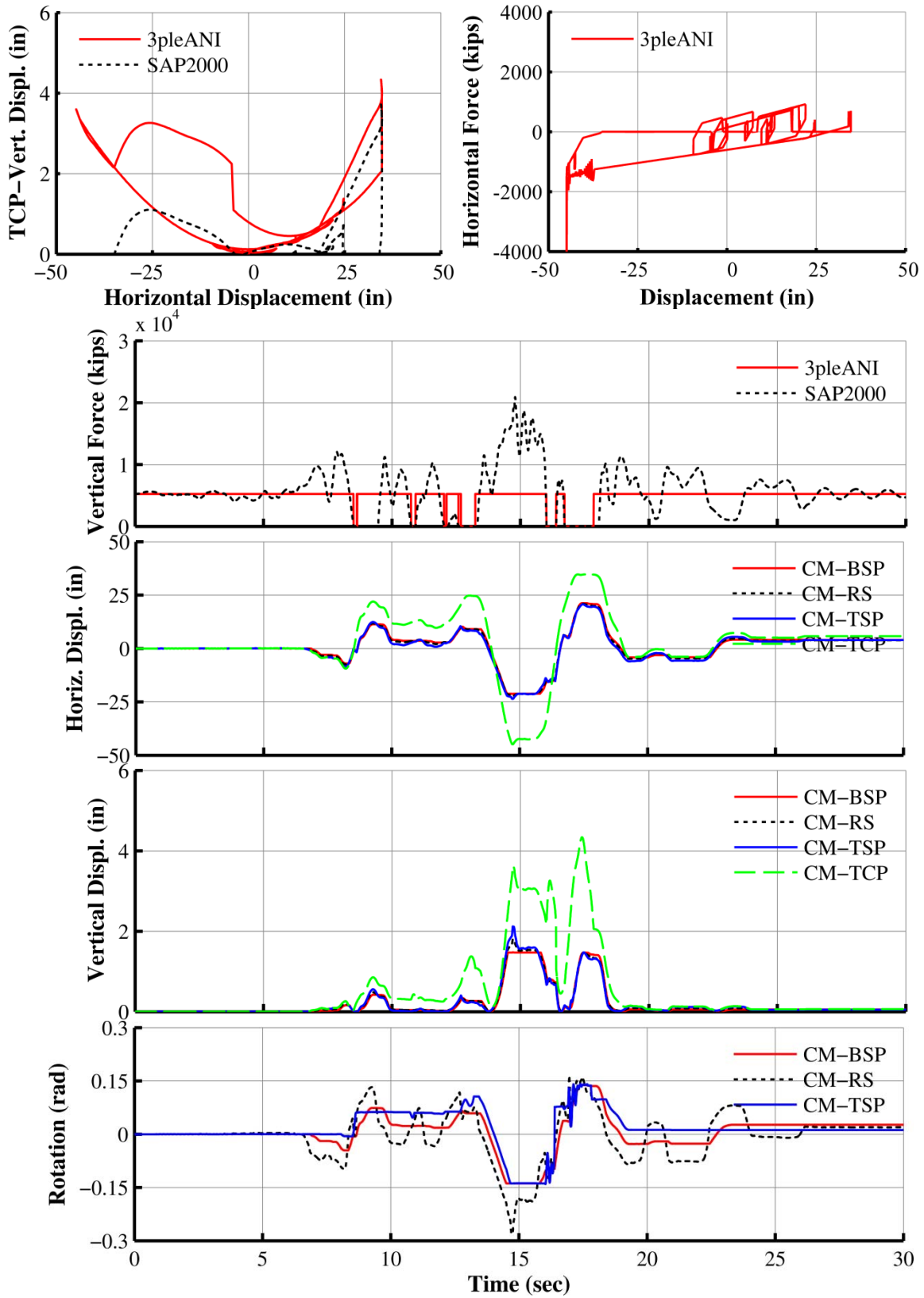


Figure 8-44: Program 3pleANI results of analysis for bearing TFP-1 using full contact theory

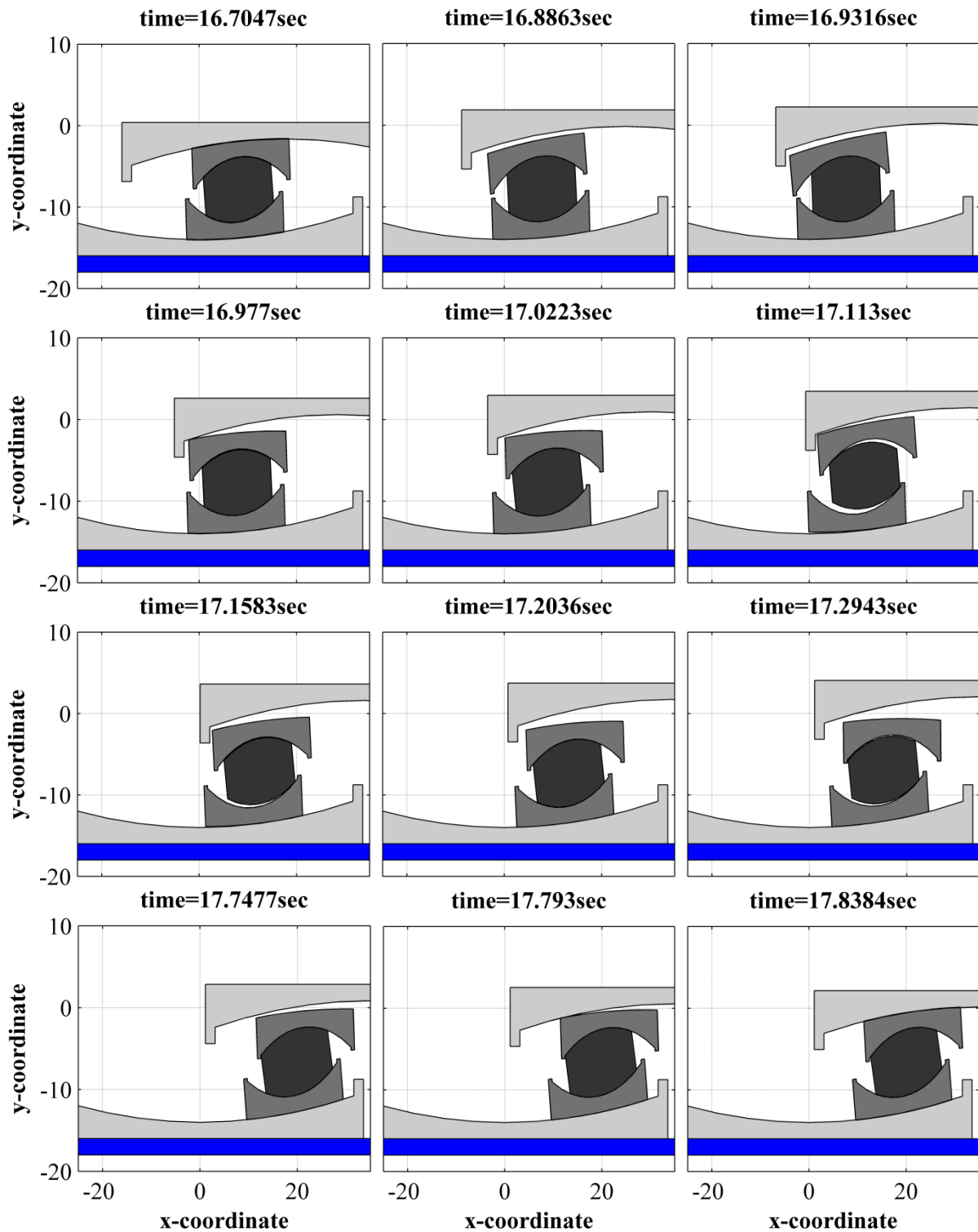


Figure 8-45: 3pleANI animation of TFP-1 isolator without seal using advanced theory

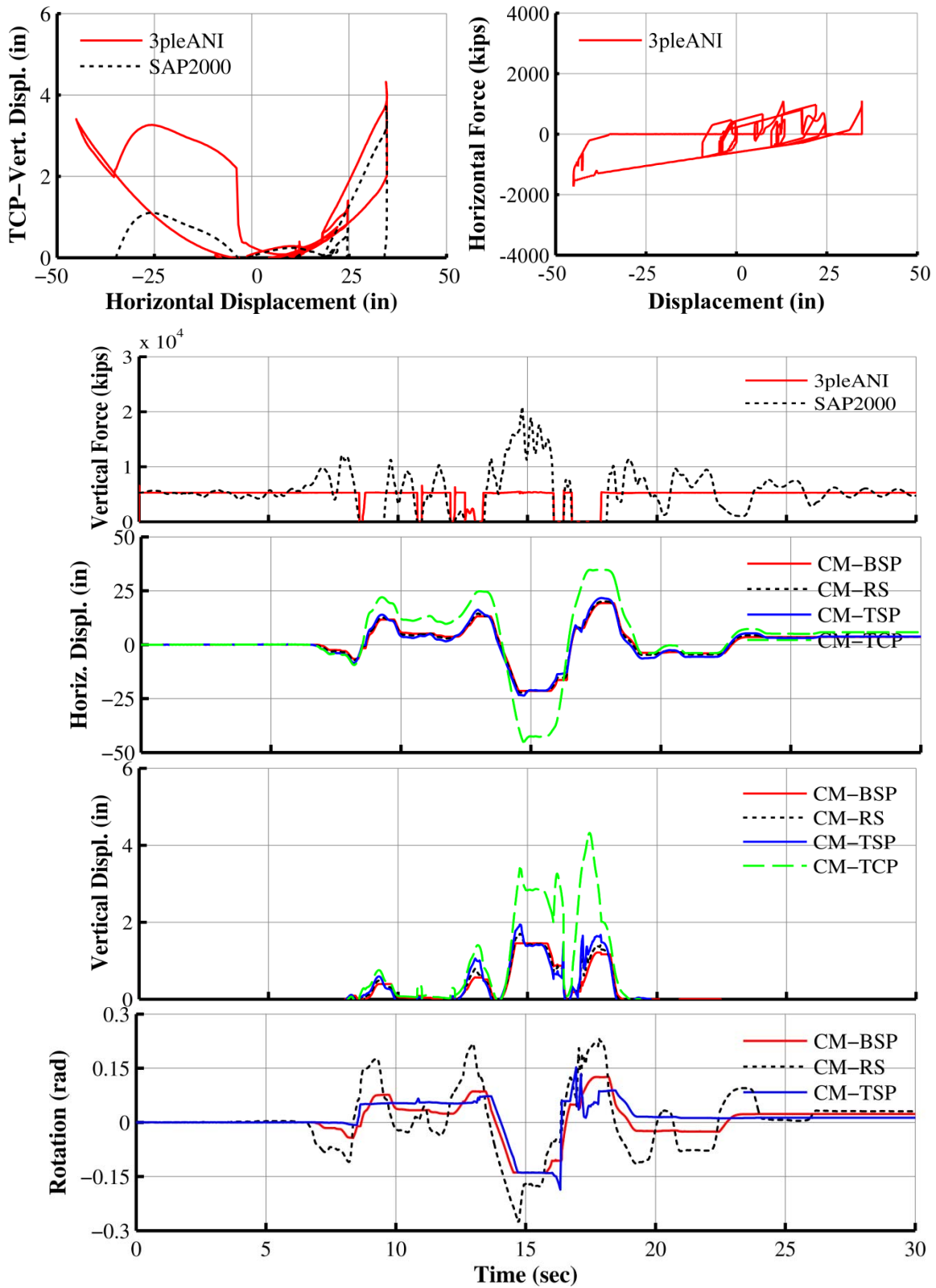


Figure 8-46: Program 3pleANI results of analysis for bearing TFP-1 using advanced theory

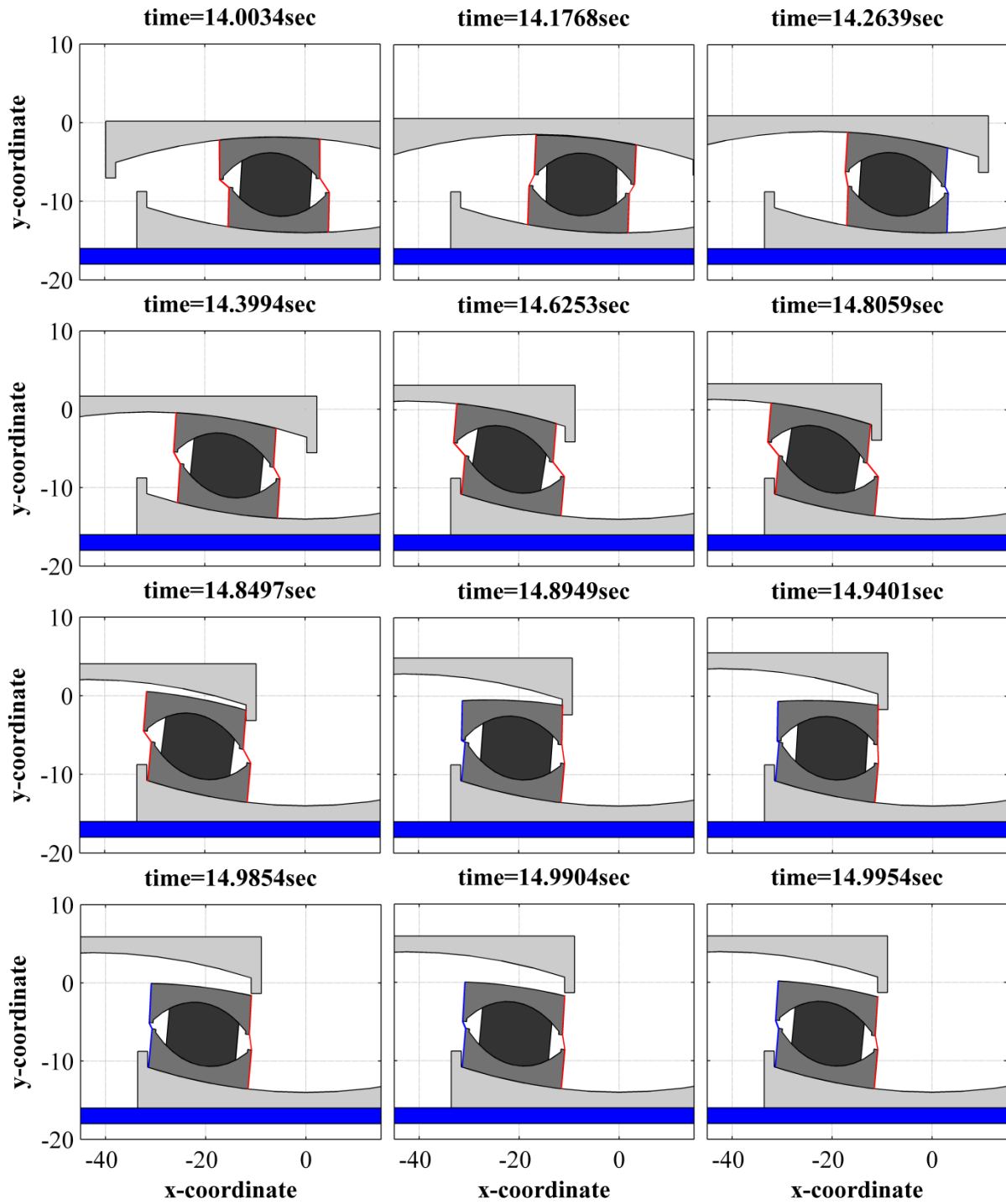


Figure 8-47: 3pleANI animation of TFP-3 isolator based on full contact theory-isolator instability

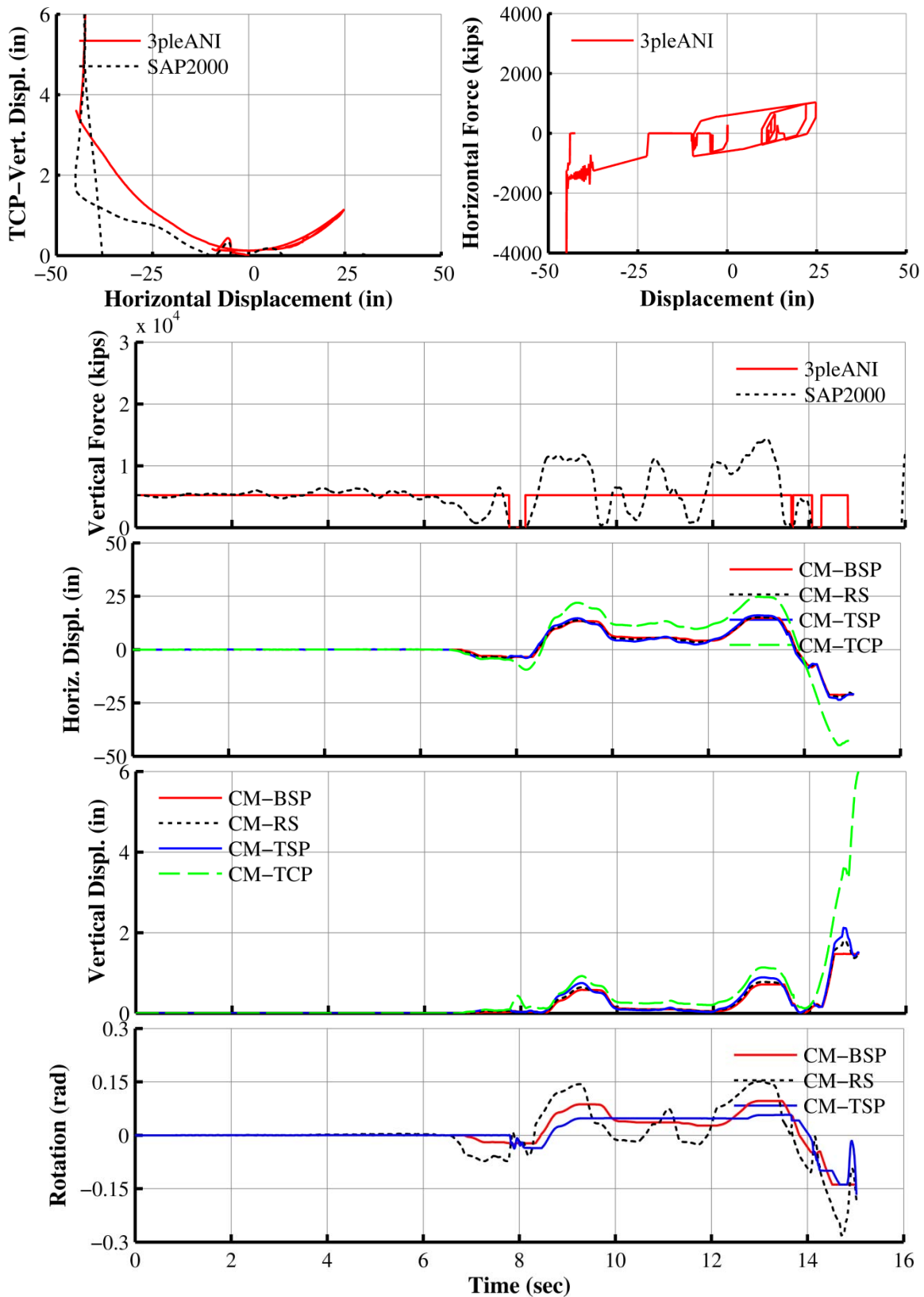


Figure 8-48: Program 3pleANI results of analysis for bearing TFP-3 using full contact theory-isolator instability

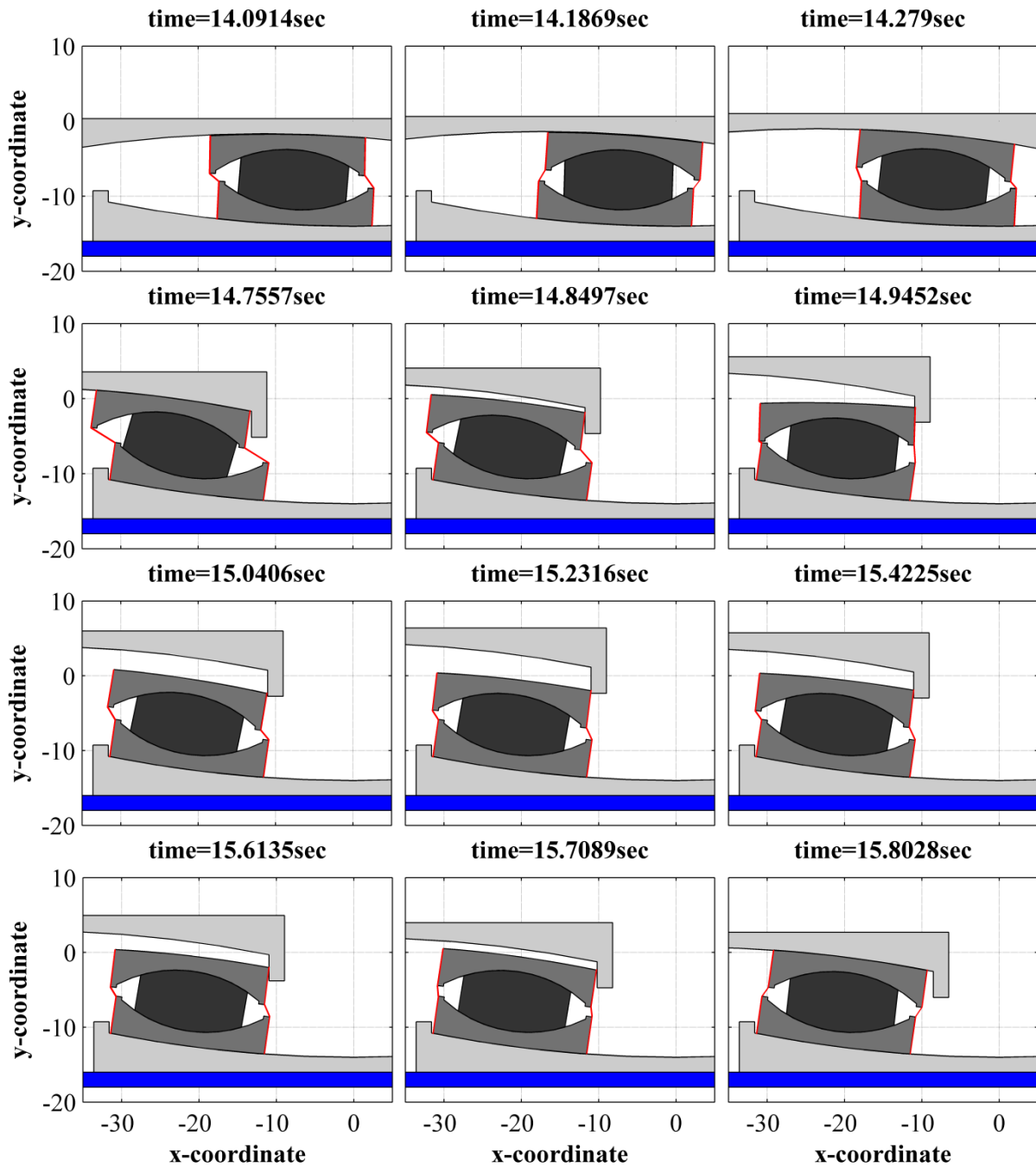


Figure 8-49: 3pleANI animation of TFP-3 modified isolator (increased restrainer height) based on full contact theory

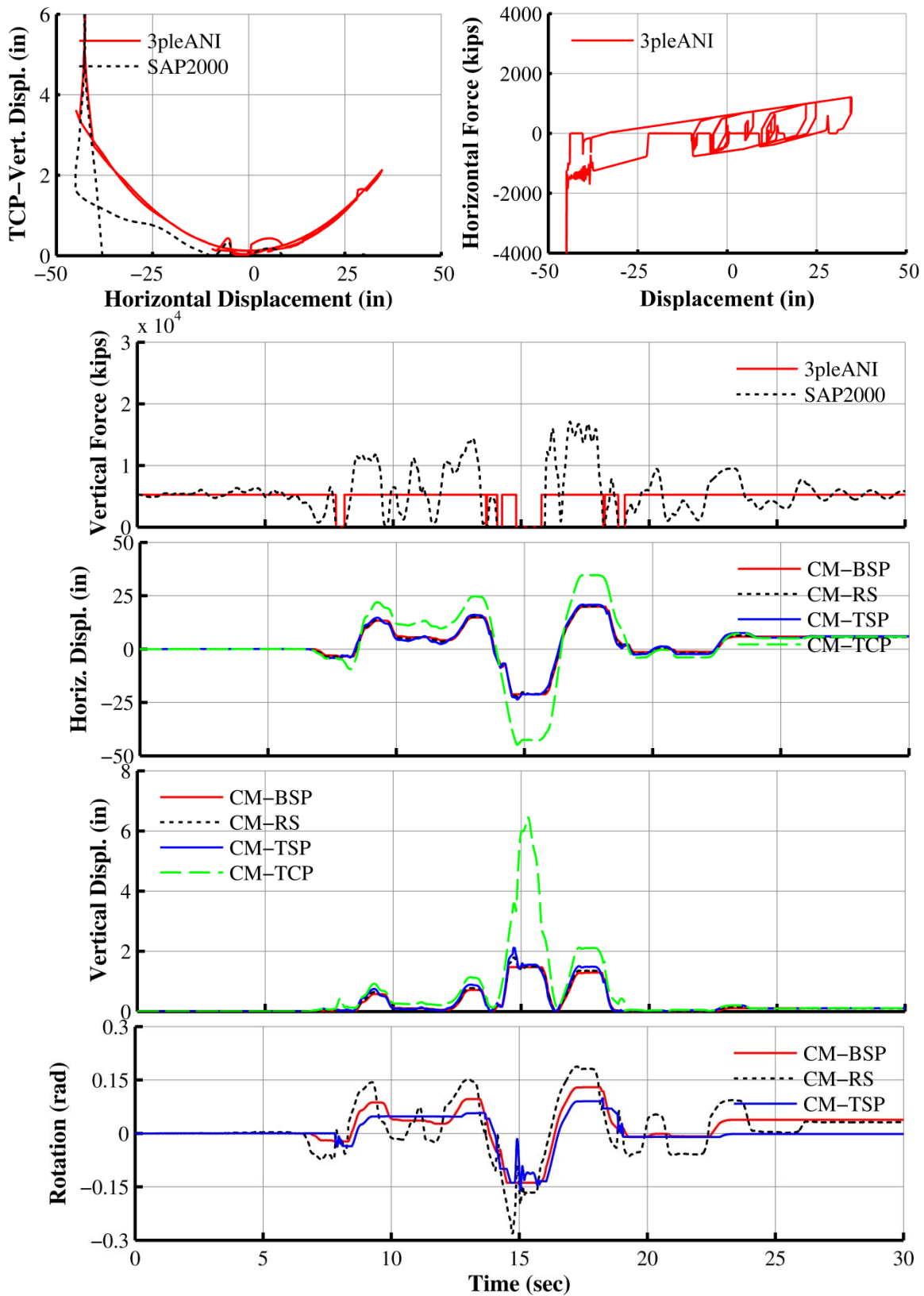


Figure 8-50: Program 3pleANI results of analysis for modified bearing TFP-3 (increased restrainer height) using full contact theory

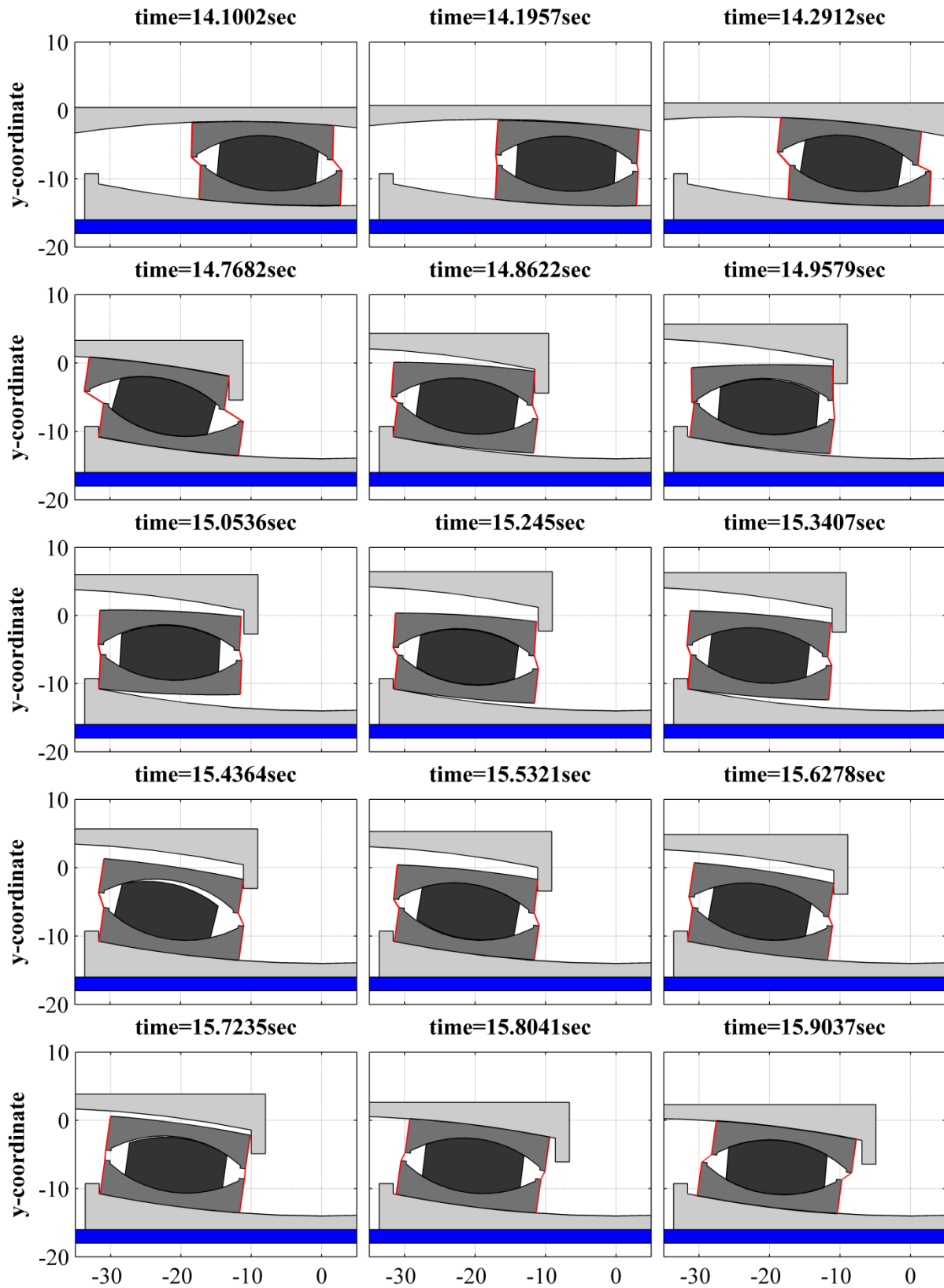


Figure 8-51: 3pleANI animation of TFP-3 modified isolator (increased restrainer height) based on full contact theory

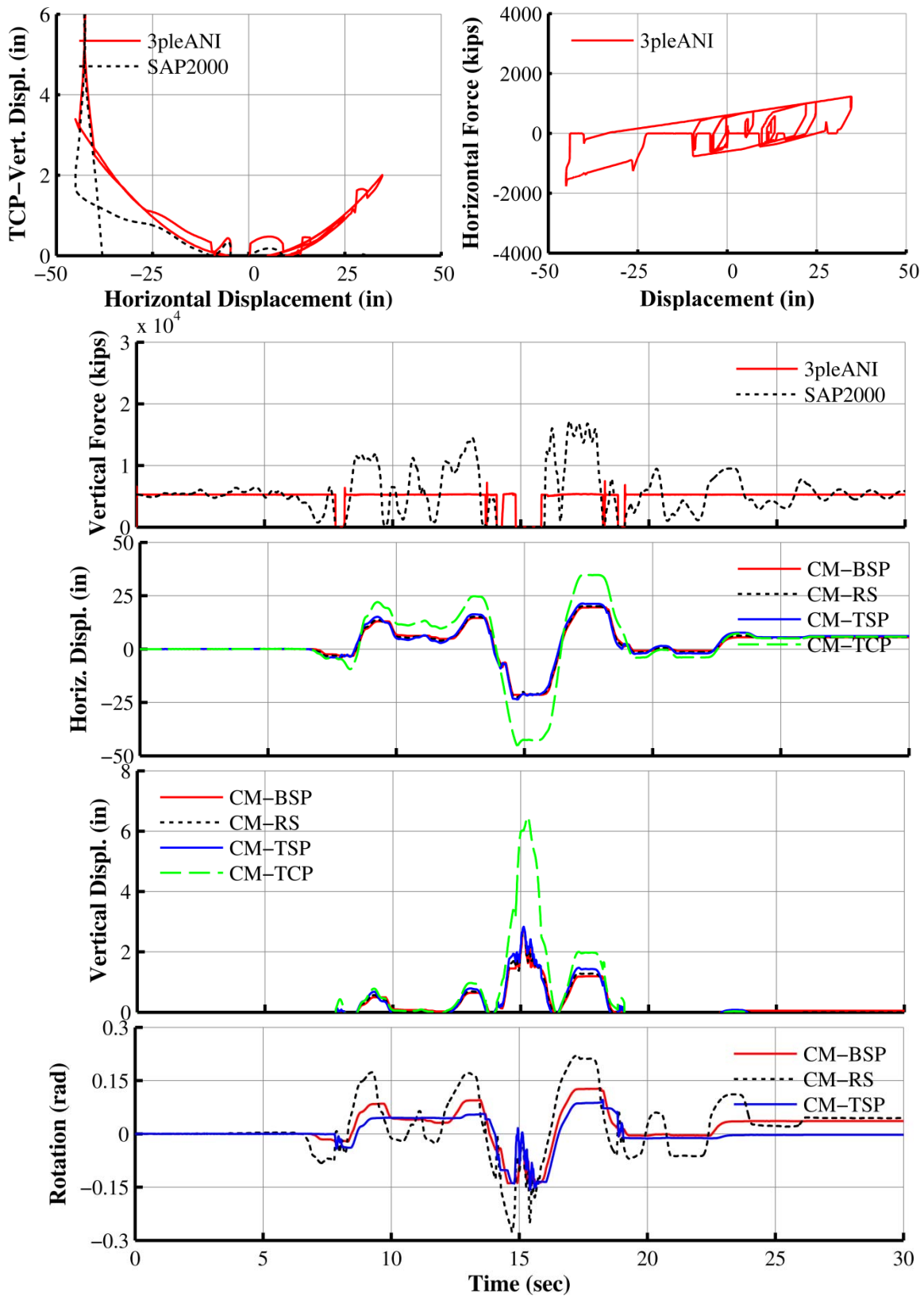


Figure 8-52: Program 3pleANI results of analysis for modified bearing TFP-3 (increased restrainer height) using advanced theory

SECTION 9

CONCLUSIONS

This report presented three new theories for the behavior of the Triple Friction Pendulum bearing. These theories and their main features are:

- 1) A theory for the behavior of the bearing under compression and with all parts being in full contact. The theory considers equilibrium of moments so that there are no restrictions on the geometric and frictional properties as in the theory of Fenz and Constantinou (2008b) and Morgan (2007). The theory explicitly predicts the motion of each part of the bearing so that heating effects and the velocity dependence of friction can be accurately considered. It has been shown that this model predicts results that are essentially the same as those of the model of Fenz and Constantinou (2008b) and Morgan (2007) provided the coefficient of friction in these models is properly interpreted. Relations to convert the actual friction values used in the presented theory to those in the Fenz and Constantinou theory have been derived.
- 2) A theory for modeling the behavior of the bearing under uplift conditions in which the Top Concave Plate of the bearing uplifts but the other parts of the bearing remain in full contact. The model is useful in obtaining first order results on the behavior of the isolator under uplift conditions and to assess its potential for instability. The main advantage of the model over a more advanced model described next is speed in execution.
- 3) An advanced theory for modeling the behavior of the bearing under uplift and landing conditions in which sliding, rocking, overturning, free fall and contact of the bearing components is simulated.

A computer program, 3pleANI, has been developed in MATLAB to implement these theories and conduct analysis of Triple Friction Pendulum isolators under prescribed vertical and horizontal motion of the top concave plate, to conduct response history analysis of seismically isolated building and bridge structures, to facilitate presentation and interpretation of the analysis results and to animate the motion of the analyzed isolator.

Several examples of analysis and comparisons to experimental results were presented that demonstrated the degree of accuracy and the utility of the theories and of the developed computer program.

It has been shown that the internal rubber seal of the bearing is important in predicting the behavior of the internal components of the bearing under uplift conditions. Accordingly, a significant effort has been spent in developing models of behavior for the seal and in implementing these options in program 3pleANI for ease in their use.

SECTION 10

REFERENCES

1. Becker, T.C, and Mahin, S.A. (2011), "Experimental and Analytical Study of The Bidirectional Behavior of the Triple Friction Pendulum Isolator." *Earthquake Engineering & Structural Dynamics*, 41(3), 355-373.
2. Chopra A. (2012), "Dynamics of Structures", Prentice Hall Inc., Upper Saddle River, New Jersey 07458. ISBN 10: 0-13-285803-7.
3. Computers and Structures Inc. (2007), "SAP2000: Integrated Finite Element Analysis And Design Of Structures", Version 11.0.8, Berkeley, CA.
4. Constantinou M.C., Mokha A. and Reinhorn A.M. (1990). "Teflon Bearings in Base Isolation. II: Modeling", *ASCE Journal of Structural Engineering*, 116(2), 455-474.
5. Constantinou, M.C., Whittaker, A.S., Kalpakidis, Y., Fenz, D. M. and Warn, G.P. (2007), "Performance of Seismic Isolation Hardware under Service and Seismic Loading", Report No. MCEER-07-0012, Multidisciplinary Center for Earthquake Engineering Research, Buffalo, NY.
6. Constantinou, M.C., Kalpakidis, I., Filiatrault, A. and Ecker Lay, R. A. (2011), "LRFD-Based Analysis and Design Procedures for Bridge Bearings and Seismic Isolators", Report No. MCEER-11-0004, Multidisciplinary Center for Earthquake Engineering Research, Buffalo, NY.
7. Dao, N. D., Ryan, K. L., Sato, E., and Sasaki, T. (2013). "Predicting the Displacement of Triple Pendulum™ Bearings in a Full-Scale Shaking Experiment Using a Three-Dimensional Element." *Earthquake Engineering & Structural Dynamics*, in press.
8. Fenz, D.M. and Constantinou, M.C. (2008a), "Mechanical Behavior of Multi-Spherical Sliding Bearings", Report No. MCEER-08-0007, Multidisciplinary Center for Earthquake Engineering Research, Buffalo, NY.
9. Fenz, D.M. and Constantinou, M.C. (2008b), "Spherical Sliding Isolation Bearings with Adaptive Behavior: Theory," *Earthquake Engineering and Structural Dynamics*, Vol. 37, No. 2, 163-183.
10. Fenz, D.M. and Constantinou, M.C. (2008c), "Spherical Sliding Isolation Bearings with Adaptive Behavior: Experimental Verification", *Earthquake Engineering and Structural Dynamics*, Vol. 37, No. 2, 185-205.

11. Fenz, D.M. and Constantinou, M.C., (2008d), "Modeling Triple Friction Pendulum Bearings for Response-History Analysis", *Earthquake Spectra*, Vol. 24, No. 4, 1011-1028.
12. Fenz, D.M. and Constantinou, M.C. (2008e), "Development, Implementation and Verification of Dynamic Analysis Models for Multi-Spherical Sliding", Report No. MCEER-08-0018, Multidisciplinary Center for Earthquake Engineering Research, Buffalo, NY.
13. Morgan, T. A. (2007), "The Use of Innovative Base Isolation Systems To Achieve Complex Seismic Performance Objectives", Ph.D. Dissertation, Department of Civil and Environmental Engineering, University of California, Berkeley.
14. Nagarajaiah, S., Reinhorn, A.M., and Constantinou, M.C. (1989) "Nonlinear Dynamic Analysis Of Three Dimensional Base Isolated Structures (3d-Basis)", Report NCEER-89-0019, National Center for Earthquake Engineering Research, State University of New York, Buffalo, NY.
15. Sarkisian, M., Lee, P., Hu, L., Doo, C., Zayas, V., Constantinou, M. and Bachman, R. (2012), "Property Verification of Triple Pendulum Seismic Isolation Bearings", Proceedings of the Structures Congress, ASCE, Chicago, Illinois, March.
16. Sarlis, A.A., Constantinou, M.C. (2010), "Modeling of Triple Friction Pendulum Isolators in Program SAP2000", supplement to MCEER Report 05-0009, document distributed to the engineering community together with executable version of program and example files, University at Buffalo.
17. Sarlis, A.A., Constantinou, M.C. and Reinhorn A.M. (2013), "Shake Table Testing of Triple Friction Pendulum Isolators under Extreme Conditions", Report No. MCEER-13-0011, Multidisciplinary Center for Earthquake Engineering Research, Buffalo, NY.

MCEER Technical Reports

MCEER publishes technical reports on a variety of subjects written by authors funded through MCEER. These reports are available from both MCEER Publications and the National Technical Information Service (NTIS). Requests for reports should be directed to MCEER Publications, MCEER, University at Buffalo, State University of New York, 133A Ketter Hall, Buffalo, New York 14260. Reports can also be requested through NTIS, P.O. Box 1425, Springfield, Virginia 22151. NTIS accession numbers are shown in parenthesis, if available.

- NCEER-87-0001 "First-Year Program in Research, Education and Technology Transfer," 3/5/87, (PB88-134275, A04, MF-A01).
- NCEER-87-0002 "Experimental Evaluation of Instantaneous Optimal Algorithms for Structural Control," by R.C. Lin, T.T. Soong and A.M. Reinhorn, 4/20/87, (PB88-134341, A04, MF-A01).
- NCEER-87-0003 "Experimentation Using the Earthquake Simulation Facilities at University at Buffalo," by A.M. Reinhorn and R.L. Ketter, not available.
- NCEER-87-0004 "The System Characteristics and Performance of a Shaking Table," by J.S. Hwang, K.C. Chang and G.C. Lee, 6/1/87, (PB88-134259, A03, MF-A01). This report is available only through NTIS (see address given above).
- NCEER-87-0005 "A Finite Element Formulation for Nonlinear Viscoplastic Material Using a Q Model," by O. Gyebe and G. Dasgupta, 11/2/87, (PB88-213764, A08, MF-A01).
- NCEER-87-0006 "Symbolic Manipulation Program (SMP) - Algebraic Codes for Two and Three Dimensional Finite Element Formulations," by X. Lee and G. Dasgupta, 11/9/87, (PB88-218522, A05, MF-A01).
- NCEER-87-0007 "Instantaneous Optimal Control Laws for Tall Buildings Under Seismic Excitations," by J.N. Yang, A. Akbarpour and P. Ghaemmaghami, 6/10/87, (PB88-134333, A06, MF-A01). This report is only available through NTIS (see address given above).
- NCEER-87-0008 "IDARC: Inelastic Damage Analysis of Reinforced Concrete Frame - Shear-Wall Structures," by Y.J. Park, A.M. Reinhorn and S.K. Kunnath, 7/20/87, (PB88-134325, A09, MF-A01). This report is only available through NTIS (see address given above).
- NCEER-87-0009 "Liquefaction Potential for New York State: A Preliminary Report on Sites in Manhattan and Buffalo," by M. Budhu, V. Vijayakumar, R.F. Giese and L. Baumgras, 8/31/87, (PB88-163704, A03, MF-A01). This report is available only through NTIS (see address given above).
- NCEER-87-0010 "Vertical and Torsional Vibration of Foundations in Inhomogeneous Media," by A.S. Veletsos and K.W. Dotson, 6/1/87, (PB88-134291, A03, MF-A01). This report is only available through NTIS (see address given above).
- NCEER-87-0011 "Seismic Probabilistic Risk Assessment and Seismic Margins Studies for Nuclear Power Plants," by Howard H.M. Hwang, 6/15/87, (PB88-134267, A03, MF-A01). This report is only available through NTIS (see address given above).
- NCEER-87-0012 "Parametric Studies of Frequency Response of Secondary Systems Under Ground-Acceleration Excitations," by Y. Yong and Y.K. Lin, 6/10/87, (PB88-134309, A03, MF-A01). This report is only available through NTIS (see address given above).
- NCEER-87-0013 "Frequency Response of Secondary Systems Under Seismic Excitation," by J.A. HoLung, J. Cai and Y.K. Lin, 7/31/87, (PB88-134317, A05, MF-A01). This report is only available through NTIS (see address given above).
- NCEER-87-0014 "Modelling Earthquake Ground Motions in Seismically Active Regions Using Parametric Time Series Methods," by G.W. Ellis and A.S. Cakmak, 8/25/87, (PB88-134283, A08, MF-A01). This report is only available through NTIS (see address given above).
- NCEER-87-0015 "Detection and Assessment of Seismic Structural Damage," by E. DiPasquale and A.S. Cakmak, 8/25/87, (PB88-163712, A05, MF-A01). This report is only available through NTIS (see address given above).

- NCEER-87-0016 "Pipeline Experiment at Parkfield, California," by J. Isenberg and E. Richardson, 9/15/87, (PB88-163720, A03, MF-A01). This report is available only through NTIS (see address given above).
- NCEER-87-0017 "Digital Simulation of Seismic Ground Motion," by M. Shinozuka, G. Deodatis and T. Harada, 8/31/87, (PB88-155197, A04, MF-A01). This report is available only through NTIS (see address given above).
- NCEER-87-0018 "Practical Considerations for Structural Control: System Uncertainty, System Time Delay and Truncation of Small Control Forces," J.N. Yang and A. Akbarpour, 8/10/87, (PB88-163738, A08, MF-A01). This report is only available through NTIS (see address given above).
- NCEER-87-0019 "Modal Analysis of Nonclassically Damped Structural Systems Using Canonical Transformation," by J.N. Yang, S. Sarkani and F.X. Long, 9/27/87, (PB88-187851, A04, MF-A01).
- NCEER-87-0020 "A Nonstationary Solution in Random Vibration Theory," by J.R. Red-Horse and P.D. Spanos, 11/3/87, (PB88-163746, A03, MF-A01).
- NCEER-87-0021 "Horizontal Impedances for Radially Inhomogeneous Viscoelastic Soil Layers," by A.S. Veletsos and K.W. Dotson, 10/15/87, (PB88-150859, A04, MF-A01).
- NCEER-87-0022 "Seismic Damage Assessment of Reinforced Concrete Members," by Y.S. Chung, C. Meyer and M. Shinozuka, 10/9/87, (PB88-150867, A05, MF-A01). This report is available only through NTIS (see address given above).
- NCEER-87-0023 "Active Structural Control in Civil Engineering," by T.T. Soong, 11/11/87, (PB88-187778, A03, MF-A01).
- NCEER-87-0024 "Vertical and Torsional Impedances for Radially Inhomogeneous Viscoelastic Soil Layers," by K.W. Dotson and A.S. Veletsos, 12/87, (PB88-187786, A03, MF-A01).
- NCEER-87-0025 "Proceedings from the Symposium on Seismic Hazards, Ground Motions, Soil-Liquefaction and Engineering Practice in Eastern North America," October 20-22, 1987, edited by K.H. Jacob, 12/87, (PB88-188115, A23, MF-A01). This report is available only through NTIS (see address given above).
- NCEER-87-0026 "Report on the Whittier-Narrows, California, Earthquake of October 1, 1987," by J. Pantelic and A. Reinhorn, 11/87, (PB88-187752, A03, MF-A01). This report is available only through NTIS (see address given above).
- NCEER-87-0027 "Design of a Modular Program for Transient Nonlinear Analysis of Large 3-D Building Structures," by S. Srivastav and J.F. Abel, 12/30/87, (PB88-187950, A05, MF-A01). This report is only available through NTIS (see address given above).
- NCEER-87-0028 "Second-Year Program in Research, Education and Technology Transfer," 3/8/88, (PB88-219480, A04, MF-A01).
- NCEER-88-0001 "Workshop on Seismic Computer Analysis and Design of Buildings With Interactive Graphics," by W. McGuire, J.F. Abel and C.H. Conley, 1/18/88, (PB88-187760, A03, MF-A01). This report is only available through NTIS (see address given above).
- NCEER-88-0002 "Optimal Control of Nonlinear Flexible Structures," by J.N. Yang, F.X. Long and D. Wong, 1/22/88, (PB88-213772, A06, MF-A01).
- NCEER-88-0003 "Substructuring Techniques in the Time Domain for Primary-Secondary Structural Systems," by G.D. Manolis and G. Juhn, 2/10/88, (PB88-213780, A04, MF-A01).
- NCEER-88-0004 "Iterative Seismic Analysis of Primary-Secondary Systems," by A. Singhal, L.D. Lutes and P.D. Spanos, 2/23/88, (PB88-213798, A04, MF-A01).
- NCEER-88-0005 "Stochastic Finite Element Expansion for Random Media," by P.D. Spanos and R. Ghanem, 3/14/88, (PB88-213806, A03, MF-A01).

- NCEER-88-0006 "Combining Structural Optimization and Structural Control," by F.Y. Cheng and C.P. Pantelides, 1/10/88, (PB88-213814, A05, MF-A01).
- NCEER-88-0007 "Seismic Performance Assessment of Code-Designed Structures," by H.H-M. Hwang, J-W. Jaw and H-J. Shau, 3/20/88, (PB88-219423, A04, MF-A01). This report is only available through NTIS (see address given above).
- NCEER-88-0008 "Reliability Analysis of Code-Designed Structures Under Natural Hazards," by H.H-M. Hwang, H. Ushiba and M. Shinozuka, 2/29/88, (PB88-229471, A07, MF-A01). This report is only available through NTIS (see address given above).
- NCEER-88-0009 "Seismic Fragility Analysis of Shear Wall Structures," by J-W Jaw and H.H-M. Hwang, 4/30/88, (PB89-102867, A04, MF-A01).
- NCEER-88-0010 "Base Isolation of a Multi-Story Building Under a Harmonic Ground Motion - A Comparison of Performances of Various Systems," by F-G Fan, G. Ahmadi and I.G. Tadjbakhsh, 5/18/88, (PB89-122238, A06, MF-A01). This report is only available through NTIS (see address given above).
- NCEER-88-0011 "Seismic Floor Response Spectra for a Combined System by Green's Functions," by F.M. Lavelle, L.A. Bergman and P.D. Spanos, 5/1/88, (PB89-102875, A03, MF-A01).
- NCEER-88-0012 "A New Solution Technique for Randomly Excited Hysteretic Structures," by G.Q. Cai and Y.K. Lin, 5/16/88, (PB89-102883, A03, MF-A01).
- NCEER-88-0013 "A Study of Radiation Damping and Soil-Structure Interaction Effects in the Centrifuge," by K. Weissman, supervised by J.H. Prevost, 5/24/88, (PB89-144703, A06, MF-A01).
- NCEER-88-0014 "Parameter Identification and Implementation of a Kinematic Plasticity Model for Frictional Soils," by J.H. Prevost and D.V. Griffiths, not available.
- NCEER-88-0015 "Two- and Three- Dimensional Dynamic Finite Element Analyses of the Long Valley Dam," by D.V. Griffiths and J.H. Prevost, 6/17/88, (PB89-144711, A04, MF-A01).
- NCEER-88-0016 "Damage Assessment of Reinforced Concrete Structures in Eastern United States," by A.M. Reinhorn, M.J. Seidel, S.K. Kunnath and Y.J. Park, 6/15/88, (PB89-122220, A04, MF-A01). This report is only available through NTIS (see address given above).
- NCEER-88-0017 "Dynamic Compliance of Vertically Loaded Strip Foundations in Multilayered Viscoelastic Soils," by S. Ahmad and A.S.M. Israil, 6/17/88, (PB89-102891, A04, MF-A01).
- NCEER-88-0018 "An Experimental Study of Seismic Structural Response With Added Viscoelastic Dampers," by R.C. Lin, Z. Liang, T.T. Soong and R.H. Zhang, 6/30/88, (PB89-122212, A05, MF-A01). This report is available only through NTIS (see address given above).
- NCEER-88-0019 "Experimental Investigation of Primary - Secondary System Interaction," by G.D. Manolis, G. Juhn and A.M. Reinhorn, 5/27/88, (PB89-122204, A04, MF-A01).
- NCEER-88-0020 "A Response Spectrum Approach For Analysis of Nonclassically Damped Structures," by J.N. Yang, S. Sarkani and F.X. Long, 4/22/88, (PB89-102909, A04, MF-A01).
- NCEER-88-0021 "Seismic Interaction of Structures and Soils: Stochastic Approach," by A.S. Veletsos and A.M. Prasad, 7/21/88, (PB89-122196, A04, MF-A01). This report is only available through NTIS (see address given above).
- NCEER-88-0022 "Identification of the Serviceability Limit State and Detection of Seismic Structural Damage," by E. DiPasquale and A.S. Cakmak, 6/15/88, (PB89-122188, A05, MF-A01). This report is available only through NTIS (see address given above).
- NCEER-88-0023 "Multi-Hazard Risk Analysis: Case of a Simple Offshore Structure," by B.K. Bhartia and E.H. Vanmarcke, 7/21/88, (PB89-145213, A05, MF-A01).

- NCEER-88-0024 "Automated Seismic Design of Reinforced Concrete Buildings," by Y.S. Chung, C. Meyer and M. Shinozuka, 7/5/88, (PB89-122170, A06, MF-A01). This report is available only through NTIS (see address given above).
- NCEER-88-0025 "Experimental Study of Active Control of MDOF Structures Under Seismic Excitations," by L.L. Chung, R.C. Lin, T.T. Soong and A.M. Reinhorn, 7/10/88, (PB89-122600, A04, MF-A01).
- NCEER-88-0026 "Earthquake Simulation Tests of a Low-Rise Metal Structure," by J.S. Hwang, K.C. Chang, G.C. Lee and R.L. Ketter, 8/1/88, (PB89-102917, A04, MF-A01).
- NCEER-88-0027 "Systems Study of Urban Response and Reconstruction Due to Catastrophic Earthquakes," by F. Kozin and H.K. Zhou, 9/22/88, (PB90-162348, A04, MF-A01).
- NCEER-88-0028 "Seismic Fragility Analysis of Plane Frame Structures," by H.H-M. Hwang and Y.K. Low, 7/31/88, (PB89-131445, A06, MF-A01).
- NCEER-88-0029 "Response Analysis of Stochastic Structures," by A. Kardara, C. Bucher and M. Shinozuka, 9/22/88, (PB89-174429, A04, MF-A01).
- NCEER-88-0030 "Nonnormal Accelerations Due to Yielding in a Primary Structure," by D.C.K. Chen and L.D. Lutes, 9/19/88, (PB89-131437, A04, MF-A01).
- NCEER-88-0031 "Design Approaches for Soil-Structure Interaction," by A.S. Veletsos, A.M. Prasad and Y. Tang, 12/30/88, (PB89-174437, A03, MF-A01). This report is available only through NTIS (see address given above).
- NCEER-88-0032 "A Re-evaluation of Design Spectra for Seismic Damage Control," by C.J. Turkstra and A.G. Tallin, 11/7/88, (PB89-145221, A05, MF-A01).
- NCEER-88-0033 "The Behavior and Design of Noncontact Lap Splices Subjected to Repeated Inelastic Tensile Loading," by V.E. Sagan, P. Gergely and R.N. White, 12/8/88, (PB89-163737, A08, MF-A01).
- NCEER-88-0034 "Seismic Response of Pile Foundations," by S.M. Mamoon, P.K. Banerjee and S. Ahmad, 11/1/88, (PB89-145239, A04, MF-A01).
- NCEER-88-0035 "Modeling of R/C Building Structures With Flexible Floor Diaphragms (IDARC2)," by A.M. Reinhorn, S.K. Kunnath and N. Panahshahi, 9/7/88, (PB89-207153, A07, MF-A01).
- NCEER-88-0036 "Solution of the Dam-Reservoir Interaction Problem Using a Combination of FEM, BEM with Particular Integrals, Modal Analysis, and Substructuring," by C-S. Tsai, G.C. Lee and R.L. Ketter, 12/31/88, (PB89-207146, A04, MF-A01).
- NCEER-88-0037 "Optimal Placement of Actuators for Structural Control," by F.Y. Cheng and C.P. Pantelides, 8/15/88, (PB89-162846, A05, MF-A01).
- NCEER-88-0038 "Teflon Bearings in Aseismic Base Isolation: Experimental Studies and Mathematical Modeling," by A. Mokha, M.C. Constantinou and A.M. Reinhorn, 12/5/88, (PB89-218457, A10, MF-A01). This report is available only through NTIS (see address given above).
- NCEER-88-0039 "Seismic Behavior of Flat Slab High-Rise Buildings in the New York City Area," by P. Weidlinger and M. Ettouney, 10/15/88, (PB90-145681, A04, MF-A01).
- NCEER-88-0040 "Evaluation of the Earthquake Resistance of Existing Buildings in New York City," by P. Weidlinger and M. Ettouney, 10/15/88, not available.
- NCEER-88-0041 "Small-Scale Modeling Techniques for Reinforced Concrete Structures Subjected to Seismic Loads," by W. Kim, A. El-Attar and R.N. White, 11/22/88, (PB89-189625, A05, MF-A01).
- NCEER-88-0042 "Modeling Strong Ground Motion from Multiple Event Earthquakes," by G.W. Ellis and A.S. Cakmak, 10/15/88, (PB89-174445, A03, MF-A01).

- NCEER-88-0043 "Nonstationary Models of Seismic Ground Acceleration," by M. Grigoriu, S.E. Ruiz and E. Rosenblueth, 7/15/88, (PB89-189617, A04, MF-A01).
- NCEER-88-0044 "SARCF User's Guide: Seismic Analysis of Reinforced Concrete Frames," by Y.S. Chung, C. Meyer and M. Shinozuka, 11/9/88, (PB89-174452, A08, MF-A01).
- NCEER-88-0045 "First Expert Panel Meeting on Disaster Research and Planning," edited by J. Pantelic and J. Stoyke, 9/15/88, (PB89-174460, A05, MF-A01).
- NCEER-88-0046 "Preliminary Studies of the Effect of Degrading Infill Walls on the Nonlinear Seismic Response of Steel Frames," by C.Z. Chrysostomou, P. Gergely and J.F. Abel, 12/19/88, (PB89-208383, A05, MF-A01).
- NCEER-88-0047 "Reinforced Concrete Frame Component Testing Facility - Design, Construction, Instrumentation and Operation," by S.P. Pessiki, C. Conley, T. Bond, P. Gergely and R.N. White, 12/16/88, (PB89-174478, A04, MF-A01).
- NCEER-89-0001 "Effects of Protective Cushion and Soil Compliancy on the Response of Equipment Within a Seismically Excited Building," by J.A. HoLung, 2/16/89, (PB89-207179, A04, MF-A01).
- NCEER-89-0002 "Statistical Evaluation of Response Modification Factors for Reinforced Concrete Structures," by H.H-M. Hwang and J-W. Jaw, 2/17/89, (PB89-207187, A05, MF-A01).
- NCEER-89-0003 "Hysteretic Columns Under Random Excitation," by G-Q. Cai and Y.K. Lin, 1/9/89, (PB89-196513, A03, MF-A01).
- NCEER-89-0004 "Experimental Study of 'Elephant Foot Bulge' Instability of Thin-Walled Metal Tanks," by Z-H. Jia and R.L. Ketter, 2/22/89, (PB89-207195, A03, MF-A01).
- NCEER-89-0005 "Experiment on Performance of Buried Pipelines Across San Andreas Fault," by J. Isenberg, E. Richardson and T.D. O'Rourke, 3/10/89, (PB89-218440, A04, MF-A01). This report is available only through NTIS (see address given above).
- NCEER-89-0006 "A Knowledge-Based Approach to Structural Design of Earthquake-Resistant Buildings," by M. Subramani, P. Gergely, C.H. Conley, J.F. Abel and A.H. Zaghaw, 1/15/89, (PB89-218465, A06, MF-A01).
- NCEER-89-0007 "Liquefaction Hazards and Their Effects on Buried Pipelines," by T.D. O'Rourke and P.A. Lane, 2/1/89, (PB89-218481, A09, MF-A01).
- NCEER-89-0008 "Fundamentals of System Identification in Structural Dynamics," by H. Imai, C-B. Yun, O. Maruyama and M. Shinozuka, 1/26/89, (PB89-207211, A04, MF-A01).
- NCEER-89-0009 "Effects of the 1985 Michoacan Earthquake on Water Systems and Other Buried Lifelines in Mexico," by A.G. Ayala and M.J. O'Rourke, 3/8/89, (PB89-207229, A06, MF-A01).
- NCEER-89-R010 "NCEER Bibliography of Earthquake Education Materials," by K.E.K. Ross, Second Revision, 9/1/89, (PB90-125352, A05, MF-A01). This report is replaced by NCEER-92-0018.
- NCEER-89-0011 "Inelastic Three-Dimensional Response Analysis of Reinforced Concrete Building Structures (IDARC-3D), Part I - Modeling," by S.K. Kunnath and A.M. Reinhorn, 4/17/89, (PB90-114612, A07, MF-A01). This report is available only through NTIS (see address given above).
- NCEER-89-0012 "Recommended Modifications to ATC-14," by C.D. Poland and J.O. Malley, 4/12/89, (PB90-108648, A15, MF-A01).
- NCEER-89-0013 "Repair and Strengthening of Beam-to-Column Connections Subjected to Earthquake Loading," by M. Corazao and A.J. Durrani, 2/28/89, (PB90-109885, A06, MF-A01).
- NCEER-89-0014 "Program EXKAL2 for Identification of Structural Dynamic Systems," by O. Maruyama, C-B. Yun, M. Hoshiya and M. Shinozuka, 5/19/89, (PB90-109877, A09, MF-A01).

- NCEER-89-0015 "Response of Frames With Bolted Semi-Rigid Connections, Part I - Experimental Study and Analytical Predictions," by P.J. DiCorso, A.M. Reinhorn, J.R. Dickerson, J.B. Radzimirski and W.L. Harper, 6/1/89, not available.
- NCEER-89-0016 "ARMA Monte Carlo Simulation in Probabilistic Structural Analysis," by P.D. Spanos and M.P. Mignolet, 7/10/89, (PB90-109893, A03, MF-A01).
- NCEER-89-P017 "Preliminary Proceedings from the Conference on Disaster Preparedness - The Place of Earthquake Education in Our Schools," Edited by K.E.K. Ross, 6/23/89, (PB90-108606, A03, MF-A01).
- NCEER-89-0017 "Proceedings from the Conference on Disaster Preparedness - The Place of Earthquake Education in Our Schools," Edited by K.E.K. Ross, 12/31/89, (PB90-207895, A012, MF-A02). This report is available only through NTIS (see address given above).
- NCEER-89-0018 "Multidimensional Models of Hysteretic Material Behavior for Vibration Analysis of Shape Memory Energy Absorbing Devices, by E.J. Graesser and F.A. Cozzarelli, 6/7/89, (PB90-164146, A04, MF-A01).
- NCEER-89-0019 "Nonlinear Dynamic Analysis of Three-Dimensional Base Isolated Structures (3D-BASIS)," by S. Nagarajaiah, A.M. Reinhorn and M.C. Constantinou, 8/3/89, (PB90-161936, A06, MF-A01). This report has been replaced by NCEER-93-0011.
- NCEER-89-0020 "Structural Control Considering Time-Rate of Control Forces and Control Rate Constraints," by F.Y. Cheng and C.P. Pantelides, 8/3/89, (PB90-120445, A04, MF-A01).
- NCEER-89-0021 "Subsurface Conditions of Memphis and Shelby County," by K.W. Ng, T-S. Chang and H-H.M. Hwang, 7/26/89, (PB90-120437, A03, MF-A01).
- NCEER-89-0022 "Seismic Wave Propagation Effects on Straight Jointed Buried Pipelines," by K. Elhmadi and M.J. O'Rourke, 8/24/89, (PB90-162322, A10, MF-A02).
- NCEER-89-0023 "Workshop on Serviceability Analysis of Water Delivery Systems," edited by M. Grigoriu, 3/6/89, (PB90-127424, A03, MF-A01).
- NCEER-89-0024 "Shaking Table Study of a 1/5 Scale Steel Frame Composed of Tapered Members," by K.C. Chang, J.S. Hwang and G.C. Lee, 9/18/89, (PB90-160169, A04, MF-A01).
- NCEER-89-0025 "DYNA1D: A Computer Program for Nonlinear Seismic Site Response Analysis - Technical Documentation," by Jean H. Prevost, 9/14/89, (PB90-161944, A07, MF-A01). This report is available only through NTIS (see address given above).
- NCEER-89-0026 "1:4 Scale Model Studies of Active Tendon Systems and Active Mass Dampers for Aseismic Protection," by A.M. Reinhorn, T.T. Soong, R.C. Lin, Y.P. Yang, Y. Fukao, H. Abe and M. Nakai, 9/15/89, (PB90-173246, A10, MF-A02). This report is available only through NTIS (see address given above).
- NCEER-89-0027 "Scattering of Waves by Inclusions in a Nonhomogeneous Elastic Half Space Solved by Boundary Element Methods," by P.K. Hadley, A. Askar and A.S. Cakmak, 6/15/89, (PB90-145699, A07, MF-A01).
- NCEER-89-0028 "Statistical Evaluation of Deflection Amplification Factors for Reinforced Concrete Structures," by H.H.M. Hwang, J-W. Jaw and A.L. Ch'ng, 8/31/89, (PB90-164633, A05, MF-A01).
- NCEER-89-0029 "Bedrock Accelerations in Memphis Area Due to Large New Madrid Earthquakes," by H.H.M. Hwang, C.H.S. Chen and G. Yu, 11/7/89, (PB90-162330, A04, MF-A01).
- NCEER-89-0030 "Seismic Behavior and Response Sensitivity of Secondary Structural Systems," by Y.Q. Chen and T.T. Soong, 10/23/89, (PB90-164658, A08, MF-A01).
- NCEER-89-0031 "Random Vibration and Reliability Analysis of Primary-Secondary Structural Systems," by Y. Ibrahim, M. Grigoriu and T.T. Soong, 11/10/89, (PB90-161951, A04, MF-A01).

- NCEER-89-0032 "Proceedings from the Second U.S. - Japan Workshop on Liquefaction, Large Ground Deformation and Their Effects on Lifelines, September 26-29, 1989," Edited by T.D. O'Rourke and M. Hamada, 12/1/89, (PB90-209388, A22, MF-A03).
- NCEER-89-0033 "Deterministic Model for Seismic Damage Evaluation of Reinforced Concrete Structures," by J.M. Bracci, A.M. Reinhorn, J.B. Mander and S.K. Kunnath, 9/27/89, (PB91-108803, A06, MF-A01).
- NCEER-89-0034 "On the Relation Between Local and Global Damage Indices," by E. DiPasquale and A.S. Cakmak, 8/15/89, (PB90-173865, A05, MF-A01).
- NCEER-89-0035 "Cyclic Undrained Behavior of Nonplastic and Low Plasticity Silts," by A.J. Walker and H.E. Stewart, 7/26/89, (PB90-183518, A10, MF-A01).
- NCEER-89-0036 "Liquefaction Potential of Surficial Deposits in the City of Buffalo, New York," by M. Budhu, R. Giese and L. Baumgrass, 1/17/89, (PB90-208455, A04, MF-A01).
- NCEER-89-0037 "A Deterministic Assessment of Effects of Ground Motion Incoherence," by A.S. Veletsos and Y. Tang, 7/15/89, (PB90-164294, A03, MF-A01).
- NCEER-89-0038 "Workshop on Ground Motion Parameters for Seismic Hazard Mapping," July 17-18, 1989, edited by R.V. Whitman, 12/1/89, (PB90-173923, A04, MF-A01).
- NCEER-89-0039 "Seismic Effects on Elevated Transit Lines of the New York City Transit Authority," by C.J. Costantino, C.A. Miller and E. Heymsfield, 12/26/89, (PB90-207887, A06, MF-A01).
- NCEER-89-0040 "Centrifugal Modeling of Dynamic Soil-Structure Interaction," by K. Weissman, Supervised by J.H. Prevost, 5/10/89, (PB90-207879, A07, MF-A01).
- NCEER-89-0041 "Linearized Identification of Buildings With Cores for Seismic Vulnerability Assessment," by I-K. Ho and A.E. Aktan, 11/1/89, (PB90-251943, A07, MF-A01).
- NCEER-90-0001 "Geotechnical and Lifeline Aspects of the October 17, 1989 Loma Prieta Earthquake in San Francisco," by T.D. O'Rourke, H.E. Stewart, F.T. Blackburn and T.S. Dickerman, 1/90, (PB90-208596, A05, MF-A01).
- NCEER-90-0002 "Nonnormal Secondary Response Due to Yielding in a Primary Structure," by D.C.K. Chen and L.D. Lutes, 2/28/90, (PB90-251976, A07, MF-A01).
- NCEER-90-0003 "Earthquake Education Materials for Grades K-12," by K.E.K. Ross, 4/16/90, (PB91-251984, A05, MF-A05). This report has been replaced by NCEER-92-0018.
- NCEER-90-0004 "Catalog of Strong Motion Stations in Eastern North America," by R.W. Busby, 4/3/90, (PB90-251984, A05, MF-A01).
- NCEER-90-0005 "NCEER Strong-Motion Data Base: A User Manual for the GeoBase Release (Version 1.0 for the Sun3)," by P. Friberg and K. Jacob, 3/31/90 (PB90-258062, A04, MF-A01).
- NCEER-90-0006 "Seismic Hazard Along a Crude Oil Pipeline in the Event of an 1811-1812 Type New Madrid Earthquake," by H.H.M. Hwang and C-H.S. Chen, 4/16/90, (PB90-258054, A04, MF-A01).
- NCEER-90-0007 "Site-Specific Response Spectra for Memphis Sheahan Pumping Station," by H.H.M. Hwang and C.S. Lee, 5/15/90, (PB91-108811, A05, MF-A01).
- NCEER-90-0008 "Pilot Study on Seismic Vulnerability of Crude Oil Transmission Systems," by T. Ariman, R. Dobry, M. Grigoriu, F. Kozin, M. O'Rourke, T. O'Rourke and M. Shinozuka, 5/25/90, (PB91-108837, A06, MF-A01).
- NCEER-90-0009 "A Program to Generate Site Dependent Time Histories: EQGEN," by G.W. Ellis, M. Srinivasan and A.S. Cakmak, 1/30/90, (PB91-108829, A04, MF-A01).
- NCEER-90-0010 "Active Isolation for Seismic Protection of Operating Rooms," by M.E. Talbott, Supervised by M. Shinozuka, 6/8/9, (PB91-110205, A05, MF-A01).

- NCEER-90-0011 "Program LINEARID for Identification of Linear Structural Dynamic Systems," by C-B. Yun and M. Shinozuka, 6/25/90, (PB91-110312, A08, MF-A01).
- NCEER-90-0012 "Two-Dimensional Two-Phase Elasto-Plastic Seismic Response of Earth Dams," by A.N. Yiagos, Supervised by J.H. Prevost, 6/20/90, (PB91-110197, A13, MF-A02).
- NCEER-90-0013 "Secondary Systems in Base-Isolated Structures: Experimental Investigation, Stochastic Response and Stochastic Sensitivity," by G.D. Manolis, G. Juhn, M.C. Constantinou and A.M. Reinhorn, 7/1/90, (PB91-110320, A08, MF-A01).
- NCEER-90-0014 "Seismic Behavior of Lightly-Reinforced Concrete Column and Beam-Column Joint Details," by S.P. Pessiki, C.H. Conley, P. Gergely and R.N. White, 8/22/90, (PB91-108795, A11, MF-A02).
- NCEER-90-0015 "Two Hybrid Control Systems for Building Structures Under Strong Earthquakes," by J.N. Yang and A. Daniellians, 6/29/90, (PB91-125393, A04, MF-A01).
- NCEER-90-0016 "Instantaneous Optimal Control with Acceleration and Velocity Feedback," by J.N. Yang and Z. Li, 6/29/90, (PB91-125401, A03, MF-A01).
- NCEER-90-0017 "Reconnaissance Report on the Northern Iran Earthquake of June 21, 1990," by M. Mehrain, 10/4/90, (PB91-125377, A03, MF-A01).
- NCEER-90-0018 "Evaluation of Liquefaction Potential in Memphis and Shelby County," by T.S. Chang, P.S. Tang, C.S. Lee and H. Hwang, 8/10/90, (PB91-125427, A09, MF-A01).
- NCEER-90-0019 "Experimental and Analytical Study of a Combined Sliding Disc Bearing and Helical Steel Spring Isolation System," by M.C. Constantinou, A.S. Mokha and A.M. Reinhorn, 10/4/90, (PB91-125385, A06, MF-A01). This report is available only through NTIS (see address given above).
- NCEER-90-0020 "Experimental Study and Analytical Prediction of Earthquake Response of a Sliding Isolation System with a Spherical Surface," by A.S. Mokha, M.C. Constantinou and A.M. Reinhorn, 10/11/90, (PB91-125419, A05, MF-A01).
- NCEER-90-0021 "Dynamic Interaction Factors for Floating Pile Groups," by G. Gazetas, K. Fan, A. Kaynia and E. Kausel, 9/10/90, (PB91-170381, A05, MF-A01).
- NCEER-90-0022 "Evaluation of Seismic Damage Indices for Reinforced Concrete Structures," by S. Rodriguez-Gomez and A.S. Cakmak, 9/30/90, PB91-171322, A06, MF-A01).
- NCEER-90-0023 "Study of Site Response at a Selected Memphis Site," by H. Desai, S. Ahmad, E.S. Gazetas and M.R. Oh, 10/11/90, (PB91-196857, A03, MF-A01).
- NCEER-90-0024 "A User's Guide to Strongmo: Version 1.0 of NCEER's Strong-Motion Data Access Tool for PCs and Terminals," by P.A. Friberg and C.A.T. Susch, 11/15/90, (PB91-171272, A03, MF-A01).
- NCEER-90-0025 "A Three-Dimensional Analytical Study of Spatial Variability of Seismic Ground Motions," by L-L. Hong and A.H.-S. Ang, 10/30/90, (PB91-170399, A09, MF-A01).
- NCEER-90-0026 "MUMOID User's Guide - A Program for the Identification of Modal Parameters," by S. Rodriguez-Gomez and E. DiPasquale, 9/30/90, (PB91-171298, A04, MF-A01).
- NCEER-90-0027 "SARCF-II User's Guide - Seismic Analysis of Reinforced Concrete Frames," by S. Rodriguez-Gomez, Y.S. Chung and C. Meyer, 9/30/90, (PB91-171280, A05, MF-A01).
- NCEER-90-0028 "Viscous Dampers: Testing, Modeling and Application in Vibration and Seismic Isolation," by N. Makris and M.C. Constantinou, 12/20/90 (PB91-190561, A06, MF-A01).
- NCEER-90-0029 "Soil Effects on Earthquake Ground Motions in the Memphis Area," by H. Hwang, C.S. Lee, K.W. Ng and T.S. Chang, 8/2/90, (PB91-190751, A05, MF-A01).

- NCEER-91-0001 "Proceedings from the Third Japan-U.S. Workshop on Earthquake Resistant Design of Lifeline Facilities and Countermeasures for Soil Liquefaction, December 17-19, 1990," edited by T.D. O'Rourke and M. Hamada, 2/1/91, (PB91-179259, A99, MF-A04).
- NCEER-91-0002 "Physical Space Solutions of Non-Proportionally Damped Systems," by M. Tong, Z. Liang and G.C. Lee, 1/15/91, (PB91-179242, A04, MF-A01).
- NCEER-91-0003 "Seismic Response of Single Piles and Pile Groups," by K. Fan and G. Gazetas, 1/10/91, (PB92-174994, A04, MF-A01).
- NCEER-91-0004 "Damping of Structures: Part 1 - Theory of Complex Damping," by Z. Liang and G. Lee, 10/10/91, (PB92-197235, A12, MF-A03).
- NCEER-91-0005 "3D-BASIS - Nonlinear Dynamic Analysis of Three Dimensional Base Isolated Structures: Part II," by S. Nagarajaiah, A.M. Reinhorn and M.C. Constantinou, 2/28/91, (PB91-190553, A07, MF-A01). This report has been replaced by NCEER-93-0011.
- NCEER-91-0006 "A Multidimensional Hysteretic Model for Plasticity Deforming Metals in Energy Absorbing Devices," by E.J. Graesser and F.A. Cozzarelli, 4/9/91, (PB92-108364, A04, MF-A01).
- NCEER-91-0007 "A Framework for Customizable Knowledge-Based Expert Systems with an Application to a KBES for Evaluating the Seismic Resistance of Existing Buildings," by E.G. Ibarra-Anaya and S.J. Fennes, 4/9/91, (PB91-210930, A08, MF-A01).
- NCEER-91-0008 "Nonlinear Analysis of Steel Frames with Semi-Rigid Connections Using the Capacity Spectrum Method," by G.G. Deierlein, S-H. Hsieh, Y-J. Shen and J.F. Abel, 7/2/91, (PB92-113828, A05, MF-A01).
- NCEER-91-0009 "Earthquake Education Materials for Grades K-12," by K.E.K. Ross, 4/30/91, (PB91-212142, A06, MF-A01). This report has been replaced by NCEER-92-0018.
- NCEER-91-0010 "Phase Wave Velocities and Displacement Phase Differences in a Harmonically Oscillating Pile," by N. Makris and G. Gazetas, 7/8/91, (PB92-108356, A04, MF-A01).
- NCEER-91-0011 "Dynamic Characteristics of a Full-Size Five-Story Steel Structure and a 2/5 Scale Model," by K.C. Chang, G.C. Yao, G.C. Lee, D.S. Hao and Y.C. Yeh," 7/2/91, (PB93-116648, A06, MF-A02).
- NCEER-91-0012 "Seismic Response of a 2/5 Scale Steel Structure with Added Viscoelastic Dampers," by K.C. Chang, T.T. Soong, S-T. Oh and M.L. Lai, 5/17/91, (PB92-110816, A05, MF-A01).
- NCEER-91-0013 "Earthquake Response of Retaining Walls; Full-Scale Testing and Computational Modeling," by S. Alampalli and A-W.M. Elgamal, 6/20/91, not available.
- NCEER-91-0014 "3D-BASIS-M: Nonlinear Dynamic Analysis of Multiple Building Base Isolated Structures," by P.C. Tsopelas, S. Nagarajaiah, M.C. Constantinou and A.M. Reinhorn, 5/28/91, (PB92-113885, A09, MF-A02).
- NCEER-91-0015 "Evaluation of SEAOC Design Requirements for Sliding Isolated Structures," by D. Theodossiou and M.C. Constantinou, 6/10/91, (PB92-114602, A11, MF-A03).
- NCEER-91-0016 "Closed-Loop Modal Testing of a 27-Story Reinforced Concrete Flat Plate-Core Building," by H.R. Somaprasad, T. Toksoy, H. Yoshiyuki and A.E. Aktan, 7/15/91, (PB92-129980, A07, MF-A02).
- NCEER-91-0017 "Shake Table Test of a 1/6 Scale Two-Story Lightly Reinforced Concrete Building," by A.G. El-Attar, R.N. White and P. Gergely, 2/28/91, (PB92-222447, A06, MF-A02).
- NCEER-91-0018 "Shake Table Test of a 1/8 Scale Three-Story Lightly Reinforced Concrete Building," by A.G. El-Attar, R.N. White and P. Gergely, 2/28/91, (PB93-116630, A08, MF-A02).
- NCEER-91-0019 "Transfer Functions for Rigid Rectangular Foundations," by A.S. Veletsos, A.M. Prasad and W.H. Wu, 7/31/91, not available.

- NCEER-91-0020 "Hybrid Control of Seismic-Excited Nonlinear and Inelastic Structural Systems," by J.N. Yang, Z. Li and A. Daniellians, 8/1/91, (PB92-143171, A06, MF-A02).
- NCEER-91-0021 "The NCEER-91 Earthquake Catalog: Improved Intensity-Based Magnitudes and Recurrence Relations for U.S. Earthquakes East of New Madrid," by L. Seeber and J.G. Armbruster, 8/28/91, (PB92-176742, A06, MF-A02).
- NCEER-91-0022 "Proceedings from the Implementation of Earthquake Planning and Education in Schools: The Need for Change - The Roles of the Changemakers," by K.E.K. Ross and F. Winslow, 7/23/91, (PB92-129998, A12, MF-A03).
- NCEER-91-0023 "A Study of Reliability-Based Criteria for Seismic Design of Reinforced Concrete Frame Buildings," by H.H.M. Hwang and H-M. Hsu, 8/10/91, (PB92-140235, A09, MF-A02).
- NCEER-91-0024 "Experimental Verification of a Number of Structural System Identification Algorithms," by R.G. Ghanem, H. Gavin and M. Shinozuka, 9/18/91, (PB92-176577, A18, MF-A04).
- NCEER-91-0025 "Probabilistic Evaluation of Liquefaction Potential," by H.H.M. Hwang and C.S. Lee, 11/25/91, (PB92-143429, A05, MF-A01).
- NCEER-91-0026 "Instantaneous Optimal Control for Linear, Nonlinear and Hysteretic Structures - Stable Controllers," by J.N. Yang and Z. Li, 11/15/91, (PB92-163807, A04, MF-A01).
- NCEER-91-0027 "Experimental and Theoretical Study of a Sliding Isolation System for Bridges," by M.C. Constantinou, A. Kartoum, A.M. Reinhorn and P. Bradford, 11/15/91, (PB92-176973, A10, MF-A03).
- NCEER-92-0001 "Case Studies of Liquefaction and Lifeline Performance During Past Earthquakes, Volume 1: Japanese Case Studies," Edited by M. Hamada and T. O'Rourke, 2/17/92, (PB92-197243, A18, MF-A04).
- NCEER-92-0002 "Case Studies of Liquefaction and Lifeline Performance During Past Earthquakes, Volume 2: United States Case Studies," Edited by T. O'Rourke and M. Hamada, 2/17/92, (PB92-197250, A20, MF-A04).
- NCEER-92-0003 "Issues in Earthquake Education," Edited by K. Ross, 2/3/92, (PB92-222389, A07, MF-A02).
- NCEER-92-0004 "Proceedings from the First U.S. - Japan Workshop on Earthquake Protective Systems for Bridges," Edited by I.G. Buckle, 2/4/92, (PB94-142239, A99, MF-A06).
- NCEER-92-0005 "Seismic Ground Motion from a Haskell-Type Source in a Multiple-Layered Half-Space," A.P. Theoharis, G. Deodatis and M. Shinozuka, 1/2/92, not available.
- NCEER-92-0006 "Proceedings from the Site Effects Workshop," Edited by R. Whitman, 2/29/92, (PB92-197201, A04, MF-A01).
- NCEER-92-0007 "Engineering Evaluation of Permanent Ground Deformations Due to Seismically-Induced Liquefaction," by M.H. Baziar, R. Dobry and A-W.M. Elgamal, 3/24/92, (PB92-222421, A13, MF-A03).
- NCEER-92-0008 "A Procedure for the Seismic Evaluation of Buildings in the Central and Eastern United States," by C.D. Poland and J.O. Malley, 4/2/92, (PB92-222439, A20, MF-A04).
- NCEER-92-0009 "Experimental and Analytical Study of a Hybrid Isolation System Using Friction Controllable Sliding Bearings," by M.Q. Feng, S. Fujii and M. Shinozuka, 5/15/92, (PB93-150282, A06, MF-A02).
- NCEER-92-0010 "Seismic Resistance of Slab-Column Connections in Existing Non-Ductile Flat-Plate Buildings," by A.J. Durrani and Y. Du, 5/18/92, (PB93-116812, A06, MF-A02).
- NCEER-92-0011 "The Hysteretic and Dynamic Behavior of Brick Masonry Walls Upgraded by Ferrocement Coatings Under Cyclic Loading and Strong Simulated Ground Motion," by H. Lee and S.P. Prawl, 5/11/92, not available.
- NCEER-92-0012 "Study of Wire Rope Systems for Seismic Protection of Equipment in Buildings," by G.F. Demetriades, M.C. Constantinou and A.M. Reinhorn, 5/20/92, (PB93-116655, A08, MF-A02).

- NCEER-92-0013 "Shape Memory Structural Dampers: Material Properties, Design and Seismic Testing," by P.R. Witting and F.A. Cozzarelli, 5/26/92, (PB93-116663, A05, MF-A01).
- NCEER-92-0014 "Longitudinal Permanent Ground Deformation Effects on Buried Continuous Pipelines," by M.J. O'Rourke, and C. Nordberg, 6/15/92, (PB93-116671, A08, MF-A02).
- NCEER-92-0015 "A Simulation Method for Stationary Gaussian Random Functions Based on the Sampling Theorem," by M. Grigoriu and S. Balopoulou, 6/11/92, (PB93-127496, A05, MF-A01).
- NCEER-92-0016 "Gravity-Load-Designed Reinforced Concrete Buildings: Seismic Evaluation of Existing Construction and Detailing Strategies for Improved Seismic Resistance," by G.W. Hoffmann, S.K. Kunnath, A.M. Reinhorn and J.B. Mander, 7/15/92, (PB94-142007, A08, MF-A02).
- NCEER-92-0017 "Observations on Water System and Pipeline Performance in the Limón Area of Costa Rica Due to the April 22, 1991 Earthquake," by M. O'Rourke and D. Ballantyne, 6/30/92, (PB93-126811, A06, MF-A02).
- NCEER-92-0018 "Fourth Edition of Earthquake Education Materials for Grades K-12," Edited by K.E.K. Ross, 8/10/92, (PB93-114023, A07, MF-A02).
- NCEER-92-0019 "Proceedings from the Fourth Japan-U.S. Workshop on Earthquake Resistant Design of Lifeline Facilities and Countermeasures for Soil Liquefaction," Edited by M. Hamada and T.D. O'Rourke, 8/12/92, (PB93-163939, A99, MF-E11).
- NCEER-92-0020 "Active Bracing System: A Full Scale Implementation of Active Control," by A.M. Reinhorn, T.T. Soong, R.C. Lin, M.A. Riley, Y.P. Wang, S. Aizawa and M. Higashino, 8/14/92, (PB93-127512, A06, MF-A02).
- NCEER-92-0021 "Empirical Analysis of Horizontal Ground Displacement Generated by Liquefaction-Induced Lateral Spreads," by S.F. Bartlett and T.L. Youd, 8/17/92, (PB93-188241, A06, MF-A02).
- NCEER-92-0022 "IDARC Version 3.0: Inelastic Damage Analysis of Reinforced Concrete Structures," by S.K. Kunnath, A.M. Reinhorn and R.F. Lobo, 8/31/92, (PB93-227502, A07, MF-A02).
- NCEER-92-0023 "A Semi-Empirical Analysis of Strong-Motion Peaks in Terms of Seismic Source, Propagation Path and Local Site Conditions, by M. Kamiyama, M.J. O'Rourke and R. Flores-Berrones, 9/9/92, (PB93-150266, A08, MF-A02).
- NCEER-92-0024 "Seismic Behavior of Reinforced Concrete Frame Structures with Nonductile Details, Part I: Summary of Experimental Findings of Full Scale Beam-Column Joint Tests," by A. Beres, R.N. White and P. Gergely, 9/30/92, (PB93-227783, A05, MF-A01).
- NCEER-92-0025 "Experimental Results of Repaired and Retrofitted Beam-Column Joint Tests in Lightly Reinforced Concrete Frame Buildings," by A. Beres, S. El-Borgi, R.N. White and P. Gergely, 10/29/92, (PB93-227791, A05, MF-A01).
- NCEER-92-0026 "A Generalization of Optimal Control Theory: Linear and Nonlinear Structures," by J.N. Yang, Z. Li and S. Vongchavalitkul, 11/2/92, (PB93-188621, A05, MF-A01).
- NCEER-92-0027 "Seismic Resistance of Reinforced Concrete Frame Structures Designed Only for Gravity Loads: Part I - Design and Properties of a One-Third Scale Model Structure," by J.M. Bracci, A.M. Reinhorn and J.B. Mander, 12/1/92, (PB94-104502, A08, MF-A02).
- NCEER-92-0028 "Seismic Resistance of Reinforced Concrete Frame Structures Designed Only for Gravity Loads: Part II - Experimental Performance of Subassemblages," by L.E. Aycaardi, J.B. Mander and A.M. Reinhorn, 12/1/92, (PB94-104510, A08, MF-A02).
- NCEER-92-0029 "Seismic Resistance of Reinforced Concrete Frame Structures Designed Only for Gravity Loads: Part III - Experimental Performance and Analytical Study of a Structural Model," by J.M. Bracci, A.M. Reinhorn and J.B. Mander, 12/1/92, (PB93-227528, A09, MF-A01).

- NCEER-92-0030 "Evaluation of Seismic Retrofit of Reinforced Concrete Frame Structures: Part I - Experimental Performance of Retrofitted Subassemblages," by D. Choudhuri, J.B. Mander and A.M. Reinhorn, 12/8/92, (PB93-198307, A07, MF-A02).
- NCEER-92-0031 "Evaluation of Seismic Retrofit of Reinforced Concrete Frame Structures: Part II - Experimental Performance and Analytical Study of a Retrofitted Structural Model," by J.M. Bracci, A.M. Reinhorn and J.B. Mander, 12/8/92, (PB93-198315, A09, MF-A03).
- NCEER-92-0032 "Experimental and Analytical Investigation of Seismic Response of Structures with Supplemental Fluid Viscous Dampers," by M.C. Constantinou and M.D. Symans, 12/21/92, (PB93-191435, A10, MF-A03). This report is available only through NTIS (see address given above).
- NCEER-92-0033 "Reconnaissance Report on the Cairo, Egypt Earthquake of October 12, 1992," by M. Khater, 12/23/92, (PB93-188621, A03, MF-A01).
- NCEER-92-0034 "Low-Level Dynamic Characteristics of Four Tall Flat-Plate Buildings in New York City," by H. Gavin, S. Yuan, J. Grossman, E. Pekelis and K. Jacob, 12/28/92, (PB93-188217, A07, MF-A02).
- NCEER-93-0001 "An Experimental Study on the Seismic Performance of Brick-Infilled Steel Frames With and Without Retrofit," by J.B. Mander, B. Nair, K. Wojtkowski and J. Ma, 1/29/93, (PB93-227510, A07, MF-A02).
- NCEER-93-0002 "Social Accounting for Disaster Preparedness and Recovery Planning," by S. Cole, E. Pantoja and V. Razak, 2/22/93, (PB94-142114, A12, MF-A03).
- NCEER-93-0003 "Assessment of 1991 NEHRP Provisions for Nonstructural Components and Recommended Revisions," by T.T. Soong, G. Chen, Z. Wu, R-H. Zhang and M. Grigoriu, 3/1/93, (PB93-188639, A06, MF-A02).
- NCEER-93-0004 "Evaluation of Static and Response Spectrum Analysis Procedures of SEAOC/UBC for Seismic Isolated Structures," by C.W. Winters and M.C. Constantinou, 3/23/93, (PB93-198299, A10, MF-A03).
- NCEER-93-0005 "Earthquakes in the Northeast - Are We Ignoring the Hazard? A Workshop on Earthquake Science and Safety for Educators," edited by K.E.K. Ross, 4/2/93, (PB94-103066, A09, MF-A02).
- NCEER-93-0006 "Inelastic Response of Reinforced Concrete Structures with Viscoelastic Braces," by R.F. Lobo, J.M. Bracci, K.L. Shen, A.M. Reinhorn and T.T. Soong, 4/5/93, (PB93-227486, A05, MF-A02).
- NCEER-93-0007 "Seismic Testing of Installation Methods for Computers and Data Processing Equipment," by K. Kosar, T.T. Soong, K.L. Shen, J.A. HoLung and Y.K. Lin, 4/12/93, (PB93-198299, A07, MF-A02).
- NCEER-93-0008 "Retrofit of Reinforced Concrete Frames Using Added Dampers," by A. Reinhorn, M. Constantinou and C. Li, not available.
- NCEER-93-0009 "Seismic Behavior and Design Guidelines for Steel Frame Structures with Added Viscoelastic Dampers," by K.C. Chang, M.L. Lai, T.T. Soong, D.S. Hao and Y.C. Yeh, 5/1/93, (PB94-141959, A07, MF-A02).
- NCEER-93-0010 "Seismic Performance of Shear-Critical Reinforced Concrete Bridge Piers," by J.B. Mander, S.M. Waheed, M.T.A. Chaudhary and S.S. Chen, 5/12/93, (PB93-227494, A08, MF-A02).
- NCEER-93-0011 "3D-BASIS-TABS: Computer Program for Nonlinear Dynamic Analysis of Three Dimensional Base Isolated Structures," by S. Nagarajaiah, C. Li, A.M. Reinhorn and M.C. Constantinou, 8/2/93, (PB94-141819, A09, MF-A02).
- NCEER-93-0012 "Effects of Hydrocarbon Spills from an Oil Pipeline Break on Ground Water," by O.J. Helweg and H.H.M. Hwang, 8/3/93, (PB94-141942, A06, MF-A02).
- NCEER-93-0013 "Simplified Procedures for Seismic Design of Nonstructural Components and Assessment of Current Code Provisions," by M.P. Singh, L.E. Suarez, E.E. Matheu and G.O. Maldonado, 8/4/93, (PB94-141827, A09, MF-A02).
- NCEER-93-0014 "An Energy Approach to Seismic Analysis and Design of Secondary Systems," by G. Chen and T.T. Soong, 8/6/93, (PB94-142767, A11, MF-A03).

- NCEER-93-0015 "Proceedings from School Sites: Becoming Prepared for Earthquakes - Commemorating the Third Anniversary of the Loma Prieta Earthquake," Edited by F.E. Winslow and K.E.K. Ross, 8/16/93, (PB94-154275, A16, MF-A02).
- NCEER-93-0016 "Reconnaissance Report of Damage to Historic Monuments in Cairo, Egypt Following the October 12, 1992 Dahshur Earthquake," by D. Sykora, D. Look, G. Croci, E. Karaesmen and E. Karaesmen, 8/19/93, (PB94-142221, A08, MF-A02).
- NCEER-93-0017 "The Island of Guam Earthquake of August 8, 1993," by S.W. Swan and S.K. Harris, 9/30/93, (PB94-141843, A04, MF-A01).
- NCEER-93-0018 "Engineering Aspects of the October 12, 1992 Egyptian Earthquake," by A.W. Elgamal, M. Amer, K. Adalier and A. Abul-Fadl, 10/7/93, (PB94-141983, A05, MF-A01).
- NCEER-93-0019 "Development of an Earthquake Motion Simulator and its Application in Dynamic Centrifuge Testing," by I. Krstelj, Supervised by J.H. Prevost, 10/23/93, (PB94-181773, A-10, MF-A03).
- NCEER-93-0020 "NCEER-Taisei Corporation Research Program on Sliding Seismic Isolation Systems for Bridges: Experimental and Analytical Study of a Friction Pendulum System (FPS)," by M.C. Constantinou, P. Tsopelas, Y-S. Kim and S. Okamoto, 11/1/93, (PB94-142775, A08, MF-A02).
- NCEER-93-0021 "Finite Element Modeling of Elastomeric Seismic Isolation Bearings," by L.J. Billings, Supervised by R. Shepherd, 11/8/93, not available.
- NCEER-93-0022 "Seismic Vulnerability of Equipment in Critical Facilities: Life-Safety and Operational Consequences," by K. Porter, G.S. Johnson, M.M. Zadeh, C. Scawthorn and S. Eder, 11/24/93, (PB94-181765, A16, MF-A03).
- NCEER-93-0023 "Hokkaido Nansei-oki, Japan Earthquake of July 12, 1993, by P.I. Yanev and C.R. Scawthorn, 12/23/93, (PB94-181500, A07, MF-A01).
- NCEER-94-0001 "An Evaluation of Seismic Serviceability of Water Supply Networks with Application to the San Francisco Auxiliary Water Supply System," by I. Markov, Supervised by M. Grigoriu and T. O'Rourke, 1/21/94, (PB94-204013, A07, MF-A02).
- NCEER-94-0002 "NCEER-Taisei Corporation Research Program on Sliding Seismic Isolation Systems for Bridges: Experimental and Analytical Study of Systems Consisting of Sliding Bearings, Rubber Restoring Force Devices and Fluid Dampers," Volumes I and II, by P. Tsopelas, S. Okamoto, M.C. Constantinou, D. Ozaki and S. Fujii, 2/4/94, (PB94-181740, A09, MF-A02 and PB94-181757, A12, MF-A03).
- NCEER-94-0003 "A Markov Model for Local and Global Damage Indices in Seismic Analysis," by S. Rahman and M. Grigoriu, 2/18/94, (PB94-206000, A12, MF-A03).
- NCEER-94-0004 "Proceedings from the NCEER Workshop on Seismic Response of Masonry Infills," edited by D.P. Abrams, 3/1/94, (PB94-180783, A07, MF-A02).
- NCEER-94-0005 "The Northridge, California Earthquake of January 17, 1994: General Reconnaissance Report," edited by J.D. Goltz, 3/11/94, (PB94-193943, A10, MF-A03).
- NCEER-94-0006 "Seismic Energy Based Fatigue Damage Analysis of Bridge Columns: Part I - Evaluation of Seismic Capacity," by G.A. Chang and J.B. Mander, 3/14/94, (PB94-219185, A11, MF-A03).
- NCEER-94-0007 "Seismic Isolation of Multi-Story Frame Structures Using Spherical Sliding Isolation Systems," by T.M. Al-Hussaini, V.A. Zayas and M.C. Constantinou, 3/17/94, (PB94-193745, A09, MF-A02).
- NCEER-94-0008 "The Northridge, California Earthquake of January 17, 1994: Performance of Highway Bridges," edited by I.G. Buckle, 3/24/94, (PB94-193851, A06, MF-A02).
- NCEER-94-0009 "Proceedings of the Third U.S.-Japan Workshop on Earthquake Protective Systems for Bridges," edited by I.G. Buckle and I. Friedland, 3/31/94, (PB94-195815, A99, MF-A06).

- NCEER-94-0010 "3D-BASIS-ME: Computer Program for Nonlinear Dynamic Analysis of Seismically Isolated Single and Multiple Structures and Liquid Storage Tanks," by P.C. Tsopelas, M.C. Constantinou and A.M. Reinhorn, 4/12/94, (PB94-204922, A09, MF-A02).
- NCEER-94-0011 "The Northridge, California Earthquake of January 17, 1994: Performance of Gas Transmission Pipelines," by T.D. O'Rourke and M.C. Palmer, 5/16/94, (PB94-204989, A05, MF-A01).
- NCEER-94-0012 "Feasibility Study of Replacement Procedures and Earthquake Performance Related to Gas Transmission Pipelines," by T.D. O'Rourke and M.C. Palmer, 5/25/94, (PB94-206638, A09, MF-A02).
- NCEER-94-0013 "Seismic Energy Based Fatigue Damage Analysis of Bridge Columns: Part II - Evaluation of Seismic Demand," by G.A. Chang and J.B. Mander, 6/1/94, (PB95-18106, A08, MF-A02).
- NCEER-94-0014 "NCEER-Taisei Corporation Research Program on Sliding Seismic Isolation Systems for Bridges: Experimental and Analytical Study of a System Consisting of Sliding Bearings and Fluid Restoring Force/Damping Devices," by P. Tsopelas and M.C. Constantinou, 6/13/94, (PB94-219144, A10, MF-A03).
- NCEER-94-0015 "Generation of Hazard-Consistent Fragility Curves for Seismic Loss Estimation Studies," by H. Hwang and J-R. Huo, 6/14/94, (PB95-181996, A09, MF-A02).
- NCEER-94-0016 "Seismic Study of Building Frames with Added Energy-Absorbing Devices," by W.S. Pong, C.S. Tsai and G.C. Lee, 6/20/94, (PB94-219136, A10, A03).
- NCEER-94-0017 "Sliding Mode Control for Seismic-Excited Linear and Nonlinear Civil Engineering Structures," by J. Yang, J. Wu, A. Agrawal and Z. Li, 6/21/94, (PB95-138483, A06, MF-A02).
- NCEER-94-0018 "3D-BASIS-TABS Version 2.0: Computer Program for Nonlinear Dynamic Analysis of Three Dimensional Base Isolated Structures," by A.M. Reinhorn, S. Nagarajaiah, M.C. Constantinou, P. Tsopelas and R. Li, 6/22/94, (PB95-182176, A08, MF-A02).
- NCEER-94-0019 "Proceedings of the International Workshop on Civil Infrastructure Systems: Application of Intelligent Systems and Advanced Materials on Bridge Systems," Edited by G.C. Lee and K.C. Chang, 7/18/94, (PB95-252474, A20, MF-A04).
- NCEER-94-0020 "Study of Seismic Isolation Systems for Computer Floors," by V. Lambrou and M.C. Constantinou, 7/19/94, (PB95-138533, A10, MF-A03).
- NCEER-94-0021 "Proceedings of the U.S.-Italian Workshop on Guidelines for Seismic Evaluation and Rehabilitation of Unreinforced Masonry Buildings," Edited by D.P. Abrams and G.M. Calvi, 7/20/94, (PB95-138749, A13, MF-A03).
- NCEER-94-0022 "NCEER-Taisei Corporation Research Program on Sliding Seismic Isolation Systems for Bridges: Experimental and Analytical Study of a System Consisting of Lubricated PTFE Sliding Bearings and Mild Steel Dampers," by P. Tsopelas and M.C. Constantinou, 7/22/94, (PB95-182184, A08, MF-A02).
- NCEER-94-0023 "Development of Reliability-Based Design Criteria for Buildings Under Seismic Load," by Y.K. Wen, H. Hwang and M. Shinozuka, 8/1/94, (PB95-211934, A08, MF-A02).
- NCEER-94-0024 "Experimental Verification of Acceleration Feedback Control Strategies for an Active Tendon System," by S.J. Dyke, B.F. Spencer, Jr., P. Quast, M.K. Sain, D.C. Kaspari, Jr. and T.T. Soong, 8/29/94, (PB95-212320, A05, MF-A01).
- NCEER-94-0025 "Seismic Retrofitting Manual for Highway Bridges," Edited by I.G. Buckle and I.F. Friedland, published by the Federal Highway Administration (PB95-212676, A15, MF-A03).
- NCEER-94-0026 "Proceedings from the Fifth U.S.-Japan Workshop on Earthquake Resistant Design of Lifeline Facilities and Countermeasures Against Soil Liquefaction," Edited by T.D. O'Rourke and M. Hamada, 11/7/94, (PB95-220802, A99, MF-E08).

- NCEER-95-0001 “Experimental and Analytical Investigation of Seismic Retrofit of Structures with Supplemental Damping: Part 1 - Fluid Viscous Damping Devices,” by A.M. Reinhorn, C. Li and M.C. Constantinou, 1/3/95, (PB95-266599, A09, MF-A02).
- NCEER-95-0002 “Experimental and Analytical Study of Low-Cycle Fatigue Behavior of Semi-Rigid Top-And-Seat Angle Connections,” by G. Pekcan, J.B. Mander and S.S. Chen, 1/5/95, (PB95-220042, A07, MF-A02).
- NCEER-95-0003 “NCEER-ATC Joint Study on Fragility of Buildings,” by T. Anagnos, C. Rojahn and A.S. Kiremidjian, 1/20/95, (PB95-220026, A06, MF-A02).
- NCEER-95-0004 “Nonlinear Control Algorithms for Peak Response Reduction,” by Z. Wu, T.T. Soong, V. Gattulli and R.C. Lin, 2/16/95, (PB95-220349, A05, MF-A01).
- NCEER-95-0005 “Pipeline Replacement Feasibility Study: A Methodology for Minimizing Seismic and Corrosion Risks to Underground Natural Gas Pipelines,” by R.T. Eguchi, H.A. Seligson and D.G. Honegger, 3/2/95, (PB95-252326, A06, MF-A02).
- NCEER-95-0006 “Evaluation of Seismic Performance of an 11-Story Frame Building During the 1994 Northridge Earthquake,” by F. Naeim, R. DiSulio, K. Benuska, A. Reinhorn and C. Li, not available.
- NCEER-95-0007 “Prioritization of Bridges for Seismic Retrofitting,” by N. Basöz and A.S. Kiremidjian, 4/24/95, (PB95-252300, A08, MF-A02).
- NCEER-95-0008 “Method for Developing Motion Damage Relationships for Reinforced Concrete Frames,” by A. Singhal and A.S. Kiremidjian, 5/11/95, (PB95-266607, A06, MF-A02).
- NCEER-95-0009 “Experimental and Analytical Investigation of Seismic Retrofit of Structures with Supplemental Damping: Part II - Friction Devices,” by C. Li and A.M. Reinhorn, 7/6/95, (PB96-128087, A11, MF-A03).
- NCEER-95-0010 “Experimental Performance and Analytical Study of a Non-Ductile Reinforced Concrete Frame Structure Retrofitted with Elastomeric Spring Dampers,” by G. Pekcan, J.B. Mander and S.S. Chen, 7/14/95, (PB96-137161, A08, MF-A02).
- NCEER-95-0011 “Development and Experimental Study of Semi-Active Fluid Damping Devices for Seismic Protection of Structures,” by M.D. Symans and M.C. Constantinou, 8/3/95, (PB96-136940, A23, MF-A04).
- NCEER-95-0012 “Real-Time Structural Parameter Modification (RSPM): Development of Innervated Structures,” by Z. Liang, M. Tong and G.C. Lee, 4/11/95, (PB96-137153, A06, MF-A01).
- NCEER-95-0013 “Experimental and Analytical Investigation of Seismic Retrofit of Structures with Supplemental Damping: Part III - Viscous Damping Walls,” by A.M. Reinhorn and C. Li, 10/1/95, (PB96-176409, A11, MF-A03).
- NCEER-95-0014 “Seismic Fragility Analysis of Equipment and Structures in a Memphis Electric Substation,” by J-R. Huo and H.H.M. Hwang, 8/10/95, (PB96-128087, A09, MF-A02).
- NCEER-95-0015 “The Hanshin-Awaji Earthquake of January 17, 1995: Performance of Lifelines,” Edited by M. Shinozuka, 11/3/95, (PB96-176383, A15, MF-A03).
- NCEER-95-0016 “Highway Culvert Performance During Earthquakes,” by T.L. Youd and C.J. Beckman, available as NCEER-96-0015.
- NCEER-95-0017 “The Hanshin-Awaji Earthquake of January 17, 1995: Performance of Highway Bridges,” Edited by I.G. Buckle, 12/1/95, not available.
- NCEER-95-0018 “Modeling of Masonry Infill Panels for Structural Analysis,” by A.M. Reinhorn, A. Madan, R.E. Valles, Y. Reichmann and J.B. Mander, 12/8/95, (PB97-110886, MF-A01, A06).
- NCEER-95-0019 “Optimal Polynomial Control for Linear and Nonlinear Structures,” by A.K. Agrawal and J.N. Yang, 12/11/95, (PB96-168737, A07, MF-A02).

- NCEER-95-0020 “Retrofit of Non-Ductile Reinforced Concrete Frames Using Friction Dampers,” by R.S. Rao, P. Gergely and R.N. White, 12/22/95, (PB97-133508, A10, MF-A02).
- NCEER-95-0021 “Parametric Results for Seismic Response of Pile-Supported Bridge Bents,” by G. Mylonakis, A. Nikolaou and G. Gazetas, 12/22/95, (PB97-100242, A12, MF-A03).
- NCEER-95-0022 “Kinematic Bending Moments in Seismically Stressed Piles,” by A. Nikolaou, G. Mylonakis and G. Gazetas, 12/23/95, (PB97-113914, MF-A03, A13).
- NCEER-96-0001 “Dynamic Response of Unreinforced Masonry Buildings with Flexible Diaphragms,” by A.C. Costley and D.P. Abrams, 10/10/96, (PB97-133573, MF-A03, A15).
- NCEER-96-0002 “State of the Art Review: Foundations and Retaining Structures,” by I. Po Lam, not available.
- NCEER-96-0003 “Ductility of Rectangular Reinforced Concrete Bridge Columns with Moderate Confinement,” by N. Wehbe, M. Saiidi, D. Sanders and B. Douglas, 11/7/96, (PB97-133557, A06, MF-A02).
- NCEER-96-0004 “Proceedings of the Long-Span Bridge Seismic Research Workshop,” edited by I.G. Buckle and I.M. Friedland, not available.
- NCEER-96-0005 “Establish Representative Pier Types for Comprehensive Study: Eastern United States,” by J. Kulicki and Z. Prucz, 5/28/96, (PB98-119217, A07, MF-A02).
- NCEER-96-0006 “Establish Representative Pier Types for Comprehensive Study: Western United States,” by R. Imbsen, R.A. Schamber and T.A. Osterkamp, 5/28/96, (PB98-118607, A07, MF-A02).
- NCEER-96-0007 “Nonlinear Control Techniques for Dynamical Systems with Uncertain Parameters,” by R.G. Ghanem and M.I. Bujakov, 5/27/96, (PB97-100259, A17, MF-A03).
- NCEER-96-0008 “Seismic Evaluation of a 30-Year Old Non-Ductile Highway Bridge Pier and Its Retrofit,” by J.B. Mander, B. Mahmoodzadegan, S. Bhadra and S.S. Chen, 5/31/96, (PB97-110902, MF-A03, A10).
- NCEER-96-0009 “Seismic Performance of a Model Reinforced Concrete Bridge Pier Before and After Retrofit,” by J.B. Mander, J.H. Kim and C.A. Ligozio, 5/31/96, (PB97-110910, MF-A02, A10).
- NCEER-96-0010 “IDARC2D Version 4.0: A Computer Program for the Inelastic Damage Analysis of Buildings,” by R.E. Valles, A.M. Reinhorn, S.K. Kunnath, C. Li and A. Madan, 6/3/96, (PB97-100234, A17, MF-A03).
- NCEER-96-0011 “Estimation of the Economic Impact of Multiple Lifeline Disruption: Memphis Light, Gas and Water Division Case Study,” by S.E. Chang, H.A. Seligson and R.T. Eguchi, 8/16/96, (PB97-133490, A11, MF-A03).
- NCEER-96-0012 “Proceedings from the Sixth Japan-U.S. Workshop on Earthquake Resistant Design of Lifeline Facilities and Countermeasures Against Soil Liquefaction, Edited by M. Hamada and T. O’Rourke, 9/11/96, (PB97-133581, A99, MF-A06).
- NCEER-96-0013 “Chemical Hazards, Mitigation and Preparedness in Areas of High Seismic Risk: A Methodology for Estimating the Risk of Post-Earthquake Hazardous Materials Release,” by H.A. Seligson, R.T. Eguchi, K.J. Tierney and K. Richmond, 11/7/96, (PB97-133565, MF-A02, A08).
- NCEER-96-0014 “Response of Steel Bridge Bearings to Reversed Cyclic Loading,” by J.B. Mander, D-K. Kim, S.S. Chen and G.J. Premus, 11/13/96, (PB97-140735, A12, MF-A03).
- NCEER-96-0015 “Highway Culvert Performance During Past Earthquakes,” by T.L. Youd and C.J. Beckman, 11/25/96, (PB97-133532, A06, MF-A01).
- NCEER-97-0001 “Evaluation, Prevention and Mitigation of Pounding Effects in Building Structures,” by R.E. Valles and A.M. Reinhorn, 2/20/97, (PB97-159552, A14, MF-A03).
- NCEER-97-0002 “Seismic Design Criteria for Bridges and Other Highway Structures,” by C. Rojahn, R. Mayes, D.G. Anderson, J. Clark, J.H. Hom, R.V. Nutt and M.J. O’Rourke, 4/30/97, (PB97-194658, A06, MF-A03).

- NCEER-97-0003 "Proceedings of the U.S.-Italian Workshop on Seismic Evaluation and Retrofit," Edited by D.P. Abrams and G.M. Calvi, 3/19/97, (PB97-194666, A13, MF-A03).
- NCEER-97-0004 "Investigation of Seismic Response of Buildings with Linear and Nonlinear Fluid Viscous Dampers," by A.A. Seleemah and M.C. Constantinou, 5/21/97, (PB98-109002, A15, MF-A03).
- NCEER-97-0005 "Proceedings of the Workshop on Earthquake Engineering Frontiers in Transportation Facilities," edited by G.C. Lee and I.M. Friedland, 8/29/97, (PB98-128911, A25, MR-A04).
- NCEER-97-0006 "Cumulative Seismic Damage of Reinforced Concrete Bridge Piers," by S.K. Kunnath, A. El-Bahy, A. Taylor and W. Stone, 9/2/97, (PB98-108814, A11, MF-A03).
- NCEER-97-0007 "Structural Details to Accommodate Seismic Movements of Highway Bridges and Retaining Walls," by R.A. Imbsen, R.A. Schamber, E. Thorkildsen, A. Kartoum, B.T. Martin, T.N. Rosser and J.M. Kulicki, 9/3/97, (PB98-108996, A09, MF-A02).
- NCEER-97-0008 "A Method for Earthquake Motion-Damage Relationships with Application to Reinforced Concrete Frames," by A. Singhal and A.S. Kiremidjian, 9/10/97, (PB98-108988, A13, MF-A03).
- NCEER-97-0009 "Seismic Analysis and Design of Bridge Abutments Considering Sliding and Rotation," by K. Fishman and R. Richards, Jr., 9/15/97, (PB98-108897, A06, MF-A02).
- NCEER-97-0010 "Proceedings of the FHWA/NCEER Workshop on the National Representation of Seismic Ground Motion for New and Existing Highway Facilities," edited by I.M. Friedland, M.S. Power and R.L. Mayes, 9/22/97, (PB98-128903, A21, MF-A04).
- NCEER-97-0011 "Seismic Analysis for Design or Retrofit of Gravity Bridge Abutments," by K.L. Fishman, R. Richards, Jr. and R.C. Divito, 10/2/97, (PB98-128937, A08, MF-A02).
- NCEER-97-0012 "Evaluation of Simplified Methods of Analysis for Yielding Structures," by P. Tsopelas, M.C. Constantinou, C.A. Kircher and A.S. Whittaker, 10/31/97, (PB98-128929, A10, MF-A03).
- NCEER-97-0013 "Seismic Design of Bridge Columns Based on Control and Repairability of Damage," by C-T. Cheng and J.B. Mander, 12/8/97, (PB98-144249, A11, MF-A03).
- NCEER-97-0014 "Seismic Resistance of Bridge Piers Based on Damage Avoidance Design," by J.B. Mander and C-T. Cheng, 12/10/97, (PB98-144223, A09, MF-A02).
- NCEER-97-0015 "Seismic Response of Nominally Symmetric Systems with Strength Uncertainty," by S. Balopoulou and M. Grigoriu, 12/23/97, (PB98-153422, A11, MF-A03).
- NCEER-97-0016 "Evaluation of Seismic Retrofit Methods for Reinforced Concrete Bridge Columns," by T.J. Wipf, F.W. Klaiber and F.M. Russo, 12/28/97, (PB98-144215, A12, MF-A03).
- NCEER-97-0017 "Seismic Fragility of Existing Conventional Reinforced Concrete Highway Bridges," by C.L. Mullen and A.S. Cakmak, 12/30/97, (PB98-153406, A08, MF-A02).
- NCEER-97-0018 "Loss Assessment of Memphis Buildings," edited by D.P. Abrams and M. Shinozuka, 12/31/97, (PB98-144231, A13, MF-A03).
- NCEER-97-0019 "Seismic Evaluation of Frames with Infill Walls Using Quasi-static Experiments," by K.M. Mosalam, R.N. White and P. Gergely, 12/31/97, (PB98-153455, A07, MF-A02).
- NCEER-97-0020 "Seismic Evaluation of Frames with Infill Walls Using Pseudo-dynamic Experiments," by K.M. Mosalam, R.N. White and P. Gergely, 12/31/97, (PB98-153430, A07, MF-A02).
- NCEER-97-0021 "Computational Strategies for Frames with Infill Walls: Discrete and Smeared Crack Analyses and Seismic Fragility," by K.M. Mosalam, R.N. White and P. Gergely, 12/31/97, (PB98-153414, A10, MF-A02).

- NCEER-97-0022 "Proceedings of the NCEER Workshop on Evaluation of Liquefaction Resistance of Soils," edited by T.L. Youd and I.M. Idriss, 12/31/97, (PB98-155617, A15, MF-A03).
- MCEER-98-0001 "Extraction of Nonlinear Hysteretic Properties of Seismically Isolated Bridges from Quick-Release Field Tests," by Q. Chen, B.M. Douglas, E.M. Maragakis and I.G. Buckle, 5/26/98, (PB99-118838, A06, MF-A01).
- MCEER-98-0002 "Methodologies for Evaluating the Importance of Highway Bridges," by A. Thomas, S. Eshenaur and J. Kulicki, 5/29/98, (PB99-118846, A10, MF-A02).
- MCEER-98-0003 "Capacity Design of Bridge Piers and the Analysis of Overstrength," by J.B. Mander, A. Dutta and P. Goel, 6/1/98, (PB99-118853, A09, MF-A02).
- MCEER-98-0004 "Evaluation of Bridge Damage Data from the Loma Prieta and Northridge, California Earthquakes," by N. Basoz and A. Kiremidjian, 6/2/98, (PB99-118861, A15, MF-A03).
- MCEER-98-0005 "Screening Guide for Rapid Assessment of Liquefaction Hazard at Highway Bridge Sites," by T. L. Youd, 6/16/98, (PB99-118879, A06, not available on microfiche).
- MCEER-98-0006 "Structural Steel and Steel/Concrete Interface Details for Bridges," by P. Ritchie, N. Kaulh and J. Kulicki, 7/13/98, (PB99-118945, A06, MF-A01).
- MCEER-98-0007 "Capacity Design and Fatigue Analysis of Confined Concrete Columns," by A. Dutta and J.B. Mander, 7/14/98, (PB99-118960, A14, MF-A03).
- MCEER-98-0008 "Proceedings of the Workshop on Performance Criteria for Telecommunication Services Under Earthquake Conditions," edited by A.J. Schiff, 7/15/98, (PB99-118952, A08, MF-A02).
- MCEER-98-0009 "Fatigue Analysis of Unconfined Concrete Columns," by J.B. Mander, A. Dutta and J.H. Kim, 9/12/98, (PB99-123655, A10, MF-A02).
- MCEER-98-0010 "Centrifuge Modeling of Cyclic Lateral Response of Pile-Cap Systems and Seat-Type Abutments in Dry Sands," by A.D. Gadre and R. Dobry, 10/2/98, (PB99-123606, A13, MF-A03).
- MCEER-98-0011 "IDARC-BRIDGE: A Computational Platform for Seismic Damage Assessment of Bridge Structures," by A.M. Reinhorn, V. Simeonov, G. Mylonakis and Y. Reichman, 10/2/98, (PB99-162919, A15, MF-A03).
- MCEER-98-0012 "Experimental Investigation of the Dynamic Response of Two Bridges Before and After Retrofitting with Elastomeric Bearings," by D.A. Wendichansky, S.S. Chen and J.B. Mander, 10/2/98, (PB99-162927, A15, MF-A03).
- MCEER-98-0013 "Design Procedures for Hinge Restrainers and Hinge Sear Width for Multiple-Frame Bridges," by R. Des Roches and G.L. Fenves, 11/3/98, (PB99-140477, A13, MF-A03).
- MCEER-98-0014 "Response Modification Factors for Seismically Isolated Bridges," by M.C. Constantinou and J.K. Quarshie, 11/3/98, (PB99-140485, A14, MF-A03).
- MCEER-98-0015 "Proceedings of the U.S.-Italy Workshop on Seismic Protective Systems for Bridges," edited by I.M. Friedland and M.C. Constantinou, 11/3/98, (PB2000-101711, A22, MF-A04).
- MCEER-98-0016 "Appropriate Seismic Reliability for Critical Equipment Systems: Recommendations Based on Regional Analysis of Financial and Life Loss," by K. Porter, C. Scawthorn, C. Taylor and N. Blais, 11/10/98, (PB99-157265, A08, MF-A02).
- MCEER-98-0017 "Proceedings of the U.S. Japan Joint Seminar on Civil Infrastructure Systems Research," edited by M. Shinozuka and A. Rose, 11/12/98, (PB99-156713, A16, MF-A03).
- MCEER-98-0018 "Modeling of Pile Footings and Drilled Shafts for Seismic Design," by I. PoLam, M. Kapuskar and D. Chaudhuri, 12/21/98, (PB99-157257, A09, MF-A02).

- MCEER-99-0001 "Seismic Evaluation of a Masonry Infilled Reinforced Concrete Frame by Pseudodynamic Testing," by S.G. Buonopane and R.N. White, 2/16/99, (PB99-162851, A09, MF-A02).
- MCEER-99-0002 "Response History Analysis of Structures with Seismic Isolation and Energy Dissipation Systems: Verification Examples for Program SAP2000," by J. Scheller and M.C. Constantinou, 2/22/99, (PB99-162869, A08, MF-A02).
- MCEER-99-0003 "Experimental Study on the Seismic Design and Retrofit of Bridge Columns Including Axial Load Effects," by A. Dutta, T. Kokorina and J.B. Mander, 2/22/99, (PB99-162877, A09, MF-A02).
- MCEER-99-0004 "Experimental Study of Bridge Elastomeric and Other Isolation and Energy Dissipation Systems with Emphasis on Uplift Prevention and High Velocity Near-source Seismic Excitation," by A. Kasalanati and M. C. Constantinou, 2/26/99, (PB99-162885, A12, MF-A03).
- MCEER-99-0005 "Truss Modeling of Reinforced Concrete Shear-flexure Behavior," by J.H. Kim and J.B. Mander, 3/8/99, (PB99-163693, A12, MF-A03).
- MCEER-99-0006 "Experimental Investigation and Computational Modeling of Seismic Response of a 1:4 Scale Model Steel Structure with a Load Balancing Supplemental Damping System," by G. Pekcan, J.B. Mander and S.S. Chen, 4/2/99, (PB99-162893, A11, MF-A03).
- MCEER-99-0007 "Effect of Vertical Ground Motions on the Structural Response of Highway Bridges," by M.R. Button, C.J. Cronin and R.L. Mayes, 4/10/99, (PB2000-101411, A10, MF-A03).
- MCEER-99-0008 "Seismic Reliability Assessment of Critical Facilities: A Handbook, Supporting Documentation, and Model Code Provisions," by G.S. Johnson, R.E. Sheppard, M.D. Quilici, S.J. Eder and C.R. Scawthorn, 4/12/99, (PB2000-101701, A18, MF-A04).
- MCEER-99-0009 "Impact Assessment of Selected MCEER Highway Project Research on the Seismic Design of Highway Structures," by C. Rojahn, R. Mayes, D.G. Anderson, J.H. Clark, D'Appolonia Engineering, S. Gloyd and R.V. Nutt, 4/14/99, (PB99-162901, A10, MF-A02).
- MCEER-99-0010 "Site Factors and Site Categories in Seismic Codes," by R. Dobry, R. Ramos and M.S. Power, 7/19/99, (PB2000-101705, A08, MF-A02).
- MCEER-99-0011 "Restrainer Design Procedures for Multi-Span Simply-Supported Bridges," by M.J. Randall, M. Saiidi, E. Maragakis and T. Isakovic, 7/20/99, (PB2000-101702, A10, MF-A02).
- MCEER-99-0012 "Property Modification Factors for Seismic Isolation Bearings," by M.C. Constantinou, P. Tsopelas, A. Kasalanati and E. Wolff, 7/20/99, (PB2000-103387, A11, MF-A03).
- MCEER-99-0013 "Critical Seismic Issues for Existing Steel Bridges," by P. Ritchie, N. Kauh and J. Kulicki, 7/20/99, (PB2000-101697, A09, MF-A02).
- MCEER-99-0014 "Nonstructural Damage Database," by A. Kao, T.T. Soong and A. Vender, 7/24/99, (PB2000-101407, A06, MF-A01).
- MCEER-99-0015 "Guide to Remedial Measures for Liquefaction Mitigation at Existing Highway Bridge Sites," by H.G. Cooke and J. K. Mitchell, 7/26/99, (PB2000-101703, A11, MF-A03).
- MCEER-99-0016 "Proceedings of the MCEER Workshop on Ground Motion Methodologies for the Eastern United States," edited by N. Abrahamson and A. Becker, 8/11/99, (PB2000-103385, A07, MF-A02).
- MCEER-99-0017 "Quindío, Colombia Earthquake of January 25, 1999: Reconnaissance Report," by A.P. Asfura and P.J. Flores, 10/4/99, (PB2000-106893, A06, MF-A01).
- MCEER-99-0018 "Hysteretic Models for Cyclic Behavior of Deteriorating Inelastic Structures," by M.V. Sivaselvan and A.M. Reinhorn, 11/5/99, (PB2000-103386, A08, MF-A02).

- MCEER-99-0019 "Proceedings of the 7th U.S.- Japan Workshop on Earthquake Resistant Design of Lifeline Facilities and Countermeasures Against Soil Liquefaction," edited by T.D. O'Rourke, J.P. Bardet and M. Hamada, 11/19/99, (PB2000-103354, A99, MF-A06).
- MCEER-99-0020 "Development of Measurement Capability for Micro-Vibration Evaluations with Application to Chip Fabrication Facilities," by G.C. Lee, Z. Liang, J.W. Song, J.D. Shen and W.C. Liu, 12/1/99, (PB2000-105993, A08, MF-A02).
- MCEER-99-0021 "Design and Retrofit Methodology for Building Structures with Supplemental Energy Dissipating Systems," by G. Pekcan, J.B. Mander and S.S. Chen, 12/31/99, (PB2000-105994, A11, MF-A03).
- MCEER-00-0001 "The Marmara, Turkey Earthquake of August 17, 1999: Reconnaissance Report," edited by C. Scawthorn; with major contributions by M. Bruneau, R. Eguchi, T. Holzer, G. Johnson, J. Mander, J. Mitchell, W. Mitchell, A. Papageorgiou, C. Scaethorn, and G. Webb, 3/23/00, (PB2000-106200, A11, MF-A03).
- MCEER-00-0002 "Proceedings of the MCEER Workshop for Seismic Hazard Mitigation of Health Care Facilities," edited by G.C. Lee, M. Ettouney, M. Grigoriu, J. Hauer and J. Nigg, 3/29/00, (PB2000-106892, A08, MF-A02).
- MCEER-00-0003 "The Chi-Chi, Taiwan Earthquake of September 21, 1999: Reconnaissance Report," edited by G.C. Lee and C.H. Loh, with major contributions by G.C. Lee, M. Bruneau, I.G. Buckle, S.E. Chang, P.J. Flores, T.D. O'Rourke, M. Shinozuka, T.T. Soong, C-H. Loh, K-C. Chang, Z-J. Chen, J-S. Hwang, M-L. Lin, G-Y. Liu, K-C. Tsai, G.C. Yao and C-L. Yen, 4/30/00, (PB2001-100980, A10, MF-A02).
- MCEER-00-0004 "Seismic Retrofit of End-Sway Frames of Steel Deck-Truss Bridges with a Supplemental Tendon System: Experimental and Analytical Investigation," by G. Pekcan, J.B. Mander and S.S. Chen, 7/1/00, (PB2001-100982, A10, MF-A02).
- MCEER-00-0005 "Sliding Fragility of Unrestrained Equipment in Critical Facilities," by W.H. Chong and T.T. Soong, 7/5/00, (PB2001-100983, A08, MF-A02).
- MCEER-00-0006 "Seismic Response of Reinforced Concrete Bridge Pier Walls in the Weak Direction," by N. Abo-Shadi, M. Saiidi and D. Sanders, 7/17/00, (PB2001-100981, A17, MF-A03).
- MCEER-00-0007 "Low-Cycle Fatigue Behavior of Longitudinal Reinforcement in Reinforced Concrete Bridge Columns," by J. Brown and S.K. Kunnath, 7/23/00, (PB2001-104392, A08, MF-A02).
- MCEER-00-0008 "Soil Structure Interaction of Bridges for Seismic Analysis," I. PoLam and H. Law, 9/25/00, (PB2001-105397, A08, MF-A02).
- MCEER-00-0009 "Proceedings of the First MCEER Workshop on Mitigation of Earthquake Disaster by Advanced Technologies (MEDAT-1), edited by M. Shinozuka, D.J. Inman and T.D. O'Rourke, 11/10/00, (PB2001-105399, A14, MF-A03).
- MCEER-00-0010 "Development and Evaluation of Simplified Procedures for Analysis and Design of Buildings with Passive Energy Dissipation Systems, Revision 01," by O.M. Ramirez, M.C. Constantinou, C.A. Kircher, A.S. Whittaker, M.W. Johnson, J.D. Gomez and C. Chrysostomou, 11/16/01, (PB2001-105523, A23, MF-A04).
- MCEER-00-0011 "Dynamic Soil-Foundation-Structure Interaction Analyses of Large Caissons," by C-Y. Chang, C-M. Mok, Z-L. Wang, R. Settgast, F. Waggoner, M.A. Ketchum, H.M. Gonnermann and C-C. Chin, 12/30/00, (PB2001-104373, A07, MF-A02).
- MCEER-00-0012 "Experimental Evaluation of Seismic Performance of Bridge Restrainers," by A.G. Vlassis, E.M. Maragakis and M. Saiid Saiidi, 12/30/00, (PB2001-104354, A09, MF-A02).
- MCEER-00-0013 "Effect of Spatial Variation of Ground Motion on Highway Structures," by M. Shinozuka, V. Saxena and G. Deodatis, 12/31/00, (PB2001-108755, A13, MF-A03).
- MCEER-00-0014 "A Risk-Based Methodology for Assessing the Seismic Performance of Highway Systems," by S.D. Werner, C.E. Taylor, J.E. Moore, II, J.S. Walton and S. Cho, 12/31/00, (PB2001-108756, A14, MF-A03).

- MCEER-01-0001 “Experimental Investigation of P-Delta Effects to Collapse During Earthquakes,” by D. Vian and M. Bruneau, 6/25/01, (PB2002-100534, A17, MF-A03).
- MCEER-01-0002 “Proceedings of the Second MCEER Workshop on Mitigation of Earthquake Disaster by Advanced Technologies (MEDAT-2),” edited by M. Bruneau and D.J. Inman, 7/23/01, (PB2002-100434, A16, MF-A03).
- MCEER-01-0003 “Sensitivity Analysis of Dynamic Systems Subjected to Seismic Loads,” by C. Roth and M. Grigoriu, 9/18/01, (PB2003-100884, A12, MF-A03).
- MCEER-01-0004 “Overcoming Obstacles to Implementing Earthquake Hazard Mitigation Policies: Stage 1 Report,” by D.J. Alesch and W.J. Petak, 12/17/01, (PB2002-107949, A07, MF-A02).
- MCEER-01-0005 “Updating Real-Time Earthquake Loss Estimates: Methods, Problems and Insights,” by C.E. Taylor, S.E. Chang and R.T. Eguchi, 12/17/01, (PB2002-107948, A05, MF-A01).
- MCEER-01-0006 “Experimental Investigation and Retrofit of Steel Pile Foundations and Pile Bents Under Cyclic Lateral Loadings,” by A. Shama, J. Mander, B. Blabac and S. Chen, 12/31/01, (PB2002-107950, A13, MF-A03).
- MCEER-02-0001 “Assessment of Performance of Bolu Viaduct in the 1999 Duzce Earthquake in Turkey” by P.C. Roussis, M.C. Constantinou, M. Erdik, E. Durukal and M. Dicleli, 5/8/02, (PB2003-100883, A08, MF-A02).
- MCEER-02-0002 “Seismic Behavior of Rail Counterweight Systems of Elevators in Buildings,” by M.P. Singh, Rildova and L.E. Suarez, 5/27/02. (PB2003-100882, A11, MF-A03).
- MCEER-02-0003 “Development of Analysis and Design Procedures for Spread Footings,” by G. Mylonakis, G. Gazetas, S. Nikolaou and A. Chauncey, 10/02/02, (PB2004-101636, A13, MF-A03, CD-A13).
- MCEER-02-0004 “Bare-Earth Algorithms for Use with SAR and LIDAR Digital Elevation Models,” by C.K. Huyck, R.T. Eguchi and B. Houshmand, 10/16/02, (PB2004-101637, A07, CD-A07).
- MCEER-02-0005 “Review of Energy Dissipation of Compression Members in Concentrically Braced Frames,” by K.Lee and M. Bruneau, 10/18/02, (PB2004-101638, A10, CD-A10).
- MCEER-03-0001 “Experimental Investigation of Light-Gauge Steel Plate Shear Walls for the Seismic Retrofit of Buildings” by J. Berman and M. Bruneau, 5/2/03, (PB2004-101622, A10, MF-A03, CD-A10).
- MCEER-03-0002 “Statistical Analysis of Fragility Curves,” by M. Shinozuka, M.Q. Feng, H. Kim, T. Uzawa and T. Ueda, 6/16/03, (PB2004-101849, A09, CD-A09).
- MCEER-03-0003 “Proceedings of the Eighth U.S.-Japan Workshop on Earthquake Resistant Design of Lifeline Facilities and Countermeasures Against Liquefaction,” edited by M. Hamada, J.P. Bardet and T.D. O’Rourke, 6/30/03, (PB2004-104386, A99, CD-A99).
- MCEER-03-0004 “Proceedings of the PRC-US Workshop on Seismic Analysis and Design of Special Bridges,” edited by L.C. Fan and G.C. Lee, 7/15/03, (PB2004-104387, A14, CD-A14).
- MCEER-03-0005 “Urban Disaster Recovery: A Framework and Simulation Model,” by S.B. Miles and S.E. Chang, 7/25/03, (PB2004-104388, A07, CD-A07).
- MCEER-03-0006 “Behavior of Underground Piping Joints Due to Static and Dynamic Loading,” by R.D. Meis, M. Maragakis and R. Siddharthan, 11/17/03, (PB2005-102194, A13, MF-A03, CD-A00).
- MCEER-04-0001 “Experimental Study of Seismic Isolation Systems with Emphasis on Secondary System Response and Verification of Accuracy of Dynamic Response History Analysis Methods,” by E. Wolff and M. Constantinou, 1/16/04 (PB2005-102195, A99, MF-E08, CD-A00).
- MCEER-04-0002 “Tension, Compression and Cyclic Testing of Engineered Cementitious Composite Materials,” by K. Kesner and S.L. Billington, 3/1/04, (PB2005-102196, A08, CD-A08).

- MCEER-04-0003 "Cyclic Testing of Braces Laterally Restrained by Steel Studs to Enhance Performance During Earthquakes," by O.C. Celik, J.W. Berman and M. Bruneau, 3/16/04, (PB2005-102197, A13, MF-A03, CD-A00).
- MCEER-04-0004 "Methodologies for Post Earthquake Building Damage Detection Using SAR and Optical Remote Sensing: Application to the August 17, 1999 Marmara, Turkey Earthquake," by C.K. Huyck, B.J. Adams, S. Cho, R.T. Eguchi, B. Mansouri and B. Houshmand, 6/15/04, (PB2005-104888, A10, CD-A00).
- MCEER-04-0005 "Nonlinear Structural Analysis Towards Collapse Simulation: A Dynamical Systems Approach," by M.V. Sivaselvan and A.M. Reinhorn, 6/16/04, (PB2005-104889, A11, MF-A03, CD-A00).
- MCEER-04-0006 "Proceedings of the Second PRC-US Workshop on Seismic Analysis and Design of Special Bridges," edited by G.C. Lee and L.C. Fan, 6/25/04, (PB2005-104890, A16, CD-A00).
- MCEER-04-0007 "Seismic Vulnerability Evaluation of Axially Loaded Steel Built-up Laced Members," by K. Lee and M. Bruneau, 6/30/04, (PB2005-104891, A16, CD-A00).
- MCEER-04-0008 "Evaluation of Accuracy of Simplified Methods of Analysis and Design of Buildings with Damping Systems for Near-Fault and for Soft-Soil Seismic Motions," by E.A. Pavlou and M.C. Constantinou, 8/16/04, (PB2005-104892, A08, MF-A02, CD-A00).
- MCEER-04-0009 "Assessment of Geotechnical Issues in Acute Care Facilities in California," by M. Lew, T.D. O'Rourke, R. Dobry and M. Koch, 9/15/04, (PB2005-104893, A08, CD-A00).
- MCEER-04-0010 "Scissor-Jack-Damper Energy Dissipation System," by A.N. Sigaher-Boyle and M.C. Constantinou, 12/1/04 (PB2005-108221).
- MCEER-04-0011 "Seismic Retrofit of Bridge Steel Truss Piers Using a Controlled Rocking Approach," by M. Pollino and M. Bruneau, 12/20/04 (PB2006-105795).
- MCEER-05-0001 "Experimental and Analytical Studies of Structures Seismically Isolated with an Uplift-Restraint Isolation System," by P.C. Roussis and M.C. Constantinou, 1/10/05 (PB2005-108222).
- MCEER-05-0002 "A Versatile Experimentation Model for Study of Structures Near Collapse Applied to Seismic Evaluation of Irregular Structures," by D. Kusumastuti, A.M. Reinhorn and A. Rutenberg, 3/31/05 (PB2006-101523).
- MCEER-05-0003 "Proceedings of the Third PRC-US Workshop on Seismic Analysis and Design of Special Bridges," edited by L.C. Fan and G.C. Lee, 4/20/05, (PB2006-105796).
- MCEER-05-0004 "Approaches for the Seismic Retrofit of Braced Steel Bridge Piers and Proof-of-Concept Testing of an Eccentrically Braced Frame with Tubular Link," by J.W. Berman and M. Bruneau, 4/21/05 (PB2006-101524).
- MCEER-05-0005 "Simulation of Strong Ground Motions for Seismic Fragility Evaluation of Nonstructural Components in Hospitals," by A. Wanitkorkul and A. Filiatrault, 5/26/05 (PB2006-500027).
- MCEER-05-0006 "Seismic Safety in California Hospitals: Assessing an Attempt to Accelerate the Replacement or Seismic Retrofit of Older Hospital Facilities," by D.J. Alesch, L.A. Arendt and W.J. Petak, 6/6/05 (PB2006-105794).
- MCEER-05-0007 "Development of Seismic Strengthening and Retrofit Strategies for Critical Facilities Using Engineered Cementitious Composite Materials," by K. Kesner and S.L. Billington, 8/29/05 (PB2006-111701).
- MCEER-05-0008 "Experimental and Analytical Studies of Base Isolation Systems for Seismic Protection of Power Transformers," by N. Murota, M.Q. Feng and G-Y. Liu, 9/30/05 (PB2006-111702).
- MCEER-05-0009 "3D-BASIS-ME-MB: Computer Program for Nonlinear Dynamic Analysis of Seismically Isolated Structures," by P.C. Tsopelas, P.C. Roussis, M.C. Constantinou, R. Buchanan and A.M. Reinhorn, 10/3/05 (PB2006-111703).
- MCEER-05-0010 "Steel Plate Shear Walls for Seismic Design and Retrofit of Building Structures," by D. Vian and M. Bruneau, 12/15/05 (PB2006-111704).

- MCEER-05-0011 "The Performance-Based Design Paradigm," by M.J. Astrella and A. Whittaker, 12/15/05 (PB2006-111705).
- MCEER-06-0001 "Seismic Fragility of Suspended Ceiling Systems," H. Badillo-Almaraz, A.S. Whittaker, A.M. Reinhorn and G.P. Cimellaro, 2/4/06 (PB2006-111706).
- MCEER-06-0002 "Multi-Dimensional Fragility of Structures," by G.P. Cimellaro, A.M. Reinhorn and M. Bruneau, 3/1/06 (PB2007-106974, A09, MF-A02, CD A00).
- MCEER-06-0003 "Built-Up Shear Links as Energy Dissipators for Seismic Protection of Bridges," by P. Dusicka, A.M. Itani and I.G. Buckle, 3/15/06 (PB2006-111708).
- MCEER-06-0004 "Analytical Investigation of the Structural Fuse Concept," by R.E. Vargas and M. Bruneau, 3/16/06 (PB2006-111709).
- MCEER-06-0005 "Experimental Investigation of the Structural Fuse Concept," by R.E. Vargas and M. Bruneau, 3/17/06 (PB2006-111710).
- MCEER-06-0006 "Further Development of Tubular Eccentrically Braced Frame Links for the Seismic Retrofit of Braced Steel Truss Bridge Piers," by J.W. Berman and M. Bruneau, 3/27/06 (PB2007-105147).
- MCEER-06-0007 "REDARS Validation Report," by S. Cho, C.K. Huyck, S. Ghosh and R.T. Eguchi, 8/8/06 (PB2007-106983).
- MCEER-06-0008 "Review of Current NDE Technologies for Post-Earthquake Assessment of Retrofitted Bridge Columns," by J.W. Song, Z. Liang and G.C. Lee, 8/21/06 (PB2007-106984).
- MCEER-06-0009 "Liquefaction Remediation in Silty Soils Using Dynamic Compaction and Stone Columns," by S. Thevanayagam, G.R. Martin, R. Nashed, T. Shenthan, T. Kanagalingam and N. Ecemis, 8/28/06 (PB2007-106985).
- MCEER-06-0010 "Conceptual Design and Experimental Investigation of Polymer Matrix Composite Infill Panels for Seismic Retrofitting," by W. Jung, M. Chiewanichakorn and A.J. Aref, 9/21/06 (PB2007-106986).
- MCEER-06-0011 "A Study of the Coupled Horizontal-Vertical Behavior of Elastomeric and Lead-Rubber Seismic Isolation Bearings," by G.P. Warn and A.S. Whittaker, 9/22/06 (PB2007-108679).
- MCEER-06-0012 "Proceedings of the Fourth PRC-US Workshop on Seismic Analysis and Design of Special Bridges: Advancing Bridge Technologies in Research, Design, Construction and Preservation," Edited by L.C. Fan, G.C. Lee and L. Ziang, 10/12/06 (PB2007-109042).
- MCEER-06-0013 "Cyclic Response and Low Cycle Fatigue Characteristics of Plate Steels," by P. Dusicka, A.M. Itani and I.G. Buckle, 11/1/06 06 (PB2007-106987).
- MCEER-06-0014 "Proceedings of the Second US-Taiwan Bridge Engineering Workshop," edited by W.P. Yen, J. Shen, J-Y. Chen and M. Wang, 11/15/06 (PB2008-500041).
- MCEER-06-0015 "User Manual and Technical Documentation for the REDARSTM Import Wizard," by S. Cho, S. Ghosh, C.K. Huyck and S.D. Werner, 11/30/06 (PB2007-114766).
- MCEER-06-0016 "Hazard Mitigation Strategy and Monitoring Technologies for Urban and Infrastructure Public Buildings: Proceedings of the China-US Workshops," edited by X.Y. Zhou, A.L. Zhang, G.C. Lee and M. Tong, 12/12/06 (PB2008-500018).
- MCEER-07-0001 "Static and Kinetic Coefficients of Friction for Rigid Blocks," by C. Kafali, S. Fathali, M. Grigoriu and A.S. Whittaker, 3/20/07 (PB2007-114767).
- MCEER-07-0002 "Hazard Mitigation Investment Decision Making: Organizational Response to Legislative Mandate," by L.A. Arendt, D.J. Alesch and W.J. Petak, 4/9/07 (PB2007-114768).
- MCEER-07-0003 "Seismic Behavior of Bidirectional-Resistant Ductile End Diaphragms with Unbonded Braces in Straight or Skewed Steel Bridges," by O. Celik and M. Bruneau, 4/11/07 (PB2008-105141).

- MCEER-07-0004 “Modeling Pile Behavior in Large Pile Groups Under Lateral Loading,” by A.M. Dodds and G.R. Martin, 4/16/07(PB2008-105142).
- MCEER-07-0005 “Experimental Investigation of Blast Performance of Seismically Resistant Concrete-Filled Steel Tube Bridge Piers,” by S. Fujikura, M. Bruneau and D. Lopez-Garcia, 4/20/07 (PB2008-105143).
- MCEER-07-0006 “Seismic Analysis of Conventional and Isolated Liquefied Natural Gas Tanks Using Mechanical Analogs,” by I.P. Christovasilis and A.S. Whittaker, 5/1/07, not available.
- MCEER-07-0007 “Experimental Seismic Performance Evaluation of Isolation/Restraint Systems for Mechanical Equipment – Part 1: Heavy Equipment Study,” by S. Fathali and A. Filiatrault, 6/6/07 (PB2008-105144).
- MCEER-07-0008 “Seismic Vulnerability of Timber Bridges and Timber Substructures,” by A.A. Sharma, J.B. Mander, I.M. Friedland and D.R. Allicock, 6/7/07 (PB2008-105145).
- MCEER-07-0009 “Experimental and Analytical Study of the XY-Friction Pendulum (XY-FP) Bearing for Bridge Applications,” by C.C. Marin-Artieda, A.S. Whittaker and M.C. Constantinou, 6/7/07 (PB2008-105191).
- MCEER-07-0010 “Proceedings of the PRC-US Earthquake Engineering Forum for Young Researchers,” Edited by G.C. Lee and X.Z. Qi, 6/8/07 (PB2008-500058).
- MCEER-07-0011 “Design Recommendations for Perforated Steel Plate Shear Walls,” by R. Purba and M. Bruneau, 6/18/07, (PB2008-105192).
- MCEER-07-0012 “Performance of Seismic Isolation Hardware Under Service and Seismic Loading,” by M.C. Constantinou, A.S. Whittaker, Y. Kalpakidis, D.M. Fenz and G.P. Warn, 8/27/07, (PB2008-105193).
- MCEER-07-0013 “Experimental Evaluation of the Seismic Performance of Hospital Piping Subassemblies,” by E.R. Goodwin, E. Maragakis and A.M. Itani, 9/4/07, (PB2008-105194).
- MCEER-07-0014 “A Simulation Model of Urban Disaster Recovery and Resilience: Implementation for the 1994 Northridge Earthquake,” by S. Miles and S.E. Chang, 9/7/07, (PB2008-106426).
- MCEER-07-0015 “Statistical and Mechanistic Fragility Analysis of Concrete Bridges,” by M. Shinozuka, S. Banerjee and S-H. Kim, 9/10/07, (PB2008-106427).
- MCEER-07-0016 “Three-Dimensional Modeling of Inelastic Buckling in Frame Structures,” by M. Schachter and AM. Reinhorn, 9/13/07, (PB2008-108125).
- MCEER-07-0017 “Modeling of Seismic Wave Scattering on Pile Groups and Caissons,” by I. Po Lam, H. Law and C.T. Yang, 9/17/07 (PB2008-108150).
- MCEER-07-0018 “Bridge Foundations: Modeling Large Pile Groups and Caissons for Seismic Design,” by I. Po Lam, H. Law and G.R. Martin (Coordinating Author), 12/1/07 (PB2008-111190).
- MCEER-07-0019 “Principles and Performance of Roller Seismic Isolation Bearings for Highway Bridges,” by G.C. Lee, Y.C. Ou, Z. Liang, T.C. Niu and J. Song, 12/10/07 (PB2009-110466).
- MCEER-07-0020 “Centrifuge Modeling of Permeability and Pinning Reinforcement Effects on Pile Response to Lateral Spreading,” by L.L Gonzalez-Lagos, T. Abdoun and R. Dobry, 12/10/07 (PB2008-111191).
- MCEER-07-0021 “Damage to the Highway System from the Pisco, Perú Earthquake of August 15, 2007,” by J.S. O’Connor, L. Mesa and M. Nykamp, 12/10/07, (PB2008-108126).
- MCEER-07-0022 “Experimental Seismic Performance Evaluation of Isolation/Restraint Systems for Mechanical Equipment – Part 2: Light Equipment Study,” by S. Fathali and A. Filiatrault, 12/13/07 (PB2008-111192).
- MCEER-07-0023 “Fragility Considerations in Highway Bridge Design,” by M. Shinozuka, S. Banerjee and S.H. Kim, 12/14/07 (PB2008-111193).

- MCEER-07-0024 “Performance Estimates for Seismically Isolated Bridges,” by G.P. Warn and A.S. Whittaker, 12/30/07 (PB2008-112230).
- MCEER-08-0001 “Seismic Performance of Steel Girder Bridge Superstructures with Conventional Cross Frames,” by L.P. Carden, A.M. Itani and I.G. Buckle, 1/7/08, (PB2008-112231).
- MCEER-08-0002 “Seismic Performance of Steel Girder Bridge Superstructures with Ductile End Cross Frames with Seismic Isolators,” by L.P. Carden, A.M. Itani and I.G. Buckle, 1/7/08 (PB2008-112232).
- MCEER-08-0003 “Analytical and Experimental Investigation of a Controlled Rocking Approach for Seismic Protection of Bridge Steel Truss Piers,” by M. Pollino and M. Bruneau, 1/21/08 (PB2008-112233).
- MCEER-08-0004 “Linking Lifeline Infrastructure Performance and Community Disaster Resilience: Models and Multi-Stakeholder Processes,” by S.E. Chang, C. Pasion, K. Tatebe and R. Ahmad, 3/3/08 (PB2008-112234).
- MCEER-08-0005 “Modal Analysis of Generally Damped Linear Structures Subjected to Seismic Excitations,” by J. Song, Y-L. Chu, Z. Liang and G.C. Lee, 3/4/08 (PB2009-102311).
- MCEER-08-0006 “System Performance Under Multi-Hazard Environments,” by C. Kafali and M. Grigoriu, 3/4/08 (PB2008-112235).
- MCEER-08-0007 “Mechanical Behavior of Multi-Spherical Sliding Bearings,” by D.M. Fenz and M.C. Constantinou, 3/6/08 (PB2008-112236).
- MCEER-08-0008 “Post-Earthquake Restoration of the Los Angeles Water Supply System,” by T.H.P. Tabucchi and R.A. Davidson, 3/7/08 (PB2008-112237).
- MCEER-08-0009 “Fragility Analysis of Water Supply Systems,” by A. Jacobson and M. Grigoriu, 3/10/08 (PB2009-105545).
- MCEER-08-0010 “Experimental Investigation of Full-Scale Two-Story Steel Plate Shear Walls with Reduced Beam Section Connections,” by B. Qu, M. Bruneau, C-H. Lin and K-C. Tsai, 3/17/08 (PB2009-106368).
- MCEER-08-0011 “Seismic Evaluation and Rehabilitation of Critical Components of Electrical Power Systems,” S. Ersoy, B. Feizi, A. Ashrafi and M. Ala Saadeghvaziri, 3/17/08 (PB2009-105546).
- MCEER-08-0012 “Seismic Behavior and Design of Boundary Frame Members of Steel Plate Shear Walls,” by B. Qu and M. Bruneau, 4/26/08 . (PB2009-106744).
- MCEER-08-0013 “Development and Appraisal of a Numerical Cyclic Loading Protocol for Quantifying Building System Performance,” by A. Filiatrault, A. Wanitkorkul and M. Constantinou, 4/27/08 (PB2009-107906).
- MCEER-08-0014 “Structural and Nonstructural Earthquake Design: The Challenge of Integrating Specialty Areas in Designing Complex, Critical Facilities,” by W.J. Petak and D.J. Alesch, 4/30/08 (PB2009-107907).
- MCEER-08-0015 “Seismic Performance Evaluation of Water Systems,” by Y. Wang and T.D. O’Rourke, 5/5/08 (PB2009-107908).
- MCEER-08-0016 “Seismic Response Modeling of Water Supply Systems,” by P. Shi and T.D. O’Rourke, 5/5/08 (PB2009-107910).
- MCEER-08-0017 “Numerical and Experimental Studies of Self-Centering Post-Tensioned Steel Frames,” by D. Wang and A. Filiatrault, 5/12/08 (PB2009-110479).
- MCEER-08-0018 “Development, Implementation and Verification of Dynamic Analysis Models for Multi-Spherical Sliding Bearings,” by D.M. Fenz and M.C. Constantinou, 8/15/08 (PB2009-107911).
- MCEER-08-0019 “Performance Assessment of Conventional and Base Isolated Nuclear Power Plants for Earthquake Blast Loadings,” by Y.N. Huang, A.S. Whittaker and N. Luco, 10/28/08 (PB2009-107912).

- MCEER-08-0020 “Remote Sensing for Resilient Multi-Hazard Disaster Response – Volume I: Introduction to Damage Assessment Methodologies,” by B.J. Adams and R.T. Eguchi, 11/17/08 (PB2010-102695).
- MCEER-08-0021 “Remote Sensing for Resilient Multi-Hazard Disaster Response – Volume II: Counting the Number of Collapsed Buildings Using an Object-Oriented Analysis: Case Study of the 2003 Bam Earthquake,” by L. Gusella, C.K. Huyck and B.J. Adams, 11/17/08 (PB2010-100925).
- MCEER-08-0022 “Remote Sensing for Resilient Multi-Hazard Disaster Response – Volume III: Multi-Sensor Image Fusion Techniques for Robust Neighborhood-Scale Urban Damage Assessment,” by B.J. Adams and A. McMillan, 11/17/08 (PB2010-100926).
- MCEER-08-0023 “Remote Sensing for Resilient Multi-Hazard Disaster Response – Volume IV: A Study of Multi-Temporal and Multi-Resolution SAR Imagery for Post-Katrina Flood Monitoring in New Orleans,” by A. McMillan, J.G. Morley, B.J. Adams and S. Chesworth, 11/17/08 (PB2010-100927).
- MCEER-08-0024 “Remote Sensing for Resilient Multi-Hazard Disaster Response – Volume V: Integration of Remote Sensing Imagery and VIEWS™ Field Data for Post-Hurricane Charley Building Damage Assessment,” by J.A. Womble, K. Mehta and B.J. Adams, 11/17/08 (PB2009-115532).
- MCEER-08-0025 “Building Inventory Compilation for Disaster Management: Application of Remote Sensing and Statistical Modeling,” by P. Sarabandi, A.S. Kiremidjian, R.T. Eguchi and B. J. Adams, 11/20/08 (PB2009-110484).
- MCEER-08-0026 “New Experimental Capabilities and Loading Protocols for Seismic Qualification and Fragility Assessment of Nonstructural Systems,” by R. Retamales, G. Mosqueda, A. Filiatrault and A. Reinhorn, 11/24/08 (PB2009-110485).
- MCEER-08-0027 “Effects of Heating and Load History on the Behavior of Lead-Rubber Bearings,” by I.V. Kalpakidis and M.C. Constantinou, 12/1/08 (PB2009-115533).
- MCEER-08-0028 “Experimental and Analytical Investigation of Blast Performance of Seismically Resistant Bridge Piers,” by S.Fujikura and M. Bruneau, 12/8/08 (PB2009-115534).
- MCEER-08-0029 “Evolutionary Methodology for Aseismic Decision Support,” by Y. Hu and G. Dargush, 12/15/08.
- MCEER-08-0030 “Development of a Steel Plate Shear Wall Bridge Pier System Conceived from a Multi-Hazard Perspective,” by D. Keller and M. Bruneau, 12/19/08 (PB2010-102696).
- MCEER-09-0001 “Modal Analysis of Arbitrarily Damped Three-Dimensional Linear Structures Subjected to Seismic Excitations,” by Y.L. Chu, J. Song and G.C. Lee, 1/31/09 (PB2010-100922).
- MCEER-09-0002 “Air-Blast Effects on Structural Shapes,” by G. Ballantyne, A.S. Whittaker, A.J. Aref and G.F. Dargush, 2/2/09 (PB2010-102697).
- MCEER-09-0003 “Water Supply Performance During Earthquakes and Extreme Events,” by A.L. Bonneau and T.D. O’Rourke, 2/16/09 (PB2010-100923).
- MCEER-09-0004 “Generalized Linear (Mixed) Models of Post-Earthquake Ignitions,” by R.A. Davidson, 7/20/09 (PB2010-102698).
- MCEER-09-0005 “Seismic Testing of a Full-Scale Two-Story Light-Frame Wood Building: NEESWood Benchmark Test,” by I.P. Christovasilis, A. Filiatrault and A. Wanitkorkul, 7/22/09 (PB2012-102401).
- MCEER-09-0006 “IDARC2D Version 7.0: A Program for the Inelastic Damage Analysis of Structures,” by A.M. Reinhorn, H. Roh, M. Sivaselvan, S.K. Kunnath, R.E. Valles, A. Madan, C. Li, R. Lobo and Y.J. Park, 7/28/09 (PB2010-103199).
- MCEER-09-0007 “Enhancements to Hospital Resiliency: Improving Emergency Planning for and Response to Hurricanes,” by D.B. Hess and L.A. Arendt, 7/30/09 (PB2010-100924).

- MCEER-09-0008 “Assessment of Base-Isolated Nuclear Structures for Design and Beyond-Design Basis Earthquake Shaking,” by Y.N. Huang, A.S. Whittaker, R.P. Kennedy and R.L. Mayes, 8/20/09 (PB2010-102699).
- MCEER-09-0009 “Quantification of Disaster Resilience of Health Care Facilities,” by G.P. Cimellaro, C. Fumo, A.M. Reinhorn and M. Bruneau, 9/14/09 (PB2010-105384).
- MCEER-09-0010 “Performance-Based Assessment and Design of Squat Reinforced Concrete Shear Walls,” by C.K. Gulec and A.S. Whittaker, 9/15/09 (PB2010-102700).
- MCEER-09-0011 “Proceedings of the Fourth US-Taiwan Bridge Engineering Workshop,” edited by W.P. Yen, J.J. Shen, T.M. Lee and R.B. Zheng, 10/27/09 (PB2010-500009).
- MCEER-09-0012 “Proceedings of the Special International Workshop on Seismic Connection Details for Segmental Bridge Construction,” edited by W. Phillip Yen and George C. Lee, 12/21/09 (PB2012-102402).
- MCEER-10-0001 “Direct Displacement Procedure for Performance-Based Seismic Design of Multistory Woodframe Structures,” by W. Pang and D. Rosowsky, 4/26/10 (PB2012-102403).
- MCEER-10-0002 “Simplified Direct Displacement Design of Six-Story NEESWood Capstone Building and Pre-Test Seismic Performance Assessment,” by W. Pang, D. Rosowsky, J. van de Lindt and S. Pei, 5/28/10 (PB2012-102404).
- MCEER-10-0003 “Integration of Seismic Protection Systems in Performance-Based Seismic Design of Woodframed Structures,” by J.K. Shinde and M.D. Symans, 6/18/10 (PB2012-102405).
- MCEER-10-0004 “Modeling and Seismic Evaluation of Nonstructural Components: Testing Frame for Experimental Evaluation of Suspended Ceiling Systems,” by A.M. Reinhorn, K.P. Ryu and G. Maddaloni, 6/30/10 (PB2012-102406).
- MCEER-10-0005 “Analytical Development and Experimental Validation of a Structural-Fuse Bridge Pier Concept,” by S. El-Bahey and M. Bruneau, 10/1/10 (PB2012-102407).
- MCEER-10-0006 “A Framework for Defining and Measuring Resilience at the Community Scale: The PEOPLES Resilience Framework,” by C.S. Renschler, A.E. Frazier, L.A. Arendt, G.P. Cimellaro, A.M. Reinhorn and M. Bruneau, 10/8/10 (PB2012-102408).
- MCEER-10-0007 “Impact of Horizontal Boundary Elements Design on Seismic Behavior of Steel Plate Shear Walls,” by R. Purba and M. Bruneau, 11/14/10 (PB2012-102409).
- MCEER-10-0008 “Seismic Testing of a Full-Scale Mid-Rise Building: The NEESWood Capstone Test,” by S. Pei, J.W. van de Lindt, S.E. Pryor, H. Shimizu, H. Isoda and D.R. Rammer, 12/1/10 (PB2012-102410).
- MCEER-10-0009 “Modeling the Effects of Detonations of High Explosives to Inform Blast-Resistant Design,” by P. Sherkar, A.S. Whittaker and A.J. Aref, 12/1/10 (PB2012-102411).
- MCEER-10-0010 “L’Aquila Earthquake of April 6, 2009 in Italy: Rebuilding a Resilient City to Withstand Multiple Hazards,” by G.P. Cimellaro, I.P. Christovasilis, A.M. Reinhorn, A. De Stefano and T. Kirova, 12/29/10.
- MCEER-11-0001 “Numerical and Experimental Investigation of the Seismic Response of Light-Frame Wood Structures,” by I.P. Christovasilis and A. Filiatrault, 8/8/11 (PB2012-102412).
- MCEER-11-0002 “Seismic Design and Analysis of a Precast Segmental Concrete Bridge Model,” by M. Anagnostopoulou, A. Filiatrault and A. Aref, 9/15/11.
- MCEER-11-0003 “Proceedings of the Workshop on Improving Earthquake Response of Substation Equipment,” Edited by A.M. Reinhorn, 9/19/11 (PB2012-102413).
- MCEER-11-0004 “LRFD-Based Analysis and Design Procedures for Bridge Bearings and Seismic Isolators,” by M.C. Constantinou, I. Kalpakidis, A. Filiatrault and R.A. Ecker Lay, 9/26/11.

- MCEER-11-0005 “Experimental Seismic Evaluation, Model Parameterization, and Effects of Cold-Formed Steel-Framed Gypsum Partition Walls on the Seismic Performance of an Essential Facility,” by R. Davies, R. Retamales, G. Mosqueda and A. Filiatrault, 10/12/11.
- MCEER-11-0006 “Modeling and Seismic Performance Evaluation of High Voltage Transformers and Bushings,” by A.M. Reinhorn, K. Oikonomou, H. Roh, A. Schiff and L. Kempner, Jr., 10/3/11.
- MCEER-11-0007 “Extreme Load Combinations: A Survey of State Bridge Engineers,” by G.C. Lee, Z. Liang, J.J. Shen and J.S. O’Connor, 10/14/11.
- MCEER-12-0001 “Simplified Analysis Procedures in Support of Performance Based Seismic Design,” by Y.N. Huang and A.S. Whittaker.
- MCEER-12-0002 “Seismic Protection of Electrical Transformer Bushing Systems by Stiffening Techniques,” by M. Koliou, A. Filiatrault, A.M. Reinhorn and N. Oliveto, 6/1/12.
- MCEER-12-0003 “Post-Earthquake Bridge Inspection Guidelines,” by J.S. O’Connor and S. Alampalli, 6/8/12.
- MCEER-12-0004 “Integrated Design Methodology for Isolated Floor Systems in Single-Degree-of-Freedom Structural Fuse Systems,” by S. Cui, M. Bruneau and M.C. Constantinou, 6/13/12.
- MCEER-12-0005 “Characterizing the Rotational Components of Earthquake Ground Motion,” by D. Basu, A.S. Whittaker and M.C. Constantinou, 6/15/12.
- MCEER-12-0006 “Bayesian Fragility for Nonstructural Systems,” by C.H. Lee and M.D. Grigoriu, 9/12/12.
- MCEER-12-0007 “A Numerical Model for Capturing the In-Plane Seismic Response of Interior Metal Stud Partition Walls,” by R.L. Wood and T.C. Hutchinson, 9/12/12.
- MCEER-12-0008 “Assessment of Floor Accelerations in Yielding Buildings,” by J.D. Wieser, G. Pekcan, A.E. Zaghi, A.M. Itani and E. Maragakis, 10/5/12.
- MCEER-13-0001 “Experimental Seismic Study of Pressurized Fire Sprinkler Piping Systems,” by Y. Tian, A. Filiatrault and G. Mosqueda, 4/8/13.
- MCEER-13-0002 “Enhancing Resource Coordination for Multi-Modal Evacuation Planning,” by D.B. Hess, B.W. Conley and C.M. Farrell, 2/8/13.
- MCEER-13-0003 “Seismic Response of Base Isolated Buildings Considering Pounding to Moat Walls,” by A. Masroor and G. Mosqueda, 2/26/13.
- MCEER-13-0004 “Seismic Response Control of Structures Using a Novel Adaptive Passive Negative Stiffness Device,” by D.T.R. Pasala, A.A. Sarlis, S. Nagarajaiah, A.M. Reinhorn, M.C. Constantinou and D.P. Taylor, 6/10/13.
- MCEER-13-0005 “Negative Stiffness Device for Seismic Protection of Structures,” by A.A. Sarlis, D.T.R. Pasala, M.C. Constantinou, A.M. Reinhorn, S. Nagarajaiah and D.P. Taylor, 6/12/13.
- MCEER-13-0006 “Emilia Earthquake of May 20, 2012 in Northern Italy: Rebuilding a Resilient Community to Withstand Multiple Hazards,” by G.P. Cimellaro, M. Chiriatti, A.M. Reinhorn and L. Tirca, June 30, 2013.
- MCEER-13-0007 “Precast Concrete Segmental Components and Systems for Accelerated Bridge Construction in Seismic Regions,” by A.J. Aref, G.C. Lee, Y.C. Ou and P. Sideris, with contributions from K.C. Chang, S. Chen, A. Filiatrault and Y. Zhou, June 13, 2013.
- MCEER-13-0008 “A Study of U.S. Bridge Failures (1980-2012),” by G.C. Lee, S.B. Mohan, C. Huang and B.N. Fard, June 15, 2013.
- MCEER-13-0009 “Database Development for Damaged Bridge Modeling,” by G.C. Lee, J.C. Qi and C. Huang, June 16, 2013.

MCEER-13-0010 “Model of Triple Friction Pendulum Bearing for General Geometric and Frictional Parameters and for Uplift Conditions,” by A.A. Sarlis and M.C. Constantinou, July 1, 2013.

3pleANI
FRICITION PENDULUM ISOLATOR
ANALYSIS AND ANIMATION
PROGRAM

USERS GUIDE AND REFERENCE
MANUAL

Apostolos A. Sarlis¹

Michael. C. Constantinou²

University at Buffalo, State University of New York

June 2013

¹ Graduate Student, Department of Civil, Structural and Environmental Engineering, University at Buffalo, State University of New York, Buffalo, NY 14260

² Professor, Department of Civil, Structural and Environmental Engineering, University at Buffalo, State University of New York, Buffalo, NY 14260.

Abbreviations and Terminology

TFP: Triple Friction Pendulum

BCP: Bottom Concave Plate

TSP: Top Sliding Plate

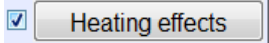
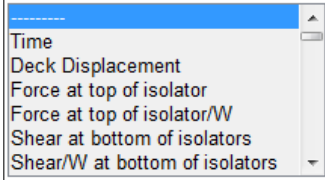
RS: Rigid Slider

BSP: Bottom Slide Plate

TCP: Top Concave Plate

DCI: Displacement Controlled Interface

DAI: Dynamic Analysis Interface

Graphics Interface Component Terminology	
Name	View
Edit box:	
Checkbox	
List box	
Pushbutton	
Popup menu	
Slider	

3pleANI was developed using MATLAB 2007b, The MathWorks Inc., Natick, MA.

1 INTRODUCTION

3pleANI is a structural analysis program capable of performing sophisticated two-dimensional analysis and animation of Friction Pendulum (FP) isolators that cannot be performed by commercially available software. The FP isolators can be modeled using two different theories developed by Sarlis and Constantinou (2013). The first and basic theory accounts for moment equilibrium and utilizes a total of eight degrees of freedom (that include horizontal displacements and contact force locations which are statically condensed to three) to trace the motion of the isolator in a single direction. The sliding isolators that can be analyzed include any isolators with four or less sliding surfaces such as the single FP (two sliding surfaces), the double FP with articulated slider (three sliding surfaces), the double FP with a rigid slider (two sliding surfaces) and the triple FP isolator (four sliding surfaces). The second and more advanced theory is based on rigid body dynamics and allows the user to conduct additional more sophisticated analyses of the FP isolator. The software offers the capability to analyze and present animation of motion of the components of isolators under (a) regular conditions when no uplift occurs and (b) uplift conditions that include bouncing of the isolator components. Output quantities include response quantities of the analyzed structural systems (accelerations, total displacements, relative displacements, forces and floor response spectra) and isolator response quantities (displacements of parts, velocities at sliding surfaces, force at sliding surfaces, heat flux and temperature rise at each sliding surface).

The program has two analysis options. Upon start of the program the interface of Figure 1-1 allows the user to select one of two options: (a) displacement control analysis or (b) dynamic analysis. Upon selection of option “displacement control analysis”, the interface of Figure 1-2 allows for input of geometric and frictional parameters, and the motion of the isolator to be analyzed. The option allows analysis and animation of motion of the components of a single isolator under specified histories of horizontal and vertical displacement (and/or varying vertical load). This option includes detailed analysis of the isolator components during normal operation and during uplift. The program can calculate all response quantities related to the sliding surfaces for any geometric parameters. Advanced analysis options include, among others, heating effects

at the sliding interfaces. The uplift analysis is the centerpiece of this interface since it allows modeling of the behavior of the inner components which cannot be done by commercial software.

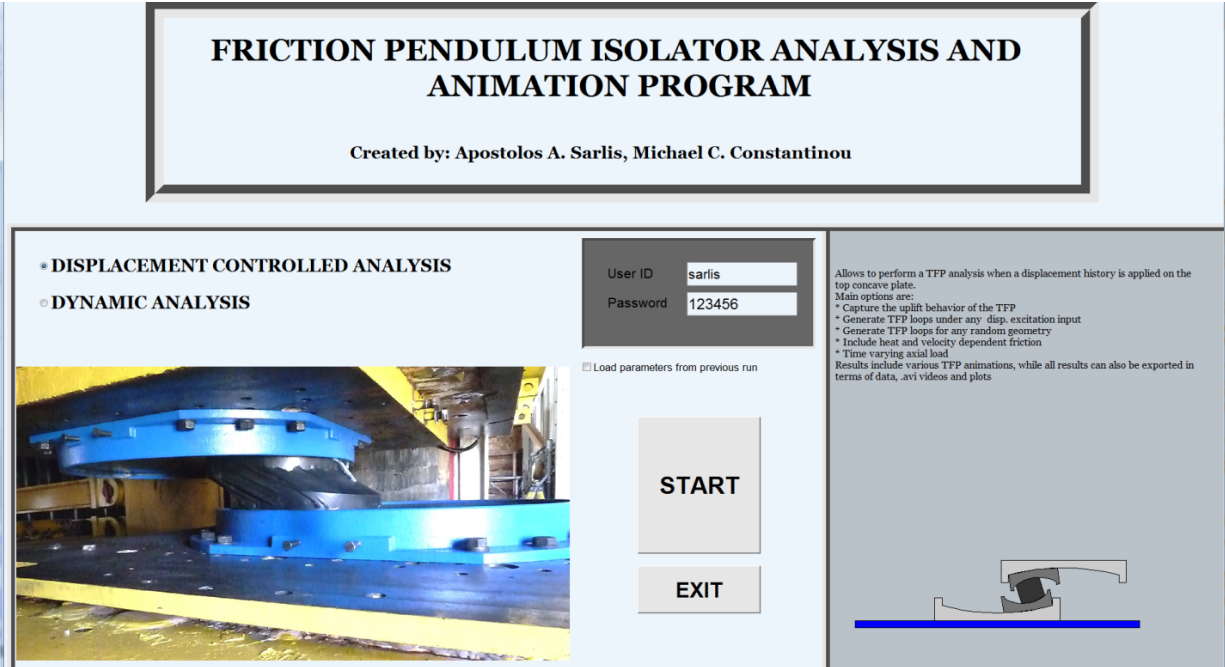


Figure 1-1: Interface for selecting analysis options

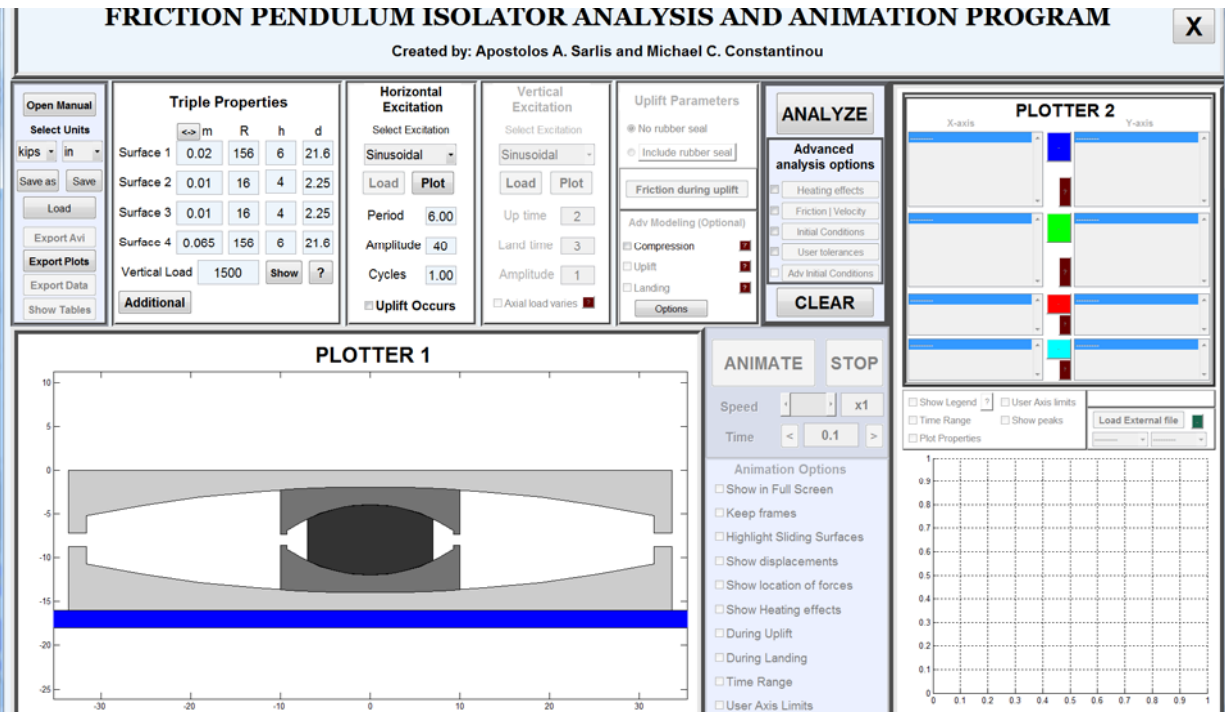


Figure 1-2: Displacement Controlled Interface (DCI)

The second option (interface shown in Figure 1-3) allows for the dynamic response history analysis of a plane seismically isolated structure or a plane seismically isolated bridge with multiple piers. Both options allow for multiple isolators of different properties and for linear viscous damping devices in the superstructure and the isolation system. The structure is modeled as a linear elastic and linear viscous system with the exception of the isolation system which is modeled as nonlinear hysteretic. The superstructure is represented as a shear building or explicitly through its mass, stiffness and damping matrices. In the case of the Shear Building representation, input parameters include the number of stories, stiffness and weight per story and damping ratio (the damping matrix is constructed based on Rayleigh damping using the specified damping ratio in the first and last modes of vibration). A library of ground motion acceleration histories allows the user to select and scale input for analysis. Analysis options include (a) calculation of response spectra of input motion, (b) calculation of periods, mode shapes and damping ratios of the superstructure (allows for quick selection of structural properties to obtain desired modal properties), (c) calculation of response of the non-isolated structure, (d) calculation of response of the seismically isolated structure, and (e) display and animation of response. In the case of a bridge, the user can use three modeling options of increasing complexity that include calculation of pier rotations, and inclusion of these rotations in the Triple FP behavior.

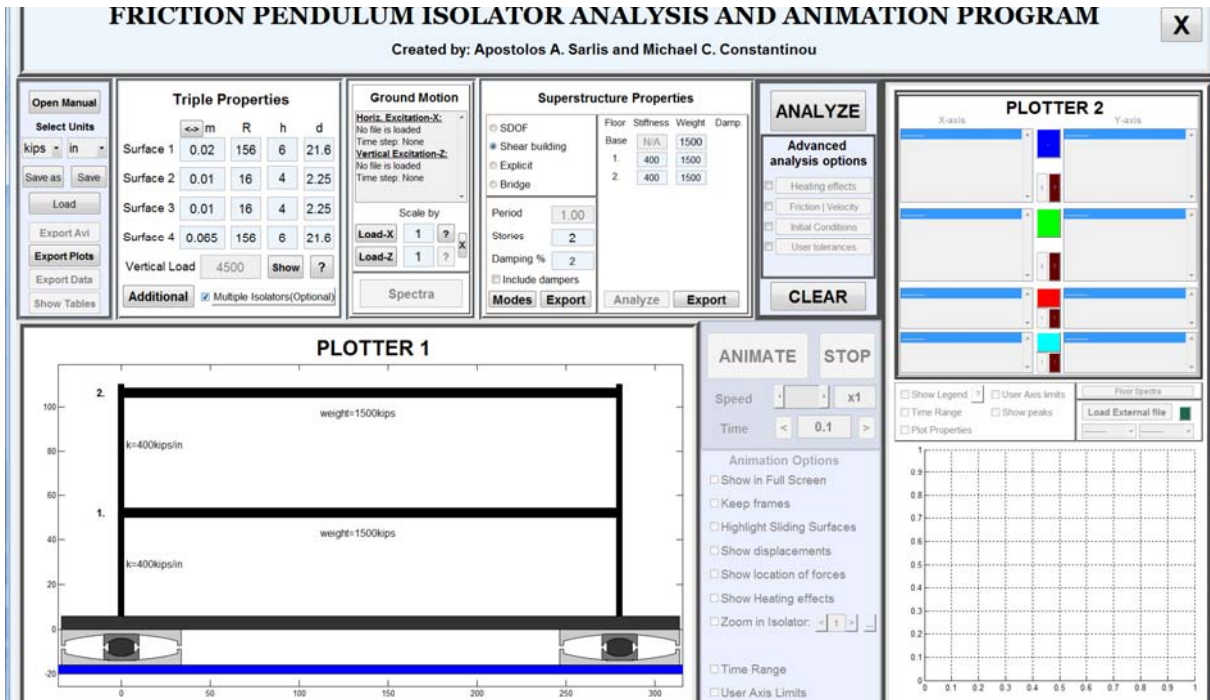


Figure 1-3: Dynamic Analysis Interface (DAI)

The theory used by the program to analyze the isolators, is described in Sarlis and Constantinou (2013). A brief overview of the theory is presented in the next section.

2 THEORY OVERVIEW

This section provides an overview of the theory that is used in program 3pleANI. For a complete presentation, see Sarlis and Constantinou (2013). Figure 2-1 shows a section of a Triple FP isolator with its geometric and frictional parameters defined together with the nomenclature and abbreviations used. The isolator can exhibit three different states during its operation as shown in Figure 2-2:

- Compression. Analysis can be performed in 3pleANI in both the Displacement Controlled Interface (DCI) and in the Dynamic Analysis Interface (DAI).
- Uplift. Analysis can only be performed in DCI.
- Landing. Analysis can only be performed in DCI.

In DAI, the isolator is assumed to be always in compression and never uplifts. In DCI, the isolator may be in any of these three states depending on the specified displacement input.

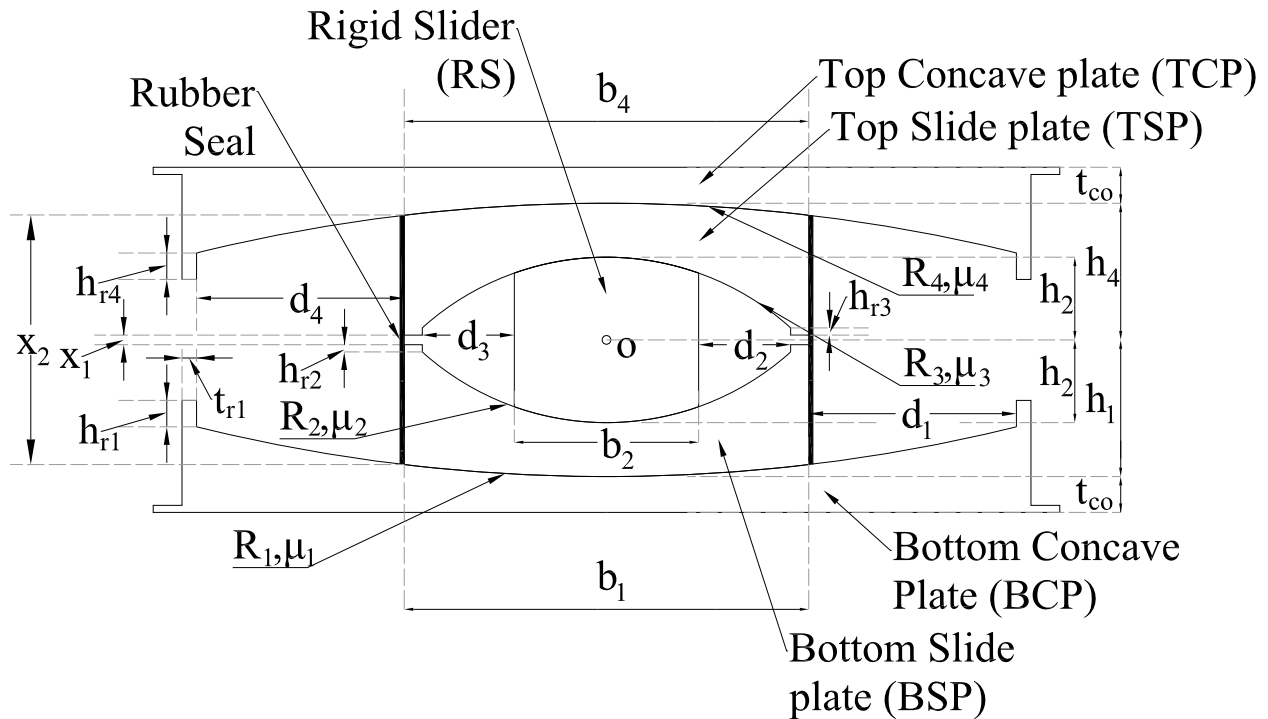


Figure 2-1: TFP isolator geometric and frictional parameters, and nomenclature

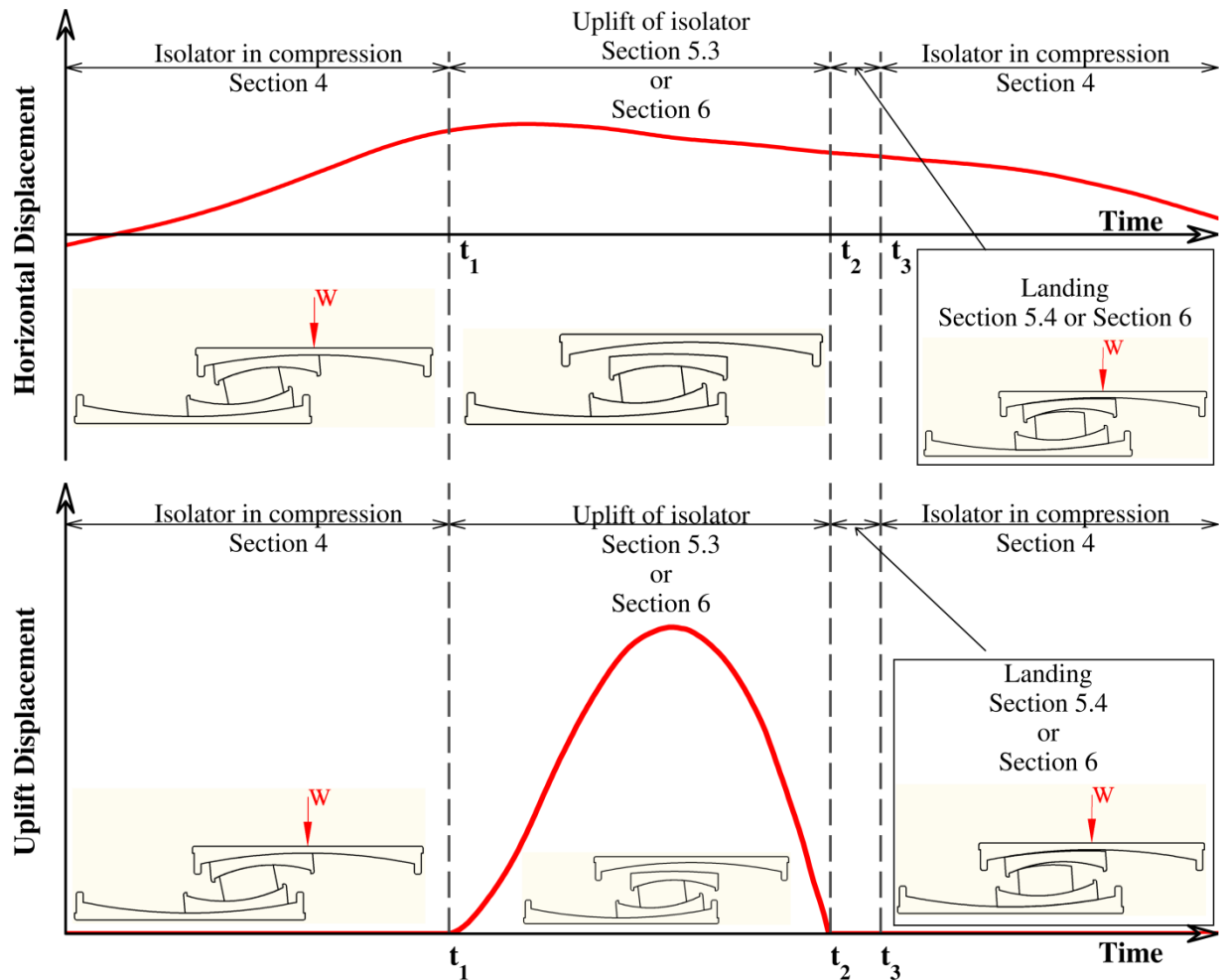


Figure 2-2: Horizontal and uplift displacement histories of TFP isolator in three states of operation (Sections are in Sarlis and Constantinou, 2013)

The program has the ability to use two independent theories in order to analyze the behavior of the TFP under any of these three states. These theories are:

- Full contact theory which represents an advancement of the theory of Fenz and Constantinou (2008a, b). This basic modeling technique is used in both DCI and DAI.
- Rigid body dynamics. This advanced modeling technique is available only in DCI.

When full contact theory is used, the equilibrium equations of the isolator are written in the deformed shape. This procedure involves horizontal and moment equilibrium of the BSP, RS, TSP and TCP (see Figure 2-1). By consideration of moment equilibrium, the resultant contact forces at each sliding interface need not be assumed to act at the center of the interface as in the theory of Fenz and Constantinou (2008a, b). As a result, there are no restrictions on the

properties of the bearing that can be analyzed. Also, the displacement and velocity of each surface can be explicitly calculated. The equations describing the behavior of the Triple FP in two-dimensional motion (one horizontal, one vertical) include eight equations with eight unknowns: the four sliding angles θ_1 , θ_2 , θ_3 and θ_4 and the four offset angles θ_{s1} , θ_{s2} , θ_{s3} and θ_{s4} as shown in Figure 2-3. Angles θ_i describe the amount of sliding that has taken place at each sliding surface. Angles θ_{si} describe the distance from the center of the surface at which the resultant contact forces apply (e.g., θ_{s1} is the angle formed between the lines connecting points 1 the center of curvature of sliding surface 1, and point 1' and similarly for the remaining surfaces). Note that in Figure 2-3 the BCP and TCP are shown rotated. These rotations are assumed constant for this discussion; however dynamic rotation can be included by the program as described later in this manual.

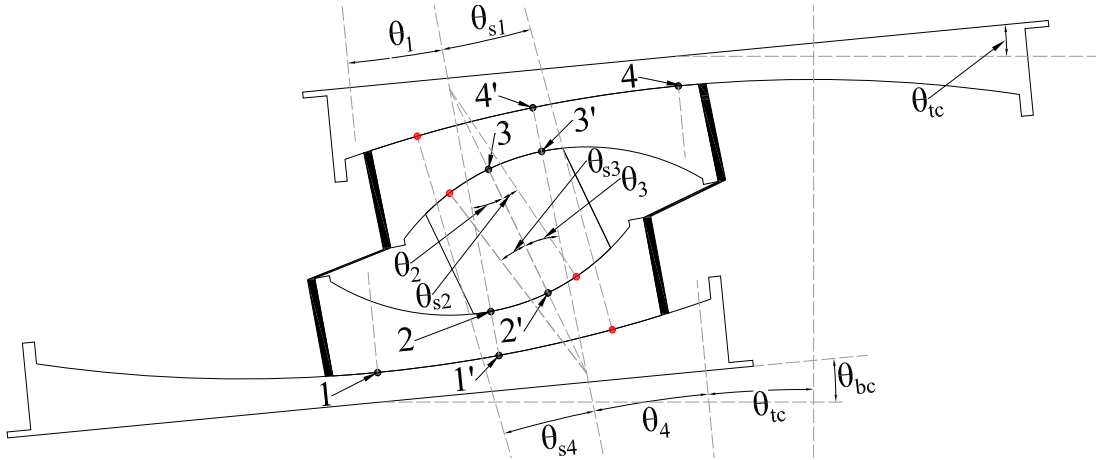


Figure 2-3: Definition of degrees of freedom in full contact theory

Due to the kinematics of the isolator, the total displacement of the TCP is related to the sliding angles through:

$$u = (R_{eff1} - h_4)\theta_1 + (R_{eff2} - h_4 - t_{co})\theta_2 + (R_{eff3} + h_4 + t_{co})\theta_3 + (R_4 + t_{co})\theta_4 - t_{co}\theta_{tc} - (h_1 + h_4 + 2t_{co})\theta_{bc} \quad (2-1)$$

Moreover for compatibility, the sliding angles need to satisfy the following condition:

$$\theta_1 + \theta_{bc} + \theta_2 - \theta_3 - \theta_4 - \theta_{tc} = 0 \quad (2-2)$$

These two kinematic equations can be substituted into the equilibrium equations to reduce the degrees of freedom by one degree to θ_1 , θ_2 , u , θ_{s1} , θ_{s2} , θ_{s3} and θ_{s4} . Following this reduction it

can be shown that the Triple FP equations of motion can be written in matrix form and partitioned as follows:

$$\begin{bmatrix} \mathbf{M}_{aa} & \mathbf{0} \\ \mathbf{M}_{ba} & \mathbf{0} \end{bmatrix} \begin{Bmatrix} \ddot{\boldsymbol{\theta}} \\ \ddot{\boldsymbol{\theta}}_s \end{Bmatrix} + \begin{bmatrix} \mathbf{K}_{aa} & \mathbf{K}_{ab} \\ \mathbf{K}_{ba} & \mathbf{K}_{bb} \end{bmatrix} \begin{Bmatrix} \boldsymbol{\theta} \\ \boldsymbol{\theta}_s \end{Bmatrix} + \begin{Bmatrix} \mathbf{S}_a \\ \mathbf{S}_b \end{Bmatrix} + \begin{Bmatrix} \mathbf{F}_{ga} \\ \mathbf{F}_{gb} \end{Bmatrix} + \begin{Bmatrix} \mathbf{F}_{ea} \\ \mathbf{F}_{eb} \end{Bmatrix} + \begin{Bmatrix} \mathbf{F}_{sa} \\ \mathbf{F}_{sb} \end{Bmatrix} = \mathbf{0} \quad (2-3)$$

Where $\boldsymbol{\theta} = [\theta_1 \ \theta_2 \ u]$, $\boldsymbol{\theta}_s = [\theta_{s1} \ \theta_{s2} \ \theta_{s3} \ \theta_{s4}]$, \mathbf{S} is a vector containing all terms related to friction forces, \mathbf{F}_g is a vector containing all terms related to restrainer forces, \mathbf{F}_e is a vector containing all excitation terms (includes terms related to ground excitation and misalignments) and \mathbf{F}_s is a vector containing the Triple FP seal forces. The offset angles θ_{si} do not cause inertia forces and can be condensed. The final equations of motion of the TFP after condensation are given by:

$$\tilde{\mathbf{M}}\ddot{\boldsymbol{\theta}} + \tilde{\mathbf{K}}\boldsymbol{\theta} + \tilde{\mathbf{S}} + \tilde{\mathbf{F}}_g + \tilde{\mathbf{F}}_e + \tilde{\mathbf{F}}_s = \mathbf{0} \quad (2-4)$$

The condensed vectors and matrices are given by:

$$\begin{aligned} \tilde{\mathbf{M}} &= \mathbf{M}_{aa} - \mathbf{K}_{ab}\mathbf{K}_{bb}^{-1}\mathbf{M}_{ba} \\ \tilde{\mathbf{K}} &= \mathbf{K}_{aa} - \mathbf{K}_{ab}\mathbf{K}_{bb}^{-1}\mathbf{K}_{ba} \\ \tilde{\mathbf{S}} &= \mathbf{S}_a - \mathbf{K}_{ab}\mathbf{K}_{bb}^{-1}\mathbf{S}_b \\ \tilde{\mathbf{F}}_g &= \mathbf{F}_{ga} - \mathbf{K}_{ab}\mathbf{K}_{bb}^{-1}\mathbf{F}_{gb} \\ \tilde{\mathbf{F}}_e &= \mathbf{F}_{ea} - \mathbf{K}_{ab}\mathbf{K}_{bb}^{-1}\mathbf{F}_{eb} \\ \tilde{\mathbf{F}}_s &= \mathbf{F}_{sa} - \mathbf{K}_{ab}\mathbf{K}_{bb}^{-1}\mathbf{F}_{sb} \end{aligned} \quad (2-5)$$

The friction force S_i at sliding surface i is modeled using the following formulation based on a modification of the Bouc-Wen model as implemented in program 3D-BASIS (Nagarajaiah et al., 1989) (special case of $A=1$, $\beta=0$, $\gamma=1$ and $\eta=2$):

$$\begin{aligned} S_i &= \mu_i W_i Z_i; \quad \dot{Z}_i = (R_i/Y)(1 - a_i Z_i^2) \dot{\theta}_i \\ a_i &= \begin{cases} 1, & \dot{\theta}_i Z_i > 0 \\ 0, & \dot{\theta}_i Z_i \leq 0 \end{cases} \end{aligned} \quad (2-6)$$

Note that parameter Y is a ‘‘yield displacement’’ for use in the visco-plastic representation of the friction force. Y should have a small value, generally less than 0.01in for full size bearings.

The restrainer forces F_{ri} of surface “i” are modeled as:

$$F_{ri} = \begin{cases} 0 & , |\theta_i| \leq d_i / R_i \\ k_{ri} (\theta_i - \text{sgn}(\theta_i) d_i / R_i) + c_{ri} \dot{\theta}_i & , |\theta_i| > d_i / R_i \end{cases} \quad (2-7)$$

The equations are written in state space after defining vector \mathbf{Q} as $\mathbf{Q} = [\boldsymbol{\theta} \quad \dot{\boldsymbol{\theta}} \quad \mathbf{Z}]^T$ so that

Equations (2-4) to (2-6) take the form:

$$\frac{d}{dt} \begin{Bmatrix} \boldsymbol{\theta} \\ \dot{\boldsymbol{\theta}} \\ \mathbf{Z} \end{Bmatrix} = \begin{Bmatrix} \dot{\boldsymbol{\theta}} \\ -\tilde{\mathbf{M}}^{-1} \tilde{\mathbf{K}} \boldsymbol{\theta} - \tilde{\mathbf{M}}^{-1} \tilde{\mathbf{S}} - \tilde{\mathbf{M}}^{-1} \tilde{\mathbf{F}} \\ \dot{\mathbf{Z}} \end{Bmatrix} \quad (2-8)$$

The equations above are combined with the superstructure or substructure (in the case of a bridge) in the Dynamic Analysis Interface.

In the Displacement Controlled interface and when the bearing is in compression, the displacement of the TCP, u , represents the specified excitation. Therefore, all terms involving u are included in the excitation vector \mathbf{F}_e and the degrees of freedom become $[\theta_1 \quad \theta_2 \quad F \quad \theta_{s1} \quad \theta_{s2} \quad \theta_{s3} \quad \theta_{s4}]$ where F is the unknown force applied at the top of the isolator. This is not associated with inertia and can be condensed so that in Equation (2-3), $\boldsymbol{\theta} = [\theta_1 \quad \theta_2]$ and $\boldsymbol{\theta}_s = [F \quad \theta_{s1} \quad \theta_{s2} \quad \theta_{s3} \quad \theta_{s4}]$. As a result, Equation (2-4) represents a 2x2 system of Equations in the DCI instead of a 3x3 in the DAI.

When uplift occurs (option available only in DCI), the TCP is subjected to a prescribed horizontal and vertical displacement and, therefore, the TCP equilibrium equations are not included in the Triple FP isolator equations of motion. Moreover, the kinematic equations (2-1) and (2-2) are no longer valid since the TCP moves independently to the rest of the isolator parts (except for potential short duration contact which is explained later). Therefore, the total number of equilibrium equations and unknown reduces to six. For the uplift case, the equations of motion are again given by Equations (2-3) with $\boldsymbol{\theta} = [\theta_1 \quad \theta_2 \quad \theta_3]$ and $\boldsymbol{\theta}_s = [\theta_{s1} \quad \theta_{s2} \quad \theta_{s3}]$, and with the addition of the force vector $\mathbf{F}_{vg} = [\mathbf{F}_{vga} \quad \mathbf{F}_{vgb}]^T$ to account for forces during possible contact

between the TCP and TSP. This force vector is a function of forces $F_{vg,l}$ and $F_{vg,r}$ described below and shown in Figure 2-4. The final uplift equations are given by:

$$\begin{aligned} \tilde{\mathbf{M}}\ddot{\boldsymbol{\theta}} + \tilde{\mathbf{K}}\boldsymbol{\theta} + \tilde{\mathbf{S}} + \tilde{\mathbf{F}}_g + \tilde{\mathbf{F}}_e + \tilde{\mathbf{F}}_s &= 0 \\ \tilde{\mathbf{F}}_{vg} &= \mathbf{F}_{vga} - \mathbf{K}_{ab} \mathbf{K}_{bb}^{-1} \mathbf{F}_{vgb} \end{aligned} \quad (2-9)$$

Landing is modeled by simply substituting the final conditions at the end of uplift as initial conditions in the compression equations.

Vertical forces $F_{vg,l}$ and $F_{vg,r}$ are activated when there is minute penetration between A and A' and B and B', respectively. Penetration is detected by comparing the coordinates of A with A' and B with B' and accounting for the horizontal and vertical displacement of the TCP as well as the curvature of surface 4. If both forces become simultaneously nonzero then the bearing is in compression and the isolator equilibrium equations are described by the compression equations. Such a case is depicted schematically in Figure 2-5. While in compression the vertical displacement of the TCP is compared to the vertical displacement that the isolator would have had if uplift was still occurring. If the latter becomes larger, then uplift initiates again. This back and forth switching between uplift and compression equations can occur many times during an uplift analysis when the height gained by the isolator parts during the uplift duration is larger than the specified uplift excitation. Such a case is usually encountered when the TCP uplift starts while the TCP is experiencing increasing lateral displacement.

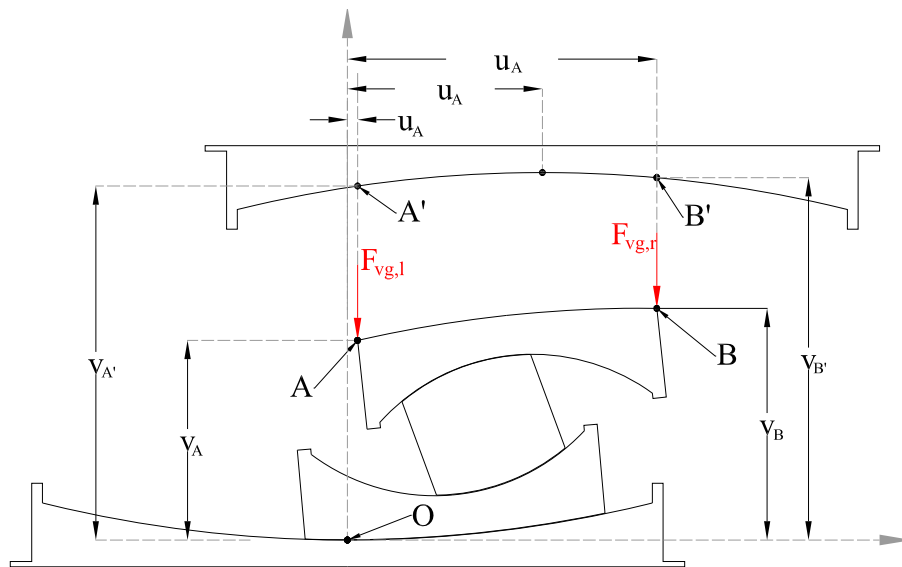


Figure 2-4: Vertical contact forces acting on the TSP

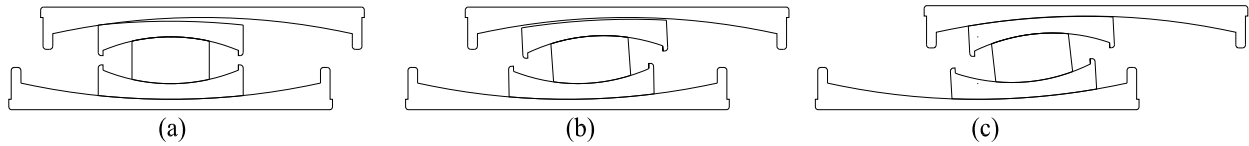


Figure 2-5: Triple FP undergoing landing prior to the end of uplift excitation

In the case of rigid body dynamics, each Triple FP part is modeled using three independent degrees of freedom located at the center of mass of each part (two translations and one rotation). These degrees of freedom are shown in Figure 2-6 in red color. The most important feature of this modeling is the distinction of each sliding interface into *contact surface* (surface of least diameter out of the two surfaces of the interface) and *sliding surface* (surface of larger diameter). Accordingly at each contact surface, two contact points (CR-i and CL-i) and their corresponding sliding points (SR-i and SL-i) are defined. Soft springs are located at contact points CR-i, CL-i. Their coordinates are continually updated based on the motion of the rigid body to which they are attached. Sliding points SL-i can be calculated as the intersection point of a vertical line that passes through each contact point and the corresponding sliding surface. Contact occurs when the contact points penetrate (by a minute amount) into the sliding points, which activates the spring forces of the contact points. The location of the sliding points and the slope of the sliding surface at these points, defines the direction of contact forces.

When advanced modeling is used, the equations describing uplift, compression and landing are the same with the exception that in the uplift case, the TCP is subjected to a prescribed horizontal and vertical displacement while for compression and landing, the vertical displacement is an additional degree of freedom.

Complete derivations for this modeling are complex and are presented in Sarlis and Constantinou (2013). It is noted that this more general formulation allows for a variety of different analyses to be conducted as, unlike the case of the full contact theory, there are no restrictions in the degrees of freedom definitions.

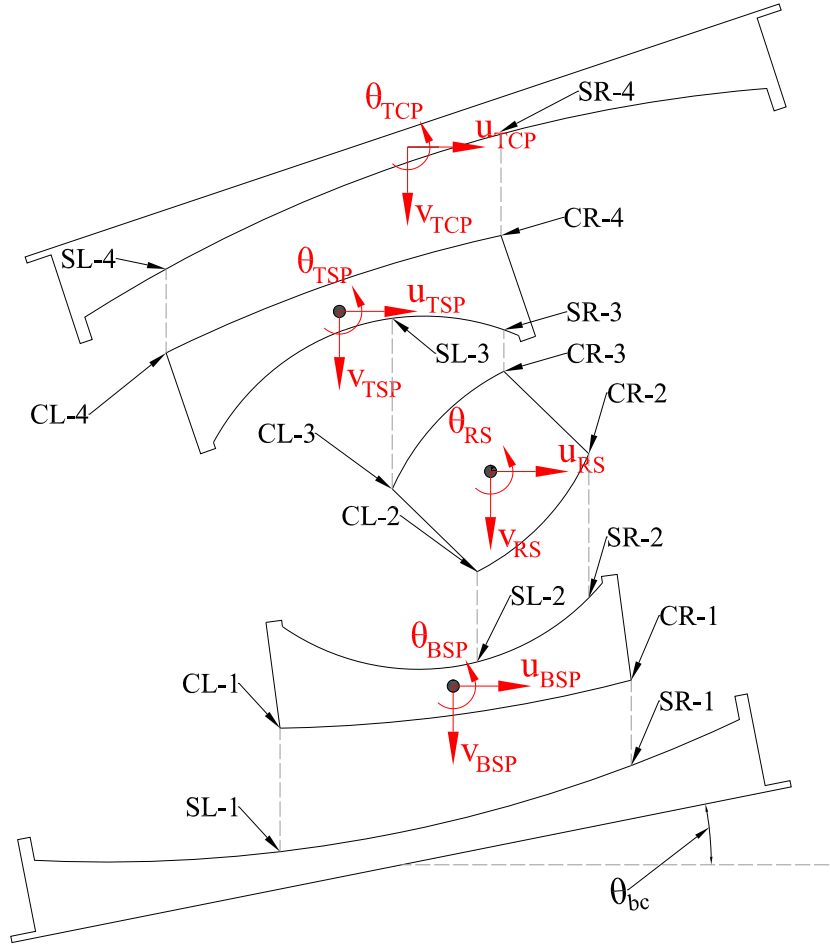


Figure 2-6: Degree of freedom definition for rigid body dynamics derivations

3 DISPLACEMENT CONTROLLED INTERFACE (DCI)

This interface can be used to analyze a Friction Pendulum (FP) isolator with four or less sliding surfaces when a displacement history is applied at the Top Concave Plate (TCP). The user can describe the isolator geometry and assign friction properties at each surface. The program can simulate the behavior of the FP isolator for any geometric and frictional properties and produce output for each surface. Animation of motion of the bearing and plots of response quantities can be generated. The program also offers the option to include a vertical displacement history in the case that uplift occurs and include, if desired, a variable vertical load (otherwise, the load is constant and abruptly reduces to zero when uplift occurs). The displacement histories can either be defined in the program or the user can import any displacement history through a “.txt” file (for example, the history of bearing motion calculated in analysis in program SAP2000 (Computers and Structures, 2007). Figure 3-1 shows the various panels of the DCI.

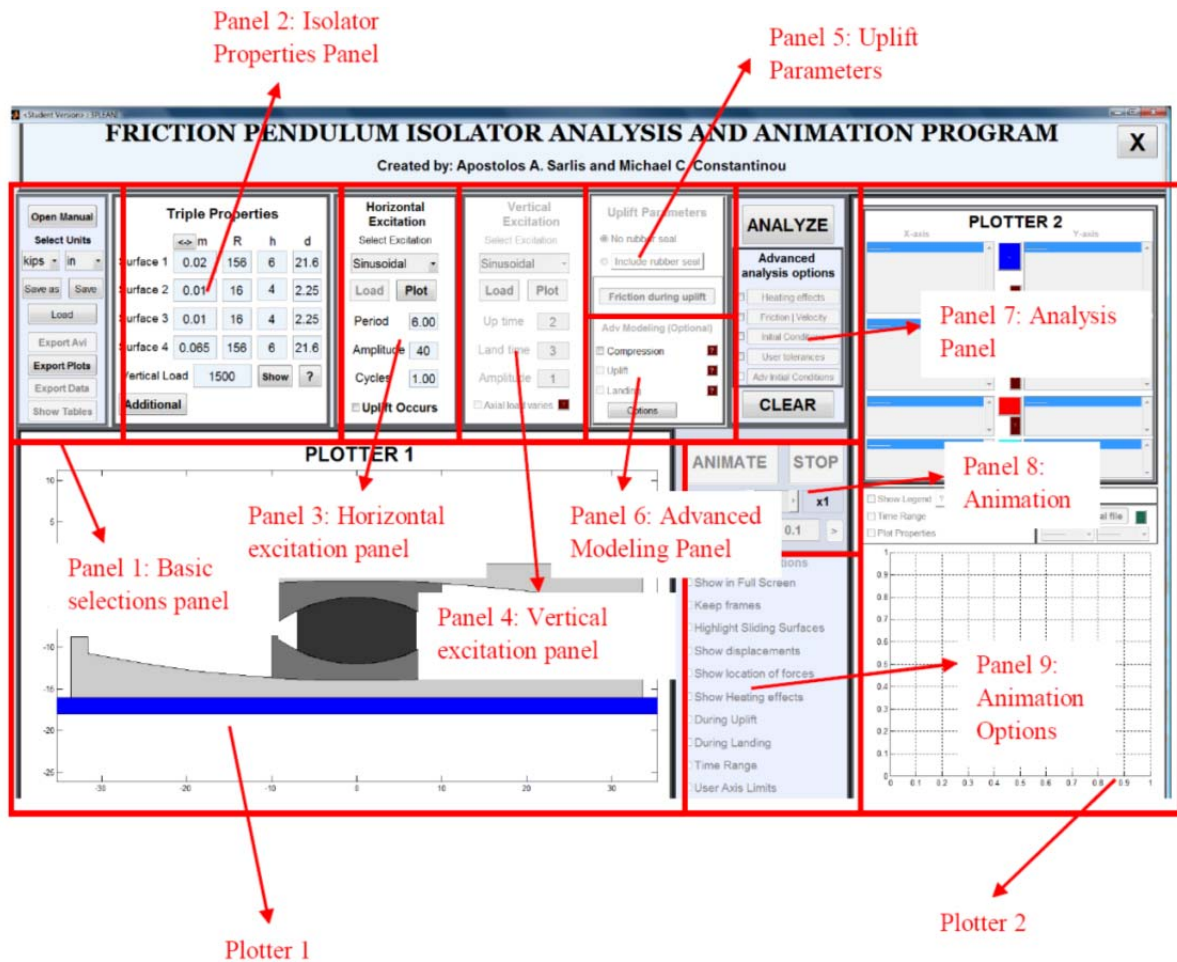


Figure 3-1: Panels of Displacement Controlled Interface

Plotter 1 in Figure 3-1 is used to display animations of the isolator and also draw the isolator while inputting parameters before running the analysis. Plotter 2 can only be used after the analysis is complete to display the analysis results together with animation of the motion of the isolator. Panel 2 is used to input the bearing parameters, while panels 3 and 4 are used to input the bearing excitation parameters. Panel 5 is used to define bearing properties if uplift occurs and Panel 6 is used to activate the rigid body dynamics theory (see section 2) for modeling the isolator behavior. Panel 7 is used to activate advanced options in the analysis such as heating and velocity effects on the friction coefficients, specify non zero initial conditions for the isolators, etc.

3.1 Panel 1: Basic selections panel

A view of panel 1 is shown in Figure 3-2. From this panel one can save the settings (geometric properties, excitation selections, etc.), load saved settings and to define the units to be used by the program. It consists of the following options:

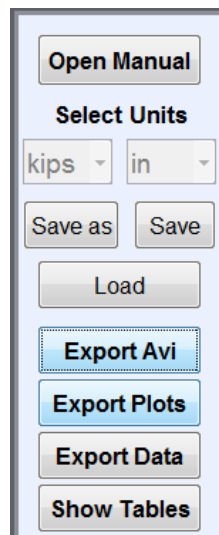


Figure 3-2: View of panel 1

Select Units: The first step is to select the units that the program will use in the analysis. All quantities that are input into the program should be in these units. Note that if the user selects one set of units (e.g., kN and mm) and later changes to another set of units (say kip, inch), this action will not transform the input to the new units. The selected units affect the calculation of quantities such as acceleration of gravity, steel density, etc. Units of time are sec.

Save: By pressing this button one can save the current state of the program in a separate file. All input parameters, imported ground motions, selections, etc. will be saved. If the user saves after an analysis is complete, all analysis results are saved. The user can load the saved file into the program by pressing the Load button. The parameters are saved in a “.udb” file.

Load: Loads previously saved files into the program.

Export Avi: When this button is pressed, the window shown in Figure 3-3 appears. This window contains two main options: a) export an “.avi” video and b) massively export “.tiff” images of the animation at selected time instances. If the user selects to export in “.avi”, then the video window size needs to be specified in inches or full screen. The user also needs to select the duration of the response to be included in the video by specifying the start and end time. The frames per second control the exported video duration. The **Auto Calculate** button calculates the required number of frames so that the duration of the exported video matches the analysis time (video is real time). Different values either slow down or speed up the video duration. Finally, the user can create a multi-screen video with different animations at each screen by selecting the multiple screens option (maximum is 3 rows and 2 columns). For example, in Figure 3-3, the exported video will be divided into a 2x2 grid. The top left screen will display the isolator animation, with the axis limits calculated automatically by the program. The bottom left screen will display the animation of the TCP displacement history, the bottom right screen will animate the force displacement loop while the top right screen will show the isolator animation with user defined axis limits (the option auto limits is not selected). The latter can be used to animate a zoomed view of the isolator motion (say zoom in to display the TSP behavior). After the **OK** button is pressed, the “.avi” animation is generated in a new window. This window should not be interrupted for the animation to be generated successfully. If the window is closed while generating the animation then only the portion of the animation that was created prior to closing the window will be saved into the “.avi” file.

If the user selects to export “.tiff” figures as shown in Figure 3-4, snapshots of the animation are exported and saved into separate “.tiff” figures, where the first figure to be exported is defined by the start time, the last figure by the end time (time instance of last figure) and intermediate figures by the increment. For example if **OK** is pressed in Figure 3-4, 32 “.tiff” files will be generated. The axis limits of the exported figures are controlled by the axis limits of plotter 1

(automatically calculated by the program or user defined by specifying axis limits at the bottom of Panel 9). The exported “.tiff” files are exported into the Exported Frame folder with each file name containing the date, time of exporting as well as the animation time of the snapshot.

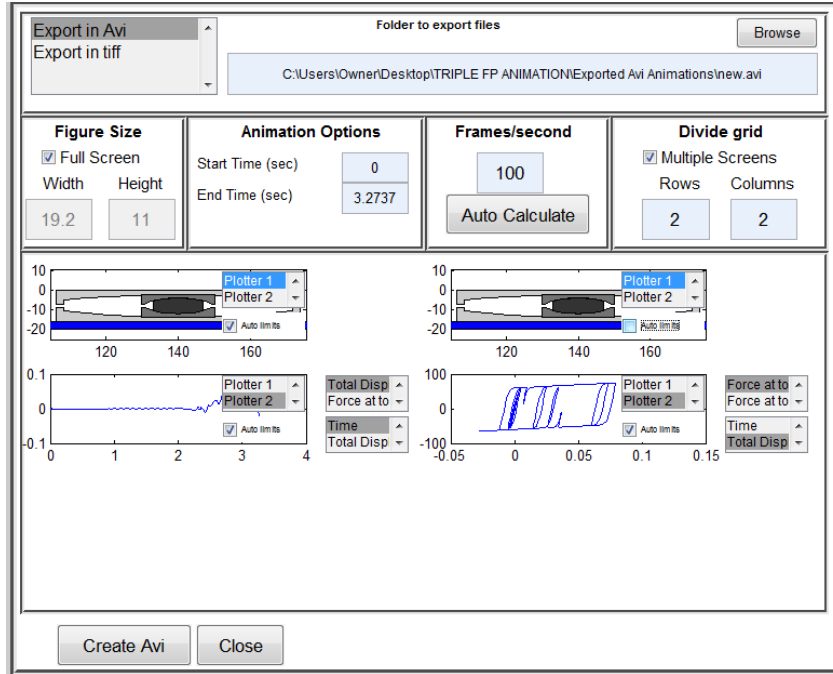


Figure 3-3: Window displayed when Export Avi is selected

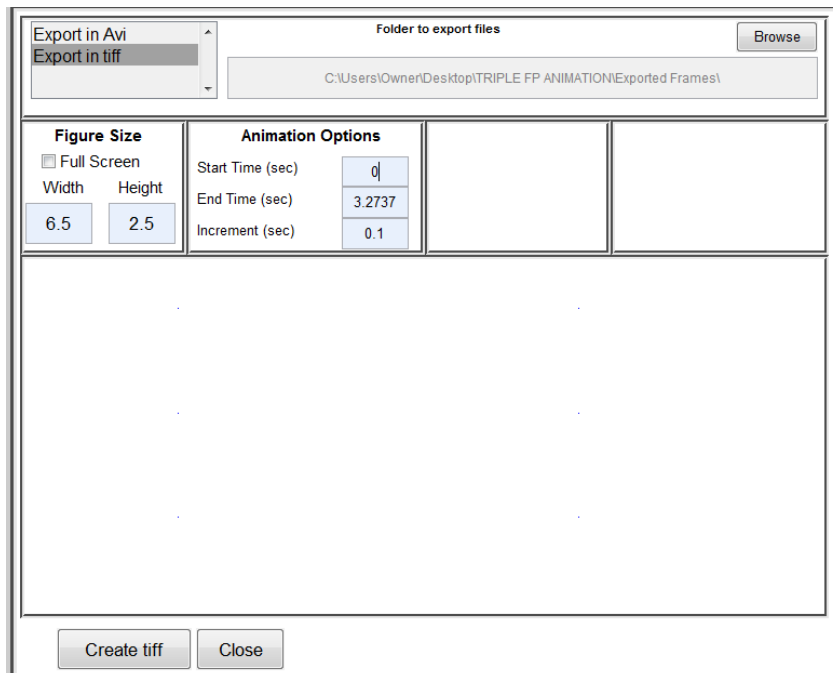


Figure 3-4: Window displayed when Export Avi is pressed and option Export in tiff is selected

Export Plots: This option can be used to export all plots that appear in Plotters 1 and 2 in Matlab figures. When this button is pressed, the window shown in Figure 3-5 appears. The user can select the size (in inches) as well as the format of the exported plot. Pressing the **View** button in Figure 3-5 will display the plot in a separate window where the user can further copy and paste into Microsoft Word or Excel or further export in tiff, jpg and other formats. Pressing the **Export** button will do the same with the addition that the user can directly save the exported plot on the hard drive. The bottom part of Figure 3-5 is used to add title and labels, and to modify the format of the plot including font size, font, weight (bold or normal) and angle (italic or normal) of all plot components, grid line style and color. Note that the user can also modify the axis limits. Leaving the entries title, x-label, y-label empty removes these components from the plots. A preview of the plot seen while the user is selecting the formatting options is shown at the bottom of Figure 3-5 (Preview Plot). The user can save the selected format into a separate file by pressing the **Save Template** button. The saved files become available by pressing the **Load Template** button. Note that the saved template file is independent of the interface that is running and can be loaded in both the DAI and DCI.

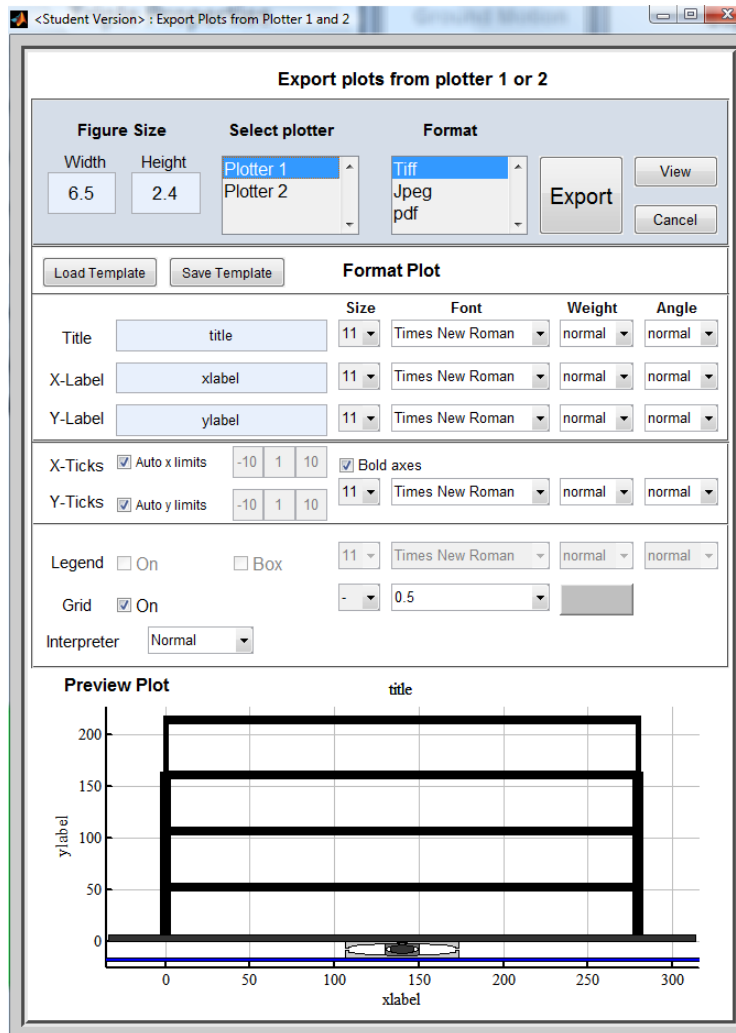


Figure 3-5: Window that appears when Export Plots is pressed

Export Data: This becomes available after the analysis is complete. Analysis results (all variables that appear in the popup menus for the variable selections of plotter 2) can be exported to an Excel file or a Matlab file. In the case of the Excel file, three spreadsheets are created that contain: a) analysis results, b) all input parameters for the analysis, and c) a picture of the interface. In the case of the Matlab (.mat) file, the user is asked to select the variables to be saved. The list of variables is the same as the one appearing in the list boxes of Plotter 2. The Matlab file is saved in a format so that it can be directly loaded back into the program by pressing **Load External File** in the Plotter 2 panel.

Show Tables: Becomes available only after an analysis is complete. A separate window is created where a variety of results are displayed in tabular form. A typical window that appears

after pressing this button is shown in Figure 3-6. The user can view the complete history for all analysis variables. If the *Specify time range* is selected, then the data for only the specified time range is displayed (useful to display results in cases where uplift occurs). Note that the *Peak value* is the maximum of the absolute values of each variable. The displayed variables can be copied for pasting into an Excel file by right clicking on the variable names.

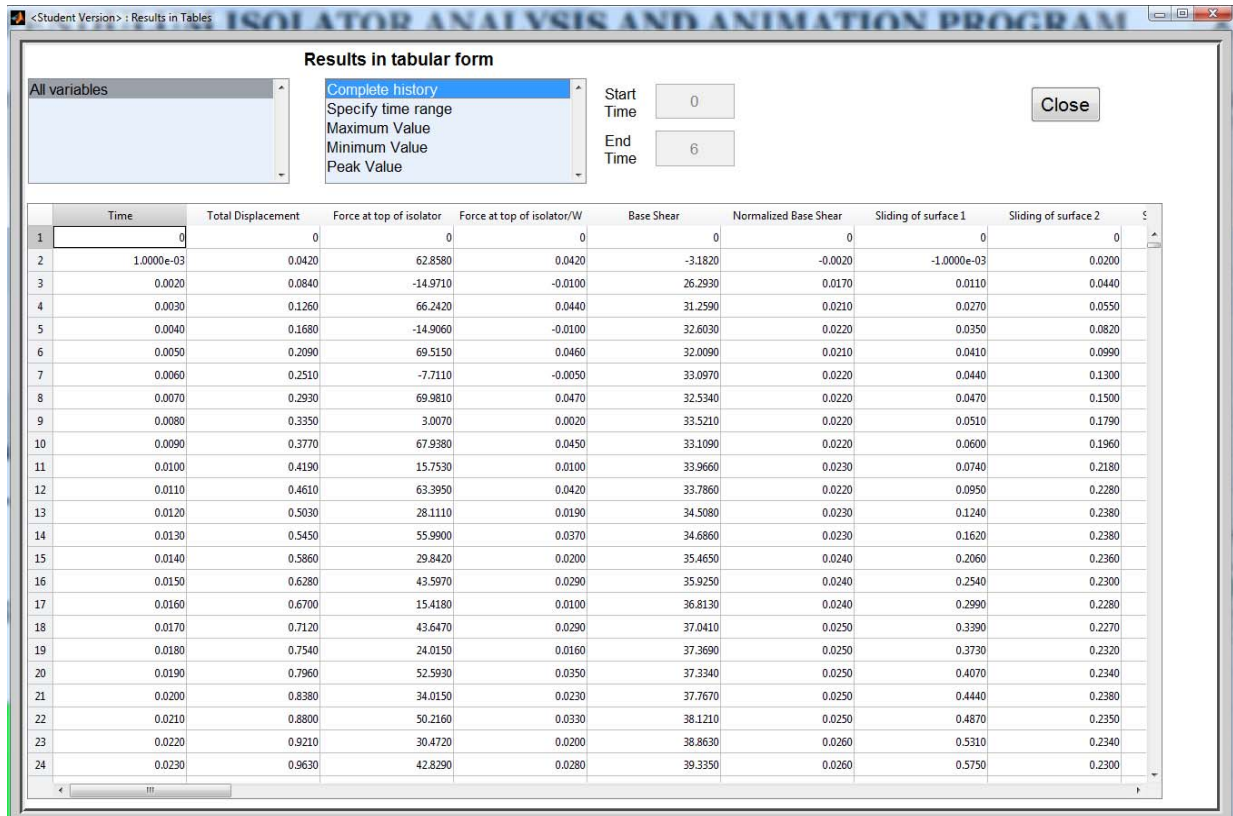


Figure 3-6: Window that appears when Show Tables is pressed

3.2 Panel 2: Isolator properties panel

Panel 2, shown in Figure 3-7, is used to describe the geometry and frictional characteristics of the isolators. The program allows the user to describe the geometry and characteristics of up to four sliding interfaces. The interface is constructed based on the geometry of the Triple FP isolator. Moreover, by appropriately selecting the geometry and friction coefficients one can also model the single FP, the double FP with articulated slider, the double FP with rigid slider, and the modified single FP (isolators with less than four sliding surfaces can be modeled by specifying large friction coefficients for some of the surfaces).

Triple Properties

Load Geometry
Save Geometry

	m \leftrightarrow	R	h	d
Surface 1	0.02	156	6	21.6
Surface 2	0.01	16	4	2.25
Surface 3	0.01	16	4	2.25
Surface 4	0.065	156	6	21.6
Vertical Load	1500	Show	?	

Additional

Figure 3-7: View of panel 2 and its components

The first column of edit boxes in panel 2 is used to assign values for the friction coefficient for each of the surfaces (μ_i in Figure 2-1); the second column to assign values for the radii of curvature (R_i in Figure 2-1); the third column to assign values for the height (h_i in Figure 2-1), and the last column to assign values for the nominal displacement capacities (d_i in Figure 2-1) of each surface. Note that Figure 2-1 is displayed by the program when the ? button is pressed. It is noted that while the user enters values for the isolator geometry, the Triple FP geometry is directly drawn in Plotter 1 and it is updated any time a geometric property is changed. The **vertical load** option is used to assign the external normal force applied on the isolator. Depending on the excitation type, the axial load may remain constant or the user has the option to include variability in the axial load. In the case where axial load variation is included, the value assigned here is used as the initial value of the axial load on the isolator. Otherwise, this value is assumed to be constant throughout the analysis and becomes zero when uplift occurs. Details on this are presented later.

An important distinction in this program is that the coefficient of friction specified is that at the sliding interface as if it were flat. By comparison when a Triple FP bearing is tested the friction values measured are affected by the spherical geometry of the sliding surfaces and the location and direction of the resultant of the tractions on each sliding surface. The frictional parameters that describe the behavior of the Triple FP bearing in the models of Fenz and Constantinou (2008a to 2008e) and Morgan (2007) ($\bar{\mu}_1, \bar{\mu}_2, \bar{\mu}_3, \bar{\mu}_4$, with the following restrictions

$\bar{\mu}_2 = \bar{\mu}_3 \leq \bar{\mu}_1 \leq \bar{\mu}_4$) utilize the values extracted from experiments of the Triple FP bearings and are not fundamental properties of the interfaces. Sarlis and Constantinou (2013) have recently shown that the true frictional values ($\mu_1, \mu_2, \mu_3, \mu_4$ without any restrictions on the friction values) are related to those in the models of Fenz and Constantinou (2008a to 2008e) by the following equations:

$$\begin{aligned}\bar{\mu}_2 &= \mu_2 \frac{R_2}{R_{eff2}} \\ \bar{\mu}_1 &= \frac{\mu_1 R_1 - \mu_2 R_2}{R_{eff1} - R_{eff2}} \\ \bar{\mu}_4 &= \frac{\mu_4 R_4 - \mu_2 R_2}{R_{eff1} - R_{eff2}}\end{aligned}\quad (3-1)$$

Program 3pleANI makes use of friction values $\mu_1, \mu_2, \mu_3, \mu_4$. The above equations should be used to convert values. The button <-> may be used to specify friction values $\bar{\mu}_1, \bar{\mu}_2, \bar{\mu}_3, \bar{\mu}_4$, then convert them to friction values $\mu_1, \mu_2, \mu_3, \mu_4$ and import them to the program.

Additional: This can be used to input additional parameters to describe the exact geometry of the isolator. The menu that appears when the **additional** button is pressed is shown in Figure 3-8. The properties include the “slide plate diameter”, “rigid slider diameter”, the “exterior restrainer thickness”, the “BCP restrainer height”, the “TCP restrainer height”, the “interior restrainer height” and the “concave plate thickness” (minimum thickness of the top and bottom concave plates, assumed to be the same for the two plates). It should be noted that the correct description of the geometry of the bearing is important because it is used to calculate the weight of individual bearing components and the rubber seal forces, which are important in the calculation of response during uplift. Also, the heights of the restrainers are important in assessing collapse of the components during uplift. For example, a case that the program identifies as collapse of the isolator is shown in Figure 3-9-the possibility of such a case occurring depends on the TCP restrainer height. The window contains a plotter on the side that redraws the bearing geometry while defining the additional bearing parameters. The notation of the variables that appear here is shown in Figure 2-1. This figure is displayed when the ? button is pressed.

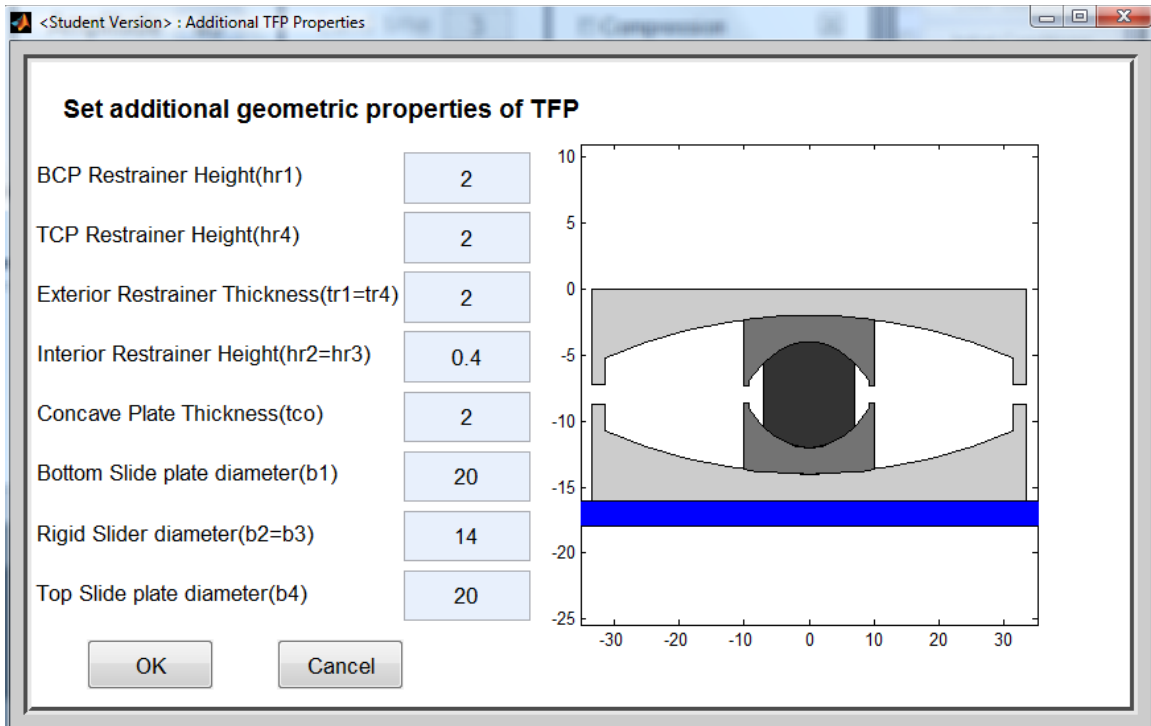


Figure 3-8: View of window displayed when Additional button is pressed

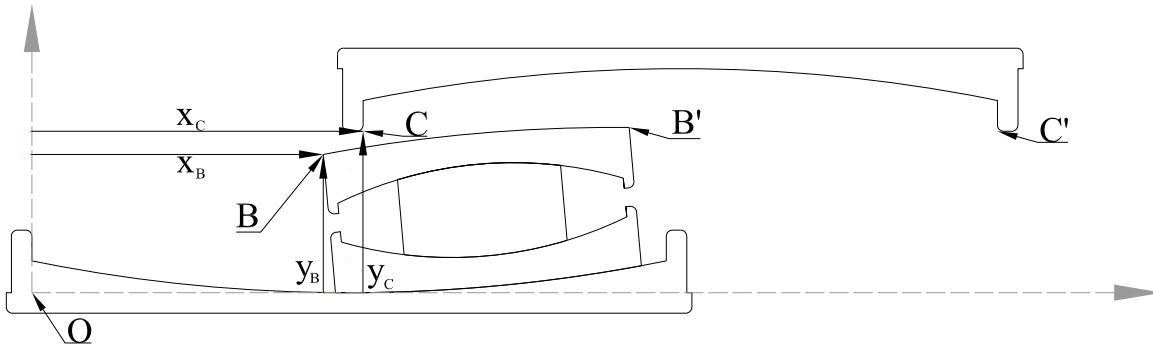


Figure 3-9: View of deformed TFP isolator when collapse occurs during uplift

Show: Shows the geometry of the isolator in a separate window that displays additional information about the isolator. This includes the sliding angle capacities (displacement capacity divided by radii of curvature), total displacement capacity of isolator (assuming infinitely rigid restrainers), apparent pressure at each surface, and weight and the location of the center of mass of each component. Note that the centers of mass are calculated for the entire three dimensional bearing and not for the two dimensional cross section that is displayed. A typical display when this button is pressed is shown in Figure 3-10. It is noted that BSP is the bottom slide plate, RS is the rigid slider, TSP is the top slide plate, TCP is the top concave plate and BCP is the bottom concave plate as shown in Figure 2-1.

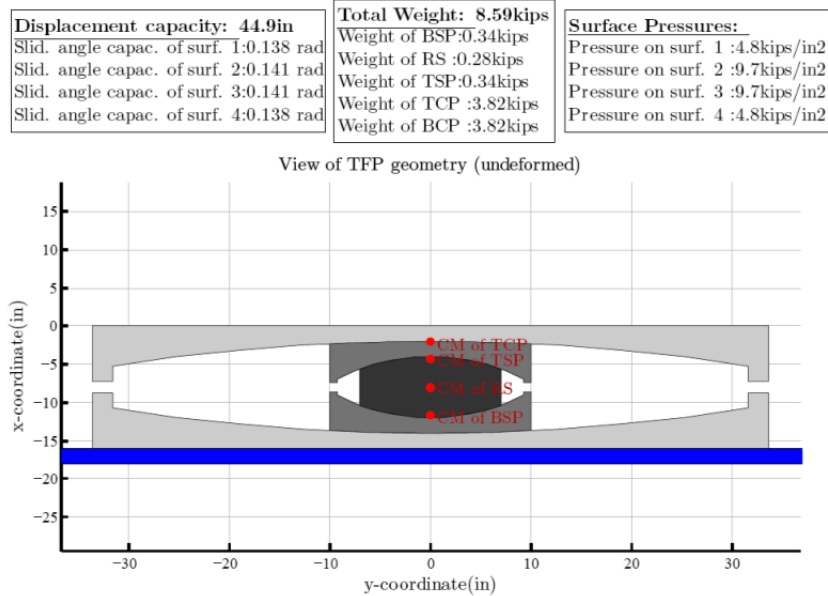


Figure 3-10: Figure appearing when the *show* button is pressed

<->: This is a tool for transforming the friction coefficients from the Fenz and Constantinou (2008a) theory to the Sarlis and Constantinou (2013) theory. Figure 3-11 shows the dialogue box that appears when this button is pressed. In Figure 3-11, the user can specify friction values $\bar{\mu}_1, \bar{\mu}_2 = \bar{\mu}_3, \bar{\mu}_4$ according to Fenz and Constantinou theory in the first column of edit boxes. The program calculates the values $\mu_1, \mu_2, \mu_3, \mu_4$ based on Equation (3-1) and displays the values in the second column of edit boxes. By pressing the ***Copy and paste into program*** button, the calculated values in the second column of edit boxes (per Sarlis and Constantinou, 2013) are pasted in panel 2 for use by the program. Note that the effective friction value (per Fenz and Constantinou) of any surface depends on the actual friction coefficients of other surfaces and vice versa. Therefore the user must specify the friction values of all surfaces prior to pressing the ***Copy and paste into program*** button. Also, the friction coefficients $\mu_1, \mu_2, \mu_3, \mu_4$ in Equation (3-1) depend on the geometry of the bearing. The transformation is done using the effective radii. Therefore, this menu should be utilized only after the final geometry of the bearing has been specified in panel 2.

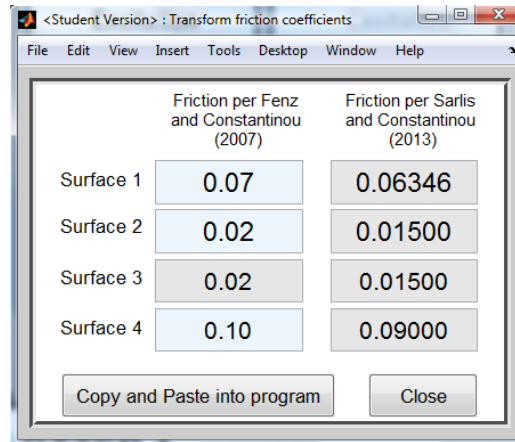


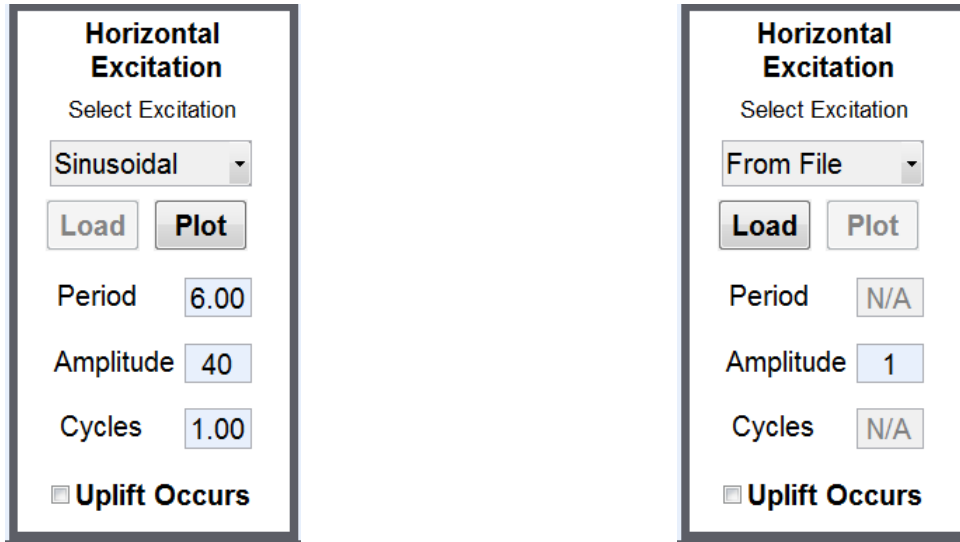
Figure 3-11: Dialogue box that assists in transforming friction coefficients from the Fenz and Constantinou theory to the Sarlis and Constantinou theory

Save Geometry: The user can save the specified properties of the bearing into a separate file. The friction coefficients, radii, heights, displacement capacities, vertical load and other geometric properties described through the *Additional* button are saved and can be later loaded into the program. Note that the saved file can be loaded into any of the two interfaces (DAI or DCI). This option should be distinguished from the Save option in Panel 1 that saves all the interface parameters.

Load Geometry: Loads all previously saved properties of an isolator into the program.

3.3 Panel 3: Horizontal excitation

Panel 3 is used to (a) define the horizontal displacement history that will be applied on the Top Concave Plate (TCP) of the isolator, and (b) define if uplifts occurs. If uplift is specified to occur, then the program prompts for specification of the uplift displacement history. Panel 3 for horizontal excitation is shown in Figure 3-12.



a) View of panel 3 for sinusoidal excitation b) View of panel 3 for excitation read from file

Figure 3-12: Horizontal excitation panel

Select Excitation This popup menu defines the type of excitation. Options are:

- **Sinusoidal** excitation, the program generates a sinusoidal motion of the specified number of *cycles*, *amplitude* and *period*.
- **From File**: The user imports a history of motion using a “.txt” file. The “.txt” file must contain columns of data (separated by spaces and read row by row). The data in the file should represent the displacement values at equal time intervals and must be consistent with the units selected in panel 1. If units are not consistent, the *amplitude* edit box can be used to make units consistent. Once one selects **From File** in the popup menu, the option **Load** becomes available as shown in Figure 3-12.

Load: Becomes available only when the **From File** option is selected in the **Select Excitation** menu and it is used to import a “.txt” file. It opens a window for the file selection. After the user selects the name of the file to import, a dialogue box will ask for the time step of the file. The **Plot** button can then be used to view the displacement history and verify that it is properly imported.

Plot: Shows the horizontal excitation that was defined by the user in this panel. A typical display when this button is pressed is shown in Figure 3-13. Figure 3-13 is obtained from an example where the horizontal excitation is **From File**. The name of the imported file and a plot of the

excitation are displayed at the bottom of the window. Also all the imported data are shown in tabular form on the “Data Values” panel. When selecting a single or multiple data points from the table these points are highlighted on the plot with a blue dot when the *Show Data Points* is selected. If the *Copy all data* is selected then the data are directly copied and can be pasted in Excel. In this window the user can format the plot as wished and export it into a separate window from which it can be further copied or saved into any desired format.

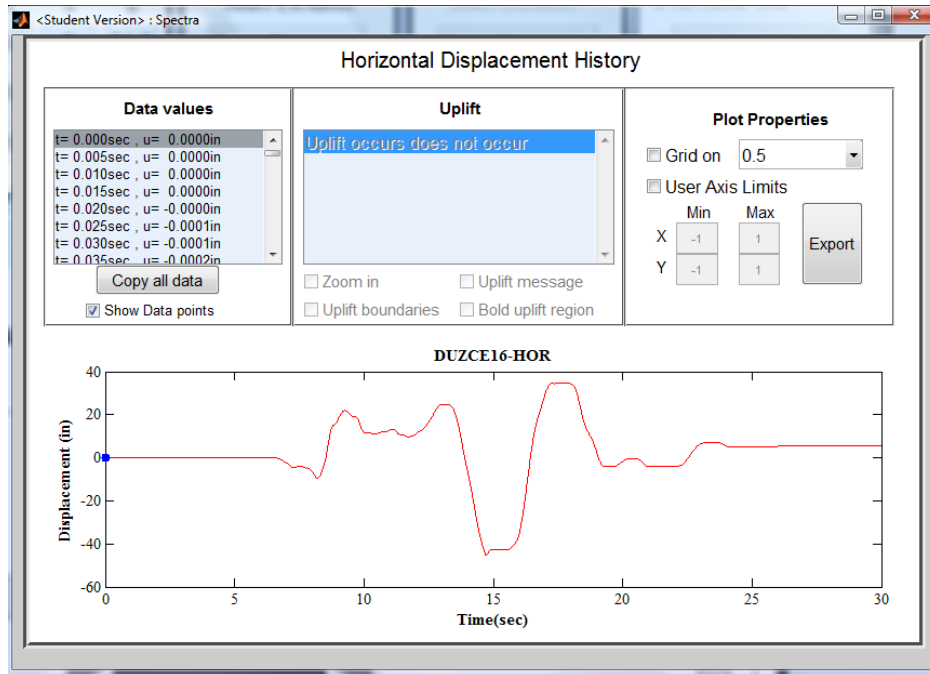


Figure 3-13: Window displayed when the Plot button is pressed in the horizontal excitation panel

Period: Is only available when the selected excitation is sinusoidal and defines the period of one cycle (it is not the duration of motion). The duration of the motion is equal to the number of cycles times the period of the motion.

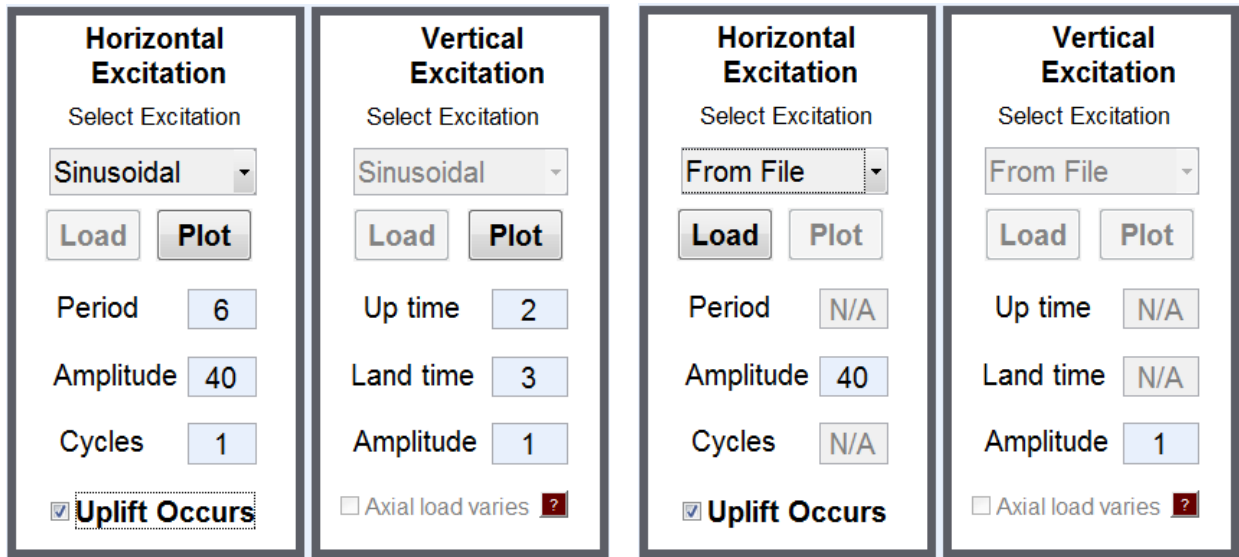
Cycles: Is only available when the selected excitation is sinusoidal and defines the number of cycles of the motion. It can have any value, including non-integer values.

Amplitude: Is used to (a) define the maximum displacement or amplitude of the motion in the case of a sinusoidal excitation and (b) define a scale factor to be applied to the motion imported from a file. This value is automatically set to 1 when importing a file but it can be changed. The value can be positive or negative.

Uplift Occurs: This option allows the user to specify that uplift occurs. If the box is left unchecked, uplift does not occur. If the box is checked, panels 4 and 5 become available in order to define the vertical excitation and additional parameters of the isolator that are relevant to capturing its uplift behavior. Note that selecting this option and specifying zero amplitude for the vertical excitation allows the user to enable other options in the analysis without occurrence of uplift. For example, the user can include variable axial load (even when uplift does not occur).

3.4 Panel 4: Vertical Excitation

Panel 4 is used to define the vertical excitation in case the user selects the **Uplift Occurs** option in panel 3. Panel 4 is shown in Figure 3-14 when two different options are selected for the horizontal excitation in the Horizontal Excitation panel.



a) View of panels 3 and 4 for **Sinusoidal**

b) View of panels 3 and 4 for **From File** option

Figure 3-14: View of panels 3 and 4

The specified uplift displacement history in this panel represents the vertical displacement of the TCP with respect to the position when uplift initiates (note that the isolator gains height when is laterally deformed). This is depicted in Figure 3-15 where v_u is the uplift excitation defined in the vertical excitation panel. This displacement is added to the vertical displacement of the TCP v_p at time t_l (when uplift occurs). For animation of the motion of the bearing, the specified vertical displacement (uplift) is superimposed to the vertical motion of the bearing components due to the pendulum motion and accounting for the conditions of compatibility of displacements (i.e., parts cannot overlap, there is no “penetration” of parts, etc.). Compatibility of

displacements has to be enforced during landing and that may require free fall of parts, which is captured in the analysis and may be animated. This case is depicted in Figure 3-15 as the instance at which there is a difference between vertical displacements v_{TCP} and v_p at the end of uplift $t=t_2$.

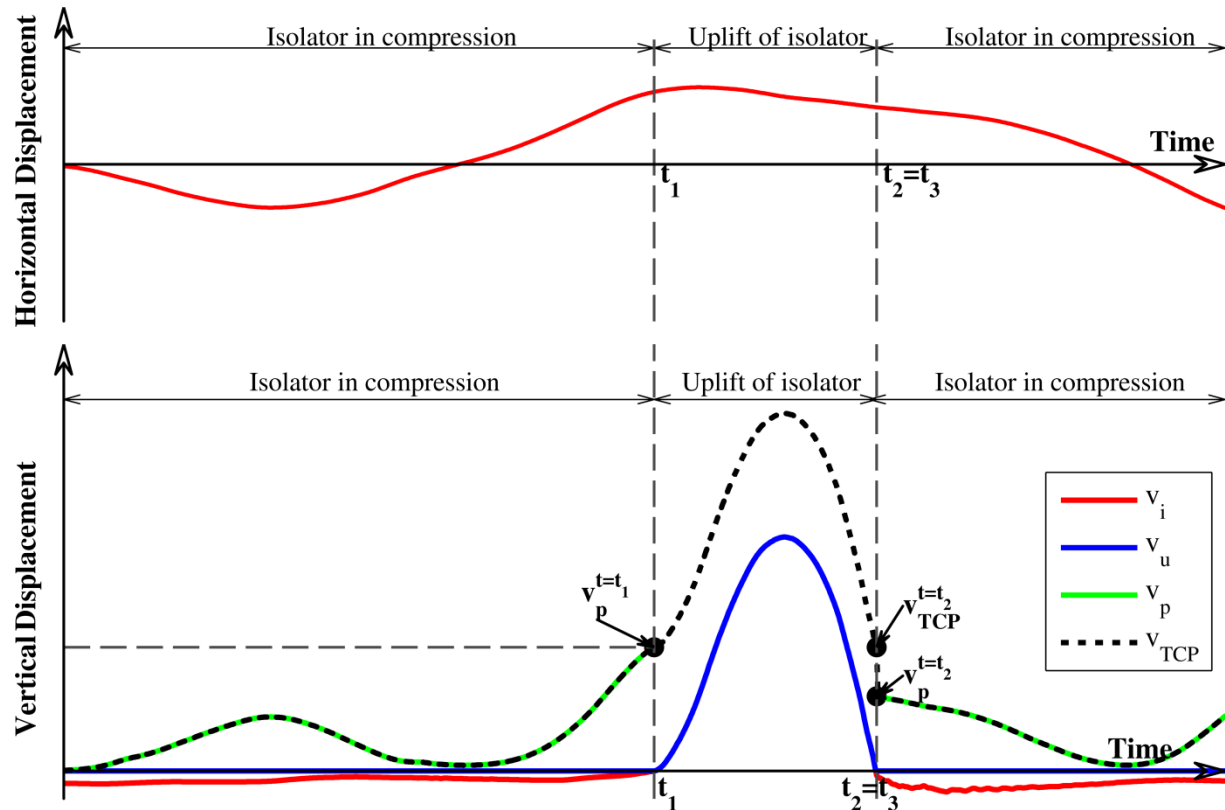


Figure 3-15: Definition of input vertical displacement for uplift analysis

Select excitation: This popup menu defines the type of the excitation. It is always disabled and the selected options depend on what is selected for the horizontal excitation as shown in Figure 3-14.

- **Sinusoidal:** If the user has selected a sinusoidal horizontal excitation, then the vertical excitation is also sinusoidal. The program generates a file that has zeros everywhere except for the duration of the uplift which the user has to define by setting the “*up time*” t_1 and “*land time*” t_2 values that are described next. Uplift will occur for the duration between times t_1 and t_2 . The program generates a half sine pulse to describe the vertical displacement of the top concave plate that has the amplitude defined by the user (in units consistent with those selected in panel 1) and frequency equal to $\pi/(t_2 - t_1)$. This guarantees that the top

concave plate will separate exactly at time t_1 and land exactly at time t_2 and that the top concave plate will reach the specified maximum displacement at time $(t_2 - t_1)/2$. It should be noted that the sinusoidal case allows for uplift to occur only once during the entire duration of the horizontal excitation. The vertical excitation input generated by the properties shown in Figure 3-14 (a) is presented in Figure 3-16 when the **Plot** button is pressed. The vertical load for this selection is constant and equal to the value set in panel 2. When uplift starts, the load is set equal to zero, and when uplift stops the load returns to the specified value. Note that although the change of the axial load at the initiation of uplift appears as abrupt, in reality it is not as some smooth transition is assumed (see “*Note on smooth transitions between bearing states*” later for more details).

- **From file:** This option becomes available only when the horizontal excitation was specified using the option **From File**. The user needs to load a “.txt” file with data points in columns that describe the vertical motion to be applied to the top concave plate. The imported file needs to contain equal or less number of points as the already imported file of the horizontal motion. If data points are less, then zeroes are added at the end of the vertical excitation in order for the two files to have equal number of points. Note that the horizontal file needs to be imported first and the time step of the horizontal and vertical file are the same. The imported file needs to contain positive and negative values. According to the software’s sign convention, the positive values represent uplift or upward displacement and negative values represent downward displacement as that caused by the application of the gravity load. This sign convention is consistent with the default convention in program SAP2000 that describes the vertical displacement history of the top joint of the isolator. A typical vertical displacement output from SAP2000 is shown in Figure 3-17 after the file was imported in 3pleANI and the **Plot** button was pressed. The program has identified that uplift occurs 5 times with durations shown in Figure 3-17 and highlighted in the vertical excitation plot (detected by identifying the zero crossing points). For the intervals of time for which uplift does not occur, the isolator is considered to be under compression. If for some reason, the imported file uses different sign convention, the user can make the conversion by use of **amplitude** with value of -1 to change the sign. Once the file is imported, all negative values are neglected (unless the **Axial Load varies** option is selected in which case the negative values are used for the axial load variation). Unlike the case of

sinusoidal, in the option *from file* there is no restriction on the number of times uplift occurs as long as the uplift duration is larger than the time step of the imported horizontal excitation file (otherwise, uplift duration is considered short and neglected). The imported file cannot start while in uplift (except for the sinusoidal case where uplift can start at time zero) and cannot end while in uplift. If a “.txt” file with all negative values is imported, uplift will not occur and the program will only consider the imported file if *Axial Load varies* has been selected. In doing so, vertical load variation will be considered but without uplift. It should be noted that importing a new file overwrites the previously imported file.

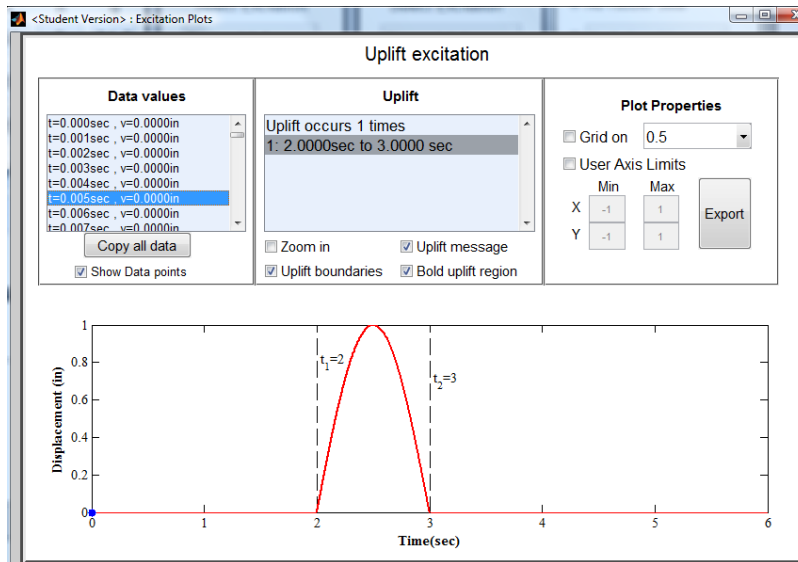


Figure 3-16: Typical vertical excitation for “sinusoidal” case

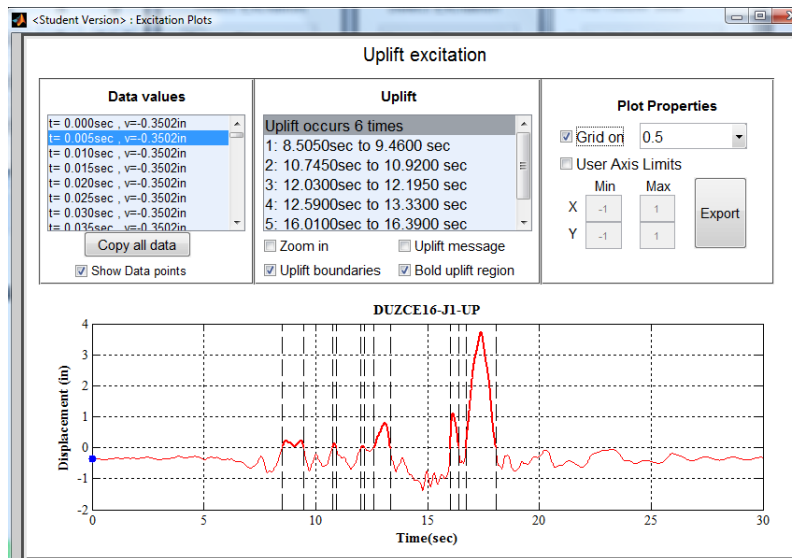


Figure 3-17: A vertical displacement history imported from SAP2000

Up time (t_1): The user defines the time at which uplift initiates (the top concave plate separates from the remaining components; see Figure 2-2). This option is only available when the excitation is *Sinusoidal*. In the case that the uplift displacement history is imported with the use of a file, this option is disabled since the detection of uplift is automatically done by the program.

Land time (t_2): The user defines the time at which uplift ends (contact is re-established between the top concave plate and the rest of the bearing; see Figure 2-2). This option is only available when the excitation is *Sinusoidal*.

Amplitude: Defines the peak value of displacement (see Figure 3-16, the peak value of unity is multiplied by the *Amplitude* value) when the *Sinusoidal* case is selected. The *Amplitude* must be positive when the *Sinusoidal* case is selected. In the case that the uplift displacement history is imported with the use of a file, *Amplitude* is used as a scale factor, which now can be positive or negative. If the amplitude is zero then uplift does not occur regardless of the imported files or the specified uplift parameters. A user may select **Uplift Occurs** in Panel 3 and then specify zero amplitude in order to activate other options such as the inclusion of the rubber seal in the analysis of the bearing in compression (which may affect the analysis results when the normal load on the bearing is small).

Axial Load varies: This option allows for variability of the axial load. The option becomes available only when the option **Uplift Occurs** is selected in panel 3 and the imported motions are from a file. The imported file for the vertical motion needs to contain some negative values. For more details see the description for **Select Excitation** (for Panel 4) earlier in this document. This option is useful when the imported file was generated in a commercial software program like SAP2000, which also calculates the history of axial load on the isolator. In such cases, fluctuations in vertical load relate to proportional fluctuations of the vertical displacement (e.g., prior to uplift the vertical load and vertical displacement are related by the vertical stiffness of the isolator). The vertical load is given as:

$$N(t) = N_o \frac{v(t)}{v(t=0)} \quad (3-2)$$

Where $v(t)$ is the imported vertical excitation history, $v(t=0)$ is the value at time $t=0$ and N_o is the vertical load specified in Panel 2. If a “.txt” file with all negative values has been imported, the

program will consider axial load variation without uplift. When the user has not selected ***Axial Load varies*** then the normal load is considered constant and equal to the value that was specified in panel 2. Figure 3-18 shows an example of axial load variation when the vertical excitation file of Figure 3-17 has been imported and the vertical load in Panel 2 is 1500kip. To display the window of Figure 3-18, the ? button next to the ***Axial Load varies*** has to be pressed.

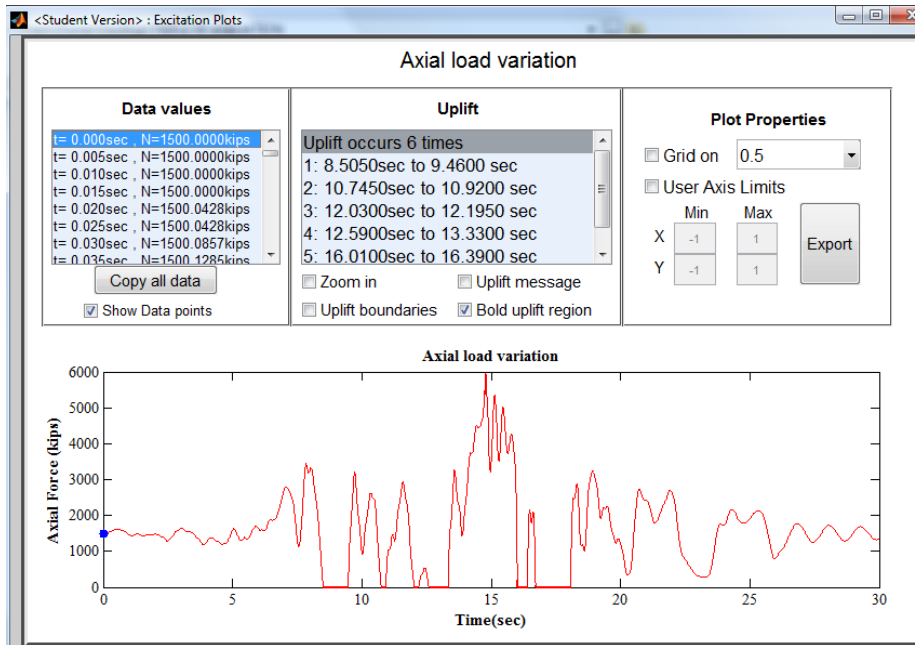


Figure 3-18: Axial load variation considered when the file of Figure 3-17 is imported

Note on smooth transitions between bearing states: Regardless of whether ***Axial Load varies*** option is selected or not and regardless of the vertical excitation type (***Sinusoidal*** or ***From File***), at the initiation of uplift the program ensures that there is a smooth transition in the vertical load from a nonzero value to the zero value. In doing so, the compression equations are solved up to time t_l when uplift starts. Then using the final conditions as initial conditions, the program solves the compression equations with a varying axial load that drops from its previous value (value in Panel 2 N_o , if axial load does not vary and value $N(t = t_l) = N_o v(t = t_l)/v(t = 0)$ if axial load varies) to zero in 0.1sec duration while the horizontal TCP displacement is constant. Only the final step of this solution is saved in the results and is used to calculate the initial displacements in the uplift equations but not the initial velocities which are calculated from the solution prior to the smooth transition.

3.5 Panel 5: Uplift Parameters

Panel 5 (see Figure 3-19) is used to define parameters related to the rubber seal that constrains the internal components of the bearing, and friction coefficients values that will be used for analysis during uplift. The rubber seal properties are important during uplift since the seal provides stability of the inner components and affects the normal load on surfaces 2 and 3.

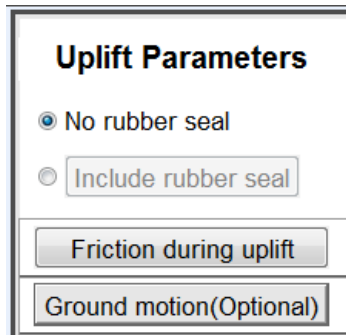


Figure 3-19: View of panel 5

No rubber seal: This option removes the rubber seal. The seal is not shown in the animation.

Include rubber seal: The seal is modeled as a linear elastic element. Two springs are considered in the analysis: one spring is connected between the top and bottom slide plate on the left side and a second identical spring is connected on the right side. When this option is selected the window shown in Figure 3-20 appears. The user has two options, a) include a seal with **constant stiffness** (Figure 3-20) and b) Include a seal with **variable stiffness** Figure 3-21. In the first case the user can either directly specify the value of stiffness of the seal or select **Auto Calculate 1** (in that case the edit box becomes disabled and just displays the calculated stiffness) which automatically calculates the seal stiffness based on the following equation and for seal properties $E=1400\text{psi}$ ($=5\text{MPa}$), thickness $t=0.06\text{in}$ (60mils) and free height x_1 (see Figure 2-1):

$$K = \frac{\pi b_1 t E}{2x_1} \quad (3-3)$$

Selecting **Use Attachments**, automatically calculates the seal stiffness based on Equation (3-3) and for the same properties but using height x_2 (instead of x_1) which is automatically calculated based on the specified seal attachment points at the bottom of the window and is given by Equation (3-4).

$$x_2 = h_1 + h_4 - R_1 + \sqrt{R_1^2 - (b_1/2)^2} - R_4 + \sqrt{R_4^2 - (b_4/2)^2} - s_{A1} - s_{A2} \quad (3-4)$$

s_{A1} and s_{A2} are the specified distances of the attachment points (can be changed through the two sliders located at the bottom of the screen) from the bottom and top edges of the contact surfaces 1 and 4. Note that specifying different attachment points significantly affects the seal behavior and this can be seen by the two plots of the TFP shown at the bottom of the windows in Figure 3-20 and Figure 3-21.

In the case of a *variable stiffness* seal (shown in Figure 3-21), large deformations effects are included and as a result, the stiffness is calculated as a function of the seal deformation. The expression of the seal stiffness as a function of its deformation u_s is given by:

$$K = \frac{\pi E b_1 x_1}{2(x_1 + u_s)^2} t \quad (3-5)$$

In the equation above, the seal is assumed incompressible so that the seal volume is equal to the initial volume prior deformation. On the basis of the assumption of incompressibility, the instantaneous thickness of the seal is given by $t' = tx_1/(x_1 + u_s)$, where t is the initial thickness. The seal length is automatically calculated from specified seal attachment points.

If the user selects any of the *Auto Calculate* or *Use Attachments* options and then presses **OK**, any change in the geometry of the bearing in Panel 2 that affects any of these quantities will be automatically updated.

Finally the user has the option to delay the engagement of the seal by specifying a “seal gap”. This option can be used to model bulging of the seal at its installed position. In that case, for the calculation of the seal stiffness, the “seal gap” is added to quantity x_l described earlier in order to calculate the initial seal length. Also the x-axis in the displayed plot of Figure 3-20 and Figure 3-21 refers to the seal deformation with respect to its installed position rather than its initial length.

The seal stiffness value is used for each of the two springs that extend between the two plates. Note that the spring is considered effective only when in tension, the spring force acts in the direction of the two points of attachment and is equal to the value of the stiffness K times the change of length of the two points of attachment (that is, the program accounts for the rotation of

the seal when it is deformed). The option *Include rubber seal only during uplift* accounts for the seal only during the uplift duration and ignores the seal when the bearing is in compression. If this option is disabled then the seal is included at all states.

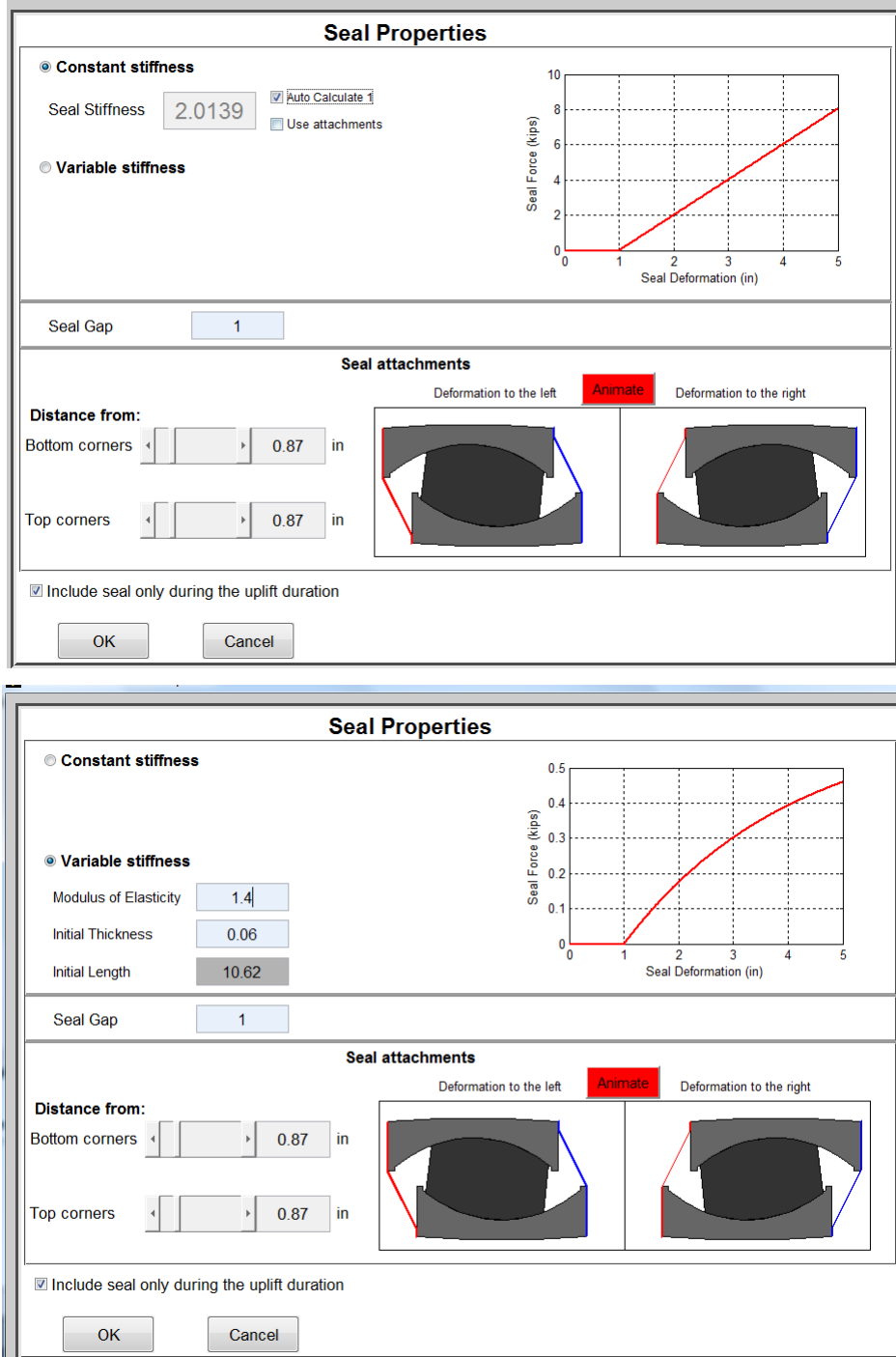


Figure 3-20: Window displayed when Include rubber seal option is selected

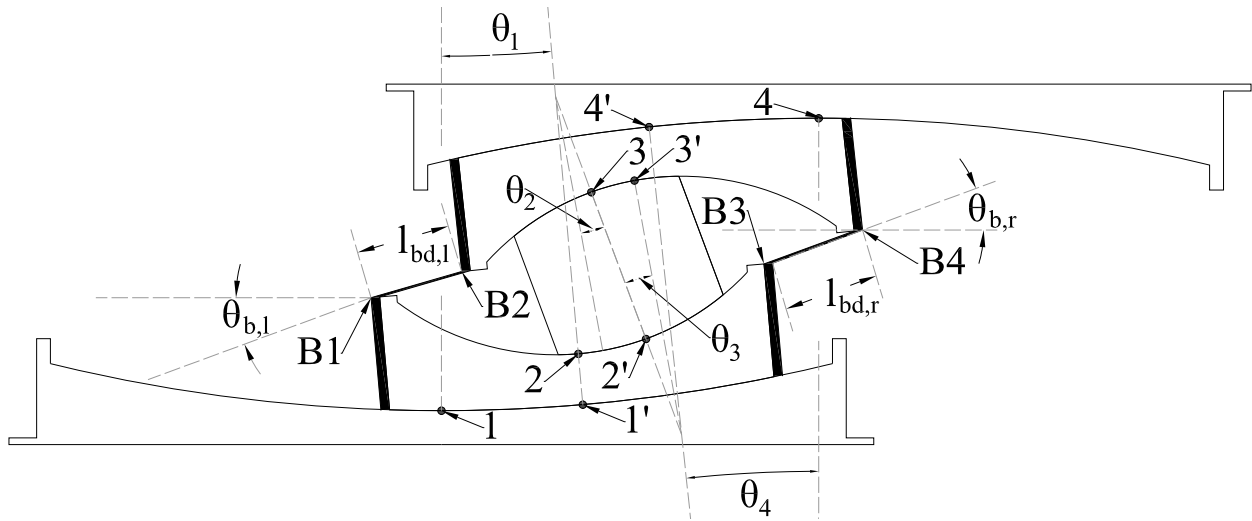


Figure 3-21: Deformed rubber seal

Friction scale factor: When this option is selected, the window shown in Figure 3-22 appears. The values of friction specified in Panel 2 apply for the conditions in which the bearing is loaded under the specified vertical load (in Panel 2). Under uplift conditions, the coefficient of friction at the sliding interfaces (that are still in contact and subjected only to the weight of the components of the bearing above them) is higher due to the low bearing pressure at the sliding interfaces. The **friction scale factor** is a factor that is used to multiply the friction coefficients of the surfaces only during the uplift duration. If no velocity or heating dependency is considered (see Panel 7 later) in the analysis, the friction coefficients specified in panel 2 are multiplied by the specified scale factor when uplift occurs. When velocity or heating dependency is enabled, the instantaneous friction coefficient including the velocity or heating effects (Constantinou et al., 2007) are multiplied by the specified scale factor during the uplift episode. In the procedure described in “*Note on smooth transitions between bearing states*” in Panel 4 earlier, when the bearing transitions from compression to uplift, the friction scale factor varies linearly from the value of 1 to the value specified in Figure 3-22. This ensures continuity of the friction forces.

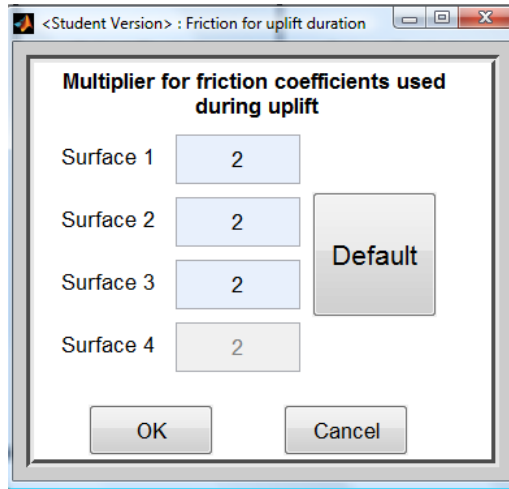


Figure 3-22: Window displayed when Friction during uplift is selected

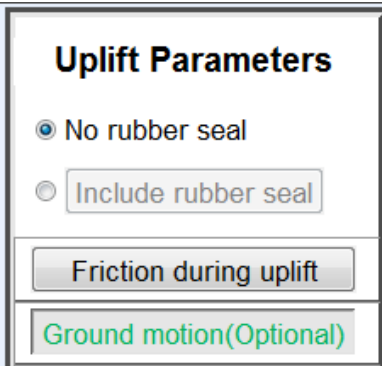
Ground Motion (Optional): This is optional and is used in order to import a horizontal and a vertical ground acceleration histories that act during the uplift duration simultaneously with the displacement histories applied to the TCP and specified in Panels 3 and 4. When this button is pressed, the text color becomes green (shown in Figure 3-23(a)) while the dialogue box in Figure 3-23(b) appears. The user can import a horizontal and a vertical ground excitation. Only the portion of the excitation that occurs during the uplift duration will be considered (red region in Figure 3-23(b) when the vertical excitation of Figure 3-17 is imported) while the remaining part (bearing in compression) will be ignored. When full contact equations are used, vertical displacements are not included in the analysis so that the vertical component only affects the variation of the normal load on each surface:

$$W_{fi} = W_i \left(1 + \ddot{u}_{vg} / g \right) \quad (3-6)$$

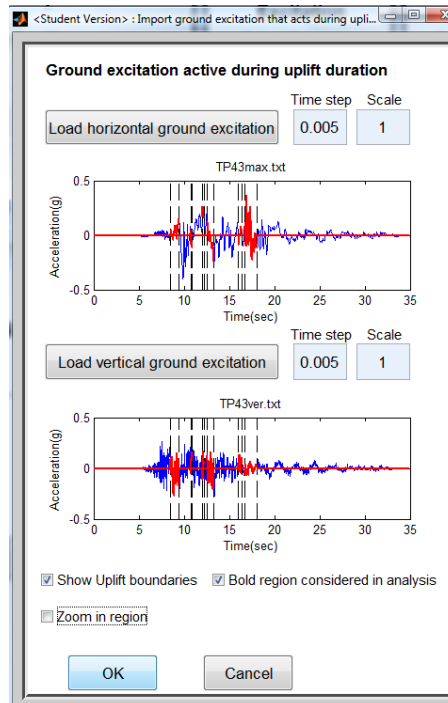
where W_i is the load on each surface due to the weight of the TFP parts (during uplift) and \ddot{u}_{vg} is the vertical acceleration history in units of g.

Note that this option can be deactivated even after the user has imported the ground motions by simply pressing **Ground Motion (Optional)** button again. When the button is displayed un-press as shown Figure 3-19 then any imported ground motion will not be considered.

Finally in Figure 3-23(b) the user can change the time step and scale factors of the imported motions.



(a) View of Panel 5



(b) View of dialogue box for importing ground motion

Figure 3-23: Import ground motion for uplift duration

3.6 Panel 6: Advanced Modeling

The view of the advanced modeling panel is shown in Figure 3-24. This panel is used to activate a different set of equations of motion that utilize rigid body dynamics in order to model the behavior of the isolator under any state (bearing in compression, uplift and landing as shown in Figure 2-2). The isolator parts are allowed to bounce and slide on the sliding surfaces with either full or point contact. This modeling is complex and often slow to execute but it allows for a more realistic account of local phenomena especially for landing. This modeling includes large rotations and can also be used when the TCP exhibits static or dynamic rotations. Details of this modeling are presented in Sarlis and Constantinou (2013) and a summary was presented in Section 2 of this report.

The user can select to use the advanced equations for any desired state with some restrictions. If advanced compression modeling is selected, the program will use advanced modeling for uplift and landing as well (options advanced uplift and landing become checked and disabled). If however only the uplift option is selected (see panel 6 in in Figure 3-24), then the isolator will be modeled using the advanced equations only for the uplift interval, whereas during the subsequent

landing and compression interval, the simpler equations that assume full contact will be used. Similar is the case when only the advanced landing modeling is selected. It is however recommended, that the same type of modeling (advanced or full contact) is used for the entire duration of the excitation. Advanced landing and advanced compression use the exact same equations but they are distinguished as options in order to allow the user to use advanced modeling for smaller portions of the analysis. It should be noted that the only difference in the formulations between the uplift interval and the compression/landing interval is that for the uplift case, the vertical displacement history of the TCP is considered as excitation (specified by the user) while for the compression case it is a degree of freedom in the equations of motion.

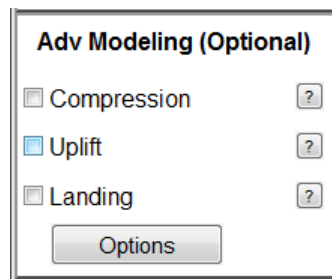


Figure 3-24: View of panel 6

Compression: This option is available even when no uplift occurs in the analysis. Activating this option means that advanced modeling will be used for all bearing states (see Figure 2-2). When this option is selected, then the option *Advanced Initial Conditions* is enabled (see Figure 3-29) which allows the user to apply non-zero initial conditions for the various parts of the isolator. In the case where there is no uplift and the excitation displacement is smaller than the isolator displacement capacity, use of *Advanced Compression* produces results that are almost identical with the full contact equations (default equations used by the program) except for the effect of large rotations that are included in advanced modeling. *Advanced Compression* can be useful if large rotation effects are significant, if the elements connected on top of the TCP are flexible (see *Options* button later), or if the displacement applied on the isolator is larger than the isolator displacement capacity. In the latter case, advanced compression modeling can capture point contact and possible overturning of components that occurs when contact with all restrainers is made. One such example of a 3pleANI analysis is presented in Figure 3-25. For this type of analysis, it is recommended that the user enables *User Tolerances* in order to ensure that the stiffness of the surface restrainers is high enough to reduce penetration.

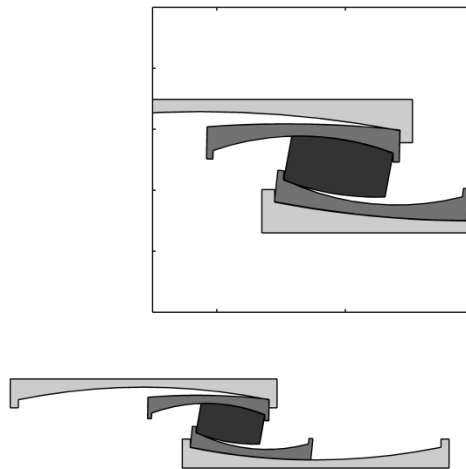


Figure 3-25: Example of 3pleANI analysis of isolator with point contact at sliding surfaces

Uplift: This option becomes available only if *Uplift Occurs* is selected and is included by default if uplift occurs and *Advanced Compression* modeling was selected. Activating this option results in use of advanced modeling when the bearing experiences uplift (for example between 2 and 3sec in the example of Figure 3-14(a)). Use of this option is particularly useful for the analysis of the uplift interval, when contact is made between the TCP and the parts below during uplift and when the isolator uplifts at a lateral displacement close to the isolator displacement capacity.

Landing: This option becomes available only if *Uplift Occurs* is selected. Activating this option results in use of advanced modeling when uplift ends (for example at time of 3sec in the example of Figure 3-14(a)) and the TCP is about to land on the components below. Note that typically, at the end of the uplift interval and due to the movement of the components below, there will be a height differential between the top concave plate and the components below. The advanced landing equations can simulate the bearing behavior when the TCP exhibits free fall under the action of the carried weight (self-weight plus specified vertical load of panel 2). If the user has selected *advanced landing* but has not activated *advanced compression*, then advanced modeling will be used from the end of the uplift duration and for a time interval of 0.2sec until compatibility of displacements and rotations are restored for the isolator. When compatibility is restored, the equations for full contact are used.

Options: When this option is selected, the window shown in Figure 3-26 appears. It allows the user to specify the stiffness of a rotational spring (in units of force-length) connected at the top concave plate as shown in Figure 3-27. This option can be used to model the rotational flexibility

of the structural components that are connected to the TCP. It allows modeling of the induced rotations to those elements (and therefore induced rotations to the TCP) due to P-Δ moments of the isolator and to account for this rotation on the isolator's behavior.

The user can also specify the stiffness and damping values of the artificial vertical springs and dampers that are used in the advanced modeling in order to determine when contact between the surfaces occurs (see Sarlis and Constantinou, 2013 and Section 2 in this report). Very small values of vertical spring stiffness will lead to some penetration between the surfaces. The vertical dampers are used to dissipate energy in relative vertical vibration that occurs between the two surfaces in near contact (note that the vertical velocity due to pendulum motion of the various bearing parts does not cause forces on these artificial vertical dampers). It is noted that the advanced modeling uses the artificial springs and dampers, and utilizes the deformed bearing geometry to detect contact between different points.

The *Auto Calculate* button calculates the stiffness and damping values based on the following equations and using a period $T=0.1$ sec and damping ratio $\zeta=0.005$.

$$\begin{aligned}k_{vi} &= \frac{4\pi^2 (N_{oi}/2)}{gT^2} \\c_{vi} &= \frac{4\pi (N_{oi}/2)}{gT} \zeta\end{aligned}\tag{3-7}$$

These values are, in most cases, sufficient to produce fast and accurate analysis results. If the analysis speed is very slow, different values could be tried as these values significantly affect the analysis speed.

The **Seal to steel friction** is the friction coefficient that is considered by the program for a calculating the vertical friction force that is developed between the TCP and TSP if contact is made between the restrainer of surface 4 and the top slide plate (see for example Figure 3-28). This friction force is also considered when there is no rubber seal but the specified coefficient of friction should then be that of steel to steel. The normal load on the interface is equal to the restrainer force of surface 4.

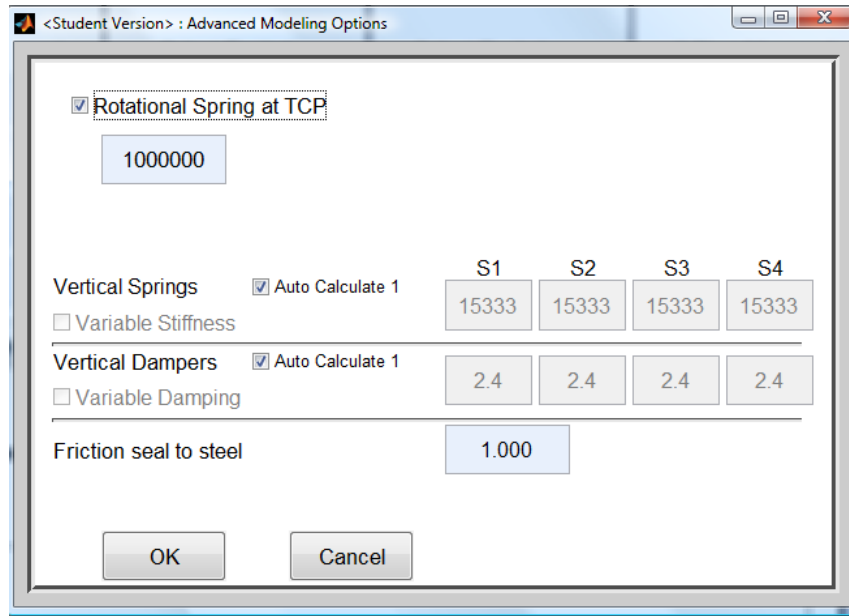


Figure 3-26: Window displayed when Options is selected

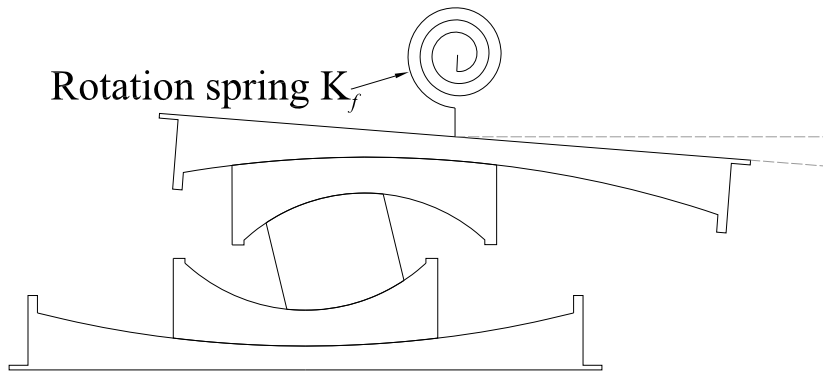


Figure 3-27: Schematic of model in 3pleANI with rotational spring connected to TCP

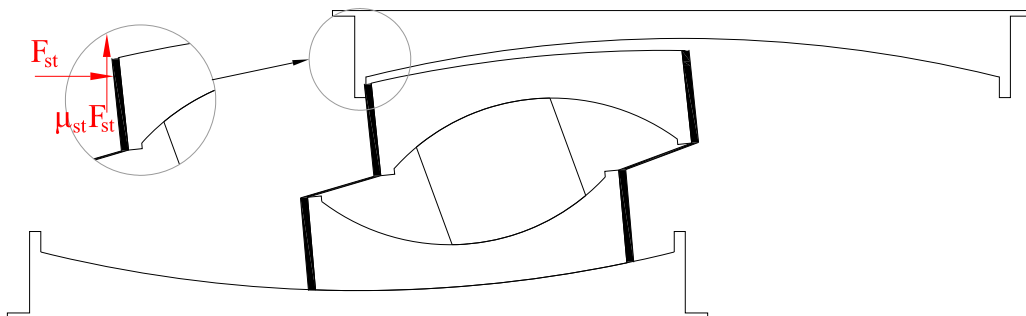


Figure 3-28: Vertical friction force developed between TCP and TSP during uplift

3.7 Panel 7: Analysis panel

This is the panel used to conduct the analysis based on the parameters defined in the previous panels. A view of this panel is shown in Figure 3-29.

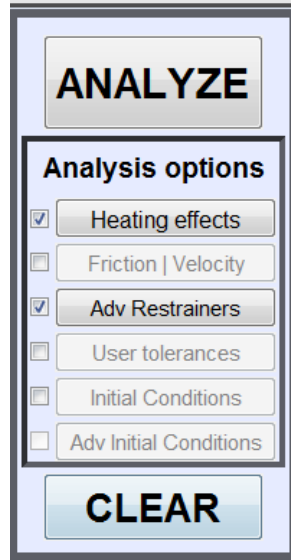


Figure 3-29: View of analysis panel

Analyze: When this button is pushed, analysis is conducted. The selection boxes below the analysis button are used to define some options that may be included in the analysis.

Clear: This button clears the analysis results so that the user can conduct a new analysis with new parameters.

Heating effects: This option calculates the heat flux and temperature rise histories at each of the four sliding surfaces of the isolator based on the theory presented in Constantinou et al (2007). For the calculation of the temperature rise, the heat flux is assumed to be supplied at the center of a sliding surface and given by

$$Q_i(t) = \begin{cases} 0 & , u_i > b_i / 2 \\ \frac{\mu_i W_i \dot{u}_i}{A_i} & , u_i < b_i / 2 \end{cases} \quad (3-8)$$

In Equation (3-8), $\mu_i, W_i, \dot{u}_i, A_i$ are the friction coefficient, vertical load, sliding velocity and area of the i-th surface of the Triple FP isolator ($i=1,2,3$ and 4), respectively. If a part of the bearing moves away from the center, the heat flux is set to zero so that the heat flux is intermittent. The

temperature rise at the center of the each surface is calculated by the following convolution integral (Constantinou et al, 2007):

$$T_i(t) = \frac{1}{k} \sqrt{\frac{D}{\pi}} \int_0^t \frac{Q_i(\tau)}{\sqrt{t-\tau}} d\tau \quad (3-9)$$

In Equation (3-9) D and k are the thermal conductivity and thermal diffusivity of the material (herein assumed to be that of stainless steel), respectively. For additional information see **Show heating effects** later in this manual.

The user has two options related to heating effects: a) Post-calculate the histories of temperature rise following analysis without accounting for the effects of heating on friction, and b) Include heating effects on the friction coefficient values during the analysis and calculate the temperature rise. In the first case-panel is shown in Figure 3-30(a)-the heat flux and temperature rise of each surface are calculated after the analysis is completed based on the calculated response quantities. The user is prompted to define the thermal conductivity and thermal diffusivity for the material stainless steel and a percentage of the total vertical load on the isolator (specified in Panel 2) that will be considered for heating effects. This is useful in the DAI where in some cases the specified load represents the weight carried by several isolators. The default values are taken from Constantinou et al (2007), are consistent with the units selected and are activated when the **Auto Calculate** button is pressed. In the second case-panel shown in Figure 3-30(b and c)-the heat flux and temperature rise are calculated at each time step and the friction coefficient values are updated at each step. The user can use two relationships between the friction coefficient and temperature. In the case of the linear variation:

$$\mu_i = \begin{cases} \mu_{\max,i} & , T_i \leq T_{\mu\max,i} \\ \mu_{\max,i} + \frac{\mu_{\min,i} - \mu_{\max,i}}{T_{\mu\min,i} - T_{\mu\max,i}} (T_i - T_{\mu\max,i}) & , T_{\mu\max,i} \leq T_i \leq T_{\mu\min,i} \\ \mu_{\min} & , T \geq T_{\mu\min} \end{cases} \quad (3-10)$$

Friction is assumed constant and equal to μ_{\max} until a specified temperature $T_{\mu\max}$ is reached. Then temperature decreases linearly until a specified $T_{\mu\min}$ temperature is reached. For larger temperature, friction remains constant and equal to a specified value μ_{\min} . Note that μ_{\max} are the friction values specified in Panel 2, whereas μ_{\min} is defined by a factor that divides the friction coefficients of Panel 2 for each surface. In the example of Figure 3-30 (c) this factor is equal to 2

so that $\mu_{min} = \mu_{max}/2$. Also in this example, $T_{\mu_{max}} = 20^{\circ}C$ and $T_{\mu_{min}} = 100^{\circ}C$. The user can also use an exponential rule for the variation of the friction coefficient with temperature given by Equation (3-11) and defined by parameters μ_{max} (specified in Panel 2), μ_{min} defined by a factor as in the linear variation case and heating rate parameter a_h .

$$\mu_i = \mu_{min,i} + (\mu_{max,i} - \mu_{min,i}) e^{-a_h T_i} \quad (3-11)$$

In the above equation, the friction coefficient is equal to μ_{max} when temperature rise is zero and decreases exponentially with rising temperature until approximately $T = 1/a_h$ when friction becomes constant and equal to μ_{min} .

Finally, when the option **Heating effect on friction coefficients** is enabled, the user can choose to a) update the friction coefficient at every integration time step or at b) upgrade at a user specified time step. The first case can significantly delay the analysis execution time due to the calculation of the convolution integral given by Equation (3-9) at each time step combined with the fact that the program uses adaptive time step. The user has the option to use an approximate procedure at which the friction coefficient values are updated only at specified time intervals as percentage of the excitation time step (equal to the time step of the imported excitation file or the duration of excitation divided by 6000 in the case of sinusoidal excitation).

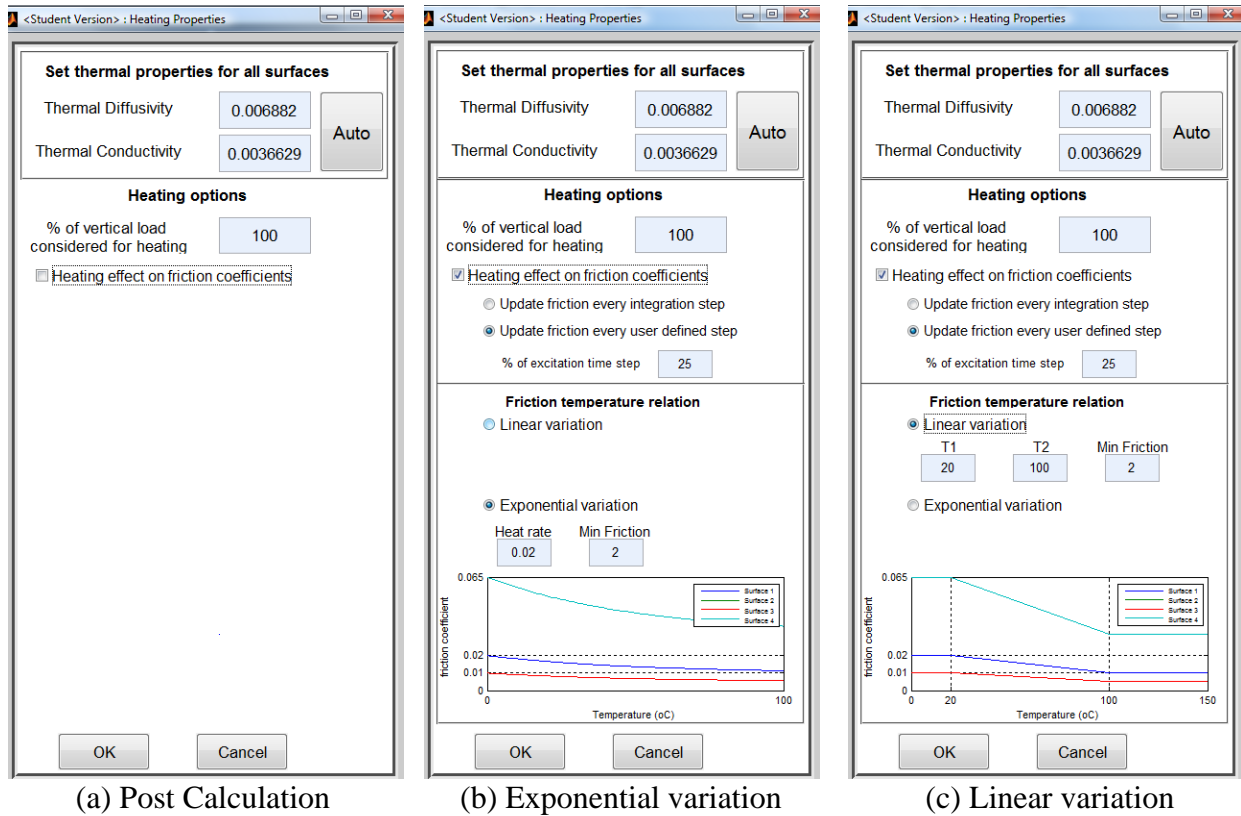


Figure 3-30: Window displayed when Heating Effects is selected

Velocity / Friction: When this option is selected, the window shown in Figure 3-31 appears. It allows specification of velocity-dependent friction (see Constantinou et al, 2007 and Sarlis and Constantinou, 2010 for details). When this option is selected, the friction coefficient values specified in Panel 1 are regarded as the high velocity values (f_{max} , or “fast” values per terminology used in SAP2000) and the user is prompted to define (a) the near zero velocity values (f_{min} or “slow” values per terminology used in SAP2000) and (b) the rate parameter for each surface. Depending on the specified parameters, this option may significantly delay the execution time. The user may expedite the analysis by changing the solution parameters using the *User Tolerances* option. The *Auto Calculate* button automatically sets the slow values as half of the specified fast friction values and sets the rate parameters to the default values obtained from Constantinou et al. (2007). When *Auto Calculate* is selected, the edit boxes become disabled and are used for display purposes. After pressing **OK**, any change in the friction coefficients in Panel 2 will automatically update the slow friction coefficients without having to revisit the menu in Figure 3-31.

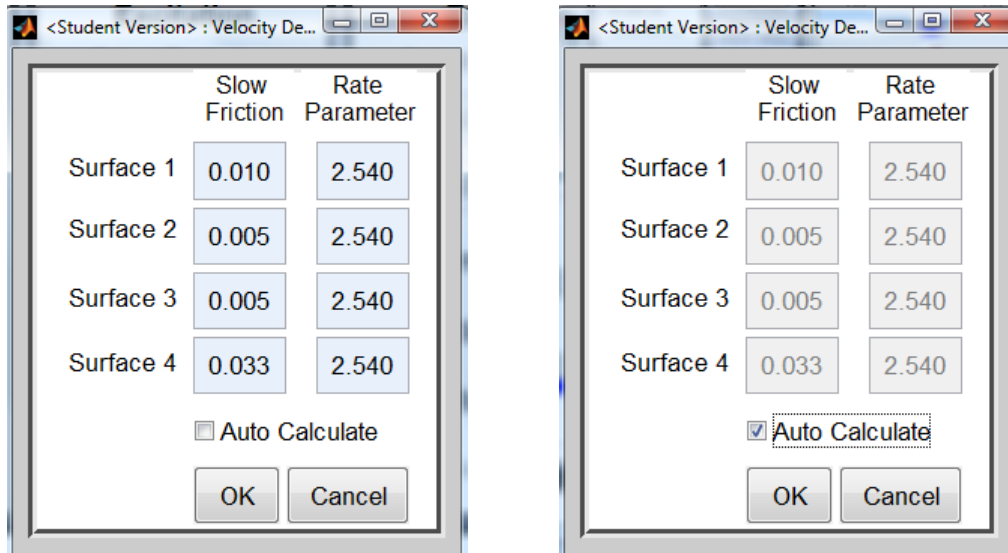


Figure 3-31: Window displayed when Friction | Velocity option is selected

Adv Restrainers: When this option is selected, the window shown in Figure 3-32 appears. This option allows the user to model the restrainers either as a) linear elastic b) inelastic assuming their failure is brittle. For the case of linear elastic restrainers, the option also allows the user to specify nonzero viscous damping for the restrainers although a value of zero is recommended for this option. The restrainer stiffness and damping values can be specified separately for each surface. The *Auto Calculate 1* calculates the stiffness of the restrainers as:

$$K_{ri} = 100 \max \left(\frac{N_{oi}}{R_i} \right) \quad (3-12)$$

In Equation (3-12), N_{oi} is the vertical load specified in Panel 2. That is, the stiffness is calculated as 100 times the stiffness resulting from the pendulum motion of the surface where the restrainer is attached. Once this option is selected, any change in the specified load will automatically update the restrainer stiffness without having to revisit this menu.

The *Auto Calculate 2* option calculates the stiffness of the restrainers as:

$$k_{ri} = \frac{\pi (t_{ri}^2 + s_i t_{ri}) F_y}{6Y_r}, \quad i = 1, 4$$

$$k_{ri} = \frac{1}{4} \frac{\pi (b_i^2 - s_i^2) t_{ri} F_y}{6Y_r}, \quad i = 2; k_{ri} = \frac{1}{4} \frac{\pi (b_4^2 - s_i^2) t_{ri} F_y}{6Y_r}, \quad i = 3 \quad (3-13)$$

Also it calculates the damping of the restrainers as:

$$c_{ri} = 2\zeta \sqrt{k_{ri} m_{TCP}} \quad (3-14)$$

In these equations, s_i is the diameter of the sliding surface given by $s_i = b_i + 2d_i$, t_{ri} is the thickness of the restrainer, F_y is the yield stress of the material, Y_r is the yield displacement of the restrainer, m_{TCP} is the mass of the top concave plate, T is some arbitrary value of period (0.1sec) and ζ is the damping ratio (5%).

For the case of inelastic restrainers, the restrainer stiffness prior to failure is again given by Equation (3-13) but for a yield displacement and an ultimate shear strength that is specified by the user. The capacity of the restrainer is assumed equal to $\pi s_i t_{ri} F_y / 6$. When this force is reached, the restrainer fails and its force drops to zero for the remainder of the excitation. Note that failure of the restrainer in one direction does not affect the restrainer in the opposite direction, which is assumed to be functional.

Finally the user has the option in Figure 3-32 to de-activate collapse detection during the uplift duration. Deactivating this option is not recommended as it might lead to unrealistic results. The user can also assume that restrainers have infinite height instead of the specified values in Figure 3-8. In this case the restrainers of surface 4 cannot move above the TSP (for the advanced modeling this applies to the restrainers of all surfaces).

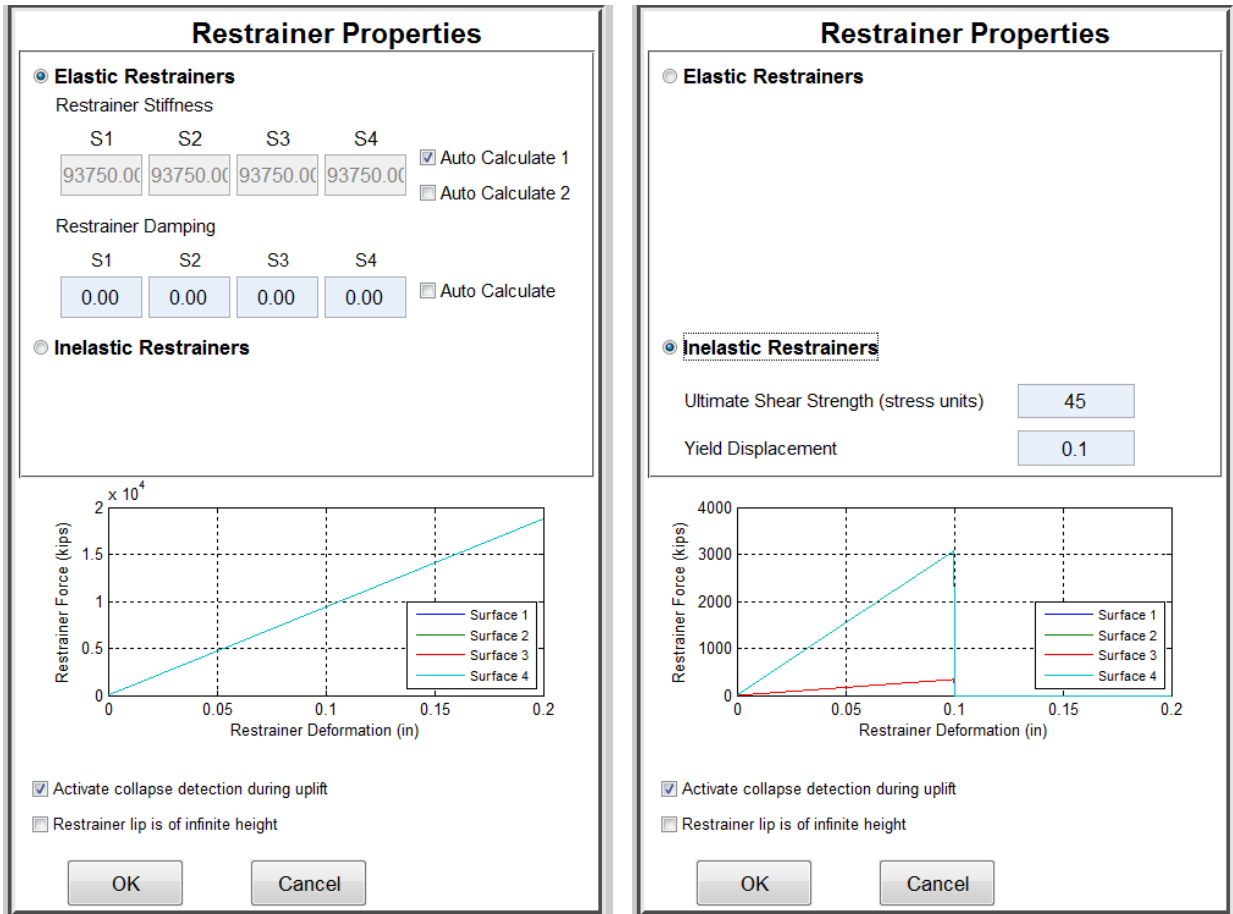


Figure 3-32: Window displayed when Advanced Restrainers option is selected

Initial conditions: When this option is selected, the window shown in Figure 3-33 is displayed. This window allows the user to specify non-zero initial conditions for the displacements of the various parts of the bearing assuming that full contact exists between all surfaces. This option is disabled if the *Advanced Compression* modeling is enabled. The user can define 3 out of 5 initial conditions for the sliding surfaces while the remaining are calculated by 3pleANI using the conditions of compatibility. The window contains checkboxes at the top where the user selects the desired surfaces for which nonzero initial conditions will be specified. In order to enable the edit boxes located below, the user must first select exactly three checkboxes. The window contains a plotter on the side that draws the initial deformed shape of the bearing while the user specifies the initial conditions. The initial conditions of the surfaces that are not selected in the checkboxes are calculated from the compatibility Equations (2-1) and (2-2). However, the specified initial conditions need to also satisfy the conditions of equilibrium under the specified starting value of load. If the specified initial conditions do not satisfy equilibrium, the program

nevertheless performs the analysis but with an abrupt change in the initial displacements at the first integration step as required for equilibrium. This becomes obvious in the display of results when at time zero, the inner components abruptly move to the locations required for equilibrium. The specified values should be in units of length, consistent with the units selected in Panel 1. The user is also allowed to enter nonzero rotations of the Top concave plate (TCP) and Bottom Concave Plate (BCP) as shown in Figure 3-34 in order to analyze a bearing with misaligned plates. Note that the misalignments are considered constant throughout the analysis. The input for such a case is shown in Figure 3-34.

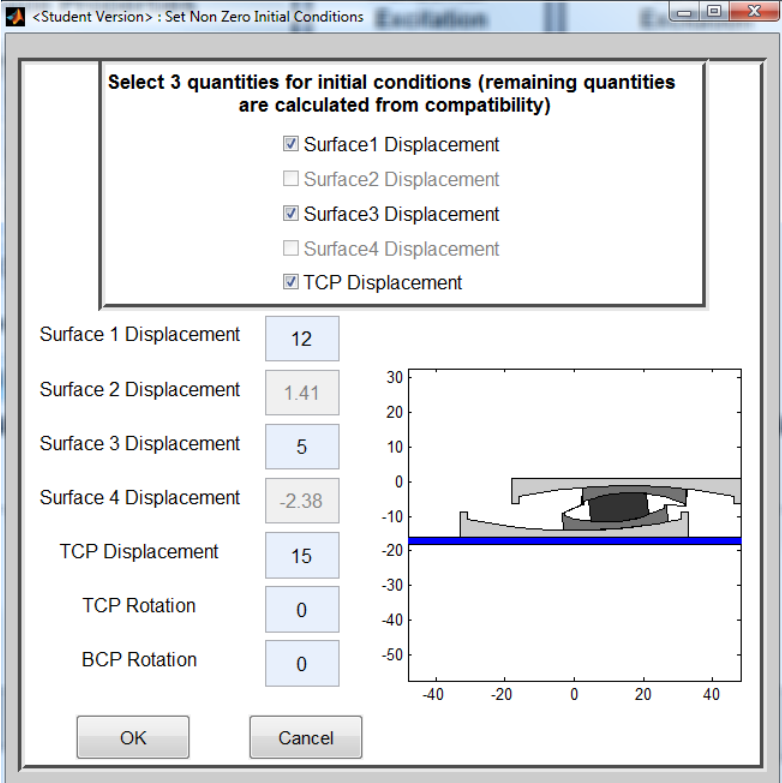


Figure 3-33: Window displayed when Initial Conditions option is selected

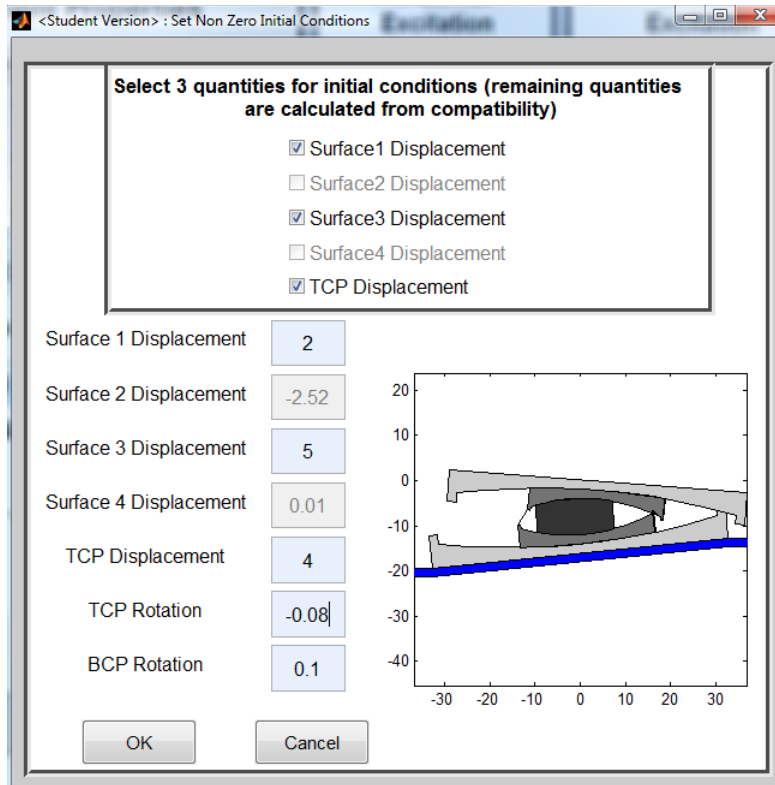


Figure 3-34: Initial conditions with misalignments of TCP and BCP

User Tolerances: When this option is selected, the window in Figure 3-35 appears. When the option is deactivated, default values are used. This option allows the user to change the numerical integration error tolerances, the solver used for the solution of the differential equations, the yield displacement for modeling friction of each surface (units are consistent with those specified in panel 1). The user is allowed to use a mass for the isolators larger than the actual mass (which is automatically calculated by the program) by specifying a value larger than 1 in the corresponding edit box. This option should never be used for uplift analysis and should always be used with caution as a value larger than 1 affects the dynamic behavior of the isolator. It also alters the normal load on each surface.

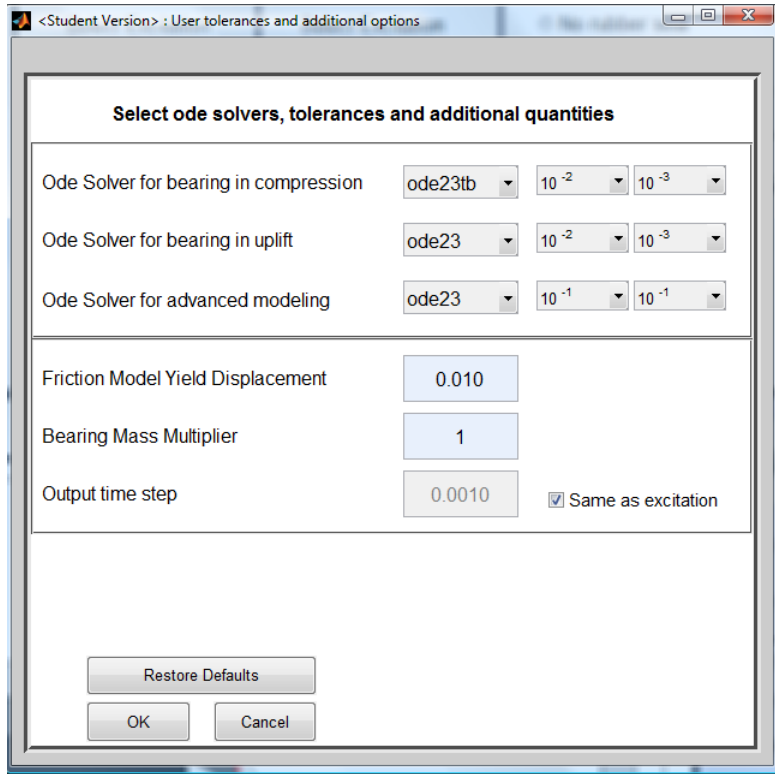


Figure 3-35: Window displayed when User Tolerances option is selected

Advanced Initial Conditions: When this option is selected, the window shown in Figure 3-36 is displayed. This option becomes available only if the **Advanced Compression** modeling is selected and becomes disabled otherwise. The reason for this distinction is that the advanced modeling option allows for non-conventional simulations as each bearing part is described by three independent degrees of freedom (horizontal translation, vertical translation and rotation about the center of mass). There are no restrictions on the initial conditions and the parts do not necessarily have to be initially in contact. This option also allows for initial rotation of the Bottom Concave Plate (BCP) which is considered constant throughout the analysis. However, penetrations between the parts should be avoided in the specification of the **Advanced Initial Conditions** as this may lead to numerical errors due to the large contact forces that develop at the start of the analysis. It is noted that if the user specifies a nonzero rotation of the Top Concave Plate (TCP) this will be considered as a constant misalignment if the rotational spring is not activated at the TCP (see Figure 3-26). Otherwise, the rotational spring will instantly cause a moment that will realign of the TCP.

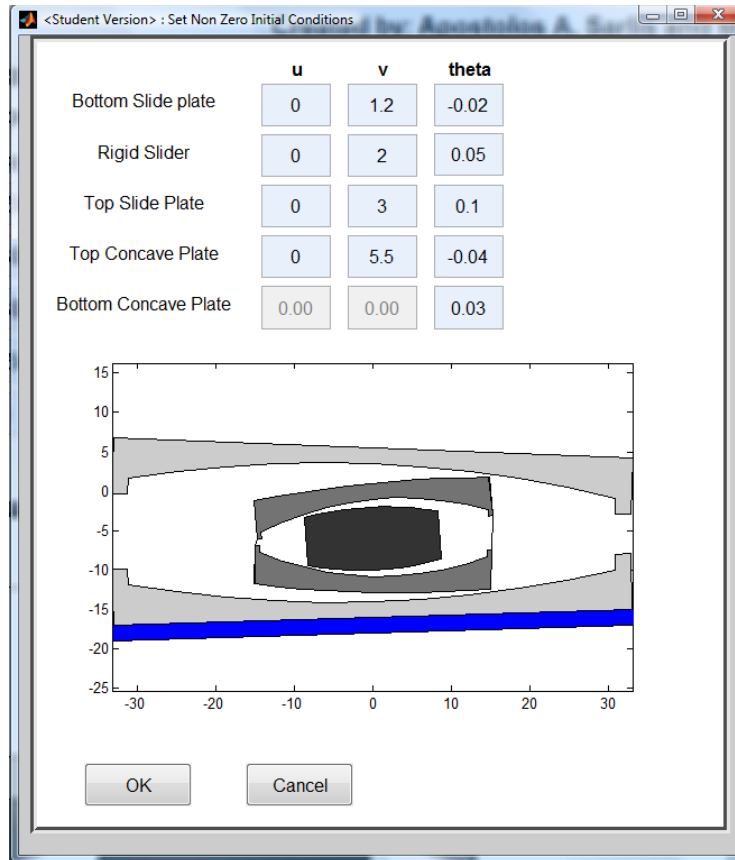


Figure 3-36: Window displayed when Advanced Initial Conditions option is selected

3.8 Plotter 1

Plotter 1, shown in Figure 3-37, is the screen where animations and drawings of the isolator are displayed. The panel is controlled by the animation panel (Panel 8) and by the animation options panel (Panel 9) shown on the right of Plotter 1 in Figure 3-1. Anything shown in plotter 1 can be extracted using *Export Plots* into a separate window from which the user can further generate “*jpeg*”, “*pdf*” and other files formats or copy and paste directly into Microsoft Word. Also any animation that is viewed in Plotter 1 can be exported into an “*avi*” file using the *Export Avi* button in panel 1. Prior to the analysis, plotter 1 is used to instantaneously draw the isolator geometry while the user inputs properties for the Triple FP isolator. The axis limits are automatically calculated by the program but the user may also specify the limits by using *User Axis Limits* in Panel 9.

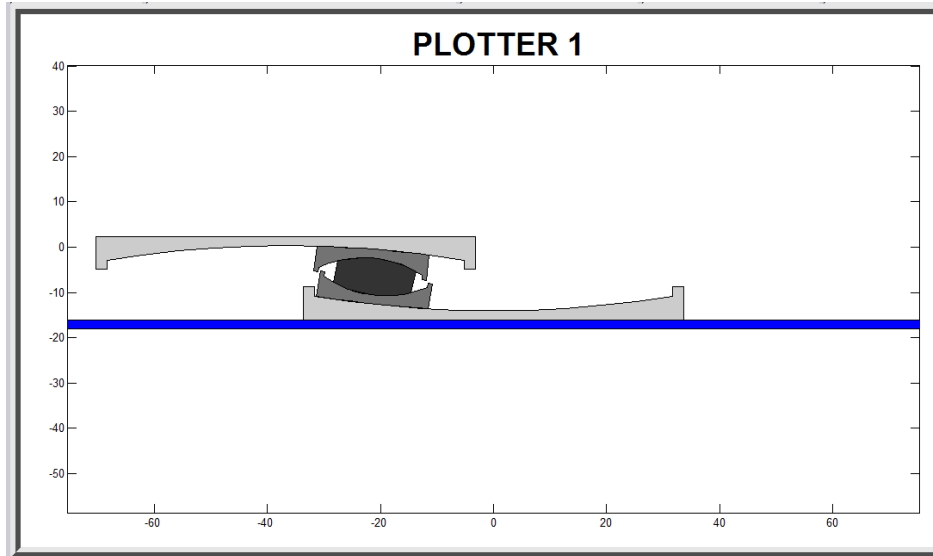


Figure 3-37: View of plotter 1

3.9 Plotter 2

Plotter 2 is used to display plots of the analysis results. The plotter is enabled after the analysis is completed. Plotter 2 is shown in Figure 3-38. On the top of the plotter 2 panel, the list box menus may be used to select the variables to be plotted on the axes shown at the bottom of Figure 3-38. The user is allowed to generate four different sets of plots. Each time the user performs an action in the list boxes, the plots are automatically updated. The x-axis variable and y-axis variable can be different for the four plots. When the **animate button** is pressed in Panel 8, plotter 2 generates graphs of the selected quantities that evolve simultaneously with the animation that is displayed on plotter 1. This way the user can monitor the visual as well as the quantitative part of the isolator response. Also, plotter 2 can be used in conjunction with the manual plotter below the *animate* button in Panel 8 when the user chooses to manually advance frames, using the < and > buttons. These buttons also manually advance the plots in plotter 1.

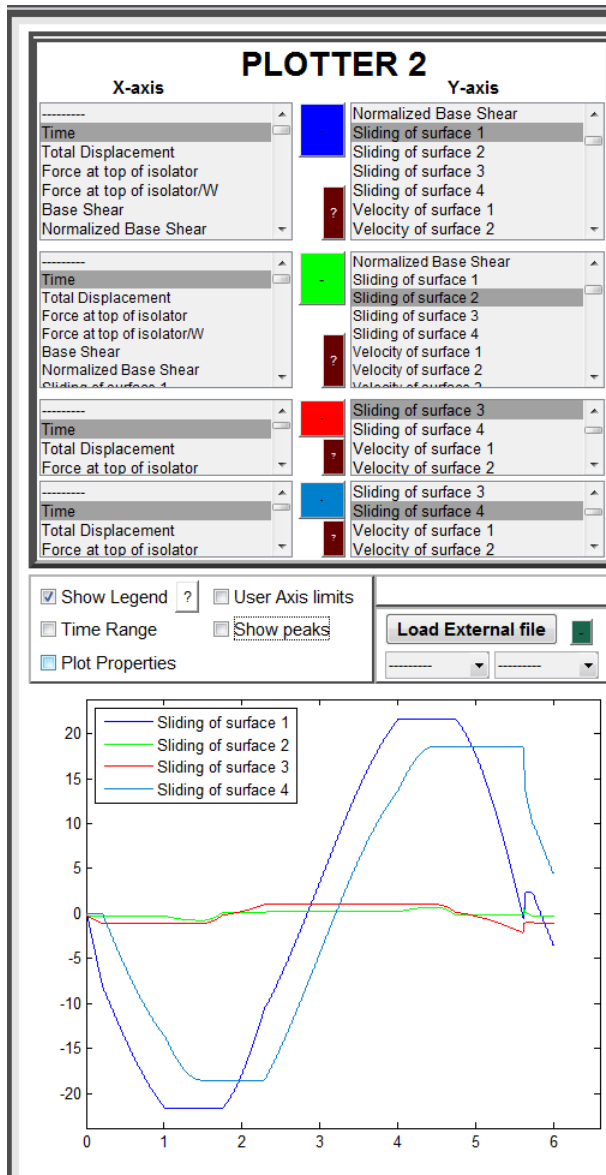


Figure 3-38 View of plotter 2

: Each set of data contains a pushbutton having the color and style of the plotted line that corresponds to that data. By pressing this button, the user can set a number of properties for the selected set of x-y data. The window that appears when pressing this button is shown in Figure 3-39. The options selected apply to both the exported plots and the ones displayed in plotter 2. The user can select the line style, thickness and color of the line. The user can also specify scale factors to multiply the selected x and y data. Note that the last two options are disabled in the DCI and are only used in the DAI.

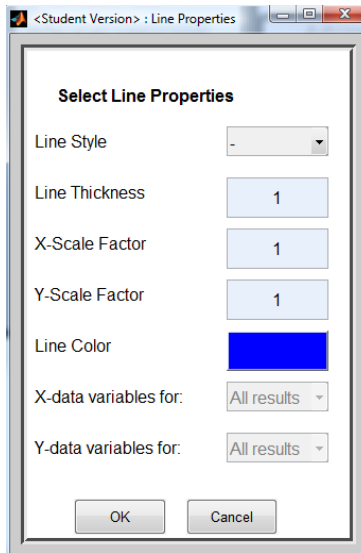


Figure 3-39: Window displayed when  button is pressed

 : This button is available for each set of x-y data. The window that appears when pressing this button is shown in Figure 3-40. This window shows the names, peak values and digital data for the selected variables. By right clicking on the labels of the digital data, the user can copy the data and paste it elsewhere (e.g., in Excel).

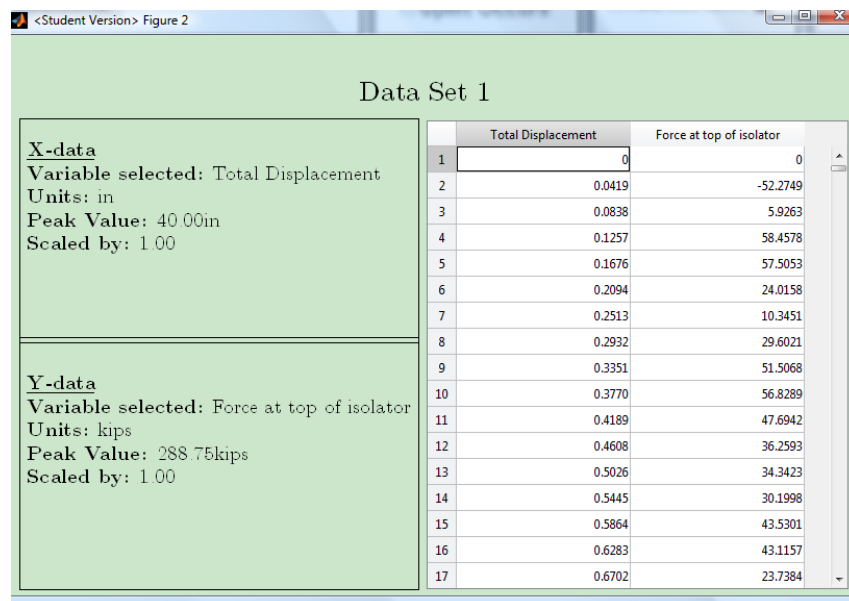


Figure 3-40: View of window that appears when ? button is pressed

User Axis Limits: By selecting this option, the user can set his own x and y limits of plotter 2. If this option is not selected, the axis limits of plotter 2 are determined automatically by the

program based on the maximum and minimum values of the quantities that are selected to be plotted with the addition of some margin.

Show peaks: This option displays on the graph the peak value of the plotted variables.

Show Legends: This option displays legends in Plotter 2 and in the exported plots. The legend names are by default obtained from the name of the variable that is selected for the y-axis. However, the user can specify any legend name by pressing the question mark button next to the **Show Legends** checkbox (for every empty entry, the default name is used). Legends are not displayed during animation (when *animate* button is pressed in Panel 8).

Time Range: The user can select the time range for which variables will be displayed. This option is particularly useful when the selected variables do not explicitly involve time (e.g., the user can view the force-displacement loop of the isolator that was calculated for the time interval 0 to 2 sec, whereas the analysis duration is much larger, say 20 sec)

External File: This panel allows the user to import into the program, data from external files. By selecting **Load file**, the window shown in Figure 3-41 appears where the user has the option to import an Excel file or a “mat” file. If the user selects Excel file then the Excel file opens, and the program prompts the user to select the region of a spreadsheet of which the data will be imported into program 3pleANI. An example of selection is shown in Figure 3-42. When selecting the region on the left figure, five variables will be imported into the program defined by each of the columns of the data selected, with names A1, A2, A3, A4 and A5. The name of each variable is defined by the first row of the selected region. If the region on the right in Figure 3-42 is selected then the variables imported are the same, however, the variable names will be assigned automatically by 3pleANI. After the desired region in Excel is selected, the **OK** button shown in Figure 3-43 must be pressed for the procedure to be complete. The imported variables will then appear in the popup menus (see Figure 3-44) of the Import Panel. If the user selects to import a Matlab file, then the selected Matlab file must contain two variables. One variable named *cledata* that contains the data in columns (each column is a variable) and another variable named *hdr* that contains the variable names in the form of a cell array of strings. If the variable *cledata* is of size $m \times n$ then *hdr* must be of size $1 \times n$. Loading “mat” files is particularly useful for comparing the results of different analyses in 3pleANI. More specifically, after the completion of

an analysis, the user may export the analysis results into a “mat” file. This may be done by pressing the button *Export Data* in panel 1 in Figure 3-1. After a new analysis is completed in 3pleANI, the exported data from the previous analysis can be loaded into the program and plotted in plotter 2 together with the results from the second analysis. Note that any file loaded into the program is overwritten when the user imports a new file.

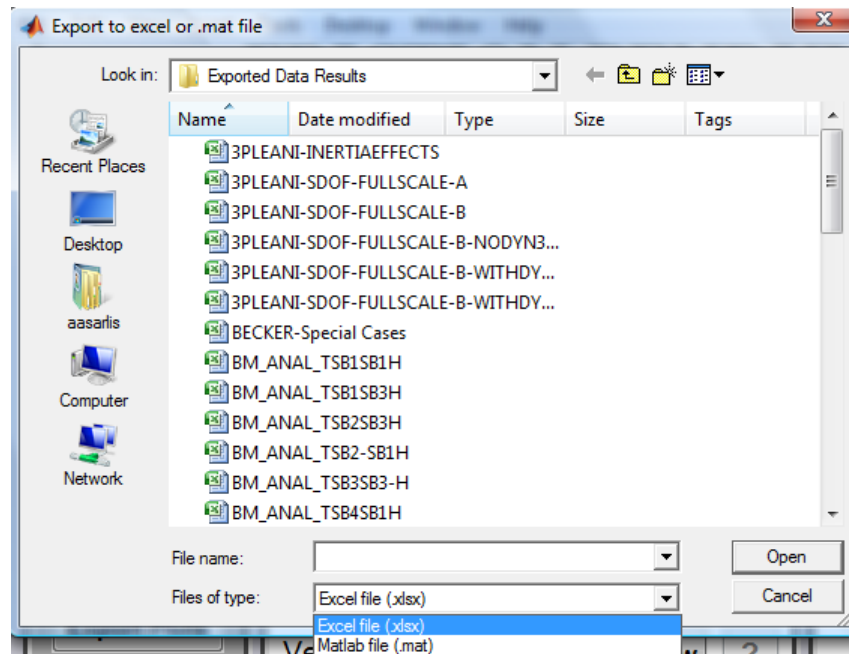


Figure 3-41: Window displayed when user selects Load File

	A1	A2	A3	A4	A5
1	A1	A2	A3	A4	A5
2	0	0	1	0.5	0.7
3	0.05	0.049979	0.99875	0.549979	0.69875
4	0.1	0.099833	0.995004	0.599833	0.695004
5	0.15	0.149438	0.988771	0.649438	0.688771
6	0.2	0.198669	0.980067	0.698669	0.680067
7	0.25	0.247404	0.968912	0.747404	0.668912
8	0.3	0.29552	0.955336	0.79552	0.655336
9	0.35	0.342898	0.939373	0.842898	0.639373
10	0.4	0.389418	0.921061	0.889418	0.621061
11	0.45	0.434966	0.900447	0.934966	0.600447
12	0.5	0.479426	0.877583	0.979426	0.577583
13	0.55	0.522687	0.852525	1.022687	0.552525
14	0.6	0.564642	0.825336	1.064642	0.525336
15	0.65	0.605186	0.796084	1.105186	0.496084
16	0.7	0.644218	0.764842	1.144218	0.464842
17	0.75	0.681639	0.731689	1.181639	0.431689
18	0.8	0.717256	0.696707	1.217256	0.396707
19	0.85	0.75128	0.659983	1.25128	0.359983
20	0.9	0.783327	0.62161	1.283327	0.32161
21	0.95	0.813416	0.581683	1.313416	0.281683
22	1	0.841471	0.540302	1.341471	0.240302
23	1.05	0.867423	0.497571	1.367423	0.197571
24	1.1	0.891207	0.453596	1.391207	0.153596
25	1.15	0.912764	0.408487	1.412764	0.108487
26	1.2	0.932039	0.362358	1.432039	0.062358
27	1.25	0.948985	0.315322	1.448985	0.015322
28	1.3	0.963558	0.267499	1.463558	-0.0325
29	1.35	0.975723	0.219007	1.475723	-0.08099
30	1.4	0.98545	0.169967	1.48545	-0.13003
31	1.45	0.992713	0.120503	1.492713	-0.1795
32	1.5	0.997495	0.070737	1.497495	-0.22926
33	1.55	0.999784	0.020795	1.499784	-0.27921
34	1.6	0.999574	-0.0292	1.499574	-0.3292
35	1.65	0.996865	-0.07912	1.496865	-0.37912
36	1.7	0.991665	-0.12884	1.491665	-0.42884
37	1.75	0.983986	-0.17825	1.483986	-0.47825
38	1.8	0.973848	-0.2272	1.473848	-0.5272
39	1.85	0.961275	-0.27559	1.461275	-0.57559
40	1.9	0.9463	-0.32329	1.4463	-0.62329
41	1.95	0.92896	-0.37018	1.42896	-0.67018
42	2	0.909297	-0.41615	1.409297	-0.71615
43	2.05	0.887362	-0.46107	1.387362	-0.76107
44	2.1	0.863209	-0.50485	1.363209	-0.80485

	A1	A2	A3	A4	A5
1	A1	A2	A3	A4	A5
2	0	0	1	0.5	0.7
3	0.05	0.049979	0.99875	0.549979	0.69875
4	0.1	0.099833	0.995004	0.599833	0.695004
5	0.15	0.149438	0.988771	0.649438	0.688771
6	0.2	0.198669	0.980067	0.698669	0.680067
7	0.25	0.247404	0.968912	0.747404	0.668912
8	0.3	0.29552	0.955336	0.79552	0.655336
9	0.35	0.342898	0.939373	0.842898	0.639373
10	0.4	0.389418	0.921061	0.889418	0.621061
11	0.45	0.434966	0.900447	0.934966	0.600447
12	0.5	0.479426	0.877583	0.979426	0.577583
13	0.55	0.522687	0.852525	1.022687	0.552525
14	0.6	0.564642	0.825336	1.064642	0.525336
15	0.65	0.605186	0.796084	1.105186	0.496084
16	0.7	0.644218	0.764842	1.144218	0.464842
17	0.75	0.681639	0.731689	1.181639	0.431689
18	0.8	0.717256	0.696707	1.217256	0.396707
19	0.85	0.75128	0.659983	1.25128	0.359983
20	0.9	0.783327	0.62161	1.283327	0.32161
21	0.95	0.813416	0.581683	1.313416	0.281683
22	1	0.841471	0.540302	1.341471	0.240302
23	1.05	0.867423	0.497571	1.367423	0.197571
24	1.1	0.891207	0.453596	1.391207	0.153596
25	1.15	0.912764	0.408487	1.412764	0.108487
26	1.2	0.932039	0.362358	1.432039	0.062358
27	1.25	0.948985	0.315322	1.448985	0.015322
28	1.3	0.963558	0.267499	1.463558	-0.0325
29	1.35	0.975723	0.219007	1.475723	-0.08099
30	1.4	0.98545	0.169967	1.48545	-0.13003
31	1.45	0.992713	0.120503	1.492713	-0.1795
32	1.5	0.997495	0.070737	1.497495	-0.22926
33	1.55	0.999784	0.020795	1.499784	-0.27921
34	1.6	0.999574	-0.0292	1.499574	-0.3292
35	1.65	0.996865	-0.07912	1.496865	-0.37912
36	1.7	0.991665	-0.12884	1.491665	-0.42884
37	1.75	0.983986	-0.17825	1.483986	-0.47825
38	1.8	0.973848	-0.2272	1.473848	-0.5272
39	1.85	0.961275	-0.27559	1.461275	-0.57559
40	1.9	0.9463	-0.32329	1.4463	-0.62329
41	1.95	0.92896	-0.37018	1.42896	-0.67018
42	2	0.909297	-0.41615	1.409297	-0.71615
43	2.05	0.887362	-0.46107	1.387362	-0.76107
44	2.1	0.863209	-0.50485	1.363209	-0.80485

Figure 3-42: Examples of selected data regions to be imported into 3pleANI from Excel

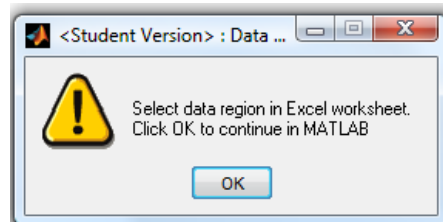


Figure 3-43: Window displayed in order to complete importing of external Excel data into 3pleANI



Figure 3-44: External File Panel

3.10 Panel 7: Animation panel

The animation panel becomes available when the analysis is completed. It is used for the following functions: (a) to automatically create an animation that keeps playing after the

Animate button is pressed, (b) to display the isolator deformed shape at any desired time, and (c) to manually advance the animation (each click of the mouse at the > or < buttons plots the subsequent or previous frame from the one already plotted). The animation panel controls both plotter 1 and plotter 2. Therefore, if the user has selected quantities to be plotted in plotter 2, then the graph in plotter 2 will gradually be drawn together with the animation of plotter 1 based on the actions performed in this panel

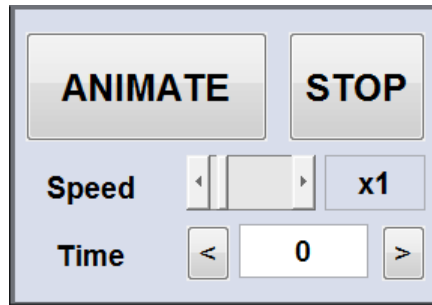


Figure 3-45: View of Animation panel

Animate: This button starts animation of the motion of the isolator in plotter 1 with simultaneous plotting of the selected variables in plotter 2. The animation starts from zero time and runs until the end unless the animation is stopped by the user or a different time range is specified in Panel 9.

Speed: This button controls the speed of the animation. Using the slider one can adjust the speed from very slow to very fast. The option *x1* does not correspond to a real time animation but rather to default speed that depends on the computer used. When the animation is exported into an “avi” file using the *Export Avi*, a real time animation can be exported by properly selecting the number of frames per second.

Time: This button is used as a monitor of the time instant if the *Animate* button is pressed or when the < and > buttons are pressed. It can also be used to display deformed shapes at a desired instant of time. For example, typing “3” will display the deformed isolator at 3sec and the history of the selected quantities in plotter 2 over the time interval of 0sec to 3sec.

The buttons < and > are used to manually advance the animation while the speed controls the number of frames advanced or reversed when the < > buttons are pressed. Every click of the >

button will display deformed shapes at subsequent time instances than the one displayed in the time monitor.

3.11 Panel 8: Animation options panel

This panel is used to include visual effects in the animations displayed in plotter 1. The panel is shown in Figure 3-46.

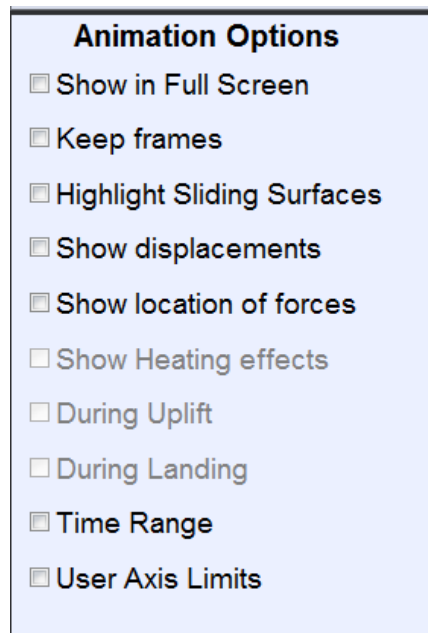


Figure 3-46: View of animation options panel

Show in full screen: When this option is selected, the animation is shown in full screen in a separate window for enlarged viewing.

Keep frames: This option allows displaying the animation without deleting the previous frames. For example, if the animation plots frames every 0.1sec then after 1sec , 10 different deformed shapes will be plotted on the screen. This is particularly useful when manual animation is used and the user wants to compare the deformed shape at two different times. To do so, the user needs to select **Keep frames** and then type the time (for example, 1.2) in the time edit box of the animation panel. This will plot the deformed shape at the specified time (at 1.2sec in this example). After typing 1.2 the user can type 2.1. This will display in plotter 1 the deformed shape at 1.2sec and 2.1sec together.

Highlight Sliding Surfaces: The option highlights the surfaces where sliding occurs. This is based on the value of the sliding velocity-different than zero. This may provide misleading information at initiation of motion or reversal of motion where the velocity instead of being exactly zero, is marginally different than zero due to numerical integration errors.

Show displacements: This option displays a dot on the top concave surface and the displacement values on the plotter during animation of motion.

Show location of forces: This option shows a dot at the location of the resultant contact tractions at each sliding surface. Values of the location of resultant contact tractions can be obtained by selecting the variables “Offset angle of surface” in Plotter 2.

Show heating effects: This option is available only when heating effects have been included in the analysis. Heating effects in plotter 1 are displayed by using different colors according to the surface temperature of each component. Colors vary from blue when the temperature rise is zero to red when the temperature reaches its maximum value. In calculating the heat flux and temperature rise, it is assumed that the friction material is a perfect insulator so that the generated heat is entirely supplied to the bare metal surface in contact with the friction material. That is, (a) the bottom concave plate heats up due to heat flux on surface 1, (b) the top concave plate heats up due to heat flux on surface 4, (c) the rigid slider is assumed insulated by the friction material on both surface 2 and 3, (d) the top slide plate heats up due to heat flux on surface 3 and (e) the bottom slide plate is heated by heat flux on surface 2. A contour bar appears that shows the different colors used for the different temperatures. Although in the animation the rigid bodies look like changing temperatures, these temperatures correspond to the middle of each sliding surface. There is no calculation of the temperature rise over the depth or width of each rigid body.

During uplift: This option is available if uplift occurs. It displays the animation only during the duration of the uplift when the **Animate** button is pressed.

Time Range: The user specifies the start and ending time of the animation to be displayed when the **Animate** button is pressed. If this option is not selected, then when pressing the **Animate** button, the animation will be displayed from the start to the end of the analysis duration.

User Limits: The user specifies the x and y axis limits of plotter 1. By default (when this option is not selected) these limits are automatically calculated by the program based on the geometry and maximum displacement of the isolator.

4 DYNAMIC ANALYSIS INTERFACE

This interface is used to perform response history analysis of two-dimensional isolated structures. Most of the panels between this interface and the *Displacement Controlled Tests* interface are common and therefore only the new ones are described below.

4.1 Panel 1: Triple Properties

This panel is shown in Figure 4-1 and it is identical to the panel described in the displacement controlled interface with the exception of the *Multiple Isolators* option. Moreover, the *Vertical Load* edit box is only used to display the total vertical load on the isolators (or weight of the structure above the isolators).

The screenshot shows a window titled "Triple Properties". It contains several controls: "Load Geometry" and "Save Geometry" buttons at the top left; a table with columns "m", "R", "h", and "d" (with a double-headed arrow between "m" and "R"); "Surface 1" through "Surface 4" rows; a "Vertical Load" input field with the value "1500" and "Show" and "?" buttons; and an "Additional" section with a checked checkbox for "Multiple Isolators(Optional)".

	m <->	R	h	d
Surface 1	0.02	156	6	21.6
Surface 2	0.01	16	4	2.25
Surface 3	0.01	16	4	2.25
Surface 4	0.065	156	6	21.6

Vertical Load: 1500 [Show] [?]

Additional Multiple Isolators(Optional)

Figure 4-1: Panel 1: View of Triple Properties panel

Multiple Isolators: When this option is not selected (default option) the isolation system consists of one isolator with constrained rotation on top. This modeling is appropriate when the analyzed structure consists of isolators of the same frictional and geometric properties, or when the isolators are represented by an equivalent single isolator with weighted average frictional properties.

When this option is selected, the window shown in Figure 4-2 appears and the user can include isolators with different frictional properties in the analysis. The geometry of all the isolators is the same and is determined by Panel 2 (Figure 4-1). The user then needs to specify the number of isolators to be included in the analysis. The minimum number is two isolators (note that each

isolator may represent a group of isolators). Then the user can shuffle through the options in the list-box of Figure 4-2 and assign the friction coefficient values of each isolator (or group of isolators). Note that the user cannot specify the friction coefficients of isolator 1 from this window since those are specified in Panel 2 (Figure 4-1). The user can also assign the vertical load on each isolator as a percentage of the total supported weight by all the isolators (this is displayed in Panel 2). The vertical load on isolator 1 is automatically calculated by the program so that the sum of all the percentages equals to 100%. The “<->” button can be used in order for the user to transform friction coefficients from the Fenz and Constantinou (2008a) theory to the Sarlis and Constantinou (2013) theory and paste the calculated values into the program. Details can be found in Section 3 for the DCI. Also, the button *Copy from* allows the user to copy the friction values of any isolator and paste them into another isolator. Note that the *Load and Save Geometry* buttons (explained earlier for the DCI) can only save properties specified in Panel 2 but cannot save properties specified in the *Multiple Isolators*. For this the *Save* button in Panel 1 should be used. Enabling the *Multiple Isolators* option affects the *Friction /Velocity* and *Heating Effect* button and the *Bridge* option. Those are discussed later.

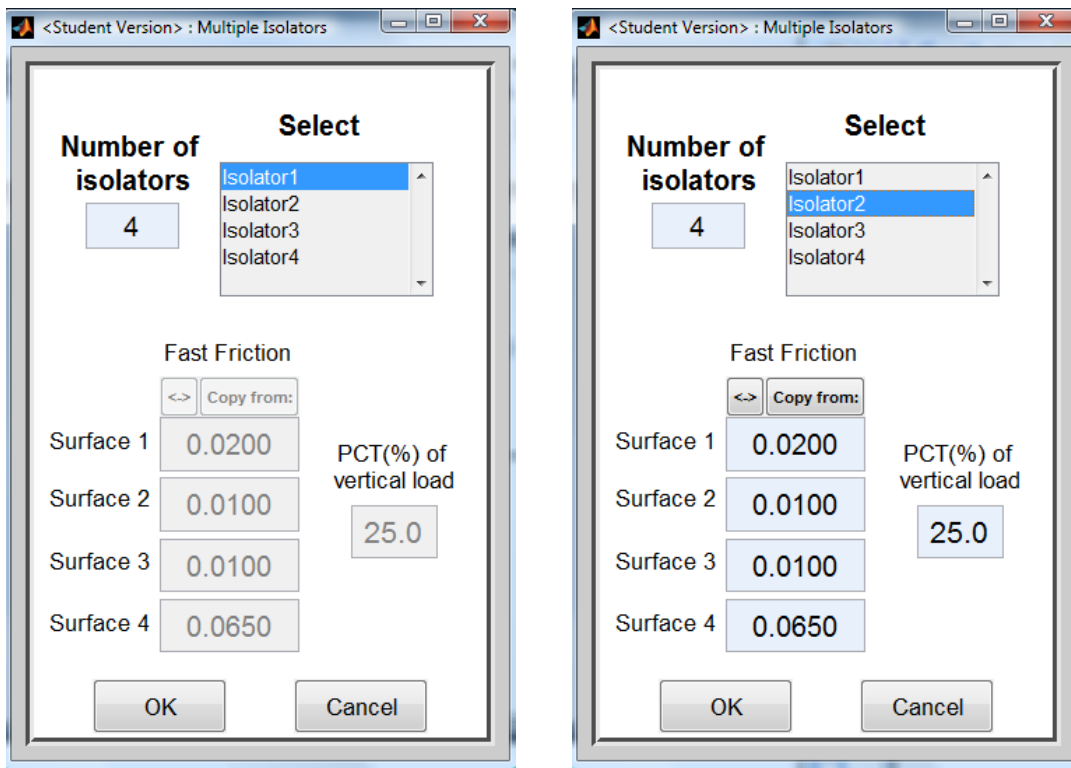


Figure 4-2: Window displayed when Multiple Isolators option is selected

4.2 Panel 3: Ground Motion

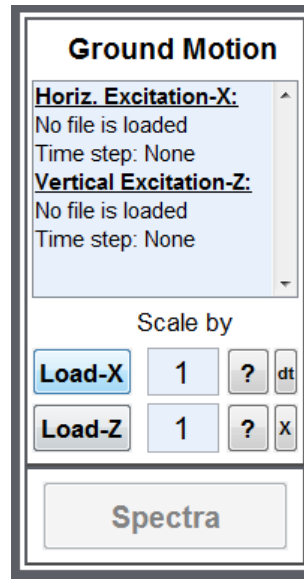


Figure 4-3: View of ground motion panel

This panel is shown in Figure 4-3 and is used to define the horizontal and vertical ground motion to be used for the response history analysis. The program accepts only input excitation from files that are loaded with the *Load-X* and *Load-Z* buttons. The selected excitations can be plotted with the ? button. Response spectra of the selected motions can be generated with the *Spectra* button. The monitor on top displays the file that is currently loaded.

Load-X: When pressing this button, the user can load into the program any “*txt*” file from the hard drive. Every time a new file is loaded, the previous file is overwritten. The “*txt*” file needs to contain columns of data (separated by spaces), which represent the horizontal ground acceleration history in units of *g*. Once the desired file is selected, the user will be prompted to input the time step of the excitation.

The program is supplied together with several historic records and other scaled motions that represent particular hazards in various areas of California. For the supplied ground motions, the time step is automatically assigned by the program. The time step can be changed by pressing the *dt* button.

? : When pressing this button, the acceleration histories that were imported in the horizontal direction (X) and the vertical direction (Z) are plotted. A separate button is used for each one. If no file has been imported, the plot will be null.

Load-Z: Same as for **Load-X** but for the vertical (Z) direction. Including a vertical excitation is optional. The time step of the vertical ground motion is assumed to be the same as that of the already imported horizontal motion. If the length of the file imported for the vertical direction is different than that of the horizontal, the analysis will be terminated when the horizontal motion terminates. If the vertical motion imported has lesser number of points than the horizontal motion, zeros are added to the vertical motion in order for the two motions to have the same duration. Exception in the latter case is when all values in the imported vertical excitation file are equal. In that case, the program assumes that the vertical acceleration is constant and adds the same values for the remainder of the excitation (in order to match the length of the horizontal excitation).

X: Removes the already imported vertical component from the memory.

dt: Button for changing the time step of the excitation.

Scale by: Button used to specify a scale factor that multiplies the imported ground motions. Separate factors can be applied in the X and Z directions.

Spectra: The spectra button becomes available only after at least one file has been imported. When pressed the window shown in Figure 4-4 appears. This window is divided into two parts: a) the input panel, and b) the output panel. In the input panel, the user can select the input excitation for the spectra. The program automatically recognizes the already imported horizontal and vertical excitations from panel 3 and includes them in the list-box. The user can also select the damping ratio for the spectra to be calculated. In order to include multiple values of damping ratio, the *ctrl* button on the keyboard must be used.

- **Options:** This button allows the user to change parameters in the construction of response spectra of the imported motions. These include the following options: (a) specification of the minimum and maximum period value and the period step for the spectra calculation, and (b) the accuracy in the calculation of the spectra in % (where 1% is more accurate than 2%). For the spectra calculation, for each value of period, the program initially performs a numerical analysis using the Newmark method with a time step equal to the time step of the excitation. Then, the time step is reduced to half and the analysis is repeated. If the result is accurate within the user defined accuracy, the results for that

period are accepted. If the accuracy is not acceptable, the time step is further reduced to half and the process is repeated. The time step will become as small as required for the user defined accuracy to be satisfied. This procedure is described in Chopra (2012).

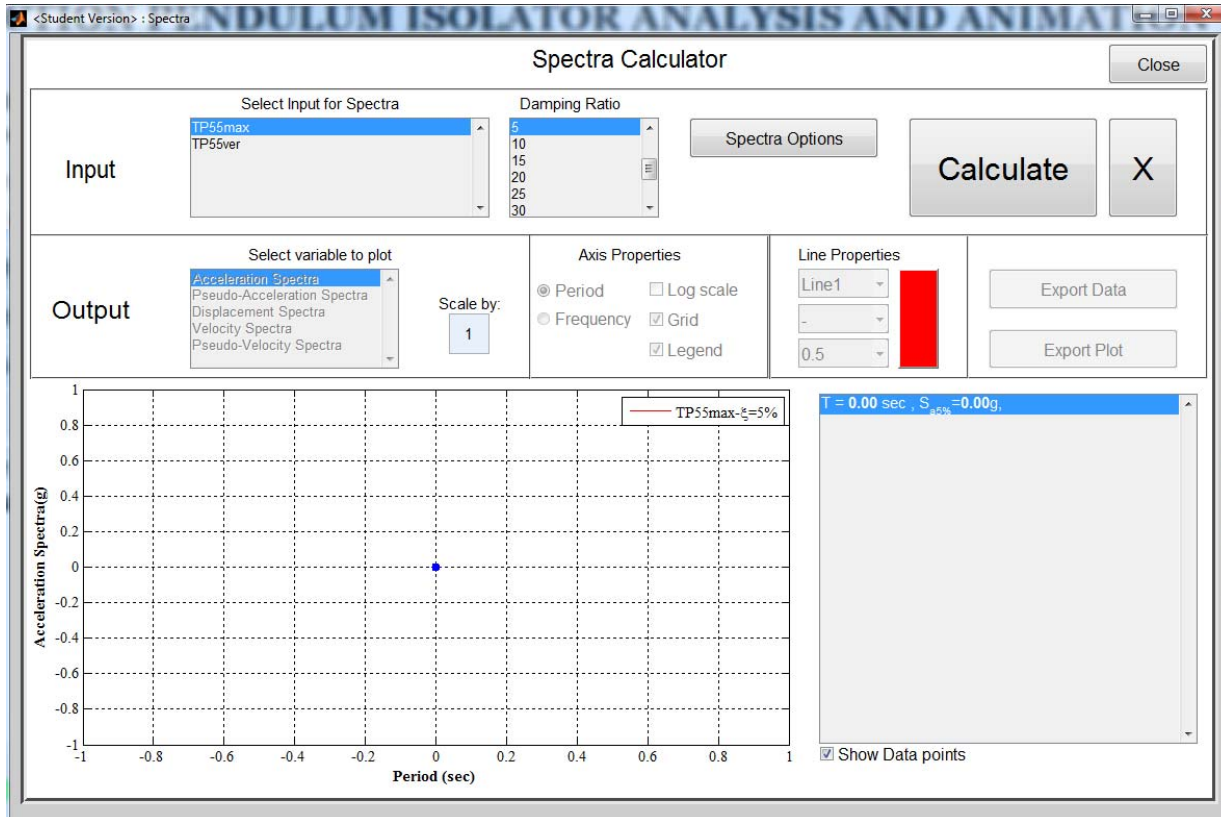


Figure 4-4: View of Spectra window prior to analysis

By pressing the *Calculate* button, the response spectra are calculated. After the analysis is complete, the output panel becomes available (see Figure 4-5). The user can select from a number of variables to be plotted (acceleration, pseudo-acceleration, displacement, velocity and pseudo-velocity spectra) and apply different scale factors to the plots. The user can plot the selected variables as functions of period or frequency and to use logarithmic scale for the x-axis. The display of the lines and of the plot can be changed. Note that the selected variable for plotting is also displayed in tabular form on the right of the plots. Any selection from the table is highlighted in the graphs when the *Show Data Points* is selected. The user can directly copy the table values into an external program by selecting *Copy All*. The plots can be exported by pressing the Export Plot button.

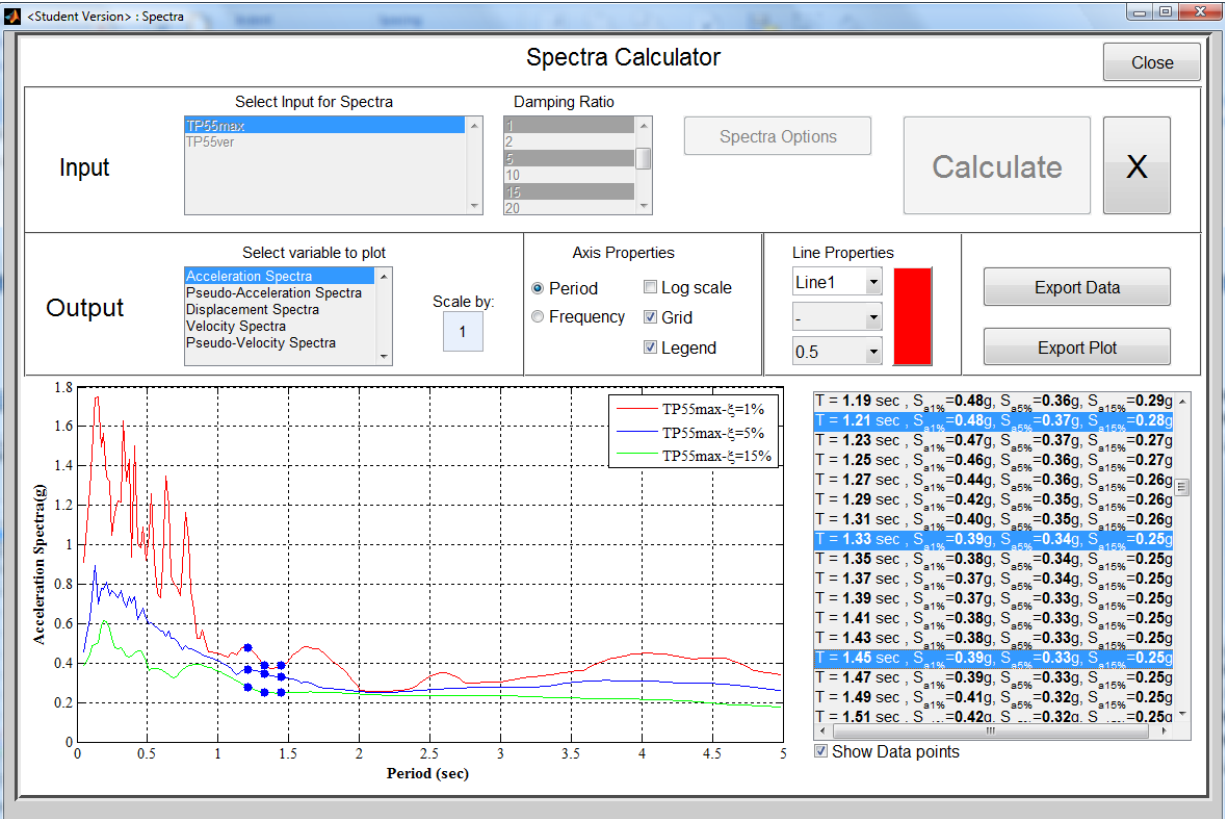


Figure 4-5: View of Spectra window after analysis is complete

4.3 Superstructure Panel

This panel is used to specify the properties of the superstructure. Options for *SDOF* (Single Degree of Freedom), *Shear building*, *Explicit* and *Bridge* exist. The panels when the four options are selected are shown in Figure 4-6. Figure 4-7 to Figure 4-9 show the displays of Plotter 1 when some of these options are selected. Depending on the selected superstructure, different options become available. These are described later.

Superstructure Properties

<input checked="" type="radio"/> SDOF <input type="radio"/> Shear building <input type="radio"/> Explicit <input type="radio"/> Bridge	Floor	Stiffness	Weight	Damp.
	Base	N/A	1500	0

a) Superstructure panel for *SDOF* system

Superstructure Properties

<input type="radio"/> SDOF <input checked="" type="radio"/> Shear building <input type="radio"/> Explicit <input type="radio"/> Bridge	Floor	Stiffness	Weight	Damp.
	Base	N/A	1500	
	1.	400	1500	
	2.	400	1500	
	3.	400	1500	
	4.	400	1500	
	5.	400	1500	
	6.	400	1500	
7.	400	1500		

Period: 3.36
 Stories: 8
 Damping %: 2
 Include dampers

b) Superstructure panel for *Shear building*

Superstructure Properties

<input type="radio"/> SDOF <input type="radio"/> Shear building <input checked="" type="radio"/> Explicit <input type="radio"/> Bridge	Floor	Stiffness	Weight	Damp.
	Base	N/A	1500	0

x 1

x 1

x 1

Period: 3.36
 Stories: 1

c) Superstructure panel for *Explicit*

Superstructure Properties

<input type="radio"/> SDOF <input type="radio"/> Shear building <input type="radio"/> Explicit <input checked="" type="radio"/> Bridge	Stiffness	Weight	
	Deck	N/A	1500
	Pier	400	1500

Advanced Modeling

Damping %: 2
 Include dampers

d) Superstructure panel for *Bridge*

Figure 4-6: View of superstructure panels for superstructure options

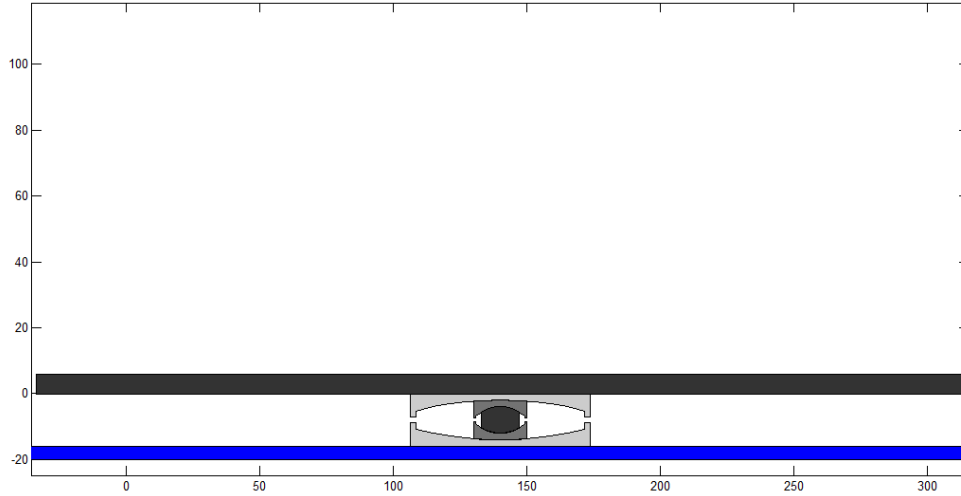


Figure 4-7: Drawing shown in plotter 1 when user specifies the properties of Figure 4-6a

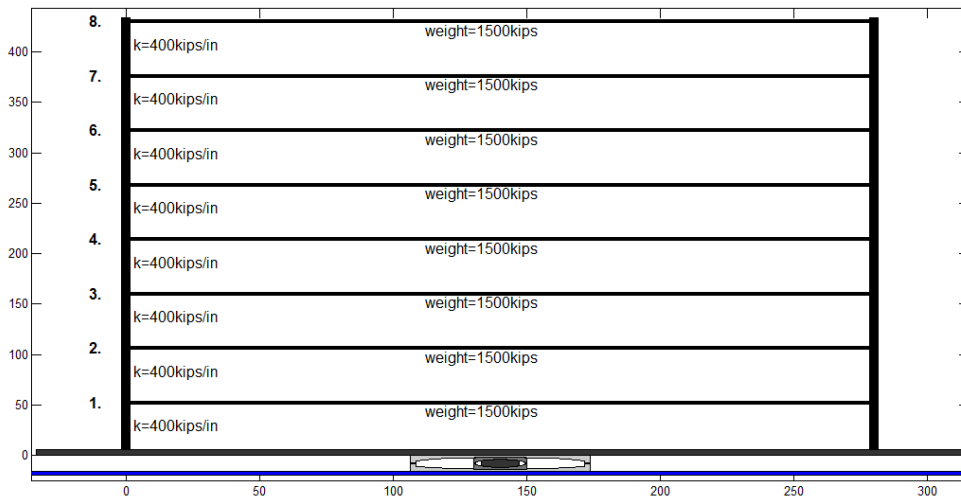


Figure 4-8: Drawing shown in plotter 1 when user specifies the properties of Figure 4-6b

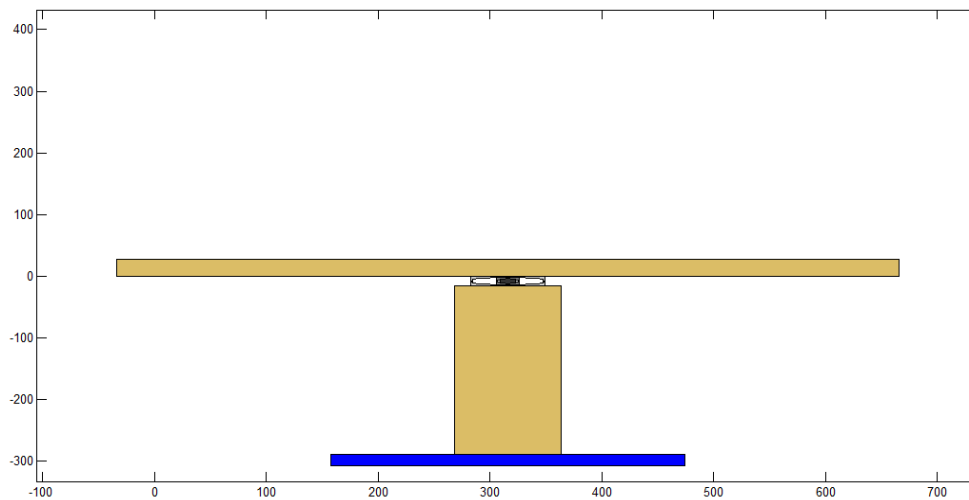


Figure 4-9: Drawing shown in plotter 1 when user specifies the properties of Figure 4-6d

SDOF: The program will perform a dynamic analysis of a rigid mass on top of an isolator (or group of isolators). The rotation of the top of the isolator is restrained. When **SDOF** is selected, the additional required input is shown in Figure 4-6(a) and is described below:

- **Weight:** the weight of the mass (in units of force) on top of the isolators. For the SDOF option, this specified weight is equal to the vertical load on the isolator(s) and it is automatically displayed in panel 2.
- **Damp.:** the damping constant of a linear viscous damper that is connected between the base and the ground (parallel to the isolators), if a damper is used. The value should be specified zero when there is no damper in the isolation system.

Shear Building: The user can model a multistory building on top of the isolators. The building is modeled with flexible columns and rigid beams. Once the **Shear building** option is selected, the **number of stories**, **damping** and **period** displays become available. Based on the specified number of stories selected, an equal number of edit boxes become visible and can be used to input the shear story stiffness and reactive floor weight. If the specified number of stories is larger than 7 (see Figure 4-6), then the last edit boxes are used to describe the properties of the selected story from the popup menu appearing at the same row. The required input when **Shear building** is selected is shown in Figure 4-6 (b) and described below.

- **Stories:** The user inputs the number of stories of the Shear Building.
- **Stiffness:** The user inputs values of the stiffness of each story in units consistent with those selected in panel 1. When the user inputs a stiffness value for the first story, the value is copied to all stories. The user can then assign the proper stiffness values of higher stories if different.
- **Weight:** The user inputs values for the reactive weight assigned to each floor of the superstructure and to the base-mat. The sum of the specified weights is the total vertical load on the isolators which is automatically displayed in Panel 2. All weights need to be input in units of force. The mass of each floor is calculated using the specified weights and dividing with the acceleration of gravity.
- **Include dampers:** This option allows the user to include linear viscous dampers between the floors and between the base and the ground. Once the box is checked, additional

columns of edit boxes appear (Figure 4-10) that allow the user to input values for the damping constant of the dampers at each floor and the base. Dampers are assumed to be placed horizontally. If the damper is at an angle θ to the horizontal, an effective damping constant in the horizontal direction should be specified (equals the damping constant of the damper times $\cos^2(\theta)$).

Superstructure Properties

SDOF

Shear building

Explicit

Bridge

Period:

Stories:

Damping %:

Include dampers

Floor	Stiffness	Weight	Damp.
Base	N/A	1500	0
1.	400	1500	1
2.	400	1500	0
3.	400	1500	1
4.	400	1500	0
5.	400	1500	1
6.	400	1500	0
7.	400	1500	0

Figure 4-10: View of superstructure panel when *Include dampers* is activated

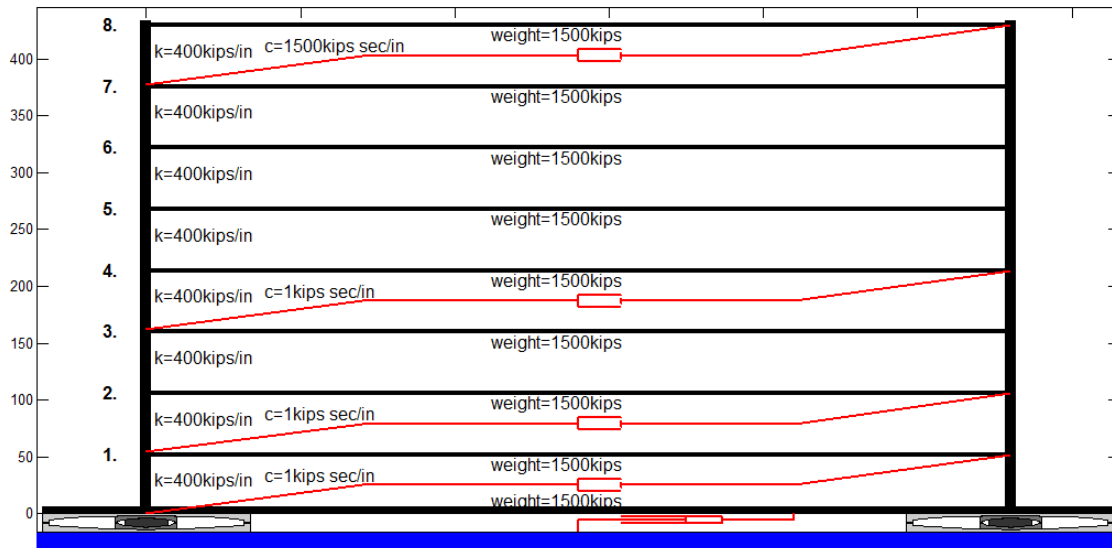


Figure 4-11: Drawing shown in plotter 1 when the user inputs the structure properties shown in Figure 4-10

- **Damp.:** Appears only when the *Include dampers* box is selected. The user can assign a damper constant at each floor and between the base and the ground for modeling supplemental damping.
- **Damping 1st mode:** This box is used to assign the inherent damping of the superstructure. The user inputs the damping ratio that will be assigned to the first and last mode of the superstructure. A superstructure damping matrix is calculated using Rayleigh damping. Accordingly, all modes will have damping ratio equal to or less than the specified value. The damping matrix resulting from inherent damping is added to the supplemental damping matrix in order to form the global damping matrix of the superstructure. The total damping ratio for all modes can be displayed by pressing the *Modes* button.
- **Modes:** When this button is pressed, complex eigenvalue analysis of the structure is performed and the exact damping ratio, period and mode shape of each mode are calculated. In the case that a mode is critically or over-critically damped, the period value displayed is incorrect and should be ignored (the exact value is infinite).. The modal characteristics can also be exported in an Excel file using the *Export* button next to the *Modes* button.
- **Period:** This button is used to display the fundamental period of the superstructure. When the user makes a change in the number of stories, the stiffness or the weight of any floor, the program performs a real eigenvalue analysis to calculate and display the period. This allows the user to easily adjust the properties of the superstructure in order to achieve a desired period.
- **Analyze:** Allows the user to perform a response history analysis of the fixed superstructure with the specified properties of the current panel and the horizontal ground motion imported in Panel 3. The vertical ground motion is ignored for this case. This allows the user to compare the response of the fixed superstructure to the response of the isolated structure. All results are displayed in a separate window. If the result windows are closed and the user presses again the *analyze* button, the results will be displayed again without conducting a new analysis. If, however, any of the structural properties or ground excitation characteristics are changed and the user presses the *analyze* button, a new analysis will be conducted using the newly specified properties.

- **Export:** Exports all fixed superstructure results to an Excel spreadsheet.

Explicit: When this option is selected, the user can import the mass, stiffness and damping matrices of the superstructure using an Excel file. The procedures for importing Excel files in 3pleANI were described in the External File Panel. In this case the user has to select rectangular regions of data only (for example, 3x3 region in Excel). The user also needs to specify the weight of the base-mat and dampers connected between the base-mat and the ground.

- **Import Mass Matrix:** When this button is pressed, a dialogue box appears where the user can select an Excel file from which the mass matrix is imported. The dimensions of the mass matrix determine the number of stories (for example, a 3x3 matrix corresponds to a 3 story building). The mass matrix must be diagonal. The sum of the mass matrix diagonal elements is used to calculate the weight of the superstructure which is added to the specified weight of the base-mat for the calculation of the total weight on the isolators that is displayed in Panel 2.
- **Import Stiffness Matrix:** When this button is pressed, a dialogue box appears where the user can select an Excel file from which a stiffness matrix is imported. The imported stiffness matrix must be of the same dimensions as the mass matrix
- **Import Damping Matrix:** When this button is pressed, a dialogue box appears where the user can select an Excel file from which a damping matrix is imported. The imported damping matrix must be the same dimensions as the mass matrix
- **Modify Mass Matrix:** Used to modify values of the already imported mass matrix
- **Modify Mass Matrix:** Used to modify values of the already imported stiffness matrix
- **Modify Mass Matrix:** Used to modify values of the already imported damping matrix
- **X:** Used to multiply the imported mass matrix, stiffness or damping matrix by a factor.

Bridge without advanced modeling: When the bridge option is selected, the user must specify the stiffness and weight of the pier and the weight of the deck. If the **Multiple Isolators** option is selected, then the number of isolators is equal to the number of piers. When **Advanced Modeling** is not selected, the bridge is modeled using the simple model shown in Figure 4-12. The piers are modeled as springs connected between the bottom of the isolators and the ground. A mass which represents the effective weight of the pier is included as shown in Figure 4-12.

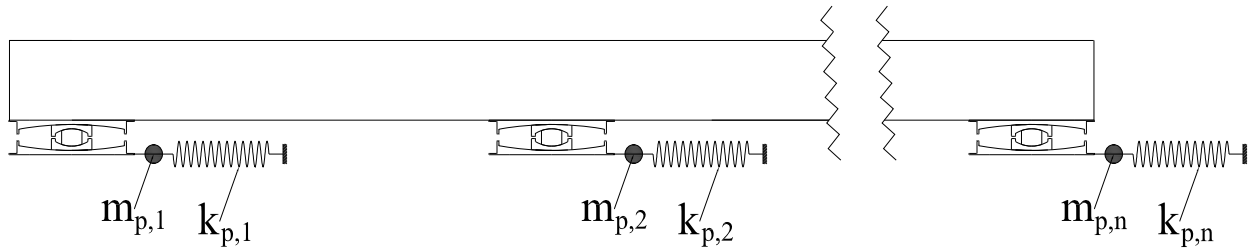


Figure 4-12: Bridge model used in 3pleANI when Advanced Modeling is not selected

- **Stiffness:** Used to specify the pier stiffness. When the *Multiple Isolators* option is selected, the user must specify the stiffness for a number of piers which is equal to the number of isolators (see Figure 4-2). When *Advanced Modeling* is not selected, each pier is modeled as a spring connected between the bottom of the isolator and the ground. The rotation of the pier and the effects of the moment at the top of the pier are ignored. *Advanced Modeling* allows the inclusion of these effects and it is described later.
- **Weight:** Used to specify the total weight of each pier. The use of the pier weight depends on the selection of modeling. In case *Advanced Modeling* is not selected, half of the specified weight is lumped at the top of the pier and half at the bottom (bottom half does not affect response). For example, in Figure 4-6(d), the user has specified 1500kip as the total weight of the pier. In the analysis, 750kip will be lumped at the top (weight corresponding to mass m_p is 750kip) in Figure 4-12. When the *Multiple Isolators* option is selected, the user must specify the total weight of a number of piers that is equal to the number of isolators. The weights assigned here do not affect the weight on the isolators.
- **Include Dampers:** Used to include a damper between the deck and each of the bridge piers if the *Multiple Isolators* option is selected. If the *Multiple Isolators* is not used, a single damper is connected between the pier and the deck. The damping constant of each damper can be specified using the third column of edit boxes.
- **Damping:** This option becomes available only if *Include dampers* option is enabled. The user must specify the damping constant of a damper connected between the deck and the pier. If the *Multiple Isolators* option is selected, then dampers between each pier and the deck need to be specified.
- **Damping %:** This is the inherent damping ratio that will be used for the piers of the bridge. The same damping ratio is used for all the piers if the *Multiple Isolators* option is selected.

Bridge with advanced modeling: When advanced modeling is selected as shown in Figure 4-13, then the window of Figure 4-14 appears that contains two main options shown with the checkboxes. By selecting, ***P-Delta Effects on Pier rotation, TFP model does not account for BCP rotation*** the analysis will account for the effect of the moment applied at the top of the pier by the isolator. This moment is given by Equation (4-1) and is due to P-Δ and any additional moment due to the shear forces applied over the height of the bearings and the restrainer forces as shown in the free body diagram of Figure 4-15 (horizontal and vertical reactions at the bottom are not shown).

$$M = W_1(\theta_1 + \theta_{s1})(R_1 + t_{co}) + (F_{g1} + S_1)t_{co} \quad (4-1)$$

The equation of motion of the pier is given by:

$$\begin{aligned} m_p \ddot{u}_p + c_p u_p + \frac{12EI}{h^3} u_p + \frac{6EI}{h^2} \theta_p &= -m_p \ddot{u}_g \\ \frac{6EI}{h^2} u_p + \frac{4EI}{h} \theta_p &= M \end{aligned} \quad (4-2)$$

Equation (4-2) after static condensation of the pier rotation results in the following equation:

$$m_p \ddot{u}_p + c_p u_p + k_p u_p + \frac{6M}{4h} = -m_p \ddot{u}_g \quad (4-3)$$

In Equation (4-3), k_p is the specified lateral stiffness of the pier given by $k_p = 3EI/h^3$ where h is the height of the pier specified in the window of Figure 4-14, m_p is the mass at the top of the pier, which is equal to half of the specified pier weight in Figure 4-13 divided by the acceleration of gravity and $c_p = 2\zeta_p \sqrt{k_p m_p}$ where ζ_p is the damping ratio of the pier which is specified by the user in the ***Damping %*** edit box.

Superstructure Properties

<input type="radio"/> SDOF <input type="radio"/> Shear building <input type="radio"/> Explicit <input checked="" type="radio"/> Bridge	<table border="1"> <thead> <tr> <th></th> <th>Stiffness</th> <th>Weight</th> </tr> </thead> <tbody> <tr> <td>Deck</td> <td>N/A</td> <td>1500</td> </tr> <tr> <td>Pier .</td> <td>40000</td> <td>800</td> </tr> <tr> <td>Pier2.</td> <td>100</td> <td>800</td> </tr> <tr> <td>Pier3.</td> <td>100</td> <td>800</td> </tr> <tr> <td>Pier4.</td> <td>40000</td> <td>800</td> </tr> </tbody> </table>		Stiffness	Weight	Deck	N/A	1500	Pier .	40000	800	Pier2.	100	800	Pier3.	100	800	Pier4.	40000	800
	Stiffness	Weight																	
Deck	N/A	1500																	
Pier .	40000	800																	
Pier2.	100	800																	
Pier3.	100	800																	
Pier4.	40000	800																	
<input checked="" type="checkbox"/> Advanced Modeling																			
Damping % <input type="text" value="2"/>																			
<input type="checkbox"/> Include dampers																			

Figure 4-13: View of Superstructure panel for Bridge with Multiple Isolators/Piers and Dampers

<Student Version> : Advanced Bridge properties

Specify the pier height for calculation of rotational stiffness. Also specify additional lumped weight(if any) at top of pier

P-Delta Effects on Pier rotation, TFP model does not account for Bottom plate rotation
 P-Delta Effects on Pier rotation, TFP model accounts for Bottom plate rotation

	Height		Height
Pier1	<input type="text" value="10"/>	Pier4	<input type="text" value="10"/>
Pier2	<input type="text" value="273"/>		
Pier3	<input type="text" value="273"/>		

Figure 4-14: View of Dialogue Box for Advanced Bridge Properties when the first option is selected

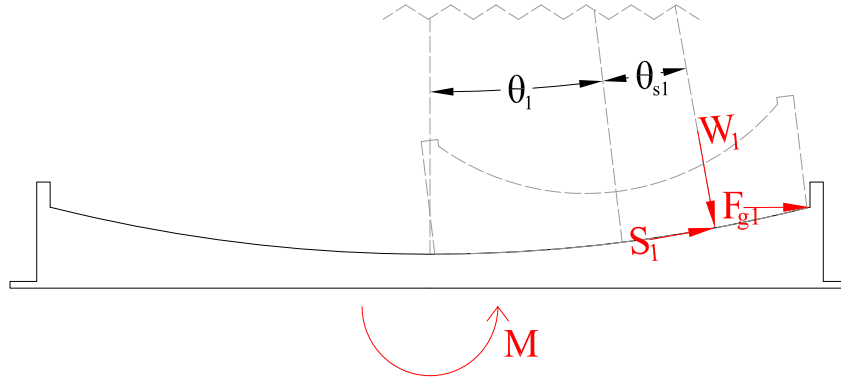


Figure 4-15: Free body diagram of BCP for calculation of bottom end plate moment

The formulation above accounts for the effect of the isolator moments on the pier displacement but it does not account for the effect of the pier rotation on the isolator behavior.

The option *P-Delta Effects on Pier rotation, TFP model accounts for BCP rotation* results in analysis that accounts for both the P-Δ moment effects and the pier top rotation on the isolator behavior. When this option is selected, the panel shown in Figure 4-16 is displayed. A schematic of the bridge model used by program 3pleANI is shown in Figure 4-17. The rotation of the pier is included as a dynamic degree of freedom. The stiffness and mass matrix of a single pier are given by:

$$K = \begin{bmatrix} 4k_p & 2k_p h \\ 2k_p h & \frac{4k_p h^2}{3} \end{bmatrix}; \quad M = \frac{m_p}{420} \begin{bmatrix} 156 & 22h \\ 22h & 4h^2 \end{bmatrix} \quad (4-4)$$

Note that the mass matrix above assumes that the specified pier weight in Figure 4-13 is distributed along the height of the pier and a consistent mass matrix formulation is used for the construction of the mass matrix in Equation (4-4). This is a significant difference in the interpretation of the pier weight when compared to previously described analysis cases.

The damping matrix is constructed using Rayleigh damping and is given by:

$$C = a_0 M + a_1 K$$

$$a_0 = \frac{2\zeta_p \omega_1 \omega_2}{\omega_1 + \omega_2}, \quad a_1 = \frac{2\zeta_p}{\omega_1 + \omega_2} \quad (4-5)$$

In Equation (4-5), ω_1 , ω_2 are the natural frequencies of the pier obtained from modal analysis using the matrices in Equation (4-4) and ζ_p is the pier damping ratio (specified in the **Damping %** edit box). The value is assumed the same for both modes of vibration.

Note that in Figure 4-16 the activation of the option **P-Delta Effects on Pier rotation, TFP model accounts for BCP rotation** allows the user to add additional concentrated weights at the top of the pier. The specified weights are included in a 2x2 diagonal mass matrix (with zero for the rotational degree of freedom) which is added to the mass matrix of Equation (4-4).

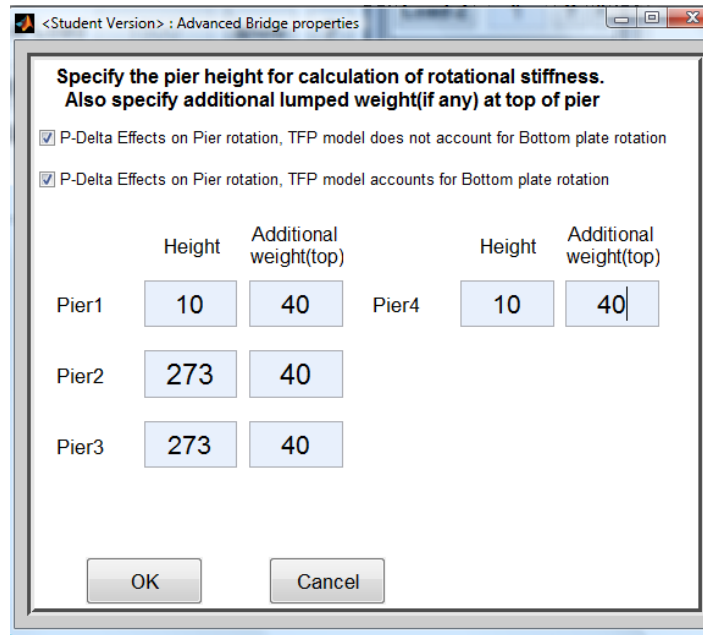


Figure 4-16: View of Dialogue Box for Advanced Bridge Properties when the second option is selected

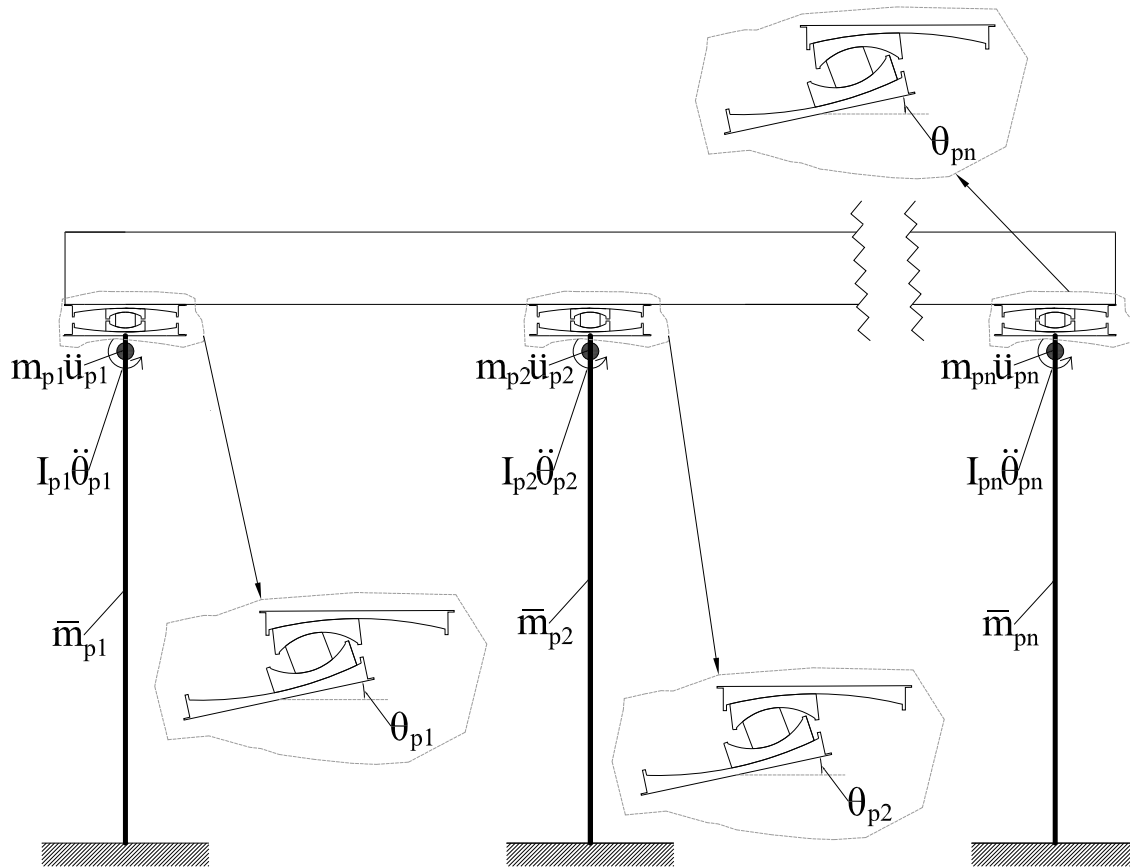


Figure 4-17: Bridge model with multiple isolators, P- Δ and pier rotation effects

4.4 Panel 7: Analysis Panel

Everything that was described in the Analysis Panel in Section 3 applies here as well with the exception that when the *Multiple Isolators* option is selected, the Friction |Velocity menu is different and is shown in Figure 4-18. The user has to input the SLOW friction coefficients for each isolator or select *Auto Calculate* so that the program automatically calculates the friction coefficients for all isolators.

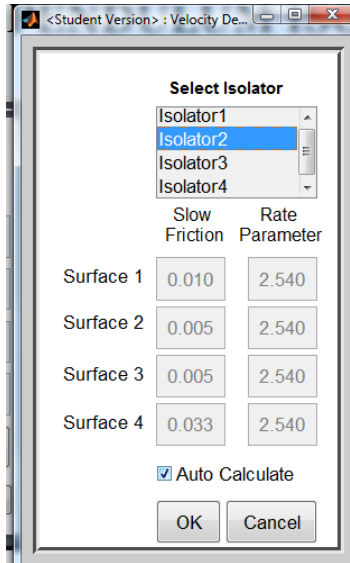


Figure 4-18: Friction |Velocity menu when Multiple Isolators option is selected

Moreover, in the *Heating Effects* window in Figure 3-30, the percentage of the vertical load that is considered for heating effects applies to the vertical load that is displayed in Panel 2 when the *Multiple Isolators* option is not selected and to the specified individual isolator load when the *Multiple Isolators* option is selected.

4.5 Panel 9: Animation Options Panel

The animation options panel is shown in Figure 4-19 and it was described in Section 3. In the case of the *Dynamic Analysis Interface* some minor changes are made in the animation options panel when compared to the same panel in the *Displacement Controlled Interface*.

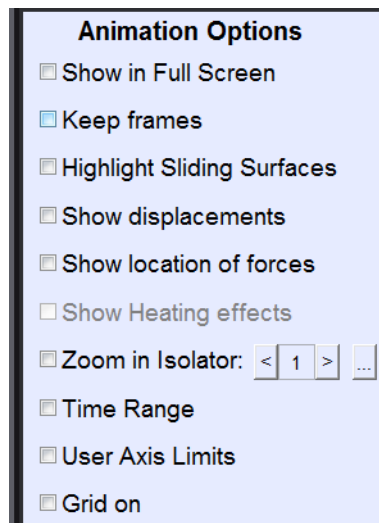


Figure 4-19: View of panel 8 in Dynamic Analysis Interface

The **Zoom in Isolator** option is used to hide the superstructure and automatically zoom to view the response of the Triple FP isolator. In the case of multiple isolators, the user can zoom in on any isolator. The superstructure animation options only affect the drawing of the superstructure. They may be used to view the structure drawn with higher stories or larger bay opening.

4.6 Plotter 2

The view of the Plotter 2 panel is shown in Figure 4-20. Plotter 2 for this interface is identical to that of the DCI with a few additional features:

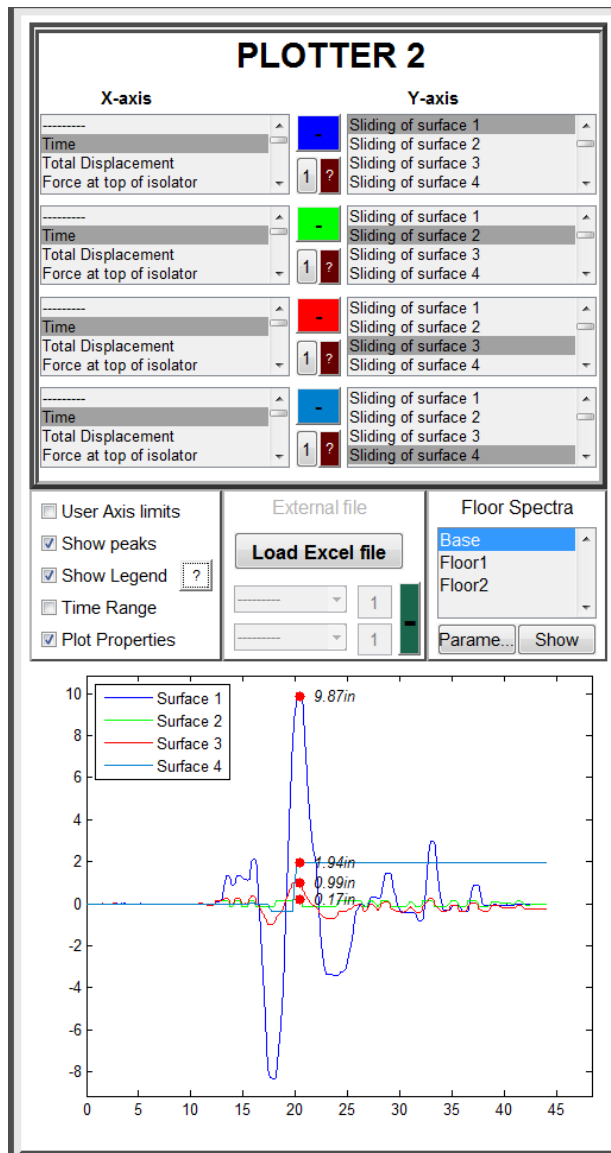


Figure 4-20: View of plotter 2

 : This button is visible only if the user has selected the **Multiple Isolators** option in Panel 2. The number shown displays the isolator for which the results in the corresponding list-boxes are shown. Note that the selected isolator number only affects the results that apply to the isolator response. Quantities related to superstructure (or deck and piers in the case of bridge) will always be available in the list-boxes regardless of the selected isolator. For example, Figure 4-20 shows the sliding displacement histories of surfaces 1, 2, 3 and 4 for isolator 1. By pressing this button the user can select another isolator to display results. The number of the selected isolator will appear on the button. Isolators are numbered from left to right of Plotter 1.

Floor Spectra: Opens the window shown in Figure 4-5. In the input list-box in Figure 4-5, the acceleration response histories of the analyzed structure are automatically displayed. As a result, the user can generate floor spectra by selecting the appropriate input for spectra calculation.

REFERENCES

1. Chopra A. (2012), "DYNAMICS OF STRUCTURES", Prentice Hall Inc., Upper Saddle River, New Jersey 07458. ISBN 10: 0-13-285803-7.
2. Computers and Structures Inc. (2007), "SAP2000: INTEGRATED FINITE ELEMENT ANALYSIS AND DESIGN OF STRUCTURES", Version 11.0.8, Berkeley, CA.
3. Constantinou, M.C., Whittaker, A.S., Kalpakidis, Y., Fenz, D. M. and Warn, G.P. (2007), "PERFORMANCE OF SEISMIC ISOLATION HARDWARE UNDER SERVICE AND SEISMIC LOADING", Report No. MCEER-07-0012, Multidisciplinary Center for Earthquake Engineering Research, Buffalo, NY.
4. Fenz, D.M. and Constantinou, M.C. (2008a), "MECHANICAL BEHAVIOR OF MULTI-SPHERICAL SLIDING BEARINGS", Report No. MCEER-08-0007, Multidisciplinary Center for Earthquake Engineering Research, Buffalo, NY.
5. Fenz, D.M. and Constantinou, M.C. (2008b), "SPHERICAL SLIDING ISOLATION BEARINGS WITH ADAPTIVE BEHAVIOR: THEORY," Earthquake Engineering and Structural Dynamics, Vol. 37, No. 2, 163-183.
6. Fenz, D.M. and Constantinou, M.C. (2008c), "SPHERICAL SLIDING ISOLATION BEARINGS WITH ADAPTIVE BEHAVIOR: EXPERIMENTAL VERIFICATION", Earthquake Engineering and Structural Dynamics, Vol. 37, No. 2, 185-205.
7. Fenz, D.M. and Constantinou, M.C., (2008d), "MODELING TRIPLE FRICTION PENDULUM BEARINGS FOR RESPONSE-HISTORY ANALYSIS", Earthquake Spectra, Vol. 24, No. 4, 1011-1028.
8. Fenz, D.M. and Constantinou, M.C. (2008e), "DEVELOPMENT, IMPLEMENTATION AND VERIFICATION OF DYNAMIC ANALYSIS MODELS FOR MULTI-SPHERICAL SLIDING BEARINGS", Report No. MCEER-08-0018, Multidisciplinary Center for Earthquake Engineering Research, Buffalo, NY.
9. Morgan, T. A. (2007), "THE USE OF INNOVATIVE BASE ISOLATION SYSTEMS TO ACHIEVE COMPLEX SEISMIC PERFORMANCE OBJECTIVES", Ph.D. Dissertation, Department of Civil and Environmental Engineering, University of California, Berkeley.
10. Sarlis, A.A., Constantinou, M.C. (2010), "MODELING OF TRIPLE FRICTION PENDULUM ISOLATORS IN PROGRAM SAP2000", supplement to MCEER Report 05-009, document distributed to the engineering community together with executable version of program and example files, University at Buffalo.
11. Sarlis, A.A., Constantinou, M.C. (2013), "MODEL OF TRIPLE FRICTION PENDULUM BEARING FOR GENERAL GEOMETRIC AND FRICTIONAL PARAMETERS AND

FOR UPLIFT CONDITIONS”, Report No. MCEER-13-xxxx, Multidisciplinary Center for Earthquake Engineering Research, Buffalo, NY.

3pleANI
FRICITION PENDULUM ISOLATOR
ANALYSIS AND ANIMATION PROGRAM

ANALYSIS AND VERIFICATION
EXAMPLES

Apostolos A. Sarlis¹

Michael. C. Constantinou²

University at Buffalo, State University of New York

June 2013

¹ Graduate Student, Department of Civil, Structural and Environmental Engineering, University at Buffalo, State University of New York, Buffalo, NY 14260

² Professor, Department of Civil, Structural and Environmental Engineering, University at Buffalo, State University of New York, Buffalo, NY 14260.

values measured are affected by the spherical geometry of the sliding surfaces and the location and direction of the resultant of the tractions on each sliding surface. The frictional parameters that describe the behavior of the Triple FP bearing in the models of Fenz and Constantinou (2008a to 2008e) ($\bar{\mu}_1, \bar{\mu}_2, \bar{\mu}_3, \bar{\mu}_4$, with the following constraints $\bar{\mu}_2 = \bar{\mu}_3 \leq \bar{\mu}_1 \leq \bar{\mu}_4$) utilize the values extracted from experiments of the Triple FP bearings and are not fundamental properties of the interfaces. Sarlis and Constantinou (2013) have recently shown that the true frictional values ($\mu_1, \mu_2, \mu_3, \mu_4$ without any constraints) are related to those in the models of Fenz and Constantinou (2008a to 2008e) by the following equations:

$$\begin{aligned}\bar{\mu}_2 &= \mu_2 \frac{R_2}{R_{eff2}} \\ \bar{\mu}_1 &= \frac{\mu_1 R_1 - \mu_2 R_2}{R_{eff1} - R_{eff2}} \\ \bar{\mu}_4 &= \frac{\mu_4 R_4 - \mu_2 R_2}{R_{eff1} - R_{eff2}}\end{aligned}\quad (1-1)$$

Program 3pleANI makes use of friction values $\mu_1, \mu_2, \mu_3, \mu_4$.

Table 1-1: Properties of TFP isolator

Parameters	Values for use in SAP2000 (Fenz and Constantinou model implemented as series or parallel model)	Values in 3pleANI (moment equilibrium model)
$R_1 = R_4$ (inch)	156	156
$R_2 = R_3$ (inch)	16	16
Displacement capacity on surfaces 1 and 4 (in)	$d_1^* = d_4^* = 20.77^1$	$d_1 = d_4 = 21.6$
Displacement capacity on surfaces 2 and 3 (in)	$d_2^* = d_3^* = 1.688^1$	$d_2 = d_3 = 2.25$
Friction surface 1 ²	$\bar{\mu}_1 = 0.02145$	$\mu_1 = 0.02$
Friction surfaces 2 and 3 ²	$\bar{\mu}_2 = \bar{\mu}_3 = 0.01333$	$\mu_2 = \mu_3 = 0.01$
Friction surface 4 ²	$\bar{\mu}_4 = 0.07232$	$\mu_4 = 0.065$
$h_1 = h_4$ (inch)	6	6
$h_2 = h_3$ (inch)	4	4
1. $d_i^* = d_i \left(\frac{R_{effi}}{R_i} \right)$, $R_{effi} = R_i - h_i$ 2. All friction values are for high velocity conditions= f_{max}		

1.1 Eigen-analysis of fixed superstructure

The eigenvalues and eigenvectors of the fixed superstructure as obtained from the two programs are shown in Table 1-2 and Figure 1-2. Note that program 3pleANI conducts complex eigenvalue analysis that includes the superstructure damping in the modal calculations. Since SAP2000 conducts real eigenvalue analysis, and for this case only, the inherent damping in 3pleANI was set to zero in order to eliminate the effect of damping in the calculated modal properties. Results from the two programs are identical.

Table 1-2: Comparison of eigenvalues obtained from 3pleANI and SAP2000

	1st mode	2st mode	3st mode	4st mode
Period (sec) 3pleANI	1.593	0.588	0.401	0.318
Period (sec) SAP2000	1.595	0.588	0.401	0.318

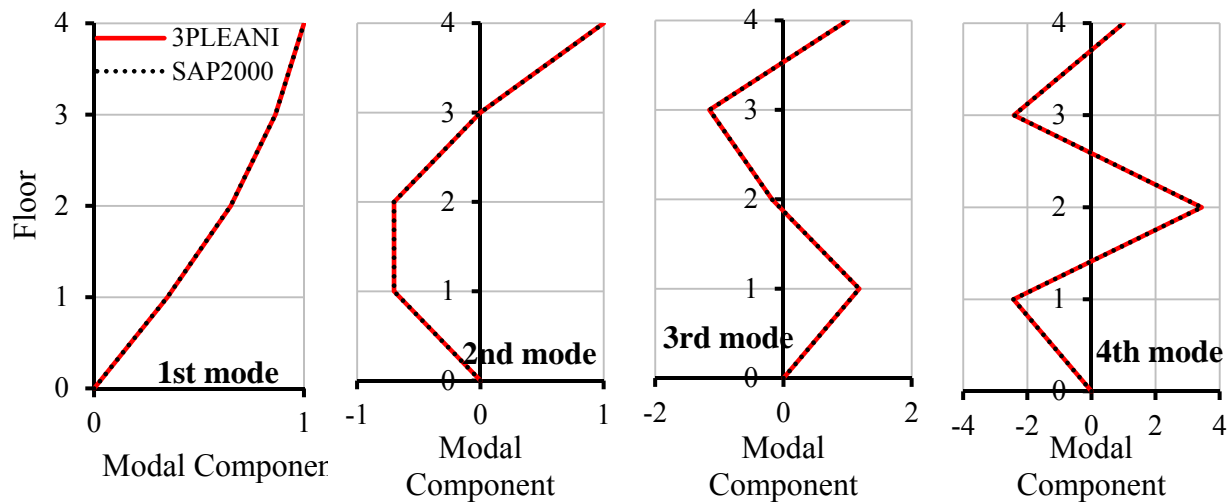


Figure 1-2: Comparison of eigen-modes obtained from 3pleANI and SAP2000

1.2 Ground motions used in analysis and response spectra

The ground motion used for response history analysis in this example is shown in Figure 1-3. The response spectra for this ground motion as obtained from 3pleANI for 2% and 10% damping ratio are compared in Figure 1-4 with the response spectra obtained from SAP2000. Results are identical.

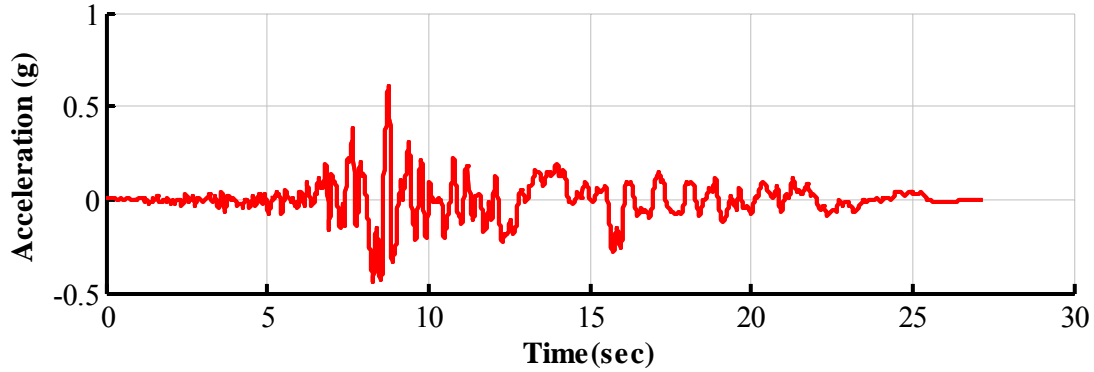


Figure 1-3: Ground motion used for response history analysis

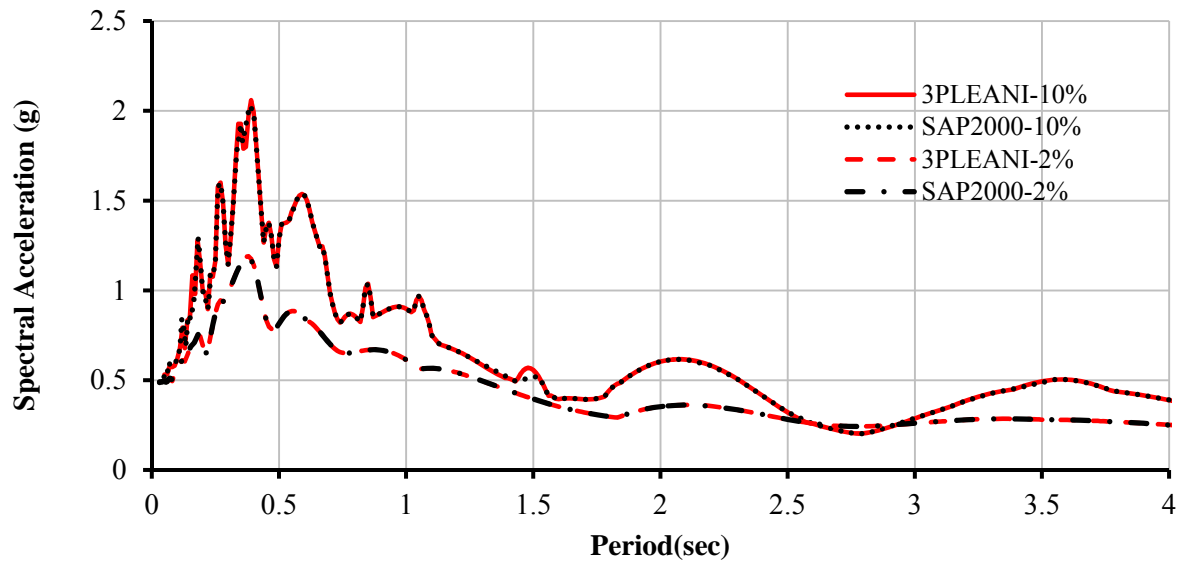


Figure 1-4: Comparison of 2-percent and 10-percent damped acceleration response spectra obtained from 3pleANI and SAP2000

1.3 Response history analysis of fixed superstructure

The superstructure fixed at its base was analyzed in programs 3pleANI and SAP2000. Structural damping was modeled in the two programs using Rayleigh damping with damping ratio of 5% in the first and the fourth modes. The results obtained from programs 3pleANI and SAP2000 are compared in Figure 1-5 for the 2nd story drift and the roof acceleration histories. The results of the two programs are essentially identical. Results for other response quantities compared equally well.

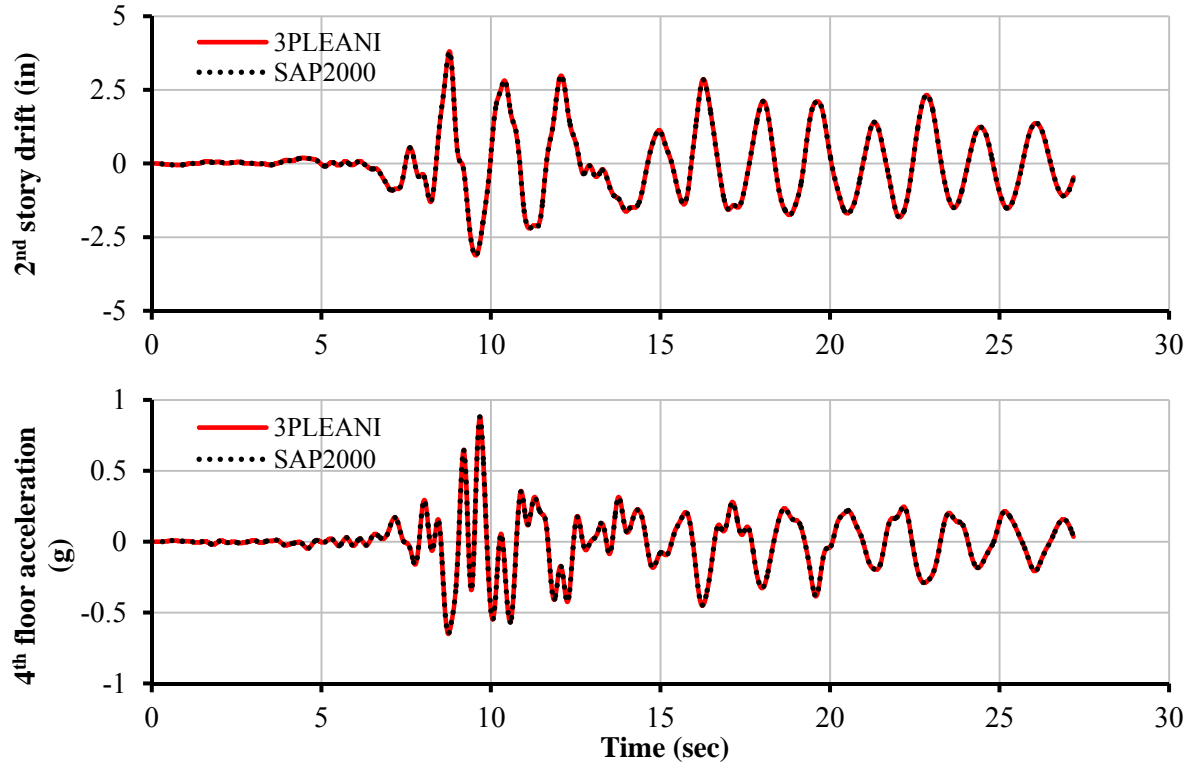


Figure 1-5: Comparison of 2nd story drift and 4th floor acceleration histories of fixed structure calculated in programs 3pleANI and SAP2000

1.4 Response history analysis of fixed superstructure with 5% inherent damping and supplemental dampers

The structure of Section 1.3 (5-percent inherent Rayleigh damping in first and fourth modes) was reanalyzed after the addition of linear viscous dampers. Dampers with damping constant (effective in horizontal direction) of 500, 300, 200 and 100 *kip – sec/in* were added to the 1st, 2nd, 3rd and 4th stories, respectively. Results comparing the 2nd story drift and 4th floor acceleration histories are shown in Figure 1-6. The results are nearly identical as were results for other response quantities not shown here.

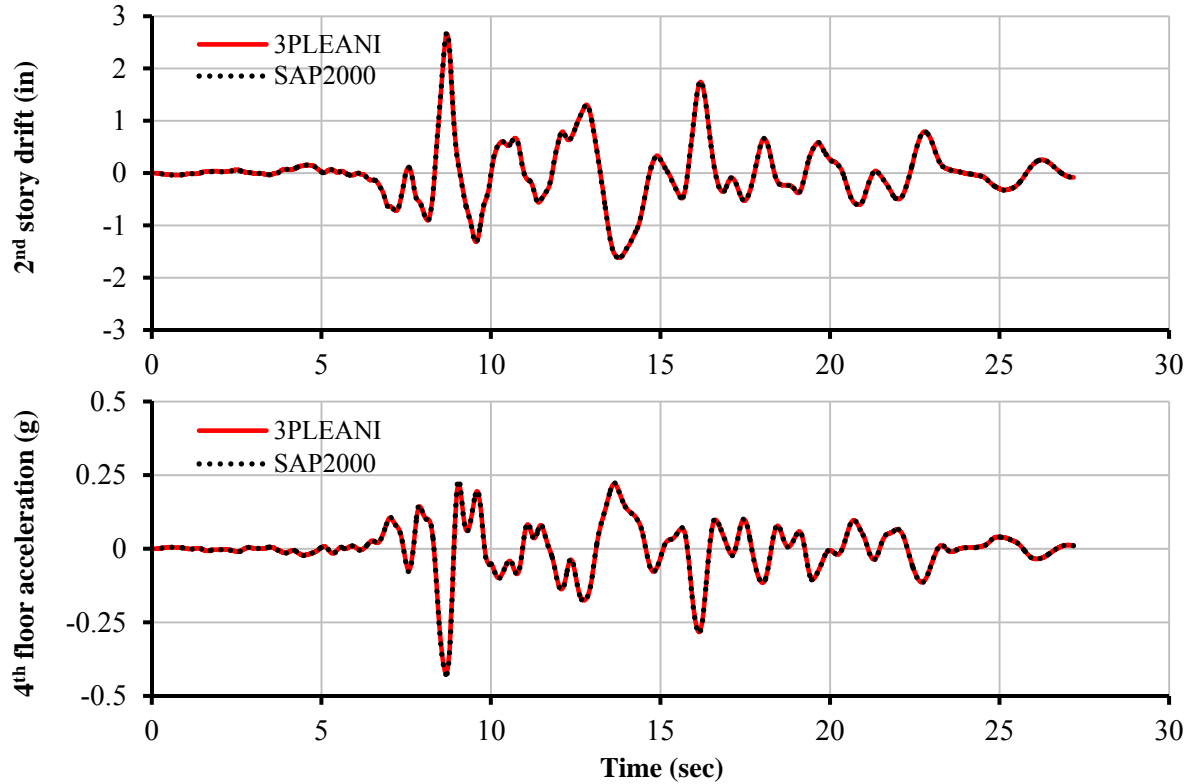


Figure 1-6: Comparisons of 2nd story drift and 4th floor acceleration histories of fixed structure with added dampers calculated in programs 3pleANI and SAP2000

1.5 Displacement Controlled Test

A single isolator with the properties shown in Table 1-1 was subjected to one cycle of sinusoidal displacement history with 6sec period and amplitude of 44.2inch. Vertical load was specified to be 15796.4kip (the vertical load on each of the three isolators in the model of Figure 1-1 which are assumed to equally carry the weight of the structure).

Figure 1-7 shows the program 3pleANI interface when specifying the parameters for this analysis. Note that the friction coefficient is considered velocity-independent in this analysis. 3pleANI uses by default 0.01in for the yield displacement for the friction of each surface. In program 3pleANI, if needed, the change from the default value can be made from the *User Tolerances* option on the Analysis options panel. Note also that the <-> button in the Triple Properties panel can be used to calculate $\mu_1, \mu_2, \mu_3, \mu_4$ (see Table 1-1) using $\bar{\mu}_1, \bar{\mu}_2, \bar{\mu}_3, \bar{\mu}_4$ based on Equation (1-1).

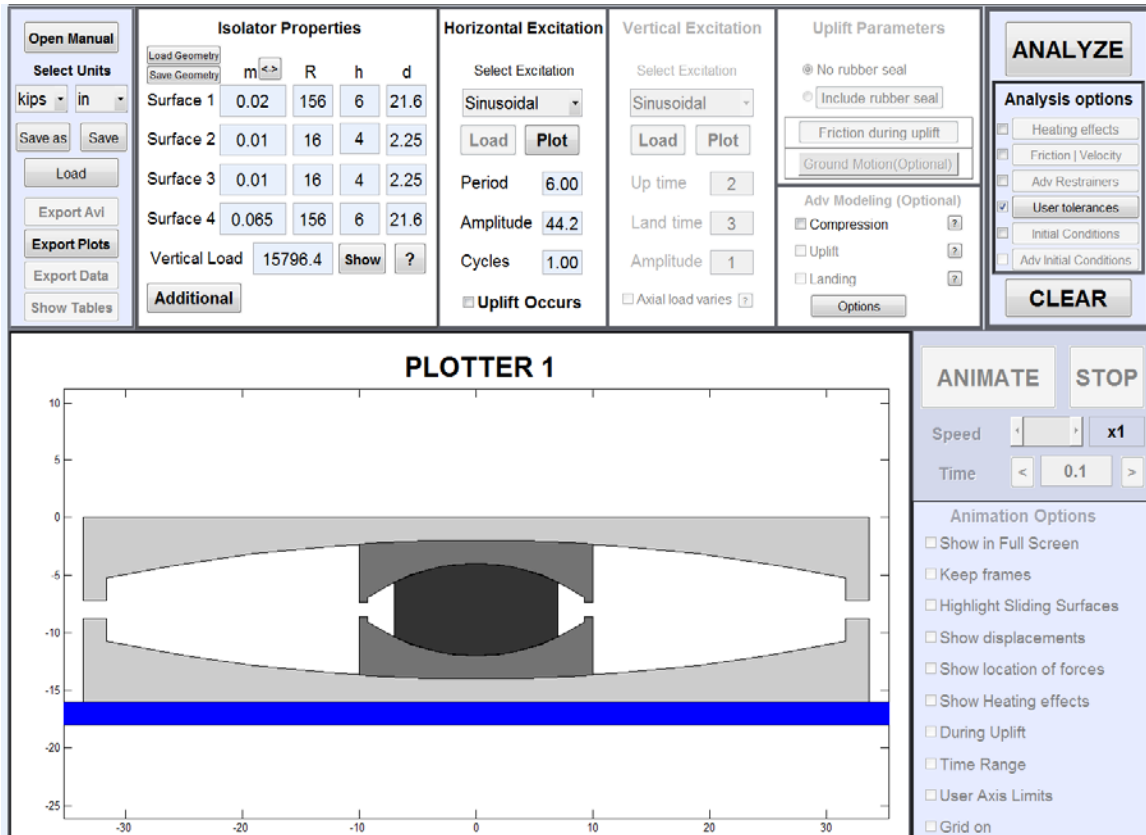


Figure 1-7: View of 3pleANI interface for single isolator analysis

In program SAP2000 the series model (Fenz and Constantinou, 2008d) was utilized subject to displacement controlled excitation and analysis was performed by direct integration. The bearing parameters are those of Table 1-1 corresponding to the Fenz and Constantinou model. When implemented in program SAP2000, the series model requires specification of properties for three friction pendulum (FP) elements and two gap elements for one-directional motion (Fenz and Constantinou 2008d and 2008e). These properties are presented in Table 1-3 and 1-4. The interested reader is referred to Fenz and Constantinou (2008d and 2008e) and Sarlis and Constantinou (2010) for more details of modeling the Triple FP isolator in program SAP2000. Note that in Table 1-3, the low velocity (SLOW) and large velocity (FAST) values of friction are the same so that friction is modeled as velocity independent.

Table 1-3: Values of parameters of the series model of isolators in SAP2000

	FP1	FP2	FP3
Element Height (inch)	8	4	8
Shear Deformation Location (in)-(distance from top joint of FP element)	4	2	4
Element Mass (kip-s ² /in)	0.00005	0.00005	0.00005
Supported Weight (kip)	15796.4	15796.4	15796.4
Vertical Stiffness (kip/in)	45000	45000	45000
Elastic Stiffness (kip/in)	21009.3	33881.6	114237.9
Effective Stiffness (kip/in)	60	11	10
Friction Coefficient SLOW	0.0133	0.02145	0.0723
Friction Coefficient FAST	0.0133	0.02145	0.0723
Radius (inch)	24	138	138
Rate Parameter (in/sec)	0	0	0
Rotational/Torsional Stiffness (R1,R2,R3)	0	Fixed	Fixed
Rotational Moment of Inertia (kip-in-sec ²)	0.0005	0	0

Table 1-4: Parameters of gap elements of the series model of Triple FP bearing in SAP2000

Element	Gap opening (in)	Stiffness after gap closing (kip/in)
GAP1	19.11	96153
GAP2	19.11	96153

Figure 1-8 compares the calculated force-displacement loop of the isolator by the two programs. The results are essentially identical.

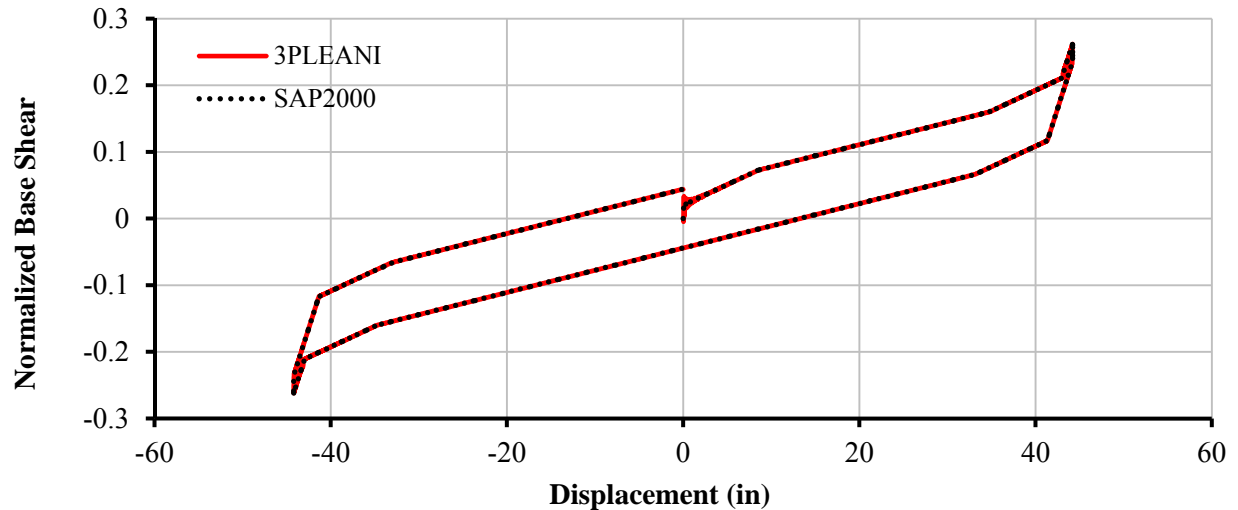


Figure 1-8: Normalized force (divided by vertical load) versus displacement loop of isolator calculated by programs 3pleANI and SAP2000

1.6 Response history analysis of isolated structure

For the analysis of the isolated structure, the ground motion shown in Figure 1-3 was scaled up by factor 1.25 in order to have a displacement demand close to the isolator’s capacity.

Figure 1-9 shows the program 3pleANI interface when specifying the parameters for this analysis. Note that velocity dependence of the friction coefficients has not been considered. Structural damping was specified as 5-percent in the first and fourth modes using Rayleigh damping (see Section 1.3).

Modeling of the isolators in program SAP2000 was described in Section 1.5. Structural damping (or inherent damping) in SAP2000 requires special handling in order to avoid or minimize “leakage” of damping in the isolation system (see Sarlis and Constantinou, 2010 for details). For this example, structural damping in SAP2000 was specified using Rayleigh damping with the same parameters as in program 3pleANI but with *Override* activated so that leakage in the isolation system is minimized following the procedures described in Sarlis and Constantinou (2010). Analysis was done by the Fast Nonlinear Analysis procedure.

Figure 1-10 and Figure 1-11 compare various response quantities obtained by programs 3pleANI and SAP2000. There is very good agreement between the results obtained by the two programs although the peak floor accelerations and peak story drifts are systematically larger-by a small amount-in the SAP2000 analysis. These differences are likely the results of many contributing factors: (a) differences in modeling structural damping (likely the main contributor to

differences), (b) modeling of the isolators (3pleANI uses a more advanced model but with insignificant differences for the analyzed isolator), (c) inability of 3pleANI to account for overturning moment effects, and (d) differences in numerical integration methods and tolerances in the two programs and (e) differences in the total elastic stiffness prior to sliding as well as the total stiffness upon contact with restrainers in programs 3pleANI and SAP2000.

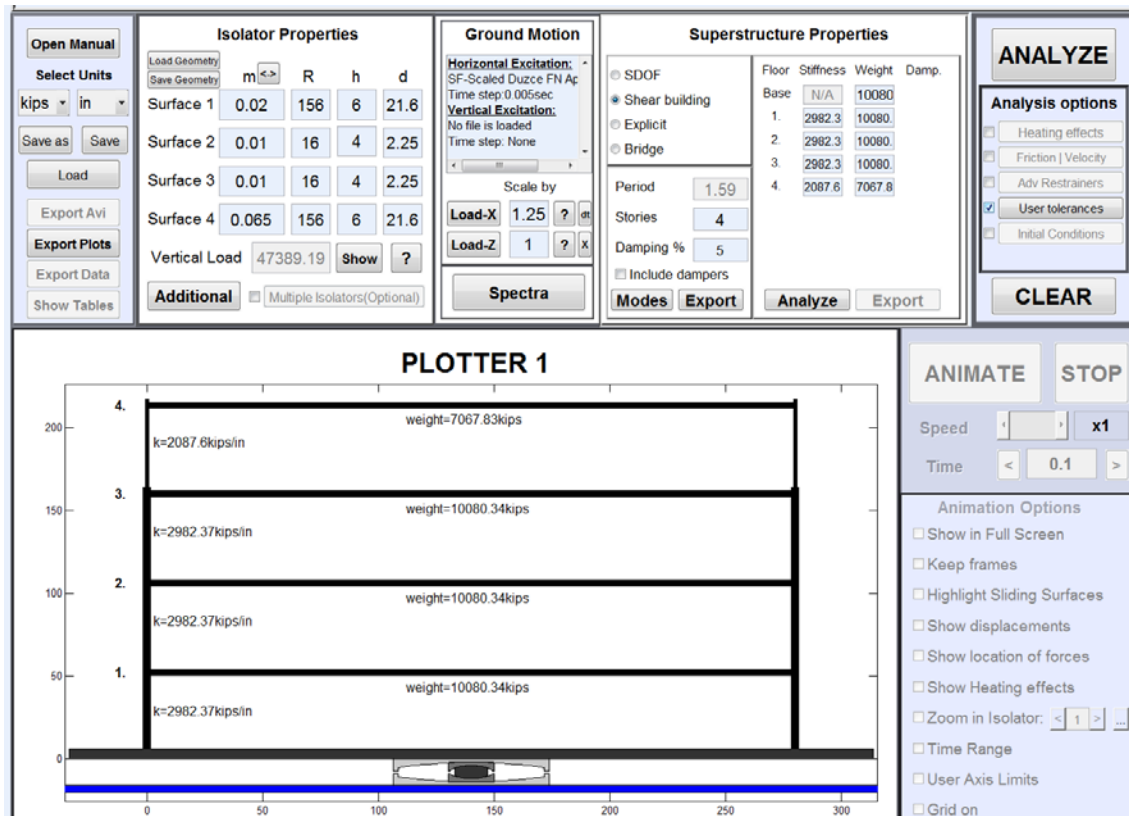


Figure 1-9: View of 3pleANI interface for analysis of isolated structure

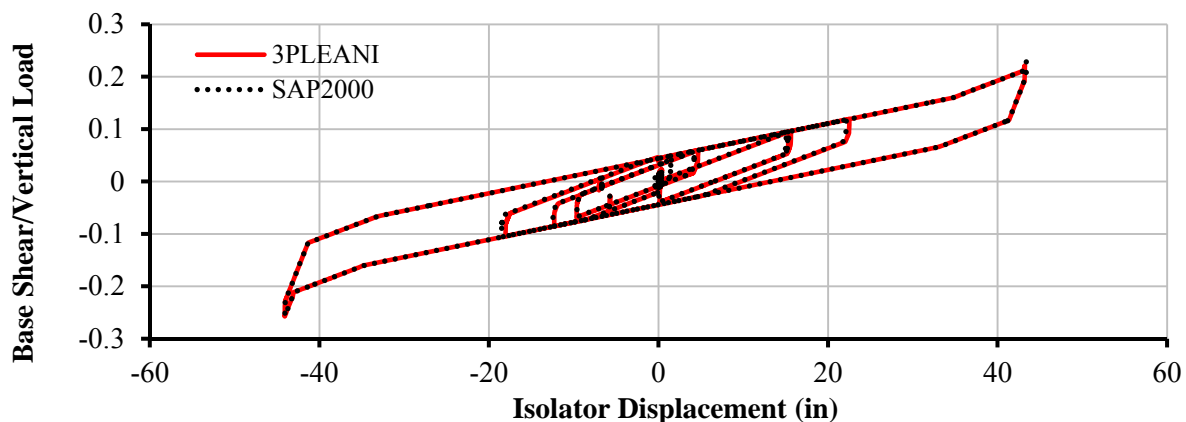


Figure 1-10: Comparison of loops of base shear/vertical load versus displacement calculated in programs 3pleANI and SAP2000 for isolated structure

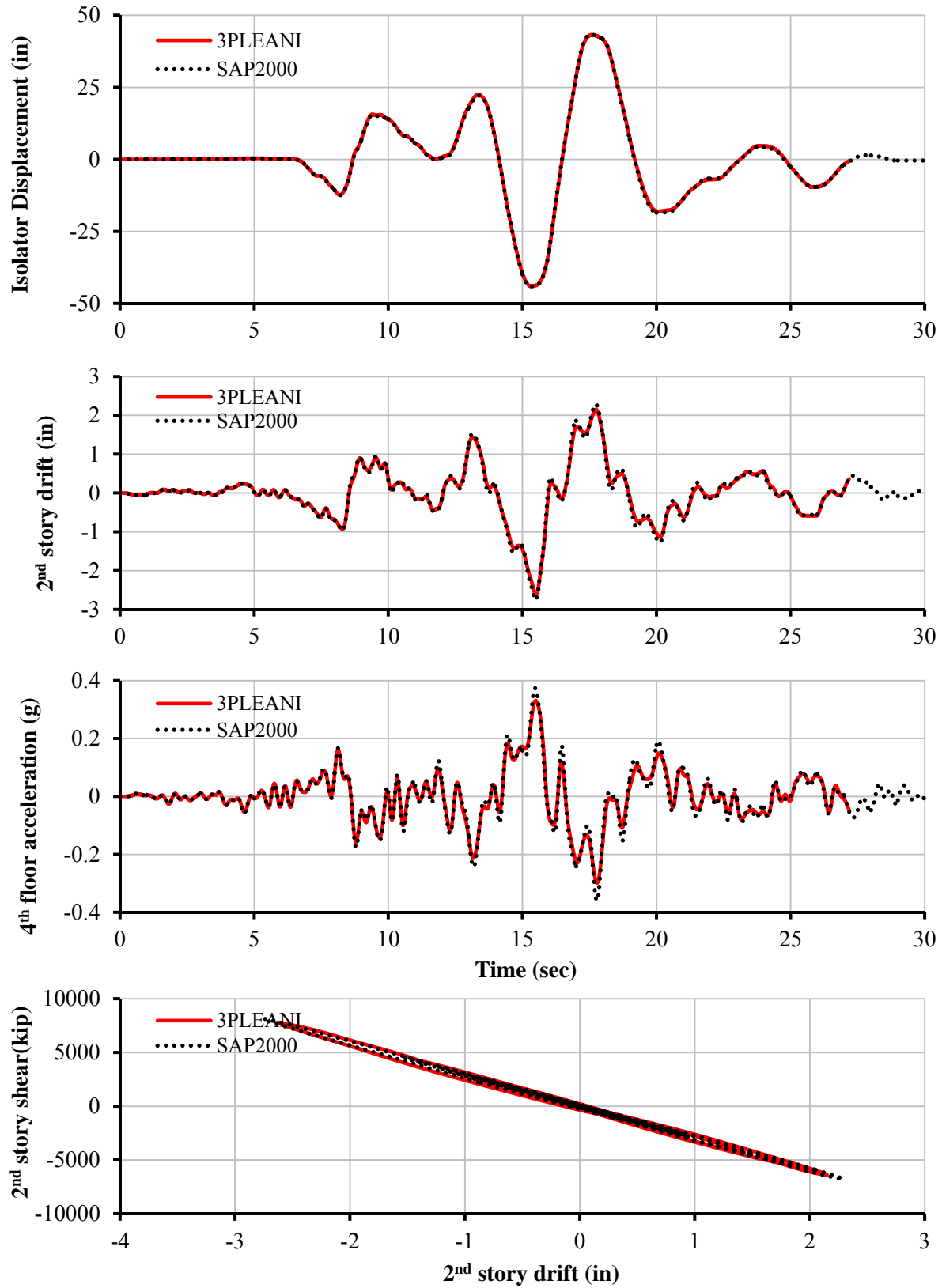
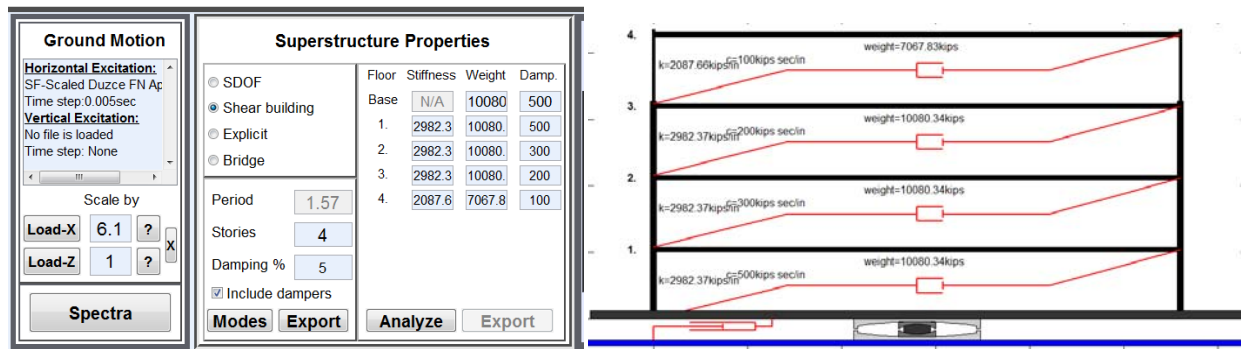


Figure 1-11: Comparison of response calculated in programs 3pleANI and SAP2000 for isolated structure

1.7 Response history analysis of isolated structure with supplemental dampers

The isolated structure analyzed in Section 1.6 was re-analyzed with linear viscous dampers added to each story and the isolation system. Figure 1-12(a) shows a partial view of the 3pleANI interface together with the values of the damping constant (effective in horizontal direction) for the added dampers. Figure 1-12(b) shows the display of Plotter 1 in 3pleANI when the properties of Figure 1-12(a) are specified. Note that the remaining parameters of the interface that are not shown in Figure 1-12 are identical to those in Figure 1-9. The ground motion used is that of Figure 1-3 but scaled up by factor 6.1.



(a) View of Superstructure Panel in 3pleANI

(b) Display in Plotter 1 in 3pleANI

Figure 1-12: View of 3pleANI interface for analysis of isolated structure with supplemental dampers

Figure 1-13 and Figure 1-14 compare various response quantities obtained by programs 3pleANI and SAP2000. There is very good agreement between the results obtained by the two programs, including the peak values of acceleration and drift. This demonstrates that the differences in the peak values of drift and acceleration obtained in the example of Section 1.6 (inherent damping of 5% and without supplemental dampers) were primarily due to differences in modeling structural damping in the two cases. In the example with supplemental dampers, the viscous damping in the isolation system is so large that “leakage” from the structural damping description in program SAP2000 adds an insignificant component.

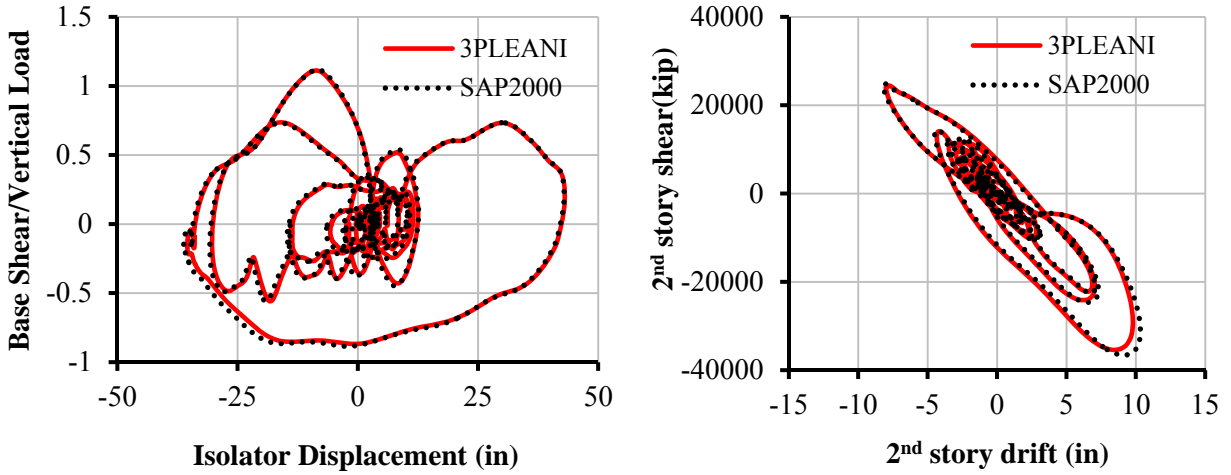


Figure 1-13: Comparison of force-displacement and shear-drift loops calculated in programs 3pleANI and SAP2000 for isolated structure with supplemental dampers

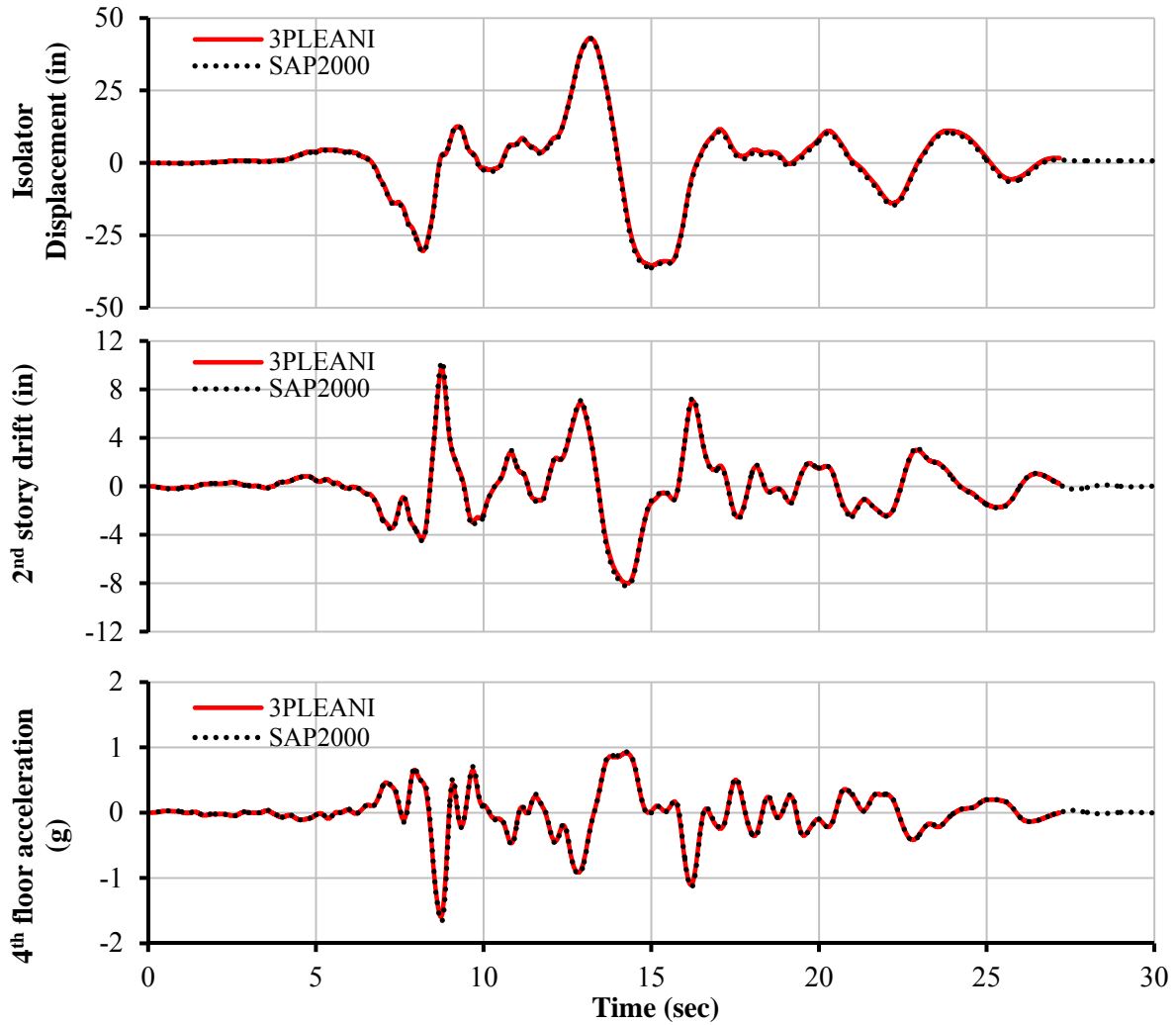


Figure 1-14: Comparison of response histories calculated in programs 3pleANI and SAP2000 for isolated structure with supplemental dampers

1.8 Response history analysis of isolated structure with multiple isolators

In the example of section 1.6 it was assumed that all three isolators in Figure 1-1 have the same frictional properties and accordingly they were “lumped” in one isolator for modeling in 3pleANI. Here we assume that all three isolators in Figure 1-1 have different frictional properties in order to verify the *Multiple Isolators* option in 3pleANI. The friction properties of each isolator for this example are given in Table 1-5 per Fenz and Constantinou (2008a) and Table 1-6 per Sarlis and Constantinou (2013) while the geometry of all the isolators is the same and described in Table 1-1. All isolators are assumed to have the same vertical load. Remaining parameters for superstructure and isolators for this example are as described in Section 1.6. For this example, the ground motion of Figure 1-3 is scaled by 1.4.

Table 1-5: Frictional properties of isolators per Fenz and Constantinou (2008a)

Element	Isolator 1	Isolator 2	Isolator 3
$\bar{\mu}_2 = \bar{\mu}_3$	0.0133	0.05	0.03
$\bar{\mu}_1$	0.0214	0.08	0.11
$\bar{\mu}_4$	0.0723	0.11	0.15

Table 1-6: Frictional properties of isolators per Sarlis and Constantinou (2013)

Element	Isolator 1	Isolator 2	Isolator 3
$\mu_2 = \mu_3$	0.01	0.0375	0.0225
μ_1	0.02	0.0746	0.0996
μ_4	0.065	0.1012	0.1350

The program 3pleANI interface is shown in Figure 1-15. In 3pleANI, the <-> button can be used in order to transform the friction coefficients from the values of Table 1-5 to the values of Table 1-6. Figure 1-15 also shows (at the bottom) the dialogue boxes that appear when the *Multiple Isolators* option is selected. Also, in Figure 1-15 each isolator carries 33.3% of the total load however, if desired, the user has the option to specify a different distribution of axial load to the isolators.

The parameters in the SAP2000 model are as described in Table 1-3 with the exception of the friction coefficients which are now calculated based on Table 1-5. The elastic stiffness was calculated using the new friction coefficients as $K_{el} = \mu W / Y$, $Y = 0.01in$.

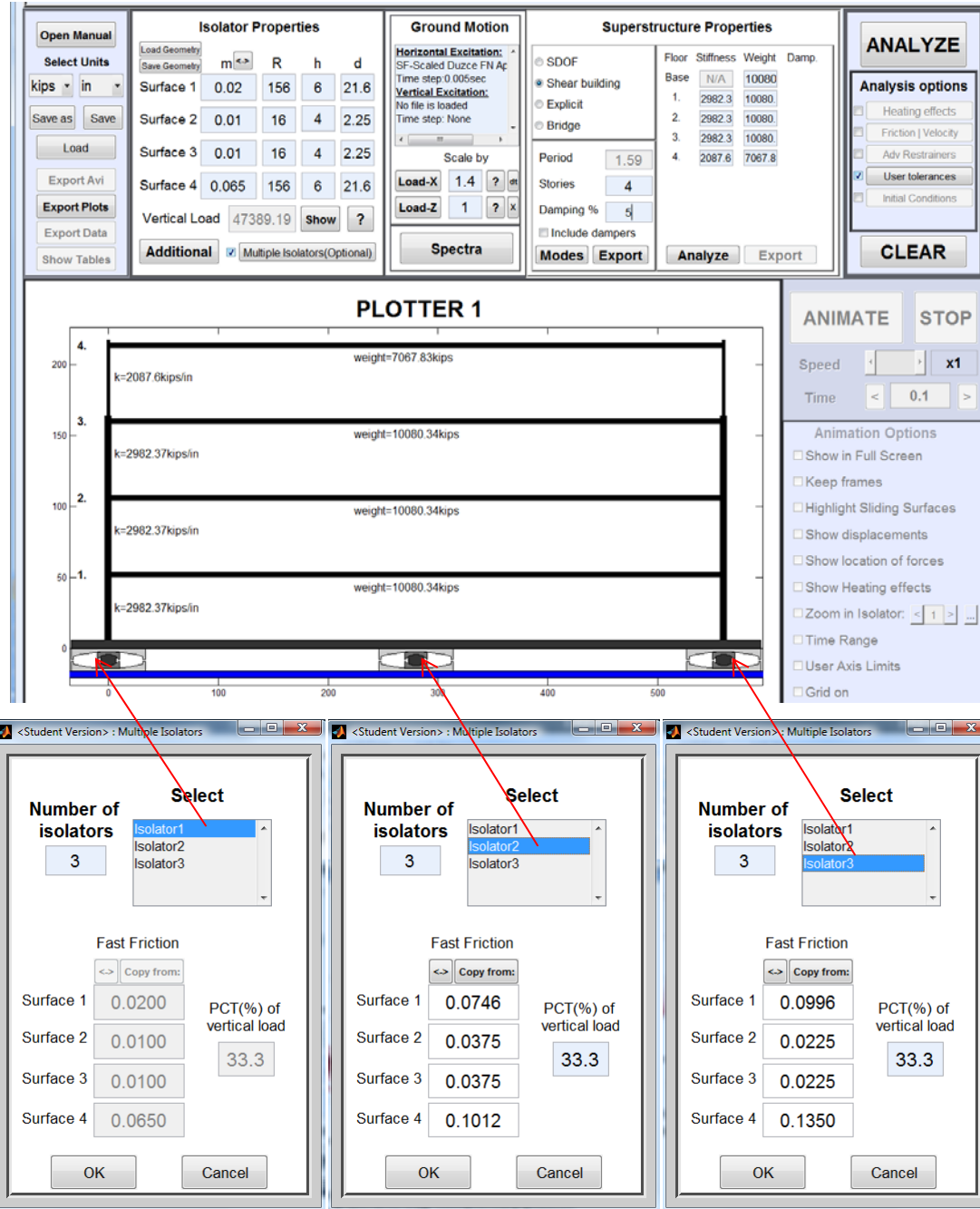


Figure 1-15: View of 3pleANI interface for response history analysis of isolated structure with multiple isolators

Results obtained from programs 3pleANI and SAP2000 are compared in Figure 1-16 and Figure 1-17. Note that the differences between the results obtained by the two programs are slightly

more noticeable here than the differences in Section 1.6. This is due to some effect of overturning moments on the base displacement because of the difference in the frictional properties of Isolators 1 and 3 (that cause asymmetry in the structure) combined with the inability of 3pleANI to capture overturning moment effects. Note that if isolators 1 and 3 were the same, then the differences would have been smaller.

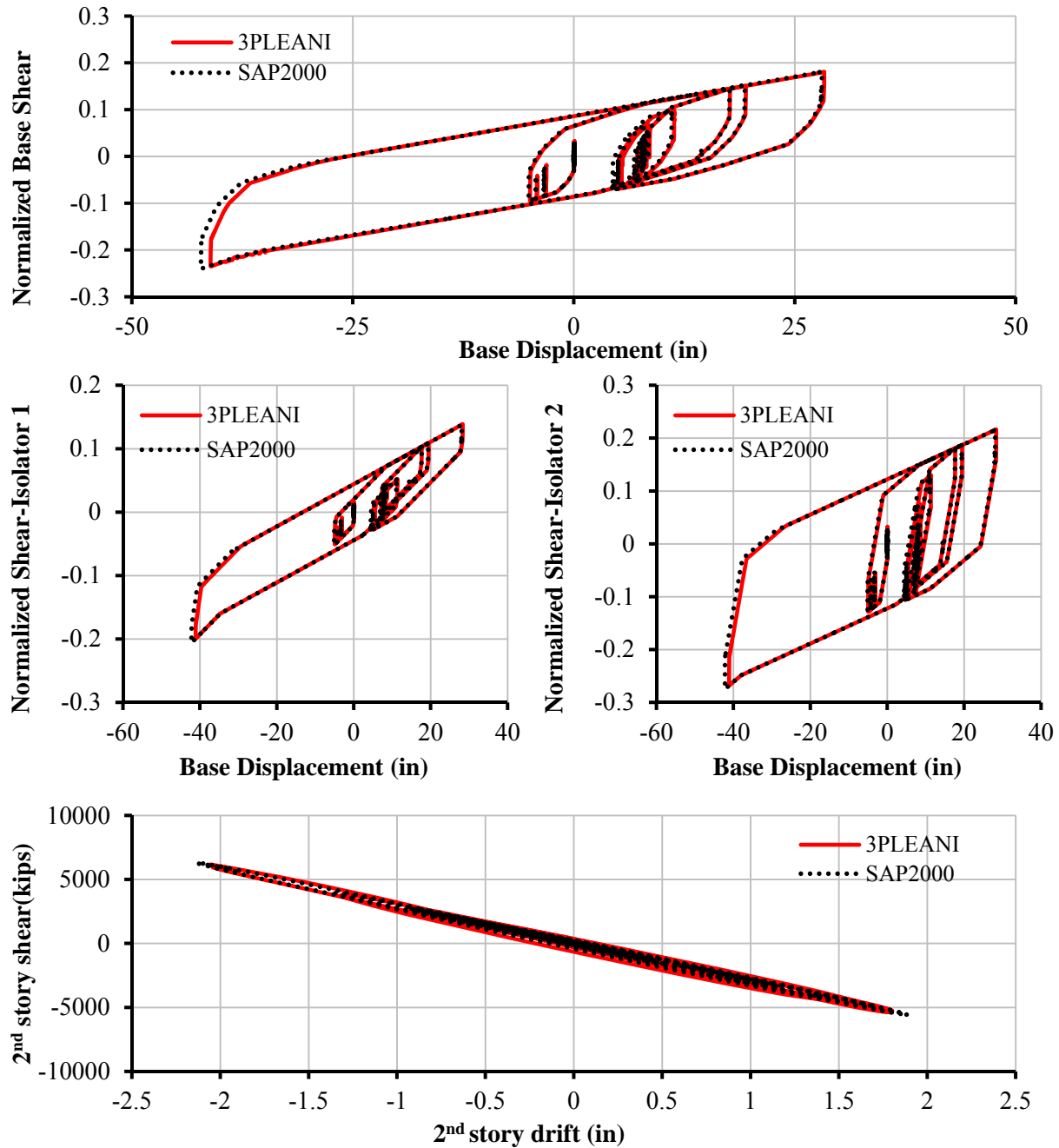


Figure 1-16: Comparison of isolator force-displacement and story shear-drift loops calculated in programs 3pleANI and SAP2000 for isolated structure with multiple isolators

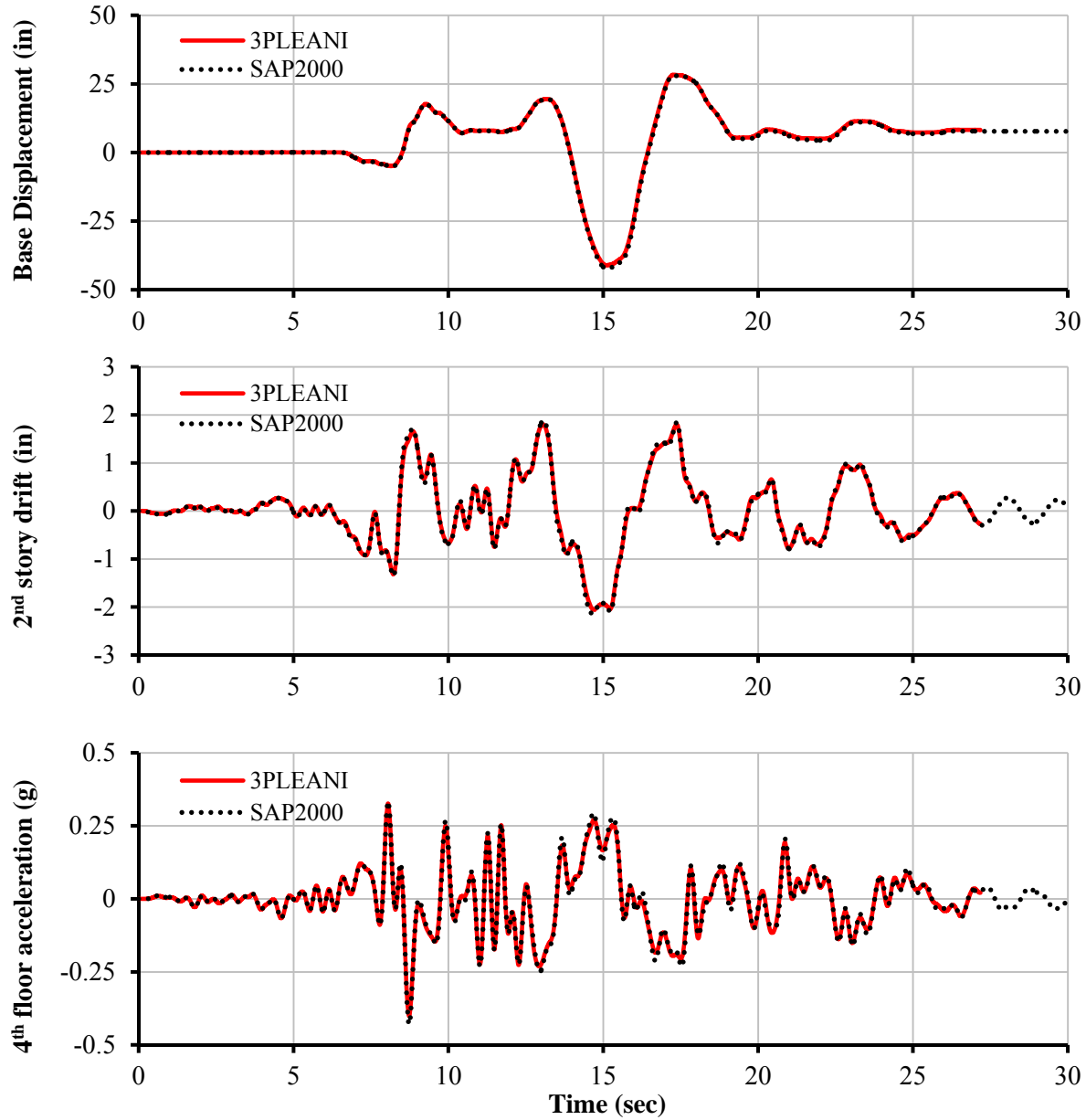


Figure 1-17: Comparison of response histories calculated in programs 3pleANI and SAP2000 for isolated structure with multiple isolators

1.9 Dynamic Analysis with Explicit structure representation

The four story structure in Figure 1-1 is modified by replacing the rigid beams with flexible beams having an area of 400in^2 and moment of inertia of 40000in^2 . As a result of this modification, the building cannot be represented as a shear building and has to be represented using the Explicit option in program 3pleANI. This requires the calculation of the mass and stiffness matrices. The stiffness matrix was calculated in SAP2000 by (a) applying unit loads at

each floor (one at a time), (b) constructing the flexibility matrix and (c) inverting the flexibility matrix in order to obtain the stiffness matrix. The mass matrix is diagonal and was easily constructed from the masses of each floor as shown in Figure 1-1. These matrices are presented below:

$$K = \begin{bmatrix} 5102.7 & -2952.1 & 763.4 & -99.3 \\ -2952.1 & 4256.0 & -2565.9 & 480.2 \\ 763.4 & -2565.9 & 3460.4 & -1511.2 \\ -99.3 & 480.2 & -1511.2 & 1110.9 \end{bmatrix} \frac{kip}{in}; \quad M = \begin{bmatrix} 26.1 & 0 & 0 & 0 \\ 0 & 26.1 & 0 & 0 \\ 0 & 0 & 26.1 & 0 \\ 0 & 0 & 0 & 18.3 \end{bmatrix} \frac{kip \cdot s^2}{in} \quad (1-2)$$

The interface in 3pleANI is shown in Figure 1-18 after the user has imported the mass and stiffness matrices above. Importing these matrices is done by pressing **Import Mass Matrix** and **Import Stiffness Matrix**. To do so, the matrices above have to be first written in an Excel spreadsheet and saved on the hard drive. By pressing the aforementioned buttons, the program will prompt the user to open any saved spreadsheet from the hard drive. Then the user must select the region of cells that encloses the mass and stiffness matrix data (one at a time). Note that the mass matrix has to be imported first. Directly after importing, 3pleANI directly recognizes the number of floors and also conducts an eigenvalue analysis.

The damping matrix was calculated so that damping of the first and fourth mode is 5%. From a modal analysis of the un-damped fixed structure in 3pleANI (damping matrix has not yet been imported and is considered to be zero) or SAP2000, the periods of these modes are $T_1 = 2.81\text{sec}$, $T_4 = 0.34\text{sec}$ so that the damping matrix is:

$$C = 0.199M + 0.00483K \quad (1-3)$$

The damping matrix was calculated in an Excel spreadsheet using Equations (1-2) and (1-3) and imported into the program by pressing **Import Damping Matrix**. From a modal analysis in 3pleANI, the final damping ratio of modes 2 and 3 was calculated (3pleANI conducts complex eigenvalue analysis which allows the calculation of the exact damping ratio of each mode) and assigned as a damping override in SAP2000. Note that modal analysis results from 3pleANI and SAP2000 of the un-damped system are almost identical, and results are omitted here for brevity.

Results obtained from programs 3pleANI and SAP2000 are compared in Figure 1-19 and Figure 1-20. The two sets of results are almost identical.

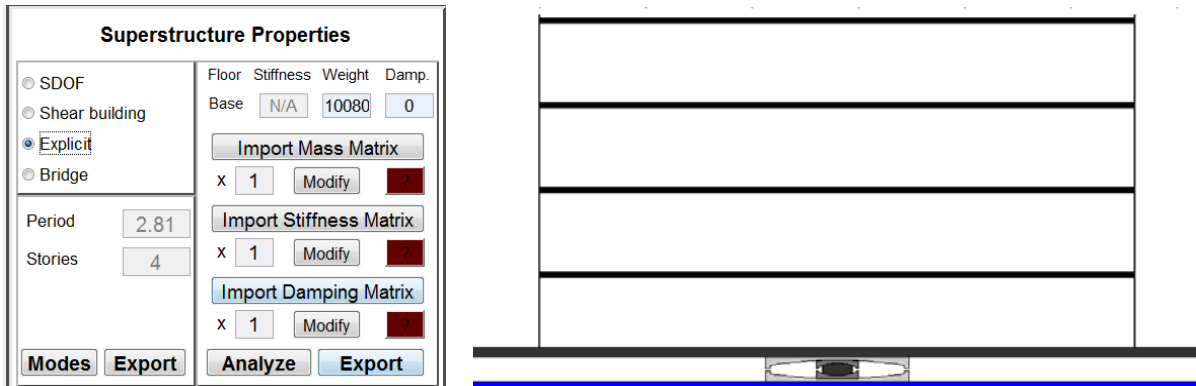


Figure 1-18: View of 3pleANI interface for response history analysis for structure with explicit matrix representation

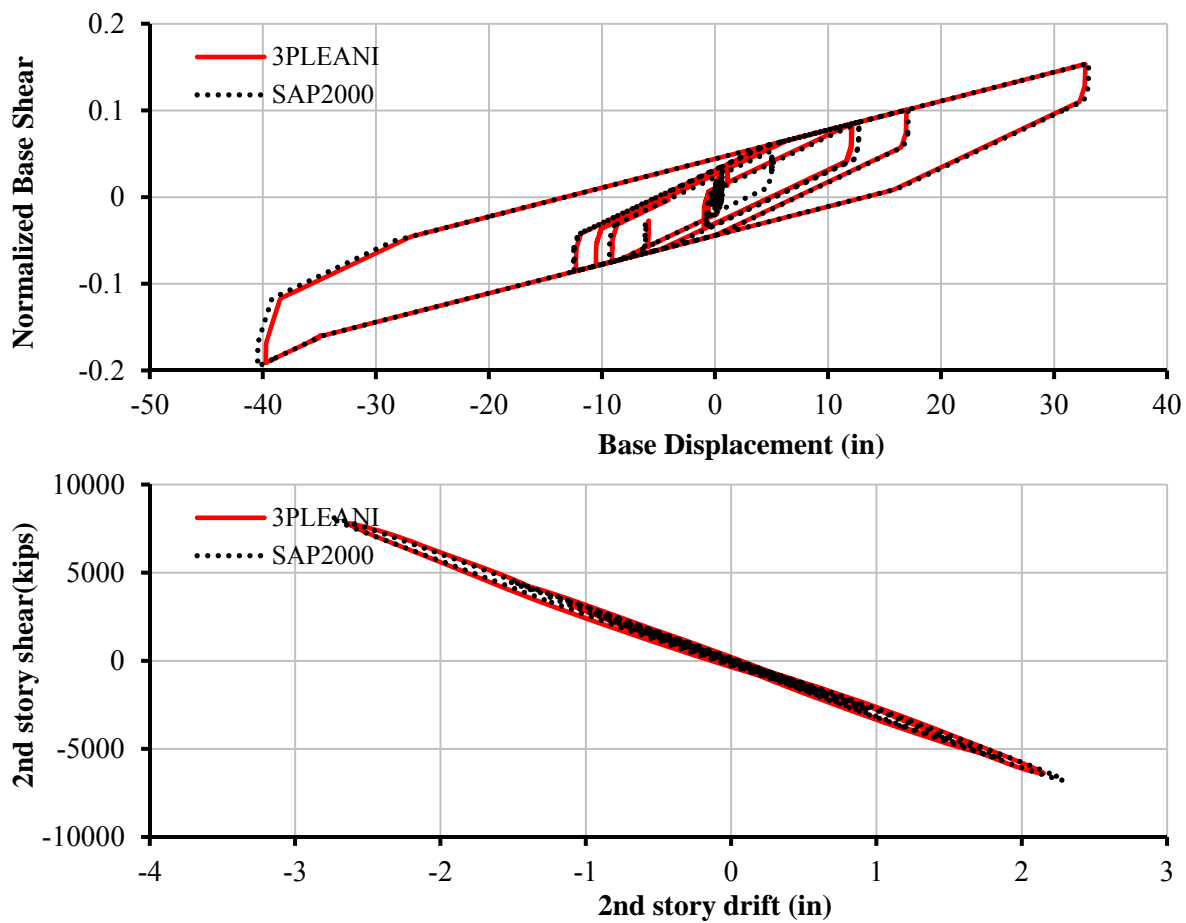


Figure 1-19: Comparison of isolator force-displacement and shear-drift loops calculated in programs 3pleANI and SAP2000 from response history analysis of structure with explicit representation

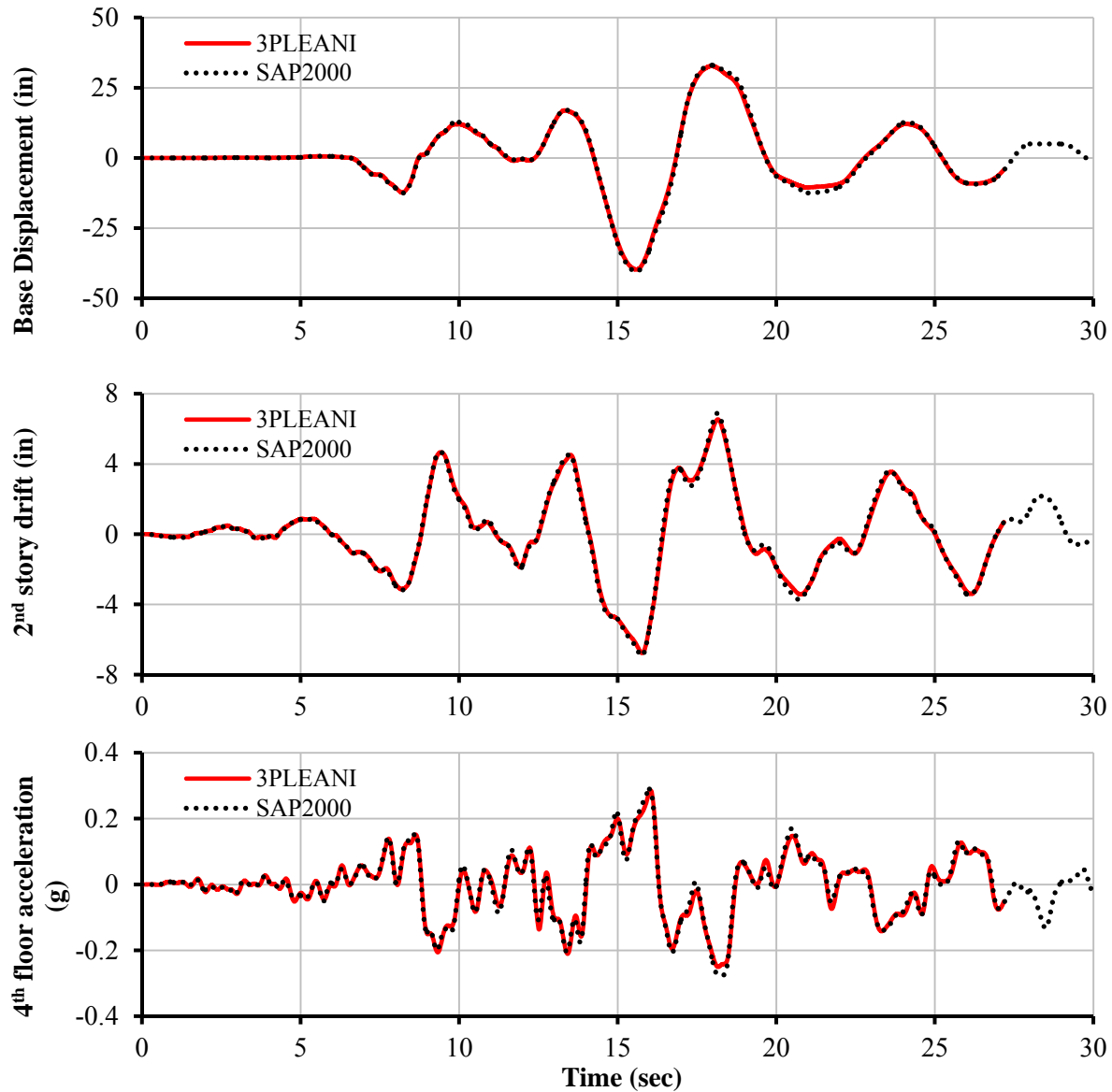


Figure 1-20: Comparison of response quantities calculated in programs 3pleANI and SAP2000 for structure with explicit representation

1.10 Response history analysis of isolated structure with isolator heating effects

In order to further demonstrate the analysis capabilities in 3pleANI, the example of Section 1.6 is re-analyzed after the activation of Heating Effects. Program 3pleANI results will not be compared with SAP2000 results since the latter does not have this analysis capability. The theory used in 3pleANI allows for the explicit calculation of displacements and velocities at each sliding surface and as a result, heat flux and temperature can be calculated using the theory presented in Constantinou et al (2007). The program uses temperature-dependent friction

coefficient at each surface given by the following equation in which T_i is the rise in temperature of sliding surface i :

$$\mu_i = \mu_{\min,i} + (\mu_{\max,i} - \mu_{\min,i})e^{-a_h T_i}, \quad i = 1, 2, 3, 4 \quad (1)$$

When the temperature rise is zero, friction is equal to μ_{\max} . The friction coefficient varies exponentially with temperature and drops to a minimum value μ_{\min} , where it remains stable (in 3pleANI the default value is $\mu_{\min} = \mu_{\max}/2$). The temperature at which the minimum value is reached is approximately equal to $1/a_h$ where a_h is a specified heat rate parameter.

The Heating effect options dialogue box with all specified parameters in 3pleANI is shown in Figure 1-22 together with a partial view of Panel 2 and the specified friction coefficients. Based on Figure 1-22 and Equation (1), the variation of the friction coefficients of all surfaces with temperature is plotted in Figure 1-21. Also, it is assumed here that the single isolator used in 3pleANI represents a total of 20 isolators in the actual structure. Therefore, for heating purposes, only $1/20^{\text{th}}$ or 5% of the total vertical load is considered for the calculation of the heat flux (see Figure 1-22). Also in order to speed up the analysis, the friction coefficient values were not updated at every integration time step but at intervals of one tenth of the imported excitation time step.

Finally, notice that the friction coefficient values specified in Figure 1-22 have double the values of those shown in Figure 1-9. The reason for this is that, it was assumed that the friction coefficients of Section 1.6 were identified from displacement controlled tests on the isolators where each surface was sufficiently heated so that friction coefficients had their minimum value μ_{\min} in Equation (1) (this can be true for surfaces 1 and 4 but is not true for surfaces 2 and 3). Also it was assumed that $\mu_{\max} = 2 \mu_{\min}$.

Results obtained in program 3pleANI are presented in Figure 1-23 and compared against the results of Section 1.6 from 3pleANI. Notice that heating effects have a noticeable effect on the base displacement. Also, Figure 1-23 shows temperature histories calculated at each surface. Note that based on the specified properties, the friction coefficient of each surface reaches the value μ_{\min} when the temperature becomes approximately equal to 200°C .

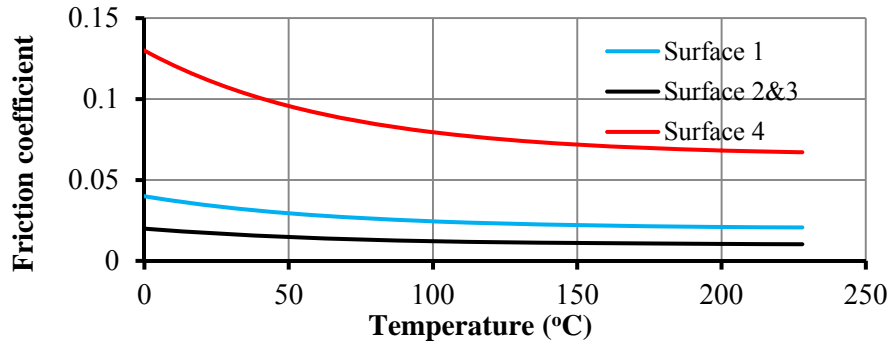


Figure 1-21: Friction coefficients plotted against surface temperature

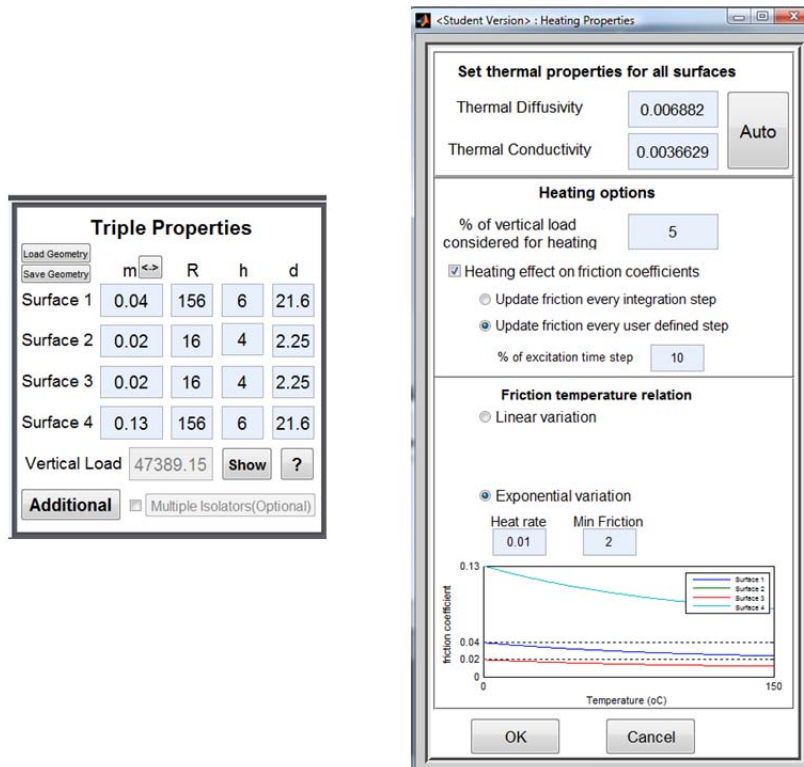


Figure 1-22: Specified parameters in program 3pleANI for dynamic analysis of isolated structure with heating effects

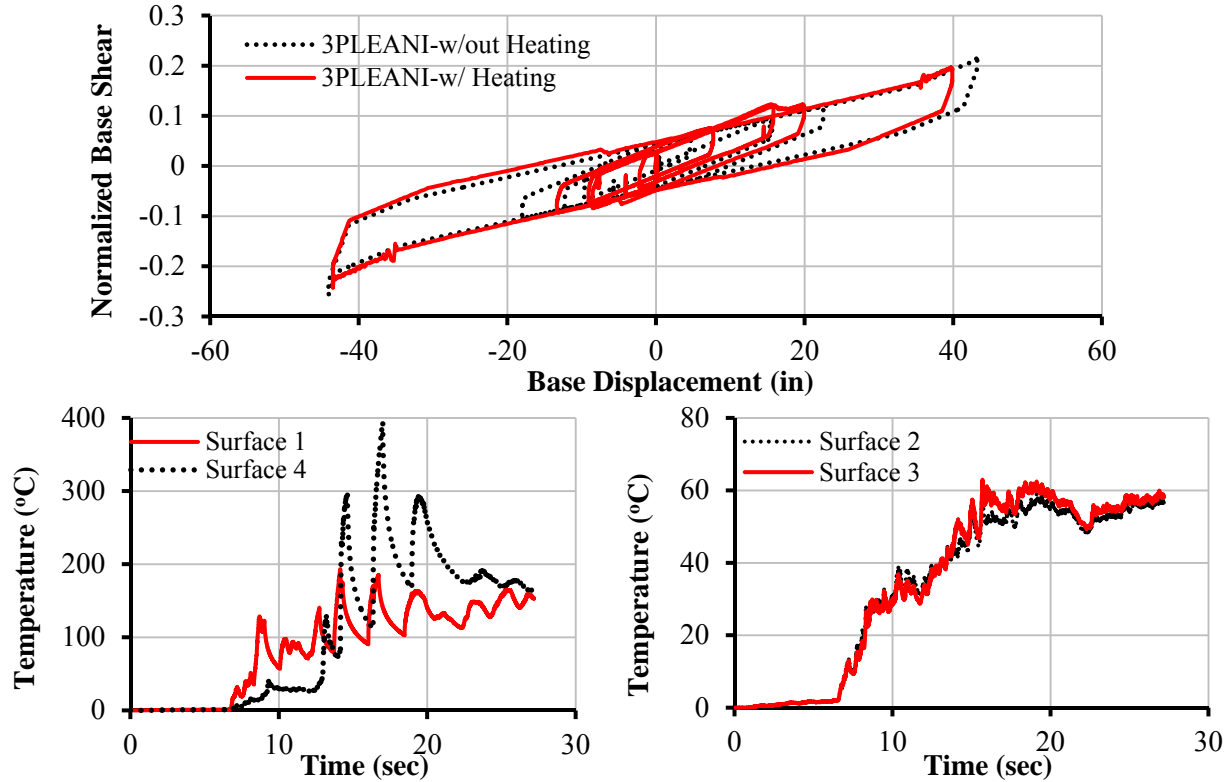


Figure 1-23: 3pleANI results from dynamic analysis of isolated structure with heating effects

Finally, the example of Section 1.8 that includes multiple isolators is reanalyzed after activation of heating effects. For this example the heating effects on each isolator are considered separately based on its individual properties and response quantities. The input parameters in 3pleANI are shown in Figure 1-24. For this example it was assumed that each of the three isolators in the analysis represents a cluster of five isolators for a total of 15 isolators in the structure. As a result, only 1/15th or 6.7% of each isolator’s load was considered for heating calculations (based on Figure 1-24, $0.33 \times 47389.2 \times 0.067 = 1048 \text{ kips}$ will be considered for heating effects on each isolator while the actual load on each of the three isolators in the model is $0.33 \times 47389.2 = 15638 \text{ kips}$). The remaining parameters were specified based on the principles described earlier.

Results from this analysis in program 3pleANI are compared in Figure 1-26 against the results that were obtained in Section 1.8 from 3pleANI without heating effects. The effect is significant although the difference is primarily due to the low value of friction used in the analysis without heating effects. Note that the analysis without heating effects was based on values of friction values equal to half of the starting values in the analysis with heating effects. It was presumed in

the analysis without heating effects that the relevant friction values for use in analysis were the lower limit values at large temperature. Also Figure 1-25 shows a snapshot of the deformed structure in which the heating effects on the isolators are depicted by the coloring of the isolator surfaces based on the calculated temperature.

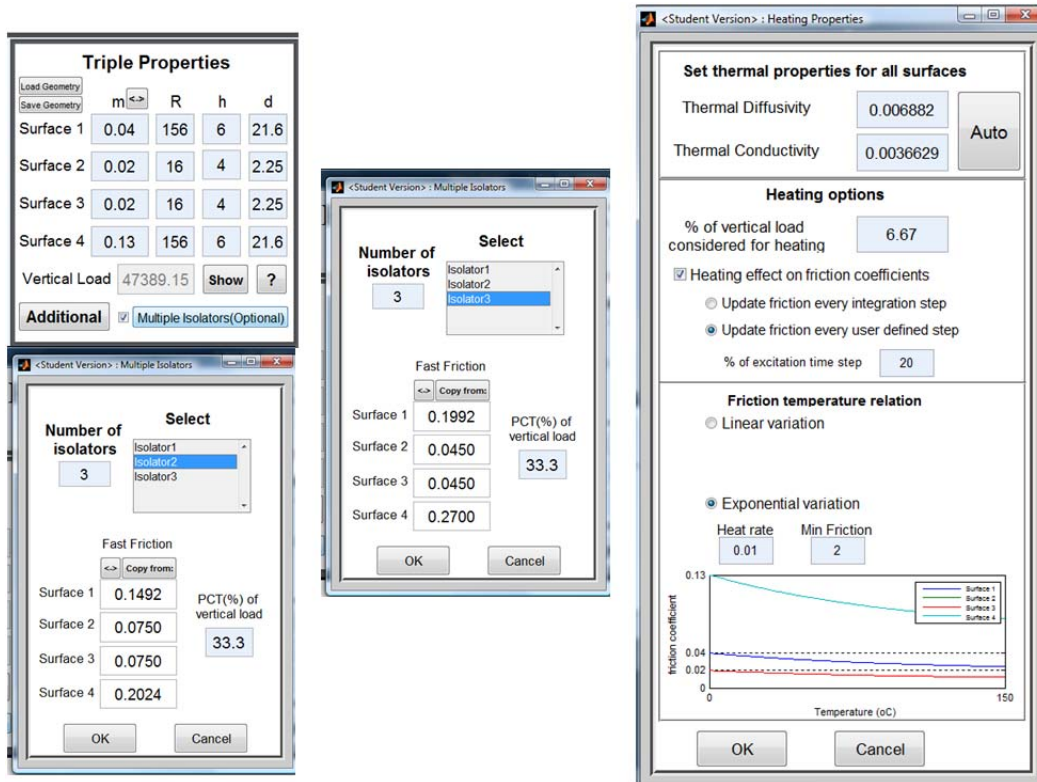


Figure 1-24: Specified parameters in program 3pleANI for dynamic analysis of isolated structure with multiple isolators and heating effects

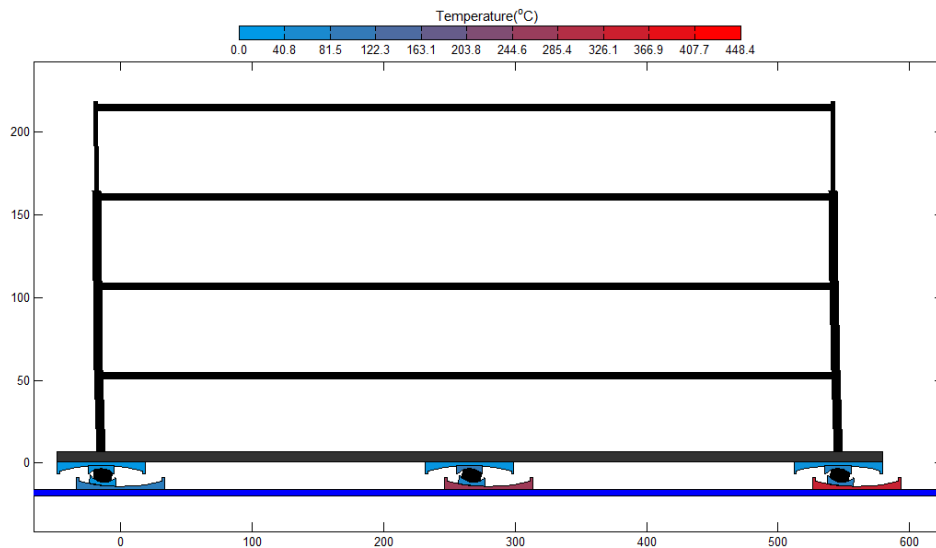


Figure 1-25: Snapshot of deformed structure with multiple isolators and heating effects

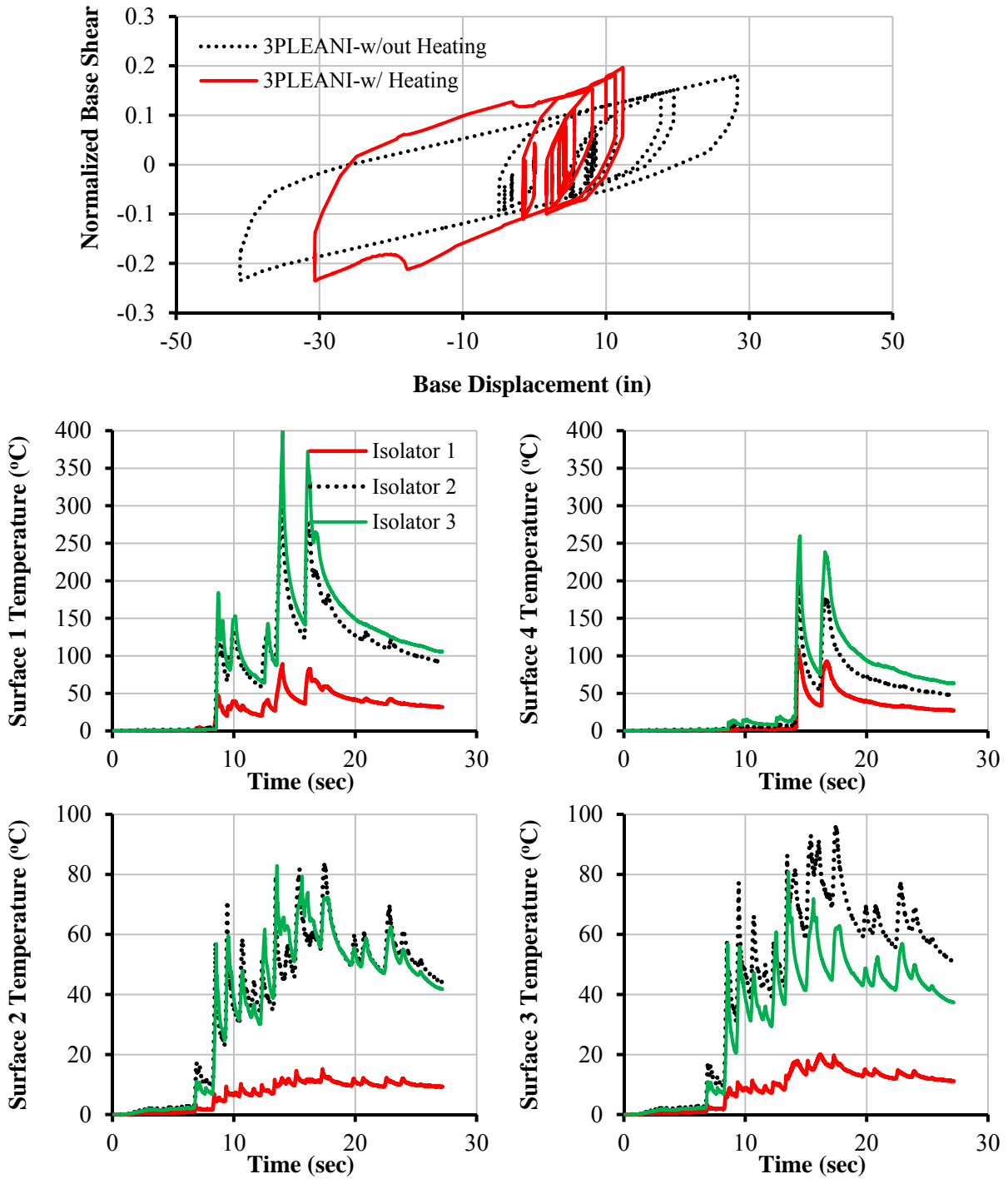


Figure 1-26: 3pleANI results of dynamic analysis of isolated structure with multiple isolators and heating effects

Note in Figure 1-26 that surface 1 is heated more than surface 4 despite the much smaller friction coefficient. The reason for this is that once motion starts on surface 1, the friction coefficient decreases and as a result sliding is harder to start on surface 4 which undergoes fewer cycles than surface 1.

1.11 Response history analysis of isolated structure with horizontal and vertical acceleration history

In this example the structure described in Section 1.6 (isolated without supplemental dampers) is analyzed with simultaneous excitation in the horizontal and vertical directions. The history of the horizontal and vertical ground accelerations are shown in Figure 1-27 and Figure 1-28, respectively. It is noted that the combination of weak horizontal and strong vertical excitation has been selected in order to interrogate the isolation system of which the behavior is dependent on the instantaneous vertical load. Analysis was first conducted in program 3pleANI with and without the vertical ground acceleration and the results are compared in Figure 1-29. The results demonstrate small effects of the vertical ground acceleration that are consistent with experimental observations (Fenz and Constantinou, 2008e; Morgan, 2007).

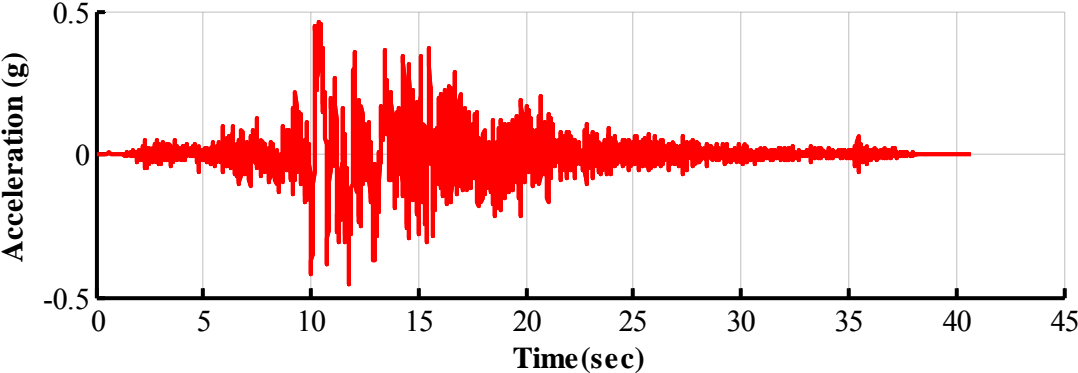


Figure 1-27: Horizontal ground motion used for analysis of isolated structure with vertical component

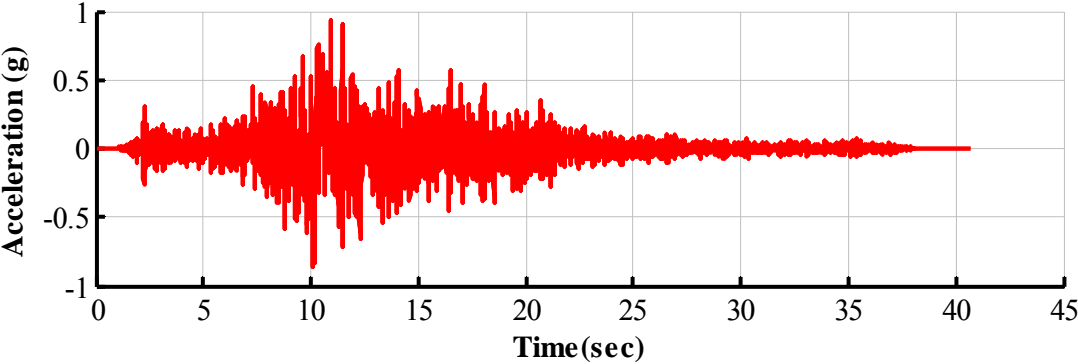


Figure 1-28: Vertical ground motion used for analysis of isolated structure with vertical component

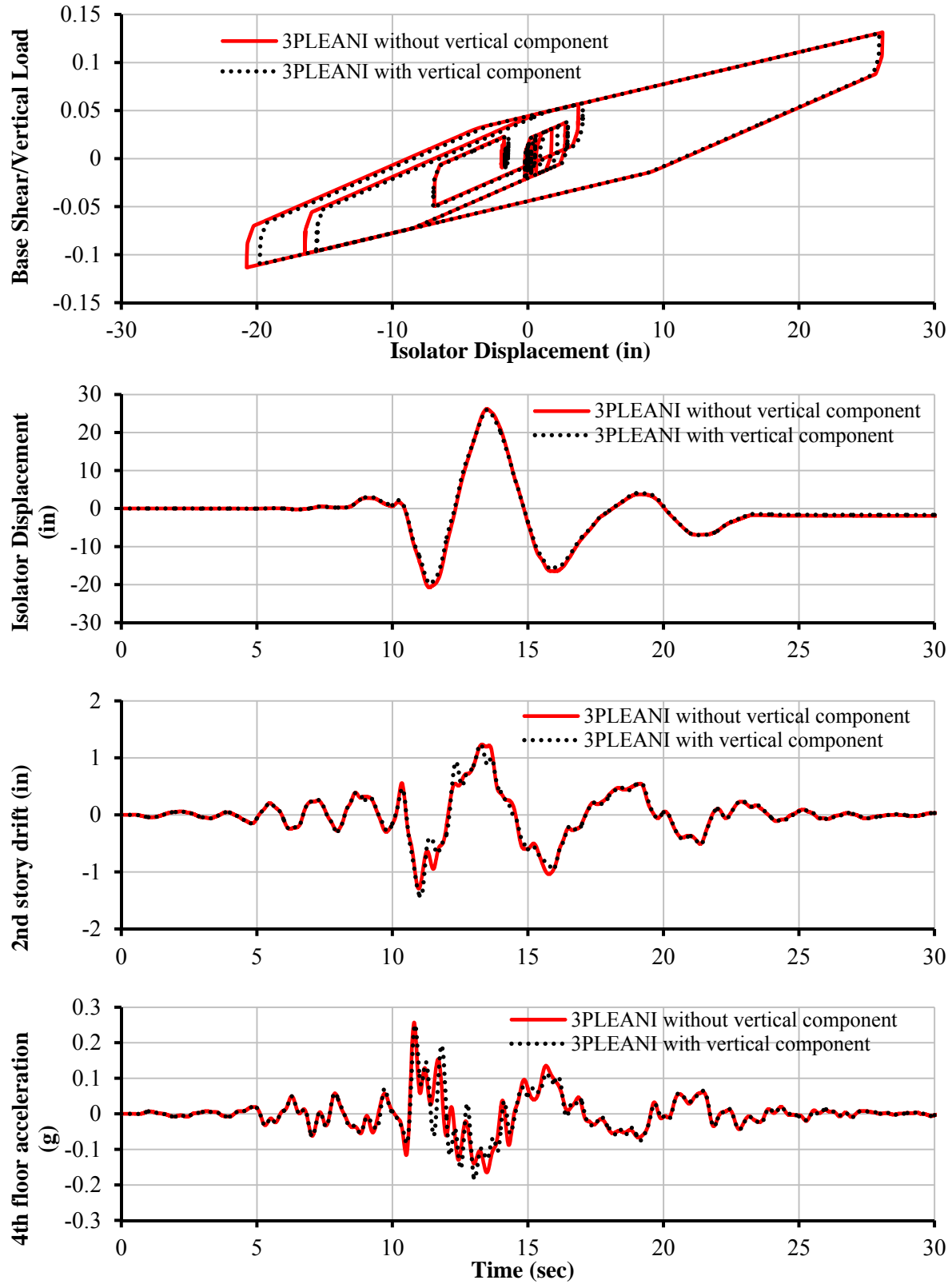


Figure 1-29: Comparison of response quantities calculated by program 3pleANI with and without vertical ground acceleration

Figure 1-30 and Figure 1-31 compare various response quantities calculated by programs 3pleANI and SAP2000 for this example. Important differences are observed in the calculation of the base vertical force (Figure 1-30) which, in turn, affects the horizontal base shear calculation (Figure 1-31). This difference is caused by the vertical flexibility of the isolator model in SAP2000 which allows for the development of parasitic vertical acceleration response. Note that when the isolators are considered vertically rigid and the superstructure masses are lumped at the vertically rigid columns (as depicted in the model of Figure 1-1), the base vertical force should fluctuate in exact proportion to the input vertical acceleration. This is not the case in the SAP2000 analysis, resulting in the wavy loops of Figure 1-31 that incorrectly over-predict the base shear. Nevertheless, the isolator displacements and drifts compare very well in the two analyses while the horizontal accelerations are somewhat over-predicted by SAP2000 due to (a) the vertical vibration effect, and (b) the structural damping specification and “leakage” of damping in the isolation system.

Note that the parasitic response obtained in SAP2000 due the vertical oscillation of the isolators cannot be corrected by increasing the vertical stiffness of the isolator as numerical instability occurs or incorrect behavior is calculated (for example, in this case multiple uplift episodes were incorrectly predicted when the vertical stiffness was increased). Solution of this problem requires that the analyst utilizes artificial vertical linear viscous dampers in the isolation system at each isolator except those that may uplift so that the parasitic oscillations are controlled, numerical stability is restored and uplift is not suppressed.

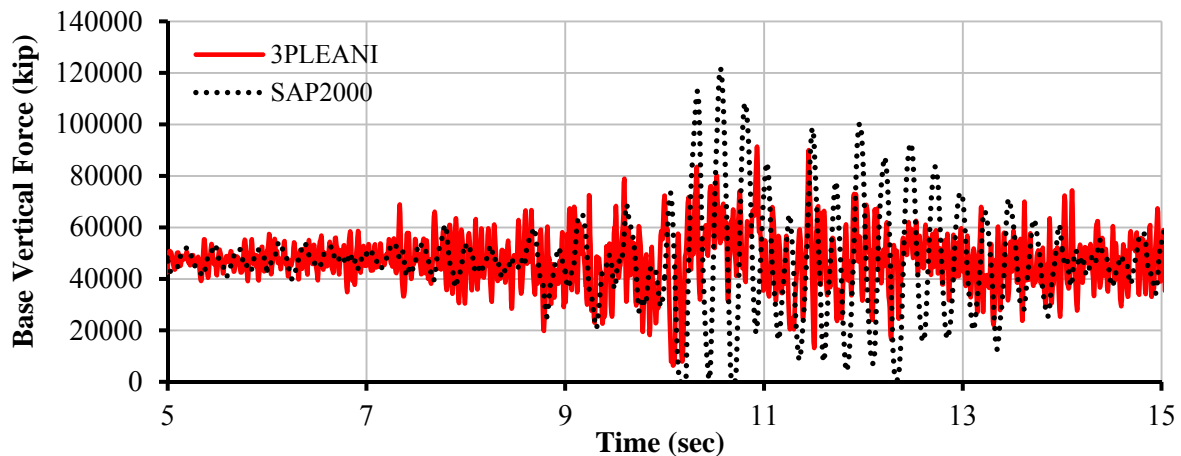


Figure 1-30: Comparison of base vertical force history calculated in programs 3pleANI and SAP2000 for isolated structure with combined horizontal/vertical ground acceleration

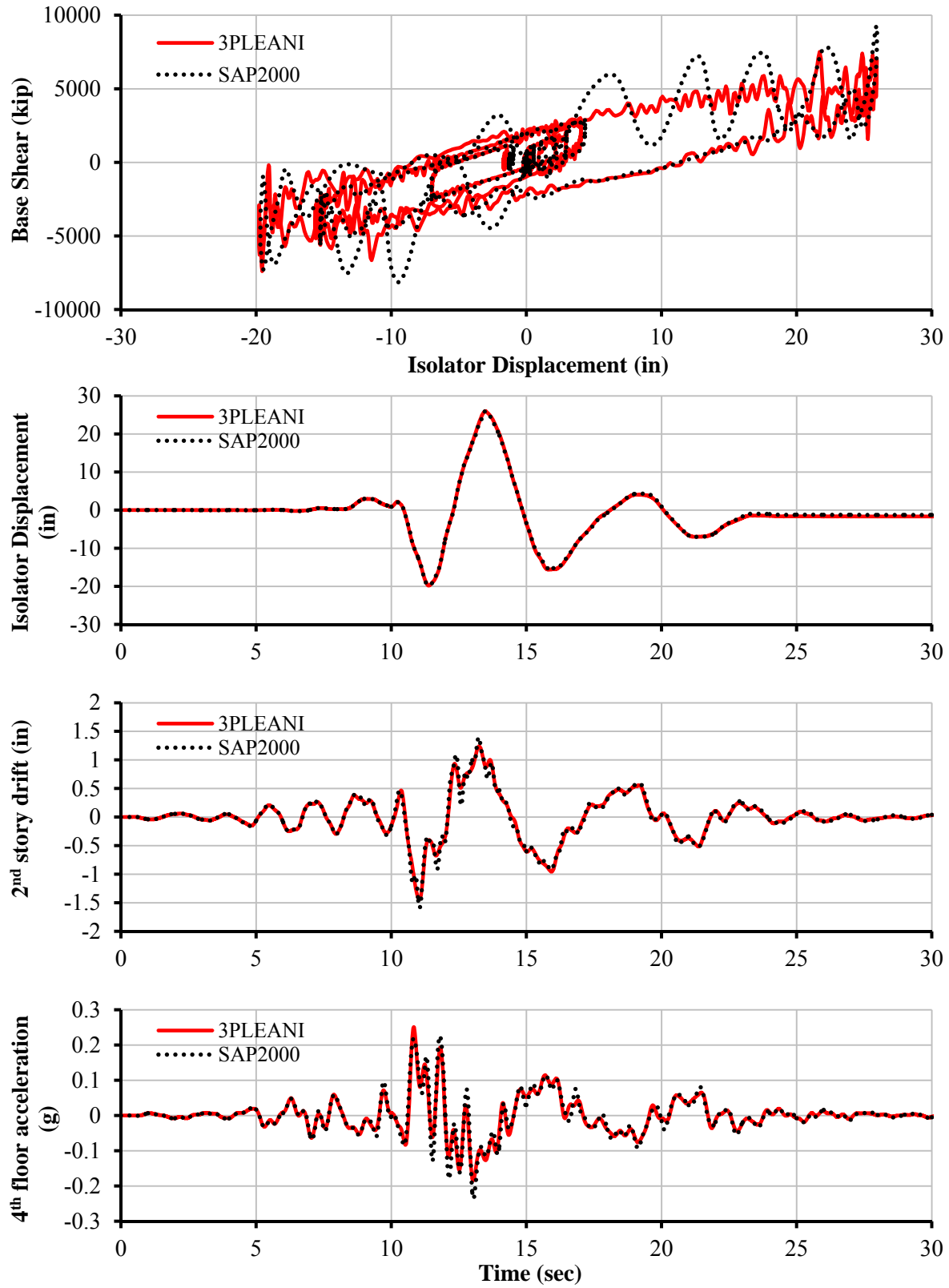


Figure 1-31: Comparison of response quantities calculated in programs 3pleANI and SAP2000 for isolated structure with combined horizontal/vertical ground acceleration

2 EXAMPLES OF DYNAMIC ANALYSIS OF A BRIDGE

This section presents analysis and verification examples for a bridge analyzed in 3pleANI and in program SAP2000. Program 3pleANI allows the user to model the bridge piers using three different methods of increasing complexity as described below:

- a) Piers are modeled as springs-mass-damper systems connected between the ground and the bottom of isolators and with only horizontal degrees of freedom. The pier top rotation is not accounted for in the isolator behavior.
- b) Piers are modeled as cantilever beams with the isolator P- Δ moment at the top of the pier included in the analysis. Again, only horizontal degrees of freedom are considered. The pier top rotation effects are not accounted for in the isolator behavior.
- c) Piers are modeled as cantilever beams with pier top rotational degree of freedom (the moment of inertia at the pier top is derived on the basis of consistent mass formulation and assuming uniform mass distribution for the pier). The isolator P- Δ moment at the top of the pier is included in the analysis. The pier top rotation effects are accounted for in the isolator behavior.

Of the three options above available in 3pleANI, program SAP2000 can only be used for the first method. For the second method, SAP2000 is unable to calculate the P- Δ moment of the isolator for the general case of the TFP isolator modeled using the series model. An exception where SAP2000 can capture the P- Δ moment of the isolator was presented in Sarlis and Constantinou (2010) for the special case isolator ($\mu_1 = \mu_4$) modeled using the parallel model. It was shown there that the isolator P- Δ effects can be either captured directly using direct integration (although this method presents implications related to modeling of damping; see Sarlis and Constantinou, 2010 for details) or indirectly by conducting an approximate P- Δ analysis using a two stage Fast Nonlinear Analysis. The third option is impossible to model in SAP2000 since the series and parallel model are artificial models and cannot capture the effect of the bottom concave plate rotation on the mechanics of the isolators. To capture these effects, the theory in Sarlis and Constantinou (2013) was implemented in program 3pleANI.

The bridge used in this example is shown in Figure 2-1. It is based on the bridge presented in Constantinou et al. (2011) with some minor modifications. Half of the original bridge is analyzed. The model consists of four isolators, two placed at the abutments and two on top of flexible piers. The load on each of the abutment isolators is 336.5kip and the load on each of the

pier isolators is 936.5kip. The properties of the isolators are shown in Table 2-1. Each pier has a height of 276in and weighs a total of 43.3kip. The weight is uniformly distributed along its height. Also each pier has an additional concentrated weight on its top due to the weight of additional elements such as the beam bent cap.

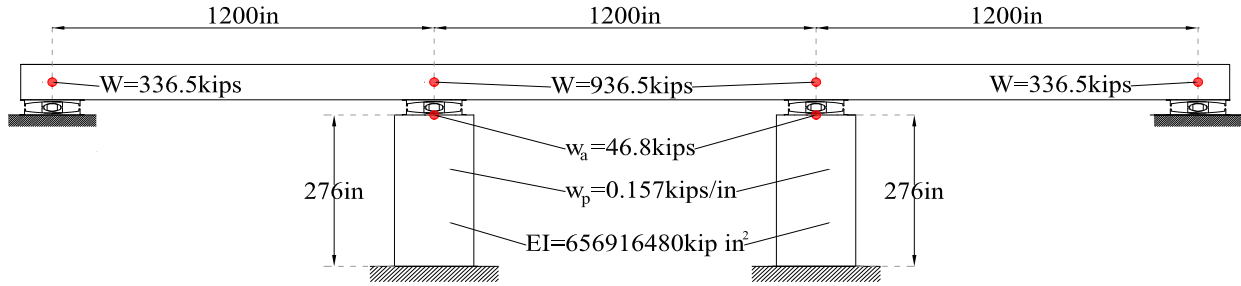


Figure 2-1: Bridge used for verification example

Table 2-1: Properties of bridge TFP isolator

Parameters	Abutment	Pier
$R_1 = R_4$ (inch)	88	88
$R_2 = R_3$ (inch)	16	16
Displacement capacity on surfaces 1 and 4 (inch)	$d_1 = d_4 = 14in$	$d_1 = d_4 = 14in$
Displacement capacity on surfaces 2 and 3 (inch)	$d_2 = d_3 = 2in$	$d_2 = d_3 = 2in$
Friction surface 1 ¹	$\bar{\mu}_1 = 0.15$	$\bar{\mu}_1 = 0.08$
Friction surfaces 2 and 3 ¹	$\bar{\mu}_2 = \bar{\mu}_3 = 0.144$	$\bar{\mu}_2 = \bar{\mu}_3 = 0.05$
Friction surface 4 ¹	$\bar{\mu}_4 = 0.18$	$\bar{\mu}_4 = 0.11$
$h_1 = h_4$ (inch)	4	4
$h_2 = h_3$ (inch)	3	3
1. All friction values are per Fenz and Constantinou (2008a) and for high velocity conditions $=f_{max}$		

2.1 Bridge with multiple piers

Prior to presenting this example, it is noted that 3pleANI offers the capability to model a bridge deck on top of a single pier. This model is appropriate when the bridge is supported by many piers and isolators with the same properties. In Figure 2-1 the presence of the abutments and isolators with different properties requires a different model. Analysis has been performed for the single pier model with and without dampers and it was found that programs 3pleANI and

SAP2000 calculated essentially the same results. These results are omitted for brevity and rather we concentrate on the more complex case of multiple piers.

The interface of 3pleANI that was used for modeling the bridge in Figure 2-1 is shown in Figure 2-2. Four isolators are specified in the *Multiple Isolators* option in order to implement the different friction properties and generate four piers. In order to model the abutments, high lateral stiffness was specified for piers 1 and 4. The total weight at the top of each pier (based on Figure 2-1) is $W = 0.5 \times 0.157 \times 276 + 46.8 = 68.5 \text{kip}$. Therefore $W = 2 \times 68.5 \text{kips} = 137 \text{kip}$ was specified in 3pleANI as the total weight of the pier. The damping ratio of each pier was 5%. The isolators in SAP2000 were modeled using the series model and the calculation of properties follows a similar to the one procedure described in Section 1.5. Piers in SAP2000 were modeled as spring-mass-damper link elements. Details are omitted here for brevity. Figure 2-3 compares results obtained from programs 3pleANI and SAP2000 when the bridge was subjected to the ground motion of Figure 1-3 scaled by factor 1.65. Results are nearly identical.

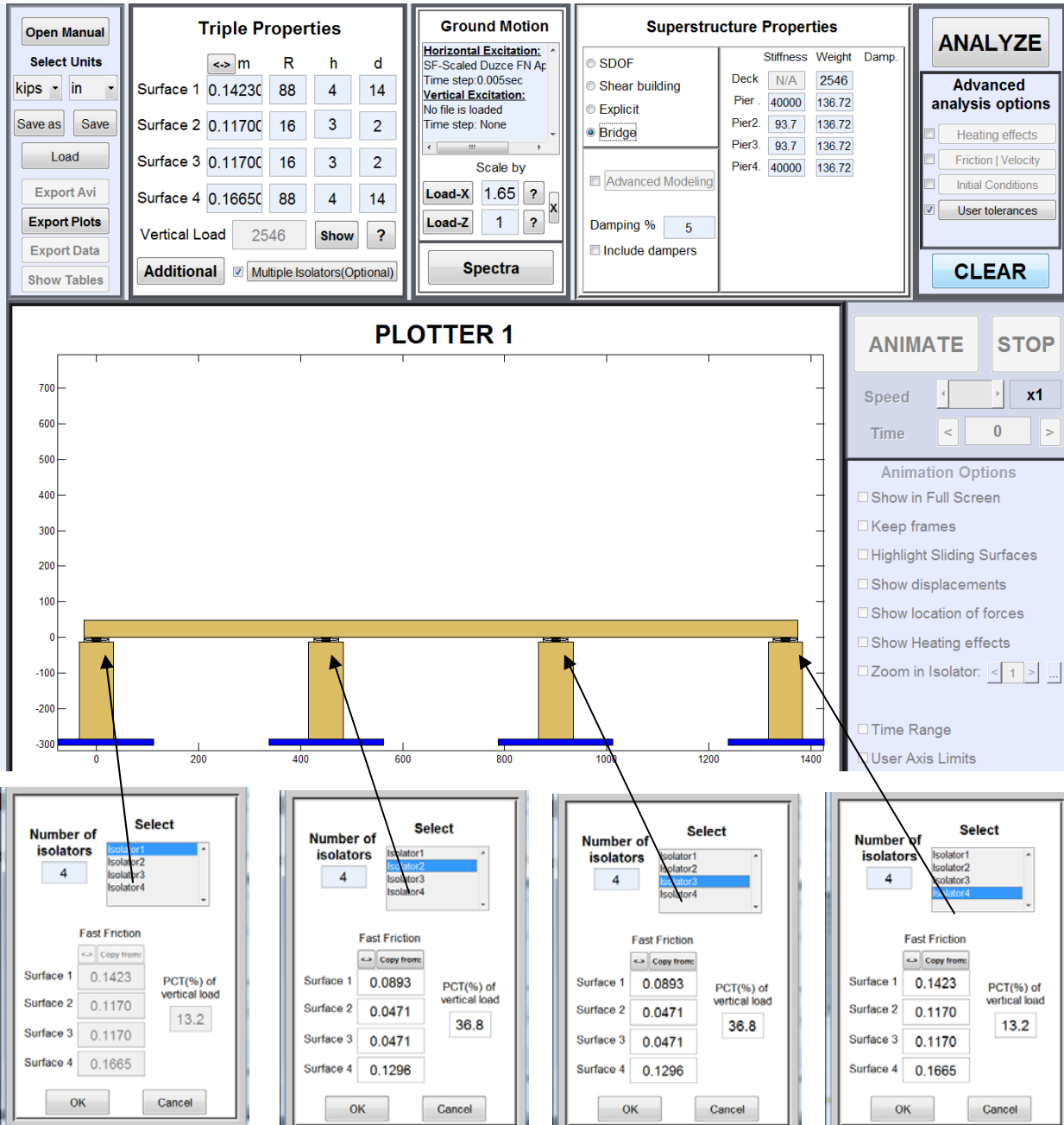


Figure 2-2: View of 3pleANI interface for analysis of bridge with multiple isolators/piers

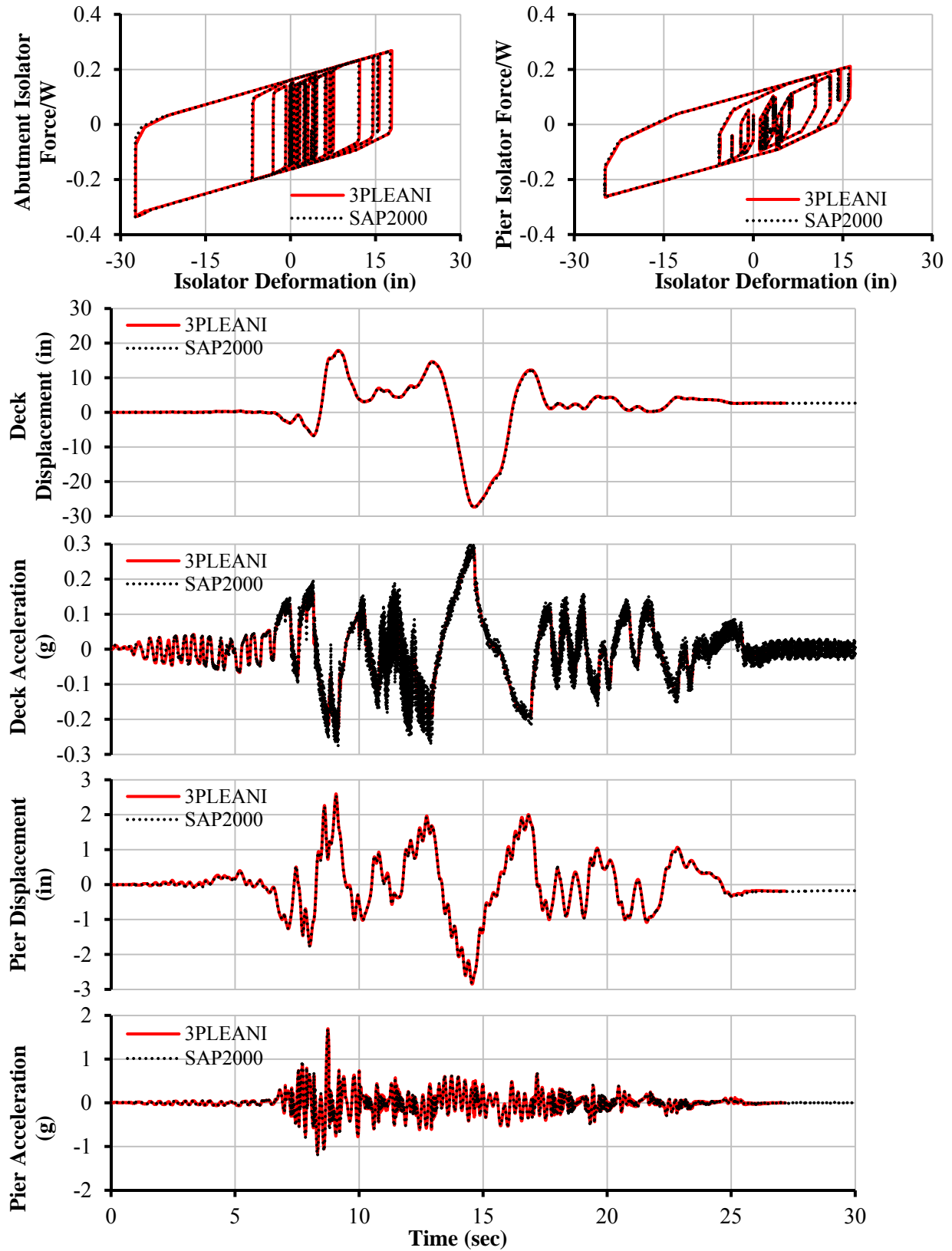


Figure 2-3: Comparison of response history analysis results calculated in programs 3pleANI and SAP2000 for bridge with multiple isolators/piers

2.2 Bridge with multiple piers and dampers

The example of section 2.1 is reanalyzed but with the addition of a linear viscous damper with damping constant 2.9kipsec/in between each pier and the deck. The superstructure panel in 3pleANI is shown in Figure 2-4. Figure 2-5 and Figure 2-6 present comparisons of results obtained from programs 3pleANI and SAP2000. Results are nearly identical.

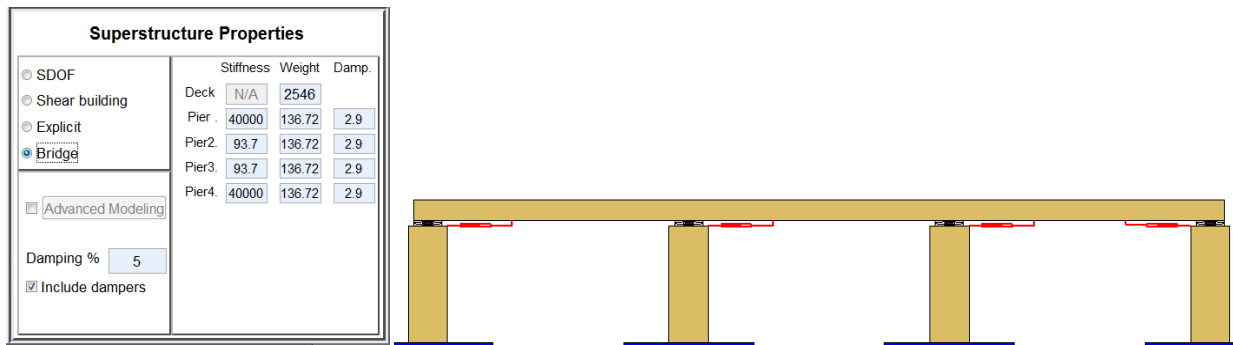


Figure 2-4: View of 3pleANI interface for analysis of bridge with multiple isolators/piers and dampers

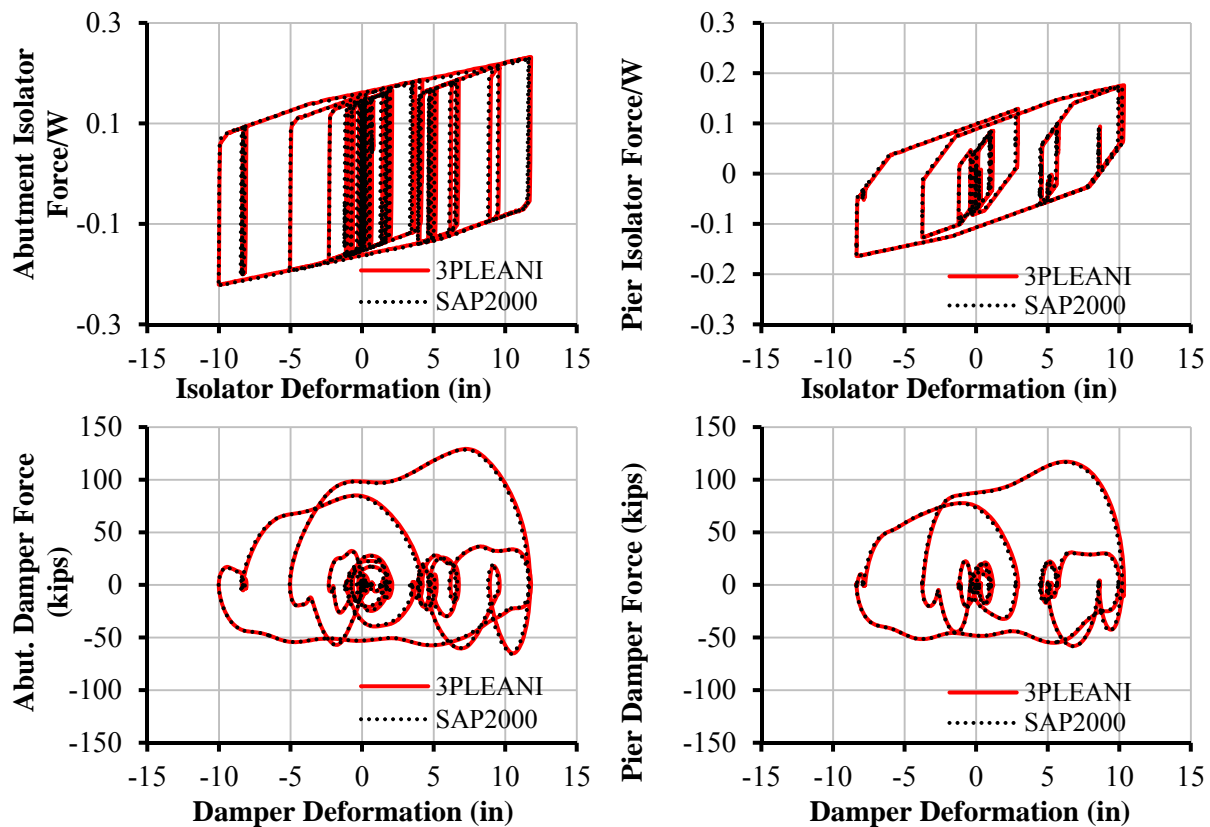


Figure 2-5: Comparison of response history analysis results calculated in programs 3pleANI and SAP2000 for bridge with multiple isolators/piers and dampers

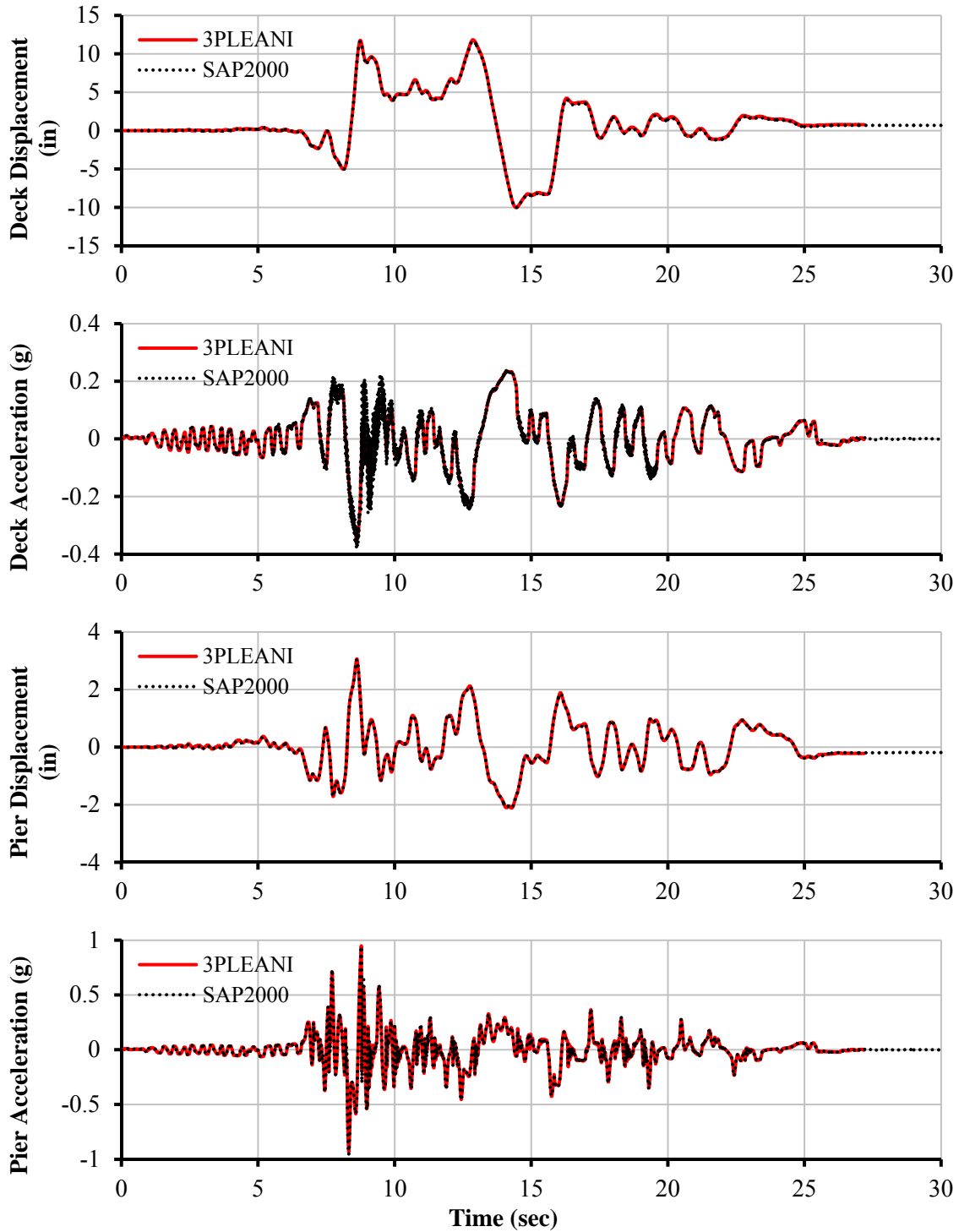


Figure 2-6: Comparison of additional response history analysis results calculated in programs 3pleANI and SAP2000 for bridge with triple isolators/piers and dampers

2.3 Bridge with advanced modeling

In Sections 2.1 and 2.2, the bridge piers in 3pleANI were modeled as springs with only horizontal degrees of freedom. This did not account for the effect of the moment applied by the isolator on the top of pier and the effect of the pier rotation in the isolator behavior. This example will demonstrate how to account for these effects in 3pleANI by use of *Advanced Modeling*.

Advanced Modeling is a unique feature of 3pleANI that does not exist in commercially available software. As a result, verification by comparison with results from SAP2000 is not possible. For this example, the results obtained in 3pleANI will be compared to the results of the analysis in Section 2.1 where these effects were not included. Two different cases will be considered:

- Isolator P- Δ moment effects are included but the rotation of the pier is ignored. This case is denoted as 3pleANI-M. The superstructure panel and the advanced modeling dialogue box for this case is shown in Figure 2-7(a)
- Isolator P- Δ moment effects and rotation of the pier effects are included. This case is denoted as 3pleANI-M&R. The superstructure panel and the advanced modeling dialogue box for this case is shown in Figure 2-7(b)

In Figure 2-7(a) the value 136.72kip that was specified includes the pier weight and the additional mass at the top of the pier shown in Figure 2-1. The program will assign half of that weight at the top of the pier (for this analysis option, the pier rotation is condensed from the equations of motion and the pier mass matrix is 1x1). However, in Figure 2-7(b), the rotation of the pier is included as a degree of freedom. The mass matrix of the pier for translation and rotation is derived using the consistent mass matrix formulation. Therefore the specified weight of the pier must be derived entirely from the pier self-weight (from Figure 2-1 this is $0.157 \times 276 = 43.3kip$). The program allows the user to specify additional concentrated weights at the top of the pier in the *Advanced Modeling* dialogue box. The concentrated weight of 46.8kip shown in Figure 2-1 is specified there.

Superstructure Properties

SDOF
 Shear building
 Explicit
 Bridge

	Stiffness	Weight	Damp.
Deck	N/A	2546	
Pier .	400000	10	
Pier2.	93.7	136.72	
Pier3.	93.7	136.72	
Pier4.	400000	10	

Advanced Modeling

Damping %

Include dampers

Superstructure Properties

SDOF
 Shear building
 Explicit
 Bridge

	Stiffness	Weight	Damp.
Deck	N/A	2546	
Pier .	400000	10	
Pier2.	93.7	43.33	
Pier3.	93.7	43.33	
Pier4.	400000	10	

Advanced Modeling

Damping %

Include dampers

<Student Version> : Advanced Bridge properties

Specify the pier height for calculation of rotational stiffness. Also specify additional lumped weight(if any) at top of pier

P-Delta Effects on Pier rotation, TFP model does not account for Bottom plate rotation
 P-Delta Effects on Pier rotation, TFP model accounts for Bottom plate rotation

	Height		Height
Pier1	<input type="text" value="10"/>		Pier4 <input type="text" value="10"/>
Pier2	<input type="text" value="276"/>		
Pier3	<input type="text" value="276"/>		

OK Cancel

<Student Version> : Advanced Bridge properties

Specify the pier height for calculation of rotational stiffness. Also specify additional lumped weight(if any) at top of pier

P-Delta Effects on Pier rotation, TFP model does not account for Bottom plate rotation
 P-Delta Effects on Pier rotation, TFP model accounts for Bottom plate rotation

	Height	Additional weight(top)		Height	Additional weight(top)
Pier1	<input type="text" value="10"/>	<input type="text" value="0"/>		Pier4	<input type="text" value="10"/>
Pier2	<input type="text" value="276"/>	<input type="text" value="46.8"/>			
Pier3	<input type="text" value="276"/>	<input type="text" value="46.8"/>			

OK Cancel

(a) Case 3pleANI-M

(b) Case 3pleANI-M&R

Figure 2-7: View of advanced modeling dialogue box

(b) Zoomed view of abutment isolator

(c) Zoomed view of pier isolator

Figure 2-10 shows a snapshot of the deformed bridge and isolators. The bottom concave plate of the pier isolator is shown rotated however this rotation is small.

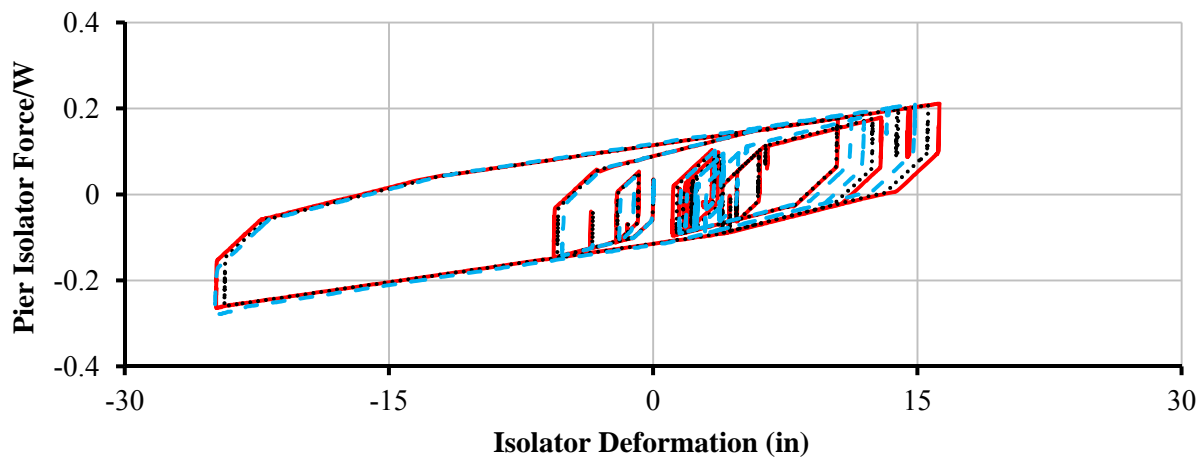
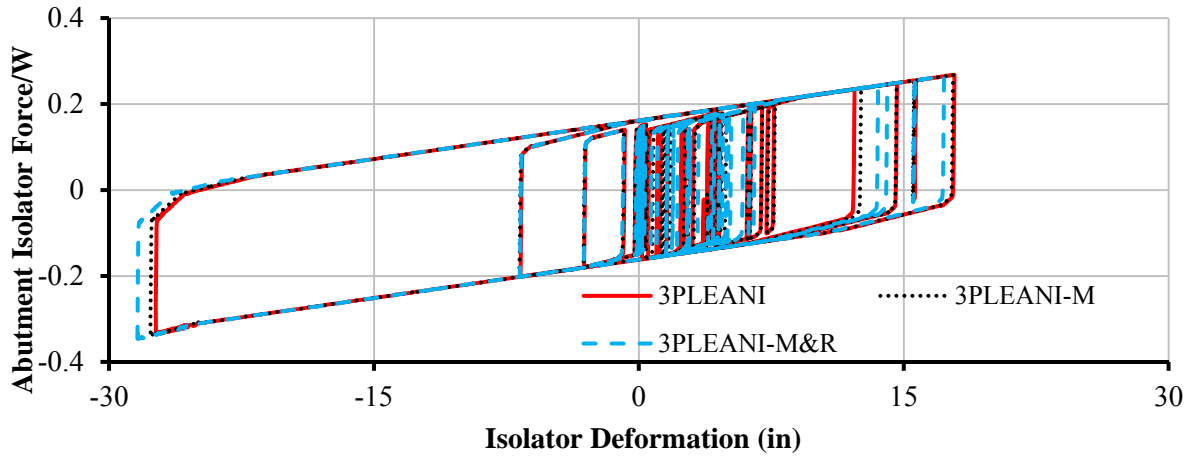


Figure 2-8: Comparison of force deformation loops calculated in program 3pleANI for bridge analyzed with three different methods

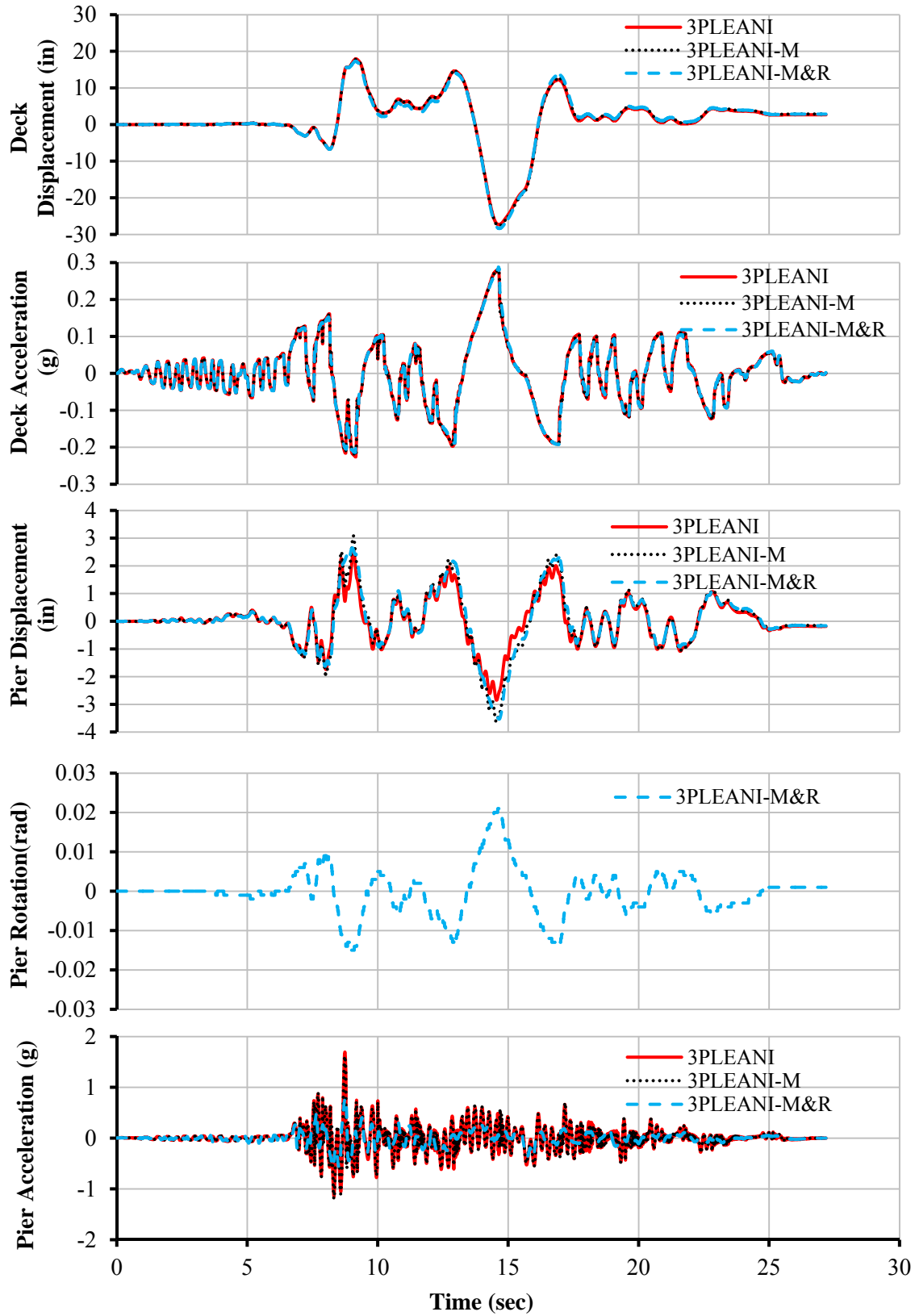
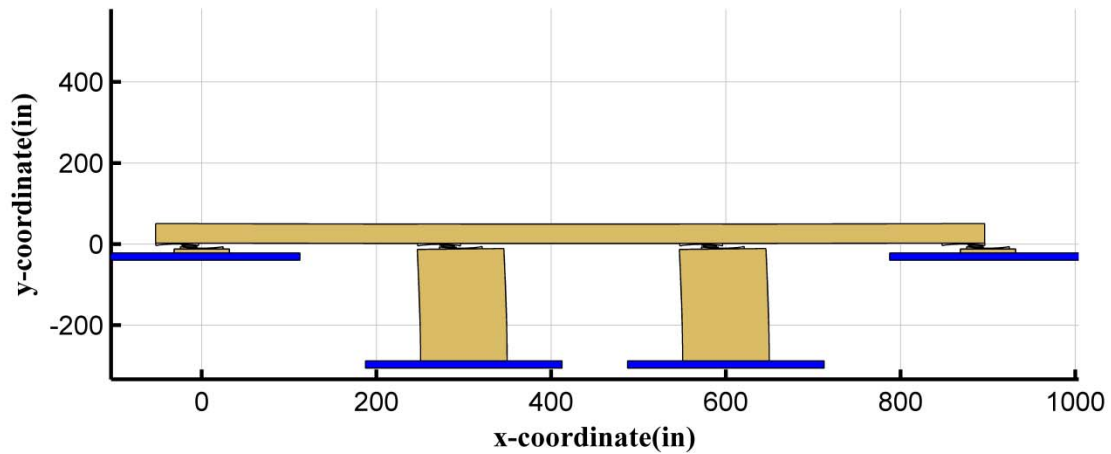
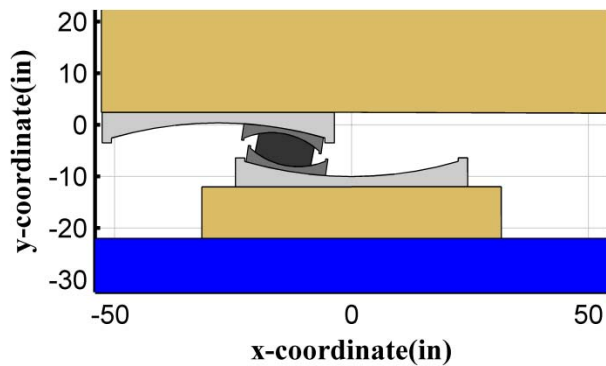


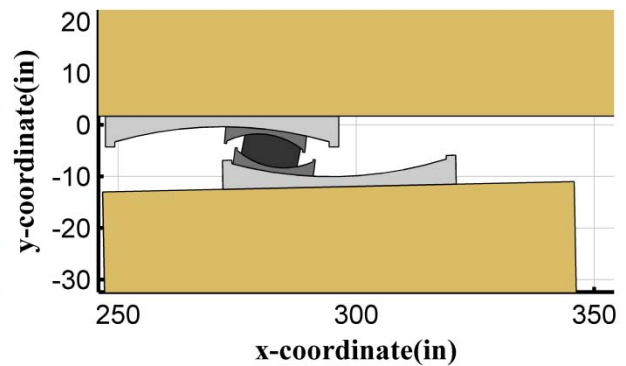
Figure 2-9: Comparison of additional response history quantities calculated in program 3pleANI for bridge analyzed with three different methods



(a) View of deformed bride



(b) Zoomed view of abutment isolator

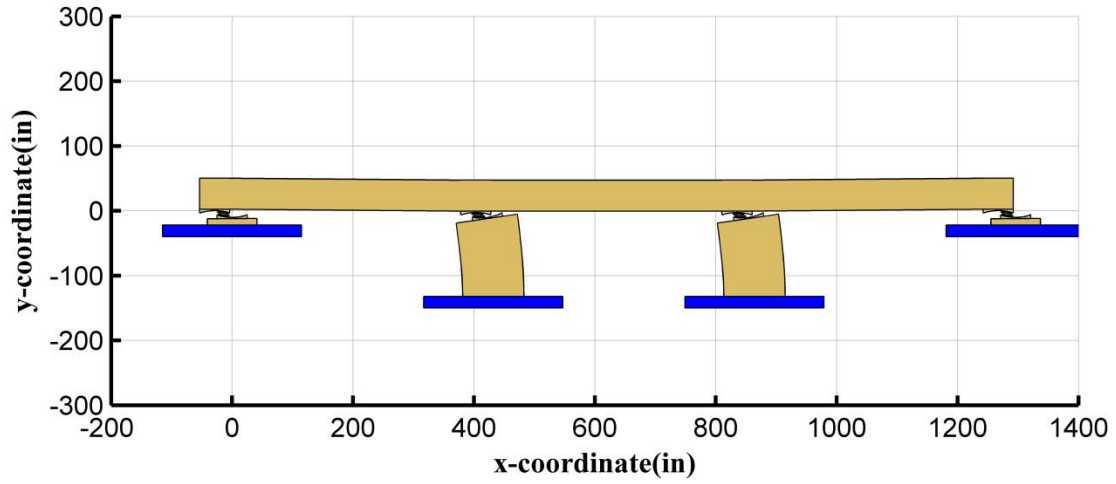


(c) Zoomed view of pier isolator

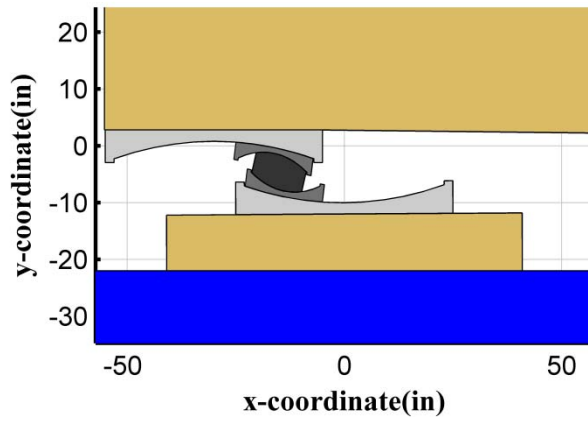
Figure 2-10: Deformed bridge and isolators from case M&R

2.4 Extreme case of pier rotation

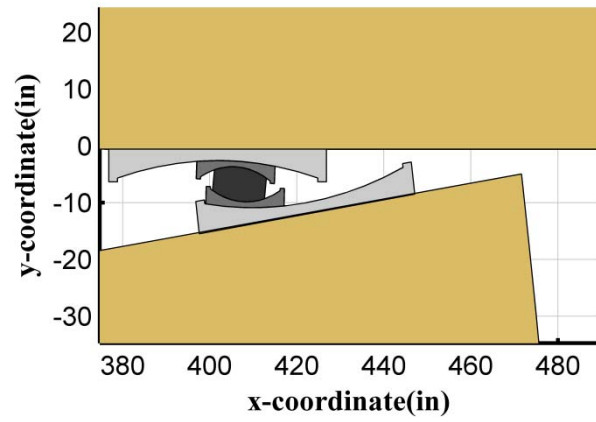
In order to further demonstrate the analysis capabilities of 3pleANI, consider that the piers of the bridge in Figure 2-1 are much more flexible so that their lateral stiffness is $k_p = 3EI/h^3 = 40kip/in$ and their height is $h=120in$. It is noted that in 3pleANI all terms of the pier stiffness matrix are calculated based on these two quantities—for example, the term $4EI/h$ is given by $4k_p h^2/3$. The results from 3pleANI are shown in Figure 2-12, whereas Figure 2-11 shows a snapshot of the deformed bridge, abutment and pier isolators. Evidently, there is significant rotation. The implications of the large pier top rotation are seen in the results of Figure 2-12 where pier rotation has significant effect on the response.



(a) View of deformed bridge



(b) Zoomed view of abutment isolator



(c) Zoomed view of pier isolator

Figure 2-11: Deformed bridge and isolators for flexible pier case

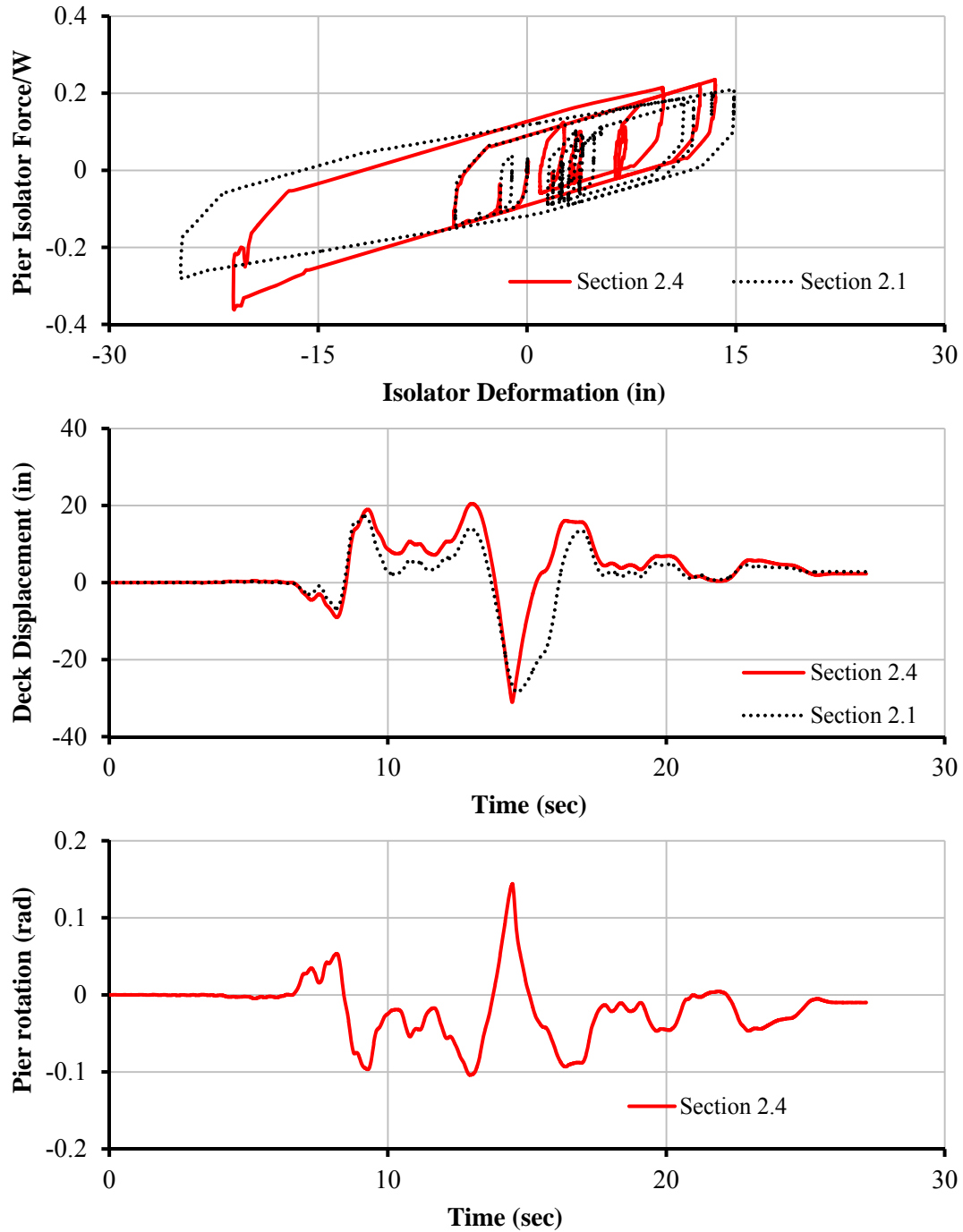


Figure 2-12: Comparison of response history quantities calculated in program 3pleANI for bridge with properties of Section 2.1 (without rotation and moment effects) and Section 2.4 (with rotation and moment effects)

REFERENCES

1. Computers and Structures Inc. (2007), "SAP2000: INTEGRATED FINITE ELEMENT ANALYSIS AND DESIGN OF STRUCTURES", Version 11.0.8, Berkeley, CA.
2. Constantinou, M.C., Kalpakidis, I., Filiatrault, A. and Ecker Lay, R. A. (2011), "LRFD-Based Analysis and Design Procedures for Bridge Bearings and Seismic Isolators", Report No. MCEER-11-0004, Multidisciplinary Center for Earthquake Engineering Research, Buffalo, NY.
3. Constantinou, M.C., Whittaker, A.S., Kalpakidis, Y., Fenz, D.M. and Warn, G.P. (2007), "PERFORMANCE OF SEISMIC ISOLATION HARDWARE UNDER SERVICE AND SEISMIC LOADING", Report No. MCEER-07-0012, Multidisciplinary Center for Earthquake Engineering Research, Buffalo, NY.
4. Fenz, D.M. and Constantinou, M.C. (2008a),"MECHANICAL BEHAVIOR OF MULTI-SPHERICAL SLIDING BEARINGS", Report No. MCEER-08-0007, Multidisciplinary Center for Earthquake Engineering Research, Buffalo, NY.
5. Fenz, D.M. and Constantinou, M.C. (2008b), "SPHERICAL SLIDING ISOLATION BEARINGS WITH ADAPTIVE BEHAVIOR: THEORY," Earthquake Engineering and Structural Dynamics, Vol. 37, No. 2, 163-183.
6. Fenz, D.M. and Constantinou, M.C. (2008c), "SPHERICAL SLIDING ISOLATION BEARINGS WITH ADAPTIVE BEHAVIOR: EXPERIMENTAL VERIFICATION", Earthquake Engineering and Structural Dynamics, Vol. 37, No. 2, 185-205.
7. Fenz, D.M. and Constantinou, M.C., (2008d), "MODELING TRIPLE FRICTION PENDULUM BEARINGS FOR RESPONSE-HISTORY ANALYSIS", Earthquake Spectra, Vol. 24, No. 4, 1011-1028.
8. Fenz, D.M. and Constantinou, M.C. (2008e),"DEVELOPMENT, IMPLEMENTATION AND VERIFICATION OF DYNAMIC ANALYSIS MODELS FOR MULTI-SPHERICAL SLIDING BEARINGS", Report No. MCEER-08-0018, Multidisciplinary Center for Earthquake Engineering Research, Buffalo, NY.
9. Morgan, T. A. (2007), "THE USE OF INNOVATIVE BASE ISOLATION SYSTEMS TO ACHIEVE COMPLEX SEISMIC PERFORMANCE OBJECTIVES", Ph.D. Dissertation, Department of Civil and Environmental Engineering, University of California, Berkeley.
10. Sarlis, A.A., Constantinou, M.C. (2010)," MODELING OF TRIPLE FRICTION PENDULUM ISOLATORS IN PROGRAM SAP2000", supplement to MCEER Report 05-009, document distributed to the engineering community together with executable version of program and example files, University at Buffalo.

11. Sarlis, A.A., Constantinou, M.C. (2013),” MODEL OF TRIPLE FRICTION PENDULUM BEARING FOR GENERAL GEOMETRIC AND FRICTIONAL PARAMETERS AND FOR UPLIFT CONDITIONS”, Report No. MCEER-13-xxxx, Multidisciplinary Center for Earthquake Engineering Research, Buffalo, NY.



EARTHQUAKE ENGINEERING TO EXTREME EVENTS

University at Buffalo, The State University of New York

133A Ketter Hall ■ Buffalo, New York 14260-4300

Phone: (716) 645-3391 ■ Fax: (716) 645-3399

Email: mceer@buffalo.edu ■ Web: <http://mceer.buffalo.edu>



University at Buffalo *The State University of New York*

ISSN 1520-295X